7th annual meeting
January 16th 2015
Het Pand, Ghent

ISMRM Benelux Chapter

Abstract book

MR SOLUTIONS Creative Solutions for MRI systems
SIEMENS
PHILIPS
MR Coils

The organizing committee of the ISMRM Benelux Chapter would like to thank all sponsors which contributed in making this meeting possible.

Gold sponsors

SIEMENS

PHILIPS

MR Coils

MR SOLUTIONS
Creative Solutions for MRI systems

Silver+ sponsors

EXprodo Software

Silver sponsors

BRUKER

TOSHIBA
Leading Innovation

Table of Contents


PHILIPS
Changing expectations and lives
The first-ever digital broadband MR is changing expectations, and lives. Even in routine imaging.
Thanks to Philips Imaging 2.0, a revolutionary new imaging approach, the Philips Ingenia 1.5T and 3.0T MR systems set a new standard in clarity, speed and expandability. Ingenia captures and digitizes the signal closest to the patient to improve SNR by up to 40%. Easier coil handling and improved patient comfort help increase productivity by up to 30%. And, Ingenia is designed to meet your demands in fast routine imaging. Discover the revolution in MR technology at www.philips.com/Ingenia30T.
innovation you
PHILIPS

SIEMENS

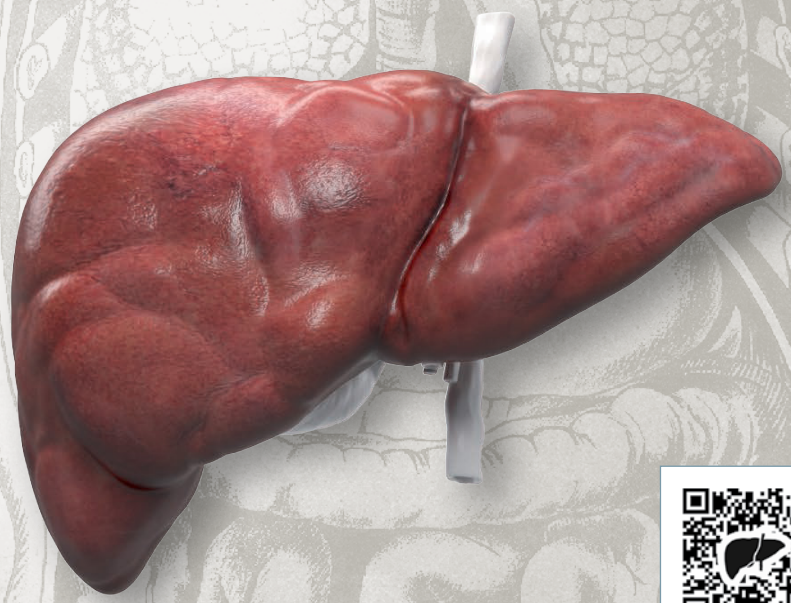

Leading.
With
MAGNETOM.

A91MR-9305-A1-7600

www.siemens.com/growth-with-BodyMRI

Growth with Body MRI

New Certainty in Liver MRI.

Body MR imaging can be challenging – motion, patient breath-hold capacity, acquisition speed, and contrast timing all have an impact on imaging results. Siemens' trendsetting application portfolio is already tackling many of these challenges – but this year we are taking the decisive step.

With **FREEZEit – our embrace motion technology** featuring TWIST-VIBE and StarVIBE – we enable you to overcome challenging motion in liver imaging, making MAGNETOM Aera and MAGNETOM Skyra even faster and the most robust MRI scanner for body imaging.

TWIST-VIBE combines for the first time **high temporal and excellent spatial resolution with full 4D coverage** for precision in dynamic liver MRI. StarVIBE delivers robust, **free-breathing and contrast-enhanced MRI** exams for patients unable to hold their breath. Both Siemens-unique sequences are part of FREEZEit and open up huge potential to expand MRI services within the body region.

Visit www.siemens.com/growth-with-BodyMRI or scan the QR code to learn more about this growth potential.
*May not be commercially available in countries outside the U.S.; future availability cannot be guaranteed.

Answers for life.

Always wanted to have more, faster, new, and better MR signals in your research?

MR Coils

can help you

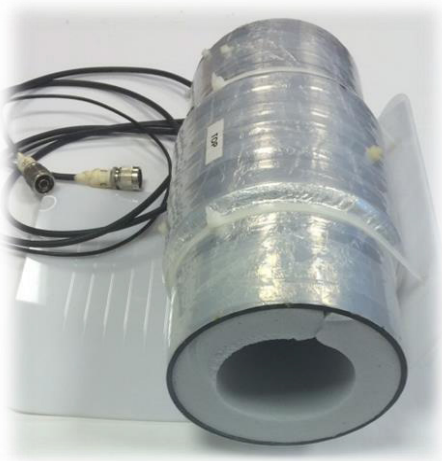
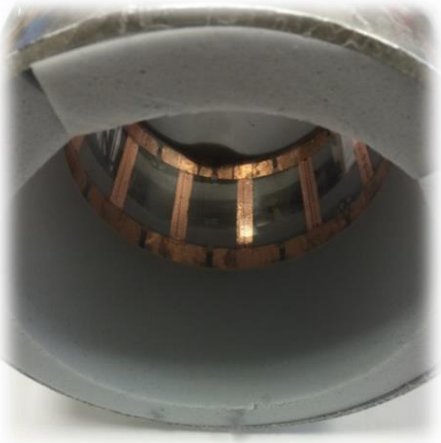
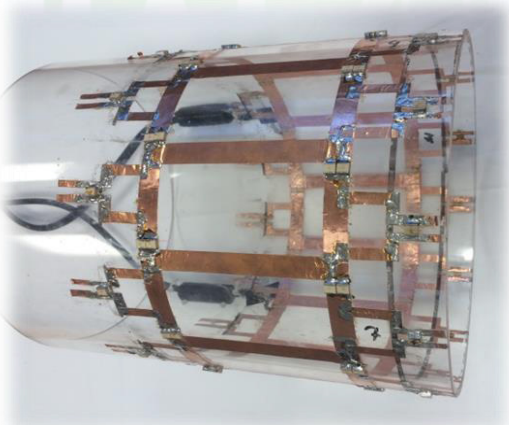
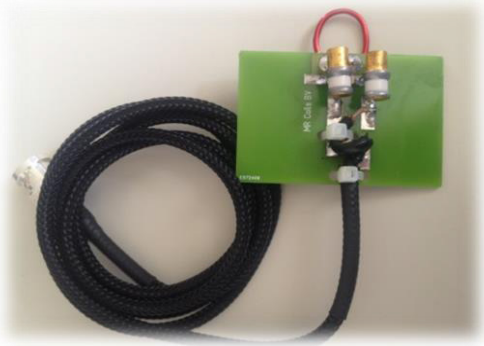



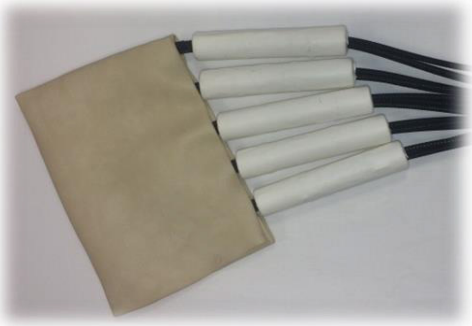

For more information please contact

- Michel Italiaander
  mitaliaander@mrcoils.com
- Dennis Klomp
  dklomp@mrcoils.com
- Or visit
  MRCoils.com

We can offer you:

- Close collaboration with the researcher
- Fast delivery time

and above all

The best MR Coils

MR SOLUTIONS

Imaging INNOVATION

- **Variable field MRI** - 0.1T to 7.0T
- **Cryogen Free**
- Integrated **PET/MRI** & **SPECT/MRI** for simultaneous or sequential imaging

Innovative technology for preclinical imaging

Calpendo

Looking for an intelligent, automated booking system for your facility?

See how Calpendo can benefit your university, hospital or research facility by contacting us and receiving your Free Demonstration.

- Best-in-class online scheduling calendar with configurable rules to control who can book what, where and when.
- A fully-featured reporting system for generating billing and auditing information.
- An integrated, intelligent system that allows for multifaceted activity bookings.
- Automated and targeted emails for activity notifications, confirmations and cancellations.
- Bespoke user accessibility, from undergraduate student to administrator or research director.
- Utilised in a multitude of MRI, MEG and PET facilities across Europe, North America and Asia.

Tel: +44 (0)1235 813458
Email: info@exprodo.com
Web: www.exprodo.com

EXprodo Software

BRUKER

Next Generation Preclinical MRI

ParaVision™

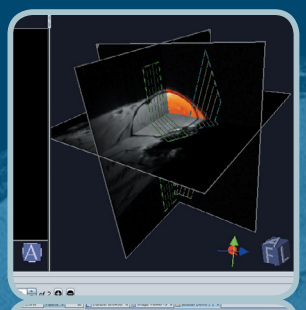

3D Scan Planning

Optimized Workflow

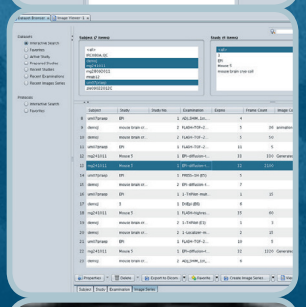

Convenient Data Management

Complete Suite of Applications and Imaging Methods

Ultimate MR-Acquisition and Processing in Preclinical and Material Research

- Comprehensive functionalities for processing, displaying and analyzing images and spectra
- Intuitive acquisition and automatic scan protocols
- Optimized application protocols for rats and mice
- High performance MR imaging methods
- 3D geometry editor
- Automatic examination report
- Intuitive data browser with image preview
- Method development environment

Discover the next generation of Preclinical MRI: www.bruker.com/paravision

Innovation with Integrity

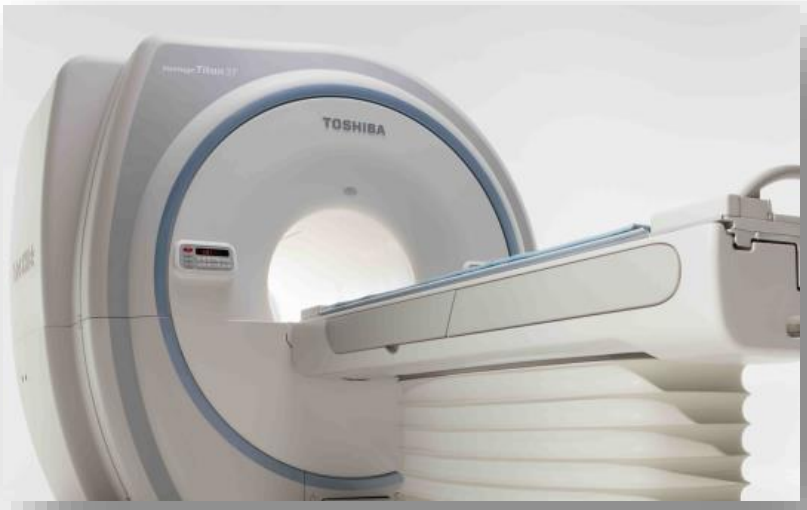

TOSHIBA

Leading Innovation

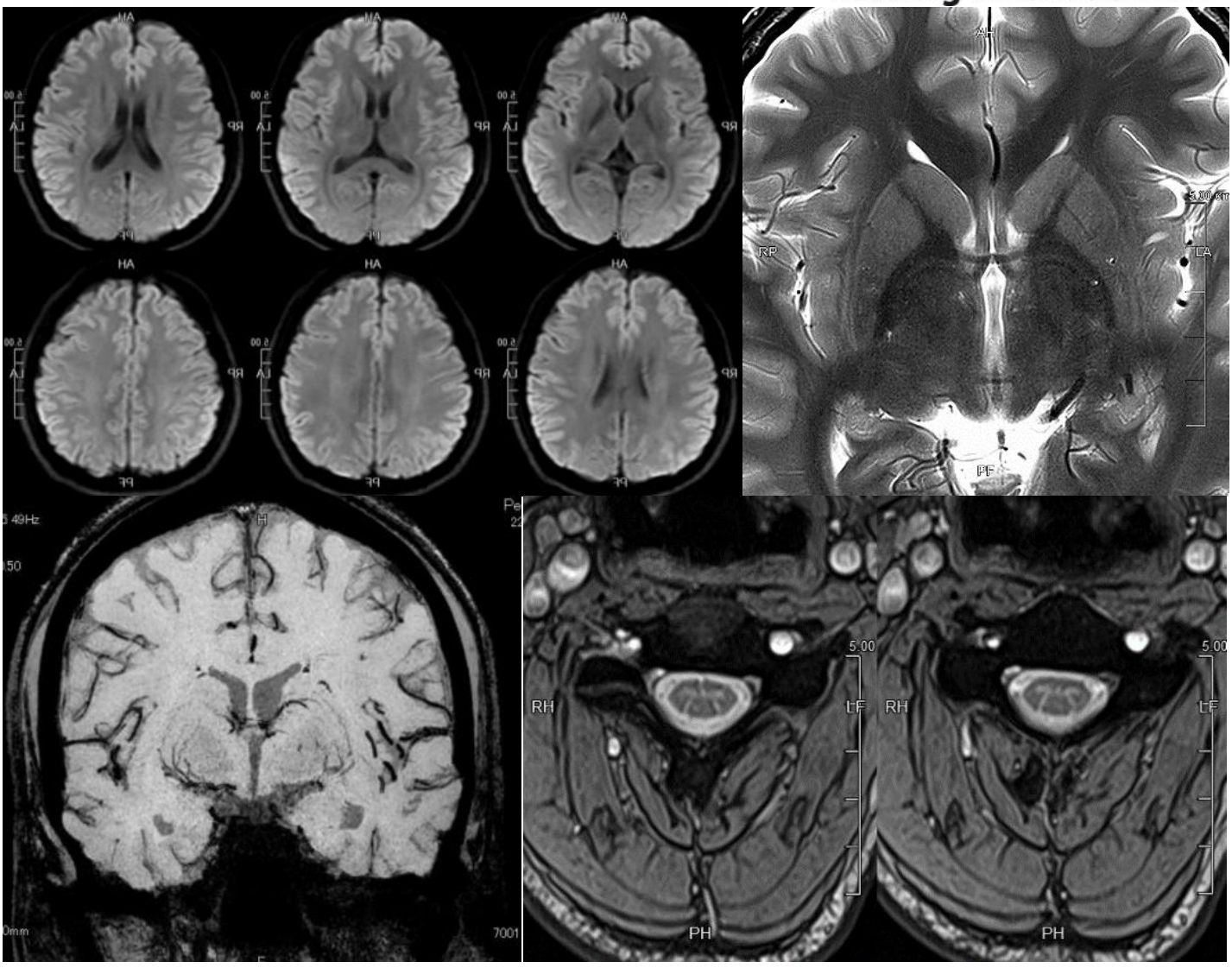

Vantage Titan 3T - MR Neuro Imaging

Diffusion Weighted Imaging, High Resolution T2-weighted,

Flow Sensitized Black Blood, Multi-Echo Imaging of the Cervical Spine

Dear Participant,

We would like to welcome you to the seventh annual meeting of the ISMRM Benelux Chapter, which is being held at Het Pand in Ghent. Het Pand is the culture and congress centre of Ghent University. It is housed in a former Dominican Monastry and is located in the historic centre of Ghent. We hope that you will enjoy this inspiring and historical environment.

The main aim of this meeting is to work and think together. As a result, new projects and collaborations will develop within the Benelux MR-community leading to bigger advancements in the field of magnetic resonance. During the meeting we provide you with different ways to share knowledge and ideas within the community. Firstly, there are three parallel sessions during which young researchers get the opportunity to present their great scientific work. In order to meet the interests of everyone, most sessions are divided into more technical (spectroscopy, MR methods, high field and RF engineering) and (pre-)clinically oriented (cancer, neuro, perfusion, muscle, diffusion) topics. Furthermore, there are two poster sessions, allowing all researchers to share and discuss their work. Lastly, we are proud to introduce a plenary power poster session this year in which the work of the ten abstracts of young investigators that were reviewed best, is presented and discussed.

Beside an extensive scientific program, you also have the opportunity to socialize and network during the breaks and lunch, with the option to keep the discussion going on over drinks and dinner. This year, we chose to have a standing buffet since we believe it improves networking. We hope you make use of these options. We also encourage you to visit the sponsor stands during the breaks and lunch, as we have advised our sponsors to, besides promoting their products, focus on young researchers by e.g. promoting job opportunities and discussing possible collaborations. We hope that the meeting leads to many new interesting collaborations and great scientific innovations.

Finally, we would like to take this opportunity to thank the following people that made this meeting possible: our sponsors, for their generous contributions; the ISMRM Benelux Chapter board, for their support; the reviewers, for rating the abstracts; the chairmen, for moderating the scientific sessions, the authors of the 119 abstracts we received this year and last but not least, I would like to thank my fellow organizers for their hard work: I loved working with all of you, you were great!

On behalf of the organizing committee 2015,

Oliver Gurney-Champion

Chair ISMRM Benelux Organizing Committee 2015

ISMRM Benelux 2015

Members of the Board

Aart Nederveen, Academic Medical Center Amsterdam, NE - *President*

Kim van de Ven, Philips Healthcare, NE - *Secretary & Company Representative*

Christine Nabuurs, Philips Healthcare, NE - *Treasurer*

Maarten Naeyaert, University of Antwerp, BE - *Website Coordinator*

Lisbeth Van Ruijssevelt, University of Antwerp, BE - *Annual Committee Representative*

Members of the Organizing Committee

Oliver Gurney-Champion, Academic Medical Center Amsterdam, NL - *Chair & Sponsoring*

Lisbeth Van Ruijssevelt, University of Antwerp, Antwerp, BE - *Board Representative*

Jules Nelissen, Eindhoven University of Technology, NL - *Communication*

Chantal Tax, University Medical Center Utrecht, NL - *Communication*

Marloes Marteijn, Eindhoven University of Technology, NL - *Treasurer*

Valerie De Meulenaere, Ghent University, BE - *Location & Proceedings*

Jasmien Orije, University of Antwerp, BE - *Sponsoring & Website*

Julie Hamaide, University of Antwerp, BE - *Location & Proceedings*

!!! GET INVOLVED !!!

Join the organizing committee for next year's meeting!

If interested, please contact this year's organizing committee (meeting2015@ismrm-benelux.org) or the members of the board.

Don't forget to join the 'ISMRM Benelux Chapter' discussion group on LinkedIn, Twitter and Facebook!

Program Overview

9.30h Welcome with Coffee & Tea

10.00h Plenary Program: Welcome and Introduction - *Refter*

10.20h Parallel Session 1
- **Cancer** - *Refter*
- **Spectroscopy** - *Rector Vermeylen*

11.15h Break & Visit sponsors

11.45h **Power Posters** - *Refter*

12.35h Lunch (runs till 14.30h)

12.35h **Posters** & **Power Posters** Session 1 (even numbers)
13.20h **Posters** & **Power Posters** Session 2 (odd numbers)
Regular posters (even & odd) - *Noordergang & Refter*
Power Posters (even & odd) - *Sacristie*

14.00h Annual Members Meeting

14.30h Parallel Session 2

14.30h **Neuro** - *Rector Vermeylen*
Muscle - *Refter*
15.15h **MR methods** - *Refter*
Perfusion - *Rector Vermeylen*

15.55h Break & Visit sponsors

16.30h Parallel Session 3

RF Engineering & **High Field** - *Refter*
Diffusion - *Rector Vermeylen*

17.50h Closing Ceremony - *Refter*

18.00h Reception

18.40h Gather at reception of Het Pand to walk together to the Marriott Hotel

19.00h Dinner @ Marriott hotel (reservation required)

Power Posters

PP001 **Sharon Janssens** - Fructose increases de novo lipogenesis in the liver of rats: an in vivo ^{1}H-[13C] MRS study

Department of Radiology, University Medical Center Utrecht, Utrecht, The Netherlands

PP002 **Bart Philips** - Spectral-Spatial-Spiral MRSI: Fast prostate MR spectroscopic imaging with low SAR on 7T

Department of Radiology and Nuclear Medicine, Radboud University Medical Center, Nijmegen, the Netherlands

PP003 **Edmond Balidemaj** - In vivo reconstructed conductivity values of cervical cancer patients based on EPT at 3T MRI

Department of Radiotherapy, Academic Medical Center, Amsterdam, the Netherlands

PP004 **Kristof Govaerts** - Increased cortical volume revealed by atlas-based volumetry in a bigenic mouse model of Alzheimer's Disease

Imaging & Pathology, KU Leuven, Belgium

PP005 **Sau May Wong** - Intravoxel Incoherent Motion Imaging exposes abnormal parenchyma and microvasculature in cerebral small vessel disease

Department of Radiology, Maastricht University Medical Center, Maastricht, the Netherlands

PP006 **Abdallah Motaal** - Carotid Pulse Wave Velocity Measurements Using Accelerated High Temporal Resolution MRI

Department of Radiology, Academic Medical Center, Amsterdam, the Netherlands

PP007 **Joep van Oorschot** - Endogenous assessment of diffuse myocardial fibrosis with T1ρ-mapping in patients with dilated cardiomyopathy

Department of Radiology, University Medical Center, Utrecht, the Netherlands

PP008 **Tom Peeters** - Glutamate dehydrogenase inhibition reduces glutamine conversion into 2HG in *IDH1*-mutated cancer cells as detected by ^{13}C MRS

Department of Radiology and Nuclear Medicine, Radboud University Nijmegen Medical Center Nijmegen, the Netherlands

PP009 **Nikki Dieleman** - Intracranial atherosclerotic lesion characteristics correlate with cerebrovascular lesion load after TIA or ischemic stroke: a 7.0 tesla MRI study

Department of Radiology, University Medical Center, Utrecht, the Netherlands

PP010 **Anita A. Harteveld** - Detection of intracranial vessel wall lesions in an elderly asymptomatic population using 7T MRI

Department of Radiology, University Medical Center, Utrecht, the Netherlands

Fructose increases de novo lipogenesis in the liver of rats: an *in vivo* ^{1}H-[^{13}C] MRS study

Sharon Janssens[1], Klaas Nicolay[1], Jeanine J. Prompers[1]

[1]Department of Biomedical NMR, Eindhoven University of Technology, Eindhoven, the Netherlands

Target audience: This work is relevant to the field of liver lipid metabolism in general and in particular dietary factors affecting liver lipid metabolism.

Purpose: Non-alcoholic fatty liver disease (NAFLD) is the most common liver disorder in Western countries and is characterized by excessive accumulation of fat in the liver (hepatic steatosis). An important contributing factor to the rapid rise in the prevalence of NAFLD is the increased consumption of carbohydrates such as glucose and fructose present in caloric sweetened beverages. This can be explained by a process termed *de novo* lipogenesis, in which excess carbohydrates are being converted to fat in the liver[1-4]. Of great value in the fight against obesity are non-caloric sweeteners such as aspartame, but their effects on liver lipid metabolism, and especially *de novo* lipogenesis, remain unknown[5]. In this study we implemented a non-invasive method for the direct *in vivo* measurement of *de novo* lipogenesis in the liver using localized ^{1}H MRS with ^{13}C editing to detect ^{13}C-labeled intrahepatocellular lipids (IHCL) after oral administration of [U-$^{13}C_6$] glucose (Figure 1). Using this method we then studied the effects of caloric and non-caloric sweeteners on *de novo* lipogenesis as well as total IHCL content in rats.

Methods: Twenty-four male Wistar rats (10-11 weeks of age; 350 ± 3 g) were divided into 4 diet groups receiving normal chow and (1) water (CON), (2) a 13% glucose solution (GLU), (3) a 13% fructose solution (FRUC), or (4) a 0.4% aspartame solution (ASP), for 7 weeks. After this diet period, baseline ^{1}H-[^{13}C] MRS measurements were performed, after which the diets were continued and the rats were administered 3.33 g/kg bodyweight [U-$^{13}C_6$] glucose, 2 times a day for 5 days by oral gavage. For all diet groups this amounted to 5.16±0.13 % of their total carbohydrate consumption. The next day, ^{1}H-[^{13}C] MRS measurements were repeated. All experiments were executed on a 7 T horizontal Bruker MR system with a ^{1}H surface coil (20 mm) combined with a ^{13}C butterfly coil (40/100 mm). A voxel of 5x2x4 mm^3 was localized in the median lobe of the liver and ^{1}H-[^{13}C] MRS was performed using the LASER sequence combined with a POCE element for ^{13}C editing[6]. The ^{13}C-editing pulse (AFP, pulse length=2 ms, bandwidth=5 kHz) was centered on the lipid methylene resonance and the POCE echo time was tuned to $1/^{1}J_{1H\text{-}13C}$ for lipid methylene protons (7.9 ms). Other LASER-POCE parameters were as follows: TR/TE=2000/26.8 ms, SWAMP water suppression, ^{13}C WALTZ decoupling, 16 averages, 64 sequential experiments, and scan time = 34 min. Spectra obtained with and without the POCE ^{13}C-editing pulse were subtracted to give a difference ^{1}H spectrum (Figure 2). Spectra were analyzed using AMARES in jMRUI. The CH_2 signal from IHCL at 1.3 ppm (Figure 2) was used to calculate total and ^{13}C-enriched IHCL contents from the spectra without ^{13}C editing and the difference spectra, respectively, and are expressed as a percentage of the unsuppressed water signal. The relative ^{13}C enrichment determined at baseline was used to correct the ^{13}C-labeled IHCL level after 5 days of [U-$^{13}C_6$] glucose administration for ^{13}C natural abundance. All data are expressed as means ± SEM. Statistical analysis was performed using ANOVA (SPSS).

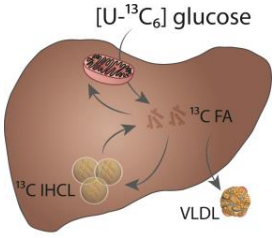

Figure 1. Overview of liver metabolism. Orally administered [U-$^{13}C_6$] glucose is oxidized or converted to ^{13}C fatty acids, that can be oxidized in mitochondria, secreted as very-low density lipoproteins (VLDL), or stored as ^{13}C IHCL.

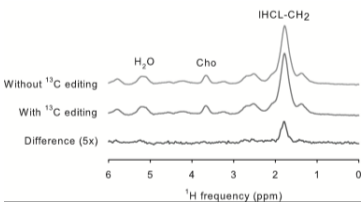

Figure 2. Example of LASER-POCE spectra of rat liver without ^{13}C editing (top), with ^{13}C editing (middle), and the calculated difference (bottom). H_2O, water; Cho, choline; IHCL, intrahepatocellular lipids.

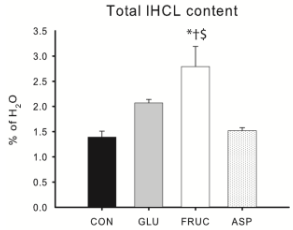

Figure 3. Total IHCL content expressed as percentage of unsuppressed water signal. * p < 0.05 vs CON, † p < 0.05 vs ASP, $ p < 0.05 vs GLU.

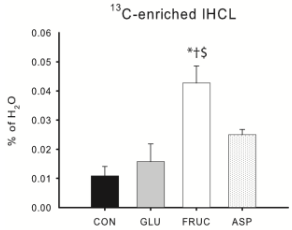

Figure 4. ^{13}C-enriched IHCL content expressed as percentage of unsuppressed water signal. * p < 0.05 vs CON, † p < 0.05 vs ASP, $ p < 0.05 vs GLU.

Table 1. Animal characteristics

	CON	GLU	FRUC	ASP
Weight gain (g)	88 ± 7	84 ± 9	104 ± 7	82 ± 3
Food intake (kJ/wk)	2322 ± 6	1184 ± 41 *†	1569 ± 34 *†$	2351 ± 4
Fluid intake (ml/wk)	181.6 ± 0.1	802.3 ± 28.3 *†	507.2 ± 24.2 *†$	219.7 ± 7.2
Energy intake (kJ/wk)	2322 ± 6	2930 ± 21 *†	2672 ± 19 *†$	2366 ± 4
Liver weight (g)	12.9 ± 0.2	13.1 ± 0.6	16.3 ± 0.6 *†$	13.2 ± 0.2
Liver glycogen content (µg/mg ww)	96.4 ± 2.8	117.7 ± 8	116.8 ± 8.2	115.2 ± 8.0

* p < 0.05 vs CON; † p < 0.05 vs ASP; $ p < 0.05 vs GLU

Results: After 7 weeks of diet, there were no differences in body weight gain among diet groups (Table 1). Although animals in the GLU and FRUC groups consumed less food compared to CON and ASP, their total energy consumption was higher due to the intake of calories from sugar in their drinking water. Liver weight of animals receiving FRUC was higher compared with the other groups. Liver glycogen content did not differ among groups. Total IHCL content was higher in the FRUC animals compared with the other groups (Figure 3). At baseline, the average relative ^{13}C enrichment of IHCL for all groups was 1.28±0.08 %, which was used to correct the level of ^{13}C-enriched IHCL after 5 days of [U-$^{13}C_6$] glucose administration for natural abundance of ^{13}C. ^{13}C-enriched IHCL content was significantly higher in FRUC animals as compared to the other groups (Figure 4), indicating an increased contribution of *de novo* lipogenesis to IHCL storage.

Discussion and Conclusion: In contrast to glucose and aspartame, fructose had marked effects on liver lipid metabolism, i.e. 7 weeks of fructose consumption increased total liver lipid content which was accompanied by an increased conversion of ^{13}C-labeled glucose to lipids in the liver. Therefore, *de novo* lipogenesis seems to be an important contributor to fructose-induced liver steatosis, which is likely explained by the activating effect of fructose on sterol regulatory element binding protein 1c[1].

References: 1. Samuel VT, Trends Endocrinol Metab 22: 60-5, 2011; 2. Schaalan M, et al., J Diabetes Complications 23: 199-208, 2009; 3. Montonen J, et al., J Nutr 137: 1447-54, 2007; 4. Schutz Y, et al., Int J Obes Relat Metab Disord 28: S3-11, 2004; 5. Wiebe N and Padwal R, BMC Med 9: 123, 2011; 6. Jonkers RAM, et al., Magn Reson Med 68: 997-1006, 2012

Spectral-Spatial-Spiral MRSI: Fast prostate MR spectroscopic imaging with low SAR on 7T

Bart Philips[1], Miriam Lagemaat[1], Mark van Uden[1], Eline Vos[1], Borjan Gagoski[2], Adam Kerr[3], Marnix Maas[1], Tom Scheenen[1]

[1]Department of Radiology and Nuclear Medicine, Radboud University Nijmegen Medical Center Nijmegen, the Netherlands
[2]Fetal-Neonatal Neuroimaging & Developmental Science Center, Boston Children's Hospital, Harvard Medical School, Boston, MA, United States
[3]Magnetic Resonance Systems Research Lab, Electrical Engineering, Stanford University, Stanford, CA, United States

Target Audience: Spectroscopists, prostate cancer clinicians

Purpose: Proton Magnetic Resonance Spectroscopic Imaging (MRSI) of the prostate can be used to discriminate cancer from non-cancer tissue and to assess the aggressiveness of prostate cancer [1, 2]. 7T offers two major advantages for MRSI (increased signal to noise ratio (SNR) and chemical shift dispersion), but also poses several technical challenges. One of the solutions to these issues is to use an external coil array and RF shimming to create a high and homogenous transmit field locally in the prostate, and to receive signals locally with an endorectal coil [3,4]. In combination with the increased chemical shift dispersion on 7T the homogenous transmit field enables the use of conventional RF pulses that are simultaneously spectrally and spatially selective. Without use of SAR intensive methods, such as outer volume suppression or adiabatic pulses, repetition times can be made short, enabling efficient MRSI. We propose to combine this technique with a spiral MRSI acquisition to optimally use the SNR gain on 7T and increase spatial resolution while maintaining feasible acquisition times.

Methods: 8 patients with prostate cancer were scanned with a multi-parametric prostate MRI protocol [5]. Measurements were performed on a 7T whole-body MR system (MAGNETOM, Siemens Healthcare, Erlangen, Germany) with use of butylscopolamine and glucagon to reduce bowel movements. An 8-channel multi transmit proton body array coil was used for B0 and B1 shimming of the prostate [6]. After localized calibration of RF power the MR signal was received with an endorectal receive coil modified from a 3T endorectal balloon (MEDRAD, Pittsburgh, PA). After T2w MRI, we used a PRESS-like volume selection with one excitation pulse (bandwidth 1200 Hz) for axial slice selection followed by two VERSE-modulated spectral-spatial refocusing pulses [7] (duration of 35.22 ms, spectral passband from 2.4 to 3.4 ppm and subpulse bandwidth of 4.1 kHz) in anterio-posterior and right-left directions for volume and frequency selection (Fig. 1). No additional water or lipid suppression was used. Acquisition was performed using spiral MRSI with a constant density spiral [8]. The echo time and repetition time were 135 ms and 1 second, respectively. The spiral acquisition was performed with a FOV of 120x120x72 mm^3 (full prostate coverage in all cases), matrix of 20x20x12, 2 time interleaves, 5 spiral interleaves, three averages and acquisition time of 7:15 min. As a comparison 4 patients were also measured using the same sequence with a conventional elliptical phase encoding acquisition (FOV of 80x80x67 mm^3, matrix of 12x12x10, one average and acquisition time of 6:59 min). A 3-dimensional 50% hamming k-space filter was used in both acquisition methods, resulting in true voxel sizes of 0.48 cc for spiral and 1.1 cc for elliptical acquisitions (the true voxel size was determined by integrating the normalized point spread function).

Results: Spectral maps in axial direction for one of the patient measurements that was performed with both the spiral and the elliptical acquisition showed similar spectra at corresponding locations with sufficient SNR and almost no water residual (Fig. 2). In some parts of the prostate, lipid contamination was present. The red and blue circles represent the voxelsize for the respective measurements. Spectra from the same location (but different voxel size) with both acquisition methods were similar, although the lower right voxel indicated in Fig.2A and D contains less lipids in the spiral acquisition due to less partial volume effect (higher resolution). Spermine signals with this sequence are generally high, because the spectral-spatial RF pulses refocus the J-coupling between the 1.8 ppm and 3.2 ppm resonances.

In the apex of the prostate of another patient with a Gleason 3+4 tumor in the left dorsolateral peripheral zone, local spectral differences were present (Fig. 3) in the group of resonances around 3.1 ppm (choline, spermine and creatine). The red voxel (B), located in this area, shows a choline peak that is clearly separable from the high spermine peak. In the voxel indicated in blue (C), on the contralateral side of the prostate, choline only appears as a slight shoulder on the spermine signal, featuring a substantially lower choline over spermine ratio. Residual lipid signals were present in the apex.

Discussion and Conclusion: Using spectral-spatial RF pulses in combination with a spiral acquisition, prostate MRSI can be performed at 7 Tesla without running into SAR limits and with high flexibility in matching SNR, FOV, resolution and acquisition time. Although the method still suffers from some lipid contamination, it offers possibilities to explore the limits of SNR and spatial resolution in 7T MRSI of the prostate. In addition, it would be a suitable method to assess the role of spermine in prostate MRSI.

Acknowledgements: Dutch Cancer Society [2014-6624], ERC Grant agreement [243115], Elisabeth Weiland and Berthold Kiefer from Siemens Healthcare, Erlangen

References: [1] Scheenen T; Invest. Radiol. 2011; 46(1):25-33; [2] Kobus T; Radiology. 2012; [3] Metzger; MRM 64:625–1639, 2010; 265(2):457-67; [4] Lagemaat et al. ISMRM 2014; abstract 4113; [5] Maas et al. ISMRM 2014 abstract 0964; [6] Maas et al MRM 71:1711-1719 (2014) [7] Kerr AB, Pauly JM. In: Proceedings of the 16th Annual Meeting of ISMRM. Toronto, Canada; 2008; [8] Andronesi O; Radiol. 2012;262:647-661;

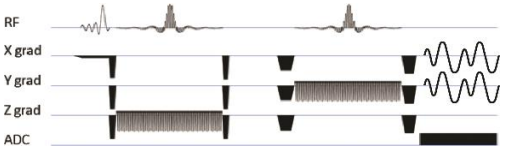

Figure 1: The spectral-spatial-spiral sequence.

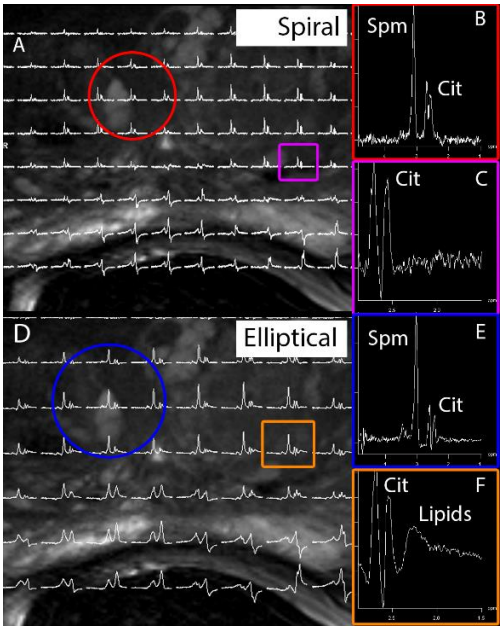

Figure 2: Spectal maps superimposed on a T2W image, of a patient measurement with a spiral (A) and an elliptical acquisition (D). B, C, E and F are spectra from correspondingly colored voxels from these measurements. B and E, and C and F are voxels from corresponding locations within the prostate.

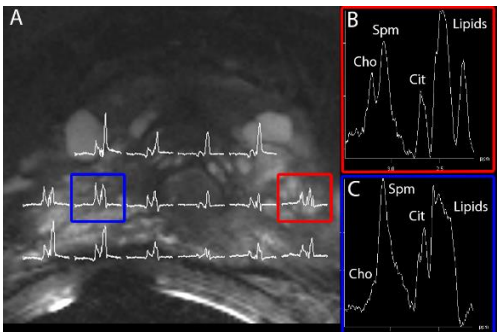

Figure 3: A is the spectral map of a patient obtained with spiral acquisition. Prostate cancer is present in the left dorsolateral peripheral zone. B is a voxel located in the tumor area. C is a voxel on the contralateral side. (This particular spiral acquisition was performed with a FOV of 160x160x70 and matrix size of 23x23x10; true voxel size: 0.77 cc, acquisition time: 6:44 min)

In vivo reconstructed conductivity values of cervical cancer patients based on EPT at 3T MRI

Edmond Balidemaj[1], Peter de Boer[1], Hans Crezee[1], Rob Remis[2], Lukas Stalpers[1], Aart Nederveen[3], Cornelis A.T. van den Berg[1]

[1]Department of Radiotherapy, Academic Medical Center, Amsterdam, the Netherlands
[2]Circuits and Systems Group, University of Technology, Delft, the Netherlands
[3]Department of Radiology, Academic Medical Center, Amsterdam, the Netherlands

Target audience: scientists working on SAR assessment and electric properties tomography

Introduction: Electric tissue properties (conductivity σ and permittivity ε_r) are essential for SAR assessment at high field MRI and other applications such as Hyperthermia Treatment Planning. An estimated whole-body SAR is normally provided during the scan, but local SAR cannot be monitored due to lack of patient-specific electric properties. To determine local SAR deposition, numerical simulations are therefore usually performed using generic body models [1]. The electric properties that are assigned to the various tissue types are generally based on the well-known Gabriel data [2]. Most of these properties have been measured ex-vivo using animal tissues. A few studies comparing in vivo and ex vivo conductivity of human tissue (e.g. liver tissue in [3]) and various animal studies (e.g. [4,5]) have shown that most tissue types have elevated conductivity values when measured in vivo. In vivo patient-specific electric properties are therefore required for more accurate SAR assessment. In this study we have performed in vivo conductivity reconstruction of muscle, bladder and tumor of 13 cancer patients.

Materials & Methods: The electric tissue conductivity values were reconstructed by Electric Properties Tomography (EPT) [6] from measured B_1^+ data. All experiments were conducted on a 3.0T scanner (Ingenia, Philips Healthcare, Best, The Netherlands) using a 16 channel receive coil. The B_1^+ amplitude map was acquired using the AFI method [7] (3D, nom. flip angle = 65° TR1 = 50 ms, TR2 = 290 ms, 16 slices). The transceive phase was acquired by an SE experiment (TR = 1200 ms, CLEAR) [6,8,9]. Conductivity values were reconstructed using a Helmholtz based reconstruction [8,9]. In vivo MR measurements of 13 cancer patients were conducted. One patient was diagnosed with uterine cancer (adeno*carcinoma)* and 12 patients were diagnosed with c*ervical cancer (*Squamous-cell carcinoma*)*. Due to scan time limitations, a more coarse resolution of 5mm isotopic was used on most of the patients. *Peristaltic motion* was reduced with the intravenous injection of *Buscopan*®. Patient scans for this study were performed in accordance with the approval of the Medical Ethics Board. Gross tumor volume (GTV) was delineated by a radiation oncologist based on mutually registered CT and T2-weighted MRI images. Mean ± standard deviation of muscle, bladder and tumor were based on manual segmentation of these tissue types based on T2-weighted images. Care was taken not to include regions where boundary artefacts were observed. As the kernel used in EPT requires many pixels of a particular tissue type, not all the patients had a tumor and bladder size that was large enough to be reliably reconstructed using EPT.

Results & Discussion: In figures 1a and 1b the T1w image and the reconstructed conductivity map of one of the patients are depicted, respectively. In fig. 1c the reconstructed muscle conductivity values (blue) of all patients are depicted and compared to the literature value (0.72S/m – light blue bar) from [2]. Elevated σ values for most patients are observed with 15-30% higher values compared to the literature value. To the best of our knowledge, there is no data available of in vivo human muscle. Reported values of in vivo σ of feline skeletal muscle at 100MHz are 0.95-0.99S/m [4] and 0.90S/m [5]. Conductivity values at 128MHz are not reported in [4,5], however, since the conductivity of muscle increases with frequency, we expect that the in vivo conductivity at 128MHz is slightly higher than the aforementioned values. In figure 1d the reconstructed conductivity of bladder/urine (purple) of 7 patients is depicted. In the same figure the bladder conductivity (light purple) is shown as used in numerical human models [1,2]. The σ of bladder reported in the literature corresponds to bladder wall tissue and does not account for highly conductive urine. It is observed that the reconstructed bladder conductivity is up to 10 times higher compared to the conductivity value used in numerical models. However, the urine conductivity reported in this work is in good agreement with the conductivity values reported in a recent study of porcine urine samples [10]. Furthermore, a relatively large conductivity spread between urine samples was also observed in [10]. In figure 1e, the conductivity values of the Squamous-cell carcinoma and adeno*carcinoma are* depicted. The conductivity of cervical tissue as reported in [2] is depicted in Fig. 1e (light red bar). No further information is available on conductivity values of cervical tumors at 128MHz. It is observed that in most patients the σ of the tumor is 5-12% higher than muscle σ. The reconstructed σ of the adenocarcinoma tumor is 22% higher than muscle conductivity.

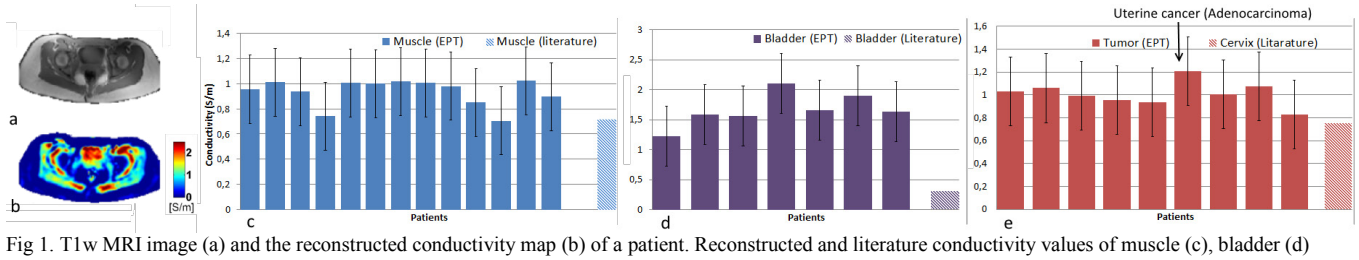

Fig 1. T1w MRI image (a) and the reconstructed conductivity map (b) of a patient. Reconstructed and literature conductivity values of muscle (c), bladder (d) and cervical tumor tissue (e).

Conclusions: We have presented first human in vivo conductivity data of muscle, bladder and cervical tumors at 3T based on EPT. Our findings regarding muscle are confirmed by scarcely available in vivo data of feline muscle tissue. The reconstructed bladder/urine conductivity values are in good agreement with the measurements of porcine urine reported in recent literature, however, the reconstructed values are much higher than the values used in numerical models. In addition, we have observed that the commonly unknown tumor conductivity is 5-12% higher compared to muscle conductivity. These results demonstrate the importance of accounting for conductivity values in living conditions when incorporating electric properties data into numerical models. Future work will, therefore, focus on the effect of these findings on SAR deposition in MR and Hyperthermia.

Acknowledgements: This study was supported by grant UVA 2010 4660 of the Dutch Cancer Society.

References: [1] Christ et al., PMB. 55:N23-N38, 2010. [2] Gabriel et.al., PMB 41:2251-2269, 1996. [3] O'Rourke et.al., PMB 52:4707-4719, 2007. [4] Stuchly et.al., Biolectromagnetics 2:93-103, 1981. [5] Surowiec et.al., PMB 31:901-909, 1986. [6] Katscher et.al., IEEE 28:1365-75, 2009. [7] Yarnykh, et.al., MRM 57:192-200, 2007. [8] Van Lier et.al., MRM 71(1):354-63, 2013. [9] Balidemaj et.al., MRM 2014. [10] Peyman, et.al., PMB 57:N339-344, 2012.

Increased cortical volume revealed by atlas-based volumetry in a bigenic mouse model of Alzheimer's Disease

Kristof Govaerts[1], Janaki Raman Rangarajan[2], Tom Struys[3], Fred Van Leuven[4], Tom Dresselaers[1], Uwe Himmelreich[1]

[1]Imaging & Pathology, KU Leuven, Belgium
[2]ESAT, KU Leuven, Belgium
[3]Morphology Research Group, Universiteit Hasselt, Hasselt, Belgium
[4]Center for Human Genetics, KU Leuven, Belgium

Target audience: This abstract is relevant for researchers interested in mouse models of Alzheimer's Disease as well as those interested in atlas-based registration and voxel-based morphometry in rodents.

Purpose

Although atrophy is a well-established MRI biomarker for Alzheimer's Disease (AD) in patients (1), results in mouse models of AD have been less consistent and depend on the model and modality used. Often, clear atrophy cannot be detected in amyloid models (2, 3, 4), while this does not seem to be the case for tauopathy models (5). In this study, we make use of the biAT model, which shows combined APP and tau pathology and also display an early behavioral phenotype representing prodromal AD (6). Atlas-based volume quantification and voxel-based morphometry (VBM) are valuable tools in clinical settings, but are not yet consistently used in pre-clinical research (e.g. mouse models). Voxel-based morphometry in particular has not seen much use in murine AD research, likely because it is constrained by the small differences expected in early stages of AD as well as due to resolution constraints. However, atrophy monitoring could provide crucial contributions to preclinical trials of novel AD treatments.

Fig. 1

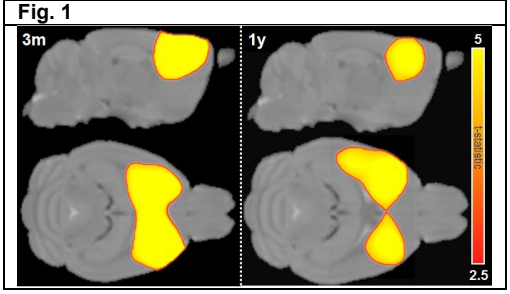

Methods

- *MRI*: Double transgenic APP.V717I x Tau.P301L (biAT) and age-matched FVB control mice were imaged at 3 (biAT: 16, FVB: 16) and 12 (biAT: 18, FVB: 19) months (mo) of age. Imaging was performed on a 9.4T Biospin small animal MR system (20cm horizontal bore, Bruker Biospin, Ettlingen, GE), using a 7 cm linearly polarized resonator for transmission and an actively-decoupled mouse brain surface coil for receiving (Rapid Biomedical, Rimpar, GE). For anatomical imaging, we utilized a 3D T_2-weighted MRI protocol (TR 1 s, TE 36 ms, rare factor 10, zero-fill factor 1.33, 160x256x88 matrix, 1.5x2.4x0.83cm FOV). To assess reproducibility of regional volume measurements, a single FVB control animal (5mo) was imaged five times on the same day, fixating the head and repositioning the coil each time.
- *Processing*: After bias field correction and intensity normalization using in-house developed Matlab scripts (The Mathworks, Natick, US) (7), spatial normalization was performed using a non-rigid registration tool (NiftyReg (8)). Atlas labels from the MDA2006 atlas (9) were propagated to a study-specific FVB template created from the 3mo FVB scans, which was used as the reference for all subsequent registrations. Regional volumes were corrected for whole brain volume and normalized to a brain volume of 500mm^3. VBM was performed on the Jacobian maps in template space using SPM5 (statistical parametric mapping, SPM, http://www.fil.ion.ucl.ac.uk/spm/), and thresholded for a family-wise error rate of 5%. Statistical analysis was performed using one-way ANOVA with Bonferroni's correction for multiple testing.
- *Histology*: 13mo animals were sacrificed by an i.p. overdose of Nembutal (300µl; Ceva) and subsequently perfused with 4% ice - cold paraformaldehyde (PFA) solution (Sigma - Aldrich). After overnight post fixation in 4% PFA, brain tissue was stored in a 0.1% sodium azide solution (Fluka, Sigma - Aldrich) at 4°C. Brains were embedded in paraffin, 7 µm sections were sliced and a Masson's trichrome staining was performed. Slices were scanned with a Mirax desk (Carl Zeiss, Oberkochen, Germany) and microscopic images were taken with the Mirax viewer software.

Fig. 2

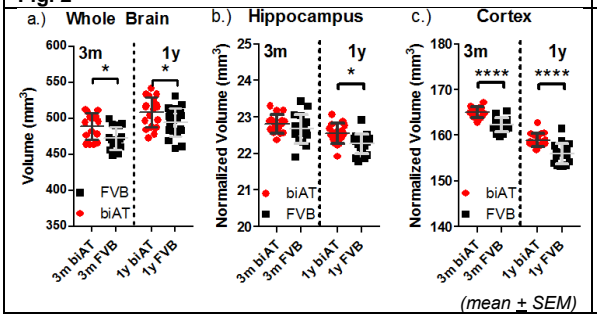

Fig. 3

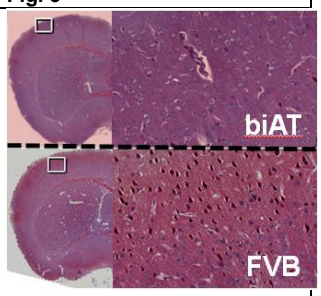

Results

biAT animals displayed a modest but significant increase in whole brain volume at 3 and 12 months *vs.* FVB (**Fig. 2a:** 3m: 489 ± 17 vs. 472 ± 15 mm^3, p=0.011, 1y: 508 ± 20 *vs.* 494 ± 19 mm^3, p=0.038). VBM (**Fig. 1**) revealed that these volume differences are largely localized to the region of the frontal cortex and basal ganglia, at both the 3 and 12 mo timepoints. Regional volumes normalized for brain volume revealed subtle but highly significant increases in volumes for the cerebral cortex of biAT mice vs FVB (**fig. 2c**, 3mo: 165.0 *vs.* 162.3mm^3, 12mo: 158.9 *vs.* 155.9 mm^3 for biAT and FVB, respectively; both p<0.0001). No significant differences in normalized volume were observed in the hippocampus at 3 mo, although a minor increase in normalized volume was found at 12mo (**Fig. 2b,** 3mo: 22.8 *vs.* 22.7, n.s., 12mo: 22.6 *vs.* 22.3, p<0.05.). Reproducibility of volume measurements in a single animal scanned repeatedly was high: standard deviations of absolute measurements were on the order of 1% (whole brain: 1.11%, hippocampus: 1.05%, cortex: 0.79%), and for normalized measurements this was 1.5% (hippocampus: 1.54%, cortex: 1.40%). Histological analysis revealed regions with a reduced neuronal density in the frontal cortex (**fig. 3,** slice with anterior commissure).

Discussion

Using *in vivo* MRI and registration-based quantification methods, we were able to reliably and reproducibly quantify volume differences of only a few percent. Increased cortical size is a counter-intuitive but not unprecedented finding in a mouse model for AD. Increased cortical thickness with a subsequent age-depended increase in cortical thinning has been reported in an APP model (2). Early and late increased cortical volume as well as late increased hippocampal volume has been reported in the TASTPM model (4). Other studies do not report clear trends suggesting global brain atrophy (3).
Considering the decreased neuronal density we observed in these regions, it is likely that the volume increases we report are the result of a secondary mechanism, most likely gliosis and/or edema. Even so, the absence of hippocampal volume changes suggests that the biAT model, although it displays many of the typical molecular and behavioral AD phenotypes (6), does not recapitulate atrophy-induced volume changes, or that the anatomical differnces are too small and the methods lack the resolution and sensitivity to reveal the expected hippocampal atrophy.

References : 1. Jack et al., Lancet Neurol. 2010, 2. Hébert et al., Neurobiol. Aging 2013, 3. Lau et al., Neuroimage 2008, 4. Maheswaran et al., Brain Res. 2009, 5. Yang et al., Neuroimage 2010, 6. Terwel et al., Am J. Pathol. 2008, 7. Vande Velde et al., Neuroimage 2012, 8. Modat et al., Comput Meth Prog Bio 2010, 9. Mackenzie-Graham, J. Anat 2004

Intravoxel Incoherent Motion Imaging exposes abnormal parenchyma and microvasculature in cerebral small vessel disease

Sau May Wong[1], Eleana Zhang[2], Frank C.G. van Bussel[1], Julie E.A. Staals[2], Cécile R.L.P.N. Jeukens[1], Paul A.M. Hofman[1], Robert J. van Oostenbrugge[2], Walter H. Backes[1], Jacobus F.A. Jansen[1]

[1]Department of Radiology, Maastricht University Medical Center, Maastricht, the Netherlands
[2]Department of Neurology, Maastricht University Medical Center, Maastricht, the Netherlands

Target Audience: Neuroscientists interested in perfusion and diffusion imaging and cerebral small vessel disease

Purpose: Cerebral small vessel disease (cSVD) is an age and vascular risk factor related microvascular disease and may clinically manifest as lacunar stroke or vascular cognitive impairment. Moreover, it can lead to physical, psychiatric and cognitive disabilities. The pathophysiology of cSVD remains largely unknown. Early changes in cSVD include loss of microstructural integrity and a possible association with hypoperfusion, which were shown by previous studies using diffusion tensor imaging and perfusion imaging, respectively.[1-2] However these studies could not distinguish between contributions of parenchymal and vascular microstructures, leaving the more precise nature of the abnormalities undetermined. To examine the parenchymal microstructure and microvasculature, Intravoxel Incoherent Motion Imaging (IVIM) was performed.

Methods: *Subjects and data acquisition:* MR imaging was conducted on 64 cSVD patients (age 70±11y) and 36 healthy controls (age 68±12y) using a 3.0 Tesla MR scanner (Philips Achieva TX). IVIM was executed using a Stejskal-Tanner diffusion weighted (DW) spin echo single shot echo planar imaging (EPI) pulse sequence (TR/TE = 6800/84 ms, FOV: 221 x 269 mm^2, acquisition matrix: 110 x 112, 58 slices, 2.4 mm voxel size). To minimize the effect of cerebral spinal fluid (CSF), an inversion recovery prepulse (TI = 2230 ms) was implemented prior to the DW sequence.[3] Fifteen DW images were acquired using b-values (0, 5, 7, 10, 15, 20, 30, 40, 50, 60, 100, 200, 400, 700, 1000 s/mm^2, in the phase encoding direction). Images obtained with b-values 700 and 1000 s/mm^2 were repeated 2 and 3 times respectively. The total IVIM scan duration was 5:13 min. For anatomical segmentation a T1-weighted scan and a FLAIR scan were performed (fig.1 A,B).
Data analysis: IVIM employs a two-compartment diffusion model.[4] A model that accounts for effects of CSF and also differences in relaxation times of blood and tissue was used.[3] A bi-exponential signal decay can be obtained (fig.2) and the two-step method[5] was used for voxel wise fitting (fig. 1C-E). First *D* (parenchymal diffusivity) was estimated using b-values higher than 200 s/mm^2, and subsequently *f* (perfusion fraction) and *D** (microvascular diffusivity) were estimated using all b-values and fixed *D*. For each participant the brain was segmented into four regions of interest (ROI): normal appearing white matter (NAWM), deep gray matter (DGM), cortex and white matter hyperintensities (WMH)[6]. Average *f*, *D**, and *D* were calculated for each ROI.
Statistical analysis: Multivariate linear regression analysis corrected for age, gender and cardiovascular risk factors hypertension, diabetes mellitus, hypercholesterolemia, smoking and atrophy was conducted. Baseline characteristics were compared using independent samples t-tests and Chi-square tests.

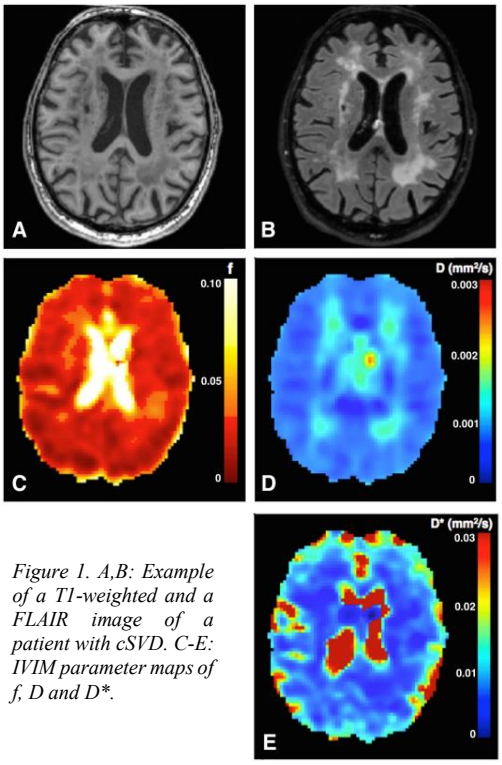

Figure 1. A,B: Example of a T1-weighted and a FLAIR image of a patient with cSVD. C-E: IVIM parameter maps of f, D and D.*

Results: Patients suffered significantly more from hypercholesterolemia (p=0.01) and significantly more smokers were present in the patient group (p=0.03). Significantly higher *f* was observed for the patient group (2.32±0.03x10^{-2}, n=64) (mean±SE, n) compared with controls (2.20±0.03x10^{-2}, n=36) in the NAWM (p=0.03). A trend towards higher *f* was found for patients (3.26±0.05x10^{-2}, n=64) in comparison with controls (2.94±0.03x10^{-2}, n=36) in the DGM (p=0.06). Significantly higher *D* was found for patients (7.32±0.04x10^{-4} mm^2/s, n=64) compared with healthy controls (7.09±0.04x10^{-4} mm^2/s, n=36) in the NAWM (p=0.02). In DGM significantly higher *D* was found for patients (7.78±0.05x10^{-4} mm^2/s, n=64) compared with controls (7.51±0.05x10^{-4} mm^2/s, n=36) (p=0.02). No differences were found for *D** or other regions.

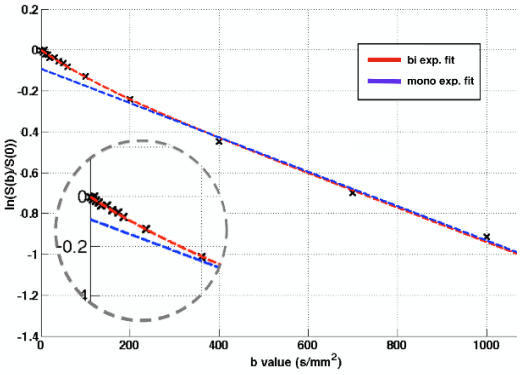

Figure 2. A two-step method was used to fit the bi-exponential decay. First a mono exponential curve is fitted for b-values larger than 200 s/mm^2 (blue line). Subsequently a bi-exponential curve was fitted for all b-values (red line) with fixed D. The inserted circle shows the bi-exponential behavior, visible for b-values <200 s/mm^2.

Discussion & Conclusion: Larger microvascular perfusion fraction *f* and higher parenchymal diffusivity *D* were found in the NAWM and DGM for patients with cSVD. The larger *f* might be related to more tortuous vessels[7] (fig. 3) that lead to a stronger dephasing of spins contributing to the fast decaying component. Furthermore the higher *D* may imply loss of parenchymal microstructural integrity. This suggests early parenchymal changes in cSVD that precede the formation of WMH. Longitudinal studies are needed to verify this. In this study, we demonstrate the potential of IVIM in providing novel pathophysiological information of the normal appearing brain tissue in cSVD.

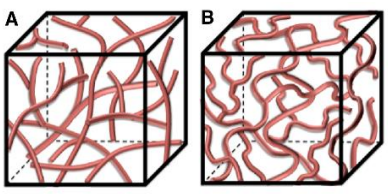

Figure 3. Illustration of voxels containing straight vessels (A) and tortuous vessels(B).

References: **1.** O'Sullivan M *et al*., Neurology 2001;57:2307-2310. **2**. Markus HS *et al.,* J Neurol Neurosurg Psychiatry 2000;69:48-53. **3.** Hales PS *et al.,* J Cereb Blood Flow Metab 2013;33, 67-75 **4.** Bihan D *et al.*, Radiology 1986; 161: 401-7 **5.** Federau *et al.,* JMRI 2014; 39: 624-632 **6.** De Boer R *et al*., Neuroimage, 2009;45(4):1151–61 **7.** Brown WR *et al.* Neuropath Appl Neuro, 2011; 37-56-74

Carotid pulse wave velocity measurements using accelerated high temporal resolution MRI

Abdallah Motaal[1], Wouter V Potters[1], Huiming Dong[2], Luc M. Florack[3], Klaas Nicolay[2], Aart Nederveen[1], Gustav J. Strijkers[4], Bram F. Coolen[1]

[1]Department of Radiology, Academic Medical Center, Amsterdam, the Netherlands
[2]Department of Biomedical Engineering, Eindhoven University of Technology, Eindhoven, Netherlands
[3]Department of Mathematics and Computer Science, Eindhoven University of Technology, Eindhoven, Netherlands
[4]Department of Biomedical Engineering and Physics, Academic Medical Center, Amsterdam, Netherlands

Purpose

Arterial stiffness is one of the major biomarkers of early atherosclerotic disease[1]. A common method to assess vessel wall stiffness is by measuring the velocity (PWV) of the pulse wave created by cardiac contraction[2]. Using phase-contrast MRI based flow measurements, PWV can be determined by measuring the time delay between the flow curves at two different slice locations. These measurements require sufficient spatial resolution for accurate flow quantification, as well as high temporal resolution with respect to the travel time of the pulse wave between the two slices. In the aorta, these measurements seem feasible using standard imaging protocols. However, in case of the carotid artery, more sophisticated acquisition strategies are needed to deal with the small lumen diameter (4-6 mm) and shorter imaging coverage of dedicated carotid coils. Here, we present a new MRI method for carotid PWV assessment, where we combine retrospective triggering and compressed sensing (CS) reconstruction, resulting in flow measurements with in-plane spatial resolution of 0.85 mm and temporal resolution of 200 frames/cardiac cycle.

Methods

MRI measurements were performed on a whole-body 3T MR scanner. A fast field echo (FFE) phase contrast MR sequence with unidirectional velocity encoding (VENC = 120 cm/s) was used with the following parameters: TE/TR/FA = 3.28 ms/10.58 ms/20°; slice thickness = 3mm; FOV = 136 mm and acquisition matrix of 160x160 resulting in a spatial resolution of 0.85 mm. We first validated the method using phantom measurements by acquiring PC MRI data for a silicon carotid model of a healthy volunteer, where a flow waveform mimicking carotid arterial blood flow pattern was applied. The fully-sampled cartesian kspace was acquired 25 times. All 25 dynamics were acquired and the klines were retrospectively binned into 200 fully-sampled frames[3]. Unlike prospective triggering, where the temporal resolution is limited by TR, retrospective triggering enables reconstructions with higher temporal resolutions. This is because the data is acquired asynchronously with the heartbeat. Additionally, a variety of undersampled random acquisition schemes were simulated by subsampling the fully-sampled data. Undersampled kt-space sampling patterns were generated using computer simulations. We aimed to achieve a 3 minute scan time per slice, and for efficient kspace sampling, half Fourier factor of 30% was used. In the simulation process random weighted sampling with different Gaussian distributions was emphasized as shown in Fig.1. Assessment of all trajectories leads to one optimum trajectory, which was used to acquire undersampled kt-space data in vivo.

In the in vivo experiments, the optimal variable density scheme is implemented on the scanner. Measurements were performed on 4 volunteers. Two axial slices were positioned to cover the common and internal carotid arteries. The resulting phase contrast data have been acquired multiple times in order to assess reproducibility of our technique. The resulting data was then subjected to a three-dimensional (2D + time) compressed sensing reconstruction[4]. Flow curves were created for each vessel and, finally, PWV analysis is performed by calculating the time-shift in flow curves between the vessels in the two axial slices. The time-shift between the curves, **t**, was determined by the maximum cross-correlation between the (time-shifted) curves. The PWV is then given by **PWV=d/t**, where **d** is distance traveled between the two slices.

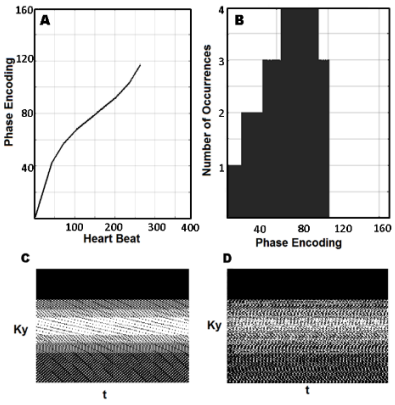

Figure 1: A) The phase encoding step as a function of time (heart beat), and the corresponding B) histogram. C, D) The simulated acquired kt spaces assuming constant heart rate and varying heart rate (5%). It can be seen small variation in heart rate shows that random weighted undersampled acquisition is achieved.

Results

In Fig.2, the top row shows the difference between linear and CS reconstructions for one of the time frames. Clearly, CS reconstruction cleans up the aliasing artifacts and better image quality with good delineation of the carotids is achieved as shown in Fig.2D. By using a retrospective triggering scheme, detailed flow curves could be estimated from the reconstructed Cine as shown in Fig.2E. In Fig.3A the normalized blood flow curves of the carotid artery of a representative case for the 2 slices are shown. Cross correlation with a dense temporal resolution scale between the two curves is calculated to estimate the time shift that yield the highest correlation value as shown in Fig3B. Repeated scans for the four volunteers have been conducted. Fig.3C shows the estimated PWV in the 2 scans of the 4 volunteers with a coefficient of variance (CV) of 16%.

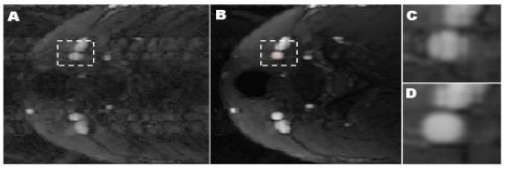

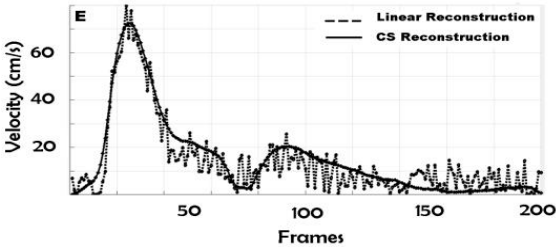

Figure 2: The difference between(A) linear and (B) CS reconstructions for a time frame. The zoomed images, C and D, show better delineation of the carotid wall for the CS reconstruction. E) The estimated flow curves for the linear and CS reconstructions.

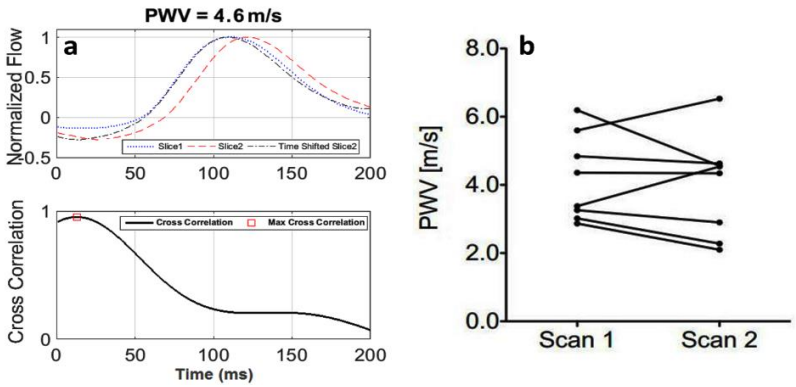

Figure 3: A) Normalized blood flow curves in the left carotid artery for the 2 slices and shifted flow curve that gives the highest correlation. B) Cross correlation between the two curves for the time difference that yields the highest correlation is calculated. By estimating the shift and by knowing the distance between the two slices, the PWV could be calculated. C) Repeated measurement for the 4 volunteers.

Conclusion

In conclusion, we showed in this abstract that by combining retrospective triggering and compressed sensing reconstruction, measuring the carotid pulse wave velocity becomes possible. Given this high temporal measurements, translation of this technique to patient and elderly people, who are expected to have higher PWV, also seems feasible

References

1. Ben-Schlomo et al. J Am Coll Cardiol 2014; 2. Wentland et al. Cardiovasc Diagn Ther 2014; 3. Coolen et al. Magn Reson Med 69:648–65 4. Motaal et al. J. Cardio Vasc. Imag. 2014

Endogenous assessment of diffuse myocardial fibrosis with T1ρ-mapping in patients with dilated cardiomyopathy

Joep van Oorschot[1], Johannes Gho[1], Sanne de Jong[2], Fredy Visser[3], Aryan Vink[2], Tim Leiner[1], Peter Luijten[1], Jaco Zwanenburg[1]

[1]Department of Radiology, University Medical Center, Utrecht, the Netherlands
[2]Department of Physiology, University Medical Center, Utrecht, the Netherlands
[3]Philips Healthcare, Best, the Netherlands

Purpose

To validate cardiac $T_{1\rho}$-mapping in patients with dilated cardiomyopathy (DCM), and correlate with ECV-mapping.

Background

It has been shown that quantitative methods such as T_1 mapping and extracellular volume (ECV) mapping provide information on diffuse fibrosis formation in patients with DCM[1]. The main drawback of these methods is the need of a gadolinium based contrast agent, with the need for a substantial delay between injection and image acquisition and possible adverse renal effects. The $T_{1\rho}$ relaxation time is known to be sensitive to changes in macromolecular content, and recently it was shown that a significantly higher $T_{1\rho}$ is found in compact myocardial fibrosis after chronic myocardial infarction[2,3]. In this study we show the feasibility of native $T_{1\rho}$-mapping for the detection of diffuse myocardial fibrosis, without the use of a contrast agent.

Methods

Ex vivo study: Three explanted hearts from DCM patients, who received heart transplantation, were sectioned in slices and scanned within 24 hours on a clinical 3T MR scanner (Philips Healthcare). $T_{1\rho}$-mapping was performed using a $T_{1\rho}$-prepared 3D gradient echo sequence. 5 images with different spin-lock (SL) preparation times with an amplitude of 500 Hz were acquired (SL = 1, 10, 20, 30, 40 ms). Other parameters: TE/TR = 1.66/3.3 ms, resolution = 0.75 x 0.75 mm^2, slice thickness = 0.75 mm, flip angle = 10 degrees. After MR Imaging heart slices were formalin-fixed, cut into small pieces, and stained with Masson's Trichrome for collagen assessment. Histological fibrosis in each piece were quantified in Matlab, and compared to the corresponding $T_{1\rho}$ value. *In vivo* study: Six DCM patients underwent a MRI exam before implantation of a left ventricular assist device (LVAD), on a Philips Achieva 1.5 T MR scanner, using a 5-channel cardiac receive coil. Five healthy young control subjects (5 male, age 25 ± 3 years) were scanned to confirm measurement of the remote tissue. Written informed consent was obtained from all subjects. A $T_{1\rho}$-map was obtained by acquiring 4 images with different SL preparation times (amplitude 750 Hz, SL = 1,13,27,45 ms). Other parameters: bandwidth/pixel = 530 Hz, TE/TR = 1.94/3.9 ms, resolution = 1.5 x 1.65 mm^2, slice thickness = 6 mm, FOV = 288x288 mm^2, flip angle = 50 degrees, 2 TFE shots, NSA = 2, SENSE = 1.5. Images were acquired in late diastole during expiration breath holds, with an R-R interval of 3 beats. In the patients corresponding T_1 maps were acquired before and 15 minutes after contrast injection (0.2 ml/kg Gadovist), using MOLLI 3(3)5 scheme[4] and blood was drawn to determine hematocrit.

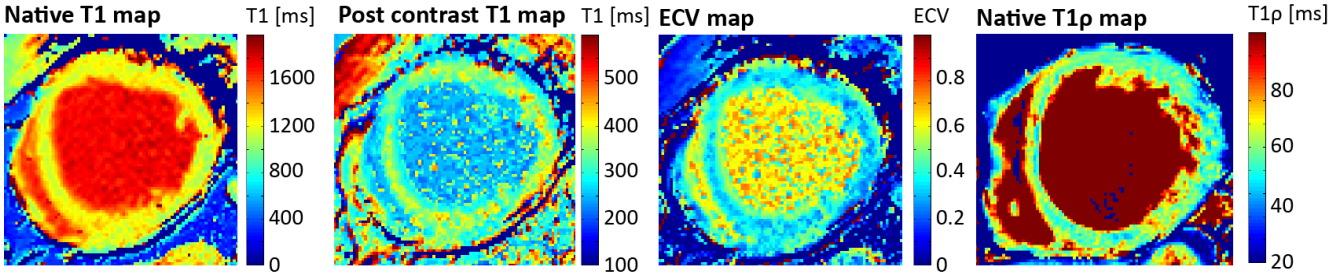

Figure 1: *In vivo* short axis pre- and post-contrast T1-map and resulting ECV-map, with corresponding $T_{1\rho}$-map in a DCM patient.

Results

$T_{1\rho}$ relaxation time was significantly higher in the DCM patients (59.5 ± 4 ms), compared to healthy young controls (50 ± 3 ms), p<0.0001. Mean left ventricular ejection fraction in the DCM patients was 23.7 ± 10%, and mean ECV was 0.25 ± 0.06. Positive trends for the *ex vivo* $T_{1\rho}$-relaxation time vs. the fibrosis fraction and for the *in vivo* $T_{1\rho}$-relaxation time vs ECV were found (Fig 2), however, these were not significant (P=0.12 *ex vivo*, and P=0.45 *in vivo*).

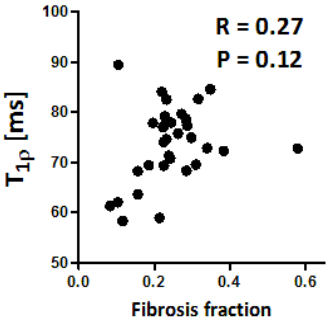

Fig. 2a: Pearson correlation $T_{1\rho}$ time and *ex vivo* fibrosis in explanted DCM hearts

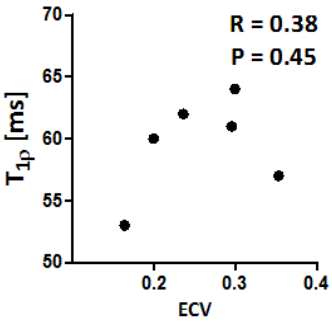

Fig 2b: Pearson correlation $T_{1\rho}$ time and *in vivo* ECV in DCM patients

Discussion

A significant higher $T_{1\rho}$-relaxation time was found in DCM patients, compared to healthy subjects. This increase in $T_{1\rho}$-relaxation time might be caused by diffuse myocardial fibrosis. However, no significant correlation was observed between the $T_{1\rho}$-relaxation times *and ex vivo* histology and *in vivo* ECV values. This may partly be due to the difficulty in exact matching of the ex vivo histology results with the MRI results. We do however observe a trend in the relation, and believe that this could become significant in a larger study with more statistical power. Native $T_{1\rho}$ –mapping requires no separate pre- and post-contrast scan with corresponding waiting delays, and no hematocrit measurement. It is, therefore, easier to incorporate in a clinical protocol, compared to ECV-mapping.

Conclusion

The $T_{1\rho}$ relaxation time was significantly higher in DCM patients, compared to healthy control subjects. We believe that $T_{1\rho}$ mapping could provide additional information on diffuse myocardial fibrosis formation.

References: [1]Kellman et al. JCMR (2012) [2]Oorschot et al. Proc. ISMRM (2012) [3]Musthafa et al. MRM (2012) [4]Messroghli et al. JMRI (2007)

Glutamate dehydrogenase inhibition reduces glutamine conversion into 2HG in *IDH1*-mutated cancer cells as detected by ^{13}C MRS

Tom Peeters[1], Vincent Breukels[1], Corina van den Heuvel[2], Anna Navis[2], Sanne van Lith[2], Jack van Asten[1], Remco Molenaar[3], William Leenders[2], Arend Heerschap[1]

[1]Department of Radiology and Nuclear Medicine, Radboud University Nijmegen Medical Center Nijmegen, Netherlands; [2]Department of Pathology, Radboud University Nijmegen Medical Center Nijmegen, Netherlands; [3]Department of Cell Biology and Histology, Academic Medical Center, Amsterdam, the Netherlands

Introduction: The cytosolic enzyme isocitrate dehydrogenase (IDH1) is involved in $NADP^+$ dependent oxidative decarboxylation of isocitrate into α-ketoglutarate (αKG) while producing NADPH (fig.1). αKG is an important intermediate for lipid synthesis and cell proliferation whereas NADPH is important for biosynthesis of metabolites that protect cells from reactive oxygen species. More than 70% of all low grade gliomas exhibit a heterozygous R132H mutation in IDH1[1] leading to a loss in isocitrate binding capacity and a conversion of αKG into *D*-2-hydroxyglutarate (2HG) by NADPH oxidation instead[2]. Depletion of the αKG and NADPH pools imposes metabolic stress and hampers cell proliferation. Although there are indications for increased dependence on glutaminolysis of $IDH1^{R132H}$ cells[3], multiple compensatory anaplerotic mechanisms that these tumor cells develop to survive are currently being studied[4]. Since it is hypothesized that in $IDH1^{wt/R132H}$ cells most 2HG is synthesized from glutamate-derived αKG[5] our goal was to investigate the effect of glutamate dehydrogenase (GDH1) inhibitor epigallocatechin gallate (EGCG)[6] on the metabolic conversion of glutamine into 2HG in IDH1 mutant human colorectal cancer cells (HCT116) with ^{13}C MRS.

Materials and methods: The heterozygous $IDH1^{wt/R132H}$ genotype was created by a knock-in of a $IDH1^{R132H}$ allele by rAAV targeting technology GENESIS. Parental $HCT116^{wt/wt}$ cells were used as control. Cells were maintained in DMEM containing 10% FBS, 5.6 mM glucose and 4mM glutamine. 17 hours prior to extraction the glutamine was replaced by an equivalent of 1-^{13}C-labeled glutamine. EGCG-treated cells were supplied with 100μM EGCG 2 hours prior to and during ^{13}C-glutamine incubation. Before extraction all cells were placed on ice and washed once with cold PBS. Subsequently cells were scraped in an ice-cold 50:50 MeOH:H_2O solution containing formic acid as reference compound. The cell suspension was centrifuged for 10 minutes at 1000 x g at 4°C. Supernatant was dried in a Savant SpeedVac evaporator and redissolved in deuterated water. All samples contained the equivalents of approximately $18 \cdot 10^7$ cells and were measured on a Bruker Avance III 500MHz spectrometer. Proton-decoupled ^{13}C spectra were acquired with a pulse-acquire experiment (TR = 5s, 90° flip angle, NS = 4150). Additional ^{1}H spectra were acquired to study total metabolite pool sizes (TR = 8s, 90° flip angle, NS = 64). ^{13}C spectra were fitted with a Lorentzian shape using Bruker Topspin software. Fits were corrected for cell number and reference compound concentration, and spectra were further analyzed with SpinWorks 4 (University of Manitoba, Winnipeg, Canada). For a proliferation assay HCT116 cells were seeded in 6-wells dishes at low density (60 cells/well) and subsequently treated with EGCG (20 μM). After two weeks colonies were stained and counted with an inverted microscope. All counts were normalized to the control groups.

Results: From the ^{13}C MR spectra it follows that 1-^{13}C-glutamine was converted via glutamate and αKG into 1-^{13}C-2HG (fig.1 and 3). Labeled 2HG was only detected in the $IDH1^{wt/R132H}$ cell line (181.35 ppm). GDH1 inhibition with EGCG resulted in a significant decrease in $IDH1^{wt/R132H}$ HCT116 cell proliferation compared to the non-treated control cells (fig.2) and reduced the production of 1-^{13}C-glutamine derived 2HG with almost 50% (fig.3). The pool sizes of 1-^{13}C-labeled glutamine and glutamate were large in all samples whereas their 2-5C resonances were in the range of intensities that originate from natural abundant ^{13}C, implying no label scrambling occurred. Label that entered the TCA cycle via 1-^{13}C-αKG was removed by oxidative decarboxylation. Furthermore, in both parental and mutated cell lines EGCG induced a decrease in total glutamate and an increase in total glutamine concentrations as observed in the ^{1}H spectra (fig.4).

Discussion: We conclude that the metabolic pathway from glutamine to 2HG is important for the generation of 2HG in $IDH1^{wt/R132H}$ HCT116 cells since the amount of glutamine-derived 2HG was considerably reduced due to the administration of EGCG. Even though multiple enzymes are co-responsible for the conversion of glutamate into αKG (e.g. BCAT1, ALT1 and AST1), we showed that the inhibition of GDH1 has a severe effect on cell proliferation. Therefore, EGCG could be a promising therapeutic agent for IDH1-mutant tumors that inhibits glutamate-dependent metabolism and exposes tumor cells to reactive oxygen species.

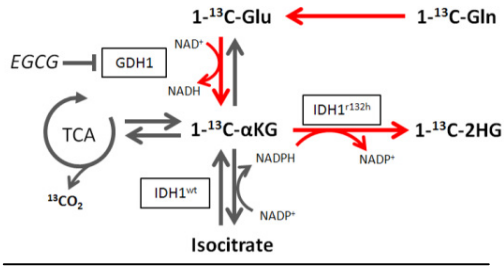

***figure 1** | schematic overview of the observed metabolic pathway. IDH1 'mutabolism' is shown in red.*

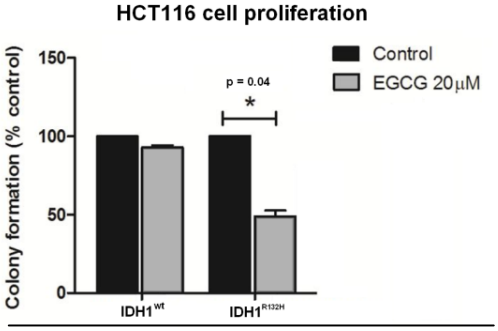

***figure 2** | cell proliferation in $IDH1^{wt/wt}$ and $IDH1^{wt/R132H}$ cells, with and without EGCG treatment (n=2).*

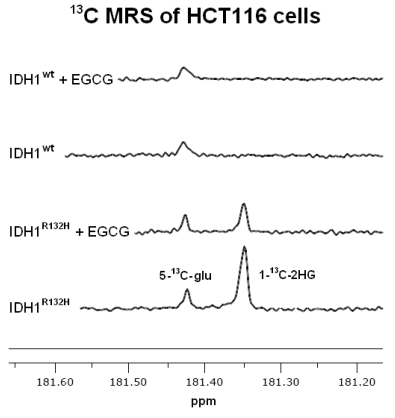

***figure 3** | proton-decoupled ^{13}C spectra showing decreased accumulation of 1-^{13}C-2HG after EGCG treatment.*

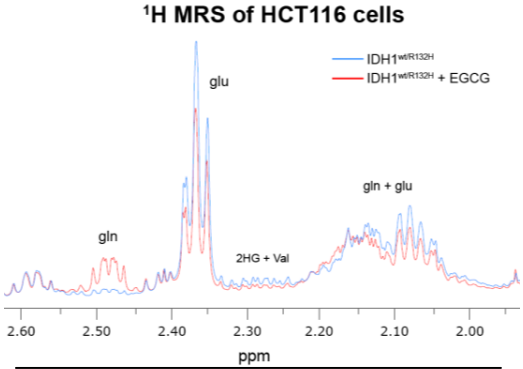

***figure 4** | ^{1}H spectra showing glu and gln total pool size alterations caused by EGCG treatment.*

References

1. Yan, H., et al., New England J of Med, 2009. **360**(8).
2. Dang, L., et al., Nature, 2009. **462**(7274).
3. Seltzer, M.J., et al., Cancer Res, 2010. **70**(22).
4. Izquierdo-Garcia, J.L., et al., PLoS One, 2014. **9**(9).
5. Van Lith, S.A.M., et al., BBA - Rev on Cancer, 2014. **1846**(1).
6. Li, C., et al., J Biol Chem, 2006. **281**(15).

Intracranial atherosclerotic lesion characteristics correlate with cerebrovascular lesion load after TIA or ischemic stroke: a 7.0 tesla MRI study

Nikki Dieleman[1], Anja van der Kolk[1], Jaco Zwanenburg[1,2], Manon Brundel[3], Anita Harteveld[1], Geert Jan Biessels[3], Fredy Visser[1,4], Peter Luijten[1], Jeroen Hendrikse[1]

[1]Department of Radiology, University Medical Center, Utrecht, the Netherlands; [2]Image Sciences Institute, University Medical Center Utrecht, Utrecht, Netherlands; [3]Department of Neurology, University Medical Center, Utrecht, the Netherlands; [4]Philips Healthcare, Best, the Netherlands

Introduction. Intracranial atherosclerosis (ICAS) is denoted as one of the most prevalent cause of stroke worldwide.[1,2] It is known that ICAS can cause different types of parenchymal injury, ranging from small lacunar infarcts to large cortical-subcortical infarcts.[3] From an ex-vivo study[4] it has been suggested that ICAS has an association with smaller (<3mm) cortical microinfarcts (CMIs) as well, but until now this was not assessed in-vivo. Moreover, from neuropathologic studies it is known that CMIs are linked to the occurrence of macroinfarcts. Given the association with macroinfarcts it has been suggested that they share a common etiology and risk factors, like ICAS.[5] Assessing both macroinfarcts and CMIs in patients with a history of cerebrovascular disease may provide additional information on the spectrum of parenchymal brain injury caused by ICAS. Therefore, in this prospective study we investigated the presence of CMIs at 7.0 tesla (7T) MRI in patients with a transient ischemic attack (TIA) or ischemic stroke of the anterior circulation and explored the relationship between ICAS, CMIs and macroinfarcts.

Materials and Methods. Institutional Review Board approval was obtained for this prospective study. All patients gave written informed consent. Patients presenting with arterial ischemic stroke or TIA of the anterior cerebral circulation were screened for inclusion in this study. Imaging was performed on a whole body 7T MR system (Philips Healthcare, Cleveland, OH, USA) with a 32-channel receive coil and volume transmit/receive coil for transmission (Nova Medical, Wilmington, MA, USA). The protocol included a T_1-weighted Magnetization Preparation Inversion Recovery Turbo Spin Echo (MPIR-TSE)[6] intracranial vessel wall sequence (acquired resolution 0.8x0.8x0.8mm^3, repetition time (TR) 3952ms, inversion time (TI) 1375ms, echo time (TE) 37ms, scan duration 11min) before and in 15 cases also after contrast administration, and a T_2-weighted Fluid-Attenuated Inversion Recovery (FLAIR) sequence (acquired resolution 0.8x0.8x0.8mm^3, TR/TE/TI 8000/300/2250ms, scan duration 13min) after contrast administration. Five minutes before acquisition of the contrast enhanced MPIR-TSE sequence, 0.1 mL/kg of a gadolinium-containing contrast agent (Gadobutrol, Gadovist 1.0 mmol/mL, Bayer Schering Pharma, Newbury, UK) was administered to the patients. Image analysis was performed with MeVisLab v2.5 (MeVis Medical Solutions AG, Bremen, Germany) and on an offline workstation (Philips). ICAS lesions, characteristics of ICAS lesions (concentric/eccentric; focal/diffuse, enhancement[7]), and ischemic lesions (CMIs and macroinfarcts) were scored by two independent raters (ND and AK) (Figure 1). The Intraclass Correlation Coefficient (ICC) and the Dice Similarity Coefficient (DSC) were evaluated for interrater reproducibility. Consensus was reached for every location. SPSS version 20 for Windows was used for statistical analysis. First, the relation between ICAS lesions, infarcts (macroinfarcts and CMIs), and baseline characteristics were examined using logistic and linear regression analyses, where appropriate. Second, linear regression analyses were used to examine relationships between calculated ratios of ICAS lesion characteristics, CMIs and macroinfarcts. Statistical significance was set at $p<0.05$ and standardized Beta coefficients are given where appropriate.

Results. Between Augustus 2011 and March 2014, nineteen patients (6 females; mean age 59 years; range 40-81 years) with a TIA (n=7) or ischemic stroke (n=12) of the anterior circulation, who fulfilled the inclusion criteria, underwent 7T imaging at a median time of 5 days after symptom onset (range 1-10 days). One patient was excluded because of poor image quality, due to motion artifacts. A total number of 101 CMIs (in 78% of patients), 31 macroinfarcts (67%) and 75 ICAS lesions (100%) were found. Eighty-one and sixty-five percent of the CMIs and macroinfarcts, respectively, were found in the same vascular territory as the ICAS lesions. A strong interrater reliability was found for both CMIs (ICC: 0.95), macroinfarcts (ICC: 0.81) and ICAS (ICC: 0.75). Interrater agreement on the evaluation of locations was good to strong (DSC for CMIs, macroinfarcts and ICAS were 0.66, 0.75 and 0.70, respectively). Age and gender were not related to vascular lesion load (macroinfarcts and CMIs) and the number of ICAS lesions did not have a relationship with the vascular lesion load either. A positive correlation existed between the number of macroinfarcts and CMIs ($\beta=0.538$, $p<0.05$); furthermore, macroinfarcts were positively correlated ($p<0.05$) to history of stroke, but CMIs and ICAS lesions were not. When examining correlations between ICAS lesion characteristics and infarcts a positive correlation was found ($\beta=0.690$, $p<0.01$) for a concentric configuration and macroinfarcts, but not for CMIs. A diffuse thickening pattern was positively correlated to macroinfarcts ($\beta=0.510$, $p<0.05$) and a weak trend was found for CMIs ($\beta=0.407$, $p=0.09$). Enhancement did not have any relationship with cerebrovascular lesion load.

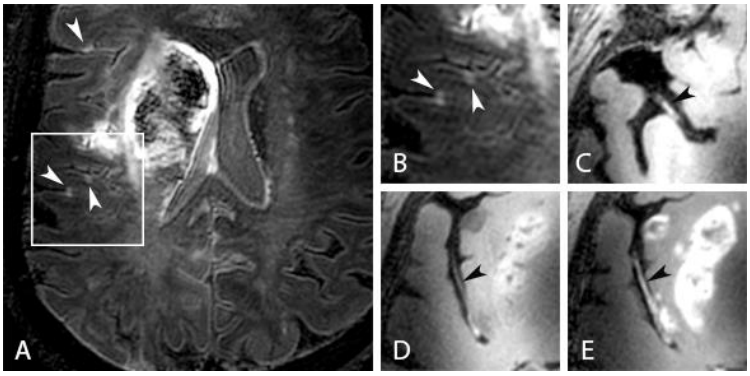

Figure 1. A 75-year-old female patient presented with ischemic stroke of the right middle cerebral artery (MCA) territory. (A) Transverse 7T T_2-weighted Fluid-Attenuated Inversion Recovery image shows an infarct of the right MCA territory and three cortical microinfarcts (**white arrowheads**); B shows a zoomed view of the box drawn in A. (C-E) Transverse 7T T_1-weighted magnetization preparation inversion recovery turbo spin echo images before (C and D) and after contrast administration (E) show thickening of the right M1 (C) and M2 (D) segments of the MCA, and enhancement of the M2 vessel wall segment after contrast administration (E) (**black arrowheads**).

Conclusion. This study shows that in patients with TIA and ischemic stroke CMIs represent a relevant portion of the total cerebrovascular lesion load and coexist with macroinfarcts. Although CMIs were only shown to have weak correlations with specific ICAS characteristics it may well be that larger studies will demonstrate that ICAS is a shared etiology between macroinfarcts and CMIs. These results shine new light on the spectrum of parenchymal damage caused by ICAS.

References. [1]Arenillas et al., Stroke, 2011; [2]Qureshi et al., Lancet, 2013; [3]Adams et al., Stroke, 1993; [4]Zheng et al., Stroke, 2013; [5]Longstreth et al., Alzheimer Dis Assoc Discord, 2009; [6]van der Kolk et al., Stroke, 2011; [7]Dieleman et al., Neurology, 2014

Detection of intracranial vessel wall lesions in an elderly asymptomatic population using 7T MRI

A.A. Harteveld[1], A.G. van der Kolk[1], H.B. van der Worp[2], N. Dieleman[1], F. Visser[1,3], P.R. Luijten[1], J.J.M. Zwanenburg[1,4], J. Hendrikse[1]

[1]Department of Radiology, University Medical Center, Utrecht, the Netherlands; [2]Department of Neurology and Neurosurgery, University Medical Center, Utrecht, the Netherlands; [3]Philips Healthcare, Best, the Netherlands; [4]Image Sciences Institute, University Medical Center Utrecht, Utrecht, Netherlands

Introduction: Intracranial atherosclerotic disease (ICAD) is one of the main causes of ischemic stroke and transient ischemic attack (TIA). Furthermore, the presence of ICAD has been associated with a higher recurrent stroke rate compared to the absence of ICAD.[1,2] Development of atherosclerotic lesions occurs silently over a long period, before they become symptomatic. Most studies have attempted to target ICAD when it is already symptomatic. Additional information regarding the prevalence of ICAD in the asymptomatic population would provide us with better insight in its development. Thus far, only transcranial Doppler has been used to assess the presence of ICAD in the asymptomatic population[3]; however, because of arterial remodeling, this technique may result in underdiagnosis of intracranial atherosclerosis. Previous studies have shown that high-resolution magnetic resonance imaging is able to reliably identify intracranial vessel wall abnormalities, even before causing luminal narrowing.[4] The aim of this study was to assess the presence of intracranial vessel wall lesions and enhancement in an asymptomatic population using intracranial vessel wall MR imaging at 7.0 tesla (7T).

Methods: This prospective study was approved by the institutional review board of our institution; all subjects provided written informed consent. Between November 2013 and August 2014, healthy volunteers aged > 60 years, without a history of cerebrovascular or ischemic heart disease, were included in this study. Imaging was performed on a 7T whole-body system (Philips Healthcare, Cleveland, OH, USA) with a 32-channel receive coil and volume transmit/receive coil for transmission (Nova Medical, Wilmington, MA, USA). The imaging protocol included a high-resolution (0.8 mm isotropic) transverse T_1-weighted magnetic preparation inversion recovery turbo spin echo (MPIR-TSE) intracranial vessel wall sequence[5] before and after contrast administration, and a 3-dimensional time-of-flight (TOF) MRA by means of a fast-field echo sequence. The following imaging parameters were used: MPIR-TSE sequence, field-of-view (FOV) 250x250x190 mm^3, acquired resolution 0.8x0.8x0.8 mm^3, TR/TI/TE 3952/1375/36 ms, and scan duration ≈11min; TOF-MRA sequence, FOV 190x190x102 mm^3 in transverse orientation, acquired resolution 0.4x0.5x0.6 mm^3, TR/TE 22/2.4 ms, flip angle 30 degrees, and scan duration ≈10min. Approximately 10 minutes before acquisition of the post-contrast MPIR-TSE sequence, 0.1mL/kg of a gadolinium-containing contrast agent (Gadobutrol, Gadovist 1.0mmol/mL, Bayer Schering Pharma, Newbury, UK) was administered. Image quality was scored with a five point scale (1=poor, 5 =excellent); volunteers with a score <3 were excluded. Two observers independently scored the vessel wall abnormalities and enhancement (location and type (concentric or eccentric, enhancing or non-enhancing)) in all the major artery segments of the circle of Willis (ACA: A1, A2 and ACoM; MCA: M1 and M2; ICA: distal part and bifurcation; PCA: P1, P2, bifurcation P1-P2 and PCoM; BA: bifurcation BA-P1, distal half, proximal half; VA: distal half, proximal half) on the MPIR-TSE scans according to the method previously described by Van der Kolk et al.[5] processing for assessment of the contrast enhancement was performed using MeVisLab (v2.6.1, MeVis Medical Solutions AG, Bremen, Germany). A consensus reading was performed with a third observer, in case of disagreement. The presence of stenosis was scored on the TOF-MRA sequence by one observer.

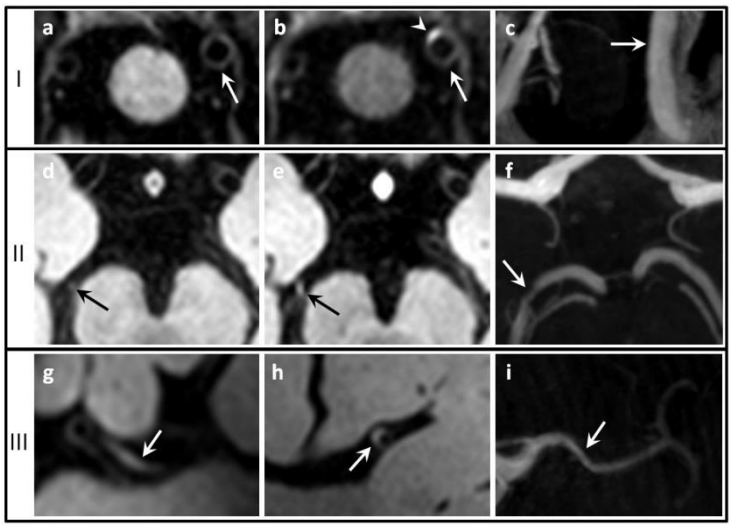

Figure 1. *Three examples of vessel wall lesions.* ***(I)*** *7T pre-contrast (a) and post-contrast (b) transverse MPIR-TSE images of the left proximal vertebral artery with concentric vessel wall thickening (arrow) and focal enhancement (arrowhead), and the corresponding location on the coronal TOF-MRA image(c).* ***(II)*** *7T pre-contrast (d) and post-contrast (e) transverse MPIR-TSE images of the right P2-segment with an eccentric vessel wall lesion (arrow) and focal enhancement, and the corresponding location on the transverse TOF-MRA image (f) showing a stenosis.* ***(III)*** *7T pre-contrast transverse (g) and sagittal (h) MPIR-TSE images of the left M1-segment with an eccentric vessel wall lesion (arrow) without enhancement, and the corresponding location on the transverse TOF-MRA image (i).*

Table 1. *Scoring of vessel wall lesions*

	Lesions	Thickening (#)		Enhancement	MRA-stenosis
	(#)	*eccentric*	*concentric*	(#)	(#)
Anterior circulation	**38**	**27**	**11**	**11**	**1**
ACA	*7*	*5*	*2*	*0*	*1*
MCA	*14*	*8*	*6*	*3*	*0*
ICA	*17*	*14*	*3*	*8*	*0*
Posterior circulation	**62**	**28**	**38**	**25**	**9**
PCA	*11*	*8*	*3*	*2*	*4*
BA	*13*	*6*	*7*	*2*	*0*
VA	*38*	*10*	*28*	*21*	*5*
Total	**100**	**51**	**49**	**36**	**10**

ACA: anterior cerebral artery; BA: basilar artery; ICA: internal carotid artery; MCA: middle cerebral artery; PCA: posterior cerebral artery; VA: vertebral artery.

Results: Twenty healthy volunteers (12 male; age 66 ± 4 years) were included in the current study. Imaging was successful in 17 subjects; three subjects with an image quality score of < 3 were excluded (the distal vertebral arteries were outside the sensitivity reach of the 7T MRI head coil in two subjects, and severe motion artifacts were present in one subject). Figure 1 shows different examples of vessel wall lesions with and without enhancement identified in the study population. Table 1 shows an overview of the number, location and thickening pattern of the identified vessel wall lesions in the main arteries of the circle of Willis, the number of lesions that showed enhancement, and the number of scored stenoses in the TOF-MRA scans. In total 100 intracranial vessel wall lesions were identified in all subjects (median per subject, 5; range, 2-11), of which 36 (36%) enhanced after contrast administration. 51 lesions (51%) were found to be eccentric, and 38 lesions were present in the anterior circulation. Enhancement of the lesions occurred more often in the vessel wall lesions of the posterior circulation (25/62, 40.3%) compared to the anterior circulation (12/38, 31.6%), however, this was not significant (χ^2(1.32), p>0.05). In the anterior circulation the ICA (distal part & bifurcation) showed the highest number of vessel wall lesions (17/38) as well as enhancements (8/11), and in the posterior circulation the vertebral arteries (38/62 vessel wall lesions, 21/25 enhancements). A total of 10 lesions in 6 subjects (35.3% of study population) showed a corresponding stenosis on the TOF-MRA images.

Discussion and conclusion: Intracranial vessel wall lesions were found in all elderly asymptomatic subjects. The total number of identified vessel wall lesions was high, especially for the posterior circulation and specifically the intracranial vertebral artery segments. Only 10% of the lesions showed a corresponding luminal stenosis on the TOF-MRA images. 36% of the detected lesions showed enhancement after contrast injection as an indication for the presence of vasa-vasorum or focal plaque inflammation. We hypothesize that with high resolution 7T MRI vessel wall imaging in asymptomatic patients small atherosclerotic lesions are detected at an early stage without luminal stenosis. Correlation of high resolution *in vivo* and *ex vivo* MRI with histopathology will be needed to validate these findings. In the future, early detection of intracranial atherosclerosis and quantification of the total burden of atherosclerosis may allow for monitoring of therapeutic interventions, proxy imaging outcomes for a faster evaluation of interventions, and provide better insight in the role of ICAD in the development of certain cerebrovascular diseases.

References: [1]Arenillas et al. Stroke 2011; [2]Qureshi et al. Lancet 2013; [3]López-Cancio et al. Atherosclerosis 2012; [4]Dieleman et al. Circulation 2014; [5]Van der Kolk et al. Stroke 2011

Oral presentations

Parallel session 1

Cancer
O001-O004

Spectroscopy
O005-O008

Parallel Session 2a

Neuro
O009-O011

Muscle
O012-O014

Parallel Session 2b

Perfusion
O015-O017

MR methods
O018-O020

Parallel Session 3

RF Engineering & **High Field**
O021-O026

Diffusion
O027-O032

Cancer

Moderators of Oral Session

Petra van Houdt

Department of Radiation Oncology, The Netherlands Cancer Institute, Amsterdam, the Netherlands

Benedicte Descamps

Infinity Lab University of Gent, Gent, Belgium

O001 **Klaassen Remy** - Correlating post-operative whole mount immunohistochemistry to functional MRI parameters in pancreatic cancer

Department of Medical Oncology, Academic Medical Center, Amsterdam, Netherlands

O002 **Sauwen Nicolas** - Hierarchical non-negative matrix factorization using multi-parametric MRI to assess tumor heterogeneity within gliomas

Department of Electrical Engineering (ESAT), KULeuven, iMinds Medical IT, Leuven, Belgium

O003 **Heethuis Sophie** - Potential of DCE-MRI for treatment response assessment in esophageal cancer

Department of Radiotherapy, University Medical Center Utrecht, Utrecht, Netherlands

O004 **Beld Ellis** - Localization of an HDR brachytherapy source using MR artifact simulation and phase-only cross correlation

Department of Radiotherapy, University Medical Center Utrecht, Utrecht, The Netherlands

Correlating post-operative whole mount immunohistochemistry to functional MRI parameters in pancreatic cancer

Remy Klaassen[1], Anne Steins[1], Oliver Gurney-Champion[2], Maarten Bijlsma[3], Hessel Wijkstra[4], Geertjan van Tienhoven[5], Marc Besselink[6], Johanna Wilmink[1], Mark van de Vijver[7], Jaap Stoker[2], Aart Nederveen[2], Hanneke van Laarhoven[1]

[1]Department of Medical Oncology, Academic Medical Center, Amsterdam, the Netherlands; [2]Department of Radiology, Academic Medical Center, Amsterdam, the Netherlands ; [3]Laboratory for Experimental Oncology and Radiobiology, Academic Medical Center, Amsterdam, the Netherlands [4]Department of Urology, Academic Medical Center, Amsterdam, the Netherlands; [5]Department of Radiation Oncology, Academic Medical Center, Amsterdam, the Netherlands; [6]Department of Surgery, Academic Medical Center, Amsterdam, the Netherlands; [7]Department of Pathology, Academic Medical Center, Amsterdam, the Netherlands

Target audience: Researchers and clinicians involved in (functional) MR imaging of pancreatic cancer.

Purpose: Despite advances in multimodality treatment options, pancreatic ductal adenocarcinoma still ranks 4th on the list of cancer-related deaths. Amongst other factors, therapy resistance is induced by the pancreatic tumor microenvironment which is characterized by an excess of stromal tissue, poor vascularization and consequently tumor hypoxia. Functional Magnetic Resonance Imaging (MRI) enables the non-invasive characterization of this tumor microenvironment. Using diffusion weighted imaging (DWI), water diffusivity can be used as measure for stromal deposition and dynamic contrast enhanced (DCE) MRI provides further insight on tumor vascularization. Although these sequences provide valuable information on macro scale, interpretation of the underlying biological processes is not unambiguous. Direct correlation of the MRI with immunohistochemical stainings for stromal deposition and vasculature would provide valuable insights how to interpret these data. However, tumor heterogeneity and scarcity of landmarks make correlation to small tissue biopsies challenging. In this study we therefore propose a method to directly project postoperative whole section tissue slices onto DWI and DCE MRI. We then use this method to correlate functional MRI parameters to local histology derived tissue characteristics.

Methods: Four patients (3 male, 1 female) with (borderline) resectable pancreatic adenocarcinoma were prospectively recruited for MR imaging. Patients were imaged directly before pylorus-preserving pancreaticoduodenectomy. Imaging was performed on a Philips Ingenia 3T MR scanner. DW-images were obtained under respiratory triggering using a single-shot echo-planar sequence: voxel size 3x3x3.7mm, 0.3mm slice gap, FOV 432x108x72mm, TE/TR 44/2300ms, BW 62.5Hz/voxel. We obtained 12 b-values (0, 10, 20, 30, 40, 50, 75, 100, 150, 250, 400 and 600 s/mm^2). Data was fitted with the intra voxel incoherent motion (IVIM) model to obtain f (perfusion fraction), D (diffusion coefficient) assuming a D^* (pseudo diffusion coefficient) of 0.0453mm^2/s.[1] The DCE protocol comprised a dynamic series consisting of a 3D FFE sequence with 30 slices; slice thickness 2.5mm (5mm non-interpolated), FOV 400x400mm, matrix size 160x160, TR/TE/FA 3.2/2.0ms/20° and a temporal resolution of 1.75s. 0.1mmol/kg of 1.0mmol/ml Gadovist® (Bayer) was administered 15s after start of the dynamic series at a rate of 5ml/s followed by a 15ml saline flush. Scanning was continued for 4.5min. Baseline T1 was measured before contrast administration by use of a Look Locker sequence. The arterial input function was automatically selected from the abdominal aorta and tissue concentration curves were fitted according to the extended Tofts model to retrieve K^{trans}-maps.[2] To minimize peristaltic movement during acquisition, 1ml of 20mg/ml Buscopan® (Boehringer Ingelheim) was administered twice; before start of the DWI and DCE acquisition. For anatomical correlation a mDIXON sequence was performed 35 seconds after injection of a second equivalent contrast bolus. All functional MRI data was projected on the mDIXON image by automated non-rigid image registration with the Elastix package, using mutual information.[3]

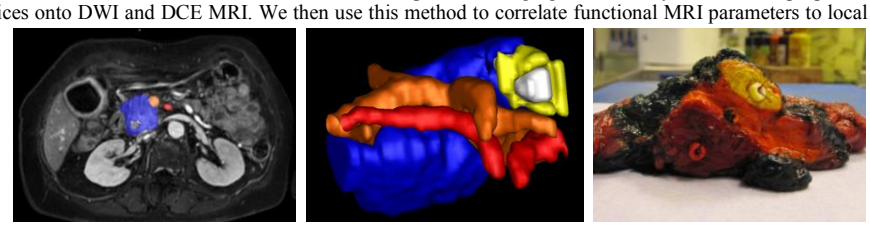

Figure 1 *Anatomical structures drawn on the MRI (left) showed good correlation with the tissue after resection (right) when rendered in 3D (middle). Blue: Pancreatic head, Yellow: pancreas dissection plane, Orange: mesenteric vein, Red: mesenteric artery, White: pancreatic duct.*

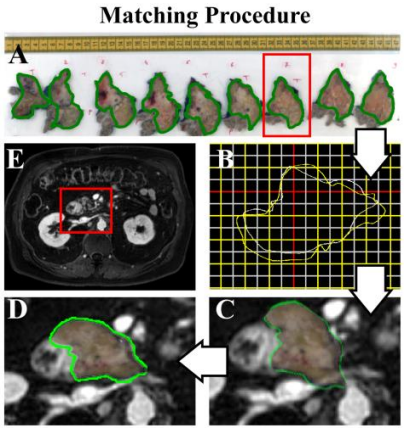

Figure 2 *Matching procedure: A. Tissue slices with drawn contours; B. Orientation of adjacent contours; C. Rotation and translation of tissue slice projected on MRI; D. Final match of tissue slice to MRI; E. Reference anatomical MRI*

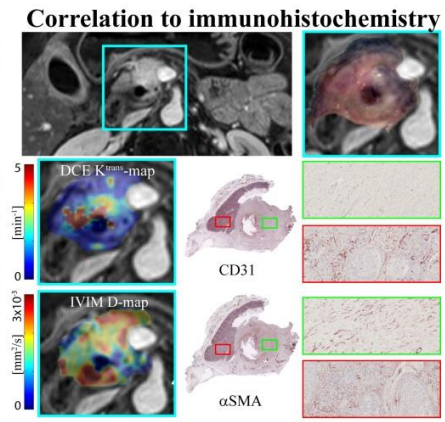

Figure 3 *Correlation of functional MRI to immunohistochemical stainings. Upper row: MRI with overlying tissue slice. Middle row: The area with high K^{trans} values shows an area with higher vessel density on CD31 staining (upper red box). Lower row: Low D-values are shown in an area with high stromal content on αSMA staining (lower green box).*

Pathology matching: After resection, the surgeon sutured colored beads to relevant anatomical structures (mesenteric vein and artery margins, bile and pancreatic duct) on the tissue specimen. Hereafter, the tissue was directly transferred to the pathology department where resection and dissection planes as well as the anatomical structures were inked by the pathologist (Figure 1). After 24 hours of fixation in formaldehyde, the tissue was sliced in the axial plane to retrieve ~5mm thick tissue slices. These slices were then numbered and photographed from both sides. One slice with evident tumor was selected for whole mount processing, embedding the complete tissue slice. Other tumor comprising slices were divided into standard pathology processing cubes (~2x2 cm). In this phase of the study all whole mount tissue slices were stained for stromal deposition (Smooth Muscle Actin (αSMA)) and vessels (CD31). On the photographed tissue slices the contour of the pancreas was manually outlined (Figure 2A). Next, contours of adjacent slices were aligned, so slight deviations between the orientations of the slices were corrected for (Figure 2B). The resulting outlined slices were stacked to form a three dimensional volume of the pancreas tissue specimen. This volume was then projected onto the anatomical MR-image (Figure 2C). Finally, the tissue volume was manually rotated and translated so anatomical structures matched corresponding features on the MRI (Figure 2D). Stained coupes were aligned with the corresponding tissue photograph and transposed to the MRI accordingly.

Results: Tissue specimens after resection showed good visual agreement when anatomical features were drawn on MRI (Figure 1). Based on corresponding anatomical structures, the post-operative tissue volume could be matched to the MRI in all 4 patients. Figure 3 shows a typical example of combined functional MRI parameters with tissue stainings. In this case, higher values on the K^{trans}-map corresponded with higher vessel density on the CD31 staining in a healthy part of the pancreas. Lower D-values were found in an area with higher stromal content on αSMA staining, corresponding with the tumor area.

Discussion & Conclusion: In this pilot study we showed the feasibility of matching post-operative axial tissue slices to in vivo MRI of the pancreas. Matching immunohistochemically stained whole mount tissue slices provides direct information on localization and local tumor heterogeneity for validation of functional MRI parameters. Expanding this work in a larger patient group will provide valuable insights on underlying biological processes of functional MRI parameters in pancreatic cancer.

References: 1. Le Bihan D et al., *Radiology.* 1988;168(2):497-505. 2. Tofts PS et al. *J. Magn. Reson Imaging*. 1999;10(3):223–32. 3. Klein S et al., *IEEE Trans. Med. Imaging* 2010;29(1):196–205.

Hierarchical non-negative matrix factorization using multi-parametric MRI to assess tumor heterogeneity within gliomas

Nicolas Sauwen[1], Diana Sima[1], Sofie Van Cauter[2], Jelle Veraart[3], Alexander Leemans[4], Uwe Himmelreich[5], Sabine Van Huffel[1]

[1]Department of Electrical Engineering (ESAT), KULeuven, iMinds Medical IT, Leuven, Belgium; [2]Department of Radiology, University Hospital, Leuven, Belgium; [3]iMinds-Vision Lab, University of Antwerp, Antwerp, Belgium; [4]Image Sciences Institute, University Medical Center Utrecht, Utrecht, Netherlands; [5]Imaging & Pathology (MoSAIC), KU Leuven, Belgium

Target audience: Clinicians and researchers interested in multi-parametric MRI (MP-MRI) for brain tumor diagnosis and follow-up.
Purpose: Advanced MR modalities such as Magnetic Resonance Spectroscopic Imaging (MRSI), perfusion-weighted MRI (PWI) and diffusion-weighted MRI (DWI) have shown their added value to non-invasively characterize brain tumors, detect full tumor extent and assess early success of therapy. Tissue characterization within gliomas is challenging due to the co-existence of several intra-tumoral tissue types within the same region and the high spatial heterogeneity in high-grade gliomas. Previous advanced MR studies have often simplified or neglected this aspect of tissue complexity. An accurate and reproducible method for brain tumor characterization and the detection of the relevant tumor substructures could be of great added value for the diagnosis, treatment planning and follow-up of individual patients.
Methods: ***Acquisition:*** 24 patients with primary glioma underwent MP-MRI, including conventional MRI (cMRI), PWI, MRSI and diffusion kurtosis imaging (DKI), (Philips Achieva 3T scanner). 11 patients were diagnosed with glioblastoma multiforme (GBM), 2 patients with anaplastic astrocytoma, 9 patients with a grade II glioma and 2 patients with grade I oligodendroglioma. cMRI consisted of T2 (TR/TE: 3000/80ms; slice/gap: 4/1 mm; turbo factor:10), T1 with contrast enhancement (TR/TE/TI: 9.7/4.6/900ms; flip angle: 8°; turbo field echo factor: 180) and FLAIR imaging (TR/TE/TI: 11000/120/2800 msec, slice/gap: 4/1 mm). Dynamic susceptibility contrast (DSC) MRI data were obtained using a gradient echo-EPI sequence (TR/TE: 1350/30ms; slice/gap: 3/0mm; 60 dynamic scans at 1s intervals). Cerebral blood volume (CBV) was calculated including leakage correction [1]. 2D-^{1}H MRSI was acquired with PRESS volume selection (TR/TE: 2000/35ms; section thickness: 10mm; receiver bandwidth: 2000Hz; samples: 2048; number of signal averages: 1; MOIST water suppression; pencil beam shimming; SENSE parallel imaging). AQSES-MRSI [2] was used for quantifying lipids (Lip), lactate (Lac), N-acetyl-aspartate (NAA), glutamine+glutamate (Glx), total creatine (Cre), total choline (Cho), myo-inositol (mI) and glycine (Gly). DKI was acquired using an EPI DWI sequence (b=0, 700, 1000 and 2800 in 10, 25, 40, and 75 uniformly distributed directions; TR/TE: 3200/90ms; d/D: 20/48.3ms; section thickness/gap: 2.5/0mm; SENSE parallel imaging). After motion and eddy current correction, diffusion and kurtosis tensors were estimated in each voxel using a constrained weighted linear least-squares algorithm [3]. Mean diffusivity (MD), fractional anisotropy (FA) and mean kurtosis (MK) maps were derived from the tensors. The diffusion maps were non-rigidly coregistered to the cMRI data to account for EPI distortion using ExploreDTI [4]. All other MR images were rigidly coregistered to the T1+contrast reference set using the normalized mutual information criterion. For MRSI, only one 2D slab was measured and only voxels within the MRSI region of interest could be analyzed.
hNMF analysis: Non-negative matrix factorization (NMF) approximately factorizes a matrix X into the product of a source matrix W and an abundance matrix H. The columns of W represent the sources and each column of H contains the abundance of the sources for one data point. In the case of our MP-MRI data, the rows of X represent the voxels and the columns represent the MP-MRI features. The sources correspond to different tissue types and each column of H contains the relative concentrations of the tissue types for one voxel. A hierarchical NMF (hNMF) algorithm was developed, consisting of 3 steps. In step1, 2-rank NMF is applied, resulting in a 'pathologic' and a 'normal' source and their abundance maps. In step2, NMF is applied to the pathologic and to the normal tissue region separately to find tissue-specific patterns. The sources are then re-combined in step3 using non-negative linear least squares fitting, to find the abundance maps. K-means clustering was applied to the abundance maps to obtain a tissue segmentation. Dice-scores were calculated with respect to a manual segmentation by a radiologist. Correlation coefficients were calculated between the pathologic tissue sources and the average feature vector within the corresponding tissue region. For the non-necrotic patients, Dice-scores and correlation coefficients were calculated for the whole tumor region, whereas for the GBM patients, validation scores are also reported for active tumor and necrosis separately. For comparison, the same hNMF analyses were also run when considering only cMRI data.
Results: Tables 1 and 2 report the Dice-scores and correlation coefficients for the non-necrotic patients and the GBM patients, respectively. Fig.1 shows some of the relevant MR parameters and the resulting abundance maps for active tumor and necrosis for a particular GBM patient.

		Dice-score tumor	Correlation coeff tumor
MP-MRI	Average	0.88	0.97
	Range	0.52 - 0.96	0.85 - 1
	Std dev	0.12	0.04
cMRI	Average	0.81	0.96
	Range	0.38 - 0.96	0.82 - 1
	Std dev	0.18	0.05

Table 1: Range, average and standard deviation of the Dice-scores and correlation coefficients of the non-necrotic patients for MP-MRI and cMRI only.

		Dice-score active tumor	Dice-score necrosis	Dice-score whole tumor	Correlation coeff active tumor	Correlation coeff necrosis
MP-MRI	Average	0.76	0.69	0.84	0.90	0.96
	Range	0.48 - 0.87	0.27 - 0.96	0.47 - 0.98	0.71 - 0.99	0.84 - 1
	Std dev	0.12	0.26	0.13	0.09	0.05
cMRI	Average	0.67	0.48	0.69	0.84	0.93
	Range	0.38 - 0.87	0.27 - 0.92	0.39 - 0.95	0.59 - 0.99	0.70 - 0.99
	Std dev	0.17	0.23	0.17	0.17	0.09

Table 2: Range, average and standard deviation of the Dice-scores and correlation coefficients for the GBM patients for MP-MRI and cMRI only.

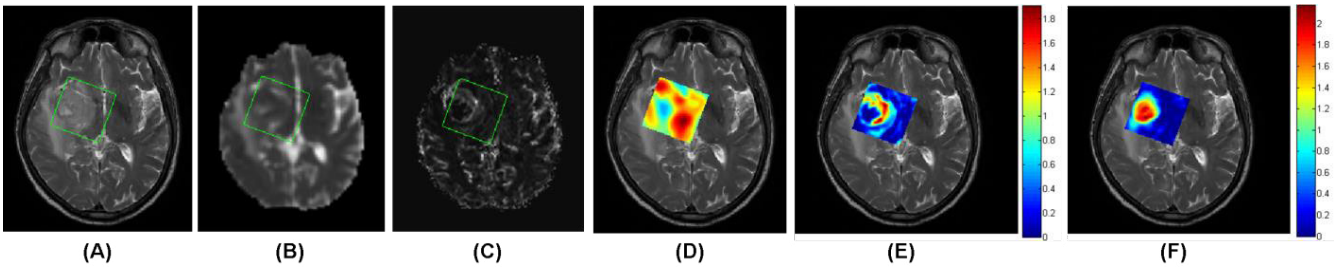

Fig.1: Coregistered MR parameter maps of different modalities for a GBM patient: T2 (A), MD (B), CBV (C) and Cre (D). The abundance maps after hNMF analysis are shown for active tumor (E) and necrosis (F).

Discussion: For MP-MRI, the average Dice-scores are higher than for state-of-the art supervised segmentation methods, which mostly use only cMRI data. For the non-necrotic tumors, the average Dice-score decreases by 7% when considering only cMRI data. For the GBM patients, a larger decrease in average Dice-scores is found: 9%, 21% and 15% for active tumor, necrosis and the whole tumor region, respectively. hNMF is therefore competitive as an unsupervised segmentation tool and the added value of using MP-MRI data has been shown. Average correlation coefficients are above 0.90 for MP-MRI, confirming that the sources can be considered as tissue-specific patterns. The hNMF method provides tissue characterization that goes beyond black-and-white segmentation. The abundance maps allow direct visual interpretation of the hNMF results, combining the information of all MP-MRI data into one map per tissue type. The relative contributions of different tissue types within the tumor region provide us with more insight in the tumor heterogeneity.
Conclusion: hNMF can be applied on a patient-by-patient basis, it does not require large training datasets nor data normalization and it provides a more refined tissue characterization compared to binary classification.
Acknowledgements: This work has been funded by: FWO G.0869.12N; IUAP P7/19/; FP7/2007-2013; EU MC ITN TRANSACT 2012 (n 316679).
References: [1] Boxerman JL, Schmainda KM, et al., AJNR Am. J. Neuroradiol. 2006;27:859–67. [2] Croitor Sava AR, Sima DM, et al., NMR Biomed. 2011;24:824–35. [3] Veraart J, Sijbers J, et al., NeuroImage 2013;81:335–346. [4] Leemans A, Jeurissen B, et al. Ann M Intl Soc Mag Reson Med. 2009; p. 3537.

Potential of DCE-MRI for treatment response assessment in esophageal cancer

Sophie Heethuis[1], Peter van Rossum[1], Irene Lips[1], Marco van Vulpen[1], Marielle Philippens[1], Jelle Ruurda[2], Gert Meijer[1], Jan Lagendijk[1], Astrid van Lier[1]

[1]Department of Radiotherapy, University Medical Center, Utrecht, Netherlands
[2]Department of Surgery, University Medical Center, Utrecht, the Netherlands

Purpose To investigate the potential of using dynamic contrast enhanced (DCE) MRI for the treatment response assessment of esophageal cancer.

Introduction In order to improve locoregional control and overall survival rates, neoadjuvant chemoradiotherapy (nCRT) is often used for the treatment of resectable esophageal cancer prior to surgery[1,2]. In 29% of the patients complete pathologic response (pCR) has been found[1]. If accurate prediction of treatment response is possible, surgery may potentially be omitted for this patient group. Changes in tumor microvasculature are reflected in DCE-MRI, which is therefore increasingly used in different sites in the body for response monitoring and prediction. In our institute the diagnostic potential of using DCE-MRI for treatment response assessment in esophageal cancer is investigated. For this purpose, semi-quantitative measures like area under the curve (AUC) are investigated during treatment.

Methods Twelve patients with biopsy proven esophageal cancer were included in this study. DCE-MRI studies were performed before treatment (pre), after 2 weeks of the start of nCRT (per) and 5 to 7 weeks after completion of nCRT, prior to surgery (post) (1.5T Philips Achieva, Best, the Netherlands). After resection pathologic assessment of the tumor regression grade (TRG) was performed following the Mandard score[3], a five point score for tumor regression. For analysis a distinction was made between a group of good responders (GR), defined as pCR (TRG 1) or near-pCR (TRG 2), and a group of poor responders (noGR) with TRG 3 or higher. **MRI protocol:** For the DCE-MRI studies 62 time frames were scanned with a resolution of 1.18x1.18x3 mm^3 and a temporal resolution of 3 s/frame (FFE T_1W, TR/TE = 3.43/1.526 ms, FA = 20°). A contrast agent (CA) was injected after the 10th time frame. Further a T_2W scan was acquired (MS-TSE, TR/TE = 1983/100 ms, resolution: 0.67x0.67x4 mm^3, with navigator). **Image processing:** To account for breathing motion within the DCE-MRI studies, registration was performed using rigid registration with a region of interest encompassing the tumor using the 41th time frame as reference image. **Analysis:** At every visit a clinician delineated the primary tumor on the T_2W image. This delineated volume was contracted with an isotropic margin of 2 mm to account for residual motion and partial volume effects. Within this contracted volume mean, median and 75th percentile (P75) of the AUC of the CA concentration was calculated. Here, the AUC was defined as the integral over the concentration curve over a period of 60 seconds after inflow of contrast agent, which was defined as the initial arterial CA increase.

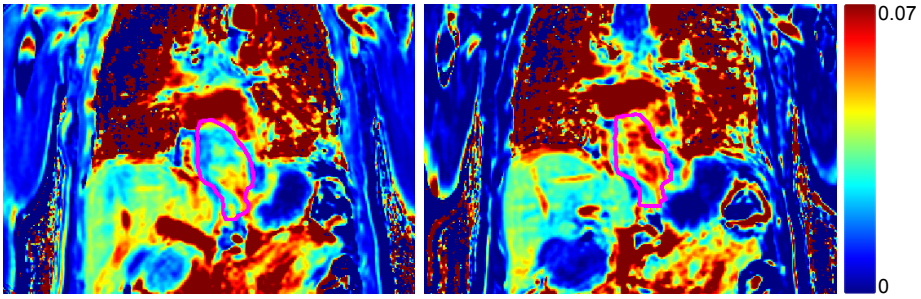

Figure 1: Coronal mean AUC maps of a poor responder, prior treatment (left) and during treatment (right). The tumor is delineated in pink in both maps. The color bar represents the accumulated concentration over a period of 60 seconds after inflow of contrast. Notice the increase in AUC in the tumor after 2 weeks of treatment.

Results and Discussion In 4 of the 12 patients pCR was found (33%) and a total of 5 patients (42%) showed a good response. Initial P75 AUC values were the same across GR and noGR. Relative changes in mean, median and P75 AUC between pre and per treatment were all found to be significant across the two groups. The same parameters comparing pre and post treatment were not found to be significant (table 1). All poor responders showed an increase in AUC comparing relative changes of per and pre treatment (fig. 1), while 80% of the good responders showed a decrease in AUC.
The relative change in P75 AUC pre-per treatment between good and poor responders was found to be the most predictive parameter (-5.7%±29.1% for GR [mean ± SD] vs. 76.2%±58.1% for noGR, p=0.005) (table 1 and fig 2). Using a cut-off value of 17.4% (horizontal grey line indicated in fig. 2) results in an area under the receiver operating characteristic (ROC) curve of 0.97, sensitivity of 80%, specificity of 100%, positive predictive value (PPV) of 100% and a negative predictive value (NPV) of 88%.

Table 1: Different AUC measures (only P75 values are reported [mean ± SD]) for both good responders (GR) and poor responders (noGR) and the corresponding p-value (Mann-Whitney U).

	GR (n=4)	noGR (n=7)	p-value
Initial P75 AUC	0.035 ± 0.024	0.038 ± 0.023	0.876
ΔP75 before-during (%)	-5.7 ± 29.1	76.2 ± 58.1	**0.005**
ΔP75 before-after (%)	-26.0 ± 46.1	15.3 ± 41.9	0.202

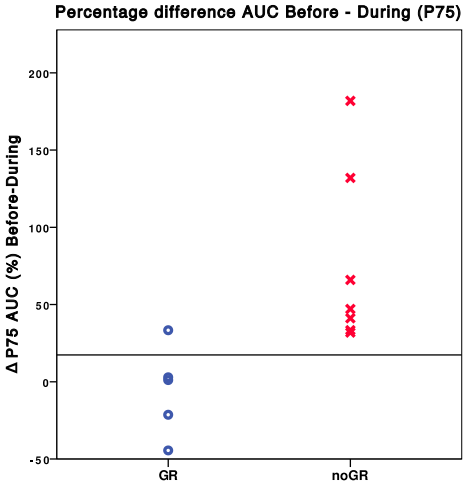

Figure 2: The relative changes in P75 AUC before and during treatment (pre-per) as a function of good or poor response. Each data point represents a patient. All poor responders (red cross) show an increase in ΔP75 AUC after 2 weeks of nCRT. A threshold line at 17.4% difference in the AUC is indicated.

Conclusion Semi-quantitative parameters from DCE-MRI studies of before and during treatment were used for treatment response prediction in patients with esophageal cancer. The change in P75 AUC after 2 weeks of nCRT compared to initial values reached high PPV and sensitivity. Although this is a limited number of patients, the use of P75 AUC for treatment response assessment, seems promising. In the future we will continue to include more patients to verify on a larger patient group whether DCE-MRI can be used as an accurate treatment response assessment for esophageal cancer.

References [1]Van Hagen et al., NEJM (2012) 366:2074, [2]Sjoquist et al. Lancet Oncol (2011) 12:681, [3]Mandard et al., Cancer (1994) 73:2680

Localization of an HDR brachytherapy source using MR artifact simulation and phase-only cross correlation

Ellis Beld[1], Marinus A. Moerland[1], Job G. Bouwman[2], Frank Zijlstra[2], Jan J.W. Lagendijk[1], Max A. Viergever[2], Peter R. Seevinck[2]

[1]Department of Radiotherapy, University Medical Center, Utrecht, the Netherlands
[2]Image Sciences Institute, University Medical Center Utrecht, Utrecht, the Netherlands

Purpose In high-dose-rate (HDR) prostate brachytherapy, needles and a high-intensity source of radiation are inserted into a tumor temporarily, to deliver a boost for focal primary or salvage treatment. Image guidance is of great importance (e.g. during needle positioning) for quality assurance and safety. MRI is the preferred imaging modality because of its excellent high soft tissue contrast. At our institution, a robotic MR-guided HDR brachytherapy procedure is being developed [1] and one of the aims is real-time tracking of the HDR source to accurately determine the positions where the dose is delivered. The materials used are primarily paramagnetic and/or conductive (e.g. titanium needles, an iridium source (Ir-192) in a steel capsule and a steel cable connecting the source to the afterloader), introducing several challenges. Firstly, the magnetic susceptibilities of these materials generate image artifacts through induced perturbations of the static B_0 field. Secondly, the steel cable may heat and experience forces due to RF pulses and gradient switching. The purpose was to investigate if an HDR source can be localized, and to what extent this depends on the materials used. This was done using gradient echo imaging in combination with artifact simulation and template matching. Simulations and experiments were performed with two types of needles (titanium and plastic) and two types of cables (steel and plastic) connected to the source.

Methods *Experimental set-up*: Measurements were done with a titanium and a plastic needle inserted into an agar phantom. Two dummy sources were constructed: one consisting of a solid steel capsule (radius: 0.45 mm, length: ~4.5 mm) welded to the distal end of a steel cable (radius: 0.45 mm) and one similarly sized steel capsule fixed in the tip of a plastic catheter. The dummy sources were brought into the needles, in the tip and at ~2 cm from the tip respectively. Measurements were done with the needles parallel to B_0 and under an angle (~20°). *Imaging parameters*: MR imaging was performed on a 1.5T MR scanner (Achieva, Philips Healthcare), using a 2D gradient echo sequence (TR/TE 9.3/3.5 ms, slice thickness 10 mm, FOV 160x160 mm, acq. matrix 160x160, flip angle 30°). *Simulations:* The geometries of the two sources and the steel cable were modeled as solid steel cylinders, on a cubic grid with voxel size 0.25^3 mm^3. The plastic cable was neglected. Since the susceptibilities of the objects were not exactly known, the susceptibility differences $\Delta\chi$ (between object and phantom) were chosen such that the simulated artifacts matched to the experimental artifacts. Forward calculations of the susceptibility induced field shifts were performed using a Fourier-based convolution method in combination with virtual zero-padding [2], at a voxel size of 0.25^3 mm^3. The influence of spatial encoding was neglected and the susceptibility induced field shifts were converted to the simulated complex MR signal. These signals were resampled to a grid with a larger voxel size of 1x1x10 mm (equal to experimental voxel size) by complex averaging, simultaneously taking dephasing into account. *Post-processing*: Phase-only cross correlation (POCC) was performed to determine the translation factor between the complex data of the experimental image $I_1(x,y)$ and the simulated image $I_2(x,y)$ containing the simulated object at its center [3]. The POCC is a normalized convolution, calculated as a multiplication in k-space: $POCC(x,y) = \mathrm{FFT}^{-1}\left[\left(I_1(k_x,k_y)\cdot I_2{}^*(k_x,k_y)\right)/\left(|I_1(k_x,k_y)\cdot I_2{}^*(k_x,k_y)|\right)\right]$. The location of the source in the experimental image followed from the coordinates of the maximum in the POCC image.

Results and discussion The $\Delta\chi$'s that were found to match the simulations to the experiments were: steel capsule connected to plastic cable: $\Delta\chi$=15.000 ppm; steel capsule connected to steel cable: $\Delta\chi$=6.700 ppm; and steel cable: $\Delta\chi$=7.200 ppm. The simulations strongly resembled the experimental data for both cases (with the source aligned with B_0 and under an angle) as shown in Fig. 1a and 1c respectively. POCC resulted in a high correlation at a single position (see Fig. 1b), providing the exact location of the source, irrespective of the presence of field distortions of the second dummy source and irrespective of the placement of the source in the needle (in tip or at ~2 cm from tip). However, validation of the position accuracy needs to be performed in the near future. The influence of the needles was small compared to the artifacts of the sources, rendering both the titanium and plastic needle suitable. Although localization of the sources was possible with both types of cables, the steel cable was less suitable for simulation, since the welding between the capsule and the cable makes accurate simulation of the artifact difficult. Moreover, when positioned at an angle with B_0, the steel cable induced large artifacts around the cable, hindering the ability to image surrounding tissue. Another important aspect is that the steel cable introduces safety concerns (risk of heating and torques). Altogether, these facts give preference to the use of a plastic drive wire.

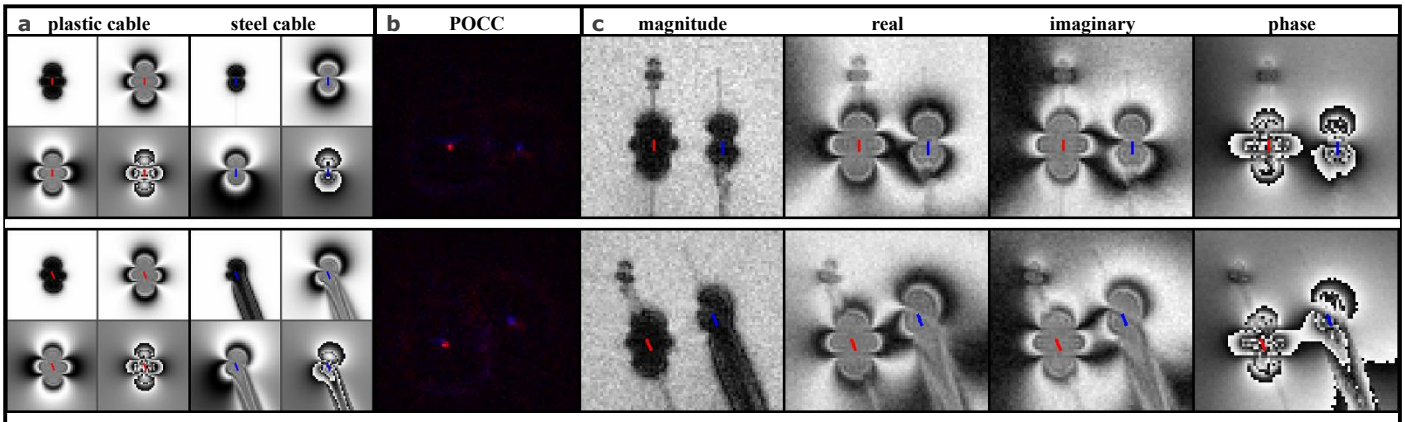

Fig 1. Example of a situation with the source with plastic cable in the titanium needle (left, indicated in red) and the source with steel cable in the plastic needle (right, indicated in blue), placed aligned with B_0 (top row) and under an angle (bottom row). ***a)*** *Simulated artifacts around the sources (magnitude, real, imaginary and phase images).* ***b)*** *The POCC's from both sources shown on top of each other (red: source with plastic cable; blue: source with steel cable).* ***c)*** *Experimental artifacts, with the positions of the sources that followed from POCC overlaid in red (plastic cable) and blue (steel cable) on the images.*

Conclusion Accurate determination of the position of an HDR source can be done retrospectively, by simulating its artifact in a gradient echo image and matching the simulated artifact to the experimental data by means of POCC. Besides, it can be concluded that it would be favorable to develop a plastic drive wire (suitable for use in an afterloader) that connects the source to the afterloader, in order to make the HDR brachytherapy treatment more appropriate for use inside the MR scanner.

References 1)Van den Bosch M.R. et al., Phys. Med. Biol. 2010; 55:N133-40. 2)Bouwman J.G. et al., MRM 2012; 68:621-30. 3)De Oliveira et al., MRM 2008; 59:1043-50.

Spectroscopy

Moderators of Oral Session

Marnix Maas

Radboud University Medical Center, Nijmegen, the Netherlands

Firat Kara

Bio-Imaging Lab, Antwerp, Belgium

O005 **Ece Ercan** - Can Diffusion Weighted Spectroscopy in brain white matter become a viable clinical tool?

C.J. Gorter Center for High Field MRI, Department of Radiology, University Medical Center Leiden, the Netherlands

O006 **Lotte Houtepen** - The effect of software processing pipelines on 7T MRS metabolite quantification

Department of Psychiatry, University Medical Center, Utrecht, the Netherlands

O007 **Ronald Zielman** - Elevated glutamate concentrations in the visual cortex of migraine without aura detected at 7 Tesla

Department of Neurology, Leiden University Medical Centre, Leiden, the Netherlands

O008 **Desiree Abdurrachim** - Cardiac metabolic adaptations in diabetic mice protect the heart from pressure overload-induced failure: a combined in vivo MRI, MRS, and PET approach

Department of Biomedical NMR, Eindhoven University of Technology, Eindhoven, the Netherlands

Can Diffusion Weighted Spectroscopy (DWS) in brain white matter become a viable clinical tool?

Ercan Ece, Emily Wood[2], Andrew Webb[1], Daniel Reich[2], Itamar Ronen[1]

[1]C. J. Gorter Center for High Field MRI, Department of Radiology, Leiden University Medical Center, Leiden, the Netherlands
[2]NeuroImmunology Branch (NINDS), National Institutes of Health, Bethesda, United States

Target Audience: Clinicians and researchers interested in studying tissue microstructure with diffusion weighted spectroscopy (DWS).

Purpose: DWS assesses the diffusion properties of intracellular metabolites such as total N-acetylaspartate (tNAA), creatine and choline compounds.[1] Compartmental localization of these metabolites means that diffusion metrics can reflect cell-type specific structure and physiology. For example the diffusion properties of tNAA have been shown to be sensitive to intraneuronal/axonal damage in a variety of pathologies, such as stroke,[2-3] tumor[3] and multiple sclerosis,[4] giving rise to changes of 30%-50% in diffusion properties of tNAA. In order to assess the diagnostic utility of DWS, the robustness and reproducibility of the technique need to be established. In this study, we have investigated the inter- and intra-subject variability of the diffusion properties of tNAA in the human corpus callosum (CC). Subsequently, we used a jackknife-like resampling approach to explore the variance of these properties in data subsets reflecting different total scan duration as well as different choices of b-values. In this fashion, we aimed to validate the DWS method for clinical studies and to help experimenters choose the optimal combination of scan parameters within the limitations of hardware and available scan time.

Methods: 6 healthy volunteers (3 men 3 women, ages 34±8 years) without known neurological abnormalities were scanned in 5 separate sessions:3 on a 3T Philips Achieva with an 8-channel head coil: 3 on a 7T Philips Achieva with a 32-channel head coil. *Data Acquisition:* The scan protocol consisted of a 3D T_1-w image (res≈1x1x1mm^3), DTI (res≈2×2×2mm^3, b=0 image, 32 DW images with b=800s/mm^2 at 3T and 15 DW images with b=1000s/mm^2 at 7T) followed by a single volume DWS scan planned on the anterior body of the CC (Fig.1). For DWS scans, PRESS with bipolar diffusion gradients was applied with 7 b-values in 2 directions: along the RL of the VOI (b=191-3050s/mm^2 at 3T and b=80-3905s/mm^2 at 7T) and perpendicular to the CC fibers (b=381-6101 s/mm^2 at 3T and b=160-7811s/mm^2 at 7T). DWS scan parameters for 3T: VOI=3.6mm^3, TR/TE: 2 cardiac cycles/110ms, spectral width=1.5kHz, 1024 sample points, 72 spectra per diffusion condition. DWS at 7T: VOI=3mm^3, TR/TE: 3 cardiac cycles/121ms, spectral width=3kHz, 1024 sample points, 40 spectra per diffusion condition. *Data Analysis:* DWS data were analyzed with custom MATLAB routines in which eddy-current, phase and frequency-drift corrections were performed. Averaged spectra were subsequently analyzed with LCModel.[5] tNAA estimates at each diffusion condition were used to calculate parallel diffusivity (D_{par}, sensitive mostly to properties of the intra-axonal medium, e.g. tortuosity) (Fig.1 panel d) and perpendicular diffusivity (D_{perp}, mostly sensitive to e.g. axonal diameter) (Fig.1 panel b) from the monoexponential decay of the signal as a function of b-value in each direction. The empirical diffusion coefficient (D_{avg}) was calculated based on the average of these two diffusivity coefficients. Cytosolic diffusion coefficient (D_{model}) was derived through a modeling routine, which accounts for the macroscopic curvature of the fiber tract within the VOI.[6] *Variability Analysis:* For inter-subject and across-session variability analysis, the entire data set from each session was used. Subsequently, a jackknife-like subsampling procedure was applied to data from all 5 sessions from two participants, one from each scanner. Within-session subsets of these data sets were randomly resampled without replacement prior to averaging. These averaged spectra were then used to calculate D_{par}, D_{perp}, D_{avg} and D_{model} for increasing number of signal averages. To investigate the effect of the choice of b-values on the variance of D_{avg} and D_{model}, these measures were calculated for various selections of b-values, shown in Fig.3, where 1 corresponds to the lowest b-value per direction.

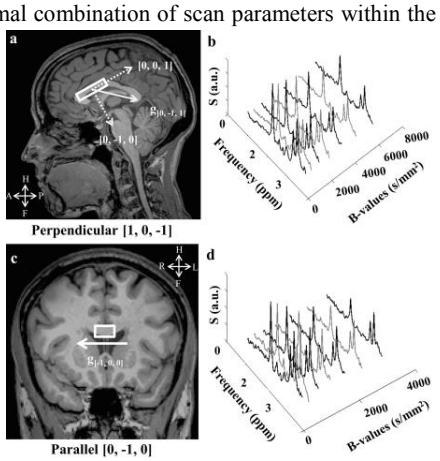

Fig.1 Planning of the VOI with perpendicular (a) and parallel (c) gradient directions. Spectra shown as a function of b-value for perp (b) and par (d) gradient directions at 3T.

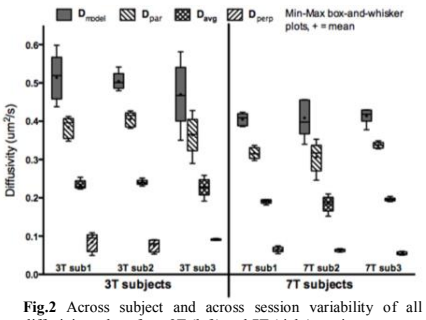

Fig.2 Across subject and across session variability of all diffusivity values from 3T (left) and 7T (right) sessions.

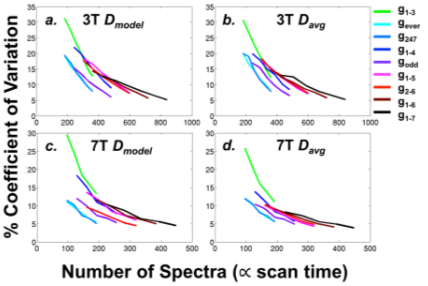

Fig.3 The coefficient of variation of D_{model} (panels a,c) and D_{avg} (panels b,d) for different b-value combinations, determined by the gradient strength g, shown as a function of number of co-added spectra

Results and Discussion: Cramér–Rao lower bounds for the tNAA peak from all spectra were between 6% and 20% at 3T and between 3% and 14% at 7T. Fig. 2 shows inter-subject and across-session variability for all participants. No significant differences in D_{par}, D_{perp}, D_{avg} and D_{model} were observed between subjects at the same field strength when one-way ANOVA with multiple comparisons was applied to the data. This, taken with the low across-session variability at 7T (average coefficient of variation 6%-8% for all measures) indicates good reproducibility of the method at 7T. At 3T, the average across-session coefficient of variation was somewhat higher (6%-11% for D_{par}, D_{avg} and D_{model} and 17% for D_{perp}). tNAA diffusivity values between patients and control in the literature[2-4] were typically substantially higher than the standard deviation in tNAA measures on both scanners, suggesting good reliability of DWS for case-control studies in both field strengths. The standard deviations of D_{avg} and D_{model} critically rely on the choice of b-values for the experiment. Fig. 3 shows the coefficient of variation (C_v) for different b-value schemes. The C_v decreases when sampling a wide b-value range. This implies DWS experiments can be performed within clinically relevant scan times (in our example, ~10 minutes for the g_{247} combination at 7T) while retaining low variance (~5%), by using a proper combination of low and high b-values.

Conclusion: Here we have shown the reproducibility of the diffusivity measures obtained through DWS experiments. Statistical assessment of the intra-subject variability shows the importance of using higher b-values for getting robust DWS measurements. Our results suggest that by choosing a combination of low and very high b-values, one can use a low number of b-values acquired and get robust results while keeping acquisition time short. **References: 1.** Nikolay, K. et al. NMR Biomed (2001) **2.** Zheng, D. et al. AJNR Am J Neuroradiol (2012) **3.** Harada et al. NMR Biomed. (2002) **4.**Wood, E.T. et al. J Neuroscience (2012) **5.** Provencher, S. MRM (1993) **6.** Ronen, I. et al. Brain Struct Funct (2013).

The effect of software processing pipelines on 7T MRS metabolite quantification

Houtepen Lotte[1], Remmelt Schür[1], Vincent Boer[2], Bart Van de Bank[3], Tom Scheenen[3], Anouk Marsman[4], Christiaan Vinkers[1], Dennis Klomp[2]

[1]Department of Psychiatry, University Medical Center, Utrecht, the Netherlands; [2]Department of Radiology, University Medical Center, Utrecht, the Netherlands; [3]Department of Radiology and Nuclear Medicine, Radboud University Nijmegen Medical Center Nijmegen, Netherlands; [4]Russell H. Morgan Department of Radiology and Radiological Science, Johns Hopkins University School of Medicine, Baltimore, United States

Introduction: 1H Magnetic resonance spectroscopy (MRS) can be used to quantify in vivo differences in brain metabolites using a linear combination of model spectra. Commercial, academic and freeware software packages are available which are based on the same model spectra, but use different implementation strategies involving a set of additional parameters that may vary between the tools or sites. Currently, it is not known to what extent the analysis pipeline used to process the MRS data affects the outcomes. To investigate whether metabolite levels of identical MRS scans are influenced by the applied software, we compared two software packages LCModel (Provencher, CA, USA)[1] and NMRWizard, a similar linear combination of model signals software implemented in Matlab[2].

Methods: 46 scans were collected in 23 healthy subjects during two different scan sessions on the same day. 1H-MRS experiments were performed using a semi LASER sequence(TE=30ms, TR=6s, 32Avg, no OVS) on the same 7Tesla whole body MR system (Philiphs,Cleveland,OH,USA). A birdcage transmit head coil was used and driven in dual transmit in combination with a 32 channel receive coil (both Nova Medical, INd., Burlington, MA,USA). Voxels(2x2x2cm^3) were located in the medial prefrontal cortex voxel. Non water suppressed spectra were obtained in order to calculate absolute concentrations of metabolites. Spectral fitting was performed with LCModel and NMRWizard using basissets simulated for the semi LASER sequence. One of the main differences between the two packages was that LCModel used a polynomial order baseline versus no baseline in NMRWizard. To illustrate the impact of the software pipeline, in this study we only report the correlation between the LCModel and NMR wizard of the highest and least overlapping resonances: total NAA, glutamate, total creatine and glutamate concentrations using Spearman regression modelling (R version 3.1.0).

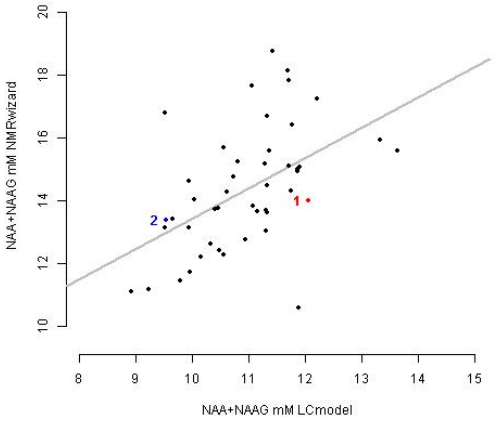

Figure 1 Comparison of the NMRwizard versus LCModel NAA concentration for all 46 scans. The grey line denotes the correlation. The fits of the two labeled scans are displayed in figure 2.

Results and discussion: Correlation (rho) ranged between 0.20 for glutamate (p=0.16) to 0.53 for total NAA (p<0.001, see figure 1). These analyses show a discrepancy between the measured metabolite concentrations between LCModel and NMRWizard, even though the fits are of similar quality (figure 2).This indicates that the processing steps used in the analysis pipeline have a major effect on the measured outcomes. While the origin of the discrepancy can be caused by the many variables included in the fits as well as processing parameters[3], we also expect differences to derive from the polynomial baseline used by LCModel, as this can vary between subjects (see figure 2B+2D).

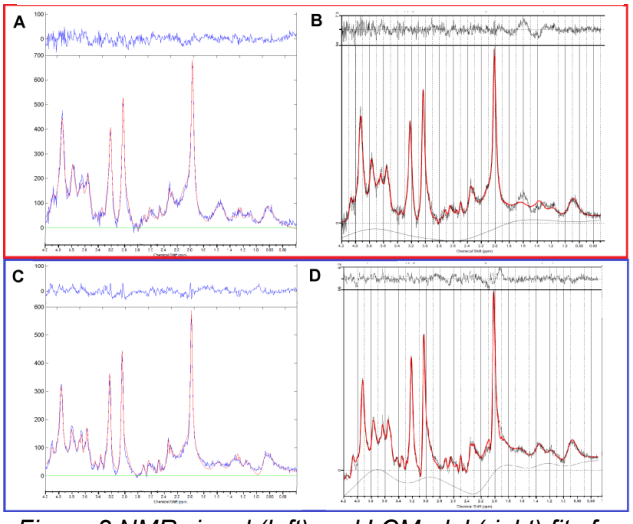

Figure 2 NMRwizard (left) and LCModel (right) fits for two selected subjects.

Conclusion: While absolute quantification of metabolites with ^{1}H-MRS would facilitate group comparisons, it must be realized that the values obtained through model fitting are severely biased by the parameters used. Even accurate fits and low CRLB does not imply accurate quantification. In this work we demonstrated that even for the most prominent signals in MRS obtained at 7T, still a systemic difference and a standard deviation of 20% is obtained by comparing two fitting settings on the same data.

References:

1. Provencher SW. *Estimation of metabolite concentrations from localized in vivo proton NMR spectra.* Magn Reson Med 1993;30(6):672-679.
2. De Graaf R.A. *NMR Processing Software for Spectroscopy, Imaging and Spectroscopic imaging.* 1999.
3. Van de Bank B. et al. *Multi-center Reproducibility of Short Echo Time Single Voxel 1H MRS of the Human Brain at 7T With Adiabatic Slice-Selective Refocusing Pulses*. 2013 ISMRM Salt Lake City USA, abstract.

Elevated glutamate concentrations in the visual cortex of migraine without aura detected at 7 Tesla

Ronald Zielman[1], J.P. Wijnen[2], G.L.J. Onderwater[1], A. Webb[3], G.M. Terwindt[1], M.D., Ferrari[1], H.E. Kan[3], M.C. Kruit[3]

[1]Department of Neurology, Leiden University Medical Centre, Leiden, the Netherlands
[2]Department of Radiology, University Medical Center, Utrecht, the Netherlands
[3]Department of Radiology, Leiden University Medical Center, Leiden, the Netherlands

Introduction: Migraine is a common, multifactorial, neurovascular disorder. The glutamatergic system is one of the pathogenetic factors. Glutamate is the main excitatory neurotransmitter of the CNS and is synthesized in neurons from glutamine and stored in synaptic vesicles.[1,2] Elevated glutamate concentrations are linked to migraine aura, trigeminovascular activation and central sensitization, mechanisms important in migraine pathophysiology.[1,3,4] The aim was to compare the glutamate concentrations in the visual cortex of interictal (between attacks) migraine patients with and without aura and age and gender matched healthy controls. As separation of glutamate and glutamine is challenging at lower field strengths, we performed this study at 7T.

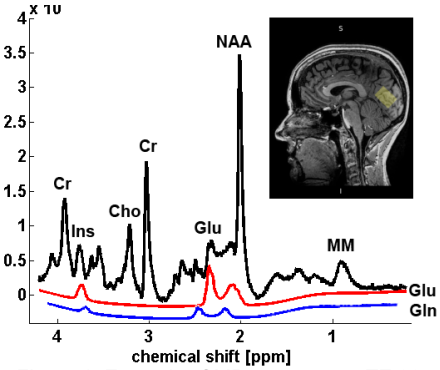

Figure 1: Example of MR spectrum at TE 30ms. The individual fit of Glu (red) and Gln (blue) is shown below the spectrum. The voxel position is displayed in the inset figure (3x2x2 cm^3).

Methods: Migraine patients with and without aura, and age and gender matched healthy control subjects were recruited. Patients were free of a migraine attack at least 3 days before the MRS scan. Patients were classified as strict interictal if they had no migraine attacks until 2 days after the examination and as pre-ictal if they had an attack within 2 days after examination. ***Acquisition:*** Participants were examined at a 7T MR system (Phillips, Cleveland, USA) using a 32 channel Rx and quadrature Tx coil driven by 2 amplifiers with fixed phase (2 times 4 kW) to reach local B_1 of 20uT. A 3D T1 weighted scan was used for voxel planning and voxel segmentation. Water suppressed (VAPOR) MR spectra in the visual cortex were acquired (12 cm^3) with a semi-LASER sequence. A B_0 map was used to optimize up to 2nd order shim gradients for each voxel position. TR/TE was 5000/30 ms, NSA was 32. A water reference scan of each measurement was used (no RF in VAPOR sequence) to correct for receive sensitivity of the coil, eddy current correction and quantification.
Data analysis: MR spectra were analyzed with LCModel[5] using a basis set of 22 metabolites and a measured macromolecular profile (Figure 1). The fraction of GM, WM and CSF within the MRS voxel was calculated (Matlab, Mathworks, Inc.). The metabolite levels were corrected for water fraction, water T1 and T2 relaxation and metabolite T2 relaxation using relaxation values from the literature.[6-9]
Statistical analysis was done in SPSS (IBM, Inc). Differences in glutamate concentrations between three groups were evaluated with ANCOVA with the fraction of GM in the voxel as covariate. Post-hoc pairwise comparisons were done with Bonferroni correction to adjust for multiple comparisons.

Results: We included 36 migraine without aura patients (age 35 ± 8, 47% male, 27 strict interictal, 11 pre-ictal), 27 migraine with aura patients (age 35 ± 9, 48% male, 23 strict interictal, 4 pre-ictal), and 24 healthy controls (age 34 ± 9, 52% male). Average migraine attack frequency was 2.7 ± 2.0 per month.
Glutamate concentration correlated with the GM fraction in the voxel (Pearson's $r(87)=0.51$, $p<0.001$), therefore the GM fraction was taken as covariate.
In the primary analysis with strict interictal migraine groups and healthy controls there was a difference in glutamate concentration between the groups ($F(2,70)=3.20$, $p=0.047$), with higher concentrations in migraine without aura (mean 7.02 ± 0.50 mM) compared to healthy controls (mean 6.40 ± 0.78 mM, $p=0.042$; Figure 2), with a fold-change of 1.06 after correction for GM fraction. No differences were found for migraine with aura. There was no difference in glutamate concentration between strict interictal migraine patients and pre-ictal migraine patients ($F(1,84)=1.96$, $p=0.16$), and no correlation between glutamate concentration and the time (days) until a next attack (Pearson's $r(36)=-0.18$, $p=0.29$). Pooling both interictal and pre-ictal migraine patients in a secondary analysis also showed higher concentrations in migraine without aura (mean 7.08 ± 0.56 mM) compared to controls (mean 6.40 ± 0.78, $p=0.006$), with a fold-change of 1.07 after correction for GM fraction, but no differences for migraine with aura.

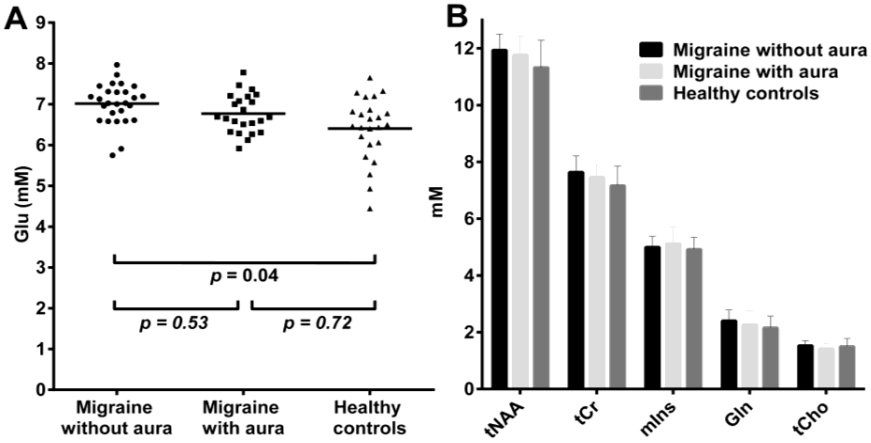

Figure 2: Comparison of strict interictal metabolite concentration between migraine without (n=27) and with aura (n=23), and healthy controls (n=24). A) Significant differences in Glu concentrations (with Bonferroni correction); B) No significant differences for other metabolites.

Discussion and conclusion: The overall CRLB's of Glu and Gln were 2.8 ± 0.95 and 8.8 ± 2.7 respectively and there were no differences between groups in linewidth, SNR or CRLB's of metabolites, indicating that at ultra-high field, glutamate and glutamine concentrations can be assessed individually. Our results support the concept that the glutamatergic system is involved in migraine. We found that glutamate concentrations in the visual cortex are higher in interictal migraine without aura patients compared to healthy controls, but not higher in migraine with aura patients. The difference is small; however, as glutamate is tightly regulated in the brain large differences are not expected. We found no relation between glutamate and the time until a next attack. The higher glutamate concentration in migraine without aura is more likely a disease trait than a reflection of a disease state (e.g. interictal, or pre-ictal). Future studies should investigate the role of glutamate in migraine in more detail, for example during different phases of a migraine attack with the focus on glutamate dynamics to learn more about the functional role of the glutamatergic system in migraine pathophysiology. Further focus on the pre-aura- and aura-phase of a migraine attack might explain why the current study unexpectedly failed to identify significant differences for the migraine with aura group.

References: *[1] Gasparini CF, 2013, IJBS 9 [2] Mckenna MC, 2007, Fates of Glutamate in Brain. [3] Scheller D, 2000, Amino Acids 19 [4] Ramadan N, 2003, CSN Spectro 8 [5] Provencher SW, 1993, MRM 30 [6] Rooney WC, 2007 [7] Bartha R, 2002, MRM 47 [8] Otazo, 2006 [9] Marjanska M, 2012, NBM* 25

Cardiac metabolic adaptations in diabetic mice protect the heart from pressure overload-induced failure: a combined in vivo MRI, MRS, and PET

Desiree Abdurrachim[1], Miranda Nabben[1], Verena Hoerr[2], Michael T. Kuhlmann[3], Philipp R. Bovenkamp[2], Michael Schäfers[3], Klaas Nicolay[1], Cornelius Faber[2], Sven Hermann[3], Jeanine J. Prompers[1]

[1]Department of Biomedical NMR, Eindhoven University of Technology, Eindhoven, the Netherlands
[2]Department of Clinical Radiology, University Hospital of Münster, Münster, Germany
[3]European Institute for Molecular Imaging-EIMI, Münster, Germany

TARGET AUDIENCE: Researchers interested in diabetes and heart failure

PURPOSE: Diabetes patients have a high risk for cardiovascular diseases. Metabolic adaptations in the diabetic heart are proposed as an important contributor to the development of heart failure in diabetes patients. However, data in this field largely originates from *ex vivo* rodent or cross-sectional human studies, which do not allow studying the time course of changes in cardiac metabolism in relation to the decline in cardiac function. We aim to investigate to what extent changes in cardiac metabolic flexibility, lipid accumulation, and energy status predict the longitudinal development of heart failure in non-diabetic and diabetic mice.

METHODS: ***Animals.*** Pressure overload heart failure was induced in non-diabetic db/+ and diabetic db/db C57BL/KsJ mice (n=3-10 per group) via transverse aortic constriction (TAC) surgery. Cine MRI, ^{1}H MRS, ^{31}P MRS, and PET were performed at baseline, and at 1, 5, and 12 weeks (wk) after TAC.
MRI/MRS. All measurements were performed using cardiac triggering and respiratory gating, on a 9.4T horizontal bore MR scanner (Bruker Biospin). For MRI and ^{1}H MRS, a 35-mm quadrature birdcage coil (Bruker Biospin) was used. For ^{31}P MRS, a 54-mm linear birdcage coil (Rapid Biomedical) and an actively decoupled surface coil with a diameter of 15 mm were used for transmission and reception, respectively.
Cine MRI. FLASH sequence was used to acquire cine images for 5-6 contiguous short axis and 2 long axis slices (thickness: 1 mm). TR/TE: 7/1.8 ms, α: 15°, matrix: 192x192, FOV: 30x30 mm^2, frames/cardiac cycle: 15-18, NSA: 6. Left ventricular (LV) lumen was semi-automatically segmented using CAAS MRV 2.0 (Pie Medical) to calculate LV mass and ejection fraction (EF).
^{1}H MRS. Localized ^{1}H MR spectra were acquired during diastole in the interventricular septum (1×2×2 mm^3 voxel) using the PRESS sequence, with CHESS water suppression, as described previously[(1)]. TR: ~2s, TE: 9.1ms, 0.41 ms 90º Hermite-shaped pulse, 0.9 ms 180º Mao-type pulses, 256 scans. Spectral analysis was performed using AMARES in jMRUI. Cardiac lipid levels were calculated from the lipid-CH_2 signal relative to the unsuppressed water peak.
^{31}P MRS. ^{31}P MRS was performed using the image selected *in vivo* spectroscopy (ISIS) sequence on a voxel of typically ~6×6×6 mm^3 covering the left ventricle, at the end of diastolic phase, as described previously[(2)]. TR: ~2s, 1.2 ms sinc-shaped excitation pulse, 6.25 ms adiabatic hyperbolic secant inversion pulses, 96 ISIS cycles (768 scans). Localized shimming was performed on the ^{1}H signal using an 11x11x11 mm^3 PRESS voxel covering the sensitive area of the surface coil. Cardiac energy status was calculated as the PCr/γ-ATP ratio, corrected for T_1 partial saturation.
^{18}F-FDG PET. To measure myocardial glucose uptake, PET (quadHIDAC; Oxford Positron System) was performed after a 12-13 hour overnight fast. The acquisition was performed for 15 minutes, at one hour after the fluorodeoxyglucose (FDG) injection (~10 MBq). Data was reconstructed into an image volume of 110×60×20 mm^3 and a voxel size of 0.4×0.4×0.4 mm^3, using a resolution recovery reconstruction algorithm[(3)] leading to an effective resolution of 0.7 mm. Quantification of segmental tracer uptake and volumes of the left ventricle were performed using an automated 3D contour detection algorithm developed in-house.
Statistical analysis. All data are presented as means ± standard deviation. Statistical analysis was performed using a two-way ANOVA (SPSS Inc), with Bonferroni-corrected post-hoc tests. Statistical significance was set at P<0.05.

RESULTS: ***Non-diabetic mice:*** In non-diabetic mice, TAC induced progressive LV hypertrophy (Fig. 1A) and dysfunction (Fig. 1B), which correlated with myocardial FDG uptake (P<0.001). Myocardial FDG uptake was increased at 1 and 5 wk post TAC, but tended to decrease again at 12 wk post TAC (Fig. 1C; Fig. 2). The decrease in FDG uptake at 12 wk post TAC was associated with a trend for lowered cardiac energy status (Fig. 1D). Myocardial lipids were not affected by TAC. ***Diabetic mice:*** At baseline, diabetic mice had lower myocardial FDG uptake (Fig. 1C), higher myocardial lipid content, and lower myocardial cardiac energy status (Fig. 1D; Fig. 3A-B), but normal cardiac function (Fig. 1B) as compared with non-diabetic mice. Surprisingly, in diabetic mice the effects of TAC on LV mass and function were much less prominent than in non-diabetic mice (Fig. 1A-B). Also in diabetic mice, myocardial FDG uptake increased upon TAC, but it remained lower than in non-diabetic mice (Fig. 1C). Myocardial lipid content and cardiac energy status in diabetic mice (Fig. 1D) were not affected by TAC.

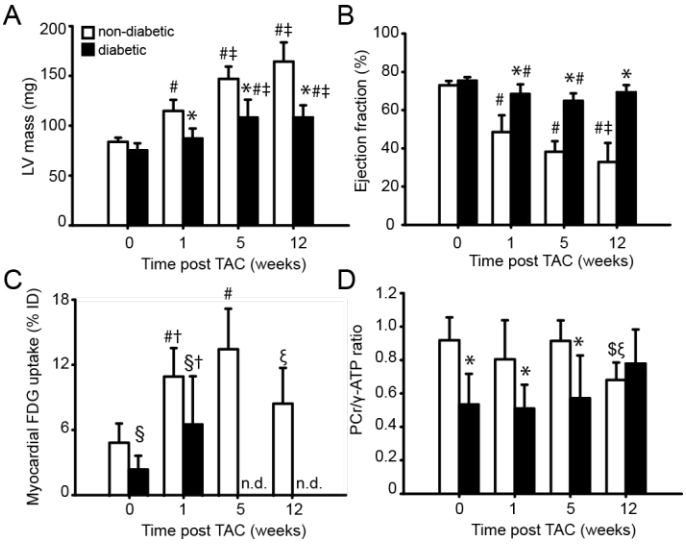

Figure 1. (A) LV mass, (B) ejection fraction, (C) myocardial FDG uptake, and (D) PCr/γ-ATP at baseline, and 1, 5, and 12 wk post TAC. *P<0.05 vs. non-diabetic mice at the same time point, §P<0.05 vs. non-diabetic mice independent of time. †P<0.05 vs. baseline independent of genotype. For the same genotype: #P<0.05 vs. baseline, ‡P<0.05 vs. 1 week post, ^P<0.05 vs. 5 wk post, $P<0.10 vs. baseline, ξP<0.10 vs. 5 wk post TAC. n.d.: data not available.

DISCUSSION & CONCLUSION: This study presents the first longitudinal *in vivo* data of cardiac metabolic, energetic, and functional adaptations during heart failure development in non-diabetic and diabetic mice. In non-diabetic mice, the progression to heart failure was correlated with increased myocardial FDG uptake, which preceded the decrease in cardiac energy status. The mild cardiac hypertrophy and dysfunction in diabetic mice, together with lower myocardial glucose uptake upon TAC, suggests that maintaining fatty acid oxidation may be beneficial for cardiac function and energetics in pressure overload-induced heart failure.

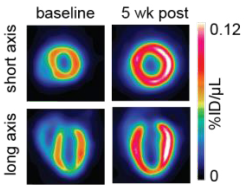

Figure 2. Cardiac FDG-PET images of a non-diabetic mouse at baseline and 5 wk post TAC. ID: injected dose.

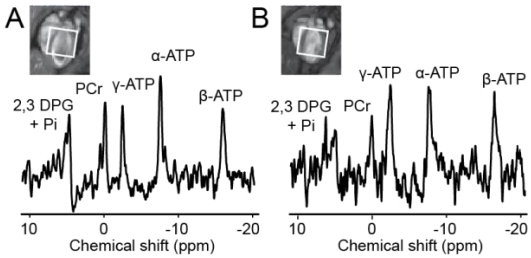

Figure 3. Representative ^{31}P MR spectra of a (A) non-diabetic and (B) diabetic mouse at baseline.

REFERENCES: (1) Bakermans AJ. *Magn Reson Med* 2014; doi 10.1002/mrm.25340; (2) Abdurrachim D. *Proc. 21st ISMRM* 2013; 117. (3) Reader A. *IEEE Trans Nucl Sci* 2002;49:693.

ACKNOWLEDGEMENT: D.A. and M.N. contributed equally to this study.

Neuro

Moderators of Oral Session

Katrien van Doorne

Biomedical NMR, Eindhoven University of Technology, Eindhoven, the Netherlands

Pim van Ooij

Academic Medical Center, Amsterdam, the Netherlands

O009 **Angelique Van Ombergen** - Regional brain alterations after parabolic flight: preliminary results

Research centre for Equilibrium and Aerospace, Department of Physics, University of Antwerp, Antwerp, Belgium

O010 **Frank Van Bussel** - Altered hippocampal white matter connectivity and memory impairment in Type 2 Diabetes Mellitus

Department of Radiology, Maastricht University Medical Center, Maastricht, the Netherlands

O011 **Harm van de Haar** - Dynamic contrast-enhanced MRI for subtle leakage of the blood-brain barrier: optimizing acquisition time

Department of Radiology, Maastricht University Medical Center, Maastricht, the Netherlands

Regional brain alterations after parabolic flight: preliminary results

Angelique Van Ombergen[1], Ben Jeurissen[2], Floris Vanhevel[3], Dirk Loeckx[4], Vincent Dousset[5], Paul M. Parizel[3], Floris L. Wuyts[1]

[1]Antwerp University Research centre for Equilibrium and Aerospace, Department of Physics, University of Antwerp, Antwerp, Belgium; [2]iMinds-Vision Lab, Department of Physics, University of Antwerp, Antwerp, Belgium; [3]Department of Radiology, University Hospital Antwerp, Edegem, Belgium [4]icoMetrix, Leuven, Belgium; [5]Department of Neuro-Radiology, CHU Pellegrin, Bordeaux, France

Target audience: Researchers interested in the vestibular system, space researchers, neuroradiologists, ENT doctors, neurologists.

Purpose: The effect of microgravity experienced during spaceflight on the human body has already been studied quite thoroughly and include cardiovascular, muscle and bone physiology[1,2]. Furthermore, it has been proposed that weightlessness can impair processes at the level of the central and peripheral nervous system[3]. However, changes of brain morphology associated with spaceflight have not yet been investigated. The purpose of this study was to investigate possible effects of short-term gravity transitions on brain connectivity and morphology. This study is part of a larger, ongoing study were we investigate neuroplasticity in astronauts after spaceflight[4,5]. We hereto use, among other MRI techniques, voxel-based morphometry (VBM)[6], an unbiased and automated technique, to assess anatomical differences throughout the brain.

Methods: *Data acquisition:* Data were acquired on a 3T GE MR 750 W (GE Healthcare, Milwaukee, Wisconsin, USA) scanner, located close to the parabolic flight (PF) site in Bordeaux, using a 32-channel head coil. 3D IR-prepared FSPGR images with a FOV of 256mm x 256mm and 176 slices were acquired with a spatial resolution of 1 x 1 x 1 mm^3 and with following acquisition parameters: TR = 8.2 ms, TE = 2.52 ms, TI = 450 ms, flip angle = 12°. *Data processing:* The data for the VBM-analysis was processed in accordance with a pipeline that relies on an improved version first proposed by Ashburner et al[6]. It mainly consists of three steps. First, a segmentation of the brain tissues is conducted in native space to classify the intensities of the original images as gray matter (GM), white matter (WM), cerebrospinal fluid (CSF), skull and an outlier class. Prior to the segmentation, the MR-image intensity is corrected for non-uniformity, using a 60mm FWHM threshold for the assumed Gaussian distribution of the bias field[7]. In a second phase, the GM and WM images are brought to the same stereotactic space, using an iteratively created template where the images are non-linearly registered to using a diffeomorphic image registration algorithm[8]. Finally, all the segmented and registered images were affinely transformed to Montreal Neurological Institute (MNI) space and smoothed using a Gaussian FWHM kernel of 8mm. As the output of this phase is very likely to be influenced by anatomical irregularities such as atrophy, we took into account the guidelines presented in Henley et al.[9]. All intermediate results were visually inspected for gross misregistration or mis-segmentation. *Subjects:* Sixteen first-time parabolic flyers were included and underwent a MRI scan before (L-2) and immediately (2-4 hours, R+0) after the parabolic flight. Gray matter (GM) differences were assessed by means of VBM. *Parabolic flight*: The parabolic flight tests were done during the 60 and 61st ESA parabolic flight campaigns in Bordeaux with the A300 Zero-G airbus. During a parabolic flight mission, once the airplane is at cruising altitude, it is 31 times consecutively subjected to phases of 1.8 g, 0 g and 1.8 g each lasting approximately 22 seconds and constituting the parabolas. In between these parabolas, the plane flies level at 1 g for 1 to 5 minutes. A mission typically lasts 3 hours.

Results: Significant clusters (p<0.001, uncorrected) of GM volume decrease (L-2 > R+0) were located in the middle frontal gyrus, the occipital lobe (cuneus included) and the middle temporal gyrus (with V5/MT area). We also found a significant increase (p<0.001, uncorrected) in GM volume (L-2 < R+0) in the anterior lobe of the cerebellum and the superior frontal gyrus (see **Fig. 1**). We did not find any significant clusters when we corrected for false discovery rate (FDR).

Discussion: The changes found above are similar to the ones earlier described in vestibular patients[10-12] having dizziness problems and this could imply that the absence of gravity or the shifts in gravity mimic a vestibular failure. The similarity between vestibular failure patients and parabolic flight participants consists among others a neurosensory mismatch. Patients lack coherent information due to a failure of the vestibular end organ, leading to a conflict between visual, proprioceptive and vestibular information. Likewise do parabolic flyers experience a sensory mismatch each time they are subjected to the gravity transitions, and in particular during the free floating phase. Additionally, most of the regions described are also involved in the cortico-limbic network and changes in these areas have been shown to be stress-related[13]. A parabolic flight is an event with a high stress load and earlier studies have already shown an increase in stress hormones and stress-related changes in electrocortical activity[14,15]. Increasing the number of subjects and including experienced PF subjects (low stress load) could help to get better insight in this matter.

Conclusion: These results suggest that alteration of gravity has an impact on brain morphology in regions that are known to play a pivotal role in the integration of neurosensory information matching vestibular, visual and proprioceptive inputs. Future research and the parallel linking of these results to long duration spaceflight is necessary to support and extend these preliminary findings and to get a first insight in the effects of spaceflight on the function and morphology of the central nervous system. This is the first experiment studying possible changes in brain morphology due to gravity alterations. It shows that short lasting gravity transitions are sufficient to induce neuroplasticity, similar to the ones experienced by vestibular patients. Identification of the regions of interest will allow better understanding of the processes involved in adaptation to microgravity environments, and this becomes more and more important in view of commercial space flight, as well as for future long duration flights e.g. interplanetary space missions and space habitats.

References

1. Aubert, A.E. et al.,*Acta Cardiol*, 60, 129-151, 2005. **2.** Stein, T.P.,*Eur J Appl Physiol,* 113, 2171-2181, 2013. **3.** Manzey, D., *Aviat Space Environ Med, 71*, A69-A75, 2000. **4.** Clément, G. et al,, *Eur J Appl Physiol,* 113, 1655-1672, 2013. **5.** Van Ombergen, A. et al., *In: 19th IAA Humans in Space: linking the challenges of space exploration with medicine on Earth. Cologne, Germany; 2013.* **6.** Ashburner, J. et al.,. *Neuroimage,* 11, 805-826, 2000. **7.** Ashburner, J. et al, *Neuroimage,* 26, 839- 851, 2005. **8.** Ashburner, J., *Neuroimage,* 38, 95-113, 2007. **9.** Henley, S.M.D. et al., *AJNR Am J Neuroradiol,* 31, 711-719, 2010. **10.** Brandt. T. et al.,, *Brain,* 128(11), 2732-41, 2005. **11.** Hüfner. K. et al., *Ann NY Acad Sci,* 1164, 383-385, 2009. **12.** Van Ombergen, A. et al., *Annual meeting ISMRM,* Milano, Italy, 2014. **13.** Li, L. et al., *Neurosci Biobehav Rev,* 43, 163-172, 2014. **14.** Schneider, S. et al., *Eur J Appl Physiol,* 100, 301-308, 2007. **15.** Schneider, S. et al., *Neuroimage,* 42, 1316-1323, 2008.

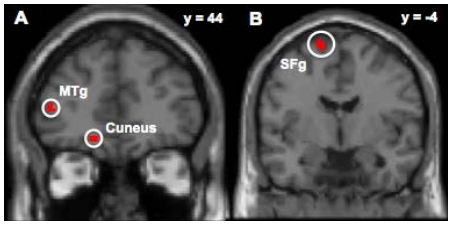

Figure 1: Brain areas showing a significant decrease (A + B) in gray matter after parabolic flight. Data are presented in normalized stereotactic space, overlaid on a high-resolution anatomical MR image with the right side of the brain shown on the left (numerical labels, y coordinates of coronal slices).

Altered hippocampal white matter connectivity and memory impairment in Type 2 Diabetes Mellitus

Frank van Bussel[1], Walter Backes[1], Paul Hofman[1], Alfons Kessels[2], Tamar van Veenendaal[1], Harm van de Haar[1], Martin van Boxtel[3], Miranda Schram[4], Coen Stehouwer[4], Joachim Wildberger[1], Jacobus Jansen[1]

[1]Department of Radiology, University Medical Center, Maastricht, the Netherlands; [2]Clinical Epidemiology and Medical Technology Assessment, University Medical Center, Maastricht, the Netherlands; [3]Department of Psychiatry and Neuropsychology, University Medical Center, Maastricht, the Netherlands; [4]Department of Internal Medicine, University Medical Center, Maastricht, the Netherlands

Target audience: Investigators interested in neuroimaging, cognition and type 2 Diabetes Mellitus.

Purpose: Type 2 Diabetes Mellitus (T2DM) is associated with cognitive decline. A prominently affected cognitive domain is memory, for which the hippocampus plays an essential role. Diffusion MRI (dMRI) enables assessment of hippocampal microstructure through the fractional anisotropy (FA), mean diffusivity (MD), and tractographic connectivity. To examine whether hippocampal abnormalities are related to verbal memory performance, T2DM, and their potential interaction, we performed dMRI in participants with and without T2DM.

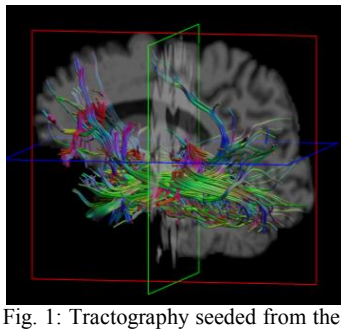

Fig. 1: Tractography seeded from the hippocampus

Methods: *Subjects and measurements*: 40 T2DM (age 64.9±6.1 y, 29 male, BMI 29.2±3.5 kg/m^2) and 38 non-T2DM (age 58.7±9.1 y, 14 male, BMI 24.7±2.9 kg/m^2) control participants were included. All participants underwent a 15-words learning memory task (15-WLT). Neuroradiological assessment revealed no abnormalities. dMRI and T1-weigthed images were obtained on a 3.0 Tesla MRI scanner (Philips Achieva TX) and a 32-element SENSE head coil. The dMRI sequence parameters are: TR/TE of 6980/84 ms, 2.4 mm isotropic voxel size, 128 diffusion sensitizing gradient directions, a b-value of 1500 s/mm^2, and acquisition time of 15 minutes. A single b0-scan was acquired. For anatomical reference, a 3D T1-weighted fast field-echo was acquired: TR/TE of 8.1/3.7 ms, 1.00 mm isotropic voxel size, 170 continuous slices, matrix size of 240x240, acquisition time of 8 minutes. *Analysis*: 3D T1-weighted fast field echo images were used for automatic segmentation of the left and right hippocampus, frontal lobe, parietal lobe, temporal lobe, occipital lobe, and subcortical gray matter with Freesurfer[1]. Motion and distortion correction of dMRI data was performed using ExploreDTI[2] (v4.8.2). The diffusion tensor was estimated using the RESTORE approach[3]. Whole brain probabilistic tractography was performed using constrained spherical deconvolution (CSD) to extract the fiber orientation distributions with a seed point volume of 1 mm^3 and a maximum deflection angle of 30°, yielding approximately 4.3M streamlines. Next, connectivity analysis was performed to obtain tract volumes seeded from each hippocampus (Fig.1). The total tract volumes seeded from both hippocampi to each brain lobe was calculated and normalized to the intracranial volume. *Statistics:* Linear regression analyses, adjusted for age, gender, education level, BMI, systolic blood pressure, relative hippocampal volume, and relative white matter lesion volume were performed (SPSS) to assess the association of hippocampal dMRI measures (FA, MD, and tractographic volumes) with verbal memory performance, T2DM status, and their interaction. When the tract volumes to specific brain lobes were significantly different between the groups, measures FA and MD of the tracts were also investigated in more detail. Furthermore, group characteristics were tested using independent samples t-test and Chi-Square tests.

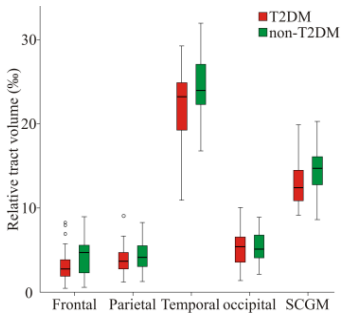

Fig. 2: Boxplots of the relative hippocampal tract volumes to the different brain lobes.

Results: T2DM participants scored significantly worse on 15-WLT total score than non-T2DM participants (39.8±10.8 vs 47.2±11.1, p≤0.05). Furthermore, age, gender, and education level were different between both groups (p<0.05). Linear regression (Fig. 3) revealed: i) no abnormalities of FA or MD in both hippocampi with T2DM or memory performance, ii) a T2DM specific decreased relative tract volume from both hippocampi to the frontal lobe (β= -0.720, p=0.017) (Fig.2,3), iii) tract volume to the temporal lobe (β= 0.235, p=0.017) decreased and tract volume to the parietal lobe (β= -0.268, p=0.042) increased for worse memory performance (Fig.3), and iv) no significant interaction of T2DM with memory performance. Additionally, the FA and MD of the tracts to the frontal lobe were not different between T2DM and non-T2DM participants.

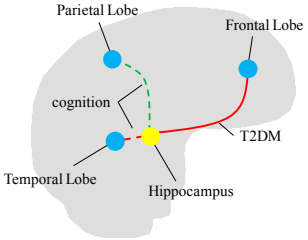

Fig. 3: Schematic overview of the connectivity results with dotted line fewer (red) and more (green) connections in participants with worse memory and less connectivity (red line) in T2DM.

Discussion & Conclusion: In this study we observed fewer connections from the hippocampus to the frontal lobe in participants with T2DM. This suggests that the transfer and integration of information between the hippocampus and frontal lobe might underlie the memory impairment. Hoogenboom et al. related impaired cognitive performance to reduced FA of specific white matter bundles in T2DM participants, although no differences in tract volumes were observed[4]. In contrary to Hoogenboom et al. our focus was specific to the hippocampus which could explain the different results. For participants who score worse on memory performance, we observed fewer hippocampal connections to the temporal lobe, but more to the parietal lobe. Possibly a compensatory mechanism is involved and therefore the cognitive reserve theory could be relevant, which specifies that individual differences in cognitive processes allow some individuals to cope better with pathology than others[5]. To conclude, impaired memory in T2DM seems to be associated with altered hippocampal white matter connectivity. The exact underlying mechanism needs to be elucidated in future studies.

References: [1] Fischl, B., et al., 2002, Neuron, vol.33, no.3, pp.341-355. [2] Leemans, A., et al, 2009, 17th Annual Meeting of ISMRM. [3] Chang, L., et al., 2005, Magn Reson Med, vol.53, no.5, pp.1088-1095. [4] Hoogenboom, W., et al., 2014, Diabetes, vol.63, no.2, pp.728-738. [5] Stern, Y. 2009, Neuropsychologia, vol.47, no. 10, pp.2015-2028.

Dynamic contrast-enhanced MRI for subtle leakage of the blood-brain barrier: optimizing acquisition time

Harm van de Haar[1], Saartje Burgmans[2], Cecile Jeukens[1], Jacobus Jansen[1], Matthias van Osch[3], Mark van Buchem[3], Paul Hofman[1], Frans Verhey[2], Walter Backes[1]

[1]Department of Radiology, Maastricht University Medical Center, Maastricht, the Netherlands
[2]Neuropsychology and Psychiatry, Maastricht University, Maastricht, the Netherlands
[3]Department of Radiology, Leiden University Medical Centre, Leiden, the Netherlands

Target audience. Neuroscientists, neuroradiologists, physicists

Purpose. Dynamic contrast-enhanced (DCE-) MRI is a non-invasive imaging technique that is often used to estimate the permeability of, for instance, tumor tissue. Recently, it has also become possible to assess the permeability of the blood-brain barrier (BBB), which is much harder to detect. This technique has been used to study lesions in multiple sclerosis, stroke, and dementia[1]. Suggestions for optimizing DCE-MRI sequences have been made in terms of minimizing influence of scanner drift and maximizing sensitivity to intrinsic tissue parameters[3], and the choice of a pharmacokinetic model[4]. For the BBB assessment, the total measurement time needed to detect the subtle BBB leakage is assumed to be quite long (~25 min) and deserves more attention to make it clinically feasible. Therefore, the aim of this study is to determine the relationship between shorter postcontrast acquisition time and the ability to detect subtle BBB leakage. This was investigated using in vivo measurements in patients with early Alzheimer's disease (AD) and healthy controls and computer model simulations.

Methods. *Acquisition:* The DCE-MRI protocol consisted of two integrated sequences with different temporal resolutions, applied on a 3T system (Achieva TX, Philips). A saturation recovery gradient recalled sequence (TR/TE 5.2/2.5 ms, 25.6x20x5 cm^3 FOV, 128x100x10 voxels, Dynamic Scan Time (DST) 3.2 s) with a 90˚ nonselective saturation prepulse given at a delay time (TD, 120 ms) was used during bolus injection for 1.5 minutes. This resulted in 29 volumes including 4 precontrast scans. Immediately afterwards, a different saturation recovery gradient recalled sequence (TR/TE 5.6/2.5 ms, 25.6x25.6x10 cm^3 FOV, 256x256x50 voxels, DST 30.5 s) with the same saturation prepulse was used for 25 minutes, resulting in 45 volumes with 3 precontrast scans. The contrast agent, gadobutrol, was injected intravenously (dose 0.1 mmol/kg, injection rate 3 ml/s) using a power injector. T1 weighted images were used for automated tissue classification (manually adjusted) of normal appearing white matter (NAWM), deep gray matter (dGM), and cortex. *Subjects*: 17 patients with early AD were included; mean age 73.6±7.9 y (mean±SD), Mini Mental State Examination (MMSE) score 26.5±1.9, Fazekas 1.7±1.0. 18 healthy controls were included; mean age 75.8±6.2 y, MMSE 29.5±0.6, Fazekas 1.4±0.9.

Analysis: After motion correction of the images, a vascular input function (VIF) was extracted from the superior sagittal sinus. Translation of signal enhancement of the VIF to contrast agent concentration was implemented using phantoms with different gadobutrol concentrations (diluted $MnCl_2$ stock solution, T1 1650 ms, comparable to human blood). A two-compartment pharmacokinetic model was applied per voxel using the Patlak graphical approach[5], to obtain measures of BBB permeability (K_i, in min^{-1}) and fractional plasma volume (v_p). Both in the simulations and the MRI analysis, 80th percentile of the K_i histogram values were used as being representative for the subjects, in order to maximize detectibility of subtle BBB leakage. Linear regression was used to test for K_i differences, corrected for age, gender, Fazekas score and diabetes incidence. Statistical significance was inferred when $p<0.05$. The acquisition time was varied by selectively removing the last volumes, after which the differences between groups were tested.

Simulations: A representative VIF was calculated from the measured VIF data of the controls by fitting a biexponential washout curve to contrast agent concentration time-courses. Signal-to-noise ratios were calculated from the acquired data and used to introduce Gaussian noise to the simulated tissue concentration curves. Realistic values of the NAWM were used, as it had the lowest K_i values and worst signal-to-noise. The simulations were used to 1) estimate the total acquisition time needed to accurately measure realistic values of K_i in the NAWM, and 2) estimate the lowest K_i which can still be distinguished from zero in the NAWM. Voxel-wise analysis was assumed, and 10K iterations ensured proper estimation of the estimated error in K_i.

Results. *MRI*: Estimated Ki values decrease with acquisition time. Eight minutes is the shortest acquisition time for which K_i was significantly higher for patients than controls (Fig. 1A), which become increasingly more significant at longer acquisition times..

Simulations: Figure 1B shows the precision of the simulations in terms of relative standard deviation of the calculated Ki. While the deviation for K_i>0.003 min^{-1} no longer improves much beyond approximately 15 minutes, K_i values between 0.001-0.003 min^{-1} require at least acquisition times of 20 minutes or longer before the relative deviation stabilizes. Even lower values are more difficult to precisely measure, even at 25 minutes acquisition time. Note that the relative deviations are on a pixel basis. Using regions of interest (i.e. multiple voxels), these deviations strongly decrease by the square root of the number of voxels. For example, for a small region of 25 voxels, a K_i of 0.001 min^{-1} can be estimated within 10% of the true K_i using an acquisition time of 17 minutes.

Conclusion/Discussion. The determination of extremely low K_i leakage values (in the order of 0.001 min^{-1}) from the NAWM of patients with dementia appears feasible when using a comparative quantification method relative to healthy controls. Acquisition times of approximately 15 minutes are suitable for this, which is feasible in a clinical setting. To obtain more precise and correct quantitative values of the leakage, longer acquisition times, i.e. 25 minutes or longer, are required.

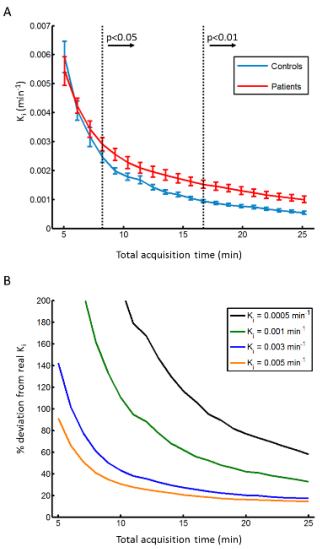

Figure 1 A: Measured K_i of patients and controls vs. acquisition time. The error bars show the standard error of the mean. Statistical significance is achieved at 8 minutes or longer acquisition time.
B: Precision in percent deviation vs. the total acquisition time for a single voxel for different K_i values.

[1] Heye et al. NeuroImage Clin., 2014. [2] Armitage PA et al. Magn. Reson. Imaging., 2011. [3] Cramer SP and Larsson HBW, J. Cereb. Blood Flow Metab., 2014. [4] Patlak CS et al., J. Cereb. Blood Flow Metab., 1983

Muscle

Moderators of Oral Session

Martijn Froeling
University Medical Center, Utrecht,
the Netherlands

Kevin Moerman
University Medical Center, Utrecht,
the Netherlands

O012 **Melissa Hooijmans** - Evaluation of skeletal muscle DTI in Duchenne Muscular Dystrophy

C. J. Gorter Center for High Field MRI, Department of Radiology, Leiden University Medical Center, Leiden, the Netherlands

O013 **Valentina Mazzoli** - Real Time fat suppressed MRI of the knee joint during flexion/extension allows the study of PCL motion

Department of Biomedical NMR, Eindhoven University of Technology, Eindhoven, the Netherlands

O014 **Linda Heskamp** - Quantification of the inflammatory process in muscles of patients with facioscapulohumeral muscular dystrophy

Department of Radiology and Nuclear Medicine, Radboud University Nijmegen Medical Center Nijmegen, Netherlands

Evaluation of skeletal muscle DTI in Duchenne Muscular Dystrophy

Melissa Hooijmans[1], Martijn Froeling[2], Maarten Versluis[3], Andrew Webb[1], Erik Niks[4], Jan Verschuuren[4], Hermien Kan[1]

[1]C. J. Gorter Center for High Field MRI, Department of Radiology, Leiden University Medical Center, Leiden, the Netherlands
[2] Department of Radiology, University Medical Center, Utrecht, the Netherlands
[3]Philips Healthcare, Best, the Netherlands
[4]Department of Neurology, Leiden University Medical Centre, Leiden, the Netherlands

Purpose: To evaluate the effects of SNR, T2 relaxation time and fat percentage on skeletal muscle DTI in patients with Duchenne Muscular Dystrophy (DMD) in assessing muscle fiber organization compared to healthy controls.

Introduction: Recently, diffusion tensor imaging (DTI) measurements have become popular for assessing skeletal muscle fiber architecture in healthy and diseased/damaged conditions. (1-4) However, from simulation based measurements it is known that the reliability of estimating DTI parameters in muscle tissue is highly affected by SNR and the percentage of fat in a particular voxel. (5-7) As fat infiltration, and associated changes in mean T2 (fat+ water), are part of the pathophysiological process in the muscles of patients with DMD, they could therefore directly affect the quality and reliability of DTI measurements in this population, and obscure the actual pathophysiological effect on the measured DTI-parameters. (8)

Methods: Multi-contrast MR images of the right lower leg were acquired in 21 DMD patients (5-16 years) and 12 age-matched healthy controls (5-14 years) using a 3T MR scanner (Ingenia, Philips Healthcare, Best, the Netherlands) with a 32-element receive coil. The MR examination contained DTI measurements (TR/TE 2990/49ms; number of signal averages 6; b-value 0,450 s/mm^2; voxel size 2x2x6mm; no gap; 12 slices; SPAIR fat suppression on the aliphatic fat and selective suppression of the olefinic fat), SE-EPI acquisition for SNR assessment (TR/TE 3020/49ms; NSA 6; b-value 0s/mm^2; 10 dynamics), T1w images for anatomical reference (TR/TE 630/30ms; voxel size 1.5x1.5x6mm; no gap) 3-point DIXON images to determine muscle fat fraction (TR/TE/ΔTE 210/4.41/0.76ms; FA 8°; voxel size 1x1x10mm; gap 5mm;) and multi spin echo images to assess the water T2 relaxation time (9)(17 echoes; TR/TE/ΔTE 3000/8/8ms; voxel size 1.4x1.8x10mm; gap 20mm;)(Fig. 1).

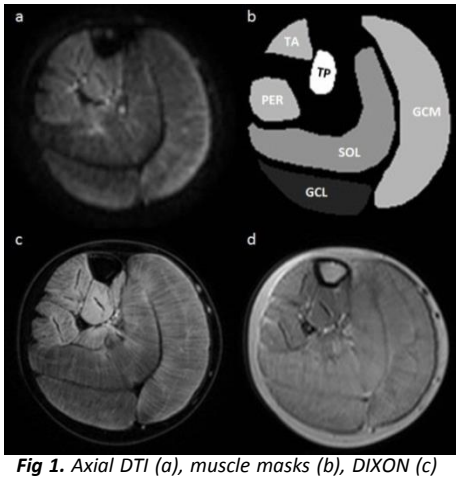

Fig 1. *Axial DTI (a), muscle masks (b), DIXON (c) and T2 image (d) in a DMD patient obtained for the individual lower leg muscles. Gastrocnemius Lateralis (GCL), Gastrocnemius Medialis (GCM), Soleus (SOL), Tibial Anterior (TA), Peroneus (PER) and Tibial Posterior (TP) muscles .*

Data Analysis: A dedicated toolbox (1) was used to calculate mean diffusivity (MD) and fractional anisotropy (FA) from the DTI data. All outcome parameters (FA, MD, %fat, DTI_SNR, water T2) were determined in the same region of interest (ROI) drawn for 6 individual lower leg muscles and presented as a mean value over multiple slices. The effect of water T2, % fat and SNR on the DTI-parameters was evaluated with a Spearman correlation. Subsequently, to ensure image quality, DTI measurements with a SNR<15 and muscles with fat infiltration> 25% were excluded from statistical analysis between groups. (7) Finally, differences in DTI parameters and mean water T2 between healthy controls and DMD patients were assessed with a general linear model, where water T2 was taken as a covariate for the analysis of the DTI-parameters. The significance level was set at p<0.05.

Results: Values of FA correlated positively with %fat (R=0.23), correlated negatively with SNR (R=-0.44) and showed no correlation with mean water T2 (fig. 2). The correlation between SNR and FA disappeared with a SNR above 25. MD did not correlate with mean water T2, %fat or SNR suggesting that the estimation of FA is more highly affected by confounders. A total of 42% (83/198) of the ROIs were excluded for the between-group analysis. Group comparisons showed increases in MD in the GCL, GCM and TA muscles in DMD patients compared to healthy controls (p<0.05). No differences in FA were observed between groups (fig. 2). All individual muscles showed a significant increased mean water T2 in DMD patients compared to controls.

Discussion and Conclusion: Our results show that the proposed quality criteria from simulation-based work (5-7) combined with an optimized and clinically feasible DTI-sequence are suitable to reliably determine MD in DMD patients and young healthy controls. However, the correlation between FA and SNR confirms that for an accurate estimation of FA in skeletal muscles higher quality levels are required (SNR>25). The positive correlation between %fat and FA in these relatively high SNR ranges is in contrast to simulation based work, in which an decrease in FA was observed with increasing fat% due to partial volume effects. (5) The absence of a correlation between the DTI measures and mean water T2 is in line with literature and confirms that minor increases in water T2 in relatively high SNR ranges have a negligible effect on the DTI parameter estimation. (6) Therefore, both the increase in MD as well as the positive correlation between FA and %fat could potentially be ascribed to pathophysiological processes. Overall, multi-parametric MRI is essential to distinguish between confounding effects and pathophysiological processes in skeletal muscle DTI.

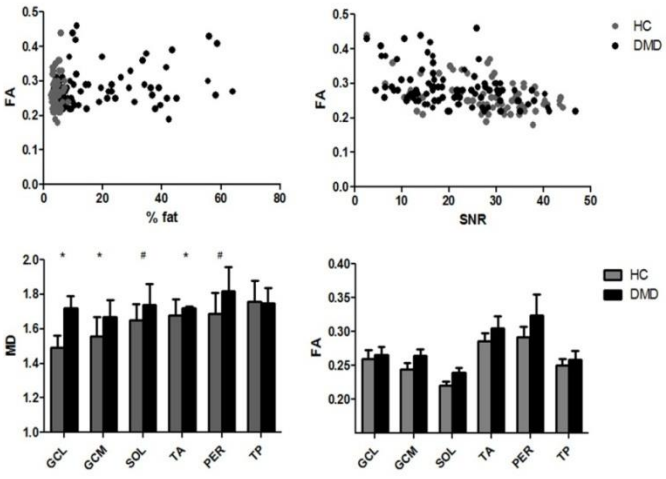

Fig 2. *Overview of the results. In the top graphs the correlation between both DTI measures (MD and FA) and SNR, DMD patients are presented in black and healthy controls in grey. Each dot presents a muscle. In the bottom graphs the mean and stdv of the MD and FA presented for the individual lower leg muscles in healthy controls and DMD patients. Significant differences between groups (p>0.05) are marked with an asterisk(*)and trends (p>0.1) are visualized with a hashtag (#).*

References: [1] Froeling et al. *MRM 2010* [2] Zaraiskaya et al. *JMRI 2006* [3] Bryant et al. *NMR in Biomed 2014* [4] Scheel et al. *NMR in Biomed 2012* [5] Damon et al. MRM 2008 [6] Froeling et al. *NMR in Biomed 2013* [7] Williams et al. *JMRI 2013* [8] Ponrartana et al. *Pediatr Radiol 2014* [9] Azzabou et al. *JMRI 2014*

Real Time fat suppressed MRI of the knee joint during flexion/extension allows the study of PCL motion

Valentina Mazzoli[1, 2, 3], Andre Sprengers[3], Aart J. Nederveen[2], Gustav J. Strijkers[1, 4], Klaas Nicolay[1], Nico Verdonschot[3, 5]

[1]Department of Biomedical NMR, Eindhoven University of Technology, Eindhoven, the Netherlands; [2]Department of Radiology, Academic Medical Center, Amsterdam, the Netherlands; [3]Orthopaedic Research Lab, Radboud University Medical Center, Nijmegen, the Netherlands; [4]Department of Biomedical Engineering and Physics, Academic Medical Center, Amsterdam, Netherlands; [5]Laboratory of Biomechanical Engineering, University of Twente, Enschede, the Netherlands

Introduction: The added value of dynamic MRI over conventional static imaging has already been demonstrated in several studies in which bone kinematics could be evaluated during both active and passive motion [1]. However dynamic imaging of soft tissues in the knee such as ligaments and tendons has been investigated less extensively, mostly due to the technical and practical challenge of dynamic fat suppressed imaging during movement of the knee joint. Fat-suppression techniques to be used in real time imaging of joints in fact should not significantly lengthen the acquisition time for a single frame and should also be relatively insensitive to B_0 homogeneity, since significant field distortions are expected as the leg is moved through the scanner bore. The **aim** of this study is to optimize and compare two different chemical shift-based methods for water-fat separation in real time at 3T, namely PS-bSSFP (Phase Sensitive balanced SSFP) and FLASH Dixon and to explore their possible application in the evaluation of posterior cruciate ligament (PCL) during active motion.

Methods: 5 healthy volunteers were scanned with a 3T scanner (Philips Ingenia, Best, The Netherlands). Subjects were placed in the lateral position to allow the maximum range of motion inside the 70 cm diameter scanner bore and asked to periodically flex and extend their knee. A single slice was planned with the knee placed in approximately 15 degrees flexion in such a way to visualize both tibial and femoral attachment point of the PCL. A foam cushion was placed underneath the subject's lateral epicondyle to provide a pivot point in order to maintain the motion of the PCL in the sagittal plane. The maximum achievable knee flexion angle was dependent on the size of the subject and ranged from 45 to 80 degrees. Data was acquired using a 16 channels Torso coil placed on top of the leg of interest, in combination with the posterior coil embedded into the scanner table. In order to minimize banding artifacts in bSSFP sequences in the patella area during motion a pillow filled with pineapple juice was placed on the anterior side of the lower leg.
Acquisition parameters common to the Dixon and bSSFP acquisition were: 2D single slice acquisition, FOV=400x400 mm^2, slice thickness=5 mm, pixel size 1x1 mm^2 and 200 ms temporal resolution. *bSSFP:* flip angle=35°, TR=2.4 ms, TE=1.2 ms. *2 points Dixon:* FLASH sequence with flip angle=8°, TR=4 ms, TE_1=1 ms, TE_2=1.8 ms. For each technique several dynamic datasets were acquired, and series were selected based on highest overall image quality, least imaging artifacts, and largest range of motion. In these series the length of the ligament was measured by manual segmentation of its posterior and anterior surface. The same acquisition parameters used for dynamic imaging were also used for acquisition of two images of the knee in a single flexion position, which were used for SNR calculation.

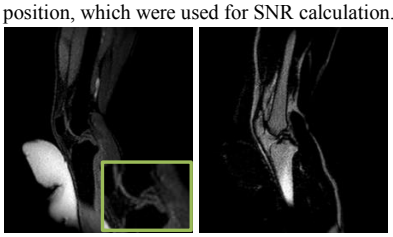

Fig 2: Selected frames with separation of water (A) and fat (B) components based on 2 points DIXON.

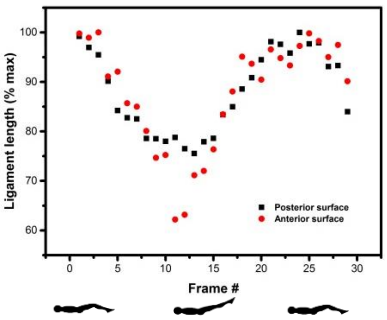

Fig 3: PCL elongation during flexion. Results are indicated as percentage of the maximum observed ligament length, which was measured when the knee was at the maximum achievable knee flexion angle.

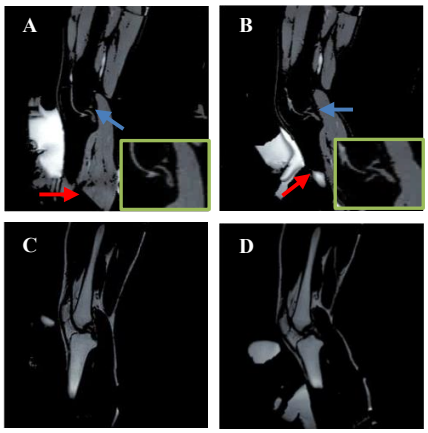

Fig 1: Selected frames with separation of water (A,B) and fat (C,D) components based on PS-bSSFP. The PCL is indicated by the blue arrow. Note the false water/fat separation indicated by the red arrow, which corresponds to banding artifacts in the original image.

Water and fat images based on Dixon were reconstructed on-line by the scanner software. For the images based on PS-bSSFP, both magnitude and phase images were exported and reconstruction was performed offline. Phase images were unwrapped and corrected using a phase errors removal algorithm, as proposed in [2]. With the selected repetition time and center frequency, the water and lipid signal show180º phase difference, and this can be exploited to separate the pixels into water and fat images.

Results: Water images obtained from PS-bSSFP (fig. 1) showed an improved SNR (SNR_{PCL}=42.0±10.0) when compared to water images reconstructed from Dixon FLASH (SNR_{PCL}=12.5±2.6) (fig. 2). The higher contrast between PCL and bone and PCL and fat in bSSFP sequences allowed for good visualization and segmentation of the structure, which was not possible in the Dixon-based water images. The PCL appeared curved at relaxed extension, and the curvature decreased for increasing flexion angle, in agreement with the hypothesis that the PCL is slack at full flexion and is increasingly loaded for increasing flexion angles of the knee. The length of the ligament was observed to increase for increasing flexion angle. Results of manual segmentation of the anterior and posterior surface of the posterior cruciate ligament in a dataset with flexion angle ranging from 0° to 80° are shown in figure 3. A gradual decrease in ligament length is observed as the knee moves from maximum flexion to full extension and a similar rate of increase in length can be seen as the knee returns to the flexed position.

Discussion and Conclusion: bSSFP in combination with Phase Sensitive reconstruction allows for robust water and fat separation in dynamic MRI imaging of the knee and for segmentation of the posterior cruciate ligament during motion. The trend of increase in length as a function of the flexion angle is in agreement with previously reported cadaveric experiments [3]. The proposed bSSFP-based imaging technique provides increased CNR of the ligaments compared to Dixon FLASH for equal temporal and spatial resolution. One of the well- known limitations of bSSFP approaches is the high sensitivity to B_0 homogeneity, which can be especially dramatic when large tissue motion occurs through the scanner bore. Since the proposed approach for water-fat separation is based on a standard bSSFP acquisition, it doesn't involve any lengthening of the repetition time and consequently doesn't result in increased sensitivity to off-resonance effects, making it suitable for the study of soft tissue structure in the knee during motion. The ability of visualizing and tracking soft tissue structures in the knee during motion, as preliminarily shown in this work, could greatly enhance biomechanical knowledge of the lower extremities and could add clinically relevant information to the conventional static images.

References: [1] d'Entremont et al, Magnetic Resonance in Medicine 69:1634–1644 (2013). [2] Hargreaves et al. Magnetic Resonance in Medicine 50:210-213 (2003). [3] Belvedere et al, Journal of Biomechanics 45:1886-1892 (2012).

Quantification of the inflammatory process in muscles of patients with facioscapulohumeral muscular dystrophy

Linda Heskamp[1], Barbara Janssen[1], Arend Heerschap[1]

[1]Department of Radiology, Radboud University Medical Center, Nijmegen, the Netherlands

Purpose

Inflammation is known to play an important role in the pathophysiological mechanism of facioscapulohumeral muscular dystrophy (FSHD)[1]. It is thought that the inflammatory process precedes the fatty infiltration and fibrotic process[2, 3]. To protect the muscle against this fat infiltration and fibrosis some therapeutic interventions aim to reduce this muscle inflammation. Therefore, it is important to accurately quantify inflammation in the muscles. Inflammation is accompanied by oedema, which appears as hyperintense lesions on T2-weighted fat-suppressed MR imaging, such as in Turbo Inversion Recovery Magnitude (TIRM) images. Currently, only semi-quantitative scales to score the presence of oedema exist[2]. However, to evaluate potential treatment effects an objective quantitative biomarker is necessary.

The *aim of this study* was to develop a method that quantifies two parameters in TIRM images, reflecting severity of inflammation: volume of inflammation and intensity of inflammation, in patients with FSHD.

Methods

Patients and study design: Three patients with genetically proven FSHD type 1 were included (3 males, clinical severity score[4]: 3, 3.5 and 3.5). They underwent an MR scan at two time-points, baseline and follow-up (12 weeks).

MRI protocol: The patients were scanned using a 3T Siemens Trio and a ^{1}H volume coil that was placed around the upper leg of the patients. T1 weighted spin echo images (TR/TE 530/16 ms, slices thickness/gap 4/0.4 mm, slices 23, FOV 175x175 mm) and TIRM images (TR/TE 4000/41 ms, IT 220 ms, slices thickness/gap 4/0.4 mm, slices 23, FOV 175x175 mm) were acquired. For the TIRM images saturation bands were placed above the upper and below the lower slice to avoid blood inflow artefacts.

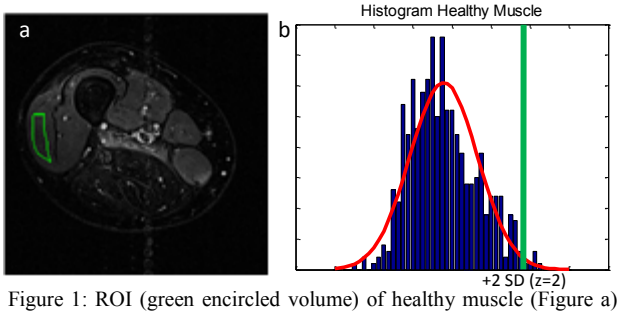

Figure 1: ROI (green encircled volume) of healthy muscle (Figure a) used to determine the threshold as + 2SD (z=2) (Figure b).

Data analysis: First, the TIRM images were visually assessed to determine which muscles were inflamed in both baseline and follow-up. These muscles were selected for further analysis. The mean value and standard deviation (SD) from healthy muscle within the same subject was obtained by drawing a region of interest (ROI) on the TIRM image. These values were used to compute a z-score for the TIRM hyperintense muscle quantifying the difference between signal intensity compared to normal. For each TIRM hyperintense muscle a region of interest (ROI) was drawn on every slice of the T1 weighted images using Matlab. We assumed that pixels with a z-score larger than 2, indicating a difference larger than 2 SD from normal (>99.7%), were inflamed (Figure 1). The number of pixels with a z-score > 2, times the pixel volume computed the volume of inflammation, expressed in cm^3 (Figure 2). For every TIRM hyperintense muscle the intensity of inflammation was expressed as the average z-score per volume of inflammation.

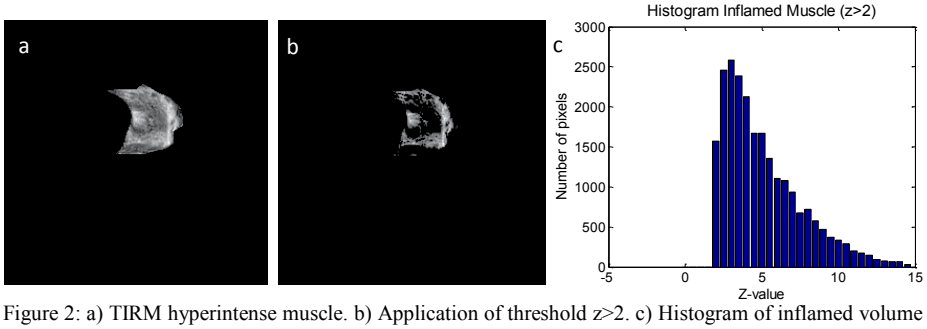

Figure 2: a) TIRM hyperintense muscle. b) Application of threshold z>2. c) Histogram of inflamed volume of the muscle.

	Baseline		Follow-up	
Muscle	Volume (cm^3)	z-value	Volume (cm^3)	z-value
1	51.5	4.9	29.3	5.2
2	13.1	3.9	22.8	4.7
3	20.7	4.7	35.6	5.8
4	67.5	5.1	30.7	4.1
5	67.8	4.3	46.5	4.8
6	57.8	5.6	43.7	5.1

Table 1: Volume and intensity of inflammation per muscle at baseline and follow-up. The muscles in of patient 1, 2 and 3 are in orange, purple and blue, respectively.

Results

During visual assessment 6 muscles were identified as inflamed during both baseline and follow-up. The volume and intensity of inflammation of these muscles are given in Table 1. In muscle 2 and 3 the volume and intensity of inflammation both increase. In muscle 4 and 6 the volume and intensity of inflammation both decrease. In muscle 1 and 5 the volume of inflammation decreases while the intensity increases.

Discussion

We developed a method that can quantify the process of inflammation in two components, intensity of inflammation and volume of inflammation. Together these express the severity of inflammation. We observed an increase in inflammation severity over time in muscle 2 and 3, while in muscle 4 and 6 the inflammation at baseline was more severe as compared to the follow-up. The decrease in inflammation severity at follow-up may indicate that the inflammatory process was followed and replaced by fatty infiltration. In muscle 1 and 5 the oedema centralized to a smaller volume. The nature of the inflammation as described by these two parameters needs to be characterised by targeted biopsy studies. The proposed method can be employed in future clinical trials to quantify these particular features of inflammation.

References

1. K. Arahata, et al., *Muscle Nerve Suppl* (1995), S56-66; 2. S. D. Friedman, et al., *Muscle Nerve,* 49 (2014), 257-60; 3. B. H. Janssen, et al., *PLoS One,* 9 (2014), e85416; 4. E. Ricci, et al., *Ann Neurol,* 45 (1999), 751-7.

Acknowledgments: Prinses Beatrix Fonds (Grant WAR08-15), ZonMW (Grant 89000003), and the FSHD stichting (WP15)

Perfusion

Moderators of Oral Session

Katrien van Doorne

Biomedical NMR, Eindhoven University of Technology, Eindhoven, the Netherlands

Pim van Ooij

Academic Medical Center, Amsterdam, the Netherlands

O015 **Lennart Geurts** - Assessment of blood flow velocity and pulsatility in cerebral perforating arteries with 7T phase contrast MRI

Department of Radiology, University Medical Center, Utrecht, the Netherlands

O016 **Nathalie Doorenweerd** - Reduced cerebral blood flow in boys with Duchenne muscular dystrophy

C. J. Gorter Center for High Field MRI, Department of Radiology, Leiden University Medical Center, Leiden, the Netherlands

O017 **Lena Vaclavu** - T1 blood correction for CBF in arterial spin labeling cannot be predicted from hematocrit in sickle cell disease

Department of Radiology, Academic Medical Center, Amsterdam, the Netherlands

Assessment of blood flow velocity and pulsatility in cerebral perforating arteries with 7T phase contrast MRI

Lennart Geurts[1], Willem Bouvy, Hugo J. Kuijf[1], Peter R. Luijten[1], L. Jaap Kappelle[2], Geert Jan Biessels[2], Jaco J. M. Zwanenburg[1]

[1]Department of Radiology, University Medical Center, Utrecht, the Netherlands
[2]Department of Neurology, University Medical Center, Utrecht, the Netherlands

Purpose: Thus far, blood flow velocity measurements with MRI were only feasible in large cerebral blood vessels. High field strength MRI may now permit velocity measurements in much smaller arteries. Our aim was to measure blood flow velocity and pulsatility of cerebral perforating arteries with 7 tesla MRI and to assess the precision by repeated measurements.

Method: A single-slice (2D) phase contrast sequence with two point velocity encoding was used to measure blood flow velocities during the cardiac cycle in perforating arteries in the basal ganglia (BG) and semioval centre (CSO), from which a mean normalized pulsatility index (PI) per region was calculated as V_{max}-V_{min}/V_{mean}. Six human subjects (age 23-29, 2 male) were scanned at 7T MRI (Philips Healthcare) with a 32 channel receive coil (Nova Medical). Scan parameters were: FOV 250x180 mm^2, TR/TE = 26/15 ms, flip angle 60°, readout BW 59 Hz/pixel (to increase the signal to noise ratio of arterial blood, which has a long T_2*), encoding velocity (V_{enc}) 4 cm/s in CSO and 20 cm/s in BG, 2 averages, and 156 ms temporal resolution (reconstructed to 10-13 cardiac phases). The scan was retrospectively triggered using a pulse-oximeter at the fingertip, and took approx. 7 minutes for a heart rate of 60 bpm. Phase contrast measurements were also performed at the M1 segment of the circle of Willis (0.5 mm resolution, Venc 100 cm/s). The precision of the measurements was determined by performing repeated scans, and testing correlations and agreement between the results of the repeated scans. Potentially confounding effects of partial volume and noise on the measurements were simulated using straightforward Bloch simulations, which included the inflow effect and imperfect slice profile of the RF pulse.

Results: The median number of arteries included was 14 in the CSO and 19 in the BG. In the CSO, the average measured velocity per volunteer ranged 0.5 – 1.0 cm/s, and the PI 0.24 – 0.39. In the BG, the average velocity ranged 3.9 – 5.1 cm/s, and the PI 0.51 – 0.62. The average and maximum velocities per artery showed a very strong correlation (ρ 0.76 - 0.86) between repeated scans. The precision of the velocities per vessel decreased with the size of the arteries (mean absolute difference between measurement one and two ± SD of Vmean was 23% ± 23% for the CSO and 14%±16% for the BG). The mean absolute difference ± SD of the PI between repeated scans was 32% ± 9% in the CSO and 18% ± 17% in the BG. The simulations proved velocities can be measured in vessels with a diameter > 80 µm, but are underestimated due to partial volume effects, while pulsatility index is overestimated (Figure 2).

Conclusion: Blood flow velocity and pulsatility in cerebral perforating arteries has been directly measured in-vivo for the first time, with moderate to good precision. This may be an interesting metric to study hemodynamic changes in ageing and cerebral small vessel disease.

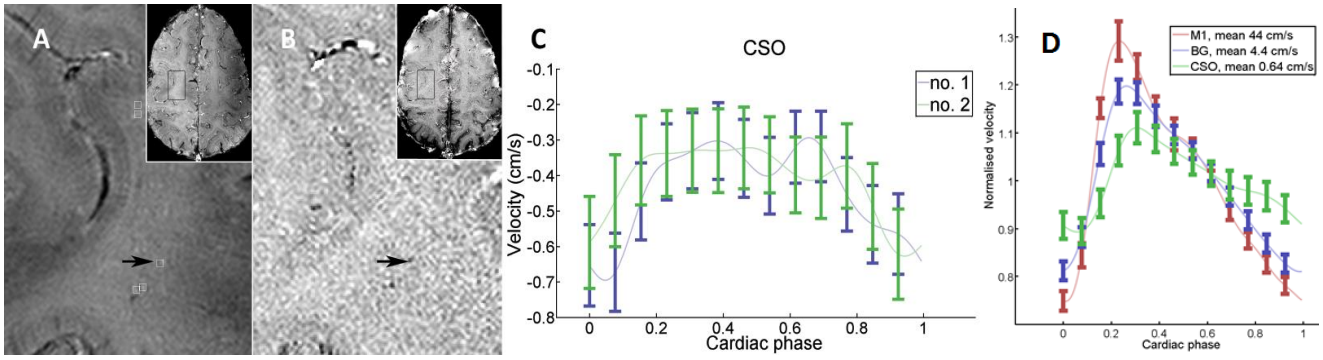

Figure 1: *CSO example data. A: mean (over cardiac cycle) magnitude. B: mean phase. Local maxima in mean velocity are indicated with white squares on the magnitude image. The black arrows point at the vessels for which the individual velocity profiles are shown. C: raw velocity curves for measurement one and two, for the individual vessel indicated with the black arrow. D: mean velocity curves over all vessels and volunteers, per region.*

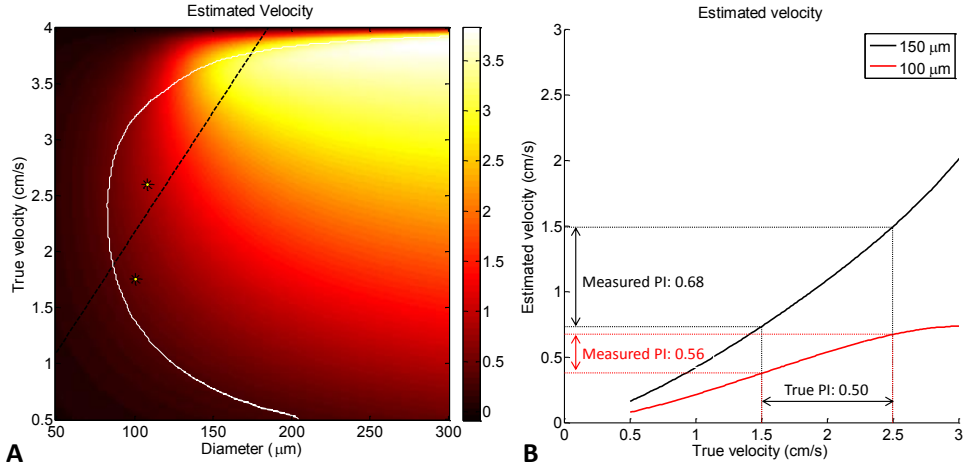

Figure 2: *Simulation data for the scan protocol used in the CSO. A: estimated velocity (color coded) as a function of the true blood velocity (vertical axis) and vessel diameter (horizontal axis). The dashed line and asterisks show literature values. The line originates from feline pial artery measurements[1)], the asterisks from human retinal arteriole measurements[2)]. The velocities in the area to the right of the white line are statistically significant. Most physiological values are within the white line and thus would be detected by our sequence. B: estimated velocity vs. true velocity for two vessel diameters. Velocities are strongly underestimated but the pulsatility is overestimated.*

References: *1.* Kobari M et al, *J Cereb Blood Flow Metab. 1984*, Blood flow velocity in the pial arteries of cats, with particular reference to the vessel diameter. *2.* Nagaoka T, *Invest Ophthalmol Vis Sci. 2006*, Noninvasive evaluation of wall shear stress on retinal microcirculationin humans.

Acknowledgment: This work was supported by the European Research Council, ERC grant agreement n°337333.

Reduced cerebral blood flow in boys with Duchenne muscular dystrophy

Nathalie Doorenweerd[1], Eve Dumas[2], Eidrees Ghariq[1], Sophie Schmid[1], Chiara Straathof[2], Pietro Spitali[3], Ieke Ginjaar[4], Beatrijs Wokke[2], Debby Schrans[5], Janneke van den Bergen[2], Erik van Zwet[5], Andrew Webb[1], Mark van Buchem[1], Matthias van Osch[1], Jan Verschuuren[2], Jos Hendriksen[5], Erik Niks[2], Hermien Kan[1]

[1]C. J. Gorter Center for High Field MRI, Department of Radiology, Leiden University Medical Center, Leiden, the Netherlands; [2]Department of Neurology, Leiden University Medical Centre, Leiden, the Netherlands; [3]Department of Human Genetics, Leiden University Medical Center, Leiden, the Netherlands; [4]Department of Clinical Genetics, Leiden University Medical Center, Leiden, the Netherlands; [5]Department of Neurological Learning Disabilities, Kempenhaeghe Epilepsy Center, Heeze, the Netherlands; [6]Department of Medical Statistics, Leiden University Medical Centre, Leiden, the Netherlands

Target audience: Researchers and physicians in the field of neuroscience and neuromuscular diseases, as this research shows the cerebrovascular involvement of a neuromuscular disorder.

Background and purpose: Duchenne muscular dystrophy (DMD) is a neuromuscular disorder known to be associated with specific learning and behavioral disabilities[1-3]. It is caused by *DMD* gene mutations leading to absence of the dystrophin protein in various cell types including neurons, astrocytes, vascular endothelial and smooth muscle cells[4,5]. The role of dystrophin in the central nervous system is not completely understood, and the pathophysiology of the learning and behavioral problems remains elusive. We previously reported reduced grey matter (GM) volume and altered white matter microstructure in DMD compared with healthy age-matched controls[6]. As dystrophin is associated with vasculature as well, we now aimed to assess whether there are changes in cerebral blood flow (CBF) in these DMD patients.

Methods: T1-weighted (TE/TR 4.6 ms/9.8 ms, res 1x1x1 mm) and pseudo-continuous arterial spin labeling (pCASL)[7] (TE/TR 14 ms/4020 ms, post-label delay 1.525 ms, label duration 1650 ms, background suppression pulses (BGS) at 1680 and 2760ms, voxel-size 3x3x7 mm) scans were obtained at 3T from 30 DMD patients and 22 age-matched controls (8-18 years). A customized analysis pipeline was employed that included subtraction of label and control conditions and registration of the CBF maps to T1 and MNI space (FSLv5). Quantification of CBF was performed as described before[7,8], slightly adapted to correct for the finite labeling duration (T_1 of blood 1664 ms[9], T_2^* of arterial blood 50ms, ρ 1.05 g/mL, labeling efficiency 0.85 and loss of label due to BGS 0.83). Quantification was performed on the mean GM CBF signal and on the CBF maps. Group statistics were performed using a T-test and AVONA for the mean GM CBF; voxel-based group analyses were performed with a GLM and age as covariate.

Results: Representative perfusion maps are shown in figure 1A. DMD patients had lower CBF at 41.1 mL/100g/min +/- 7.8 versus 49.9 +/- 8.7 in controls (p=0.002) (Fig 1B). The reduced CBF was found throughout the brain irrespective of age. The differences remained significant after correcting for grey matter volume, which was also reduced in these patients. The biggest difference with controls was found in patients predicted to miss both the full length and Dp140 isoforms of dystrophin (DMD_Dp140-) (fig.1C bottom). Patients predicted to miss only the full length dystrophin (DMD_Dp140+) also had reduced CBF but to a lesser extent (fig. 1C top).

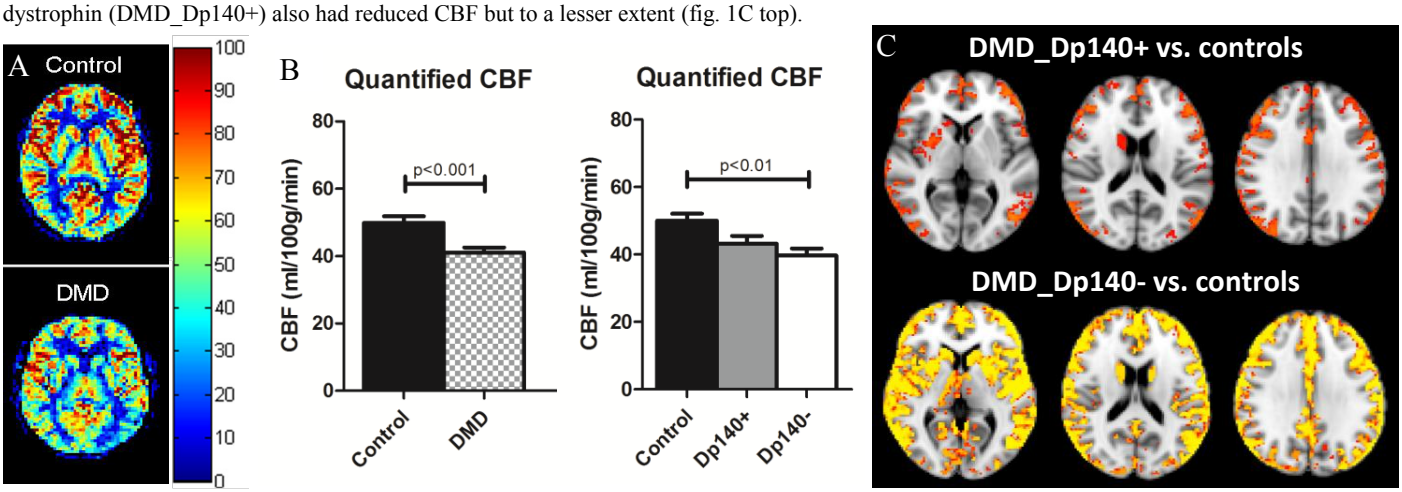

Figure 1. ***A)*** *Representative cerebral blood flow maps of a healthy 10y old control (top) and a 9y old boy with DMD (bottom). Color coded values are in ml/min/100g.* ***B)*** *The quantified CBF showing significant CBF reduction in the whole patient group versus controls (left) and in DMD_Dp140- versus controls specifically (right).* ***C)*** *Localization of the reduced perfusion in statistical maps ranging from p<0.05 (red) to p<0.001 (yellow) showing differences throughout the grey matter in both DMD_Dp140+ and DMD_Dp140 versus controls.*

Discussion and conclusions: Boys with DMD have a 17.6% reduced cerebral blood flow compared to age-matched controls. Patients predicted to miss both full length dystrophin and isoform Dp140 show the lowest CBF compared with controls. However, voxel-based analysis show that the group missing only full length dystrophin also has significantly reduced CBF throughout the brain compared with controls. A recent study in *mdx* mice, an animal model for DMD, also showed reduced CBF (15%) in addition to leaky blood-brain-barrier permeability and increased arteriogenesis[10]. That study proposed increased intracranial pressure as underlying cause for the reduced CBF. However, as the greatest differences here reported are in patients missing both full length and Dp140, whereas *mdx* mice only miss full length dystrophin, more research is required to further assess the vascular involvement in the brain pathophysiology in DMD.

References: [1]Cotton S *et al* Dev Med Child Neurol. 2007;[2]Hendriksen JG *et al* J Child Neurol 2008;[3]D'Angelo MG *et al* Pediatr Neurol 2011;[4]Waite A *et al* Trends Neurosci. 2012;[5]Loufrani L *et al* 2008 Circulation 2001;[6]Doorenweerd *et al* Ann Neurol 2014;[7]Alsop DC *et al* Magn Res Med 2014; [8]Chalela JA *et al* Stroke. 2000; [9]Lu H *et al* Reson Med. 2004;[10]Goodnough CL *et al* Neuroimage 2014 .

T_1 blood correction for CBF in arterial spin labeling cannot be predicted from hematocrit in sickle cell disease

Lena Vaclavu[1], Henk-Jan Mutsaerts[1], Veronica van der Land[2], Dennis Heijtel[3], Karin Fijnvandraat[2], Marjon Cnossen[4], Aart Nederveen[1]

[1]Department of Radiology, Academic Medical Center, Amsterdam, the Netherlands; [2]Department of Hematology, Academic Medical Center, Amsterdam, the Netherlands; [3]Philips Medical Systems, Best, the Netherlands; [4]Erasmus Medical Center, Rotterdam, the Netherlands

Introduction: $T1_{blood}$ is required for perfusion (CBF) calculations from arterial spin labelling (ASL) experiments, and a standard T1 value of 1650ms is generally deemed suitable[1]. In populations with significantly different hematocrit (Hct) values there is an inverse linear relationship between $T1_{blood}$ and Hct[2]. Low Hct is characteristic of sickle cell disease (SCD) due to anemia. We hypothesized that a) the inverse relationship between $T1_{blood}$ and Hct may be disturbed due to changes in blood properties in SCD and b) using a measured T1 in the CBF model improves the CBF calculation.

Method: T1 in venous blood was measured in 40 children diagnosed with SCD (genotype HbSS or HbSβ^0, 12.3 ± 2.4 years, 58% male) on a 3.0T Philips Ingenia scanner. A 180° non-selective inversion pulse preceded a single slice Look-Locker EPI readout in the sagittal sinus (**Fig. 1a.**) to obtain an inversion recovery curve, as described previously[2]. Data from ten voxels with highest intensity from each patient were fitted to a 3-parameter model[3] (**Fig. 1b.**). Perfusion was measured with a background suppressed single-shot GE-EPI pseudo-continuous ASL sequence in 17 slices with a resolution of 3x3x7mm^3; TE/TR 17/4000ms; flip angle 90°; labeling duration 1650ms; post-label delay 1525ms, and analyzed with a dual-compartment model using a labeling efficiency of 0.85; tissue transit time of 1500ms; and either fixed T1 of 1650ms[1], Hct-modelled T1 values as described previously[4] or measured T1 values. These were compared against CBF calculated from 2D phase-contrast (2D PC) obtained from a single-slice 4mm thick at the level of the cervical arteries (labeling plane), TE/TR 5.14/15ms, 4 averages, flip angle 15°. CBF was calculated from PC-MRI by dividing the total mean flow by the volume of the gray and white matter brain segmentations derived from SPM, and assuming a brain density of 1.05g/L. Venous Hct was measured from blood drawn from an antecubital vein.

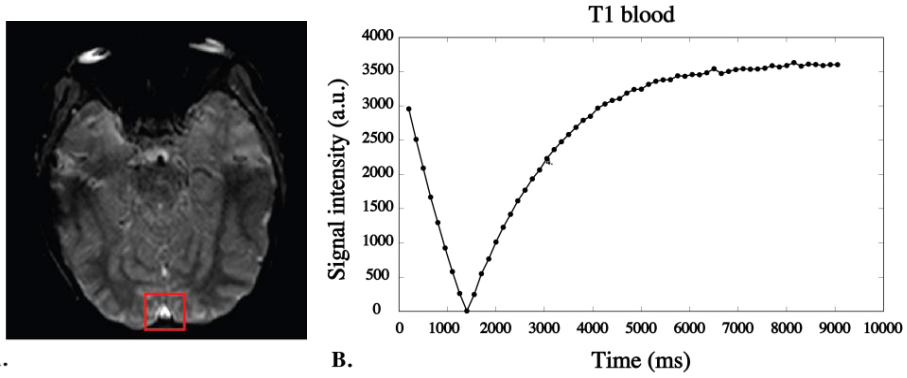

Fig 1. (a) Single slice readout was placed perpendicular to posterior sagittal sinus (red square). **(b)** example of inversion recovery data (points) fitted to an inversion recovery curve (line) in 10 voxels from one patient.

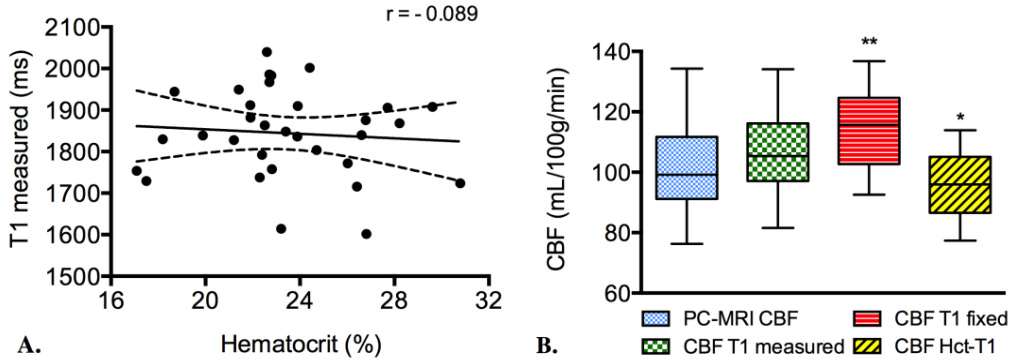

Fig. 2. (a) shows the relationship between measured T1 of blood and Hct.

(b) shows the different ASL flow calculations compared against PC-derived whole brain CBF on the left.

** <0.001, *p<0.05, significantly different from PC-derived CBF.

Results and Discussion: Measured $T1_{blood}$ did not correlate with Hct (mean 23±3%) despite the wide range of both Hct and $T1_{blood}$ values obtained (**Fig. 2a**). The measured $T1_{blood}$ (mean 1810± 158 ms) was lower than Hct-modelled $T1_{blood}$ and hence resulted in a higher CBF estimation (CBF T1 measured) compared with CBF (Hct-T1). CBF (T1 measured) agreed most with the PC-derived CBF calculations, indicating an improvement in the CBF calculation, compared with CBF T1 fixed and CBF Hct-T1 (**Fig. 2b**). We suspect that, since Hct was not found to be related to $T1_{blood}$ in SCD, that other factors might play an important role in driving the T1 relaxation time of blood. Changes in rheology, viscosity and blood content such as mean corpuscular volume of red blood cells (RBCs), and hydration status of RBCs could be important in SCD also. We cannot rule out that venous T1 might be different from arterial T1, and that even Hct could be different between arterial and venous blood or between locations of measurement. Moreover, differences between arterial and venous $T1_{blood}$ could arise from differences in oxygenation[4] and in sickling of RBCs between patients.

Conclusion: Due to the apparent breakdown of the T1-Hct relationship in pediatric SCD, we suggest the measured $T1_{blood}$ values ought to be used to improve CBF estimations from ASL experiments. Divergent factors of SCD blood such as changes in blood content and rheology are likely additional factors influencing the $T1_{blood}$ in SCD instead of Hct alone.

1. Alsop et al. MRM 2014; 2. Varela, M. et al. NMR 2011; 3. Zhang, X. et al. MRM. 2013; 4. de Vis, J.B. et al. Neuroimage 2004.

MR methods

Moderators of Oral Session

Martijn Froeling
University Medical Center, Utrecht, the Netherlands

Kevin Moerman
University Medical Center, Utrecht, the Netherlands

O018 **Bjorn Stemkens** - Estimating dynamic 3D abdominal motion for radiation dose accumulation mapping using a PCA-based model and 2D navigators

Department of Radiotherapy, University Medical Center, Utrecht, Netherlands

O019 **Vitaliy Khlebnikov** - Modulation and regulation of intracellular pH in healthy human brain studied by means of Chemical Exchange Saturation Transfer (CEST) at 7T

Department of Radiology, University Medical Center, Utrecht, the Netherlands

O020 **Ronald Mooiweer** - Squashing the g-factor: Ultra high scan acceleration factors in reduced Field of Excitation imaging

Image Sciences Institute, University Medical Center, Utrecht, The Netherlands

Estimating dynamic 3D abdominal motion for radiation dose accumulation mapping using a PCA-based model and 2D navigators

Bjorn Stemkens[1], Rob Tijssen[1], Baudouin Denis de Senneville[2], Jan Lagendijk[1], Cornelis van den Berg[1]

[1]Department of Radiotherapy, University Medical Center, Utrecht, the Netherlands
[2]Image Sciences Institute, University Medical Center Utrecht, Utrecht, the Netherlands

PURPOSE Respiratory-induced motion is a well-known problem in treating abdominal tumors using external beam radiotherapy. The recent introduction of MR-Linacs[1], which enables MR-guidance during radiation, will allow real-time tracking of highly mobile tumors, such as pancreatic tumors, using multiple fast 2D image navigators. However, this type of imaging will only provide information on the centroid of the tumor, whereas information of surrounding tissue is unavailable. In order to calculate the dose deposition to the entire tumor and surrounding healthy tissue, dose accumulation estimation is required for the complete radiation field, which necessitates dynamic 3D information. In this work we propose a PCA-based motion model to characterize the dynamic 3D motion of the surrounding tissue outside the field-of-view of the 2D image navigators in order to estimate the deposited dose during treatment, and have the 3D motion information of the centroid of the target during treatment, based on the 2D image navigators. For this purpose, a PCA model was formed, based on a previously described 4D-MRI method[2], and updated using the 2D navigator information.

METHODS Three healthy volunteers were scanned on a Philips Achieva 1.5T. Model formation: First, a 4D-MRI data set (3D bTFE with radial in-plane sampling TE/TR=1.45/3.0 ms, α=30°, FOV=350x350x96 mm^3, voxel-size=2.0x2.0x4.0 mm^3, 30 dynamics) was acquired during free-breathing for 10:12 minutes and subsequently sorted into ten respiratory phases, φ (see **Fig. 1**)[2]. Non-rigid registration was performed using a 3D optical flow algorithm using the exhale phase as reference phase[2,3]. A PCA analysis was performed over the ten respiratory phases, resulting in ten 3D eigenvectors for each voxel, representing the eigencomponents, as described by King *et al.*[4]. Next, two orthogonal (coronal to update the model, and sagittal to measure the model accuracy independently) 2D cine-MRI slices (MS 2D bTFE, TE/TR=1.0/2.0 ms, α=50°, FOV=350x350 mm^2, pixel-size=1.76x1.76 mm^2, slice thickness=8 mm, dynamic scan time per slice=0.145ms, SENSE=2), positioned on the pancreas, were acquired for 1:35 minutes. Processing: The goal of the model is to find the optimal eigencomponent-weightings for each 2D acquisition time point. The PCA model is described by $\hat{p} = \bar{p} + Uw$, in which $\hat{p}$ is an instance of the 3D motion vector field, $\bar{p}$ the mean displacement, U is a matrix comprising only the first two eigencomponents with the highest eigenvalues, and w a vector with the weights for each eigencomponent, which are calculated based on the 2D coronal cine-MRI. Two components were used to reduce dimensionality and noise propagation, while still being able to model the motion[5]. For each 2D slice, the optimal weights are calculated using $w = \text{argmax}_w\, Sim(I_w, I_{2D-cor})$[4]. Here, I_w represents the 3D image warped with the motion field computed using the PCA-weights w, I_{2D-cor} represent the 2D coronal slice and Sim is the image similarity index. The similarity was solely calculated on the overlapping 2D anatomy. To allow for differences in contrast between the 4D-MRI and 2D navigator data, a gradient-based similarity index[6] was used. A pattern search was used to maximize the similarity. After optimization, the full 3D motion vector field was calculated for each 2D acquisition time point by applying the weightings to the model. To assess the motion calculated by the model, the pancreatic motion was also estimated on the 2D cine-MR images, using a 2D optical flow algorithm[3]. Spatial maps of the root-mean-squared error (RMSE) were calculated for the sagittal slice, as an independent measure for the model accuracy, and for the coronal slice, to quantify the correctness of the fit between the 3D volume and the 2D cine-MR images.

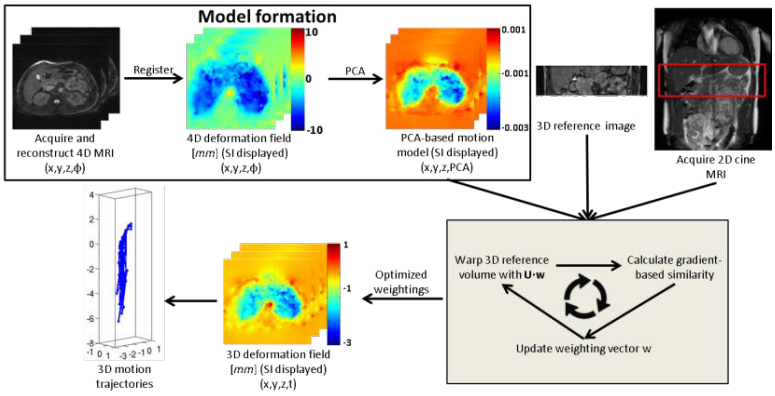

Fig. 1 *Schematic overview of the workflow. First, a PCA-based model is formed using a retrospective binned 4D-MRI. Next, the PCA-weightings are calculated by maximizing the gradient-based similarity of the warped 3D reference image and the 2D coronal slice. This results in a 3D displacement field for each 2D acquisition time point, which is used to calculate the 3D motion of the pancreas*

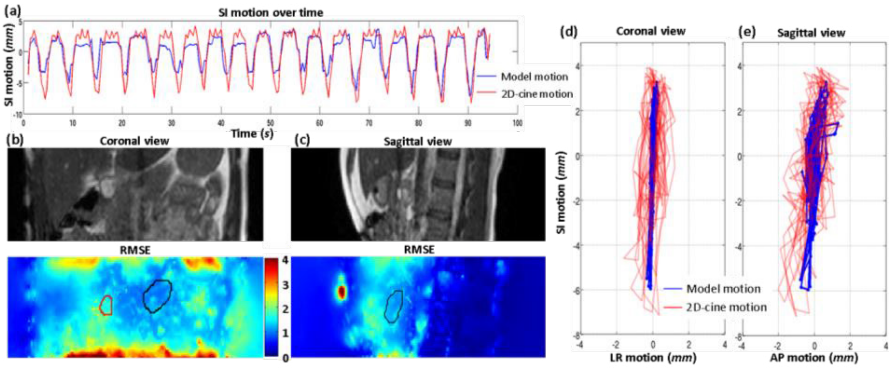

Fig. 2 *(a) SI motion calculated by the model (blue) and estimated on the sagittal 2D slice. Anatomical reference and the RMSE on the coronal slice (b) and sagittal slice (c) with the pancreas delineated. (d) coronal and (e) sagittal view of the motion trajectories of the pancreas calculated using the model (blue) and using the 2D-cine MR images (red).*

RESULTS AND DISCUSSION **Fig. 2a** displays the SI motion of the pancreas estimated on the 2D sagittal cine-MR image (red) and calculated using the model (blue) for one subject. Differences between the curves are primarily observed for the inhale phase. **Fig. 2b** and **c** display the spatial RMSE maps, alongside an anatomical reference image for the coronal and sagittal slice, with the pancreas delineated in black. The RMSE of the SI-motion within the pancreas was, on average, 1.45 mm when compared to the SI motion on the sagittal slice, whereas the RMSE in LR and AP direction were smaller than 1 mm for all subjects. Moreover, other structures close to the pancreas, such as the duodenum (delineated in red on coronal view), which is an organ-at-risk in radiation treatment of pancreatic cancer, showed errors below 2 mm, which equals the voxel size. The larger errors on the upper and lower borders of the maps are induced by the reduced amount of information available for warping the 3D volume in these areas. **Fig. 2d** and **e** displays the motion trajectories of the pancreas calculated using the model (blue) and estimated on the 2D cine-MRI (red) for the coronal and sagittal view. Cardiac-induced AP motion was observed on the sagittal 2D slices, contributing to larger intra-cycle variation in the motion trajectories, which is difficult to model using the PCA-based motion model, since it is formed using a respiratory sorted 4D-MRI. Future studies will focus on improving the fit between the 3D volume and the 2D cine-MR images and improving the model accuracy.

CONCLUSION We presented a method to retrospectively calculate 3D motion vector fields for dose accumulation studies, while still acquiring real-time imaging data for MR-guided radiotherapy treatments. This allows dynamic monitoring of all structures in 3D in the radiation field. This methodology is based on a PCA motion model, calculated on 4D-MRI data, which is data-driven by 2D cine-MRI data. Using this model, we can investigate both the intra- and inter-cycle respiratory motion of all critical structures within the radiation field, which is necessary for retrospective dose accumulation calculations.

REFERENCES **1.** Lagendijk JJW, et al. *Radiot Oncol*, 2008;86:25-29 **2.** Stemkens B, et al. *Int J Radiat Oncol Biol Phys* 2014, *In press*, **3.** Roujol S, et al. *IEEE Trans on Med Imag* 2011;30:1737-1745 **4.** King AP, et al. *Med Imag Anal*, 2012;16:252-264 **5.** Zhang Q, et al. *Med Phys* 2007;34:4772-4781 **6.** Sun Y et al. IEEE ICIP 2004, 1923-1926

Modulation and regulation of intracellular pH in healthy human brain studied by means of Chemical Exchange Saturation Transfer (CEST) at 7T

Vitaliy Khlebnikov[1], Alex Bhogal[1], Jeroen Siero[1], Michel Italiaander[2], Vincent Boer[1], Peter Luijten[1], Hans Hoogduin[1], Dennis Klomp[1]

[1]Department of Radiology, University Medical Center, Utrecht, the Netherlands
[2]MR Coils BV, Drunen, the Netherlands

Abstract. pH homeostasis is vital to normal functioning of cells. ^{31}P Magnetic Resonance Spectroscopy (^{31}P MRS) is currently a gold standard for the non-invasive measurements of intracellular pH (pHi) using inorganic phosphate (Pi) as a probe. However, this method suffers from low resolution and limited pH sensitivity. The purpose of this work was to show that Amide Proton Transfer (APT) imaging is a great alternative to ^{31}P MRS offering both high resolution and pH sensitivity.

Methods. All experiments were carried out on a 7T whole body MR system (Philips, Best, the Netherlands) using a 32 channel transmit-receive head coil for CEST and a coil for ^{31}P MRSI (MR Coils BV, Drunen, The Netherlands). 6 volunteers participated in the experiments (3 for hypocapnia and 3 for hyperventilation). Brain pH was modulated using Respiract (Thornhill Reasearch Inc., Toronto, Canada) by changing PCO_2 (+10 mmHg and -10 mmHg for hypocapnia and hyperventilation, respectively) from the baseline level (**Fig. 1**). The challenge duration was 4 min for hypocapnia and 8 min for hyperventilation. The CEST sequence (B_1 2.3μT for hypocapnia and 1 μT for hypeventilation) used was published earlier [1]. Asymmetry was calculated as MTRasym=CEST(-ώ ppm)/M_0-CEST(ώ ppm)/M_0 in the region from 3 to 4 ppm from the whole brain averaged for white matter (WM) and gray matter (GM) using their binary masks and corrected for variations in B0 and B1. A B_1map was acquired based on a dual TR sequence [2]. A T_1-weighted anatomical scan (3D TFE, TR/TE/FA= 5.5ms/2.0ms/6°, voxel size 1mm) was used for co-registration of the CEST data and B_1map. The anatomical scan was used to create masks of WM and GM from their partial volume masks using a fixed threshold. 3D ^{31}P chemical shift imaging (CSI, 25x25x25mm^3, 5min) was performed to measure pH using Pi as a probe: 3.27 ppm (Pi acidic form), 5.69 ppm (Pi basic form) and PCr (phosphocreatine) as a reference (6.72 pKa). Both co-registration and segmentation were done in FSL (FMRIB v6.0, UK). All data analysis was done in MATLAB®.

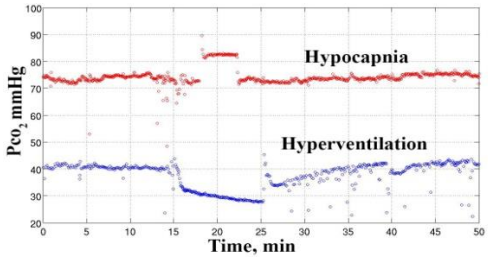

Fig. 1. Traces of partial pressure of CO_2 vs time for two challenges: hypocapnia (top) and hyperventilation (bottom). Hypocapnia trace was shifted by 40 mmHg.

Results and discussion.

pH modulations in vivo in response to different breathing patterns were measured by ^{31}P (**Fig. 2**). Both hypocapnia and hyperventilation induced pH change was estimated to be ~0.1pH units. This pH change corresponds to a 10mmHg change in PCO_2. Thus, average brain buffering capacity is approximately 100mmHg (PCO_2)/pH. However, the low spatial resolution of ^{31}P does not allow estimating buffering capacity of WM distinctively from GM in vivo. High resolution APT imaging was used to get an estimate on buffering capacity of different brain compartments, i.e. WM and GM. Although MTRasym is heavily NOE (Nuclear Overhauser Enhancement)-weighted, since NOE is not pH dependent [3] all variation in MTRasym is expected due to pH sensitive APT effect. MTRasym comparison reveals higher sensitivity of WM to hyperventilation challenge (**Fig. 3 A**) compared to GM ($p<0.01$). The slopes from normal (1) to hyperventilation (2) breathing pattern were 30.3 and 142.93mmHg (PCO_2)/MTRasym for WM and GM, respectively. The slopes from hyperventilation (2) to recovery (3) breathing pattern were 76.9 and 111.1 3mmHgPCO_2)/MTRasym for WM and GM, respectively. The difference in the 1 to 2 breathing pattern slope is most likely a result of different buffering mechanisms in WM and GM in response to alkalosis. Both WM and GM show very similar sensitivity to hypocapnia challenge (**Fig. 3 B**). Slopes 1 to 2 and 2 to 3 breathing patterns were 58.8/40.0 mmHg (PCO_2)/MTRasym and 27.8/15.8mmHg (PCO_2)/MTRasym for WM and GM, respectively. The results suggest that GM and WM have similar mechanism to counter acidosis. The slopes give an estimate about WM and GM buffering capacity in healthy human brain.

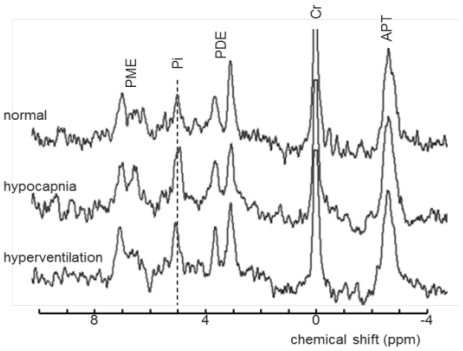

Fig. 2. 31P spectra from a healthy human brain during normal breathing pattern (top), hypocapnia (middle) and hyperventilation (bottom). The vertical dashed line represents the position of Pi during normal breathing pattern. APT (adenosine triphosphate), Cr (phosphocreatine), PDE (phosphodiesters), Pi (inorganic phospate) and PME (phosphomonoesters).

Conclusions. The work shows that APT imaging can be used to estimate pH buffering capacity of different brain compartment. The findings of this study suggest that WM has higher than GM sensitivity to hyperventilation challenge probably due to different anti-alkalosis buffering mechanism. On the other hand, both WM and GM had similar response to hypocapnia challenge, assuming similar anti-acidosis buffering mechanisms.

References. [1] Jones CK et al. MRM 2012. [2] Yarnykh VL. MRM. 2007. [3] Jin T et al. MRM 2013.**This work was funded by the European Commission (FP7-PEOPLE-2012-ITN-316716).**

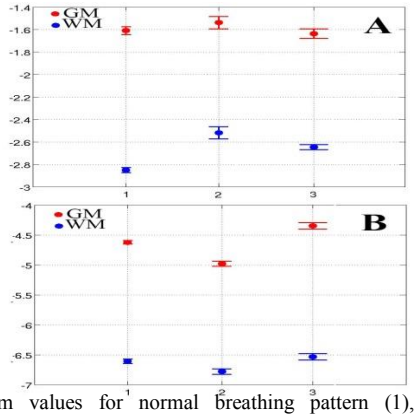

Fig. 3. MTRasym values for normal breathing pattern (1), challenge (2): hyperventilation (A) and hypocapnia (B) and post challenge normal breathing pattern after 10min recovery (3).

Squashing the g-factor: Ultra high scan acceleration factors in reduced Field of Excitation imaging

Ronald Mooiweer[1], Alessandro Sbrizzi[1], Alexander Raaijmakers[1], Cornelis A.T. van den Berg[1], Peter R. Luijten[1], Hans Hoogduin[1]

[1]University Medical Center, Utrecht, the Netherlands

Motivation Parallel imaging using SENSE (1) is routinely used to shorten MR scans. Separately, efforts have been made to reduce the Field of Excitation (rFOX) to the desired region of interest to facilitate reduced Field of View (rFOV) imaging (for faster scanning) (2,3) and/or to avoid artifacts from nearby moving tissue (4). In this work, we explore the combination of both methods, in part suggested by Coristine et al (5). We show that the unfolding capabilities of SENSE can be improved in scans where spin excitation is reduced along two directions.

Theory In SENSE imaging, the acquisition time is shortened by undersampling the k-space. The resulting folded images are unfolded using the spatial sensitivity distributions of the receive coils. Voxels outside the imaged object, with insignificant signal contribution, are usually excluded from the reconstruction (6). This reduces the local degree of aliasing and, as a result, the reduced system matrix used for the unfolding step has a lower condition number. The unfolded image will show a lower noise level. The noise perturbation from the unfolding is quantified by the g-factor, which relates to the SNR of the image as $SNR(R)=SNR^{full}/[g(R)\sqrt{R}]$. R is the acceleration factor, SNR^{full} is the SNR without SENSE acceleration and $\sqrt{R}$ is the signal loss inherent to acquiring fewer data points. In rFOX scans, many more voxels can be excluded from the unfolding process if their locations are known, leading to a far better posed inversion problem, lower g-factor and thus even lower noise in the obtained image compared to a full FOX image.

Experiments SENSE acceleration factors of 3x3 and 5x5 (APxRL) were used to scan a healthy volunteer on a 7 T MR scanner (Philips) using a 32 channel receive coil (Nova Medical). The FOX was limited in the transverse plane by using a 2D SSE RF pulse that was designed to excite an elliptical shape with axis lengths of 1/3rd the dimensions of the head. Several 3D FFE scans were acquired in sagittal orientation, covering the complete head, with TR/TE: 75/25ms, FA: 15˚, EPI factor: 9, resolution: 0.5 mm isotropic. Also, an rFOV image was acquired with the FOV matching the excitation profile. SENSE reference maps were acquired with regular RF excitation pulses (full FOX, scan time: 1m6s) and with the 2D SSE RF pulse scaled to 1˚FA (rFOX, scan time: 2m28s). Raw data was reconstructed offline using the ReconFrame platform (Gyrotools, Zurich, Switzerland) in MATLAB (The MathWorks, Inc., Natick, Massachusetts, United States). G-factor maps for a number of acceleration factors were calculated based on the SENSE reference maps. Their mean values over the rFOX were used to estimate the SNR.

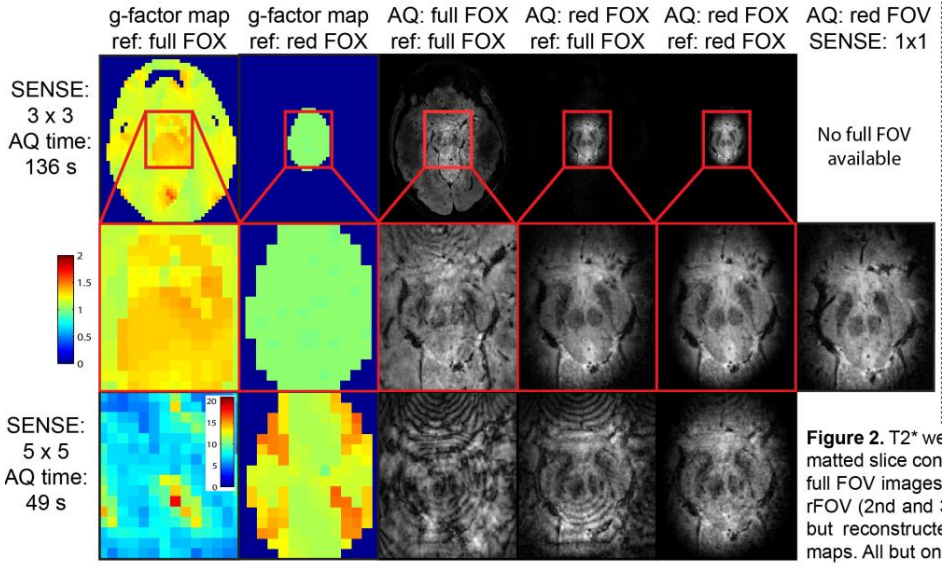

Figure 2. T2* weighted images and g-factor maps of a transverse reformatted slice containing the substantia nigra and the nucleus ruber. The full FOV images (1st row) are cropped around the rFOX, similar to the rFOV (2nd and 3rd rows). The rFOX acquisitions were scanned once, but reconstructed both using the fullFOX and the rFOX sensitivity maps. All but one of the g-factormaps are color coded from 0 to 2.

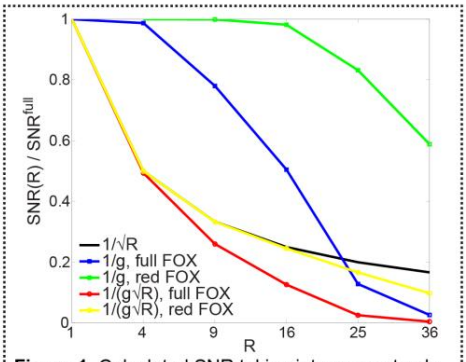

Figure 1. Calculated SNR taking into account only √R or g, and their combined contribution to the SNR, for reference maps with full and reduced FOX.

Results Fig.1 shows that the SNR of the rFOX reconstruction (yellow line) stays close to the 1/√R-line of theoretical maximum SNR. The red line for the full FOX reconstruction decreases much more rapidly. Fig. 2 shows the same: the g-factor remains below 2 even at a 25-fold acceleration combined with rFOX, compared to ~10 at full FOX. Thus, a significant gain in SNR can be expected at high acceleration factors. This is reflected in the T2* images: those acquired using rFOX at SENSE 3x3 show a much better image quality than the full FOX SENSE accelerated images. Even greater improvements are observed at SENSE 5x5, in the images that are reconstructed using the reference map acquired using rFOX. As expected, the rFOV image is of similar quality as the SENSE accelerated scan of the same acquisition time.

Discussion Highly accelerated scans benefit from rFOX inclusion in the SENSE image reconstruction. In practice, the usefulness shall depend on the specific geometries that are excited, also with respect to the spatial distribution of the receive coils. Also, the SNR of the unaccelerated scan should be high enough to support the inherent 1/√R-loss in SNR. Without g-factor penalty, the SNR of a SENSE accelerated acquisition is the same as a scan in which the FOV is reduced by the same factor. If the signal suppression outside the rFOV is not perfect, it will fold back into the image. We expect the selective SENSE approach to be able to unfold this unwanted signal to its spatial origin, at the cost of a slight g-factor penalty in SNR, making it preferential over the rFOV approach. The scan time of the reference map was increased as result of the longer RF excitation pulse, this might be avoided by masking the full coil sensitivity data with a predicted rFOX. We reduced the FOX by using 2D SSE, but in theory the extended voxel exclusion technique is also applicable to any other scan in which the FOX is limited, for instance by spatial saturation.

Conclusion Including the rFOX in the SENSE reconstruction results in a substantial reduction of the g-factor penalty in SNR and enables highly accelerated scans. Images of good quality were obtained at a 25-fold acceleration, using a 32-channel receive coil.

References **1**. Pruessmann KP *et al.* Magn. Reson. Med. 1999;42:952–62, **2**. Schneider JT *et al.* Magn. Reson. Med. 2013;69:1367–78, **3**. Abd-Elmoniem KZ *et al.* Magn. Reson. Med. 2012;68:822–9, **4**. Edelman RR *et al.* Radiology 1988;166:231–6, **5**. Coristine AJ *et al.* Magn. Reson. Med. 2014, **6**. Weiger M *et al.* MAGMA 2002;14:10–19.

RF Engineering

Moderators of Oral Session

Beenakker Jan-Willem
University Medical Center, Leiden, the Netherlands

Siero Jeroen
University Medical Center, Utrecht, the Netherlands

O0021 **Plantinga Birgit** - Structural connectivity mapping and parcellation of the human subthalamic nucleus using ultra-high field diffusion MRI

Department of Neuroscience, Maastricht University, Maastricht, Netherlands

O022 **Diana Khabipova** - Human cortical surface maps of three quantitative imaging parameters:R_1, R_2* and Magnetic Susceptibility

Centre d'Imagerie BioMédicale, Ecole Polytechnique Fédérale de Lausanne, Lausanne, Switzerland

O023 **Roy Haast** - Comparing different contrasts for myelin-related cortical mapping at 7T

Department of Cognitive Neuroscience, Maastricht University, Maastricht, Netherlands

Structural connectivity mapping and parcellation of the human subthalamic nucleus using ultra-high field diffusion MRI

Birgit Plantinga[1], Alard Roebroeck[2], Matteo Bastiani[2], Valentin Kemper[2], Maartje Melse[1], Kâmil Uludag[2], Mark Kuijf[3], Ali Jahanshahi[1], Bart ter Haar Romenij[4], Yasin Temel[5]

[1]Department of Neuroscience, Maastricht University Medical Center, Maastricht, Netherlands; [2]Department of Cognitive Neuroscience, Maastricht University Medical Center, Maastricht, Netherlands; [3]Department of Neurology, Maastricht University Medical Center, Maastricht, the Netherlands; [4]Biomedical Image Analysis, Eindhoven University of Technology, Eindhoven, the Netherlands; [5]Department of Neurosurgery, Maastricht University Medical Center, Maastricht, Netherlands

Target audience

Neuroscientists, neurosurgeons, and neurologists interested in high resolution MR basal ganglia anatomy

Purpose

The subthalamic nucleus (STN) is a relatively small deep brain structure that is involved in motor, limbic, and associative processes[1]. Deep brain stimulation (DBS) of the STN is used to treat basal ganglia disorders such as Parkinson's disease and obsessive compulsive disorder[2,3]. Good clinical outcome requires the targeting of either the motor or the limbic part of the STN, respectively. Although the STN can be well delineated at ultra-high field MRI[4], with current clinical imaging techniques it is not possible to derive its functional zones due to its small size (around 106 mm^3 [5]), which typically only comprises a few voxels (size 2 × 2 × 2 mm^3 [6]). In this study we investigate the structural connectivity profile to parcellate the STN with the aid of ultra-high field *ex vivo* MRI at very high spatial resolution.

Methods

A human post mortem specimen originally kept in formalin, including the left STN, substantia nigra, red nucleus, and globus pallidus, was scanned in PBS using a 7 T MRI scanner (Magnetom 7 T, Siemens). The protocol consisted of two scans: a) 0.3 mm nominal isotropic resolution, gradient echo (GRE) imaging (TE = 11 ms, TR = 37 ms), and b) 0.5 mm isotropic resolution diffusion weighted segmented spin echo 3D EPI (TE = 60 ms, TR = 500 ms, 60 diffusion directions and 8 b0s, b-value = 2800 s/mm^2, total scan time = 65 hours). After FSL's eddy current and motion correction[7], constrained spherical deconvolution-based probabilistic fiber tracking was performed on the whole specimen (2,313,310 tracks) with MRtrix[8] (parameters: step size = 0.05 mm, minimum curvature = 0.1 mm, FOD amplitude cutoff = 0.3, FOD amplitude cutoff for initiation = 0.01) from which only the fibers intersecting the STN (65,182 tracks) were subsequently filtered. The included basal ganglia nuclei and white matter bundles were manually delineated with ITK-SNAP[9]. The relative number of fibers connected to each region as well as the origin of these fibers within the STN (expressed as the percentage of fibers of each voxel connected to that specific region) were computed.

Results

An overview of the projection sites of the STN and their abbreviations is shown in Table 1. Only structures receiving more than 1 % of the STN fibers are listed. Figure 1 shows the origin of these fiber bundles within the STN. This shows that the large amount of fibers that follow the ascending IC mainly originate in the posterior and dorsal parts of the STN. Fibers to the SN originate in the ventrolateral posterior part of the STN. Many projections are also found towards both the GPe and the GPi. Although there is overlap, the anteromedial STN gives rise to more projections to the *anterior* GPe and in the posterolateral STN originate more connections to the *posterior* GPe. The majority of the fibers to the GPi (99 %) run through the anterior half of the GPi (vs. 23 % through the posterior half) and originate in the anteromedial tip of the STN. The STN is also connected to the brain stem, with 17 % of the fibers following the ML, which mainly originate in the ventrolateral part of the STN. Finally, 10 % of the fibers run in lateral direction along the course of the sublenticular part of the IC, which mainly originate in the medial part of the STN. Figure 2 displays the connectivity profile within the SN. Although a similar amount of fibers cross both the SNc and SNr, in the SNc these comprise a bigger volume.

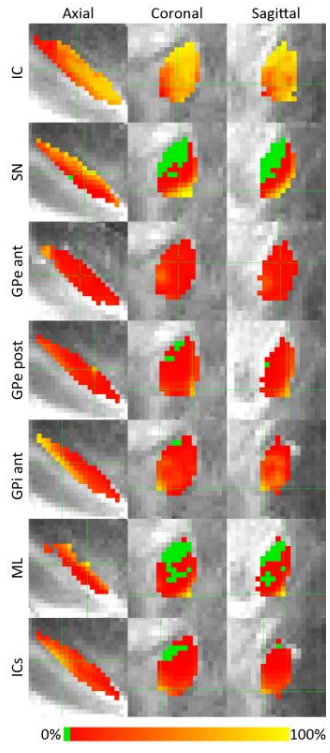

Figure 1. Percentage of fibers per voxel that are connected to the specified region overlaid on the STN (green = no connection).

Table 1. Overview of the projection sites of the STN, with the percentage of all fibers through the STN that project onto it. Individual fibers may intersect multiple structures.

Site	Full name	%
STN	Subthalamic nucleus	100
IC	Internal capsule	30
SN	Substantia nigra:	17
SNc	SN pars compacta	15
SNr	SN pars reticulata	14
GP	Globus pallidus:	14
GPe	External GP	9
GPi	Internal GP	8
ML	Medial lemniscus	9
ICs	Sublenticular IC	5

Discussion

Because fibers that coursed towards but did not fully reach the identified nuclei were discarded, the percentages in Table 1 might be underestimated. Nevertheless, the strong posterior dorsal connection of the STN to the IC and the connection of the medial tip of the STN to the anterior GPi indicate the existence of a gradual division between the motor and limbic parts of the STN, respectively. The posterior and dorsal part is putatively primarily involved in motor processes and the medial side in limbic processes. Furthermore, the STN-SNc connection appears stronger than the STN-SNr connection, which is in contradiction to rodent studies[10]. This suggests that the STN-SNc connection in humans may be more pronounced than what is currently assumed. Although more specimens should be analyzed to assess the reliability of this segregation, these findings may aid in improving clinical pre-operative targeting of DBS patients.

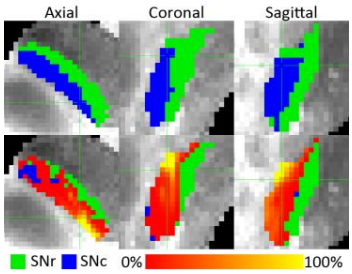

Figure 2. Destination in the SN of fibers connecting to the STN. The upper row shows the manual division of the SN.

References

[1] Temel, Y., et al., Prog Neurobiol, 2005. 76(6): p. 393-413. [2] Benabid, A.L., et al., Lancet Neurol, 2009. 8(1): p. 67-81. [3] Chabardes, S., et al., World Neurosurg, 2013. 80(3-4): p. S31 e1-8. [4] Abosch, A., et al., Neurosurgery, 2010. 67(6): p. 1745-56; discussion 1756. [5] Massey, L.A., et al., Neuroimage, 2012. 59(3): p. 2035-44. [6] Brunenberg, E.J.L., et al., PLoS One, 2012. 7(6): p. e39061-e39061. [7] Jenkinson, M., et al., Neuroimage, 2012. 62(2): p. 782-90. [8] Tournier, J.-D., et al., Int. J. Imaging Syst. Technol., 2012. 22(1): p. 53-66. [9] Yushkevich, P.A., et al., Neuroimage, 2006. 31(3): p. 1116-28. [10] Benazzouz, A., et al., Neurosci Lett, 1995. 189(2): p. 77-80.

Human cortical surface maps of three quantitative imaging parameters: R_1, R_2^* and Magnetic Susceptibility

Diana Khabipova[1], Rolf Gruetter[1,2], José P. Marques[1]

[1]CIBM, EPFL, Lausanne, Switzerland
[2]Department of Radiology, University of Lausanne and Geneva, Switzerland

TARGET AUDIENCE: researchers interested in cortical surface maps of quantitative contrasts; quantitative susceptibility mapping, R_1 and R^*_2.

PURPOSE: Longitudinal (R_1) and apparent transvrse (R^*_2) relaxivity rates have been used to study the cortical structure of the human brain [1, 2] and shown to reveal cortical cytoarchitecture, particularly enhancing the primary sensory cortices. As both these quantitative contrasts are sensitive to iron and myelin, the quantitative susceptibility mapping (QSM), which is sensitive to the same components but with opposite sign, might provide additional information regarding what is being observed. This study compares the ability of the different contrasts (R_1, R^*_2 and χ) to provide insights into the cortical structure.

METHODS: Data from six subjects were acquired on a 7T scanner (Siemens) according to a protocol accepted by the local ethics committee using the following sequences:

1. T1w imaging MP2RAGE: $TR/TI_1/TI_2$ = 6/0.8/2.7s, α_1/α_2 = 7°/5°, res= 0.6mm , T_{acq}=10min 25sec
2. B1 map Sa2RAGE:$TR/TI_1/TI_2$ = 2.4/0.045/1.8s, α_1/α_2 = 4°/10°, res= 2.0mm, iPAT=3x1, T_{acq}=1min 55sec
3. T2*w imageing 3D GRE: TR/TE_1-TE_5=42/4.97-37.77ms, α=10°, res= 0.66mm, iPAT=2x2, T_{acq}=11 mins. The scan was repeated 4 times with the subject's head oriented along different orientations.

Quantitative R_1 maps were calculated using the MP2RAGE and Sa2RAGE data and the processing protocol as described in [3]. The relative head positions were computed by co-registering using FSL-FLIRT. Field maps were computed as in [4] and χ maps were calculated with multiple orientation acquisitions (COSMOS) [5]. The magnitude T_2^*-w image was used to co-register the R*2 and χ volumes with the R_1 maps. The processing procedure for the cortical surface maps of quantitative contrasts (R_1, R^*_2 and χ) is shown in Fig.1.

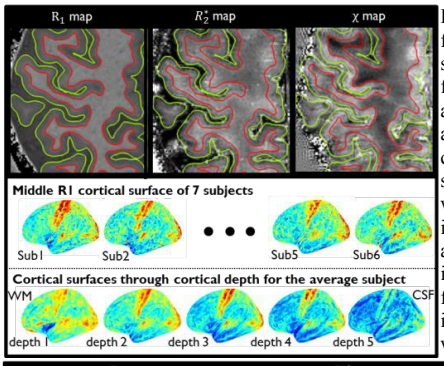

Fig. 1 shows the processing procedure for cortical surface maps: i) cortical surface models were reconstructed from R_1 maps using FreeSurfer and applied to R^*_2 and χ maps (detail of an axial slice of at the level of sensory cortex is shown), ii) all maps were sampled along the normal to gray-white matter (GM-WM) surface vertex in steps of 20% of cortical thickness across the entire cortical hemisphere, iii) an average dataset was calculated for all quantitative contrasts and the information on the different depths was kept (average R1 maps shown).

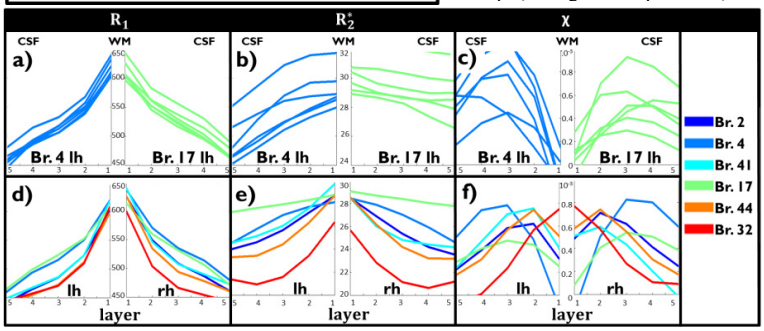

Fig. 2 Plots of the for different quantitative contrasts (R_1,R^*_2 and χ) as a function of the layer number (layer 1 being closest to the GM-WM surface and layer 5 closest to the pial). The first row (a-c) shows the left hemisphere (lh) of Brodmann 4 (left) and right hemisphere (rh) of Brodmann are 17 (right) for all 7 subjects. The second row (d-f) shows average subject where the different colors correspond to different Brodmann regions (Brodmann 2 somatosensory, 4 primary motor cortex, 17 primary visual cortex, 41 auditory cortex, 44 Broca's area and 32 cingulate region).

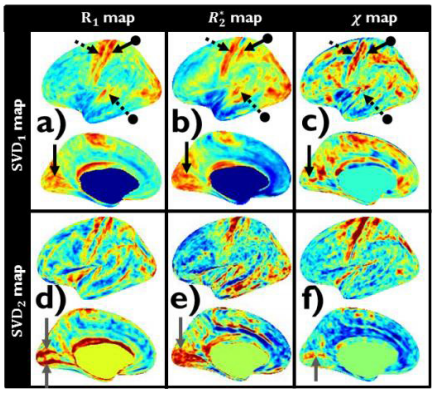

Fig. 3 shows on first, second and third column the surface maps of the left hemisphere for i) R_1, ii) R^*_2 and iii) χ contrast for the first component (a-c) and the second component (d-f) of the singular value decomposition. Black solid arrow points the visual cortex, the dashed arrow shows the motor cortex, the dot-ended solid arrow points the somatosensory cortex while the dot-ended dashed points the auditory cortex. The gray arrow shows the separation between primary and supplementary visual cortex.

RESULTS: The quality of the used data is shown for one subject in Fig.1. The FreeSurfer [6] calculated cortical surfaces (green and red lines in Fig.1 i) correspond well to the underlying R_1 contrast (from which they were calculated), the R^*_2 and χ contrast reveal dissimilarities that are not attributed to poor co-registration. While in the outer layer (the pial surface) the χ contrast is significantly noisier due to the background removal, the mismatches in the grey white-matter surface for both the R^*_2 and χ is solely due to the different mechanisms generating the contrast.

Fig. 2 a-c) shows that for all contrasts the through layer behaviour on the R_1, R^*_2 and χ was in good agreement between the 6 subjects and varied between different brain regions. It should be noted that the variability of the χ curves is due to the arbitrary offset, but the shapes are maintained. Figure 2 d-f) shows for a wider set of ROIs, the behaviour of the contrasts when averaged over the subjects. While the behaviours are different between different ROI, they are coherent between left and right hemisphere.

To benefit from this information without the need to rely on segmentation, singular value decomposition (SVD) was performed for each contrast to separate cortical maps with different through layer behaviour. The first component of the SVD (SVD1) of R_1, and R^*_2 shows similar maps (enhancing all primary sensory regions, see Fig 3.a,b) and describes a relaxivity decay (as in Fig. 2d,e). The χ SVD1 has a curvature like behaviour (as in Fig. 2 c,f). While the R_1 contrast shows both the motor and somatosensory cortex, the R^*_2 and χ only enhance the motor cortex and show low contrast for the somatosensory cortex (dot-ended arrow in Fig. 3). SVD2 performs a separation of the primary visual cortex and the cortex variation is similar for all three contrasts (gray arrow in Fig. 3).

DISCUSSION/CONCLUSION: The cortical R_1 and R^*_2 maps shown show similar contrast to that reported by other groups [1,2]. The observation that χ, as opposed to R_1 maps and R^*_2, does not decrease monotonically from inner surfaces to outer surfaces, suggests that myelin and iron contributions are cancelling each other and might have distinguishable cortical distributions that could be studied using this data. This will be the object of future research. Furthermore, combination of information using different contrasts at different depths could provide useful information for cortical segmentation as is supported by the reproducibility of the single subject data.

REFERENCES

[1] J.Cohen-Adad et al, NeuroImage et al., vol 60, 2012, [2] M. Sereno et.al. Cereb.Cortex, vol.23, 2013, [3].J.P.Marques at al., PLoSOne, vol. 8, e69294,2013, [4] D.Khabipova et al, ISMRM, Nr 0602, 2014, [5] T. Liu et.al.,MRM, vol.61, no. 1, pp. 196-204, 2009, [6] http://freesurfer.net/

Comparing different contrasts for myelin-related cortical mapping at 7T

Roy Haast[1], Dimo Ivanov[1], Kâmil Uludag[1]

[1]Department of Cognitive Neuroscience, Maastricht University, Maastricht, the Netherlands

TARGET AUDIENCE: Neuroscientists and clinicians interested in cortical mapping using (high-field) MRI.

INTRODUCTION: Several papers showed that differences in cortical myelin content measured by tissue staining is comparable with the changes in intensity observed in T_1(-weighted) and $T_{2(*)}$(-weighted) images[1,2]. Areas with high myelin content are hyperintense compared to areas with low myelin content in the T_1w and quantitative R_1 images. In T_2w images and quantitative T_2 and T_2*, myelin content decreases signal intensity. This myelin-related contrast can be enhanced and the bias field removed by calculating the T_1w/T_2w ratio[3]. However, as T_1w and T_2w images are non-linear functions of T_1- and T_{2*}-values, this ratio might misrepresent presumed myelin content. Therefore, the aim of this study is to determine commonalities and differences for all previously proposed weighted and quantitative contrasts in order to get further insights into the biophysical basis of myelin imaging with MRI.

METHODS: *Subjects and MRI:* Four healthy volunteers (aged 25-35, 2 females) participated in this study. MP2RAGE and multi-echo GRE data were acquired using a whole-body 7T magnet (Siemens Medical Systems, Erlangen, Germany) using 32-channel phased-array coil (Nova Medical, Wilmington, USA). Both datasets were acquired with a 0.7 mm isotropic resolution using the following parameters (MP2RAGE: TE 2.47 ms, TI1 900 ms, TI2 2750 ms, TR 5000 ms, GRAPPA 3 and GRE: TR 33 ms, TE1 2.53 ms, TE2 7.03 ms, TE3 12.55 ms, TE4 20.35 ms, GRAPPA 2). *Analysis:* First, MP2RAGE and GRE datasets were aligned with each other using SPM8 (Welcome Department of Imaging Neuroscience, University College London, London, UK). Next, T_2* was obtained from the GRE data using a monoexponential fit, whereas the GRE image acquired at TE4 was divided by the image acquired at TE1 to obtain a T_{2*}-weighted image corrected for receive bias fields. T_1w/T_2w and R_1/T_{2*} ratio images were computed using the mitools software package. Subsequent anatomical analysis was performed using MIPAV 7.1.1 (Center for Information Technology, NIH, Bethesda, USA) and CBS tools 3.0.2 (Max Planck Institute for Human Cognitive and Brain Sciences, Leipzig, Germany). The standard high-res analysis pipeline provided with the CBS tools package was used[4]. Minor changes were applied to the parameters to enhance the performance of the difference modules. The different contrasts (Figure 1A) were mapped to the mid-thickness surface of the individual inflated brains.

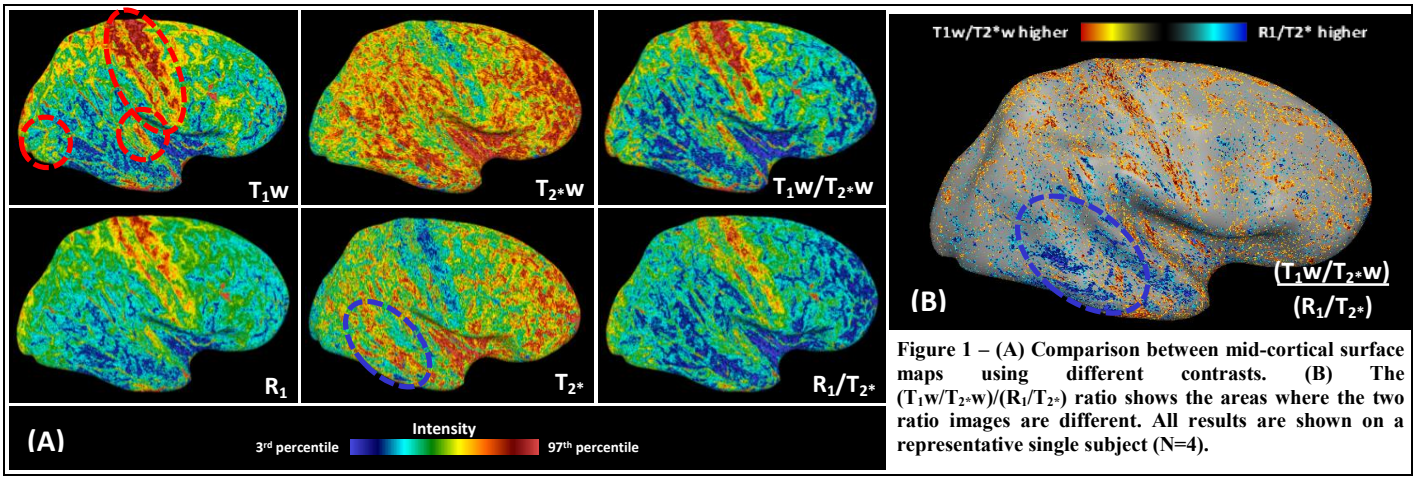

Figure 1 – (A) Comparison between mid-cortical surface maps using different contrasts. (B) The (T_1w/T_{2*}w)/(R_1/T_{2*}) ratio shows the areas where the two ratio images are different. All results are shown on a representative single subject (N=4).

RESULTS: Similar intensity patterns, though with minor differences, are observed between the different contrasts (Figure 1). In all contrasts, the 'classical' highly myelinated areas, including the sensorimotor cortex, auditory cortex (highlighted with red in Figure 1A) and visual cortex, show increased contrast compared to other areas. Minor differences are observed between the weighted and quantitative images for T_1 and T_2* with regards to the size of these areas. Slightly larger areas are detected in the T_1w images compared to the quantitative R_1 ($1/T_1$) images. The opposite is true for the T_2* contrasts. Moreover, the intensity distribution shows a more patchy pattern in the quantitative T_2* images compared with the T_2*w images. Besides, the temporal lobe shows differences in intensity between the T_2*w and the T_2* images (highlighted with blue in Figure 1A/B). Both the patchy distribution and difference in temporal lobe intensity disappear in the quantitative R_1/T_2* ratio. Results were consistent between all four subjects.

DISCUSSION: The present results show that comparable 'myelination' patterns are detectable across all the investigated contrasts at 7T, though minor differences exist. Most of these differences seems to be induced by T_2* effects. We are currently investigating whether these differences might be partially explained by orientation dependency of T_{2*}, in particular in the temporal lobe [4]. Susceptibility artifacts in the inferior temporal and frontal lobe, which are exacerbated at 7T, may also affect the intensity pattern. Nevertheless, quantitative measurements are more directly related to physical or physiological tissue properties than weighted measurements and the differences between the two cannot be attributed solely to artifacts. More detailed (quantitative) analysis, that take potential confounds like cortical thickness and curvature into account, is important to compensate for possible differences induced by these anatomical factors.

REFERENCES: [1] Bock NA, Hashim E, Janik R et al. *Neuroimage*. 2012; [2] Stüber C, Morawski M, Schäfer A et al. *Neuroimage*. 2014 [3] Glasser MF & Van Essen DC. *Journal of Neuroscience*. 2011; [4] Bazin PL, Weiss M, Dinse J et al. *Neuroimage*. 2014 [5] Cohen-Adad J, Polimeni JR, Helmer KG et al. *Neuroimage*. 2012

High Field

Moderators of Oral Session

Beenakker Jan-Willem
University Medical Center, Leiden, the Netherlands

Siero Jeroen
University Medical Center, Utrecht, the Netherlands

O024 **Robin Navest** - Cardiac activity detection with noise variance of a receive array at 7T

Imaging Division, University Medical Center, Utrecht, the Netherlands

O025 **Mark Gosselink** - Converting digital MRI receivers built for 1.5T into 7T receivers using Surface Acoustic Wave filters

University Medical Center, Utrecht, the Netherlands

O026 **MJ van Uden** - ^{31}P MRSI of the brain at 3T with an improved 8-channel receive array and whitened singular value decomposition for optimal combination of ^{31}P array signals

Department of Radiology and Nuclear Medicine, Radboud University Nijmegen Medical Center Nijmegen, the Netherlands

Cardiac activity detection with noise variance of a receive array at 7T

Robin Navest[1], Cornelis van den Berg[1], Alexander Raaijmakers[1], Peter Luijten[1], Jan Lagendijk[1], Anna Andreychenko[1]

[1]Imaging Division, University Medical Center, Utrecht, the Netherlands

Purpose: Cardiac activity often results in artifacts in human cardiac MR images, fMRI studies and MR spectroscopy. Currently ECG is the standard sensor in MRI to detect cardiac activity. However, the electric potential measured in the ECG may be altered by the induced electric field in the body generated by the interaction between the blood flow and a strong magnetic field. This magnetohydrodynamic (MHD) effect mainly occurs in the aortic arch, because the blood velocity there is large and roughly orthogonal to the magnetic field. At higher magnetic field strength (e.g. 7T) the MHD increases [1] and causes the ECG to become unstable.
It has been shown that thermal noise variance of the receive RF coil can effectively pick up the respiratory motion [2]. Here, we investigate whether the thermal noise variance is also sensitive to cardiac activity.

Methods: Free breathing experiments on healthy volunteers were performed on 1.5/3/7T MR scanners with 16/32/8 channel arrays. The 16 and 32 channel body receive arrays consisted of overlapping loop coils and the 8 channel transcieve array consisted of dipole antennas [3]. The arrays were positioned to cover the thorax and, thus the heart. Noise samples were acquired by switching off the RF and gradients during a 2D balanced gradient recalled echo (GRE) sequence (cine MRI frames). Signal was collected with TR=3.1/3.9/2.5 ms and 672/688/480 data samples per TR at 1.5/3/7T respectively. Instead of turning off RF and gradients (as is done here) it is also possible to collect sufficient noise samples from the MR signal free part of 2D balanced GRE cine MRI frames, with a maximum sampling rate resulting from an FOV extended in read-out direction. For all experiments the time per frame was kept constant at 0.3 s and 120 frames were recorded, so the total acquisition time was 36 s. For every individual coil the measured signal was normalized to its median and band-pass filtered between 0.6-2 Hz (i.e. 36-120 beats per minute). During these measurements the ECG was also recorded to serve as a reference. Power spectra were calculated of both noise variance and ECG signals to compare their dominant frequencies and also their time signals was compared.

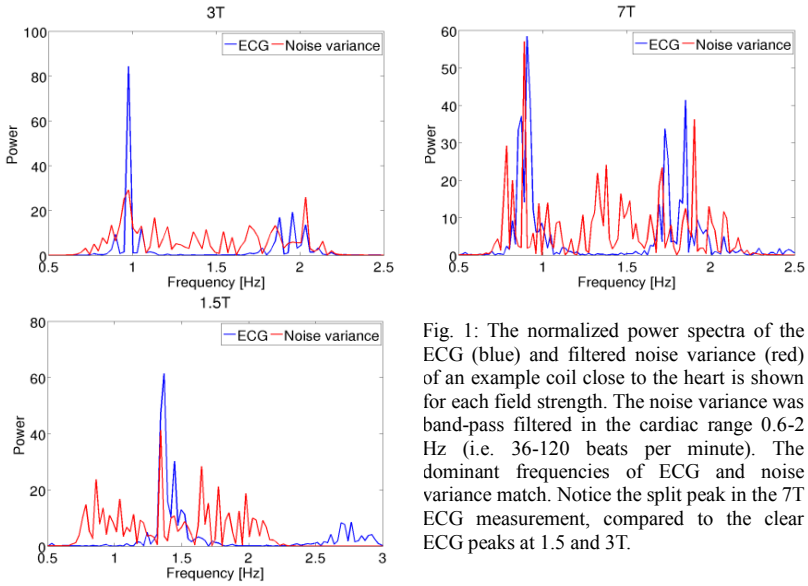

Fig. 1: The normalized power spectra of the ECG (blue) and filtered noise variance (red) of an example coil close to the heart is shown for each field strength. The noise variance was band-pass filtered in the cardiac range 0.6-2 Hz (i.e. 36-120 beats per minute). The dominant frequencies of ECG and noise variance match. Notice the split peak in the 7T ECG measurement, compared to the clear ECG peaks at 1.5 and 3T.

Results and discussion: All measurements show the clearest cardiac activity in coils which were in close proximity to the heart. The dominant frequency of cardiac activity could easily be distinguished in the power spectrum of the noise variance fluctuations of at least one of the coils close to the heart for all field strengths. The power spectrum of one such a coil per field strength is shown in Fig. 1. Notice the normalized power of the dominant frequency of the noise variance compared to the ECG is lower at 3T than at the other field strengths. The respiratory component (outside of the cardiac frequency range shown in the graph) that is orders of magnitude larger than the cardiac activity present in the measured noise variance of this particular coil suppresses the components in the cardiac frequency range. The same frequency was dominant in the power spectrum of the ECG signal. The power spectrum of the noise variance has more sidebands compared to the ECG, but this can be solved by using an adequate filter instead of just a band-pass filter between 0.6-2 Hz. To show this, a narrower band-pass filter was applied around the cardiac frequency to the same coils shown in Fig. 1. The resulting power spectrum and temporal modulation of this narrower filtered noise variance are shown in Fig. 2. The filter widths were 1.2-1.5/0.8-1/0.8-1 Hz for 1.5/3/7T respectively. The amplitude variation over the observation time of the noise variance fluctuations is most likely caused by the used band-pass filter or the remaining side bands. The temporal modulation of the ECG and noise variance fluctuations match in frequency. In the time domain there is a different time shift between the peak of the noise variance and ECG for the different field strengths. This can be explained by the fundamental differences between the physical processes that underlie the noise and ECG measurements. The ECG measures electric activation of the heart directly, whereas noise arises from the entire body volume, spatially weighted by the coils RF electric fields. This means that noise variance consists of a complex convolution of cardiac and anatomical activity (e.g. breathing, aorta pulsation, atrial and ventricular contraction).As a result, it is possible to detect the dominant cardiac frequency with each of the three shown coils, but due to their different locations with respect to the body and operating wavelengths the temporal signals are shifted. To improve sensitivity of the noise variance to the cardiac activity, principal component analysis (PCA) of multiple coils close to the heart will be investigated in the future.

Conclusion: The cardiac activity is present in the noise variance fluctuations at multiple field strengths (i.e. 1.5, 3 and 7T). The proposed method doesn't require additional hardware (e.g. ECG electrodes and wires). An application of this technique could be retrospectively sorting of dynamic cardiac data (e.g. read out lines) in case ECG triggering was not available or problematic. For real time triggering the signal processing has to adapted as the applied band-pass filters lead to phase lag. In that case Kalman filtering of noise data could be an alternative.

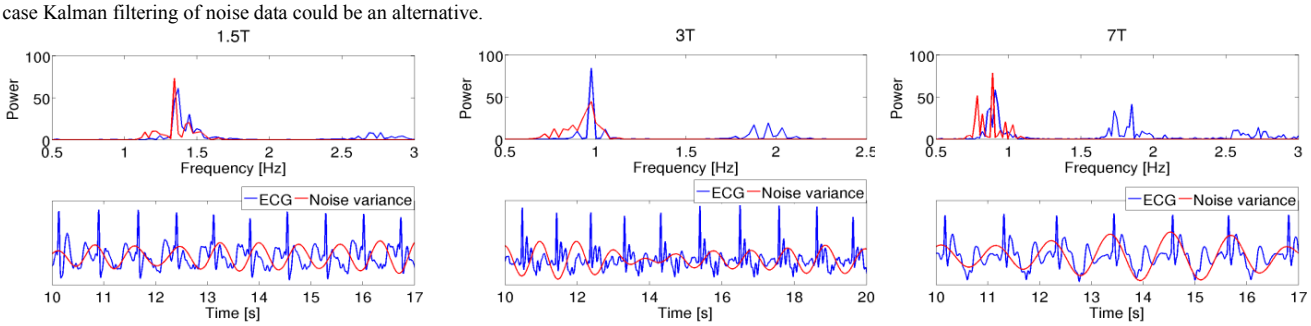

Fig. 2: The power spectrum and temporal modulation of the ECG (blue) and filtered noise variance (red) of an example coil close to the heart for each field strength. Each noise variance signal was band-pass filtered around the specific cardiac frequency of the volunteer and only 10 heart beats were shown to improve visibility. Notice that the temporal modulation of the noise variance matches the ECG.

References: [1] Martin V, et al. (2012) Phys Med Biol 57:3177; [2] Andreychenko A, et al. (2013) ISMRM 21:92; [3] Raaijmakers A, et al. (2014) ISMRM 22:314.

Converting digital MRI receivers built for 1.5T into 7T receivers using Surface Acoustic Wave filters

Mark Gosselink[1], Andrea Anzellotti[2], Giel Mens[2], Marco Boutelje[2], Bart Voermans[2], Hans Hoogduin[1], Peter R. Luijten[1], Cecilia Possanzini[2], Dennis W.J. Klomp[1]

[1]University Medical Center, Utrecht, the Netherlands
[2]Philips Healthcare, Best, the Netherlands

Introduction: 7T MRI can improve SNR and spatiotemporal resolution compared to 3T and 1.5T.Therefore the dynamic range in acquired signals increases (more SNR), as well as the need for more receiver channels (to increase SENSE acceleration). In order to achieve high channel counting at 7T, we made use of Philips digital receivers developed at 1.5T (Philips, Best, The Netherlands) and we have investigated the use of under-sampling and Surface Acoustic Wave (SAW) filters to adapt existing 1.5T to 7T digital receivers.

Methods: The sampling frequency of the ADC is 38MHz, enabling detection of the 298MHz after 8-fold aliasing. The filters inside the digital receivers have been adapted to pass the 298MHz signal. To preserve the noise figure, the filters are required to suppress the side bands of which the closest will be at 310MHz and 272MHz. SAW filters (RF Monolithics, Inc) were installed at the output of the preamplifier (WanTcom, Inc) (Fig 1). Noise figure was measured by comparing the noise obtained by the MRI system using a 50 ohm terminator either connected directly to the input of the preamplifier, or via another calibrated preamplifier with known noise figure and gain. Scaling and gain corrections were obtained by using signals from an external RF synthesiser connected at the input of the preamplifier. A total of 16 receivers were modified to enable MRI acquisition with a 16 channel head coil (NOVA).

Figure 1. Photograph of external preamplifiers with SAW filters at 298MHz (7T) connected to the adapted digital 1.5T receivers.

Results: The adapted filter inside the digital receiver could be tuned to 298MHz, obtaining attenuation at 310 MHz and 272MHz of only 5.1dB and 5.3dB respectively. This resulted in an increased noise figure of 2.0 dB without the SAW filter (Fig 2) (the noise figure of the preamplifier is 0.7dB).The inclusion of the SAW filter attenuated the side bands by 56dB and 59dB respectively (Fig 2). After merging the software of the 7T console with the 1.5T software, 7T MRI could be obtained with the adapted digital receivers (Fig 4).

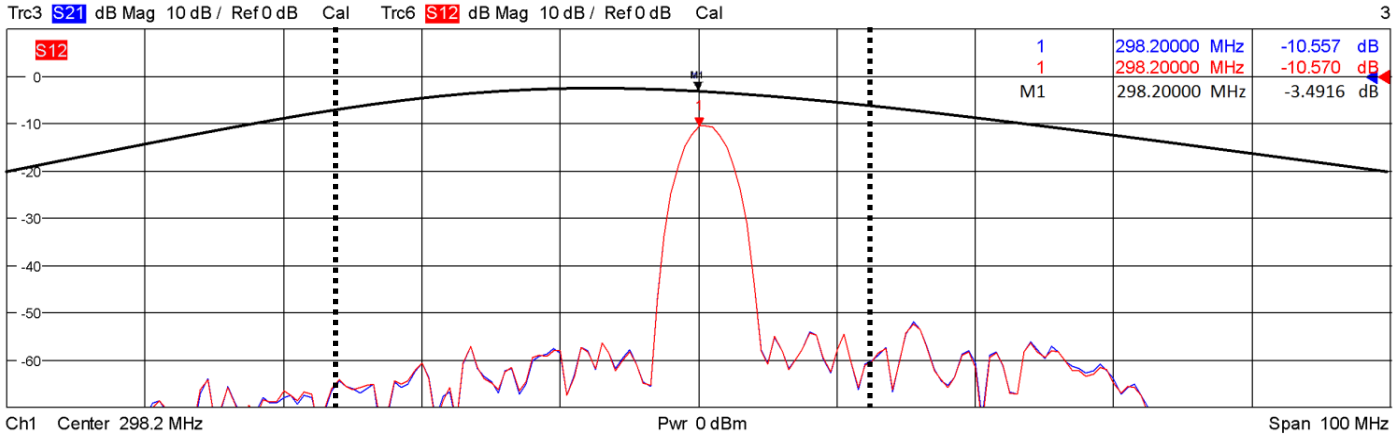

Figure 2. Frequency response (S12) of the adapted filter inside the digital receiver (Black, M1) and the SAW filter (red, 1). Based on the sample frequency of 38MHz of the digital receiver and the proton frequency of 298MHz at 7T, the sidebands of the 7th and 8th harmonic are indicated by the dashed lines. Note that the SAW filter attenuates the side bands of the aliased noise bands by more than 50dB.

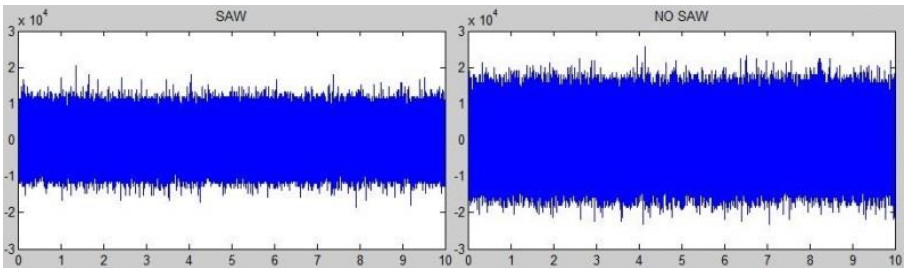

Figure 3. 27dB amplified 50 ohm noise detected with (left) and without (right) the SAW filter, scaled to obtain identical signal level.

Discussion/conclusion: We have shown that digital 1.5T receivers can be used to acquire MRI signals at 7T with a low noise figure by including a SAW filter after the RF coil preamplifier. The high gain of the preamplifier could overcome the substantial loss in the pass band of the SAW filter. Having shown proof of operation with digital 7T MRI, the limits in high coil density receiver arrays at 7T can now be explored.

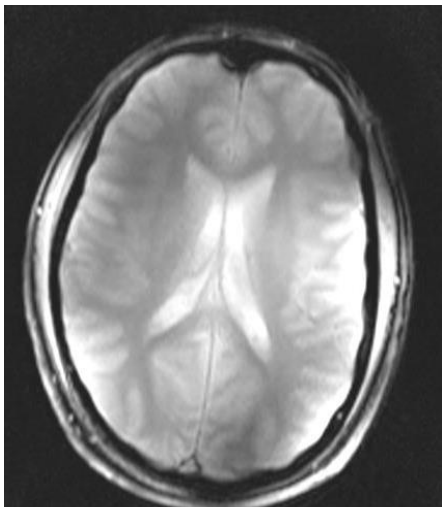

Figure 4. MRI obtained at 7T with 16 modified digital 1.5T receivers.

^{31}P MRSI of the brain at 3T with an improved 8-channel receive array and whitened singular value decomposition for optimal combination of ^{31}P array signals

M.J. van Uden[1], A. Rijpma[2], Bart Philips[1], C.T. Rodgers[3], T.W.J. Scheenen[1], A. Heerschap[1]

[1]Department of Radiology and Nuclear Medicine, Radboud University Medical Center, Nijmegen, the Netherlands
[2]Department of Geriatric Medicine, Radboud University Medical Center, Nijmegen, the Netherlands
[3]OCMR, RDM Cardiovascular Medicine, University of Oxford, Oxford, United Kingdom

Target audience: RF-coil designers, researchers with interest in ^{31}P MR spectroscopy

Purpose: Phosphorus MR Spectroscopy (^{31}P MRS) provides valuable information about energy and phospholipid metabolism in neurological diseases like Alzheimer's disease[1] and brain tumors[2]. The low intrinsic ^{31}P sensitivity can be increased not only by the use of higher magnetic fields, but also by the use of an array of smaller coils to receive the MR signal. This approach is particularly attractive in combination with a volume transmit coil as conventional block pulses can be used for homogeneous excitation as has been reported for 4T and 7T MR-systems with arrays of smaller receive only coils to cover the full volume of the head [3,4,5]. When signals in MRS have a low intensity, the accumulation, phasing , and weighting of the signals from an array becomes challenging [6]. Here we demonstrate an improved 8-channel ^{31}P head array insert combined with a dual-tuned ^{1}H/^{31}P birdcage transmit coil with homogenous transmit field, for ^{31}P MRSI at 3T. It allows ^{1}H decoupling and NOE to further enhance sensitivity. We also compared the performance the methods Time-Domain[7] and Whitened Singular Value Decomposition (WSVD)[8] to combine ^{31}P from our arrays.

Methods: A home built 8-channel ^{31}P head array (diameter 24.5cm) was combined with a quadrature TxRx ^{31}P/^{1}H birdcage coil (RAPID Biomedical GmbH.) detunable at the ^{31}P frequency[9]. Improvements to the head array insert consisted of replacing all ^{1}H tank circuits by an improved trap circuit[10] and removal of all fuses. Fuses were "replaced" by an electronic circuit that detects if a direct current is flowing through the PIN-diode, which prevents scanning whenever there is no direct current flowing. The probe was tested at 3T (TRIO Siemens, Erlangen) on 2 volunteers and a ^{31}P phantom . For both frequencies γB_1 was calibrated. A 3D ^{31}P MRSI dataset was acquired with a hard excitation pulse of 500µs (flip=40°, TR=2s, 10x10x10 (16x16x16 interpolated), voxel size after apodization 51.9 cc) and using WALTZ16 ^{1}H decoupling. Signal was received with the birdcage or with the ^{31}P head array when present. The ^{31}P MRSI data acquired with the receive array were combined using both Time-Domain and WSVD methods. The ^{31}P SNR was calculated by dividing the total peak integral (HLSVDpro) by the standard deviation of the time domain noise of the same voxel.

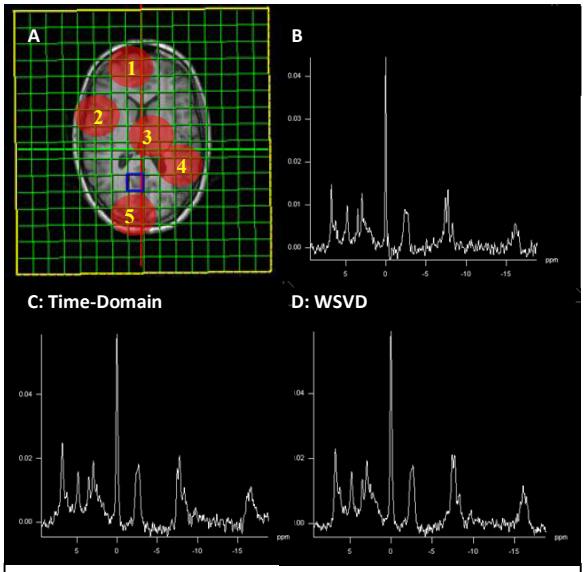

Figure. 1: a) transversal slice with ^{31}P MRSI grid voxel locations and true size; sSpectra shown from voxel 5;

Results: No loss in transmit efficiency for ^{1}H and a 20% loss for ^{31}P was detected in the birdcage after introduction of the 8-channel array coil. The SNR of the ^{31}P MR spectra varied across the brain when the array coil was used, with higher SNR closer to the individual receive elements (e.g. voxel 1, 2 and 5 in figure 1). Table 1 shows the SNR differences between the two RF-coil setups and coil combination methods for all volunteers.

Voxel	Vol 1	Vol2	Vol 1	Vol2
	WSVD/ birdcage		WSVD/ Time-Domain	
^{31}P 1	4.19	3.97	1.48	1.56
^{31}P 2	1.54	1.32	1.3	1.16
^{31}P 3	1.11	0.86	1.05	1
^{31}P 4	1.98	1.23	1.16	1.23
^{31}P 5	2.48	1.53	0.99	1.14

Table 1: ^{31}P SNR increase by WSVD of the five voxels shown in figure 1

Discussion: An improved 8-channel head array in combination with WSVD resulted in a 2 fold SNR increase with respect to earlier presented work[9]. Our alternatives for lossy circuits and components provide the gain in SNR. This gain is hard to quantify exactly because inter-element decoupling, tuning and matching all have an influence on the performance of the RF-coil and will confound such a comparison. The comparison of the WSVD and Time-Domain coil combination methods showed a substantial SNR increase (up to 56% in the frontal lobe where spectral SNR is low) for the WSVD method with the RF-coil insert configuration as detailed above.

Acknowledgement: CTR is funded by the Wellcome Trust and the Royal Society [098436/Z/12/Z]
References: [1]Mandal,P.K. Concepts in MR(2007); [2]Maints,D. ea. NMR Biomed(2002); [3]Avdievich,N.I. ea. J.Magn.Reson.(2007); [4]Zhang,X. ea. ISMRM(2005); [5]Avdievich,N.I. ea, ISMRM(2010); [6]Wright,S. ea. NMR Biomed(1997); [7] Brown,M.A. MRM(2004); [8]Rodgers,C.T. ea. MRM(2010); [9]van Uden,M.J. ea ESMRMB(2013); [10]Meyerspeer,M. ea. MRM(2014)

Diffusion

Moderators of Oral Session

Pim Pullens
University Hospital, Antwerp, Belgium

Anneriet Heemskerk
University Medical Center, Utrecht, the Netherlands

O027 **Gaetan Duchene** - Estimation of pore size distributions with diffusion MRI: feasibility for clinical scanners

Department of Medical Imaging, Université Catholique de Louvain, Brussels, Belgium

O028 **Daan Christiaens** - Can label priors in global tractography resolve crossing fibre ambiguities?

Medical Image Computing, Department of Electrical Engineering, KU Leuven, Belgium

O029 **Gwendolyn Van Steenkiste** - Super-resolution structural connectivity and anatomy of the zebra finch brain

iMinds-Vision Lab, University of Antwerp, Antwerp, Belgium

O030 **Haakma Wieke** - Diffusion tensor imaging of the lumbar and sacral plexus in post mortem subjects

Department of Radiology, University Medical Center, Utrecht, the Netherlands

O031 **David Szabolcs** - The influence of various diffusion MRI processing pipelines

Image Sciences Institute, University Medical Center Utrecht, Utrecht, Netherlands

O032 **Tom Dela Haije** - Reconstruction of Convex Polynomial Diffusion MRI Models Using Semi-definite Programming

Department of Mathematics and Computer Science, Eindhoven University of Technology, Eindhoven, Netherlands

Estimation of pore size distributions with diffusion MRI: feasibility for clinical scanners

Gaetan Duchene[1], Frank Peeters[1], Thierry Duprez[1]

[1]Department of Medical Imaging, Université Catholique de Louvain, Brussels, Belgium

TARGET AUDIENCE: This study should be of interest for people interested in the quantification of pore size distributions using diffusion MRI.

PURPOSE: Pore size distribution (PSD) estimation has been proposed[1] through the application of a d-PFG (double pulsed field gradients) sequence (double wavevector encoding) with zero mixing time and infinite diffusion time Δ under the short gradient pulse approximation. Such an idealization is not valid for clinical scanners. In this work, we investigate the effect of finite gradient durations δ on PSD's estimation and assess the feasibility of the technique on clinical scanners on the basis of simulations. We also discuss the choice of experimental parameters and the influence of noise.

METHODS: Application of a d-PFG-sequence with varying gradient strengths G and relative angles Φ between the two pairs of gradient pulses leads to an integral equation for the PSD. In discrete form it can be written as a matrix equation[2]: $\boldsymbol{E} = K \cdot \boldsymbol{P}$. Here the PSD is a vector $\boldsymbol{P}$ with components $P_i = P(a_i)$ (a_i is the i-th pore size), $\boldsymbol{E}$ is a vector with the measured signal attenuations $S(q)/S(0)$ for different pairs (q, Φ) ($q = \gamma G \delta / 2\pi$) and the kernel matrix K depends on the pore's geometry as well as the gradient waveform and can be calculated numerically with the Multiple Correlation Function (MCF) method[3]. Inverting this equation to get $\boldsymbol{P}$ constitutes an ill-posed problem: the least-squares method will yield unstable solutions. We solved the problem using Tikhonov regularization[4] .
As our 'ground-truth' distribution, we used a Gaussian PSD (mean $25\mu m$ and standard deviation $6.25\mu m$) of cylinders with radii a ranging from 0 to $50\mu m$. In each simulation, $\boldsymbol{E}$ was generated with a 100 points distribution (with resolution 0.5 μm to mimic a continuum of pores) for q and ϕ ranging equidistant as $0 \rightarrow q_{Max} = \gamma G_{Max} \delta / 2\pi$ and $0 \rightarrow 180°$ respectively and taking the exact gradient waveform into account. The estimation was then performed to obtain a 20 points $\boldsymbol{P}$ from which the estimation's error (EE) was assessed through the sum of squared differences with the ground-truth PSD. The influence of δ on EE was investigated for conditions corresponding to two clinical and one pre-clinical MR-scanners with maximum gradient strengths of 40, 80 and 400 mT/m and with $\Delta = 200ms$. We also evaluated the consequences of changing the number of (q, ϕ) values and the effect of adding noise.

RESULTS: Figure (**A**) represents 4 estimated PSD's for data $\boldsymbol{E}$ generated using increasing gradient durations δ while the estimation of $\boldsymbol{P}$ used an ideal gradient ($\delta = 0$) kernel K . The influence of δ on the EE for 3 gradient strengths (16 q-values , 10 Φ-values) is shown on Fig (**B**). The effect of decreasing the number of q values is shown on Fig (**C**). Finally, Fig (**D**) displays systematic and random errors on the PSD when using a 3% noise corrupted signal. Note that, unlike in Fig (**A**), in Figs (**B**), (**C**) and (**D**) the estimation kernel K was calculated using the exact gradient waveform ($\delta \neq 0$).

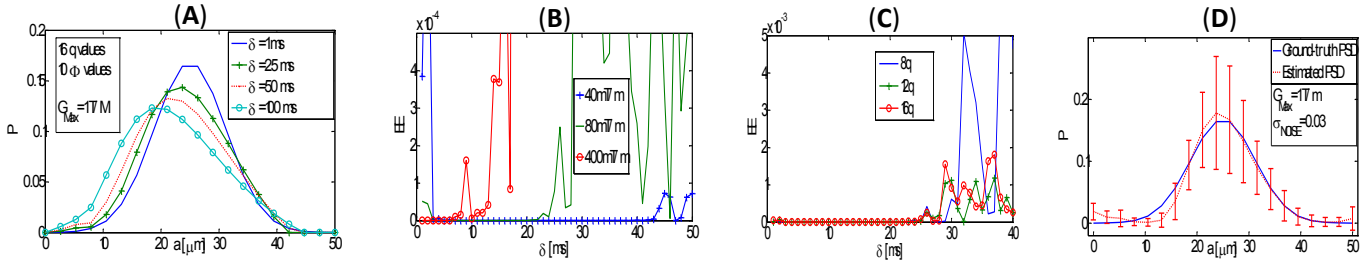

FIGURE: (**A**) Four estimated PSD's for increasing δ ($\Delta \rightarrow \infty$). (**B**) EE versus δ for 3 G_{Max} values (16 q and 10 Φ values, $\Delta = 200ms$). Note the cut-off of EE axis at 5.10^{-4}. (**C**) EE versus δ for varying number of q values ($G_{Max} = 80mT/m$,10 Φ values, $\Delta = 200ms$). (**D**) Influence of noise (a bar represents 1 standard deviation, $\Delta \rightarrow \infty$) .

DISCUSSION: The shift to smaller pore sizes that affects PSD's when δ increases (Fig. (**A**)) is consistent with the 'pore shrinkage effect' of finite gradient-pulse widths described in reference[5]. Although this artefact could suggest a increasing EE with δ, the curves in Fig (**B**) exibhit rather a plateau at minimum EE, surrounded by two areas of inaccurate estimation. The plateau can be explained by the fact that (unlike in Fig(**A**)) the estimation has been done with a kernel K that accounts for the actual temporal profile of the gradient ($\delta \neq 0$). However, as δ is increased, so is q_{Max} (with G_{Max}fixed) and so the attenuations E become to smal for any Φ, leading to inaccurate estimations (i.e. too many data are measured in the noise in practice). On the other hand, at to short δ (too small q_{Max}), the undersampled signals cannot detect pore-induced signal variations leading again to inaccurate estimations. Figure (**C**) shows that decreasing the number of q-values has no significant effect except in the inaccuate region. Varying the number of Φ values (not shown here) leads to similar conclusions. Figure (**D**) shows that noise induced systematic errors occur when estimating PSD for small sizes. This can be understood by noting that smaller pores are those for which higher q-values are needed and thus noisier signal attenuations are used. Large fluctuations can arise due to the noise (see bars standard deviation) and when designing an experiment, one should keep in mind that selecting δ, and thus q_{Max}, requires a trade-off between completely sampling $\boldsymbol{E}$ and avoiding noisy data. Finally, as we used $\Delta = 200ms$ in (**B**) and (**C**) the free mean displacement during the diffusion period may be approximated by $\sqrt{2D\Delta} = 30\mu m$ (D the water diffusion coefficient). Nevertheless, we correctly estimated PSD's up to $50\mu m$, which is larger than the mean displacement encountered in about 15% of our pores. This was also recently observed in reference[6].

CONCLUSION: Accurate quantification of pore size distributions seems possible on clinical MR-scanners as long as the exact gradient waveform and the pores geometry are taken into account in the estimation procedure and if the data are not too noisy. Extension of the method to more complex pore geometries and with intra- and extracellular compartments is in progress.

REFERENCES: **[1]** P.T. Callaghan, *Translational Dynamics & Magnetic Resonance*, Oxford University Press (2011) **[2]** D. Benjamini & al., J. Chem. Phys. 137, 224201 (2012). **[3]** E. Özarslan & al., J. Chem. Phys.130, 104702 (2009). **[4]** R. Aster, B. Borchers, C. Thurber, *Parameter estimation and inverse problems*, Academic Press (2012) **[5]** P.P. Mitra & al., J. Magn. Reson. A 113:94, (1995). **[6]** Y. Katz & al., J. Chem. Phys. 140, 164201 (2014).

Can label priors in global tractography resolve crossing fibre ambiguities?

Daan Christiaens[1], Frederik Maes[1], Stefan Sunaert[2], Paul Suetens[1]

[1]Medical Image Computing, Department of Electrical Engineering, KU Leuven, Belgium
[2]Translational MRI, Imaging & Pathology, KU Leuven, Belgium

TARGET AUDIENCE – The diffusion tractography community.

PURPOSE – Conventional tractography suffers from ambiguous local fibre configurations, due to partial voluming and the symmetry of DWI data[1,2]. It is, for example, not possible to discriminate between crossing and kissing fibre bundles (Fig. 1) or between bending and fanning configurations, a leading cause of spurious (false positive) fibre tracks. Global tractography methods can be more robust against this issue by optimizing the fibre density in the entire image[2–4]. Here, we propose to use fibre bundle labels (e.g., *green* and *orange* in Fig. 1) as an additional prior in global tractography, and hypothesize that such prior will reduce false positive fibres.

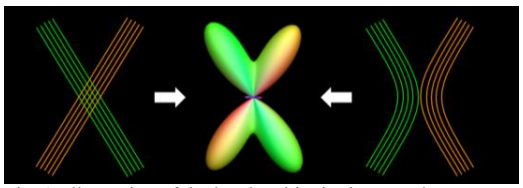

Fig. 1: Illustration of the local ambiguity in DWI data.

METHODS – *Global tractography:* Energy-based global tractography aims to reconstruct the full-brain tractogram M that best explains the data D as a whole[2–4], maximizing $P(M|D) \propto P(D|M)P(M)$. The tracks are modeled by chains of segments, that each have a fixed and equal contribution to the simulated data in the form of a fibre response function, estimated from the data[4]. The optimization, which strives for maximal similarity to the measured data subject to smoothness and connectivity priors, relies on a Markov Chain Monte Carlo technique that generates random proposals for creating, deleting, and moving segments and for (dis)connecting neighbouring segments. *Label Prior:* We introduce a white matter atlas that provides, at every position $\mathbf{x}$, the probability $p(L_\mathbf{x} = l)$ of a bundle label $L_\mathbf{x}$[5,6]. We assume that for all $\mathbf{x}$, $\sum_l p(L_\mathbf{x} = l) = 1$, and use a uniform prior in unlabelled regions. The label probability of a track t is then defined as

$$p(L_t = l) = \frac{1}{Z} \prod_{\mathbf{x} \in t} p(L_\mathbf{x} = l) \quad ,$$

where Z is the normalization across all labels l. As such, a track connecting two disjoint bundles has prior probability 0, while a track within a single bundle will have label probability 1 for that bundle. In practice, bundle label maps will overlap in crossings and due to atlas uncertainty and the attributed probabilities will not be binary. The acceptance probability (Green's ratio) of a connection proposal between tracks t_1 and t_2 is then weighted by the probability of their labels to be equal, i.e., $p(L_{t1} = L_{t2}) = \sum_l p(L_{t1} = l)p(L_{t2} = l)$. Move proposals are similarly adapted to incorporate the prior.

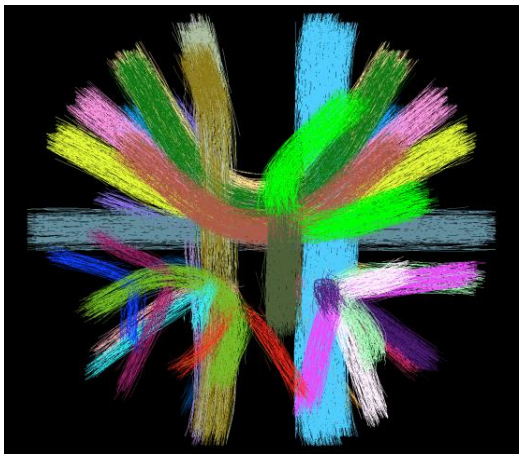

Fig. 2: Labelled track reconstruction on the Phantomas data.

RESULTS – *In silico phantom:* We use the Phantomas software[7] to generate data with known ground truth fibre bundles. The data is sampled at the HCP gradient scheme (see below), at signal-to-noise ratio 30. The label probability atlas is based on the ground truth fibre bundles, using uniform probability outside white matter regions. Fig. 2 shows the reconstructed tracks, coloured by their maximum likelihood label. We compare the Tractometer metrics of this result to those without the prior in Table 1. In both cases, all 27 valid bundles (VB) are found; the number of invalid bundles (IB) is strongly reduced. With the prior, invalid connections (IC) are suppressed in favour of valid connections (VC) and at the cost of slightly increased no connections (NC). *In vivo data:* Data of a single subject is provided by the NIH Human Connectome Project, WU-Minn Consortium[8]: 18 gradients at b=0s/mm^2, 3 x 90 gradients at b=1000s/mm^2, 2000s/mm^2, and 3000s/mm^2, 1.25mm isotropic voxel size. We use the publicly available, manually segmented DTI tractography atlas of Catani and Thiebaut de Schotten[9] for creating the label probability maps (30 labels in total), normalizing all label probabilities and using a uniform prior in unlabelled regions, and register this atlas to subject-space with FSL FNIRT. The output tracks with label probability above 95% are shown in Fig. 3 for 5 bundles in the cerebrum. The forceps major substructure is segmented via an inclusion ROI in the mid-sagittal plane on reconstructions with and without label prior (Fig. 4). Imposing the prior reduces false positive fibres.

Table 1: Tractometer metrics

	VC	IC	NC	VB	IB
no prior	15.9%	6.9%	77.1%	27	56
prior	19.2%	0.2%	80.6%	27	9

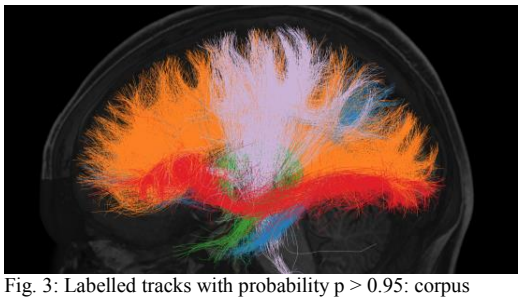

Fig. 3: Labelled tracks with probability p > 0.95: corpus callosum (*orange*), cingulum (*blue*), fornix (*green*), inferior fronto-occipital fasciculus (*red*) and corona radiata (*violet*).

DISCUSSION – The results on the in silico phantom demonstrate that imposing a "perfect" label prior effectively suppresses false positive connections. The few invalid connections that do occur either run through the grey matter area (uniform prior), or are misclassified due to edge effects at the target ROIs. In real data, bundle labelling is more difficult for two main reasons. First of all, the atlas is inherently incomplete, i.e., not all bundles are (and may never be) labelled, and some bundles are undersegmented due to the tensor-based nature of this particular atlas, e.g., the radial projections of the corpus callosum. Secondly, registration artefacts affect the labelling at the edges between neighbouring bundles, say the corpus callosum and the fornix. Nevertheless, acceptable bundle segmentations can be obtained by thresholding the label probability, and a reduction of spurious fibres demonstrates that the proposed label prior can improve the track reconstruction itself. Future work should first of all focus on building a more detailed atlas. Multi-atlas techniques may help to alleviate registration effects.

CONCLUSION – We have introduced a label prior in global tractography, which allows for probabilistic white matter labelling and reduces the amount of false positive fibres.

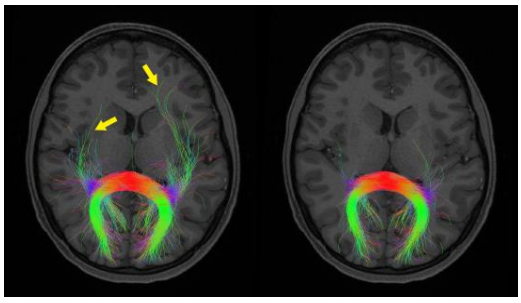

Fig. 4: Segmentation of the forceps major without label prior (*left*) and with label prior, p > 95% corpus callosum (*right*).

REFERENCES – **1.** Jbabdi and Johansen-Berg, *Brain Connectivity 1(3):169–183* (2011); **2.** Mangin et al., *NeuroImage 80:290–296* (2013); **3.** Reisert et al., *NeuroImage 54(2):955–962* (2011); **4.** Christiaens et al., *ISMRM 22:270 (2014)*; **5.** Ziyan et al., *Int J Comput Vis 85(3):279–290* (2009); **6.** Yendiki et al., *FNINF 5(23)* (2011); **7.** Caruyer et al., *ISMRM 22:2666* (2014); **8.** Van Essen et al., *NeuroImage 80: 62–79* (2013); **9.** Catani and Thiebaut de Schotten, *Cortex 44:1105–1132* (2008).

Super-resolution structural connectivity and anatomy of the zebra finch brain

Gwendolyn Van Steenkiste[1], Julie Hamaide[2], Ben Jeurissen[1], Dirk H.J. Poot[3, 4], Johan Van Audekerke[2], Jan Sijbers[1], Marleen Verhoye[2]

[1]iMinds-Vision Lab, University of Antwerp, Antwerp, Belgium; [2]Bio-Imaging Lab, University of Antwerp, Antwerp, Belgium; [3]Medical Informatics and Radiology, Erasmus Medical Center, Rotterdam, the Netherlands; [4]Imaging Science and Technology, University of Technology, Delft, the Netherlands

TARGET AUDIENCE: Scientists and clinicians interested in high resolution diffusion imaging of small animals.

PURPOSE: So far, structural investigation of the zebra finch (*Taeniopygia guttata*) brain was mainly performed by invasive methods such as histology [1]. This methodology, however, does not allow quantitative investigation of whole-brain structural connectivity. A recent proof-of-principle study using *in vivo* diffusion tensor imaging (DTI) in adult zebra finches revealed a novel sexual dimorphism in the song control system [2]. However, the diffusion weighted (DW) data acquired in that study, had a low spatial resolution of (0.19x0.19x0.24) mm^3. In order to better understand of the anatomical substrate underlying the observed differences, DTI data with a higher and preferably isotropic spatial resolution is required. Acquiring DW data at such a high isotropic spatial resolution covering the entire brain is, however, not feasible in a reasonable acquisition time using a conventional spin echo DW (SE-DW) or SE-EPI sequence. Therefore, a super-resolution (SR) *ex vivo* DTI protocol and reconstruction (SR-DTI), that improves the trade-off between acquisition time, spatial resolution and SNR of DTI parameters [3], was implemented. The SR-DTI method was combined with track density imaging (TDI) [4], as it has been shown in other small animal studies that TDI facilitates delineation of a large number of brain regions and small white matter bundels [5-6]. Here, the data set of an adult male zebra finch, obtained by the combination of SR-DTI and TDI is presented.

METHODS: *Sample preparation*: One adult male zebra finch kept in normal, non-breeding housing conditions was euthanized by an intramuscular injection of pentobarbital (60 mg/kg) and transcardially perfused first with ice-cold saline and second with an ice-cold 4% paraformaldehyde (PFA) in 0.1 M Phosphate Buffered Saline (PBS; pH 7.4) solution supplemented with gadolinium (1% Dotarem, 0.05 mmol/ml gadoteric acid). Next, the brains were post-fixed overnight with 4% PFA in 0.1 M PBS enriched with 1% Dotarem after which the tissue was transferred to 0.1 M PBS with 1% Dotarem and kept at 4°C. *Acquisition:* Eight hours prior to *ex vivo* imaging the brains were removed from the refrigerator in order to acclimatize to the ambient bore temperature. The zebra finch head was imaged with a spin echo sequence on a 9.4 Tesla MR with a circular polarized transmit resonator, quadrature receive surface coil and a 600 mT/m gradient insert. Fifteen sets of low resolution (LR) images were acquired, each with a different slice orientation, which was rotated around the phase encoding axis at incremental steps of 12°. Each of these sets consisted of 1 non DW image (b=0 s/mm²) and 6 DW images (b=2500 s/mm²) with following acquisition parameters: FOV (15x15) mm2, TE 26 ms, TR 10000 ms, acquisition matrix (192x137) zero-filled to (192x192), in-plane resolution of (0.078x0.078) mm², 37 slices, slice thickness 0.32 mm, b-value 2500 s/mm², δ 6 ms, Δ 14 ms, 1 repetition. Per slice orientation, the scanning time was 2h 40min. As the diffusion gradient directions were different for each slice orientations, a total of 90 unique diffusion gradient directions was acquired. The brains were kept in the skull during the entire procedure as to prevent mechanical damage throughout the different tissue processing and imaging steps. All experimental procedures were approved by the local Ethics Committee for Animal Experiments. *SR reconstruction*: The SR-DTI reconstruction combines the DTI model with an acquisition model, which allows the direct reconstruction of high resolution (HR) DTI parameters from the LR DW images with different slice orientations and diffusion gradient directions. The HR DTI parameters benefit from the high SNR of the LR DW images and the large set of diffusion gradient directions. A set of HR DTI parameters with isotropic voxel size (0.078x0.078x0.078) mm^3 was reconstructed from the acquired data set with this SR-DTI technique. *TDI*: From these HR DTI parameters, the fiber orientation density functions (ODF) with lmax=6, were estimated. Next, 10^8 streamlines, with a threshold of 0.1 on the ODF amplitude, a maximum angle of 9° and a step size of 0.00781 mm, were launched throughout the brain using probabilistic streamlines tractography by second order integration over fiber orientation distributions [7] in MRtrix3 [8]. This tractography result was then used to calculate a track density image with voxel size (0.04x0.04x0.04) mm^3.

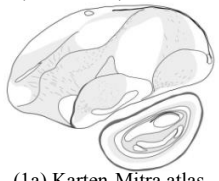

(1a) Karten-Mitra atlas

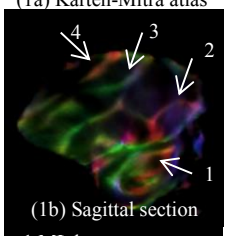

(1b) Sagittal section

1 MLd
2 arcopallium
3 Lamina mesopallialis
4 Lamina frontalis superior

RESULTS: The directionally encoded color SR-TDI maps provide clear anatomical contrast of several components of the song control (e.g. Area X, LMAN, RA; Fig 2b-c), auditory (e.g. FieldL, MLd; Fig 1b-2d) and visual system (e.g. Entopallium; Fig 2b). Structural connectivity such as tracts connecting distinct brain areas (e.g. tractus OM) and laminae subdividing the zebra finch brain in separate parts (e.g. LFS, LaM etc. Fig 1b), are most clearly visualized on the individual and color-coded SR-TDI maps (Fig 2). The obtained TDI maps (Fig 1b) show great similarities with online available myelin stained histological slices (Karten-Mitra atlas, Fig 1a) and with previously published high-resolution starling DTI data [9].

DISCUSSION: The current data set enables 3D whole-brain qualitative assessment of structural connectivity of several areas of the zebra finch brain. The obtained resolution of the acquired dataset and clear anatomical contrast allows delineation of brain regions of interest. This *ex vivo* experiment illustrates that the combination of SR-DTI and TDI can provide clear delineation of the anatomy of the song control system, without proportionally extending the acquisition time. The possibility to perform targeted or even whole-brain fiber tractography on the obtained high-resolution dataset might lead to a further insight into zebra finch brain connectivity both in health, e.g. throughout the critical period of vocal learning, and along the course of pathology.

CONCLUSION: In conclusion, the combination of SR-DTI and TDI has been successfully applied in preclinical small animal research, paving the way for exciting future studies aimed at the establishment of structural connectivity in early development or assessing (early) defects in structural connectivity attributed to neurodegenerative disorders.

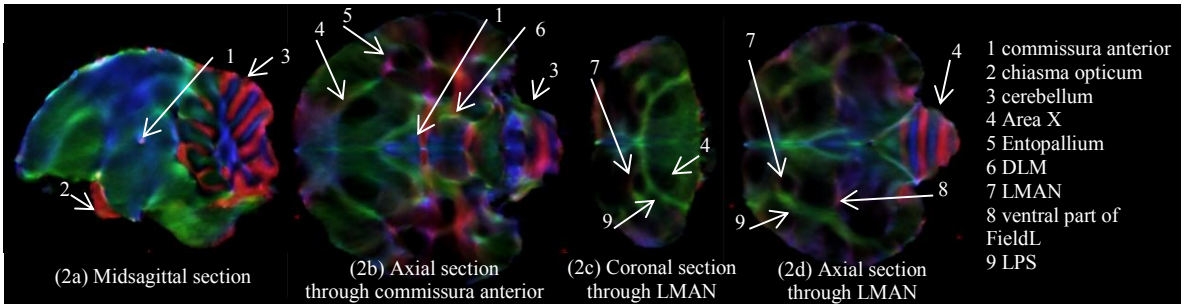

(2a) Midsagittal section | (2b) Axial section through commissura anterior | (2c) Coronal section through LMAN | (2d) Axial section through LMAN

REFERENCES: [1] Nottebohm et al., Science 194:211-213, 1976; [2] Hamaide et al., ISMRM 22:4553, 2014;[3] Van Steenkiste et al., ISMRM 22:2572, 2014; [4] Calamante et al., NeuroImage 53:1233-1243, 2010; [5] Richards et al., NeuroImage 102:381-392, 2014 [6] Ullmann et al., Brain Struct Funct 1-12, 2013; [7] Tournier et al., ISMRM 18:1670, 2010; [8] Tournier et al., Int J Imag Syst Tech 22:53-66, 2012; [9] De Groof et al., NeuroImage 29:754-763, 2006.

Diffusion tensor imaging of the lumbar and sacral plexus in post mortem subjects

Wieke Haakma[1,2], Michael Pedersen[3], Martijn Froeling[1], Lars Uhrenholt[2], Jeroen Hendrikse[1], Alexander Leemans[4], Lene Warner Thorup Boel[2]

[1]Department of Radiology, University Medical Center, Utrecht, the Netherlands; [2]Department of Forensic Medicine and Comparative Medicine Lab, Aarhus University, Aarhus, Denmark; [3]Department of Clinical Medicine and Comparative Medicine Lab, Aarhus University, Aarhus Denmark; [4]Image Sciences Institute, University Medical Center Utrecht, Utrecht, the Netherlands

Audience: Clinicians and researchers interested in the visualization of nerves with diffusion tensor imaging in post mortem subjects

Background and purpose: Diffusion tensor imaging (DTI) allows evaluation of microstructural properties of tissue and therefore is an emerging imaging technique to investigate post-mortem (PM) tissue. However DTI of PM nervous tissue remains challenging, particularly due to PM autolysis which is occurring shortly after death. Combined with bacterial degradation, which facilitates tissue decomposition, nervous tissue will quickly degrade.[1] Therefore, most PM DTI research has been performed on formaldehyde fixated tissue. However, fixation changes the diffusion characteristics and reduces proton density as well as T2.[2] Moreover, PM studies have mainly focused on brain research.[1] Whether DTI can be used in peripheral nervous tissue such as the lumbar and sacral nerves PM remains to be shown. This information is relevant as it can be helpful in the PM identification of death-related injuries. Furthermore, it is expected to be helpful to better understand peripheral nerve pathologies as it can be combined with histology. In this work we investigate the feasibility of DTI to examine the nerves in the lumbosacral plexus after death in PM non-fixated subjects and to identify trauma in one case.

Methods: Six non-fixated PM subjects with normal anatomy of the lower spine were included; 5 men and 1 women (1-8 days after death) with a mean age of 44 years (range 30–55 years). In addition a female PM subject (35 years) with a crushed lower lumbar vertebrae occurred during life was included. Subjects were scanned at the level of the lumbosacral plexus on a 1.5 Tesla MR system (Achieva; Philips Healthcare, Best, The Netherlands) using a 16-channel phased-array surface coil. DTI was performed with diffusion-weighted spin echo single-shot echo planar imaging (EPI) in the coronal plane with the following parameters; TE = 82 ms, TR = 13538 ms, SENSE factor 2, number of excitations = 8, FOV 384 × 216 mm², matrix size 128 × 72, 35 slices with thickness = 3.0 mm, resulting in a voxel size of 3.0 × 3.0 × 3.0 mm³, EPI factor: 35, SPIR fat suppression, b-values 0 en 2000 s/mm², and 15 gradient directions. The total acquisition time was 29:06 minutes. This protocol was repeated 4 times. For anatomical reference, a 3D Turbo Spin Echo (3D-TSE) scan was acquired according to the protocol described by van der Jagt et al[3]. The DTI scans were concatenated into one dataset. Fiber tractography (FT) was performed with the diffusion MRI-toolbox *ExploreDTI* to determine the fractional anisotropy (FA), mean diffusivity (MD), axial diffusivity (AD), and radial diffusivity (RD) of the lumbar and sacral nerves. As a reference, 6 healthy living controls with a mean age of 30 years (range 25-42 years), were scanned on a 3 Tesla Philips MRI scanner. Nerves at the level of L3 to S2 for FA, MD, AD, and RD were compared between PM subjects and healthy controls with the non-parametric Mann-Whitney U test.

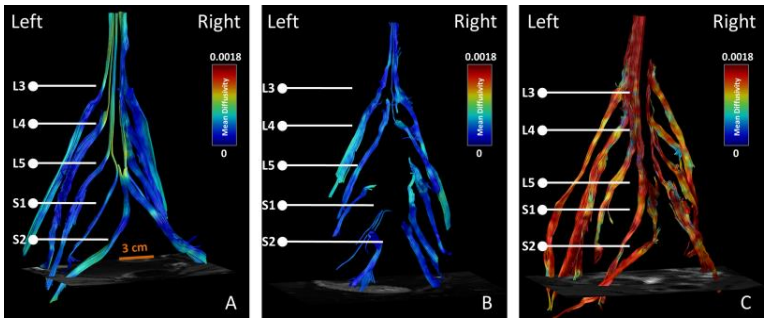

Figure 1: Lower lumbar and sacral nerves color coded with mean diffusivity, A) post-mortem, B) post-mortem subject with spinal cord injury with disorganization of spinal nerve roots, C) healthy living control

Results: This DTI study was able to reconstruct the 3D architecture of the lumbar and sacral plexus in all 7 PM bodies, detailing the individual pathway trajectories and the microstructural properties of L3-S2. The FT results were similar to in vivo measurements in healthy adults (see figure 1). In cases where the nerves and cauda equina were exposed during autopsy the FT results were similar in architecture found during autopsy (see figure 2).
Diffusion values showed a higher FA in PM cases ($p<0.05$). MD, AD and RD values were approximately 4 times lower than in vivo results (see table 1).
In one case disorganization of the nerves at the lower lumbar level was found (figure 1B). Here, the lower lumbar vertebrae was crushed due to trauma during life, years before death occured. Clinical background information of this case showed incontinence problems and less sensibility in the legs. This is comparable to the results found in spina bifida patients described by Haakma et al[4].

Table 1 Diffusion parameters (FA, MD, AD, and RD) of PM and in vivo healthy controls

Nerve	Diffusivity (mm²/s) x 10^{-3}							
	FA		MD		AD		RD	
	In vivo	PM	In vivo	PM	In vivo	PM	In vivo	PM
L3**	0.27±0.05	0.33±0.07	1.47±0.16	0.35±0.05	1.90±0.17	0.48±0.05	1.25±0.16	0.29±0.05
L4**	0.27±0.04	0.33±0.07	1.43±0.17	0.36±0.05	1.84±0.18	0.49±0.05	1.22±0.17	0.29±0.05
L5**	0.29±0.03	0.35±0.06	1.41±0.17	0.36±0.03	1.87±0.19	0.51±0.04	1.18±0.16	0.29±0.03
S1**	0.26±0.04	0.31±0.06	1.47±0.17	0.38±0.05	1.89±0.16	0.51±0.05	1.26±0.17	0.31±0.06
S2**	0.25±0.03	0.29±0.06	1.49±0.10	0.38±0.06	1.88±0.12	0.50±0.07	1.29±0.10	0.31±0.06

** At all levels for each diffusion value in vivo vs PM: $p<0.05$

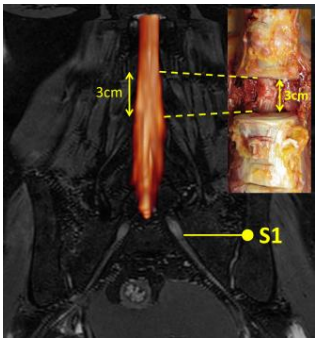

Figure 2: 3D TSE image with nerve tracts of the cauda equina found with FT (vertebrae not shown) and the matching images of the autopsy

Conclusion: This DTI study shows the feasibility of DTI to identify the architecture of the lumbar and sacral plexus in 7 PM bodies with DTI and FT. We demonstrate the difference in diffusion parameters between in vivo and PM nervous tissue. The architectural configuration of the nerves and cauda equina found on the DTI images was equivalent to the visual examination during autopsy. Disorganization of the nerves in the trauma case showed the potential of DTI and FT to be used to identify nerve injuries PM. The observed differences in MD, AD and RD are presumed to be caused by temperature difference[5] and PM changes of the nervous tissue. DTI PM allows the possibility to identify other peripheral nerve pathologies which can be helpful in the contribution of better understanding pathogenesis and disease progression as it can be compared with histology and other techniques. We expect that this technique can provide a valuable contribution to the identification of nerve injuries in complex PM trauma cases.

References:

[1] D'Arceuil et al. Neuroimage. 2007;36(1):64-8; [2] Miller et al. Neuroimage. 2011;57(1):167-81; [3] van der Jagt et al. Neuroimage. 2012;62(3):1792-9;
[4] Haakma et al. Journal of Urology. 2014; [5] D'Arceuil et al. Neuroimage. 2007;35(2):553-65

The influence of various diffusion MRI processing pipelines

David Szabolcs[1], Chantal M. W. Tax[1], Max A. Viergever[1], Anneriet Heemskerk[1], Alexander Leemans[1]

[1]Image Sciences Institute, University Medical Center Utrecht, Utrecht, the Netherlands

Target audience: Researchers with an interest in diffusion MRI tractography

Introduction: With advanced diffusion-weighted (DW) MRI methods becoming more popular to investigate white matter properties in clinical and biomedical applications, a lot of efforts are being made to optimize the pipeline to analyse the data [1]. Different steps and settings during processing procedures (e.g. corrections to subject motion, eddy current induced distortions and EPI deformations, spatial normalization, and tensor estimation methods) can influence the resulting outcome and may complicate interpretation and statistical inferences [2, 3]. The purpose of this work was to investigate whether the choice of (a) interpolation strategy (linear vs. cubic spline) during subject motion / eddy current distortion correction and (b) the tensor estimation procedure (robust vs. ordinary linear least squares – OLLS) would *significantly* affect the outcome, which in this work was confined to an example of a tractography based analysis of the uncinate fasciculus.

Methods: Acquisition: Ten healthy volunteers were scanned on a 3T MR system with a diffusion MRI scan protocol consisting of: 60 DW images with b-value of 1200 s/mm^2; 6 non-DW images; isotropic voxel size of 2.4 mm (more details are provided in [4]). Processing: All datasets were processed with ExploreDTI [5] using four different pipelines: linear and cubic spline interpolation during correction for subject motion and eddy current distortions [6] in combination with two diffusion tensor estimation methods: REKINDLE [7] and the OLLS approach [8]). Analysis: An automated atlas based fiber tractography based on the framework presented in [9] was used to reconstruct the right uncinate fasciculus (R-UNC). Details of the ROI protocol to extract the R-UNC are described in [10]. Statistical evaluation: Fractional anisotropy (FA), volume, and mean diffusivity (MD) of the R-UNC tracts are compared between the four processing pipelines using paired t-tests. Combinations in which both the tensor estimation and the interpolation approach are different were not examined.

Results: Fig. 1 illustrates the differences in trajectories of the R-UNC between the four different processing pipelines for a representative subject. Generally, small differences are observed in the length and the overall configuration of the tract pathways. Fig. 2 shows the spatial heterogeneity of the FA difference between REKINDLE and OLLS for the linear interpolation strategy. We found, however, *significant* differences in FA values between the tensor estimation methods for a given interpolation approach and between the two interpolation approaches for a given tensor estimation method (Fig. 3 A). As shown in Fig. 3 B, predominantly the interpolation method affected the MD estimates. There was only a minor effect of estimation method on the volume of the tract (Fig. 3 C).

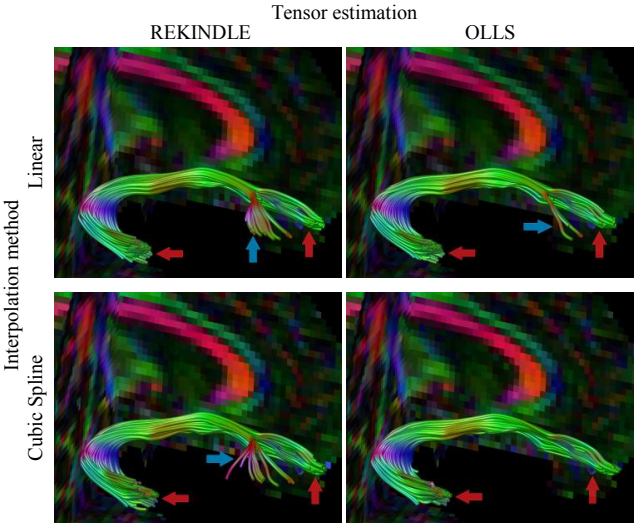

Fig. 1: *Tracts representing the right uncinate fasciculus reconstructed with four different preprocessing strategies from the same subject. Arrows indicate differences in architectural configurations.*

Discussion and Conclusion:

In this work, we have shown that the influence of tensor estimation and interpolation methods on a typical diffusion analysis is significant. Both the interpolation method and the tensor estimation method result in small local, yet significant differences in the diffusion metrics. Comparisons of data from different processing pipelines should be interpreted with care. Considering the interaction of the processing parameters there is *no significant difference* in the effect size of tensor estimation and interpolation strategy in the case of FA. For MD the outcome is more affected by the interpolation method, while volume is more sensitive to the choice of tensor fitting algorithms.

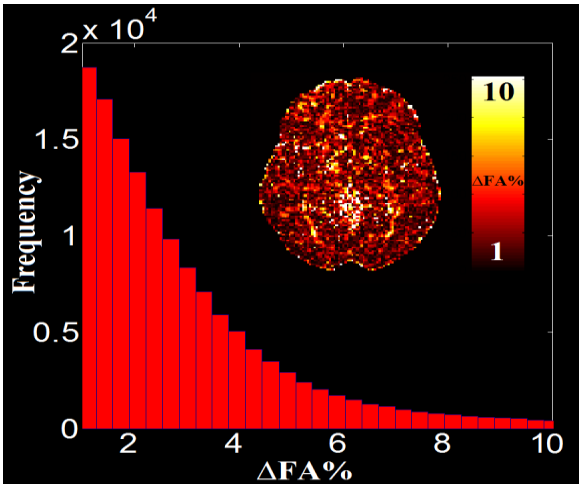

Fig. 2: *Voxel wise difference in FA between OLLS and REKINDLE for a representative subject. Image scale and histogram X axis indicate FA differences between 1% and 10% value.*

References:[1] Sotiropoulos SN, et al. Neuroimage. 2013 Oct 15;80:125-43.;[2] Jones DK, et al. Neuroimage. 2013 Jun;73:239-54;[3] Jones DK, et al. NMR Biomed. 2010 Aug;23(7):803-20.;[4] Vos SB, et al. Neuroimage. 2011 Apr 15;55(4):1566-76.;[5] Leemans et al.ISMRM, Hawaii,USA; 2009:3537.;[6] Leemans A et al. Magn Reson Med. 2009 Jun;61(6):1336-49.;[7] Tax CMW et al. Magn Reson Med. 2014 Mar 31;[8] Veraart J et al. Neuroimage. 2013 Nov 1;81:335-46.;[9] Lebel C et al. Neuroimage. 2008 Apr 15;40(3):1044-55;[10] Aarnink SH et al. Neuroimage. 2014 Feb 1;86:404-16

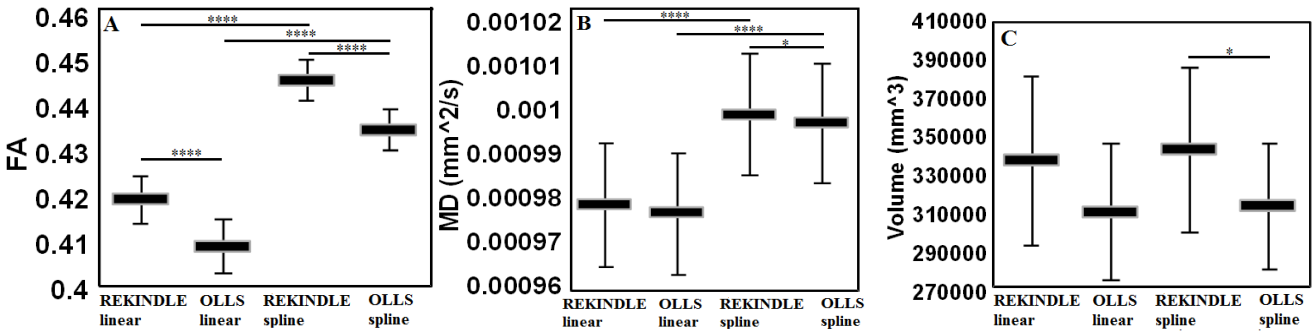

Fig. 3: *Average and standard error of the mean FA (A), MD (B) and volume (C) of all ten R-UNCs. Significant differences can be found between all the FA and some of the MD values; however volumetric difference only occurs between REKINDLE and OLLS with cubic spline interpolation. Data sets that are significant at different levels: * p<0.05, ** p<0.01, *** p<0.001, **** p<0.0001.*

Reconstruction of convex polynomial diffusion MRI models using semi-definite programming

Tom Dela Haije[1], Andrea Fuster[1], Luc Florack[1]

[1]Department of Mathematics and Computer Science, Eindhoven University of Technology, Eindhoven, the Netherlands

Purpose: Polynomial basis functions form the backbone of many current signal models in diffusion MRI. These models typically impose constraints like positive semi-definiteness and symmetry, combining heuristics, physically motivated assumptions, and computational complexity arguments. In order to incorporate these constraints the reconstruction algorithms used to determine the polynomial coefficients have to be adapted accordingly. Here we consider convexity of a general polynomial model as an additional constraint, which among other things is one of the requirements when performing (Finsler) geodesic tractography.[1] Since verifying the convexity of a polynomial is generally NP-hard, we consider a subset of all convex polynomial functions called sum-of-squares polynomials, following the approach outlined by Magnani et al.[2] In this work we explain their method and show that the resulting optimization procedure is feasible for use in typical diffusion MRI reconstruction tasks.

Theory: We will consider a degree $2m$ polynomial diffusion MRI model $P_{\boldsymbol{y}}(\boldsymbol{q})$ that is linear in its coefficients $\boldsymbol{y}$ and where $\boldsymbol{q} \in \mathbb{R}^3$ is a gradient vector that parameterizes the measurement space in diffusion MRI. $P_{\boldsymbol{y}}(\boldsymbol{q})$ is convex if and only if its Hessian $\nabla^2 P_{\boldsymbol{y}}$ is positive semi-definite. Our goal is to find $\boldsymbol{y}$ such that the measurements $\{\hat{P}(\boldsymbol{q}_i)\}_{i=1}^N$ are best represented by a convex $P_{\boldsymbol{y}}(\boldsymbol{q})$ in the least squares sense, and so we want to minimize the residual sum of squares $\|\boldsymbol{r}_{\boldsymbol{y}}\|^2 := \sum_{i=1}^N [P_{\boldsymbol{y}}(\boldsymbol{q}_i) - \hat{P}(\boldsymbol{q}_i)]^2$ over $\boldsymbol{y}$ subject to $\nabla^2 P_{\boldsymbol{y}}(\boldsymbol{q}) \succcurlyeq 0$, where $\succcurlyeq 0$ indicates positive semi-definiteness. There are no known techniques to tractably solve this problem, and so following Magnani et al.[2] we impose the stronger restriction that $\nabla^2 P_{\boldsymbol{y}}(\boldsymbol{q})$ be the sum of a number of squared polynomials, which directly guarantees convexity of $P_{\boldsymbol{y}}(\boldsymbol{q})$. The sum-of-squares constraint is formulated as a linear matrix inequality $V(\boldsymbol{y}) \succcurlyeq 0$, where the associated Gram matrix $V(\boldsymbol{y})$ is any matrix such that for a given vector $\boldsymbol{e}(\boldsymbol{s},\boldsymbol{q})$ of all monomials up to degree m in $\boldsymbol{s} \in \mathbb{R}^3$ (order 1) and $\boldsymbol{q}$ (up to order $m-1$) we have $\boldsymbol{s}^T \cdot \nabla^2 P_{\boldsymbol{y}}(\boldsymbol{q}) \cdot \boldsymbol{s} = \boldsymbol{e}(\boldsymbol{s},\boldsymbol{q})^T \cdot V(\boldsymbol{y}) \cdot \boldsymbol{e}(\boldsymbol{s},\boldsymbol{q})$.

Methods: We introduce a bound τ on the objective function, i.e., $\|\boldsymbol{r}_{\boldsymbol{y}}\|^2 \leq \tau$, and define an analogous optimization problem with a linear objective function:

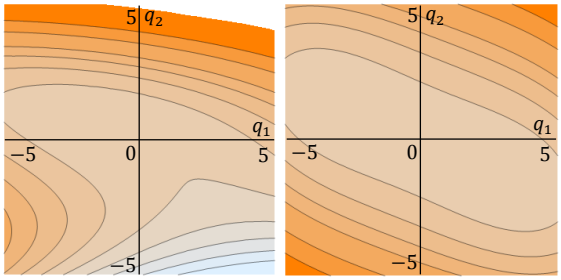

Fig 1. Left: The ground truth data $\hat{P}(\boldsymbol{q}) = (q_1)^2 + 4(q_2)^2 + 3q_1q_2 + (q_2)^3$, sampled equidistantly on a Cartesian grid from -5 to 5 in steps of 0.5. Right: Results of the reconstruction algorithm fitting a fourth order convex-constrained polynomial $P_{\boldsymbol{y}}(\boldsymbol{q})$. Displayed are the level sets $\{-200, -175, \ldots, 200\}$, with colors indicating the approximate function value (light blue – low; orange – high).

$$\min_{\tau,\boldsymbol{y}} \tau \quad \text{subject to} \quad \begin{pmatrix} V(\boldsymbol{y}) & 0 & 0 \\ 0 & I & \boldsymbol{r}_{\boldsymbol{y}} \\ 0 & (\boldsymbol{r}_{\boldsymbol{y}})^T & \tau \end{pmatrix} \succcurlyeq 0. \qquad (1)$$

Since both the constraint and the objective function are linear in the optimization parameters, this is a convex optimization problem called a semi-definite programming problem. [3] For a given model and data we write this problem to an SDPA file, which is a standard format supported by the majority of solvers. For all experiments shown we use the SDPA solver[4] with default settings for the optimization. An illustration of an optimized fourth order convex-constrained polynomial (with even order monomials) is shown in Fig. 1, where we took $\boldsymbol{q} \in \mathbb{R}^2$ for simplicity.

As proof of concept we further consider the diffusion model $\hat{P}(\boldsymbol{q}_i) = -\log E(\boldsymbol{q}_i)$, $\|\boldsymbol{q}\|^2 \sim b$, used in the context of Finsler tractography by Melonakos et al.[1], where E is the normalized diffusion-weighted signal in a given voxel. $P_{\boldsymbol{y}}(\boldsymbol{q})$ is given by an even order polynomial with even order monomials. The reconstruction is tested on 10 random voxels from a data set of the Human Connectome Project[5] (subject ID 100307) consisting of 270 $\boldsymbol{q}_i$ evenly distributed on shells with $b \approx 1000, 2000, 3000\, s/mm^2$. The baseline image is estimated by averaging the 18 available $b \approx 0\, s/mm^2$ images.

Results: Optimization for a fourth order model required $2.58 \pm 0.03\, s/voxel$ (mean $\pm$ std) on an Intel i7-2600 CPU clocking at 3.40GHz (8 cores). Reducing the number of used measurements to 60 per voxel brought the running time for this model down to $0.46 \pm 0.03\, s/voxel$. A second order convex-constrained model took $2.18 \pm 0.04\, s/voxel$ on the full data, while a sixth order constrained model could be reconstructed in $5.71 \pm 0.18\, s/voxel$. When dropping the convexity constraint the algorithm converged in similar time spans (due to the relatively small size of $V(\boldsymbol{y})$ in the constraint). The per-voxel overhead is around $0.25\, s$ in the current implementation. The impact of the convexity constraint on the residual sum of squares (RSS) was typically small, suggesting that for this data convexity may be a reasonable assumption. Fig. 2 shows $\hat{P}(\boldsymbol{q}_i)$ for the $b \approx 3000\, s/mm^2$ shell, together with the estimated profiles produced by the reconstruction algorithm.

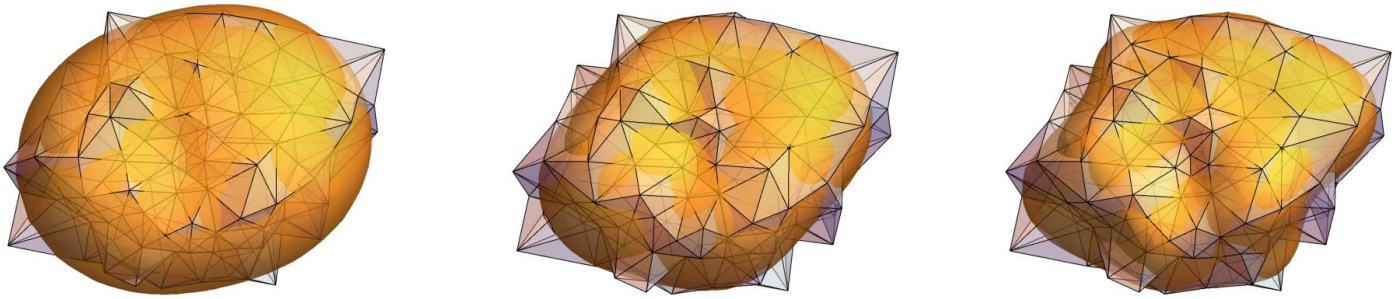

Fig 2. Left: Second order convex-constrained model, with a residual sum of squares $RSS = 10.33$. Middle: Fourth order convex-constrained model, $RSS = 4.82$. Right: Sixth order convex-constrained model, $RSS = 4.40$. The plots show $\hat{P}(\boldsymbol{q}_i)$ for the $b \approx 3000\, s/mm^2$ shell (purple triangulated mesh, with vertices $\hat{P}(\boldsymbol{q}_i)\, \boldsymbol{q}_i/\|\boldsymbol{q}_i\|$), together with the estimated profiles (smooth orange surface, defined as the set $\left\{P_{\boldsymbol{y}}(\boldsymbol{q})\frac{\boldsymbol{q}}{\|\boldsymbol{q}\|} \,\middle|\, b = 3000\, s/mm^2\right\}$, comparable to an ADC profile). The considered voxel is located in the occipital lobe.

Discussion: Generally the algorithm scales somewhat poorly in both the number of measurements per voxel and in model complexity, as both significantly increase the problem size of the semi-definite program. The timings presented here show that for a fairly large data set (270 measurements) and a moderately complex model (21 degrees of freedom for the fourth order polynomial model), reconstruction of a full data set (~750,000 relevant voxels) would take around three weeks. The same model reconstructed on a typical clinical data set, consisting of 60 measurements per voxel and 300,000 voxels, would take roughly a day. The overhead per voxel can be essentially eliminated by fixing the model choice, which would reduce the computation time for a clinical scale data set to half a day. Further improvements can be gained by exploiting parallelization of the reconstruction and by fine-tuning the solver settings, both of which are expected to result in significant speed-ups.

Conclusion: In this work we apply the fitting techniques described by Magnani et al.[2] to reconstruct a polynomial diffusion MRI model subject to convexity constraints. Convexity is enforced by requiring that the Hessian function of the polynomial model is sum-of-squares. We show that the resulting model fitting procedures are feasible for diffusion MRI reconstruction tasks. Future work will consist of improving the implementation and applying convex-constrained models in existing geodesic tractography.

References: [1] Melonakos et al. *IEEE Trans. Pattern Anal. Mach. Intell.* 2008; 30(3):412–23. [2] Magnani et al. *IEEE 44th CDC-ECC* 2005; 1672–77. [3] Vandenberghe et al. *SIAM Rev.* 1996; 38(1):49–95. [4] Yamashita et al. *Tokyo Tech Report* 2010; B-460. [5] Van Essen et al. *NeuroImage* 2013;80:62. [6] B. Borchers. *Optimization Meth. & Soft.* 1999:11(1-4):613–23.

Posters

Angiography and pulsatility of small intracranial vessels at 7 Tesla

Roald S. Schnerr[1], Jaap F. Jansen[1,2], Paul A. Hofman[1,2], Joachim E. Wildberger[1,2,3], Kâmil Uludag[4], Robert J. van Oostenbrugge[2,3,5], Walter H. Backes[1,2,3]

[1]Department of Radiology, Maastricht University Medical Center, Maastricht, the Netherlands
[2]Research School for Mental Health & Neurosciences (MHeNS), Maastricht University Medical Center, Maastricht, the Netherlands
[3]Cardiovascular Research Institute Maastricht (CARIM), Maastricht University Medical Center, Maastricht, the Netherlands
[4]Maastricht Brain Imaging Centre (M-BIC), Maastricht, the Netherlands
[5]Department of Neurology, Maastricht University Medical Center, Maastricht, the Netherlands

Background: Cerebral small vessel disease (SVD) is a term that covers a large range of neuropathological disorders and clinical symptoms which are considered to be related and often manifest in global neurological dysfunction and dementia. Observable features of SVD on MRI include white matter lesions, microbleeds and lacunar infarcts[1]. However, the direct pathology of small cerebral blood vessels in terms of occlusions or increased vessel wall stiffness has not yet been visualized. The rationale behind this research is that the pulsatility of the perforating arteries should be related to vessel condition, which would allow us to investigate the role of vessel wall deterioration in SVD and provide a functional imaging biomarker.

Objective: Our goal is to directly image small (perforating) arteries of the brain and to characterize their pulsatile condition. We have selected the lenticulostriate arteries (LSAs), where previous research[2] has focused on small arteries above the corpus callosum. The LSAs are small perforating vessels, which branch from the middle cerebral arteries (MCAs, see Fig. 1) and supply the basal ganglia with blood. They are larger than most other penetrating vessels and easily identified using the MCAs as a landmark.

Methods: To achieve the required spatial resolution to image the LSAs, we have used ultra-high field MRI imaging (7 Tesla Magnetom MRI, Siemens Healthcare, Erlangen, Germany) with a 32-channel send-receive head coil. We applied three-dimensional high spatial resolution (0.2 mm isotropic voxel size) time-of-flight (TOF) arteriography to image the intracranial vessels and velocity-sensitized (phase-contrast) MR angiography to measure flow speeds as a function of the cardiac phase. The cardiac cycle was registered with an acoustic sensor.

Results: We have obtained high resolution three dimensional arteriography measurements of eight healthy volunteers at 7-Tesla. An example maximum intensity projection (MIP) of the area around the circle of Willis is shown in Fig. 1. In these images we can recognize all the major arteries and clearly identify the LSAs. After identifying the LSAs, these images were used to geometrically plan the slice to measure the velocity of the blood stream as a function of the cardiac cycle. We determined the flow velocity for both MCAs and LSAs.

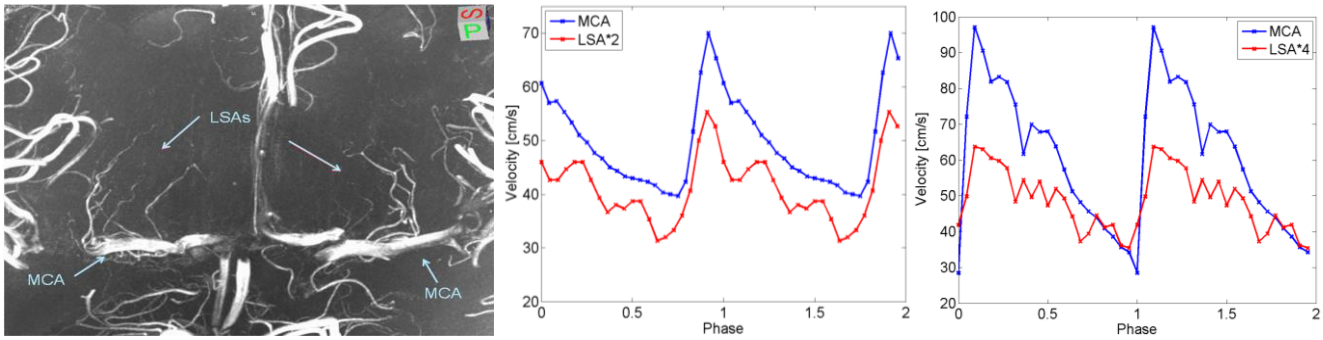

Figure 1: The LSAs are arteries that branch from the MCAs and penetrate the basal ganglia. These can be clearly visualized in a maximum intensity projection (MIP) of arteriography measurements at 7T (left), here viewed from posterior to anterior. Velocity profiles as a function of cardiac phase of two healthy volunteers (middle and right). Two cardiac cycles are displayed to show the periodicity of the average velocity profile. Pulsatility is clearly seen in both the MCAs and LSAs. The LSA blood velocity has been multiplied by 2 (middle) and 4 (right) to improve its visibility.

Conclusions: The high spatial resolution that can be achieved with 7-Tesla MRI allows us to clearly identify the lenticulostriate arteries (LSAs) in healthy volunteers using time-of-flight arteriography. We measured significant blood flow velocity profiles in both the MCAs and LSAs as a function of the cardiac phase. In the LSAs the flow velocities were found to be an order of magnitude larger than in the perforating arteries above the corpus callosum[2]. For the first time we have visualized the pulsatility of LSAs. Further analysis will allow us to determine the reproducibility of these results, and their applicability for clinical research.

References

[1]Wardlaw, J.M., Smith, C. and Dichgans, M. Mechanisms of sporadic cerebral small vessel disease: insights from neuroimaging. The Lancet Neurology 2013; 12(5):483-97
[2]Bouvy, W., Biessels, G.J., Kappelle, L.J, et al. Blood flow velocity and pulsatility analysis of cerebral small perforating arteries with 7 Tesla quantitative flow MRI, ISMRM Benelux 2014, poster PT3-01 (http://benelux-ismrm.org/annual-meetings/annmeeting14/proceedings)

Whole heart DTI using asymmetric bipolar diffusion gradients

Martijn Froeling[1], Gustav J. Strijkers[2], Aart J. Nederveen[3], Peter R. Luijten[1]

[1]Department of Radiology, University Medical Center, Utrecht, the Netherlands
[2]Department of Biomedical Engineering and Physics, Academic Medical Center, Amsterdam, the Netherlands
[3]Department of Radiology, Academic Medical Center, Amsterdam, the Netherlands

Introduction: Cardiac diffusion weighted imaging (DWI) using a spin echo sequence is challenging because of its high sensitivity to bulk motion. When the displacement, velocity or acceleration are constant and coherent but not equal for all spins within a voxel, it will cause signal attenuation due intra voxel de-phasing as an effect of first or second order moment encoding errors. This signal attenuation cannot be distinguished from that originating from diffusion weighting. To compensate for these effects bipolar gradients have been proposed that compensate for first order moment encoding [1]. However, this method will only work under the assumption of a uniform non-accelerated motion. Therefore, the aim of this study was to develop SE-based cardiac diffusion MRI protocol with second order moment nulling, thus also compensating for acceleration, and to compare its performance to that of Stejskal-Tanner and bipolar gradients waveforms.

Methods: Five healthy volunteers were scanned on a 3T scanner (Philips, Achieva) using a 16-channel coil (Torso XL). DWI was performed using a SE sequence with cardiac triggering in free breathing with Stejskal-Tanner, bipolar and asymmetric bipolar gradients (**figure 1**) and additional flow compensation for the slice and readout gradients [2]. The echo times were, 42, 60 and 66 ms, respectively. Further imaging parameters were; TR = 8 heart beats; FOV = 280 x 150 mm^2 (using outer volume suppression); slices = 12 (2 interleaved 6 slice packages); voxel size = 6 x 2.5 x 2.5 mm^3; acquisition matrix = 112 x 58; SENSE factor = 2; partial Fourier= 0.85; EPI train = 37; EPI duration = 23.2 ms; EPI bandwidth = 36 Hz/pix; averages = 4; trigger delay = 200 ms; gradient directions = 12; b-value = 400 s/mm^2; G_{max} = 62 mT/m; max slope = 100 mT/m/ms and acquisition time = 10 min.

Results: DWI data acquired in different cardiac phases (100 to 800 ms) using Stejskal-Tanner, bipolar and asymmetric bipolar diffusion encoding gradients are shown in **figure 2**. Signal dropout due to motion was reduced most with the asymmetric bipolar gradients (**figure 2C**). Maps showing the trans-mural changes in helix angle, which were calculated from data acquired with these gradients, are shown in **figure 3**.

Conclusion: In this study whole heart DTI using second order moment nulling diffusion gradients was performed. Using this approach we have shown that it is feasible to quantify the transmural helix angle for the entire heart. The DTI data was acquired in free breathing with a 10 min protocol, making this protocol well suited for clinical applications.

References: **[1]** U.Gamper, MRM;2007, 57:331–337; **[2]** M.Froeling, JCMR 2014; 16(Suppl 1):O15

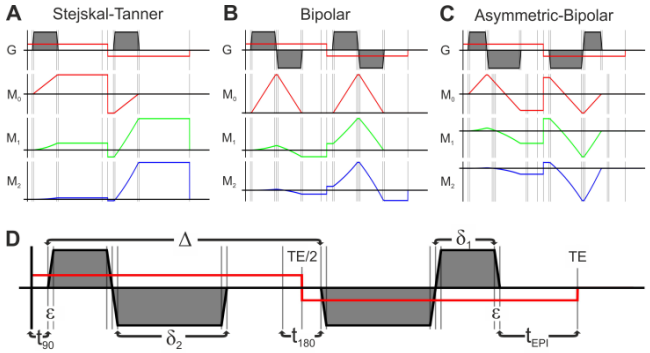

Figure 1: *Diffusion weighted SE sequence with Stejskal-Tanner (**A**), Bipolar (**B**) and asymmetric bipolar (**C**) diffusion weighted gradients together with their gradient moments $M_n(t)$ (Red: M_0; Green: M_1; Blue: M_2). **D**) The timing of the asymmetric bipolar gradient waveform. Its first and second order gradients moments are zero when* $\delta_1 = (-\Delta\delta_2 + \delta_2\epsilon)/(\Delta + 2\delta_2 + \epsilon)$.

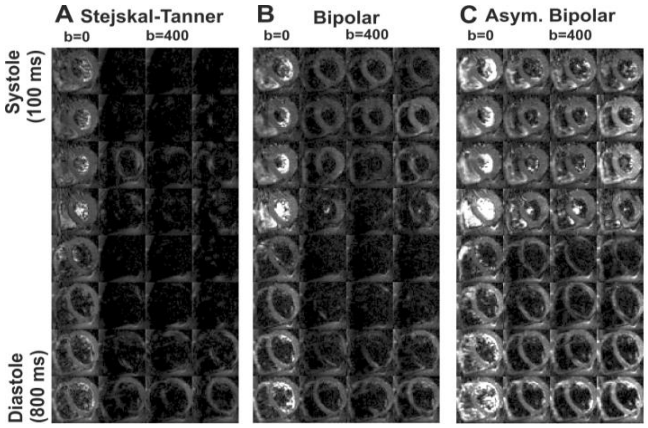

Figure 2: A-C) *Diffusion weighted imaging using Stejskal-Tanner (**A**), bipolar (**B**) and asymmetric bipolar (**C**) diffusion encoding gradients in different cardiac phases (100 to 800 ms in steps of 100 ms). For each sub-figure left column shows the non-weighted images (b=0s/mm^2) and the right three columns show the diffusion weighted images (b=400 s/mm^2) in the x, y and z directions, respectively.*

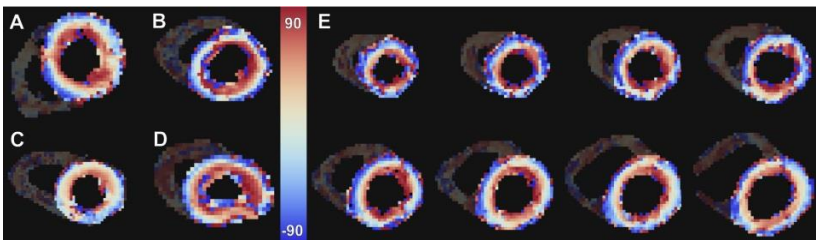

Figure 3: *Helix angle maps for all 5 volunteers, calculated form DTI data acquired with asymmetric bipolar diffusion gradients. **A-D)** Helix angle map of the middle slice for 4 volunteers **E)** Helix angle map of apical to basal slices for one volunteer.*

Noninvasive three-dimensional mapping of endothelial dysfunction in cardiac ischemia by dynamic contrast enhanced magnetic resonance imaging using Albumin-based contrast agent

Katrien Vandoorne[1], Moriel H. Vandsburger[2], Yue Han[1], Igor Jacobs[1], Hagit Dafni[3], Klaas Nicolay[1], Gustav Strijkers[1]

[1]Department of Biomedical Engineering, Eindhoven University of Technology, Eindhoven, the Netherlands
[2]Department of Physiology, University of Kentucky, Lexington, United States
[3]Department of Veterinary Resources, Weizmann Institute of Science, Rehovot, Israel

Target audience: Cardiovascular magnetic resonance researchers.
Purpose: Myocardial endothelial dysfunction after a myocardial infarction results in leakage of albumin from the intravascular space. This study aimed to develop a noninvasive method to quantify the dynamics of an albumin-based blood pool contrast agent for mapping the myocardial microvascular density and the rate of extravasation from myocardial blood vessels using in vivo dynamic contrast enhanced magnetic resonance imaging (DCE-MRI).

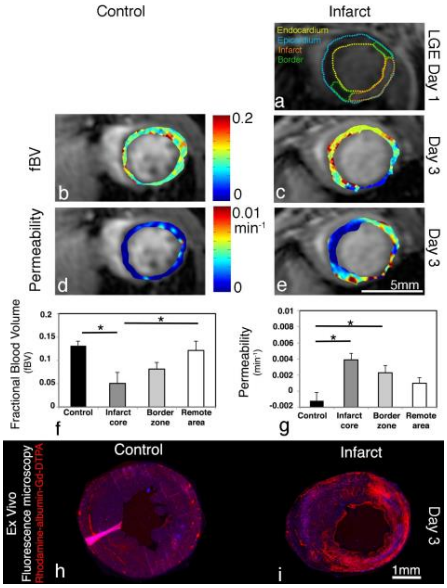

Fig. 1. (a) Late gadolinium-enhanced (LGE) images acquired 1 day after MI to define the regions of interest (ROIs) for analysis of DCE-MRI. Representative midventricular cardiac MR images in gray of the first postcontrast scan with in color parametric (b,c) fBV and (d,e) permeability maps of the myocardium. Values for (f) fBV and (g) permeability in different regions. (h,i) Ex vivo fluorescence microscopy of myocardium 30min after injection of albumin-based contrast agent.

Methods: C57BL/6 mice were imaged before (n=6) and 3 days (n=7) after a myocardial infarction (MI). Late gadolinium enhanced (LGE) MRI using Gd-DTPA was performed one day after MI to verify similar infarct sizes. LGE-MR images defined infarct core (hyper intense signal) and border zone (2mm area circumferentially away from the infarct core; Fig.1 a). Measurements were performed on a 9.4T Bruker scanner using a 72-mm volume coil with a 4-channel phased-array coil (Bruker Biospin, Ettlingen Germany). Three-dimensional (3D) Intragate FLASH images of the entire heart with retrospective gating were acquired before and after intravenous injection of macromolecular albumin-Gd-DTPA (10mg/mouse in 200μl; Relaxivity r_1=130mM^{-1}s^{-1}; SyMO-Chem, Eindhoven, The Netherlands). After a series of precontrast 3D-FLASH images with increasing flip angle (2°, 5°, 8°, 11°, 13°) to determine the endogenous R_1, albumin-Gd-DTPA was injected through an indwelling tail vein catheter at a rate of 50μl/min. Consequently the dynamics of the contrast agent were imaged by 6 consecutive scans with flip angle = 13° (1,2). MRI parameters included: RFpulse of 1ms sinc pulse (10lobes, 20kHz); FOV 30x30x10mm; Matrix128x64x15 with zerofilling to 128x128x15; TE=1.784ms; TR=10ms; repetitions=22; and scantime=4min. For the navigator slice parameters included RFpulse=1.5ms; Gauss pulse (Bandwidth=1830kHz); slice thickness=3mm. Maps of fractional blood volume (fBV) and permeability surface area product (Permeability) were calculated in MATLAB (Mathworks, Natick, MA, USA) using a linear regression of the first 24min, after normalizing the concentration of contrast material in the selected ROIs (i.e., healthy (control) myocardium, remote myocardium, infarct core and border zone) by the concentration in the hepatic vein (2). Red fluorescent rhodamine covalently bound to the albumin-based contrast agent was used to validate the MR finding by ex vivo fluorescence microscopy.

Results: Three days post-MI fBV at the infarct core appeared significantly reduced compared to both healthy control mice and remote myocardium. In the border zone fBV values were reduced compared to healthy control tissue, but elevated compared to infarcted tissue (Fig. 1b,c,f). The permeability surface area product was elevated in the infarct core and border zone compared to healthy control and non-infarcted remote tissue (Fig. 1d,e,g). Additionally these permeability findings were quantified and validated by ex vivo fluorescent microscopy. The myocardial percent area of red fluorescennt rhodamine-albumin-Gd-DTPA was significantly elevated in the infarct core and border zone compared to healthy control and non-infarcted remote tissue (Fig.1h,i). **Discussion:** The previously developed 3D cardiac R_1 mapping to monitor the accumulation of macromolecular contrast agents in a murine myocardial infarction (3) appeared robust enough to follow dynamics of albumin-Gd-DTPA with DCE-MRI and to measure myocardial fBV and permeability. Measurements of reduced fBV in infarcted myocardium reflect the decreased (micro)vascular density in the infarct core. In healthy myocardial tissue, fBV values were comparable to previously published data (4).
Conclusion: This method enabled noninvasive 3D quantitative mapping of microvascular density and initial rate of extravasation of high-molecular-weight contrast materials in the distinct regions of infarcted myocardium with altered endothelial function and has the potential to longitudinally track endothelial dysfunction in models of myocardial healing.

References:

1. Coolen BF, Geelen T, et al. NMR in biomedicine 2011;24(2):154-162.
2. Dafni H, Gilead A, et al. 2003;50(5):904-914.
3. Coolen BF, Geelen T, et al. J cardiovascular magnetic resonance 2011;13:56.
4. Waller C, Kahler E, et al. Radiology 2000; 215(1):189-97.

The effect of Ivabradine on plaque size, biomechanics, and microvasculature in atherosclerotic rabbits measured using MR and Ultrasound Imaging

Raf H.M. van Hoof[1], Evelien Hermeling[1], Julie Salzmann[2], Judith C. Sluimer[3], Sylvia Heeneman[3], Arnold P.G. Hoeks[4], Jérôme Roussel[2], Harry Struijker-Boudier[5], Joachim E. Wildberger[1], M. Eline Kooi[1]

[1]Department of Radiology, Maastricht University Medical Center, Maastricht, the Netherlands; [2]Institut de Recherches Internationales Servier, Suresnes, France; [3]Department of Pathology, Maastricht University Medical Center, Maastricht, the Netherlands; [4]Department of Biomedical Engineering, Maastricht University Medical Center, Maastricht, the Netherlands; [5]Department of Pharmacology, Maastricht University Medical Center, Maastricht, the Netherlands

Target Audience: Researchers interested in imaging techniques and new treatment strategies for atherosclerosis.
Purpose: Atherosclerotic plaque development is associated with increased oxidative stress, promoting angiogenesis, lipid oxidation and uptake, and ensuing cell death. In addition, biomechanical stress (blood-pressure variations with every heart beat), may further enhance plaque vulnerability. Ivabradine, a heart-rate lowering drug, is associated with reduced oxidative stress and diminished atherosclerotic plaque formation in mice[1]. Yet it's role on plaque microvasculature and biomechanical stress is unknown. The purpose of the present study was to investigate the effect of Ivabradine on plaque formation using MR and ultrasound (US) imaging.
Methods: Atherosclerosis formation was induced in 19 New-Zealand White rabbits with a high cholesterol diet (1.0% for 10 weeks and 0.3% for 4 weeks). After two weeks, endothelial denudation (balloon-injury) of the abdominal aorta was performed[2]. Nine rabbits were treated with Ivabradine (17 mg/kg/day) dissolved in their drinking water during the entire study period. After 14 weeks, MRI (7.0 T Bruker BioSpec 70/30, Bruker, Germany) and US (Esaote Picus, Genoa, Italy) examination of the rabbits was performed. Plaque size was measured using contrast-enhanced T1w-Double Inversion Recovery black-blood MR images[3] (TR/TE/TI: 1000/10/350 ms, FOV 120x120 mm, acq/reco matrix 384x384/512x512), while plaque microvasculature was determined using a dynamic T1w black blood TSE pulse sequence[4] (TR/TE/TI: 300/9.5/120 ms, FOV 120x120 mm, acq/reco 192x192/384x384 matrix, temporal resolution 7.2 sec, 100 time phases) with 0.2 mmol/kg Gadobutrol (Bayer Healthcare, Germany) injected after one minute through a marginal ear vein. Quantification of DCE-MRI was done both semi-quantitatively by means of the area under relative signal time-enhancement curve (AUC) and quantitatively by means of pharmacokinetic modelling using a muscular region as reference[5], with K^{trans} and v_e values of muscle taken from literature[6]. Pulse pressure and relative distension were measured using a pressure catheter in the central auricular ear artery and high frame-rate ultrasound, respectively.
Results: Failure of contrast injection occurred in one rabbit and three rabbits died during the study period. Therefore, successful MRI and US examination was performed on 15 rabbits (six Ivabradine treated animals). Ivabradine resulted in a 15% heart rate reduction, both in conscious state (p=0.026) and under anaesthesia (p=0.031). Pulse pressure and relative distension, as measured with US, were similar between the Ivabradine and control group (both p>0.5). But, due to the reduction in heart-rate, the aorta's in the Ivabradine group are less often exposed to the biomechanical stress. MRI plaque size (Figure 1) was similar between the groups (p=1.0). DCE-MRI analysis showed a decrease in plaque microvasculature with a 25% decrease in the AUC from 0 till 7 minutes after contrast injection (p=0.029) and a 30% decrease in K^{trans} (p=0.040) for Ivabradine-treated animals compared to controls.
Discussion and Conclusion: Use of Ivabradine led to lowered AUC and K^{trans} on DCE-MRI, indicating decreased plaque microvascular density, flow, or leakiness, which is thought to be an important determinant of reduced plaque vulnerability. Ivabradine did not lead to reduced vessel wall area, despite reduced repetitive biomechanical stress. Histological analysis is still ongoing and is expected to provide further insights on the effect of Ivabradine on atherosclerosis.
References: [1]Custodis et al., Circulation. 2008;117:2377-87, [2]Lobbes et al., Radiology. 2009;250:682-91, [3]Phinikaridou et al., Circ Cardiovasc Imaging. 2010;3:323-32, [4]Calcagno et al., ATVB. 2008;28:1311-17, [5]Yankeelov et al. MRM. 2005;23:519-29, [6]Jaspers et al., Med Phys. 2010;37:5746-55. **Acknowledgements**: This research was performed within the framework of CTMM, project PARISk (grant 01C-202), and supported by the Netherlands Heart Foundation.

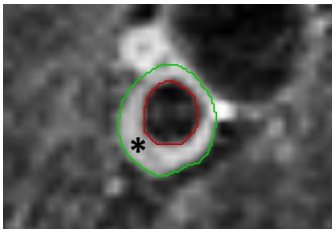

Figure 1: Contrast-enhanced T1w-DIR BB MR image showing the atherosclerotic plaque in the rabbit aorta (indicated with *).

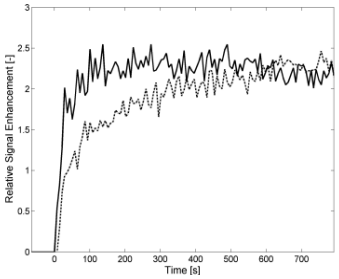

Figure 2: Relative signal enhancement-time curve of DCE MRI for a control rabbit (black line) and a rabbit that was treated with ivabradine (dashed line).

A novel method to estimate labeling efficiency for pseudo-continuous arterial spin labeling imaging

Zhensen Chen[1], Xingxing Zhang[1], Andrew Webb[1], Xihai Zhao[2], Matthias van Osch[1]

[1]C. J. Gorter Center for High Field MRI, Department of Radiology, Leiden University Medical Center, Leiden, the Netherlands
[2]Center for Biomedical Imaging Research, Department of Biomedical Engineering, School of Medicine, Tsinghua University, Beijing, China

Introduction: Labeling efficiency is one of the most important factors affecting quantification of pseudo-continuous ASL (pCASL) perfusion imaging and is conventionally assumed as constant for different subjects and obtained from simulations[1]. However, labeling efficiency of pCASL is vulnerable to factors, such as field inhomogeneity and flow velocity, which may vary across scans, subjects and arteries. Therefore, acquisition of labeling efficiency for each artery and scan might improve the accuracy of pCASL perfusion quantification. Previously, it was proposed to use phase-contrast MRI (PC-MRI) to estimate the labeling efficiency[2], but this approach showed unsatisfying repeatability[3]. In this study, we proposed a novel method to estimate the labeling efficiency by performing multi-phase pCASL imaging distal to the labeling plane.

Theory: The ASL-signal (i.e. the subtracted signal) in an arterial cross section is made up of labeled spins that have various velocity (Fig 1A). Both labeling efficiency and the transit time are velocity-dependent. Therefore, to calculate the labeling efficiency a separate T1 decay correction should be done for each velocity. The labeling efficiency in labeling plane can be denoted as: $ASL(t)=\int_0^{v_{max}} P(v)D(v)E(v,t)dv$ (1), where M_0 is the total equilibrium blood magnetization in the arterial cross section; $\alpha(v)$ and $M(v)$ are the labeling efficiency and longitudinal magnetization of spins with velocity v. The ASL-signal in the imaging plane can be described as: $ASL(t)=\int_0^{v_{max}} P(v)D(v)E(v,t)dv$ (2), where $D(v)=e^{-TT(v)/T_{1b}}$ is T1 decay experienced by the spin; $E(v,t)=rect(t-TT(v))$ denotes the presence of spin in the imaging plane, which is assumed to be a rectangle window pulse with a width equal to the labeling duration and a time shift equal to the spin's transit time $TT(v)$. The above problem of obtaining $\bar{\alpha}$ can be solved numerically, whereas the transit time of the fastest spin is detected as the latest time-point with maximum ASL intensity (e.g. indicated by the arrows in Fig 1B). This prior information is utilized to improve the numerical solving algorithm.

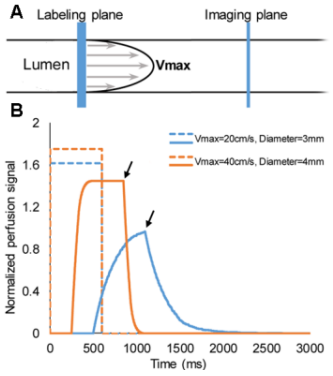

Fig 1. A) Schematic plot of the simulations. B) Simulated ASL-signal curves of one pixel in labeling (dotted line) and imaging plane (solid line) for two arteries with different diameter and blood velocity.

Methods: The ASL-signal as detected in the arterial cross section is simulated using a laminar flow model[4] for the velocity distribution (Fig 1A). Subsequently, labeling efficiencies are derived using equation (1) and (2). In vivo multi-phase single slice pCASL imaging was performed in two healthy subjects on a 3T MR scanner (Philips healthcare) equipped with a 32-channel head coil. The imaging parameters were as follows: post labeling delay 5ms, 2D EPI readout with 90° excitation RF pulse, half Fourier factor 0.71, number of phases 42, phase interval 37.5ms, number of averages 15. For the first subject, the labeling plane was placed just below the carotid bifurcation and the imaging plane about 25mm below skull base. Slice thickness of the imaging plane was 5mm. The imaging was performed for labeling durations of 400, 600, 800 and 1000ms. Then two additional scans were performed with labeling duration 400ms, but with the imaging plane either moved to the skull base or to the level of the basilar artery. These 3 imaging locations were denoted as low, middle and high, respectively. For the second subject, slice thickness was reduced to 3mm with a labeling duration of 600ms. These scans were performed with 6 different flip angles of the pCASL RF labeling pulse: 5°, 7.5°, 10°, 15°, 25° and 30°. Furthermore, quantitative flow imaging was conducted in the labeling plane to obtain the mean blood velocity of each artery, which was used for simulation of the theoretical relationship between pCASL labeling efficiency and pCASL RF flip angle. Cardiac triggering with pulse oximeter was used for all above labeling efficiency imaging. An additional scan without cardiac triggering was also performed in the second subject. The M_0 was obtained from the mean of the last ten control phases and was used to normalize the ASL-signal time curve before averaging over the ROI containing the artery. The average normalized ASL-signal curve was them smoothed and interpolated, followed by manual detection of the transit time of the fastest spin and calculation of labeling efficiency.

Results: Fig 1B showed simulated ASL-signal curves for two arteries with different diameter and blood velocity. The labeling efficiency can be perfectly restored from the simulated ASL-signals (data not shown). ASL-signal curves with different labeling durations of the first subject's left internal carotid artery (LICA) are shown in Fig 2. The calculated labeling efficiencies of the same artery at three different imaging locations are shown in Table 1. The ASL control signals with and without cardiac triggering were shown in Fig 3. Measured in vivo labeling efficiencies for different pCASL flip angles are shown in Fig 4A. The Fig 4B showed simulated curves based on quantitative flow measurements by PC-MRI.

Table 1 Estimated labeling efficiencies for different imaging locations

	RVA	LVA	RICA	LICA
Low	0.531	0.813	0.686	0.684
Middle	0.370	0.760	0.568	0.657
High	0.518		0.508	0.635

* RVA=right vertebral artery, BA=basilar artery, LVA=left vertebral artery, RICA=right internal carotid artery, LICA=left internal carotid artery. "Low" means about 25mm below skull base, while "Middle" means skull base, "High" means the level of basilar artery.

Discussion and Conclusions: The proposed labeling efficiency estimation method works well on simulated data. The shape and amplitude of the measured ASL-signal as depicted in e.g. Fig 2 are largely consistent with the expected curves from simulations. Furthermore, the dependency of the in vivo measured labeling efficiencies for different pCASL flip angles are in line with theory as well. However, the measured labeling efficiency of the same artery measured at different imaging locations varied too much and in some measurements (see Fig 4A) unrealistic high labeling efficiencies were obtained. It is postulated that these measurement errors arise due to imperfect estimation of M_0, which may be caused by cardiac pulsation (see Fig 3) affecting spin velocity and transit times or partial volume effects that result from the low resolution or non-perpendicular sections through some arteries. In summary, a new, fast method for estimation of the labeling efficiency is proposed that is promising, although further improvements in robustness and quantification are needed.

References: 1. Alsop, MRM epub, 2014; 2. Aslan *et al*, MRM 63:765-771, 2010; 3. Dolui *et al*., Proc. Intl. Soc. Mag. Reson.Med. 22(2014). 0212; 4. Gallichan *et al*, MRM 60:53-63, 2008.

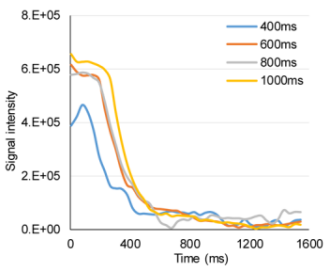

Fig 2. ASL-signal curves of one pixel within LICA acquired with different labeling durations.

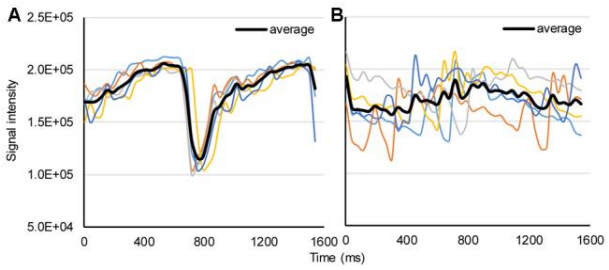

Fig 3. ASL control signals acquired with A) and without B) cardiac triggering. Signals of 5 individual dynamic scans were shown with the color curves, and their average was shown with black bold curve. Distinct effect of cardiac pulsation on the ASL signals can be seen.

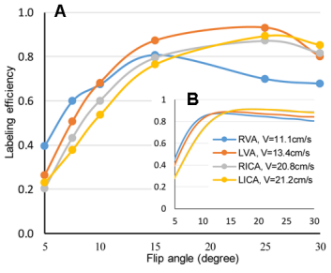

Fig 4. Labeling efficiency for different pCASL RF flip angles. A) In vivo labeling efficiency; B) Simulated labeling efficiency with blood velocity obtained from phase contrast MRI as input.

Hemodynamics of the cerebral border zone regions in healthy, young volunteers

Sophie Schmid[1], Wouter Teeuwisse[1], Hanzhang Lu[2], Matthias van Osch[1]

[1]C. J. Gorter Center for High Field MRI, Department of Radiology, Leiden University Medical Center, Leiden, the Netherlands
[2]University of Texas Southwestern Medical Center, Dallas, Texas, United States

Targeted audience Researchers and clinicians interested in new developments in ASL and compartmentalization of spins.

Purpose The tissue regions supplied by the distal end branches of the cerebral arteries are called the cerebral border zone or watershed regions. It is known that these regions are more vulnerable to ischemia and infarction and have a longer arterial transit time (ATT) compared to the central regions of the flow territories[1]. It is, however, unclear whether transport through the microvascular tissue is also delayed. In this study we employed time encoded (aka. Hadamard encoded) pseudo Continuous Arterial Spin Labeling (te-pCASL)[2] combined with T_2-Relaxation-Under-Spin-Tagging (TRUST)[3] to evaluate the hemodynamics of the posterior and middle cerebral artery (MCA) border zone region, which lies between the cortical branches of the MCA and the posterior cerebral artery. The aim of this study was to assess hemodynamic properties of the border zone regions in the brains of young healthy volunteers.

Methods Eight healthy volunteers (age 21-30 y, 5 female, 3 male) were scanned at 3T (Achieva, Philips Healthcare) with a 32-channel head coil. te-pCASL was combined with TRUST to distinguish spin transition from the vasculature to the tissue compartment based on their T_2. This method is more time efficient, while still keeping an equal SNR, compared with separate multi-time point pCASL scans[4]. For te-pCASL, the total labeling duration of 3700 ms was divided into 7 blocks of 1300, 600, 3x400 and 2x300 ms, comprising 8 encoding patterns, followed by a minimum post labeling delay (PLD) of 265 ms. The T_2-preparation module was performed at 4 effective echo times (eTE): 0, 40, 80 and 160 ms (0, 4, 8, and 16 composite 180° pulses with their signs arranged in an MLEV pattern). General te-pCASL-TRUST protocol: imaging module with single shot FFE-EPI, 3.2×3.2×7 mm voxel size, 11 slices and TR/TE/fa = 4423ms/17ms/90°, background suppression FOCI pulses at 1900 and 3400 ms. 72 acquisitions (9x8 encodings) were acquired with vascular crushing (V_C = 5 cm/s) in a total scan time of 22:34 min. After subtraction, according to the appropriate Hadamard scheme, the ASL signal was calculated for the different eTEs and PLDs. A Regional Perfusion Imaging scan was performed to determine the 3 major flow territories: left and right MCA flow territory and posterior flow territory. 10 voxels were selected on either side of the posterior border and in the central region of each flow territory. The average signal in these voxels was fitted to the kinetic perfusion model of Buxton[5] to estimate CBF and ATT. For each PLD the T_2 was calculated with a mono-exponential fit on the average signal of these voxels. The hemodynamic properties were statistically compared using paired t-tests.

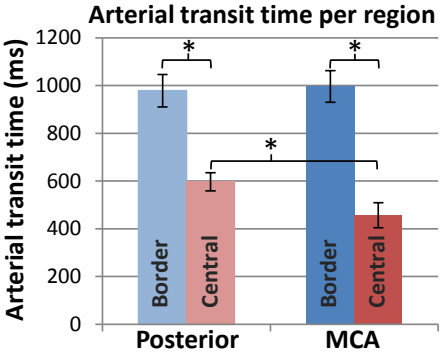

Figure 1 Arterial transit time in the posterior and MCA flow territory sampled from the border and central regions. * is p<0.05

Results and discussion On average, the ATT was 1.9 times longer in the border regions compared with the central regions, as shown in figure 1. The ATT in the central posterior region was also significantly longer than in the central MCA region (p<0.05). A significantly lower CBF was found in the border region compared with the central region: 37.8 ± 2.5 (mean±sem) and 47.8 ± 2.5 in the posterior flow territory, and 38.6 ± 2.6 and 50.1 ± 2.6 mL/100g/min in the MCA flow territory. In figure 2 a clear delay and lower ASL signal can be seen in the border regions. The same delay as in the ATT was found in the moment of transition of the signal from the vascular to the tissue compartment, as can be concluded from figure 3 by the significantly later decrease of the T_2 in the border zones (T_2 around 165 ms is expected for the labeled spins in the arteries and 90 ms for spins in the grey matter tissue[3]). To see whether the transition of the label from the vascular to tissue compartment occurs with the same timing, the T_2-curve of the border zone is shifted by the difference in ATT between the border and central part of that flow territory (shown in green in figure 3). This shows that the central and border zone regions seem to provide similar timing of the T_2-curves, although at a PLD around 1650 ms a slightly higher T_2 can be observed.

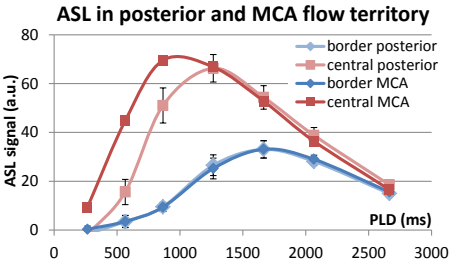

Figure 2 The ASL signal in the posterior and MCA flow territory sampled from the border and central regions.

Conclusion The arterial transit time in the border zone is significantly longer compared to the central region. However, the exchange of the label from the arterial to the tissue compartment appears to be at a similar rate.

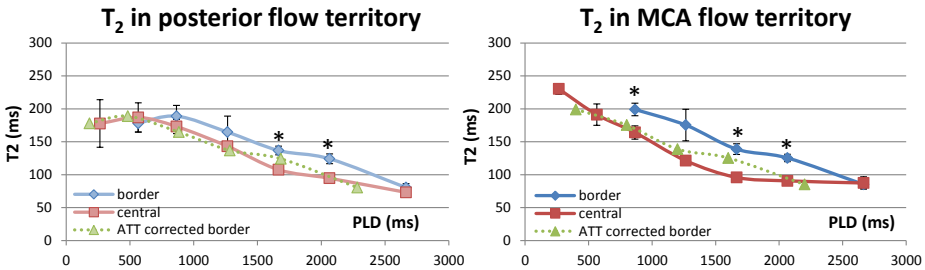

Figure 3 The T_2 in the posterior (left) and MCA (right) flow territory over time sampled from the border and central regions (* is p<0.05). The arterial transit time corrected border T_2 is the T_2-curve of the border zone is shifted by the difference in ATT between the border and central part of that flow territory.

References
1. I. Momjian-Mayor, Stroke 2005; 36:567–577;
2. M. Günther, ISMRM 2007; abstract 380;
3. H. Lu et al, MRM 2008; 60:357-363;
4. W. Dai et al, MRM 2013; 69:1014–1022;
5. R.B. Buxton, et al, MRM 1998; 40:383-396.

Acknowledgement This research is supported by the Dutch Technology Foundation STW, applied science division of NWO and the Technology Program of the Ministry of Economic Affairs.

Arterial spin labeling spectroscopy for cerebral perfusion measurement

Xingxing Zhang[1], Itamar Ronen[1], Wouter Teeuwisse[1], Andrew Webb[1], Matthias van Osch[1]

[1]C. J. Gorter Center for High Field MRI, Department of Radiology, Leiden University Medical Center, Leiden, the Netherlands

Target audience: Researchers interested in new acquisition approaches in arterial spin labeling

Purpose: Although arterial spin labeling (ASL) has been widely implemented to measure cerebral blood flow in gray matter, white matter perfusion has proved difficult to detect due to low perfusion, long transit time, low SNR and significant partial volume effects [1,2]. It has previously been proposed to use pulsed ASL with a single voxel PRESS spectroscopic read-out (PASL PRESS) to enhance sensitivity, but this leads to long acquisition time [3]. In this study, time encoded pseudo-continuous ASL [4] and single voxel PRESS (te-pCASL PRESS) were combined to detect cerebral perfusion in white matter as well as in gray matter in an efficient manner.

Methods: ASL spectroscopy is based on a normal ASL preparation in combination with a PRESS read-out. In this study, ASL preparation was achieved by te-pCASL enabling temporal data to be acquired within a single scan instead of multiple scans as previously used in PASL PRESS. Te-pCASL was performed with an 8 Hadamard encoding scheme using asymmetric and relative long Hadamard block durations (1500, 1500, 1500, 1500, 1000, 500 and 500 ms) to increase the sensitivity in deep white matter. The Hadamard scheme (8 acquisitions) was repeated 10 times resulting in a total scan duration of ~13 min. Perfusion data with PRESS were acquired in two similarly-sized ROIs in gray and white matter and were compared to the perfusion data of a similar te-pCASL scan with traditional single shot echo planar imaging (EPI) readout.

Six healthy volunteers were scanned under a local IRB approved protocol. Te-pCASL PRESS and traditional te-pCASL imaging were implemented on a 3T MRI scanner (Philips Healthcare) using a 32ch head coil; for all scans the post labeling delay (PLD) was 1000 ms, flip angle was 90°, linear shimming was performed in the labeling plane and in the ROI separately. Equilibrium magnetization (M0) scans were acquired for both the PRESS and imaging read-out. A large voxel of 47×9×7 mm^3 was carefully placed within the white matter, avoiding gray matter contamination, based on a 3D T1-scan and a similarly-sized ROI was selected in gray matter (Fig.1).

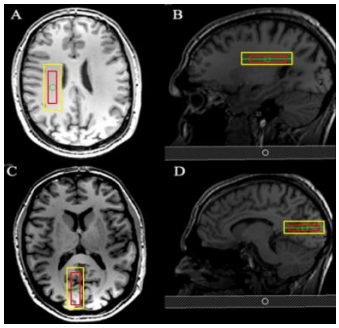

Figure 1: Region of interest selection of a large voxel (red) and volume shimming box (yellow) in white matter (A, B) and gray matter (C, D) based on 3D T1 anatomical images.

The data were processed using off-line scripts (Matlab, The MathWorks). The free induction decays (FIDs) of each acquisition of te-pCASL PRESS were phase corrected, filtered with an apodization of 20 Hz, 4-fold zero filled and Fourier transformed. The resulting spectra were Hadamard decoded and the central 200 points of the Hadamard decoded water spectra were used for quantification. Images acquired by traditional te-pCASL imaging were Hadamard decoded, and signals from the same ROI covered the same anatomical region as in PRESS read-out were extracted and compared to the perfusion signals obtained by te-pCASL PRESS.

Results: Figure 2 shows time courses of the normalized perfusion signal (ASL signal divided by M0 and the duration of the specific labeling block). The amplitudes of the perfusion signals in white matter are much smaller than in gray matter demonstrating lower perfusion. Also white matter perfusion signal decays much more slowly representing longer and more dispersed transit times. Figure 3 shows comparable temporal SNR (tSNR) for te-pCASL PRESS as compared to the traditional imaging technique in both white matter and gray matter.

Discussion: Both perfusion measurement by te-pCASL PRESS and normal imaging show similar results and tSNR in white matter. So far all te-pCASL PRESS scans were performed with linear shimming, and second order shimming might improve the tSNR by diminishing the phase difference in such a large voxel. Partial volume effects were avoided by careful planning, and outer volume suppression could theoretically eliminate some residual gray matter contamination. In gray matter, imaging showed a higher perfusion signal at a very short post labeling delay probably due to vascular signals, whereas such vascular signals would be saturated in te-pCASL PRESS because of the two 180° pulses after the 90° excitation pulse. Lower perfusion signal and faster decay in gray matter, especially between PLDs of 2000-4000 ms, could potentially be explained by the fact that PRESS is insensitive to T_2^* dephasing while EPI could result in ~25% signal loss due to T_2^*.

Conclusion: Te-pCASL PRESS can be used to measure localized white matter perfusion changes with a comparable SNR as traditional te-pCASL imaging. Second order shimming and outer volume suppression will be evaluated in the future.

Acknowledgement: This research is supported by the Dutch Technology Foundation STW, applied science division of NWO and the Technology Program of the Ministry of Economic Affairs.

References: [1]. van Gelderen et al, MRM 2008;59(4):788-795. [2]. van Osch et al, MRM 2009;62(1):165-173. [3]. Pohmann, MRM 2010;64(4):1109-1113. [4]. Teeuwisse et al, MRM 2014.

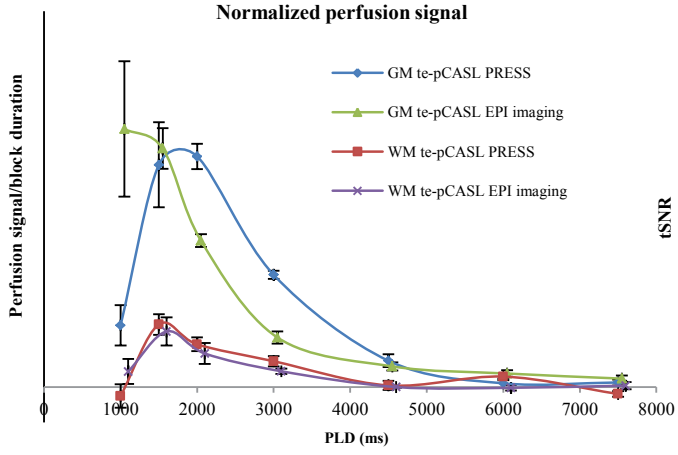

Figure 2: Time courses of normalized perfusion signal and standard error in white matter and gray matter acquired by te-pcASL PRESS and EPI imaging.

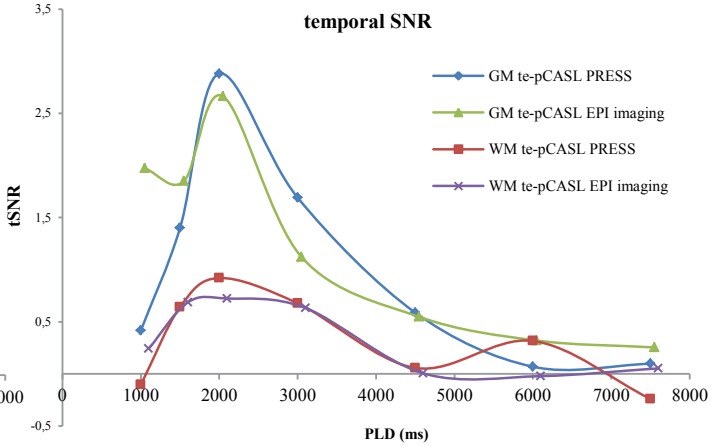

Figure 3: tSNR as a function of post-labeling delay (PLD) showing similar values for te-pCASL PRESS and te-pCASL EPI imaging

Improving the arterial input function in dynamic contrast enhanced MRI by fitting the signal in the complex plane

Frank Simonis[1], Alessandro Sbrizzi[2], Ellis Beld[1], Jan Lagendijk[1], Cornelis van den Berg[1]

[1]Department of Radiotherapy, University Medical Center, Utrecht, the Netherlands
[2]Department of Radiology, University Medical Center, Utrecht, the Netherlands

Target audience Physicists and clinicians working on DCE data analysis

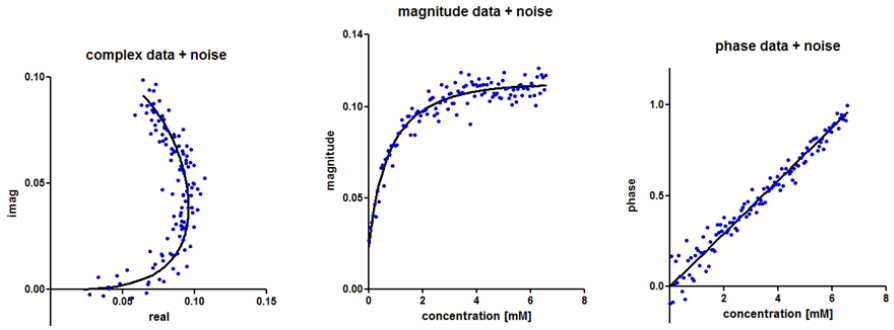

Fig. 1. Influence of noise on concentration determination. Although the complex noise is equal over the complete signal, the error it causes when using magnitude data is larger at higher concentrations. The error in phase data is larger at smaller concentrations

Purpose Acquiring an accurate arterial input function (AIF) is essential in dynamic contrast-enhanced (DCE) MRI analysis; the AIF serves as the input for models that estimate tissue properties. Determining patient specific AIFs using MR magnitude data faces challenges due to experimental difficulties such as inflow, B_1 non-uniformity and saturation effects. By using the phase of the MR data, most of these difficulties can be overcome and an attractive linear relationship between contrast agent (CA) concentration and phase shift is obtained[1-3]. However, at low CA concentrations the relatively low amplitude of the signal causes high noise levels in the phase resulting in wrong estimation of the baseline and the tail of the AIF. Magnitude data provides a more reliable estimation at these low CA concentrations, but at high CA concentrations where T_2^* effects dominate the signal, estimation based on magnitude is highly affected by physiological and/or thermal noise (see Figure 1). Recent work by Brynolfsson et al.[4] pointed out the use of magnitude and phase simultaneously for CA concentration estimation using a statistical modelling approach on simulated data. Here we demonstrate that fitting the enhancement data in the complex plane, originally proposed by van Osch et al[5]. for Dynamic Susceptibility Contrast enhanced MRI, can also be used in DCE AIF estimation to mitigate noise and bias that arise from solely using phase or magnitude data. The technique is applied to 3T DCE-MRI data of 3 prostate cancer patients.

Materials and methods The DCE-MRI exams were performed on a 3T MR scanner (Achieva, Philips Healthcare), using a 3D spoiled gradient echo sequence (20 transverse slices, slice thickness 5.0 mm, TR/TE 160, FOV 40 cm, flip angle 8°, 120 dynamics at 2.4 s time interval). In each patient 0.1 mL/kg gadobutrol was injected (1.0 M Gadovist, 1 or 2 mL/s, followed by a saline flush)[3]. For the AIF determination vascular voxels of the femoral arteries were selected. The complex AIF signal S was fit to the following model[6]:

$$\frac{S(C(t))}{S_0} = \frac{\left(1-e^{-TR(R_{10}+r_1C(t))}\right)}{\left(1-e^{-TR\cdot R_{10}}\right)} \cdot \frac{1-cos(\alpha)e^{-TR\cdot R_{10}}}{1-cos(\alpha)e^{-TR(R_{10}+r_1C(t))}} \cdot e^{-TE(r_2C(t))} \cdot e^{i(F\omega_0\chi_m TE\, C(t)+\varphi_0)}$$

where $C(t)$, r_1/r_2 and χ_m are the concentration at time point t, the relaxivities and the molar susceptibility of gadobutrol respectively. R_{10} is the longitudinal relaxivity of blood, F is a geometry factor of the artery, ω_0 is the resonance frequency of protons, α is the flip angle, φ_0 is an offset phase, TR equals the repetition time and TE the echo time. All variables were assumed to be equal to literature and sequence values, so only $C(t)$, φ_0 and α had to be fit. DCE-CT data of the same patients was used as a gold standard.

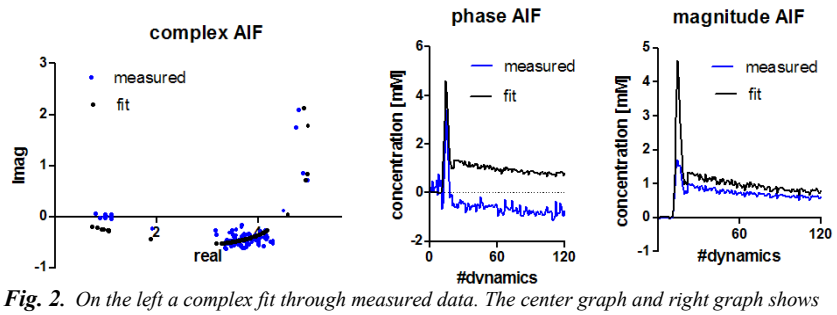

Fig. 2. On the left a complex fit through measured data. The center graph and right graph shows the phase AIF and magnitude AIF as they were measured compared to the fit. Note the saturation effect in the magnitude data and the large error in phase and for low concentrations as baseline.

Results and discussion Figure 2 shows the AIFs obtained using only magnitude or phase and when the complex signal is used. The applied fit strongly improved the shape of the AIFs, now showing a clear first pass peak, recirculation and a slowly decreasing tail. Although the model is still affected by inflow and B_1 inhomogeneities, their effects are regularized by also taking the phase into account. In Figure 3 we compare the complex fit AIFs from DCE MRI to the AIFs from DCE CT for the same patients.

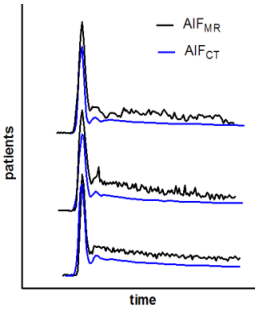

← ***Fig.3.*** *The AIF concentrations found by DCE-CT and DCE-MR of three patients*

Conclusion By modeling the complex signal from DCE-MRI, AIFs can be greatly improved, making it a more stable input for DCE models. The correction method will be tested on a larger group of patients to confirm its applicability and confirm the resulting absolute concentrations.

References 1) Akbudak E. et al, MRM 1996; 36:809-815. 2) Garpebring A. et al, Magn Reson Mater Phy 2011; 24:233-245 3) Korporaal J.G. et al, MRM 2011; 66:1267-1274. 4) Brynolfsson et al. Magn Reson Med. 2014 Oct 16. 5) Van Osch et al. Magn Reson Med. 2001; 45:477–485. 6)Schabel et al. Phys. Med. Biol. 2008;53:2345–2373.

Influence of the cardiac cycle on pCASL: the effect of triggering the end-of-labeling on signal stability

Jasper Verbree[1,2], Matthias J.P. van Osch[1,2]

[1]Department of Radiology, Leiden University Medical Centre, Leiden, the Netherlands
[2]C. J. Gorter Center for High Field MRI, Department of Radiology, Leiden University Medical Center, Leiden, the Netherlands

Purpose – Investigating the contribution of the cardiac cycle on pCASL signal stability

Background – Pseudo continuous ASL (pCASL) label generation is dependent on the velocity of the blood, number of spins flowing through the labeling plane, and also the transport to, and exchange of, the label in the tissue compartment, all of which are influenced by the cardiac cycle. Introducing cardiac triggering at the start of every dynamic has been shown to reduce variability in pulsed ASL[1,2], but not pCASL[2]. Due to variation in the cardiac cycle, T1 decay and the longer labeling period in pCASL, the blood tagged at the end-of-labeling period is expected to contribute most to the perfusion signal. Triggering the moment of end-of-label might therefore be more important to reduce the physiological variability introduced by the cardiac cycle. We assessed the signal contribution of the end-of-labeling period by prospectively triggering the start- and end-of-labeling in pCASL.

Methods – Data from six human volunteers (3 male, 3 female, 25-56 years) were acquired on a Philips 3T Achieva MRI system with a 32 channel head coil. The build-in pulse oximeter was attached to the finger to detect the pulse wave for cardiac triggering. High resolution anatomical images were acquired using a 3DT1 sequence. The blood flow velocity through the labeling plane was assessed using a retrospectively triggered phase-contrast scan with 15 cardiac phases. Flow profiles in the main arteries were determined in manually drawn ROIs using QFLOW (Philips, Best, NL) software. (See bottom of the abstract for imaging parameters.)

The vendor supplied pCASL sequence was modified to incorporate triggering of start- and end-of-labeling (ASLtrig). To isolate the effect of triggering the end-of-labeling, the minimum labeling duration was set to 7 sec. Following the detection of the trigger, the labeling was stopped in a specific phase of the cardiac cycle. Three distinct cardiac phases (a), (b) and (c) were determined for each subject according to the acquired pulse wave (Figure 1). The control scans were triggered at start-labeling and had the same labeling duration as the preceding label scan. The triggered scan was acquired continuously, cycling through the cardiac phases a-b-c-a-b…, after each label-control pair. The order of phases was randomized between subjects.

The non-triggered ASL scan (NTASL) had the same imaging parameters as the triggered scan. In addition, the labeling duration was increased to 7500ms to have a comparable mean labeling duration. For quantification purposes an M0 scan was also acquired. The order of the ASLtrig, NTASL and M0 scans were randomized between subjects. ASL images were quantified[3], aligned to the first dynamic and scaled using the M0 scan. The anatomical scan was segmented and the gray matter voxels with probability>0.9 were selected as a mask. Differences across scans were assessed using repeated measures ANOVA supplemented with post-hoc tests when appropriate. All analyses and statistics were performed in MATLAB with the SPM8 toolbox.

Results – Heart rate (p=0.26) and mean labeling duration (p=0.47) did not differ significantly between scans. Mean CBF was higher in NTASL (p=0.035) compared to ASLtrig of cardiac phase (b). No correlation between mean labeling duration and CBF was observed. The temporal standard error was comparable between the triggered and non-triggered scans (p=0.44) (Figure 3). The moment of imaging with respect to the cardiac cycle varied equally for non-triggered (27%) and triggered scans (23%).

Discussion - Triggering of the start- and end-of-labeling in pCASL did not reduce the temporal variation of the gray matter perfusion and no relation with the cardiac cycle was observed. A possible limitation of this study was the varying labeling duration and repetition time for each triggered dynamic due to the cardiac cycle. By increasing the labeling duration to 7 sec, the influence of longer variable labeling period was minimal, thereby enabling the isolation of the effect of triggering the moment of end-of-labeling period. Moreover, no correlation was observed between repetition time and mean CBF. Another limitation of the current study was that peripheral pulse oximeter triggering was used instead of ECG, which could possibly have resulted in less accurate triggering.

Conclusion – Triggering the moment of end-of-labeling does not to improve pCASL perfusion measurements on a per-subject basis.

References – [1] Fushimi, et al. NMR biomed. 2013; (jan) [2] Wu et al. IEEE TMI. 2007;26(1): 84-92 [3] Heijtel et al. MRM. 2014;92(C):182-192

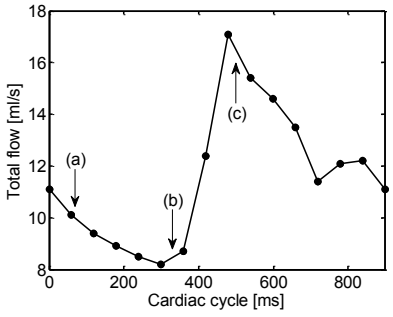

Figure 1: *Total flow though brain feeding arteries with the three cardiac phases indicated.*

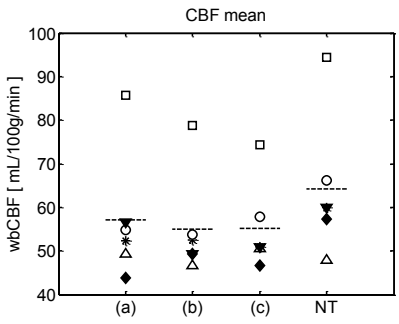

Figure 2: *whole brain gray matter perfusion of all six subjects during the three cardiac phases and non-triggered ASL (NT).*

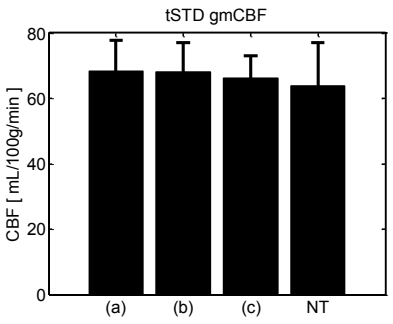

Figure 3: *mean voxel-wise temporal standard deviation for of all six subjects.*

Phase-contrast: TR/TE= 13/8.1 ms; flip angle = 10°; Field-of-View = 150x103 mm^2; matrix = 128x88; slice thickness = 6 mm; VENC = 200 cm/s; heart phases = 15, retrospective triggering. **ASLtrig:** minimum labeling duration = 7000ms; post labeling delay = 1800; TE = 14 ms; flip angle = 90°; FOV = 240x240x119 mm^3; matrix = 80x79; slice thickness = 7 mm; number of dynamics = 60 (20 per cardiac phase); EPI factor = 35; **NTASL:** same as triggered, labeling duration = 7500; dynamics = 20; **M0:** TR/TE/TE2 = 2000/11/14 ms; FOV = 220x220x102 mm^3; matrix = 72x69; slice thickness = 6 mm; number of averages = 10; EPI factor =25;

Understanding brain perfusion modifiers in normal subjects

Patricia Clement[1], Henk-Jan Mutsaerts[2], Eidrees Eidrees[3], Marion Smits[4], Marjan Acou[1], Egill Rostrup[5], Francesca B. Pizzini[6], Jorge Jovicich[7], Mervi Könönen[8], Ritva Vanninen[8], António Bastos-Leite[9], Roland Wiest[10], Elna-Marie Larsson[11], Eric Achten[1]

[1]Radiology and nuclear medicine, Ghent University, Ghent, Belgium; [2]Academic Medical Center, Amsterdam, the Netherlands; [3]Leiden University Medical Centre, Leiden, the Netherlands; [4]Erasmus Medical Center, Rotterdam, the Netherlands; [5]University of Copenhagen, Glostrup, Denmark; [6]University Hospital Verona, Verona, Italy; [7]University of Trento, Mattarello, Italy; [8]Kuopio University Hospital, Kuopio, Finland; [9]University Porto, Porto, Portugal; [10]University Hospital Bern, Bern, Switzerland; [11]Uppsala University, Uppsala, Sweden

PURPOSE

Interpretation of quantitative perfusion measurements with arterial spin labeling as biomarker of brain health is biased by a battery of perfusion modifying factors, such as patient characteristics, lifestyle and medication use. Standardization of measurement conditions and correction for important modifiers is essential to increase the accuracy of perfusion derived parameters, e.g. for individual patient diagnosis and follow-up, and to reduce variance in large multicenter studies. This study summarizes the results of an extensive review of modifying factors found in the literature and their reported effects on brain perfusion. The effects from prescribed medication use are not included in the current review.

METHODS

An extensive literature search was performed for factors influencing quantitative perfusion measurement in the brain and which were not related to prescribed medication use. Only human studies were included. Perfusion measurement techniques were Xe-CT, PET, SPECT, ASL, or TCD. This information was used to build a database summarizing all factors and their effects, and a standard operation procedure was constructed to take the impact of the most important confounding factors into account.

RESULTS AND DISCUSSION

A total of 58 studied perfusion modifiers where categorized in four groups. Several of the reported factors induce a significant effect on brain perfusion and in most cases the results for a modifier are consistent between different studies. This is the case for modifiers such as caffeine, aging and blood gasses. For a few factors, their confounding value is subject to discussion, due to contradictory results or lack of research.

From this literature review, a standard operating procedure to reduce methodological noise and to correct for the most important modifiers is proposed. To account for the immediate effects on perfusion from the MRI environment and the physical and psychological state of individuals, we suggest to monitor end-tidal CO2, heart rate, respiratory rate and wakefulness as these factors can have profound effects on perfusion measurements. The effect of hematocrit is also important, therefore a blood sample is advised. A mood sensing test is suggested for each subject as well. Furthermore, a questionnaire was constructed to inquire for several additional important modifiers of perfusion such as medication use, lifestyle, and gender related effects. Every subject should also have a minimum of neuropsychological testing to assess mental abilities and to rule out psychiatric comorbidity.

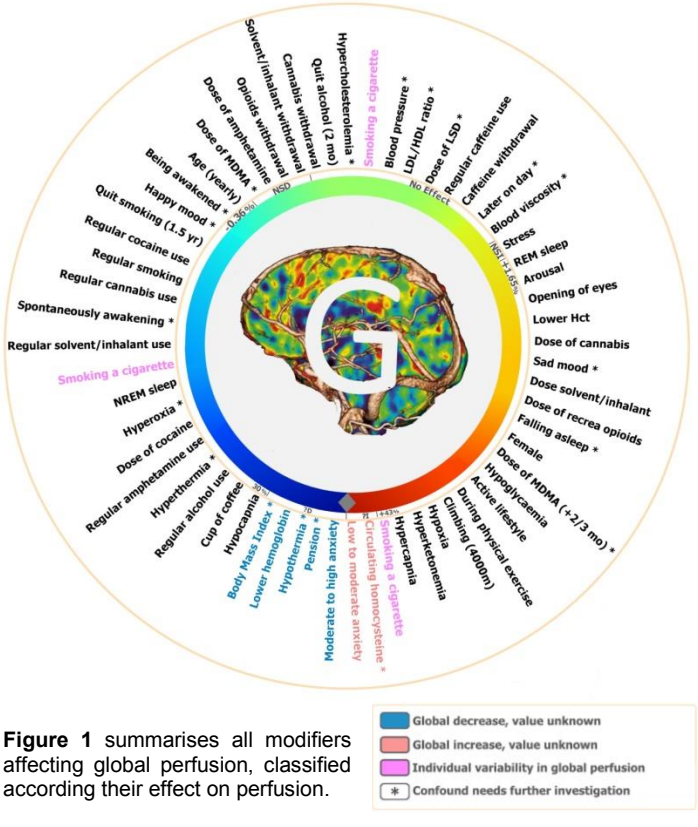

Figure 1 summarises all modifiers affecting global perfusion, classified according their effect on perfusion.

Acquiring such data will allow for deep MRI phenotyping, the tailoring of expected normal MRI signals to personalized reference data taking the modifiers into account. The hypothesis is that this approach will allow for a more accurate and early diagnosis of neurodegenerative and psychiatric diseases.

CONCLUSION

This review underlines the importance of several modifiers of perfusion quantification and perfusion patterns in the brain. To account for these factors in ASL perfusion measurements, we compiled a questionnaire and standard operating procedure from this survey.

This study is founded within the COST Action BM1103.

Validation of quantitative blood flow with 3D Gradient Echo (GRE) dynamic contrast-enhanced Magnetic Resonance Imaging (DCE-MRI) using blood pool contrast medium in skeletal muscle of swine

Stefan Hindel[1], Anika Sauerbrey[1], Marc Maaß[2], Lutz Lüdemann[1]

[1]Strahlenklinik und Poliklinik, Universitätsklinikum Essen, Essen, Germany
[2]Evangelisches Krankenhaus Wesel GmbH, Wesel, Germany

Purpose: To validate the feasibility of absolute regional perfusion quantification by dynamic contrast-enhanced magnetic resonance imaging (DCE-MRI) with shared k-space sampling and a blood pool contrast agent in low-perfusion tissue in an animal model.

Material and Methods: A total of seven female pigs were investigated. An ultrasonic Doppler probe was attached to the right femoral artery to determine the total flow in the hind leg musculature. The femoral artery was catheterized to enable continuous local administration of adenosine to increase blood flow up to four times the baseline level. Three different stable perfusion levels were induced [1]. The MR protocol included a 3D gradient-echo sequence with a temporal resolution of approximately 1.5 seconds. Before each dynamic sequence, static MR images were acquired with flip angles of 5°, 10°, 20° and 30°. Both, static and dynamic images were used to generate relaxation rate change maps with a flip angle method. 0.1 mL/kg body weight of blood pool contrast medium was injected via the central venous catheter, delivery rate: 5 mL/s. The right hind leg was segmented in 3D in: medial, cranial, lateral and pelvis thigh muscles, lower leg, bones, skin and fat. The first 80 seconds of the relaxation rate change-time curves of the voxels in these segments were used for model fitting. The temporal resolution of the curves was increased to 0.1 seconds using interpolation. The arterial input function (AIF) was measured in the aorta. The perfusion of the different anatomic regions was calculated using a one- and a two-compartment models with delay and dispersion corrected AIFs (as suggested by [2]). The F-test for model comparison was used to decide whether to use the results of the one- or two compartment-model fit (Fig. 1). The total flow was calculated by integrating the volume weighted perfusion values over the whole measured region.

Results: The resulting values of delay, dispersion, blood volume, mean transit time and flow were all in physiologically and physically reasonable ranges. In 107 of 160 ROIs the blood signal was separated using a two compartment model into a capillary and an arteriole signal contribution, proven by the F-test. The overall flow of the hind leg muscles, as measured by the ultrasound probe, highly correlated with the total flow from the MRI measurement, $r = 0.89$ and $P = 10^{-7}$ (Fig. 2B). Linear regression yielded a slope of 1.2 and a y-axis intercept of 259 mL/min. With respect to the mean total volume of the investigated muscle tissue this corresponds to a offset perfusion of 4.7 mL/(min·cm³). Exclusive use of the one-compartment model yielded a significant lower correlation, $r = 0.51$ and $P = 0.02$ (Fig. 2A).

Conclusions: The DCE-MRI technique of the present study using blood pool contrast media (as suggested in [3]) in combination with a two-compartment tracer kinetic model allows for the absolute perfusion quantification of low perfused organs like muscles.

References: [1] Sauerbrey et al. Biomed Res Int, 390506 (2014). [2] Calamante et al. MRM, 55(5):1180–1185 (2006).
[3] Sourbron et al. NMR BIOMED, 26(8):1004–1027 (2013).

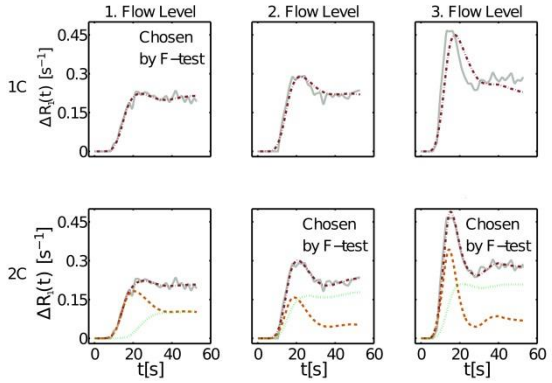

Figure 1: Fitting results for the two different models (one-compartment (1C) and two-compartment (2C)) and for different flow levels. The solid line represents the tissue blood data and the dashed-dotted line represents the fitting result. The dotted (dashed) line shows the fitting result for the capillary (arteriole) compartment.

Figure 2: Regression of the DCE-MRI model results with the Doppler flow values for the one-compartment model (A) and for the F-test selection method (B).

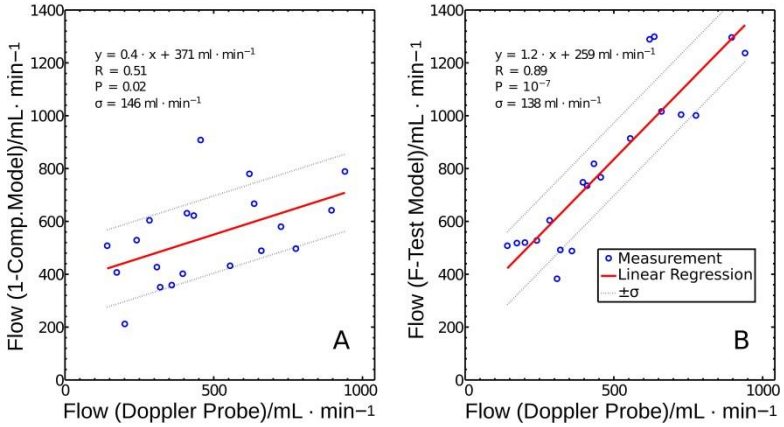

Deformation-induced damage in rat skeletal muscle: role of the vascular system

Jules Nelissen[1,2], Willeke Traa[3], Kevin Moerman[4], Cees Oomens[3], Aart Nederveen[4], Klaas Nicolay[1], Gustav Strijkers[1,2]

[1]Department of Biomedical Engineering (Biomedical NMR), Eindhoven University of Technology, Eindhoven, the Netherlands
[2]Department of Engineering and Physics, Academic Medical Center, Amsterdam, the Netherlands
[3]Department of Soft Tissue Biomechanics and Engineering, Eindhoven University of Technology, Eindhoven, the Netherlands
[4]Department of Radiology, Academic Medical Center, Amsterdam, the Netherlands

Target audience
(Pre) clinical scientists interested in vascular system, skeletal muscle damage, pressure ulcer research and musculoskeletal MRI.

Purpose
To investigate the relationship between the status of the arterial blood supply during prolonged skeletal muscle loading and the development of muscle injury, a study was performed in a rat model of skeletal muscle damage. The rat model involved the indentation of the Tibialis Anterior (TA) skeletal muscle with an MR compatible indentation setup to induce sustained skeletal muscle loading.[1,2] Muscle damage in both Sprague-Dawley (SD) and Brown-Norway (BN) rat types was investigated.

Materials & Methods
Rat model: 11-week-old SD rats (♀, 214-272 g, n=6) and BN rats (♀, 152-180 g, n=6) were used. The right leg of the rat was shaved and placed in a plastic profile filled with alginate mold for fixation, while keeping the TA muscle accessible for indentation. Indentation was performed with a previously described MR compatible indentation setup.[1] Indentation of the TA muscle, for a period of 2 hours, took place inside the MR scanner.
In vivo MRI: A Bruker 7.0T small animal MRI scanner was used with a 2 cm diameter receive surface coil, placed on top of the TA muscle inside the indentation device, in combination with a 86 mm excitation volume coil. Skeletal muscle injury and blood flow were assessed with T2 mapping (Spin-Echo, 20 slices, FOV = 2.5 x 2.5 cm^2, MTX = 256 x 256, TE = 6.95 – 180.7 ms, 26 echoes, TR = 4 s, fat suppression), and Time-Of-Flight (TOF) angiography (FLASH, 120 slices, FOV = 4 x 4 cm^2, MTX = 256 x 256, TE = 3.8 ms, TR = 12 ms) protocols. All measurements were performed pre, during and up to 2 h after indentation. During the MRI scans and indentation isoflurane (1-2%) was used as anesthetic and temgesic 0.05 mg/kg as analgesia.
Data analysis: Quantitative T_2 maps were obtained by fitting the MR signal pixel wise. Pixels with $R^2 < 0.9$ were excluded. Region of interest based T_2 analysis on the whole TA muscle was performed. The TOF angiograms were processed by visualizing maximum intensity projections (MIP) in OsiriX (Pixmeo) and visual inspection of occlusion of the saphenous artery.

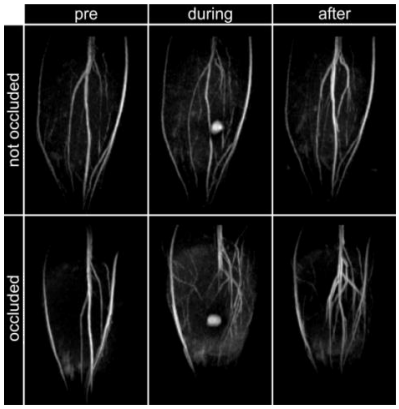

Fig. 1. Not occluded vs. occluded saphenous artery MIPs of TOF angiograms of pre, during and after end of indentation of two SD rats.

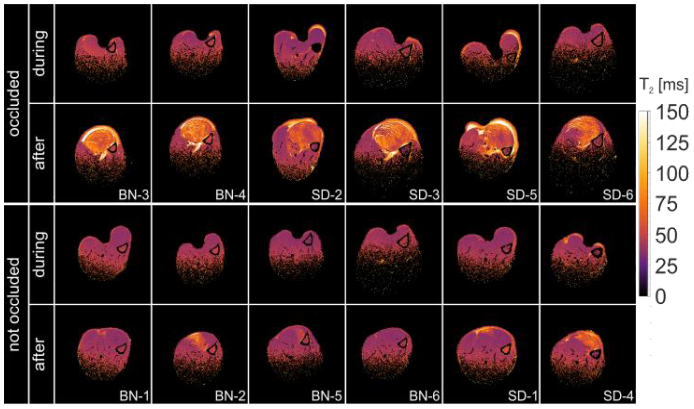

Fig. 2. Quantitative T_2 maps during and 90 min after end of indentation of 6 BN and 6 SD rats with occluded or not occluded saphenous artery.

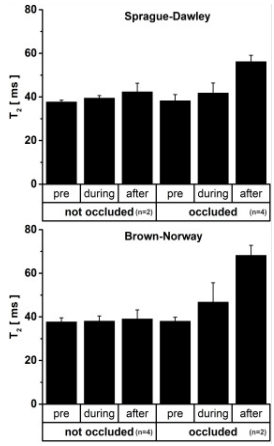

Fig. 3. ROI T_2 analysis for both BN and SD rats pre, during and 90 min after end of indentation, grouped into not occluded vs. occluded.

Results and Discussion
Fig. 1 shows angiography MIPs pre, during and after indentation, during deformation the indentor is clearly visible through its filling with 1g/L $CuSO_4$ solution. In some cases, the saphenous artery, responsible for the main blood supply to the lower leg, was occluded (bottom middle) during indentation. In other cases, it was not (top middle). Multiple small vessels became visible during indentation in the occluded cases, which indicates a compensatory mechanism in collateral vessels to account for loss of blood supply. In the cases where the saphenous artery was not collapsed during indentation a small increase in the number of visible small vessels was observed which indicates a larger demand of blood to the muscle in response to the deformation. Within a few minutes after load release multiple small vessels became apparent for both the occluded and non-occluded cases and all vessels were better visible. This is likely caused by an increase in blood flow and indicative for a hyperemic effect. This hyperemic effect was observed up to 90 min after end of indentation, which was the time point of last scan, and was more pronounced in the occluded cases. In **Fig. 2** quantitative T_2 maps of a slice in the center of deformation during and 90 min after end of indentation of the TA muscle are shown for both BN and SD rats. T2 values are grouped in occluded and not occluded saphenous artery subjects. In both groups increased T_2 values were found, indicative for the formation of edema and skeletal muscle damage. The percentage of elevated T_2 pixels ($T_2 \geq T_2$ mean prior to indentation + 3 x Std dev) in the TA was significant larger in those rats for which the saphenous artery was collapsed during indentation (paired t-test, $p<0.001$, 23.7 ± 12.8 % and 74.3 ± 10.7 %, for not occluded and occluded, respectively). The T_2 enhancement was patchy with a structure that resembled the peri- and endomysium organization of skeletal muscle. In addition, edema between muscle and skin was observed for most of the occluded cases. No difference in response on skeletal muscle deformation between the BN and SD rat type was observed. The reason that the saphenous artery for some subjects was occluded and for some not, is most probably related to the strength and position of the indentation, which differed between animals due to small anatomical differences. **Fig. 3** shows the ROI T_2 analysis of the whole TA muscle pre, during and 90 min after end of indentation for SD and BN rats. T2 values were again grouped for the occlusion and not occlusion cases. Both rat strains showed a similar T2 enhancement and T2 was more elevated in case of occlusion of the saphenous artery 90 min after end of indentation, indicative of more skeletal muscle damage in the latter case.

Conclusion
This study showed that skeletal muscle damage due to application of a sustained mechanical load is aggravated in cases where the loading leads to collapse of a major supplying blood vessel. In a rat model, the combination of skeletal muscle deformation and occlusion of a main supplying vessel, led to high T2 values in the muscle indicative of edema and muscle damage. T_2 enhancement due to skeletal muscle damage appeared highly structured and matched the peri- and endomysium organization of skeletal muscle.

Acknowledgement This research was supported by the Dutch Technology Foundation STW (NWO), and the Technology Program of the Ministry of Economic Affairs
References 1) Nelissen *et al.* ISMRM, 2014 2) Stekelenburg *et al.* Med. Eng. Phys, 2006

Multi-modality imaging in a pre-clinical model of developing rat brain metastases: initial results

Valerie De Meulenaere[1], Benedicte Descamps[2], Sara Neyt[3], Olivier De Wever[4], Elke Decrock[5], Filip J. De Vos[3], Christian Vanhove[2], Karel Deblaere[1]

[1]Department of Radiology and Nuclear Medicine, Ghent University, Ghent, Belgium; [2]iMinds Medical IT - Medisip - Infinity lab, Ghent University, Ghent, Belgium; [3]Department of Radiopharmacy, Ghent University, Ghent, Belgium; [4]Department of Experimental Cancer Research, Ghent University, Ghent, Belgium; [5]Department of Basic Medical Sciences, Ghent University, Ghent, Belgium

Introduction

Development of brain metastases is a major problem in oncology. Current medical imaging techniques such as positron emission tomography (PET) or magnetic resonance imaging (MRI) are unable to detect (micro)metastases at an early stage, hence hampering research of their underlying mechanisms. Injection of cancer cells which are labeled with iron oxide particles, allows cell tracking from the single-cell stage until the appearance of full-blown metastases, and could therefore overcome this issue.

We established a rat model which allows the follow-up of brain metastasis development up to six weeks post-induction using molecular MRI, PET and histology.

Materials and Methods

Green fluorescent protein-transfected MDA-MB-231Br breast cancer cells were labeled with micron-sized particles of iron oxide (MPIO; 1µm, Dynabeads MyOne, Invitrogen).

Two six-weeks old female rats (Crl:NIH-Foxn1rnu, Charles River; mean 128.4g) were intracardially injected with 10^5 MDA-MB-231Br/EGFP cells, using ultrasound (US) guidance to target the left ventricle (1).

MRI was performed on a 7T system (PharmaScan 70/16, Bruker) at day 1, and then weekly until 6 weeks post-injection. T2*w (GRE FLASH, 120µm isotropic resolution, TR/TE 50/14ms), T2w (SE RARE, 109µm in plane-resolution, TR/TE 6346/37ms), and contrast-enhanced T1w (SE RARE, 117µm in plane-resolution, TR/TE 1382/9.7ms; 2 mmol/kg, Dotarem, Guerbet) sequences were run with a total acquisition time less than 90 minutes. MPIO-induced hypointensities were counted on the T2*w images; T2-visible lesions were coregistered with T2*w images.

Following the final MRI session, a static, whole-body ^{18}F-FDG PET acquisition (Triumph-II, Trifoil, 37MBq, 30 minutes uptake, 30 minutes acquisition) was performed to determine metastasis development outside the brain.

Finally, haematoxylin and eosin staining was performed on paraffin-embedded slices of cerebrum, cerebellum and lungs.

Results and Discussion

The US guidance allowed successful cell injection into the left ventricle.

The T2*w images acquired one day post-injection, showed the initial distribution of MPIO-labeled cells in the rat brain The amount of hypointensities decreased week after week (>300 hypointensities at day 1 to around 50 at week 6). At week 3 to 4 first signs of metastasis development were visible as hyperintensities on T2w images. All metastases visible on T2w images at week 6 could be correlated to their corresponding hypointensities on T2*w images and histology.

Whole-body PET imaging suggested some hot spots outside the brain. Histological slices confirmed the presence of local cellular alterations. Contrary to the claim of Yoneda et al (2), we observed metastasis in the top of the left lung, amongst others.

Conclusion

We demonstrate that the development of single MPIO-labeled cancer cells into metastases can be detected at three to four weeks post-injection. This model will allow further investigation of brain metastasis development and novel treatment strategies.

References

(1) Balathasan et al, Am J Pathol 2013, 183:26-34

(2) Yoneda et al, J Bone Miner Res 2001, 16:1486-95

Development of a molecular approach for the monitoring and treatment of diabetic patients

Deborah Crombez[1], Sophie Laurent[1], Géraldine Scaux[1],Luce Vander Elst,[1] Robert Muller[2], Carmen Burtea[1]

[1]Laboratory of NMR and Molecular Imaging, UMONS, Mons, Belgium
[2]Center for Microscopy and Molecular Imaging, Charleroi, Belgium

Diabetes is one of the major causes of premature illness and death worldwide due to the severe long-term complications, such as cardiovascular disease, visual disability, limb amputation, renal failure, and neuropathy. The main pathological hallmark of diabetes mellitus consists in a progressive decline of the pancreatic beta cell mass (PBCM), which is responsible of the insufficient insulin secretion and hyperglycemia[1]. No reliable method is available nowadays to measure non-invasively the PBCM in diabetic patients. On the other hand, adipokines play an important role in the pathophysiology of obesity-related disorders, including diabetes and metabolic syndrome, due to their ability to regulate inflammatory and metabolic processes. Adiponectin is an adipokine, a protein hormone secreted in the blood circulation by the adipose tissue. It interacts with two main receptors: AdipoR1, mostly expressed in skeletal muscles, and AdipoR2, mostly expressed in the liver.[2, 3] In diabetic and obese patients, adiponectin blood levels are decreased, while its replenishment has an anti-diabetic effect by improving insulin sensitivity and cell survival, including that of PBC.[3, 4]

The first research strategy is thus focused on the development of a PBC-targeted imaging probe, which will allow the quantification of PBCM by molecular imaging, the monitoring of its decrease during the pathological process and to adopt novel therapeutic strategies. In this last context, the second part of the present work is dedicated to the identification of a therapeutic peptide able to modulate the activity of adiponectin receptors. Our therapeutic agent would act as an adiponectin agonist, replacing its diminished endogen production in diabetic patients. The improved PBC survival produced by this therapeutic agent could be evaluated by the PBC-targeted imaging probe.

The first part of our work aimed to validate *in vitro* an imaging probe (USPIO-P88) able to target the PBC[5] by interaction with a specific biomarker, the protein FXYD2-gamma-a[6]. The imaging probe was developed by coupling to ultrasmall particles of iron oxide (USPIO) a peptide (P88) that is specific to FXYD2-gamma-a, previously discovered by phage display in our laboratory. Aiming to develop a therapeutic agent, the AdipoR agonist has been searched within a combinatorial library of random peptides that was screened against a C-terminal fragment of AdipoR (AdipoR-9C) that is homologous in both receptors in humans and mice.

P88 does not bind to the exocrine pancreas and is able to detect by MRI down to ~156 human pancreatic islets/mm^3 after conjugation to USPIO. On human histological sections, USPIO-P88 is specific to PBC, but not to duodenum, stomach or kidney tissues.

Two peptides have been identified as promising potential agonists of both AdipoR receptors. They have shown a good affinity, efficacy and specificity for AdipoR-9C, as well as for human AdipoR1. The histological tests performed on control mouse liver and muscle are promising by corroborating the affinity for the tissue-expressed AdipoR. These peptides are being evaluated *in vitro* on hepatic cells, seeking to confirm their expected pharmacological effects. Our preliminary data have shown that both peptides are able to stimulate up to twice the AMPK phosphorylation, a key enzyme in the cellular energy homeostasis.

To conclude, USPIO-P88 and AdipoR-targeted peptide agonists represent novel and promising tools both for treatment and monitoring of PBCM in diabetic patients.

1. Cnop Met al. Diabetes 2005; 54 (Suppl. 2): S97–S107.
2. Maury E et al. Mol Cell Endocrinol 2010;314(1): 1-16.
3. Kadowaki T & Yamauchi T. Endocrine Reviews 2005; 26: 439–451.
4. Lee YH, Magkos F, Mantzoros CS, Kang ES. Metabolism. 2011; 60(12): 1664-1672.
5. Burtea C, Laurent S, Muller RN, Sermeus C, Eizirik D, EP2537859A1/26-12-2012.
6. Flamez D et al. Diabetologia 2010;53:1372–1383.

Multiparametric Magnetic Resonance to investigate aggression: a study at 11.7T on the BALB/cJ mouse model

Houshang Amiri[1], Amanda Jager[2], Sjaak van Asten[3], Arend Heerschap[3], Jeffrey Glennon[4]

[1]Department of Radiology and Nuclear Medicine, Radboud University Medical Center, Nijmegen, the Netherlands
[2]Department of Cognitive Neuroscience, Radboud University Medical Center, Nijmegen, the Netherlands
[3]Department of Radiology, Radboud University Medical Center, Nijmegen, the Netherlands
[4]Department of Cognitive Neuroscience, Radboud University Medical Center, Nijmegen, the Netherlands

Target audience – Radiologists, Psychiatrists, Psychologists and Neuroscientists.

Purpose – Juvenile aggression and antisocial behavior in childhood and adolescence particularly conduct disorder (CD), represents an increasing socioeconomic burden due to the persistent and repeated nature of offences. The age of onset varies but cases with childhood onset are at increased risk of developing antisocial personality disorder in adulthood and when coupled to callous unemotional traits typically present with more severe treatment aggression and antisocial behavior. Aggressive behaviour is a key symptom domain of CD. Therefore, animal models of aggression could provide more knowledge about the neural substrates underlying CD and could eventually provide new insights in possible treatments to treat or prevent this disorder. The BALB/cJ mouse has been reported to exhibit aggressive behavior when compared to its genetically related substrain, BALB/cByJ. In the current study, we first extensively phenotyped the BALB/cJ mice in terms of aggression, anxiety, impulsivity, compulsivity and attention. Following this, a multiparametric magnetic resonance experiment including diffusion tensor imaging (DTI), arterial spin labelling (ASL), and magnetic resonance spectroscopy (MRS) was performed on the same animals. Three brain regions involved in cognitive processing, i.e. anterior cingulate cortex (ACC), orbitofrontal cortex (OFC) and dorsomedial striatum (DMS) were selected for further study.

Methods – A total of 64 mice (32 BALB/cJ, 32 BALB/cByJ) were included in the study. A cognitive profile of the mice was created by testing aggression in the resident-intruder test, attention and impulsivity in the touchscreen operant boxes and locomotion and anxiety in the open field and elevated plus maze. Interactions took place for 5 consecutive days. In each interaction, C57BL/6J intruders of lower weight were randomly assigned to a different resident. Aggressive behavior was analyzed on the last interaction day using The Observer XT (Noldus). Open field and elevated plus maze experiments were performed for 5 min. Locomotion activity and place preference was quantified using Ethovision (Noldus). Since CD is highly comorbid with ADHD [1], the BALB/cJ mice were tested in the five-choice serial reaction time task in touchscreen operant chambers (Campden Instruments) to assess impulsivity, compulsivity and attention. MR experiments were performed using an 11.7T scanner (Biospec, Bruker). To visualize the brain anatomy a gradient echo sequence in three orthogonal orientations was used. For DTI experiments, 20 axial slices covering the whole brain were acquired with a spin-echo echo-planar imaging (EPI) sequence (b=0 and 1000 s/mm^2) along 30 non-collinear directions; resolution was 156×156×500µm^3 and total acquisition time (TA) was 18 min. Pulsed-ASL data were acquired by a flow sensitive alternating inversion recovery (FAIR) EPI sequence with the resolution as 195×260×1000µm^3 and TA=12min. Brain metabolite concentrations were quantified by single-voxel ^{1}H-MRS using PRESS sequence (TR/TE=2500/11.6ms, TA=17min) with a voxel size of 3.75µL (for DMS) and 2.74µL (for ACC and OFC) and LCModel software. Metabolite concentrations are reported relative to the total Creatine (tCr) as it was found to be unchanged in our models when using water concentrations as references. Imaging data were analyzed using ParaVision software (5.2, Bruker) and MATLAB scripts. Statistical analysis were performed using GraphPad Prism software p-values less that 0.05 were considered significant.

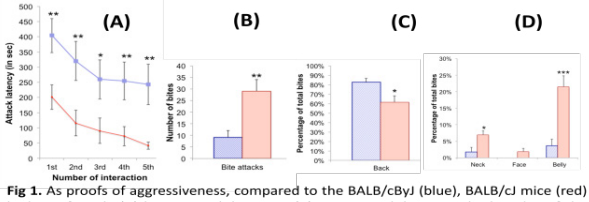

Fig 1. As proofs of aggressiveness, compared to the BALB/cByJ (blue), BALB/cJ mice (red) had significantly (A) lower attack latencies (B) more attack bites on the last day of the interactions (C,D) lower percentage of bites directed to the back and higher to the vulnerable body parts.

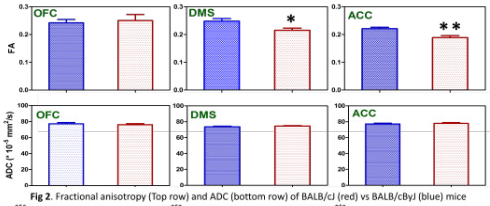

Fig 2. Fractional anisotropy (Top row) and ADC (bottom row) of BALB/cJ (red) vs BALB/cByJ (blue) mice

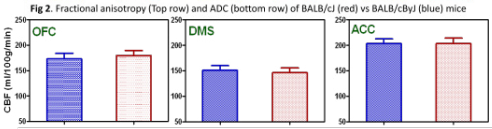

Fig 3. Cerebral blood flow (CBF) in the OFC, DMS and ACC of BALB/cJ (red) vs BALB/cByJ (blue) mice

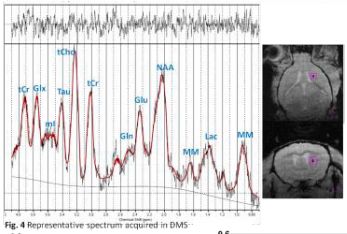

Fig. 4 Representative spectrum acquired in DMS

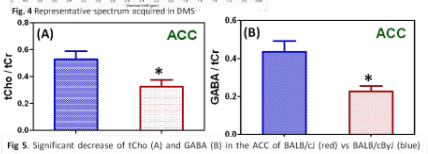

Fig 5. Significant decrease of tCho (A) and GABA (B) in the ACC of BALB/cJ (red) vs BALB/cByJ (blue) mice.

Results – As shown in Fig. 1, increased pathological aggression (reduced attack latency ($p<0.01$), atypical pattern ($p<0.001$) and increased number of bites ($p<0.01$) were observed in the BALB/cJ mice. Phenotyping of anxiety demonstrates increased freezing behavior (not shown), a marker for anxiety, in the open field test ($p<0.01$) and increased preference (not shown) for the closed arms in the elevated plus maze ($p<0.01$), a marker for increased anxiety in BALB/cJ versus BALB/cByJ mice. No deficits were found in impulsivity and compulsivity, as measured by respectively the number of premature responses and the number of time-out responses. Interestingly, the aggressive BALB/cJ mice were associated with global attention-deficits ($p<0.001$) as measured by an increased number of omissions (not shown). DTI of the BALB/cJ mice showed a reduced directional diffusivity measured by fractional anisotropy (FA) in both the ACC ($p<0.01$) and the DMS ($p<0.05$) with no change in the mean diffusivity (Fig. 2). No change was seen in cerebral blood flow (CBF, Fig. 3) measured by ASL. A representative spectrum acquired in the DMS is shown in Fig. 4. We found that BALB/cJ exhibited a significant decrease in GABA ($p<0.01$) and total choline (tCho, $p<0.05$) in the ACC compared to the BALB/cByJ (Fig. 5). No significant change in the DMS metabolites was observed. The aforementioned alterations in the brain structure and metabolism did not alter cerebral blood flow measured by the ASL.

Discussion – The results from the resident-intruder test proved that BALB/cJ mice have elevated levels of aggression which might be related to the more anxious phenotype observed in the open field and elevated plus maze. Significant differences observed in global attention processing suggest possible comorbidity of aggression and inattention. Reduced FA and changes in the white matter (WM) organization is likely related to the aggression, which also has been reported in traumatic brain injury patients possessing aggressive behavior [2]. Reduced inhibitory GABA tone in the ACC seems to be linked to aggression, which confirms similar findings in aggression in humans. In addition, prefrontal GABA tone is associated with anxiolytic effects, therefore the increased anxiety in the BALB/cJ mice may be explained by decreased GABA tone. Therefore understanding GABAergic tone might be important in a fuller understanding of aggression linked to anxiety. tCho levels are a precursor for the neurotransmitter acetylcholine and were also significantly decreased in the ACC in the BALB/cJ mice. Interestingly, reduced acetylcholine tone has been reported to be linked to aggression [3]. Whether this is linked to inattention (also observed in the BALB/cJ mice) remains an open question.

Conclusion – The BALB/cJ mouse model shows marked aggression coupled to increased anxiety and a global attention deficit with no evidence for increased impulsivity and compulsivity when compared to the controls, BALB/cByJ mice. Our data indicates that pathological aggression observed in the BALB/cJ mice is likely related to structural and neurochemical changes leading to inattention and anxiety; such that BALB/cJ mice are insensitive to environmental cues resulting in inappropriate behavior such as antisocial behavior and aggression. In summary, BALB/cJ mice may serve as a suitable model to investigate potential therapeutic approaches for CD such as modulation of anterior cingulate cortical GABA and acetylcholine tone.

References – [1] Buitelaar J. K., et al., Eur. Child Adolesc Psychiatry, 2013 Feb; 22 Suppl 1:S49-54. [2] Wozniak J. R., et al., Arch Clin Neuropsychol. Jun 2007; 22(5): 555–568. [3] Chan A., et al., J Nutr Health Aging,2008 Apr;12(4):252-61.

Magnetisation transfer contrast imaging reveals white matter pathology in the APP/PS1 mouse model of amyloidosis

Jelle Praet[1], Christian Bigot[1], Jasmien Orije[1], Maarten Nayaert[1], Marleen Verhoye[1], Annemie Van der Linden[1]

[1]Bio-Imaging Lab, University of Antwerp, Antwerp, Belgium

Abstract:

Target Audience: People aiming to develop Magnetisation Transfer Contrast imaging (MTC) as tool for the early diagnosis of Alzheimer's Disease (AD).

Purpose: While no definitive cure for AD exists yet, current treatments would benefit greatly from an early diagnosis. We have previously shown that MTC is able to detect amyloid β plaques in old APP/PS1 mice [1]. In the current study we investigated if MTC is also able to visualize early amyloid-induced pathological changes.

Materials and methods: In a cross-sectional study, we used wild type (n=61) and APP/PS1 mice (n=76) [2] of 2, 4, 6, 8 and 24 months of age. Mice were imaged at the respective ages and sacrificed thereafter for histological analysis. MTC was acquired on a 7T Pharmascan MRI system (Brucker, Germany) using a Turbo Spin Echo sequence (number of echoes = 1, TE = 33.0 ms, TR = 3000 ms, matrix size = 256 × 256, field of view = 2.0 × 2.0 cm^2, slice thickness = 1 mm, NA = 1). Turbo Spin Echo images were acquired without an off-resonance RF pulse (unsaturated) and with an off-resonance RF pulse (saturated) applied (pulse strength = 12 µT, number of pulses = 36, pulse length = 40 ms, saturation time = 1440 ms) at an offset frequency of -16875 Hz.

Results: We first validated our previous results using 24 month old mice as, compared to our previous study [1], we acquired the MTC images using a different sequence and a lower field strength MRI scanner. We observed an increased MTC ratio in grey matter regions of APP/PS1 mice, validating our previous results. Next, we observed that young mice consistently showed decreased MTC ratios in the splenium of 4, 6 and 8 month old APP/PS1 mice. Analysis of the MTC values of cortical regions is currently still ongoing. For the splenium, MTC values correlated to the histological markers 4G8 (amyloid plaques), IBA1 (microglia) and GFAP (astrocytes) but not MBP (myelin). Again, analysis of histological data of the cortical regions is still ongoing.

Conclusion: MTC is able to visualize early amyloid-induced white matter pathology in the splenium of APP/PS1 mice.

References:

[1] Bigot C, Vanhoutte G, Verhoye M, Van der Linden A. *Magnetization transfer contrast imaging reveals amyloid pathology in Alzheimer's disease transgenic mice*. 2014. Neuroimage 87:111-9.

[2] Radde R, Bolmont T, Kaeser SA, Coomaraswamy J, Lindau D, Stoltze L, Calhoun ME, Jäggi F, Wolburg H, Gengler S, Haass C, Ghetti B, Czech C, Hölscher C, Mathews PM, Jucker M. *Aβ42-driven cerebral amyloidosis in transgenic mice reveals early and robust pathology*. 2006. EMBO Rep. 7: 940–946.

Basal metabolic state does not modulate cerebrovascular reactivity response to common hypercapnic stimuli

Jeroen C.W. Siero[1], Carlos C. Faraco[2], Megan K. Strother[2], Jeroen Hendrikse[1], Manus J. Donahue[2]

[1]Dep Department of Radiology, University Medical Center, Utrecht, the Netherlands
[2]Radiology and Radiological Sciences,Nashville, Vanderbilt University School of Medicine, Tennessee, United States

Introduction: BOLD cerebrovascular reactivity (CVR) measurements with hypercapnic stimuli are commonly used for measuring cerebrovascular reserve capacity in patients with cerebrovascular disease and for calibrating neuronal BOLD responses [1-2]. However, basal physiological parameters such as cerebral blood flow (CBF), venous blood oxygenation (Yv), oxygen extraction fraction (OEF) and cerebral metabolic rate of oxygen consumption (CMRO2) may add variability in BOLD CVR, as has been shown to be the case for neuronal stimuli [3]. Potential BOLD CVR modulators can be included as regressors to increase statistical power in detecting group differences. This study investigated whether these parameters (basal CBF, Yv, OEF, and CMRO2) modulate the BOLD CVR response for two common hypercapnic stimuli (5%CO2 + balanced room air, and carbogen; 5%CO2 + 95%O2).

Materials and Methods: Healthy volunteers (n=11; 2F/9M; age=28.2±3.2 yrs) were scanned at 3T (Philips) with a nasal cannula for EtCO2 monitoring and a non-rebreathing oxygen mask for gas administration. BOLD CVR data (GE-EPI, TR/TE=2000/35ms; spatial resolution 3x3x3.5mm^3, slices 31, SENSEfactor=1.8, flip angle=80°) were acquired during a hypercapnic stimulus paradigm; subjects were presented with two blocks of the following hypercapnic stimuli; room air interleaved with hypercapnic-normoxia (90s), and room air interleaved with hypercapnic-hyperoxia (carbogen; 90s). Subjects were randomly assigned each of the two stimulus orderings. BOLD data were corrected for drift, motion and slice timing using FEAT (FSL [4]). BOLD signal changes (%) were normalized by the measured end-tidal CO2 (EtCO2).
Yv measurements were performed on the sagittal sinus using TRUST MRI (TR=3s, TI=1.2s, voxel size=3.4×3.4×5mm^3, 4 T2 weightings (effective TEs: 0, 40, 80, and 160ms), with a tCPMG=10ms; repeats=2 [5-6]. Whole brain CBF measurements (ventricles excluded) were performed using pCASL MRI, and subsequently registered to MNI space. Acquisition parameters and CBF quantification method follow those in [7]. Post label delay=1.7s, label duration=1.5s, TR=3.9s, averages=13, voxel size=3x3x7mm^3, slices=17. OEF was computed as $([O_2]_a - [O_2]_v)/[O_2]_a$, and $CMRO_2 = CBF*([O_2]_a - [O_2]_v$ Total arterial O2 content ($[O2]_a$), venous O2 content ($[O2]_v$), and pvO2 was computed using physiological models of O2 hemoglobin saturation and plasma-dissolved O2 [8]. Hct values of 0.42 for males and 0.4 for females were assumed.

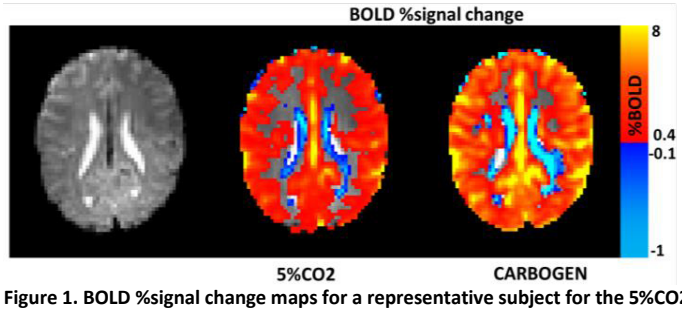

Figure 1. BOLD %signal change maps for a representative subject for the 5%CO2 and carbogen stimuli.

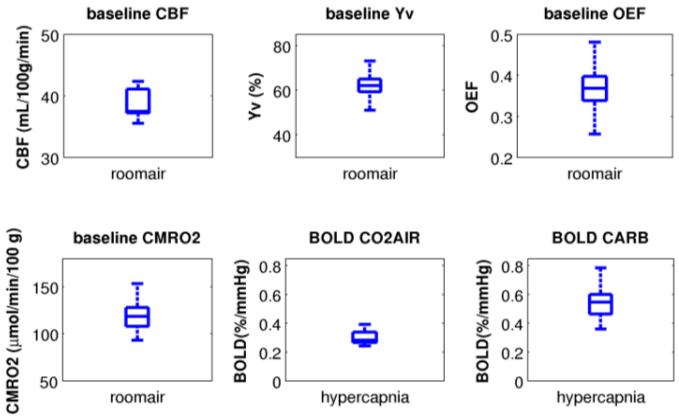

Figure 2. Box plots of the basal CBF, Yv, OEF and CMRO2 and BOLD signal changes (%/mmHg) for all subjects (N=11).

Results & Discussion: As expected carbogen induces higher BOLD signal changes compared to 5%CO2 due to elevated [HbO2]/[dHb] in veins (**Fig1, 2**). Note that negative BOLD signals changes were observed in the ventricles (vessel dilation causing fractional CSF displacement) in line with [9], and were highest for carbogen which is likely due to amplified extravascular ΔR2* effects in the ventricular (CSF) space due to hyperoxia. Correlation analysis between basal CBF, Yv, OEF, CMRO2 and BOLD signal changes showed no significant correlations for both the 5%CO2 and carbogen stimuli (**Table1**). Basal CBF and basal Yv were found to be correlated (**Fig3.**), likely caused by the increased influx of HbO2 in venous blood with elevated CBF. Earlier reports focused on regional BOLD fMRI signal changes with neuronal activation found a similar relationship between basal CBF and Yv [3]. Lu et al. indicated that basal CBF and Yv modulate regional BOLD fMRI signal changes in response to neuronal stimuli, suggesting that including these parameters as regressors in BOLD fMRI studies would reduce inter-subject variability. In the current study, however, we find that basal CBF, Yv, OEF and CMRO2 do not significantly modulate global vascular BOLD signal changes elicited by 5%CO2 and carbogen (5%CO2/95%O2) vasoactive gas stimuli. This discrepancy could be explained by modulatory effects manifesting only
on local regional scale (visual cortex), or known differences in how neurotransmitter-mediated vasodilation and pH-mediated vasodilation differ in their dependence on basal metabolic state. In addition, neuronally-induced BOLD responses include CMRO2 changes which decrease the BOLD signal changes compared to pure vascular BOLD signal changes for similar ΔCBF and ΔCBV. Investigating modulatory effects of basal CBF, Yv, OEF and CMRO2 on global resting-state BOLD fMRI results could shed light on a possible neurovascular origin. These findings should be useful for confirming that CVR studies measure 'pure' vascular effects, and suggest that normalization by basal metabolic state in such experiments may not be necessary. Further, certain assumptions in calibrated BOLD that similar physiology is being probed by vascular and neuronal stimuli may have to be revisited.

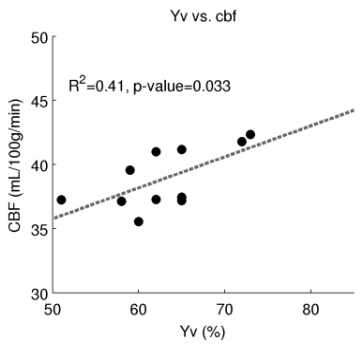

Figure 3. Basal CBF versus basal Yv.

[1] Spano et al. Radiology 2013, [2] Donahue et al. Stroke 2014, [3] Lu et al MRM2008, [4] Smith SM et al. NI2004, [5] Xu et al. MRM2012, [6] Lui et al. MRM 2013, [7] Alsop et al. MRM2014 [8] Dash et al. Ann. Biom. Engin. 2010, [9] Thomas B et al. NI2013

Pearson Correlation (R-squared, p-value), n=11		
Basal parameters	5%CO2	Carbogen
CBF	0.02, p=0.67	0.23, p=0.14
Yv	0.17, p=0.21	0.13, p=0.28
OEF	0.17, p=0.21	0.13, p=0.28
CMRO2	0.18, p=0.19	0.08, p=0.40

Table 1: correlation between basal CBF, Yv, OEF CMRO2 and BOLD signal changes (%/mmHg) for 5%CO2 and carbogen

Network analysis of EEG related functional MRI changes due to medication withdrawal in focal epilepsy

Kees Hermans[1], Pauly Ossenblok[2], Petra van Houdt[1], Liesbeth Geerts[3], Rudolf Verdaasdonk[4], Paul Boon[1], Albert Colon[5], Jan C. de Munck[4]

[1]Department of Research and Development, Academic Center for Epileptology Kempenhaeghe & Maastricht University Medical Center, Heeze, the Netherlands; [2]Department of Clinical Physics, Academic Center for Epileptology Kempenhaeghe & Maastricht University Medical Center, Heeze, the Netherlands; [3]Philips Healthcare, Best, the Netherlands; [4]Department of Physics and Medical Technology VU University Medical Center, Amsterdam, the Netherlands; [5]Department of Neurology, Academic Center for Epileptology Kempenhaeghe & Maastricht University Medical Center, Heeze, the Netherlands

Introduction: EEG correlated functional MRI (EEG-fMRI) studies revealed substantial predictive value compared to invasive EEG and surgical outcome in patients with refractory focal epilepsy [1]. In this study we applied network analysis strategies to investigate EEG related fMRI changes due to withdrawal of anti-epileptic drugs (AEDs) to elaborate the clinical usefulness for epilepsy surgery candidates.

Methods: EEG-fMRI was acquired for 10 patients with focal epilepsy who were candidates for epilepsy surgery. Patients were scanned before the start of standard pre-surgical video-EEG when still on the usual medication (condition A) and at the end of the video-EEG session, after anti-epileptic drug (AED) withdrawal (condition B). EEG-fMRI data were analyzed using both the general linear model (GLM) approach and independent component analysis (ICA). The EEG-fMRI correlation pattern obtained in condition B was used for spatial correlation with all the independent components to select the epileptic independent component (ICE). A similar procedure was used to select the well-known resting state components or networks (RSNs). Next, the difference in functional connectivity between conditions A and B was quantified using a GLM approach applied to the concatenated time series of the selected components. A functional connectivity difference parameter $\Delta\alpha$ was estimated.

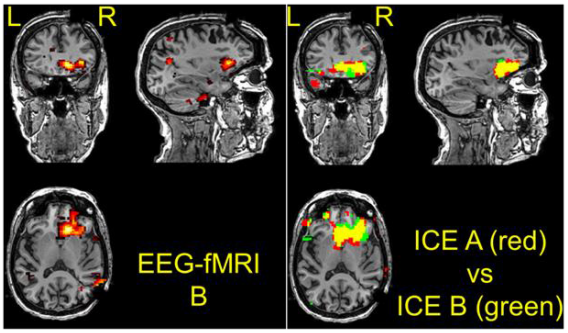

Fig. 1: Comparison of EEG-fMRI results of one patient in condition B, with the ICEs in condition A (red) and B (green) and their spatial overlap (yellow).

Results: We were able to identify an ICE for both conditions A and B, even if the GLM analysis of EEG-fMRI was inconclusive. Standard GLM analysis was inconclusive in condition A for 7 out of the 10 patients studied. Spatially, these ICEs were similar for both conditions (see Fig. 1 for an example of one patient), before and after withdrawal of AEDs. Furthermore, mean $\Delta\alpha$ (see Fig. 2 for an example of a matrix with $\Delta\alpha$ values for one patient) values were found to be significantly different from zero ($p<0.05\%$, Wilcoxon signed rank test), which indicates that a significant increase in general functional connectivity of all selected resting state components was found for each patient after medication withdrawal.

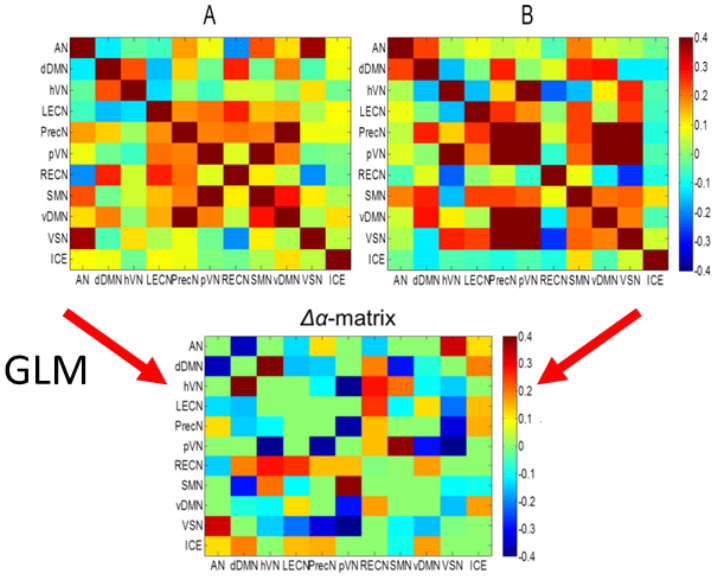

Fig. 2: In the top row the Pearson's correlation matrices are shown for the conditions A and B, for the same patient as in Fig. 1. On the bottom row the matrix containing the functional connectivity difference values ($\Delta\alpha$) is shown. A negative value means that the functional connectivity is higher in condition B compared to A. Correlation values are shown for the following RSNs: AN = auditory network; dDMN = dorsal default mode network; hVN = higher visual network; LECN = left executive control network; PrecN = precuneus network; pVN = primary visual network; RECN = right executive control network; SMN = sensorimotor network; vDMN = ventral default mode network; VSN = visuospatial network; ICE = epileptic independent component.

Conclusions: The results of this study suggest that sensitivity of EEG-fMRI as diagnostic tool is improved at the end of the video-EEG monitoring session. Our results indicate that the underlying reason is related to the increased excitability of the brain which is reflected in a general increased functional connectivity after withdrawal of AEDs.

REFERENCES

[1] P.J. van Houdt, P.P.W. Ossenblok, A.J. Colon, P.A.J.M. Boon, J.C. de Munck, A framework to integrate EEG-correlated fMRI and intracerebral recording, NeuroImage, Vol. 60, pp. 2042-53 (2012)

Investigating the effects of hypercapnia and hyperoxia on T2* and S0 calculated from multi-echo BOLD data at 7T

Alex Bhogal[1], Jeroen C.W. Siero[1], Marielle E. Philippens[2], Esben Petersen[1], Martijn Froeling[1], Peter Luijten[1], Jeroen Hendrikse[1], Manus J. Donahue[3], Hans Hoogduin[1]

[1]Department of Radiology, University Medical Center, Utrecht, the Netherlands
[2]Department of Radiotherapy, University Medical Center, Utrecht, the Netherlands
[3]Vanderbilt University School of Medicine, Nashville, United States

Purpose: To investigate the effect of hyperoxia and hypercapnia on fitted T_2* and S_0 calculated from high-field multi-echo BOLD EPI data.

Introduction: Hypercapnia and hyperoxia, induced using controlled gas challenges, may be used to probe physiological effects related to the Blood Oxygenation Level-Dependent (BOLD) contrast. Hypercapnia is a vasoactive stimulus which elicits increases in cerebral blood flow (CBF) and cerebral blood volume (CBV), with a concomitant decrease in venous de-oxyhemoglobin (dHb) saturation. Hyperoxia also reduces venous dHb by increasing hemoglobin saturation and dissolved plasma O_2. The latter has the effect of shortening blood water T_1 relaxation times which in turn can increase the intensity of the measured BOLD signal. Therefore, gas challenges may be used to modulate T_2* and S_0, which may give information on underlying physiological processes when performed in controlled manner with high signal-to-noise ratio. As such, the aim of this study was to examine the effects of hyperoxia and hypercapnia on these parameters by utilizing a controlled breathing apparatus at high field (7T). We interpret the findings in the context of existing physiological models.

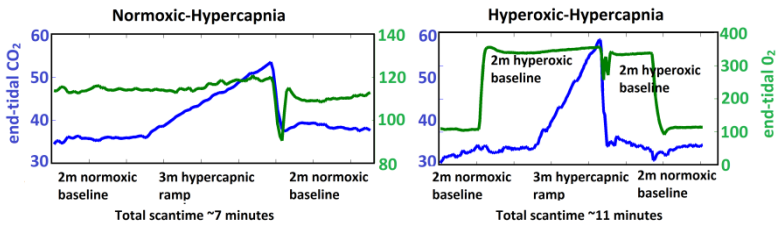

Fig 1: example end tidal CO_2 and O_2 traces used as regressors for general linear model. The timing of the breathing paradigms for NH and HH are given.

Methods: Healthy (n=3) volunteers were scanned on a Philips 7T scanner using a 32 ch receive coil (NOVA Medical). Multi-echo GE-BOLD (α= 90°, TR= 3000 ms, TE= 4.38,28.01,51.56ms, EPI/SENSE 39/3, resolution = 1.5x1.5x2mm, FOV= 216 x 40x 192mm, slices=20) were acquired during two (normoxic-hypercapnia (NH) and hyperoxic-hypercapnia (HH)) targeted breathing challenges (fig 1) delivered by a RespirAct gas control system (Thornhill Research Inc, Toronto, Can). Motion correction was performed using Elastix (Image Sciences Institute, UMC Utrecht). Voxel-wise T_2* and S_0 parameters ($S(t) = S_0*\exp(-TE/T_2*)$ were calculated for each image volume using log-linear regression. S_0 and T_2* maps were analyzed using a general linear model (FEAT – FSL FMRIB, Oxford) using end-tidal CO_2 and O_2 traces (temporally resampled to match TR) as regressors (see fig 1). Data were spatially smoothed (Gaussian: 2mm FWHM). Z-statistic maps were produced which independently examined the effects of the NH and HH stimuli, on the fitted S_0 and T_2* timeseries data. Z-values were thresholded between -3 and -5 for negative correlations and 3 to 10 for positive correlations.

Results: ***Regressor = end-tidal CO_2 (fig 2-A):*** Results for the NH challenge showed negative T_2*- and S_0-related Z-values in the ventricles (arrows fig 2A), and to a lesser extent, white matter regions in all three subjects. This correlation was less apparent for the HH challenge (fig 2A – bottom row). T_2* Z-values were high in the grey matter for both challenges, but were generally lower for the HH challenge (fig 2A – left column. ***Regressor = end-tidal O_2 (fig 2-B):*** Positive T_2* changes were observed for both breathing challenges (fig 2-B: left) with diffuse, negatively correlated T_2* changes throughout (not shown). For the S_0 maps, positive Z-values were observed in regions that apparently correlated with large vessels, such as the sagittal sinus (arrow fig 2-B), and those located along the sulci. Clusters of negative S_0 Z-values were observed throughout (data not shown).

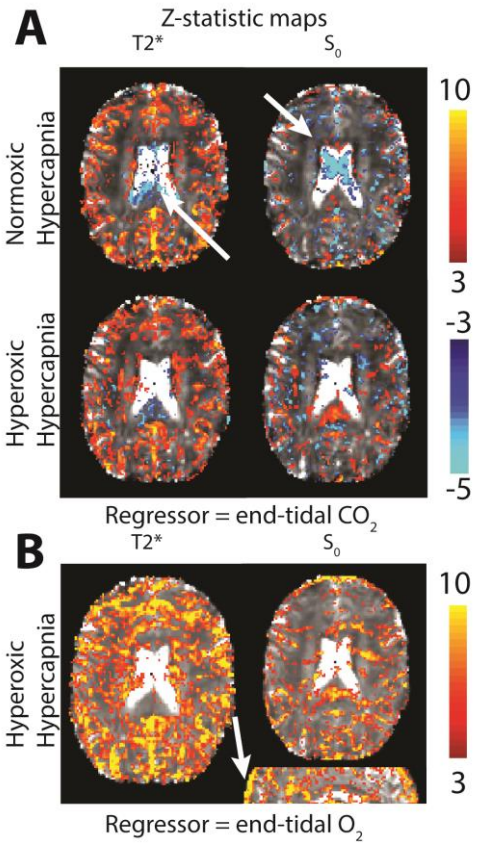

Fig 2A: Z-statistic maps when using end-tidal CO_2 as a regressor. Negative T_2* and S_0 Z-values (top arrows) seen in ventricles under normoxia but not hyperoxia. A significant T_2* response seen in GM for both challenges. Fig 2B: Significant positive T_2* response due to hyperoxia (left). Significant positive S_0 response correlating with large vessels seen in response to hyperoxia. White arrow highlights saggital sinus (right-bottom).

Discussion: The negative T_2* Z-values observed in the ventricles (particularly the choroid plexus), and within the sulci support results shown in [1] and can be explained via changes in relative tissue/blood and CSF fractions. Hypercapnia causes an increase in CBV leading to a decrease in S_0 in voxels where CSF and venous blood signals are averaged as reported by Thomas et. al [1]. In addition to their findings, we observe T_2^* decreases for these regions which are likely caused by reduced extravascular BOLD contribution due to displacement by CSF [2]. Under hyperoxia, shortening of blood water T_1 can lead to an increase in S_0. Furthermore, increased venous Hb saturation due to hypercapnia related CBF increases (BOLD effect) reduces the maximum permissible T_2* changes. These effects may combine to counteract the negative correlation in CSF and white matter observed under NH and explain the reduced T2* Z-values seen under hyperoxia. The end-tidal O_2 regressor revealed a positive correlation between O_2 and signal changes amongst large vessels, particularly the sagittal sinus. Here, shortening of T_1 due to increased venous oxygenation likely leads to an increase of the extravascular steady state signal as suggested by the increased S_0-, and associated Z-values. The large positive T_2* correlation seen across the entire brain is related to the increase in venous oxygenation under hyperoxia. Ongoing work will investigate the effects of different stimulus paradigms to shed further light on the influence of hypercapnia and hyperoxia on T_2* and S_0. Accurate understanding of the vascular effects of HN and HH stimuli is necessary when employing these stimuli for assessing CVR in disease and health.

Conclusion: Hypercapnia and hyperoxia can be used to modulate both T_2* and S_0 which may shed a light on the physiological phenomena underpinning the BOLD effect in different areas of the brain.

References: [1] Thomas et al, Neuroimage 2013 [2] Scouten et al, MRM 2008

This study was part of the EU Artemis High Profile Project

Relating cognitive adverse events of antiepileptic drugs to functional network efficiency

Tamar van Veenendaal[1], Dominique Ijff[2], Richard Lazeron[2], Walter Backes[1], Paul Hofman[1], Marielle Vlooswijk[3], Anton de Louw[2], Albert Aldenkamp[2], Jacobus Jansen[1]

[1]Department of Radiology, Maastricht University Medical Center, Maastricht, the Netherlands
[2]Kempenhaeghe Epilepsy Center, Heeze, the Netherlands
[3]Department of Neurology, Maastricht University Medical Center, Maastricht, the Netherlands

Target audience: Researchers interested in epilepsy, antiepileptic drugs and resting state fMRI

Introduction: Cognitive adverse events, such as mental slowing, often arise when antiepileptic drugs (AEDs) are prescribed to treat patients with epilepsy[1]. On the basis of previous epilepsy research, in which cognitive performance is linked to the efficiency of brain networks[2], we hypothesize that cognitive problems due to AEDs are associated with a less efficient brain network. To this end, the relation between graph theoretical measures derived from resting state fMRI, AED use, and cognitive function was investigated.

Methods: Two groups of epilepsy patients were included: a 'low risk' group (30 epilepsy patients using lamotrigine or levetiracetam; AEDs associated with only mild cognitive adverse events) and a 'high risk' group (17 patients using topiramate or phenytoin; AEDs associated with more severe cognitive adverse events)[1].

The Computerized Visual Searching Task (CVST) was used to measure mental slowing. A 3.0T MRI scanner (Philips, Achieva) was used to perform resting state fMRI (EPI sequence, 195 volumes, 32 slices, voxel size: 2x2x4 mm, TR/TE: 2000/35 ms, flip angle: 90°) and a T1-weighted scan (resolution: 1x1x1 mm, TR/TE: 8/4 ms, 180 slices, flip angle: 8°).

The preprocessing[3] included FreeSurfer for anatomical parcellation of the T1 scan into 82 cortical and subcortical brain areas. The functional images were corrected for differences in slice timing and motion, coregistered to the T1 image, spatially filtered (FWHM 6 mm), temporally filtered (band pass 0.01 – 0.1 Hz) and corrected for variations in the white matter and CSF signal by linear de-regression. Subsequently, an association matrix was created by calculating the Pearson's correlation coefficient between the average time signal of each combination of two regions. Correlations lower than 0.01 were set to zero.

Linear regression analysis was employed to test if the graph measures normalized characteristic path length and clustering coefficient, were associated with AED use and cognitive functioning with the covariates risk group, CVST score and age.

Results: High risk patients had a slower response on the CVST than low risk patients, although this difference was not significant (15.3±5.3s versus 13.5±5.5s, mean±sd). Significant associations were found between clustering coefficient and risk group: high risk patients had a lower clustering coefficient than low risk patients ($\beta<-0.217$, $p<0.01$ at all sparsity levels, Figure 1). Significant associations were also found between clustering coefficient and age ($\beta>0.008$, $p<0.03$ at all sparsity levels). At a sparsity level of 0.9, a significant association was found between clustering coefficient and CVST score ($\beta=-0.04$, $p=0.04$) and between characteristic path length and CVST score ($\beta=0.009$, $p=0.001$, Figure 2). No consistent significant associations were found between path length and any of the covariates at other sparsity levels.

Conclusion: Epilepsy patients using AEDs associated with a high risk on cognitive adverse events showed a lower local efficiency compared to patients using low risk AEDs. Furthermore, an association between decreased efficiency and mental slowing was shown in these patients. These results support our hypothesis that cognitive problems due to AEDs are associated with a less efficient brain network.

References: [1] P Kwan, MJ Brodie, The Lancet 357.9251: 216-222 (2001), [2] MCG Vlooswijk et al, Neurology 77:938-944 (2011), [3] E Bullmore, O Sporns, Nat. Rev. Neurosci. 10 (2009)

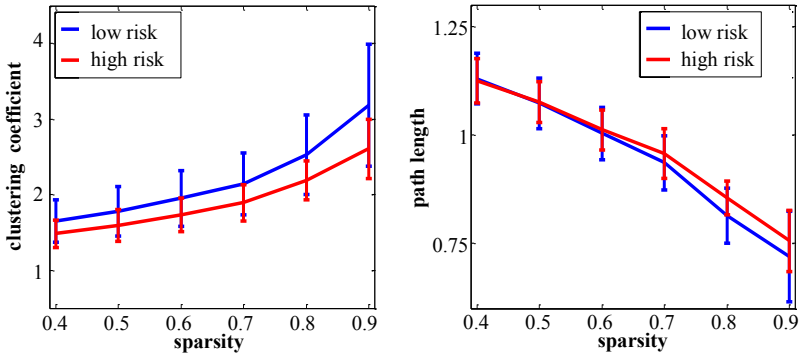

Figure 1. Clustering coefficient (left) and path length (right) at different sparsity levels for the low and high risk group (mean ± standard deviation, uncorrected for other variables).

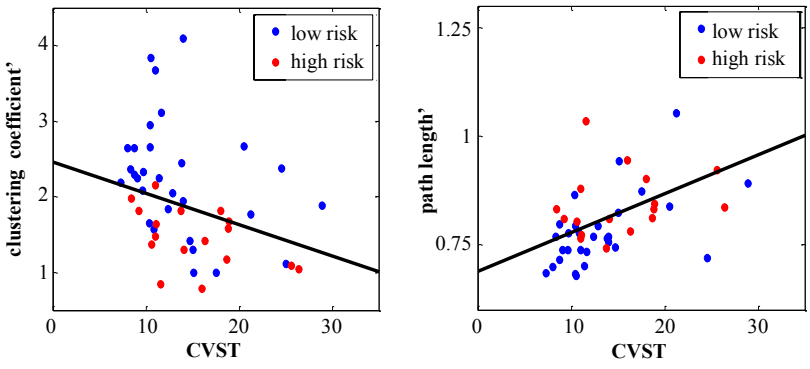

Figure 2. Clustering coefficient (left) and path length (right) versus CVST score. Both clustering coefficient and path length are corrected for age and at a sparsity level of 0.9.

Theoretical study of the free water elimination model

Quinten Collier[1], Jelle Veraart[1,2], Ben Jeurissen[1], Arnold J. den Dekker[1,3], Jan Sijbers[1]

[1]iMinds-Vision Lab, University of Antwerp, Antwerp, Belgium
[2]Center for Biomedical Imaging, New York University Langone Medical Center, New York, United States
[3]University of Technology, Delft, the Netherlands

Target audience: Researchers using diffusion MRI

Purpose: In diffusion MRI, multiple brain structures exist with sizes of the same order of magnitude as the voxel size, which typically range from 2 mm to 3 mm. This makes that partial volume (PV) effects are an important issue in diffusion MRI. This is especially true for brain structures close to cerebrospinal fluid (CSF) regions because the diffusivity of water in CSF can easily be up to 3 times larger than the water diffusivity in white matter brain tissue. This often leads to large biases in the estimation of the diffusion parameters. One way to account for CSF effects is to incorporate a free water component in the diffusion model. The 'Free Water Elimination' (FWE) model proposed by Pasternak et al. [1] is one of the most widely applied models. Despite being used in multiple studies, a thorough theoretical analysis of the FWE model is yet to be performed. In this work, we address this issue by studying the Cramér-Rao lower bound (CRLB) and using it to determine the optimal experimental design and justify the need for regularization.

Methods: The FWE model describes the diffusion weighted (DW) signal S_i with a bi-exponential function consisting of a tissue compartment and a 'free water' compartment linked by a relative volume fraction f [1,2]: $S_i = S_0\left[(1-f)e^{-b\boldsymbol{g}^T\boldsymbol{D}\boldsymbol{g}} + fe^{-bd}\right]$, with S_0 the signal without diffusion weighting, $\boldsymbol{g}$ the diffusion weighting unit gradient, $\boldsymbol{D}$ the diffusion tensor as known from the DTI model, and $d = 3 \times 10^{-3}\ mm^2/s$ the diffusivity of free water at body temperature. Studying the CRLB of the FWE model provides insights in the highest attainable precision with which the FWE model parameters can be estimated unbiasedly. Additionally, the optimal diffusion weighting gradient directions and strengths in terms of maximal precision of an unbiased estimator of the parameters of interest can be determined by minimizing the trace of the CRLB in function of the experimental design [3]. The CRLB is calculated by taking the inverse of the so-called Fisher Information Matrix (FIM) $I(\boldsymbol{\theta})$ [4]: $I(\boldsymbol{\theta}) = -E\left[\frac{\partial^2}{\partial\boldsymbol{\theta}^2}\log p(X;\boldsymbol{\theta})\middle|\boldsymbol{\theta}\right]$, with $p(X;\boldsymbol{\theta})$ the Rician probability density function of the observations X given the model parameters $\boldsymbol{\theta} = [S_0, D_{xx}, D_{xy}, D_{xz}, D_{yy}, D_{yz}, D_{zz}, f]$. The CRLB was minimized for a diffusion tensor with mean diffusivity of 1,2 × 10^{-3} mm^2/s and variable FA and CSF fractions. Initialization was done using the multi-shell optimized FWE acquisition scheme proposed by Pasternak et al. [5], having the following number of directions per respective b-value shell [s/mm^2]: 1 × b=0, 3 × b=50, 6 × b=200, 10 × b=500, 30 × b=900 and 16 × b=1400. The optimized gradient set was restricted to the same maximum b-value and number of measurements. Monte Carlo simulations were performed for all combinations of FA and CSF fraction. Rician noise was imposed with a signal-to-noise ratio of 20 on the non-diffusion weighted images and 1000 noise realizations per voxel. An FWE fit was also performed on a real data set of a healthy volunteer. The acquisition scheme was: 6 × b=0, 25 × b=600 and 45 × b=1200.

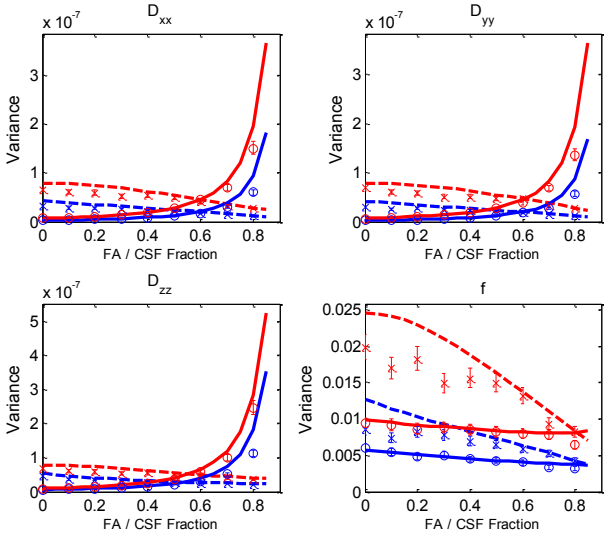

Figure 1: The CRLB in function of the CSF fraction (full line, FA fixed on 0.8) and FA (dashed line, f fixed on 0.5) with their respective simulation results (CSF: o; FA: x) of the three diagonal DT elements (D_{xx}, D_{yy}, D_{zz}) and the estimated CSF fraction (f). The initial and optimized acquisition schemes are shown in red and blue, respectively. Errorbars indicate the 95% confidence interval.

Mask	S_0	D_{xx}	D_{xy}	D_{xz}	D_{yy}	D_{yz}	D_{zz}	f
Low FA (%)	0.00	5.81	2.54	1.80	6.32	2.59	5.81	1.52
High FA (%)	0.00	0.23	1.24	0.40	0.17	0.23	0.06	0.11

Table 1: Percentage of voxels in a mask from a real data set where the estimation of a model parameter exceeds a predetermined threshold.

Results and discussion: Minimization of the trace of the CRLB matrix resulted in an acquisition protocol with 4 distinct b-value shells (s/mm^2): 3 × b=0, 15 × b=422, 10 × b=592, 38 × b=1400. This result appears independent of the initial acquisition scheme. When looking at the diagonal CRLB elements and corresponding simulation results in figure 1, it is clear that a significant gain in terms of attainable precision can be obtained with the optimized acquisition scheme. However, we see that in voxels with a high CSF fraction, the variance of the distribution of the estimated diffusion parameters becomes increasingly larger. Similarly, the precision of the estimation of f will decrease significantly for voxels with tissues with low FA. Due to the absence of a ground truth in the real data set, we tried to quantify the need for regularization by counting the number of times an estimated parameter exceeds a certain threshold, beyond which it could be considered incorrect and regularization is thus needed. This threshold was defined as the median of each parameter over all voxels ± 10 times the median absolute deviation of the parameter distributions. Two masks of the data set were studied separately based on their FA (from a DTI estimation): 1) low FA mask: 0.05 < FA < 0.2, and 2) 'high' FA mask 0.3 < FA < 0.9. The low FA mask will also encompass voxels with high CSF fractions since these voxels typically have very low FA values. The results are presented in table 1. We note that in the low FA mask, considerably more voxels exhibit erroneous parameter estimates when compared to the high FA mask. These findings confirm our theoretical and simulation results.

Conclusion: From the results we can conclude that using the optimized acquisition protocol enables the user to achieve a significantly higher precision when estimating the diffusion parameters. Furthermore, in voxels containing a large CSF fraction or a low FA value, the FWE model becomes ill-conditioned and additional regularization and/or constraints become necessary. These theoretical findings are confirmed by both simulation and real data experiments.

References:**[1]** Pasternak et al.,MRM 62, 717-30, 2009; **[2]** Pierpaoli et al., Proc. ISMRM, 2004:1215; **[3]** Poot et al., TMI 29, 819-29, 2010; **[4]** van den Bos, Wiley, 51-53, 2007; **[5]** Pasternak et al.,MICCAI 15, 305-12, 2012

Robust diffusion-prepared neurography of the complete brachial plexus facilitated by an optimized shimming strategy

Jos Oudeman[1], Bram Coolen[1], Camiel Verhamme[2], Mario Maas[1], Andrew Webb[3], Gustav Strijkers[4], Aart Nederveen[1]

[1]Department of Radiology, Academic Medical Center, Amsterdam, the Netherlands
[2]Department of Neurology, Academic Medical Center, Amsterdam, the Netherlands
[3]Department of Radiology, Leiden University Medical Centre, Leiden, the Netherlands
[4]Department of Medical Engineering and Physics, Academic Medical Center, Amsterdam, the Netherlands

Introduction: Diagnosis of treatable immune-mediated diseases affecting peripheral nerves such as multifocal motor neuropathy (MMN) commonly relies on the specific abnormalities on nerve conduction studies such as a conduction block. However, conduction studies cannot properly assess the roots and the most proximal parts of the plexus brachialis, so that the diagnosis may be missed. New imaging methods for qualitative and quantitative imaging of the brachial plexus may be useful for diagnosing and monitoring patients with immune-mediated neuropathies [1,2]. In this study, we utilized the 3D diffusion prepared iMSDE sequence suggested by Yoneyama et al. [3] and optimized it to include the full brachial plexus and shoulders. Although the sequence gives excellent contrast of the nerves, image quality is often compromised by poor fat-suppression and a poor signal to noise ratio (SNR). The origin of these artifacts may be found in poor homogeneity of the magnetic field (B_0) and inhomogeneous distribution of the RF-signal (B_1). Both B_0 and B_1 can be improved by respective shimming methods. However when multiple tissue-air transitions are present -as is the case in the neck- shimming can become unreliable. The **aim** of this work was therefore to develop the optimal (combination of) methods to overcome problems with fat suppression and low SNR of brachial plexus imaging. To improve the B_0 and B_1 homogeneity we used a neck-pillow filled with pineapple juice (Pillow) for susceptibility matching. The pillow provides a large susceptibility-matched volume which facilitates improved shimming [4,5], but at the same time has low signal on T2-weighted imaging due to the paramagnetic effect of manganese in the pineapple juice [6]. Next we compared image based (IB) shimming to volume shimming. IB-shimming uses a 2nd order shim based on an automatic segmentation which follows the contours of the anatomy [7].

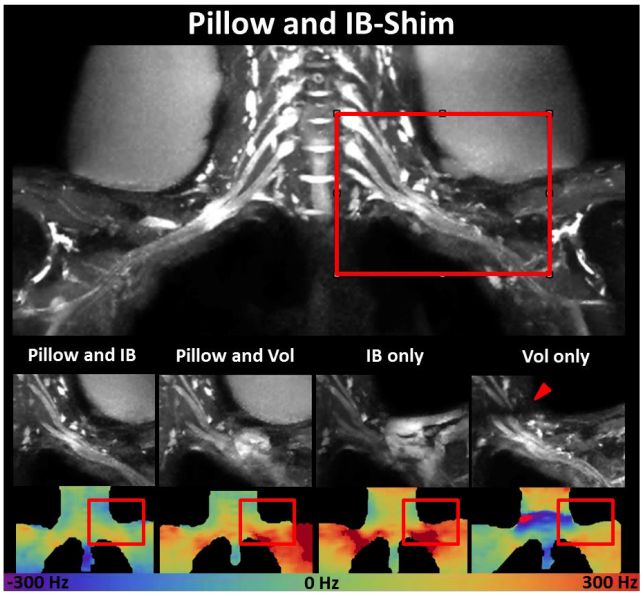

Figure 1: Maximum intensity projection (MIP) of the whole neck area using Pillow and IB-shimming (top). Magnifications of the infraclavicular space for different set-ups (middle row), corresponding B_0 maps in Hz in a mid-coronal plane (lower row). Strong inhomogeneities in B_0 resulted in poor fat-suppression or low SNR in the anatomical images (red arrow).

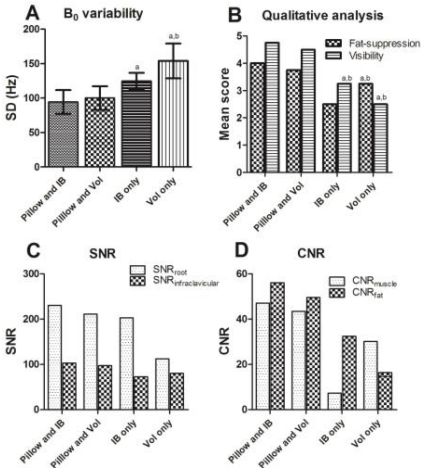

Figure 2: (A) Variability of the B_0 field in Hz; (B) mean score on fat-suppression and visibility; (C) SNR of the nerve at the root and in the infraclavicular space; D) CNR of the nerves (a = significant difference to Pillow and IB, b = significant difference to Pillow and Vol ($p < 0.05$)).

Methods: 4 healthy volunteers (3 male, 1 female, age 25-30) were positioned supine with the pillow placed anteriorly. Scanning was performed in the following order: pillow with IB-shim (Pillow and IB), pillow with volume shim (Pillow and IB), IB-shim only (IB only) and volume shim (Vol only). The study was performed on a 3 Tesla Philips Ingenia MRI-scanner (Best, The Netherlands). iMSDE: coronal TSE acquisition with RARE readout; FOV: 300x450 mm2; TEeff/TR 61/2500 ms; TSE factor: 100; echo spacing: 4.0 ms; voxel size: 1.1×1.1×1.1 mm3; fat suppression: SPAIR; duration of 7 min 13 s; SENSE 3.5 in right-left (RL) direction and 1.5 in the anterior-posterior (AP) direction. For B_0 and B_1 measurements the FOV; shim settings and SENSE factor were kept identical. B_1: 3D FFE; TR/TE; 20/2.2 ms; voxel size 4x4x4 mm3 and a duration of 2 min 27 s [8]. B_0: 3D FFE; TR/TE_1/TE_2; 3.6/1.23/2.3 ms; voxel size 2x2x2 mm3; flipangle of 10˚ and a duration of 15 s. We masked the nerves and its surroundings and calculated the variability of the B_0 and B_1. Scoring was performed for nerve visibility over the whole image (1=not visible, 2=visible but not suitable for analysis, 3=visible and suitable for analysis, 4=good visibility and 5=excellent visibility) and fat-suppression (1=poor and in area of interest, 2=poor, however not in area of interest but hindering analysis, 3=incomplete but not hindering analysis, 4=some incomplete fat-suppression but overall good, and 5=excellent). SNR was calculated for the nerves of the brachial plexus at the roots and at the infraclavicular space. For contrast to noise (CNR) evaluation we concentrated on the infraclavicular spaces in which image quality was most hindered by poor fat-suppression and low SNR. We compared the signal of the nerve with the surrounding fat (CNR_{fat}) in the infraclavicular space, but also with the deltoid muscle (CNR_{muscle}).

Results & discussion: The pillow significantly ($p < 0.05$) improved the B_0-homogeneity over the area around the nerves (Figure 2) and resolved the strong feet to head gradient (Figure 1). B_1-maps did not reveal significant differences for the different set-ups. The B_0-inhomogeneity produced drops in SNR and poor fat-suppression (red triangle in Figure 1). With the pillow, both IB and Vol shim provided good to excellent visibility of the nerves over the whole image from the myelum to the shoulders in all subjects. For all of the measured outcomes, there were no significant differences between 'Pillow and IB' and 'Pillow and Vol'. Nevertheless, 'pillow and IB' scored higher on all measures and therefore we consider this the best option.

Conclusion: The use of the pillow filled with pineapple juice in combination with IB-shimming resulted in the best overall visibility of the brachial plexus with minor to no artifacts. Furthermore, the application of the pillow, may find application for other sequences (e.g. diffusion tensor imaging) and for other anatomical areas where B_0-homogeneity is required.

References: [1] Chhabra et al. Am J Neuroradiol 34 (2013) 486-497; [2] Van Schaik et al. J Peripher Nerv Syst. 15 (2010) 295-301; [3] Yoneyama et al. Magn Reson Med Sci 12 (2013) 111-114; [4] Cox et al. Am J Neuroradiol 16 (1995) 1367–1369; [5] Maeharaet al. Magn Reson Imaging 32 (2014) 440–445; [6] Riordan et al. Br J Radiol 77 (2004) 991–999; [7] Schär et al. Magn Reson Med 51(2004) 799; [8] Yarnykh et al. Magn Reson Med 57 (2007) 192-200.

Two methods to study the small-worldness measures of human brain structural network

Shouliang Qi[1,2,3], Stephan Meesters[2,4], Klaas Nicolay[3], Bart M. ter Haar Romeny[1,3], Pauly Ossenblok[1,2,3]

[1]Sino-Dutch Biomedical and Information School, Northeastern University, Shenyang, China; [2]Academic Center for Epileptology, Kempenhaeghe Epilepsy Center & Maastricht University Medical Center, Heeze & Maastricht, the Netherlands; [3]Department of Biomedical Engineering, Eindhoven University of Technology, Eindhoven, the Netherlands; [4]Department of Mathematics and Computer Science, Eindhoven University of Technology, Eindhoven, the Netherlands

Purpose: The human brain is a complex structural network that can be represented by nodes and edges. The nodes represent different gray matter regions generated by brain parcellation using the anatomical MR images. The edges connecting pairs of nodes represent the connectivity strength, as assessed by the reconstruction of the white matter fibers using diffusion weighted imaging (DWI). Once the structural network is constructed in the form of an adjacency matrix, graph theoretical network measures can be calculated and analyzed. To study the small-worldness measures of the human brain structural network, we investigated two different methods for whole brain tractography: diffusion tensor imaging (DTI)[1] and constrained spherical deconvolution (CSD)[2]. Furthermore, the influences of the seed region, number of streamlines, tracking algorithm (deterministic and probabilistic) and termination criteria on the network measures are assessed.

Methods: MRI data were acquired using a 3.0T MR scanner. The T1-weighted structural images were obtained using a Turbo Field Echo (TFE) sequence. The DWI acquisition was performed using the Single-Shot Spin-Echo Echo-Planar Imaging (SE-EPI) sequence in 32 directions with a b-value of 1000 s/mm^2. After applying EPI distortion correction, motion correction and b-matrix rotation to the DWI data, the local fiber orientation can be computed by fitting a tensor or by computing a fiber orientation distribution (FOD), for DTI and CSD respectively. Next, the MRTrix tracking algorithm[2] is applied for whole brain tractography. The nodes are generated from the AAL atlas[3] which are transformed to the subject-specific space using the structural MR images and the MNI-152 template. The adjacency matrix can be calculated by counting the number of streamlines connectingthe pairs of nodes. Finally, the network measures are calculated by Brain Connectivity Toolbox[4], and compared with known sparsity ($1.0 - \mathrm{Edge}_{\mathrm{Available}}/\mathrm{Edge}_{\mathrm{Potenstial}}$).

Results: A binary undirected network was obtained as visualized in Fig.1 where the node size is proportional to the degree. The resulting brain structural network shows small-worldness attribute (i.e., σ>1.0), as shown in Table 1. It can be seen that CSD generates the network with larger σ than DTI for a similar sparsity s. For both DTI-derived and CSD-derived networks, using the whole brain as the seed region yields a higher σ than using the white matter mask thresholded by fractional anisotropy (FA)>0.7. While increasing the termination criteria of FA or FOD amplitude cutoff from 0.1 to 0.2, σ rises for DTI-derived network, but drops for CSD-derived one. While decreasing the number of streamlines from 100,000 to 10,000, σ drops for DTI-derived network, but increases for CSD-derived one. For CSD-derived network, probabilistic tracking algorithm leads to higher σ than deterministic one. In all the situations, the normalized characteristic path length λ changes onlys lightly. The variation of σ mainly results from the normalized clustering coefficient γ.

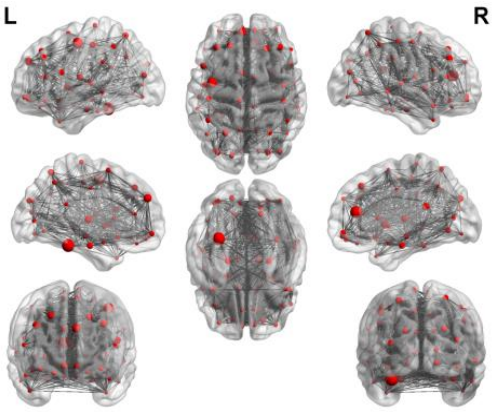

Fig. 1 Obtained brain structural network where the node size indicates the node degree

Table 1. Small-worldness measures of human brain structural network drivenby two methods

Methods		Parameter	Specific value	λ	γ	σ	s
1	DTI	Seed point mask (100,000 streamlines, FA cutoff=0.1)	FA>0.7 (white matter)	1.07	1.48	1.38	0.90
			Whole brain	1.10	2.11	1.92	0.81
		Number of streamlines (FA>0.7, FA cutoff=0.1)	10,000	1.05	1.27	1.21	0.95
		Termination criteria (100,000 streamlines, FA>0.7)	FA cutoff = 0.2	1.07	1.77	1.66	0.92
2	CSD	Tracking algorithm (FA>0.7, 100,000 streamlines, FOD cutoff=0.1)	Probabilistic	1.00	1.00	1.00	0.43
			Probabilistic	1.09	1.57	1.44	0.89
			Deterministic	1.04	1.39	1.33	0.89
		Seed point mask (probabilistic, 100,000 streamlines, FOD cutoff=0.1)	Whole brain	1.15	2.95	2.57	0.91
		Number of streamlines (probabilistic, FA>0.7, FODcutoff=0.1)	10,000	1.14	2.95	2.58	0.91
		Termination criteria (probabilistic, FA>0.7, 100,000 streamlines)	FOD cutoff = 0.2	1.12	1.37	1.23	0.91

λ - normalized characteristic path length, γ - normalized clustering coefficient, σ -small-worldness index (γ/λ), s - sparsity ($1.0 - \mathrm{Edge}_{\mathrm{Available}}/\mathrm{Edge}_{\mathrm{Potenstial}}$), FA - fractional anisotropy, FOD- fiber orientation distribution

Discussions: DTI is the most common approach to estimate the local fiber orientation, but it has the downside of being unable to handle regions of crossing fibers, while crossing fibers have been observed in about 90% of the brain white matter voxels[2]. Alternative to resolve fiber crossing is CSD or Q-ball reconstructions based on high-angular resolution diffusion imaging (HARDI). It is reported that DTI results in higher small-worldness than Q-ball based on HARDI, but the sparsity is not clearly given.

Conclusions: The CSD method generates the human brain structural network with a higher small-worldness than DTI for a similar sparsity. It results from higher γ and steady λ. For both methods, the seed point mask, number of streamlines, and termination criteria also affect the small-worldness measures, but the trends are not the same. Comparison of small-worldness measures across studies must clarify the trajactography method and related parameters.

References:

1. Mori S, Crain BJ, Chacko VP, et al. Three-dimensional tracking of axonal projections in the brain by magnetic resonance imaging, Ann. Neurol. 1999;45, 265-269.
2. Tournier JD, Calamante F, Connelly A, MRtrix: diffusion tractography in crossing fiber regions, Int. J. Imaging Syst. Technol. 2012;22, 53-66.
3. Tzourio-Mazoyer N, Landeau B, Papathanassiou D, et al. Automated anatomical labeling of activations in SPM using a macroscopic anatomical parcellation of the MNI MRI single-subject brain. NeuroImage 2002;15 (1), 273-289.
4. Rubinov M, Sporns O, Complex network measures of brain connectivity: Uses and interpretations, NeuroImage 2010;52:1059-69.

Age-related microstructural changes quantified using myelin water imaging and advanced diffusion MRI

Thibo Billiet[1], Mathieu Vandenbulcke[2], Burkhard Mädler[3], Ronald Peeters[4], Thijs Dhollander[5], Hui Zhang[6], Sabine Deprez[1], Bea RH Van den Bergh[7], Stefan Sunaert[1], Louise Emsell[1]

[1]Translational MRI, Imaging & Pathology, KU Leuven, Belgium; [2]Old Age Psychiatry, KU Leuven, Belgium; [3]Department of Neurosurgery, University of Bonn, Bonn, Germany; [4]Department of Radiology, University Hospitals Leuven, Leuven, Belgium; [5]Florey Institute of Neuroscience and Mental Health, Melbourne, Australia; [6]Computer Science & Centre for Medical Image Computing, University College, London, United Kingdom; [7]Department of Psychology, Tilburg University, Tilburg, the Netherlands

Target Audience: Basic scientists and clinicians with an interest in diffusion MRI, neuroscience, neuroimaging and oncology.

Purpose: Age-related microstructural changes have been detected using diffusion tensor imaging (DTI)[1]. Whilst DTI is sensitive to the effects of aging, it is not specific to any underlying biological mechanism, including demyelination. Combining multi-exponential T2 relaxation (MET2) and multi-shell diffusion magnetic resonance imaging (dMRI) techniques may elucidate such processes. This study therefore aimed to characterise how advanced dMRI and MET2 parameters evolve during adulthood.

Methods: Multi-shell dMRI (b700 x 25d, b1000 x 45d, b2800 x 75d) and MET2 data were acquired on 59 healthy adults aged 17-70 years (3T Philips). Whole brain and regional age-associated correlations of multiple dMRI measures (DTI, diffusion kurtosis imaging[2] (DKI), neurite orientation dispersion and density imaging[3] (NODDI)) and myelin sensitive MET2[4] metrics were assessed using both region-of-interest (JHU atlas labels) and voxel-based analysis (custom-made white matter template and lateral ventricle exclusion mask).

Results: DTI and NODDI revealed widespread increases in measures of isotropic diffusivity with increasing age, with the most significant changes located at the cortical white matter boundary and in the fornix. In frontal white matter, fractional anisotropy (FA) linearly decreased with age, paralleled by increased 'neurite' dispersion (Orientation Dispersion Index). Myelin water fraction (MWF) remained stable, with minimal increases in deep WM. DKI measures related more to MET2 metrics than to DTI measures.

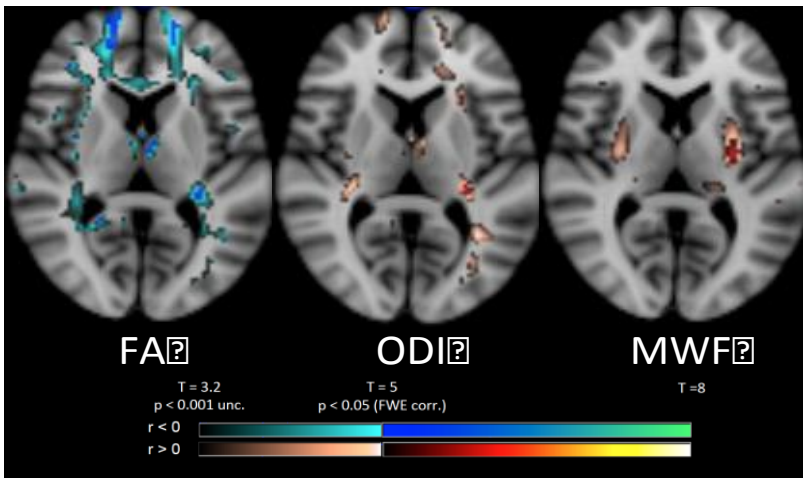

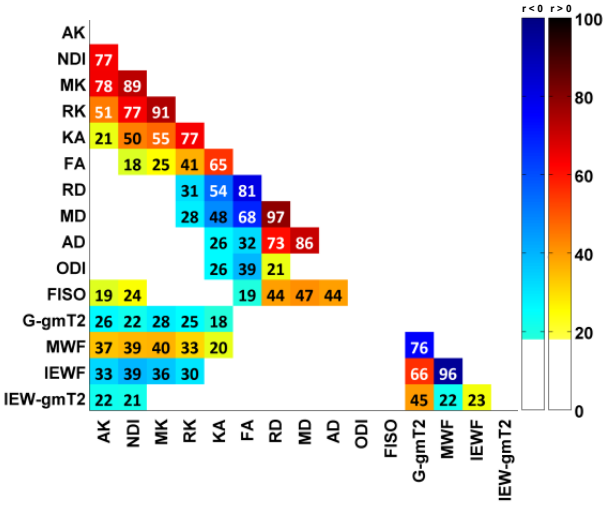

Fig. 1 (left) Significant voxel-wise correlations with age on axial T1 slice. Results for clusters surviving FWE correction thresholds at p=0.001(unc) and pFWE=0.05 are shown. The decrease in frontal FA was not paralleled by a change in MWF but by an increase in ODI, reflecting axonal dispersion. (Right) Percentage shared variance between all parameters. DKI metrics correlated most strongly with MET2 metrics. Red scale = positive, blue = negative correlation.

Conclusion: DTI estimates remain among the most sensitive markers for age-related alterations in white matter. NODDI, DKI and MET2 indicate that the initial decrease in frontal FA in late adulthood (50-60 years) may be due to increased axonal dispersion rather than demyelination. These findiings confirm the added value of combining multiparametric microstructural imaging measures to assess human aging *in vivo*.

References:[1] Sullivan, E.V. and A. Pfefferbaum, Neuroscience and Biobehavioral Reviews, 2006. **30**(6): p. 749-61. [2] Jensen, J.H. and J.A. Helpern, NMR in biomedicine, 2010. **23**(7): p. 698-710. [3] Zhang, H., et al., Neuroimage, 2012. **61**(4): p. 1000-16. [4] MacKay, A., et al., Magnetic resonance imaging, 2006. **24**(4): p. 515-25.

Potential gain of a 256 channel head coil at 7T: combined measurements and g-factor calculations

Arjan Hendriks[1], Michel Italiaander[2], Natalia Petridou[1], Dennis Klomp[1,2]

[1]Department of Radiology, University Medical Center, Utrecht, the Netherlands
[2]MR Coils BV, Drunen, the Netherlands

Introduction

Recently it was demonstrated that UHF MRI combined with high density receiver arrays can facilitate laminar fMRI, bringing neuroimaging of the human brain to a completely new level [1]. A level at which we are closer to the small spatial scale in which the brain is organized. Using the high BOLD sensitivity at 7T combined with uncompromised image accelerations of the high density arrays, fMRI activations can be observed, at close to 0.5 mm isotropic resolution. This can be acquired within functionally relevant scan times (order of sec). However, as the optimal size of the receiver elements at 7T can be as small as 1x2cm (remaining in tissue load dominance; i.e. minimal electronic noise), a 32 channel setup, as commonly available, will provide a limited field of view of the brain. In fact, in order to cover the entire human brain with these receiver elements, close to 256 receivers (Fig. 1) would be required to obtain the full potential of ultra-high resolution fMRI of the human brain at 7T. In this study, while in progress of installing the receivers, we investigated the acceleration performance of a 256 channel high density head coil by measuring the sensitivity profiles (SENSE reference scans) and corresponding g-factor maps.

Figure 1: Concept of the 256 channel receiver coil. The blue squares indicate the size and position of the coil elements. The pre-amplifier boards (green) are stacked behind the head and are small enough to fit inside the transmit coil.

Method

Measurements were performed on a healthy volunteer in a 7 Tesla Achieva system (Philips, Cleveland, OH, USA). Eight different SENSE reference scans were made with 2x16 channel surface coils (MR Coils BV, Drunen, the Netherlands), using a volume headcoil as a transmitter (Nova Medical, MA, USA). The used MR sequence is a SENSE reference scan, with the following properties: 3D FFE acquired interleaved with receiver arrays and volume coil; TE/TR= 1.22/8.0 ms, 2x2x2 mm^3 voxel, 20x20x20 cm^3 FOV, acquisition time= 1 min.

For each SENSE reference scan, the surface coils were shifted to a different part of the head. In this way these 8 shifted reference scans constitute a virtual 256 channel coil. To correct for head displacement in between the reference scans, images acquired for each coil position were aligned to the images of the first position using AFNI. Alignment parameters (rotation & translation) were calculated, using the reconstructed magnitude images from the reference scan, and then applied on the calculated sensitivity matrices per coil position. For comparison, a SENSE reference scan was also made with the standard 32-channel Nova receive array. From the SENSE reference scans, the g-factor (corresponding to noise amplification) was calculated with the following equation from Pruessman et al. [2]:

$$g_\rho = \sqrt{[(S^H \Psi^{-1} S)^{-1}]_{\rho,\rho} \, (S^H \Psi^{-1} S)_{\rho,\rho}}$$

Where S defines the sensitivity matrix (N_{coils} x $N_{folding\_locations}$) and ψ is the N_{coils} x N_{coils} receiver noise matrix. The g-factor was calculated for the same slice of the brain with different acceleration factors.

Results

The g-factor comparison of the standard 32 channel head coil and the virtual 256 channel is in Fig. 2 displayed. The 32 channel head coil shows acceptable g-factors at an acceleration factor of less than 9 (3x3 APxFH). For the virtual 256 channel head coil similar g-factors are obtained at a SENSE factor of 24 (6x4 APxFH).

Discussion

More than a factor 2 in acceleration performance is expected, when comparing a 256 channel headcoil with a 32 channel headcoil at 7T. Note that the data to obtain the g factor maps is obtained sequentially in time, preventing the inclusion of the full noise correlation matrix. However, it is expected that the dominant noise coupling was already included since at each scan the 32 elements were situated as two dense arrays.

Conclusion

The results show very good g-factor performance for the virtual 256-channel coil, up to an acceleration factor of 6x4. This implies a gain in SNR or acceleration factor. Also, the results suggest that the benefits achieved in spatial/temporal fMRI resolution by using the high-density 32-channel configuration, can be extended to 256-channels with full head coverage.

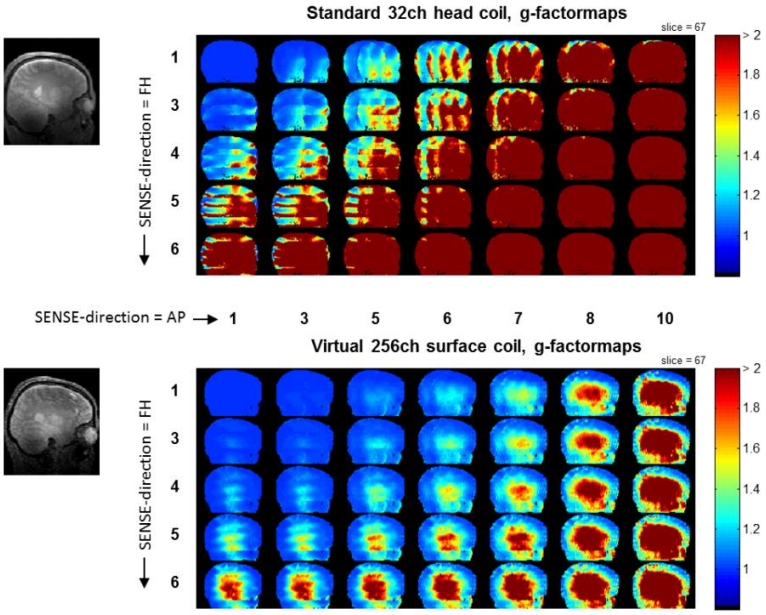

Figure 2: g-factormaps for different SENSE acceleration factors. Shown is the standard 32 channel head coil (up) and the virtual 256 channel surface coil (bottom). The 32 channel head coil shows acceptable g-factors at an acceleration factor of 3x3 (APxFH). The virtual 256 channel surface coil shows similar g-factors at an acceleration factor of 6x4 (APxFH).

References: [1] N. Petridou et al. NMR Biomed. 2013; 26: 65–73, *Pushing the limits of high-resolution functional MRI using a simple high-density multi-element coil design.*
[2] K.P. Pruessman et al. Magn Reson Med 1999; 42:952–962, *SENSE: Sensitivity Encoding for Fast MRI*.

Acknowledgment: The Netherlands Organization for Scientific Research (NWO), grant number: ALW-834.14.004

Investigating possible recovery of chemotherapy-induced structural changes in cerebral white matter and its relation with cognitive functioning in breast cancer patients

Sabine Deprez[1], Thibo Billiet[1], Frederic Amant[2], Ann Smeets[2], Ronald Peeters[1], Marie-Rose Christiaens[2], Mathieu Vandenbulcke[3], Stefan Sunaert[1]

[1]Translational MRI, Imaging & Pathology, KU Leuven, Belgium
[2]Oncology KU Leuven & Multidisciplinary Breast Center, University Hospital Gasthuisberg, Leuven, Belgium
[3]Department of Psychiatry, KU Leuven & University Hospitals Leuven, Belgium

Target Audience

Researchers and Clinician interested in the longitudinal effects of chemotherapy on cerebral white matter and cognitive functioning.

Purpose

In a previous *longitudinal* diffusion tensor imaging (DTI) study, we reported changes in cerebral white matter (WM) 3-4 months after chemotherapy-treatment[1]. Those changes were correlated with decreased cognitive functioning. The current study used DTI to investigate if the previously observed microstructural changes are still present 3 years after ending chemotherapy.

Patients and Methods

Subjects: Thirty-four women with early-stage breast cancer exposed to chemotherapy (C+) underwent neuropsychological testing and DTI before the start of chemotherapy (t1), 4 months (t2) and 3 years (t3) after treatment. Whole brain DTI SE-EPI images with 45 non-collinear directions and a b-value of 800 s/mm2, were acquired on a 3T scanner. Sixteen patients not exposed to chemotherapy (C-), and 19 age-matched healthy controls (HC) underwent the same assessment at matched intervals. ***Analysis:*** DTI pre-processing was performed using *ExploreDTI* consisting of motion and distortion correction with reorientation of the b-matrix and an iterative nonlinear tensor estimation process. The individual DTI datasets were non-rigidly registered to a population-based atlas. SPM8 whole-brain voxel-based-repeated-measures ANOVA was used to study changes in WM fractional anisotropy (FA) within the C+ group. Additionally, FA values were extracted in 4 regions previously associated with chemotherapy-related changes from t1 to t2 (CT-ROI)[1] (Fig.1). Neuropsychological tests previously showing decreased performance after chemotherapy[1] were selected for further analysis using a linear-mixed-effects-modeling approach.

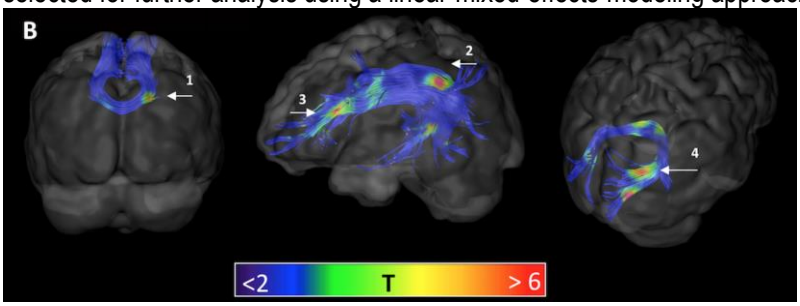

Fig 1. Regions showing significant decrease in FA in chemotherapy-treated patients at t2 vs t1. These 4 ROI are selected for region-based analysis at t3

Results

In the C+ group, whole-brain-voxel-based-analysis showed decreased FA ($p<0.05$) in frontal, parietal and occipital WM tracts from t1 to t2, while no differences were found with t3. Region-based analysis in the CT-ROI, showed significantly decreased FA from t1 to t2 followed by significant increase to t3 ($p<0.05$)(Fig 2). Interestingly, significant group x time interactions were found for psychomotor speed and memory tests reflecting a decreased performance from t1 to t2 and increased performance from t2 to t3 for the C+ group ($p<0.05$).

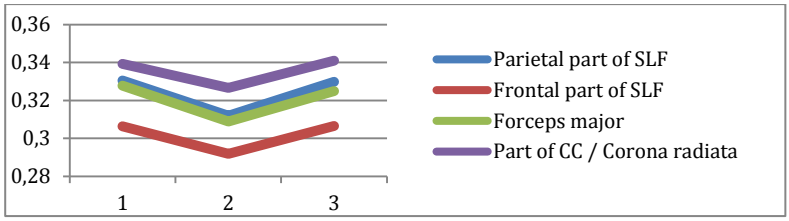

Fig.2. Adjusted mean FA values at the 3 timepoints in regions previously associated with chemotherapy-related changes

Conclusion

No remaining differences in FA could be detected 3 years after chemotherapy. This could indicate possible recovery of chemotherapy-induced microstructural changes in cerebral WM [1].

References

1. Deprez S, Amant F, Smeets A, et al: Longitudinal assessment of chemotherapy-induced structural changes in cerebral white matter and its correlation with impaired cognitive functioning. Journal of clinical oncology : official journal of the American Society of Clinical Oncology 30:274-81, 2012

Thyroid cancer imaging: peptidic targeting of galectin-1 as a diagnostic tool

Deborah Fanfone[1], Nadège Despretz[1], Sophie Laurent[1], Vanessa Arcolia[2], Robert N. Muller[3], Luce Vander Elst[1], Sven Saussez[3], Carmen Burtea[1]

[1]Department of General, Organic and Biomedical Chemistry, Laboratory of NMR and Molecular Imaging, UMONS, Mons, Belgium
[2]Department of Anatomy and Cell Biology, Mons, Belgium
[3]Center for Microscopy and Molecular Imaging, Charleroi, Belgique

The worldwide incidence of the thyroid cancer, the most common endocrine malignancy, is still increasing nowadays. The main challenge is to diagnose the patients who really need a surgery. Indeed, despite the frequency of thyroid nodules, 90% of surgeries are made for benign lesions. Current diagnosis approaches imply painful and often useless thyroid surgeries. Thereby, this project aims to develop a new and non-invasive diagnosis approach of papillary carcinoma, which is the most frequent thyroid malignancy.

This work is based on the targeting of galectin-1 (gal-1) as a diagnostic tool for well-differentiated thyroid cancers. Gal-1 is a small adhesion protein expressed in muscles, neurons and some embryonic tissues in non-pathologic conditions. Mostly secreted in the extracellular compartment, this protein can also be found in the cytoplasm and the nucleus. It is involved in cellular adhesion, aggregation, migration, cytoskeleton reorganisation and cell cycle regulation phenomena. Moreover, gal-1 is overexpressed in a large variety of cancers (head and neck, skin, lungs, bladder, prostate, ovaries, colorectal region) and also in thyroid cancers. In fact, gal-1 is implied in tumour-induced immunosuppression, angiogenesis, hypoxia and metastasis.

During this project, the phage display technique has been used to identify peptides targeting gal-1. Six successive rounds have been performed by exposing the immobilized target to a phage library. Each phage clone wears on its capsid a different random peptide sequence. The pre-selection has been carried out on a control protein and after washing and elution steps, the phages bound to gal-1 have been collected and amplified to start a new round. The affinity towards gal-1 of these 6 outputs has been evaluated by ELISA and showed an increase along the rounds. From the sixth output, 50 clones have been isolated and their affinity evaluated. Two clones over fifty showed a good specific affinity towards gal-1. The peptide sequence has been revealed after DNA extraction and the two peptides were synthesized.

The affinity of these two molecules has been evaluated by ELISA ($K_d^{gal\text{-}1} = 2{,}38 \times 10^{-6}$ and $4{,}1 \times 10^{-8}$ for Peptide 1 and Peptide 8 respectively) and their cellular localization has been demonstrated by immunohistochemistry on human well-differenciated thyroid cancer slices. Clone 8 and its respective peptide appeared to be the best, according to ELISA. However, Peptide 1 has shown a better specific affinity on histological sections. Moreover, peptide 1 has perfectly co-localized with gal-1 on biopsy sections of thyroid cancers as demonstrated by immunofluorescence. Interest will be henceforth focused on this peptide, which will be thereafter synthesized and conjugated to a contrast agent like USPIO in order to visualize tumours *in vivo* by MRI.

Peptide 1 seems to be a promising targeting agent against gal-1 for the thyroid cancer imaging, once used to functionalize a contrast agent for MRI.

Multiparametric MRI analysis for the evaluation of MR-guided High Intensity Focused Ultrasound treatment

Igor Jacobs[1], Stefanie Hectors[1], Edwin Heijman[2], Jochen Keupp[3], Monique Berben[2], Gustav Strijkers[1,4], Holger Gruell[1,2], Klaas Nicolay[1]

[1]Department of Biomedical NMR, Eindhoven University of Technology, Eindhoven, the Netherlands
[2]Oncology Solutions, Philips Research Europe, Eindhoven, the Netherlands
[3]Tomographic Imaging Systems, Philips Research Europe, Hamburg, Germany
[4]Department of Biomedical Engineering and Physics, Academic Medical Center, Amsterdam, the Netherlands

Introduction For the clinical application of High Intensity Focused Ultrasound (HIFU) treatment of malignant lesions, accurate treatment evaluation is of key importance. In a previous study, in which the HIFU treatment was performed outside the high-field preclinical MR scanner, we have shown that successfully HIFU-treated tumor tissue can be identified using a multiparametric MRI analysis based on T_1, T_2 and apparent diffusion coefficient (ADC) data [1]. In subsequent studies, we have demonstrated that amide proton transfer (APT) imaging [2] and $T_{1\rho}$ mapping [3] are additional MRI methods that are sensitive to HIFU-induced tissue changes. In the present study, we have employed a multiparametric MRI protocol combining all these promising MRI methods to evaluate HIFU treatment of rat tumors in a clinical 3T MR-HIFU system, which facilitated real-time temperature monitoring during treatment. Cluster analysis was performed on the multiparametric MRI data and the optimal set of MR parameters to identify successfully treated tumor was determined by quantitative comparison with histology.

Materials and Methods 9L glioma tumor-bearing (hind limb) Fischer 344 rats were subjected to MRI before (n=12), directly after (n=12) and 3 days after (n=6) HIFU treatment. In addition, a non-treated control group (n=6) was included. All animals were positioned in a rat MR-HIFU setup [4] placed on the tabletop of a clinical Philips 3T Sonalleve MR-HIFU system. Partial tumor ablation (4 mm diameter treatment cell) was performed with an acoustic power of 35 W and duration of 90 s. MR thermometry (PRFS method), from which thermal dose maps were calculated, was performed during treatment. The multiparametric MRI protocol consisted of quantitative T_1, T_2, ADC, APT, $T_{1\rho}$ and dynamic contrast-enhanced MRI (DCE-MRI) acquisitions. DCE-MRI was only performed after ablation. After the last MR experiments, tumors were marked, excised and sliced according to the orientation of the central MRI slice. NADH-diaphorase staining was performed to determine non-viable tumor fractions. K-means clustering with 4 clusters and all possible feature vectors (i.e. all different combinations of MR parameters) was performed on the MR parameter values in the tumor (excluding the DCE-MRI results because of absence of DCE-MRI data before treatment). Clusters in which the fraction of pixels significantly increased after MR-HIFU treatment were classified as non-viable. The optimal feature vector for identification of ablated tumor was determined by correlation analysis between clustering-derived and histology-derived non-viable tumor fractions. To compare the multiparametric MRI analysis results with conventional HIFU monitoring and evaluation methods, the histology-derived non-viable tumor fractions were also quantitatively compared with non-perfused tumor fractions (derived from the level of contrast enhancement in the DCE-MRI measurements) and 240 EM tumor fractions (*i.e.* thermal dose > 240 equivalent minutes at 43°C, which is generally considered as a lethal thermal dose [5]).

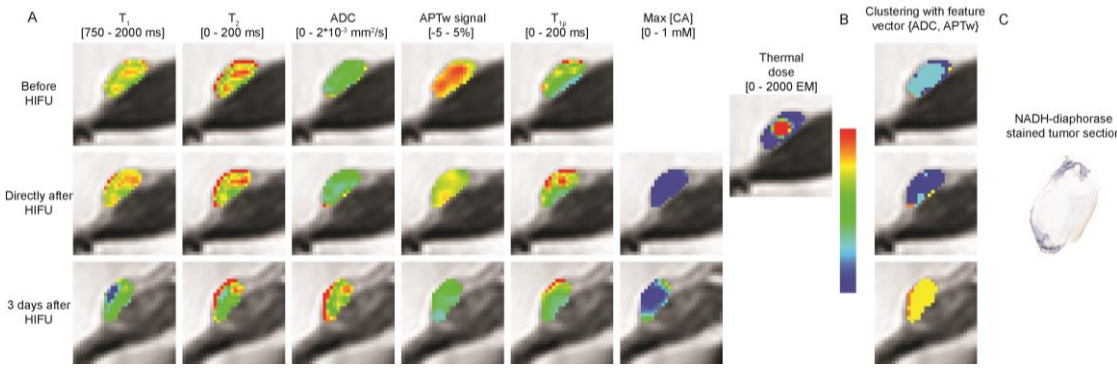

Fig 1 A) Representative MRI parameter maps in the tumor tissue overlaid on T_2-weighted images. The max [CA] maps represent the maximum tissue contrast agent concentration derived from the DCE-MRI data. B) Results of k-means clustering with feature vector {ADC, APTw signal}. The different colors represent different clusters. The yellow and orange clusters were classified as non-viable. C) NADH-diaphorase stained tumor section obtained at 3 days after HIFU at approximately the same location as the shown MRI slice, showing a large region of pale, non-viable tumor tissue.

Results Representative MR parameter maps are shown in Fig 1 A. Changes in the individual MR parameter values after HIFU treatment were rather subtle and heterogeneous between the different endogenous contrast parameters. The maximum contrast agent concentration maps derived from the DCE-MRI measurements showed that the tumor was largely non-perfused directly after treatment, while the perfusion was partly restored at 3 days after treatment. The thermal dose map showed a circular region in which a high thermal dose was reached. Clustering with feature vector {ADC, APTw signal} resulted in distinct regions of tumor tissue classified as non-viable (consisting of the combined yellow and orange clusters) after HIFU treatment. These regions corresponded to non-viable tissue in histology (Fig 1 B/C). For this feature vector, a strong one-to-one correspondence (R^2 to line of identity ($R^2_{y=x}$)=0.92 and strong correlation (r=0.92) was observed between the histology-derived and clustering-derived non-viable tumor fractions when combining all groups. In Fig 2 A, B and C correlation plots between histology-derived and clustering-derived non-viable tumor fractions are shown for this particular feature vector for the individual groups (animals sacrificed directly after HIFU, at 3 days after HIFU and non-treated control animals, respectively). The correlation and one-to-one correspondence was largest at 3 days after HIFU treatment ($R^2_{y=x}$=0.97, r=0.87, Fig 2 B). The correlation between histology-derived non-viable tumor fractions directly after HIFU and the 240 EM fractions was high, but not significant (Fig 2 D). The non-perfused fractions overestimated the extent of non-viable tumor tissue directly after HIFU treatment (Fig 2 E), while an underestimation was seen at 3 days after HIFU (Fig 2 F).

Fig 2 Correlation plots between: histology-derived non-viable fractions and clustering-derived non-viable fractions for feature vector {ADC, APTw signal} for animals sacrificed directly after HIFU treatment (A), animals sacrificed 3 days after HIFU treatment (B) and non-treated control animals (C); histology-derived non-viable fractions and 240 EM fractions for animals sacrificed directly after HIFU (D); histology-derived non-viable fractions and DCE-MRI-derived non-perfused fractions directly after HIFU (E); histology-derived non-viable fractions and DCE-MRI-derived non-perfused fractions at 3 days after HIFU (F).

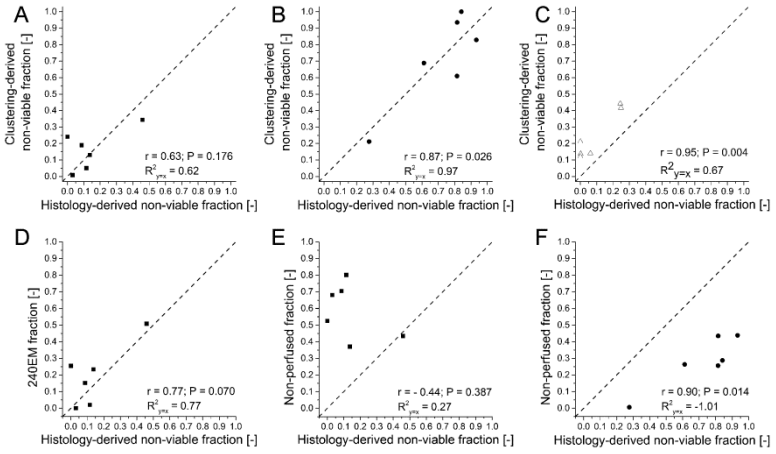

Discussion and conclusion We have shown that a multiparametric MR analysis, based on the ADC and the APT-weighted signal measured at 3 Tesla, can accurately determine the extent of non-viable tumor tissue after HIFU treatment. We expect that this method can be incorporated in the current clinical workflow of MR-HIFU ablation therapies.

Acknowledgement This research was supported by the Center for Translational Molecular Medicine (VOLTA).

References 1. Hectors et al. PloS One 2014;9(6):e99936, 2. Hectors et al. Magn Reson Med. 2014;72:1113-22, 3. Hectors et al. Magn Reson Med. 2014;doi:10.1002/mrm.25269, 4. Hijnen et al. Int J Hyperthermia 2012;28:2, 5. McDannold et al. Radiology 2000;216:517-523.

Qualification of a new method to measure lipid T_1 relaxation, a marker of tumor oxygenation

Thanh Trang Cao Pham[1], Chrystelle Po[1], Ly Binh An Tran[1], Nicolas Joudiou[1], Florence Colliez[1], Vincent Gregoire[2], Bernard Gallze[1], Bénédicte Jordan[1]

[1]Biomedical Magnetic Resonance Group, Université Catholique de Louvain, Brussels, Belgium
[2]Center for Molecular Imaging, Radiotherapy and Oncology, Université Catholique de Louvain, Brussels, Belgium

Introduction: Tumor hypoxia has long been known as a big challenge in solid tumor treatment. It is considered to be one reason for the failure of radiotherapy, of chemotherapy as well as for surgery. However, there is still no accommodating method for mapping oxygenation of solid tumors available for routine clinical practice. Direct quantitative methods are either invasive or require an injection of the reporter probe. Promising methods rely on MRI, which is non-invasive and widely available. Nowadays, there are two MRI methods used for monitoring tumor oxygenation. The first one_ the T1 based method measures oxygen soluble in tissues. Yet, the significant limitation of this method is its lack in sensitivity. The second one_ the T2* based method measures oxygen in blood vessels. However, it is influenced by other compartments unrelated to the change of oxygen like hematocrit or blood volume. Therefore, our group has suggested an innovative method using MRI for noninvasive mapping oxygen_ MOBILE. The method is based on the higher solubility of oxygen in lipid than in water and measures T1 longitudinal relaxation rates in lipids instead of the aforementioned method measuring the T1 of water. Yet, the initial MOBILE sequence using a look-locker approach, with water suppression, suffers from problems of quality of T1 fitting. Therefore, another way to extract the T1-lipids parameter was considered using a bi-exponential deconvolution of T1 global relaxation rate which composes of fast lipid relaxation and slow water relaxation. The aim of this work is to qualify the new version of MOBILE (T1 of lipids extracted from global T1) as a marker of response to radiation therapy, and benchmark it with its parent parameters (global T1 and T1 of water), with T2* based method and with the quantitative but invasive method, EPR oximetry, as a marker of response to radiation therapy.

Methods: Male adult Fisher 344 rats were inoculated with 5.10^6 cells of 9L-Glioma in right thighs. Tumors were allowed to grow to the size of 15-20mm in diameter at the beginning of experiments. They were subjected to T1 imaging, then compared to the T2* based method and EPR oximetry_ a quantitative but invasive method that allows to assess the value of pO_2 through the linewidth of the EPR spectra. Three parameters could be extracted from T1 imaging using a bi-exponential approach: global T1, T1 of water and T1 of lipids. Each experiment was conducted under both air-breathing and carbogen-breathing conditions to assess the sensitivity of the method changes in oxygenation. Then, the rats were randomly divided to two subgroups for radiation therapy: air breathing or carbogen breathing. Tumors were monitored individually for the tumor growth delay experiment.

Result and conclusion: All 3 parameters extracted from T1 mapping show a significant decrease indicating a rise of oxygen in tissue after carbogen challenge. These results are in agreement with the increase in T2* and in actual pO_2 assessed by EPR oximetry. In conclusion, the oxygen level in 9L-Glioma increases in response to the carbogen challenge. The three T1- parameters were able to assess this change in tumor oxygenation, including T1 of lipids ("MOBILE"). In two subgroups of rats going through different irradiation conditions, preliminary results show a significant difference between air-breathing group and carbogen-breathing group in terms of regrowth delay. This suggests that the higher level of oxygen conducts to a better response to radiotherapy and that T1 of lipids could be considered as a marker of tumor response to radiation therapy in further studies using models that are more radioresistant or radiosensitive.

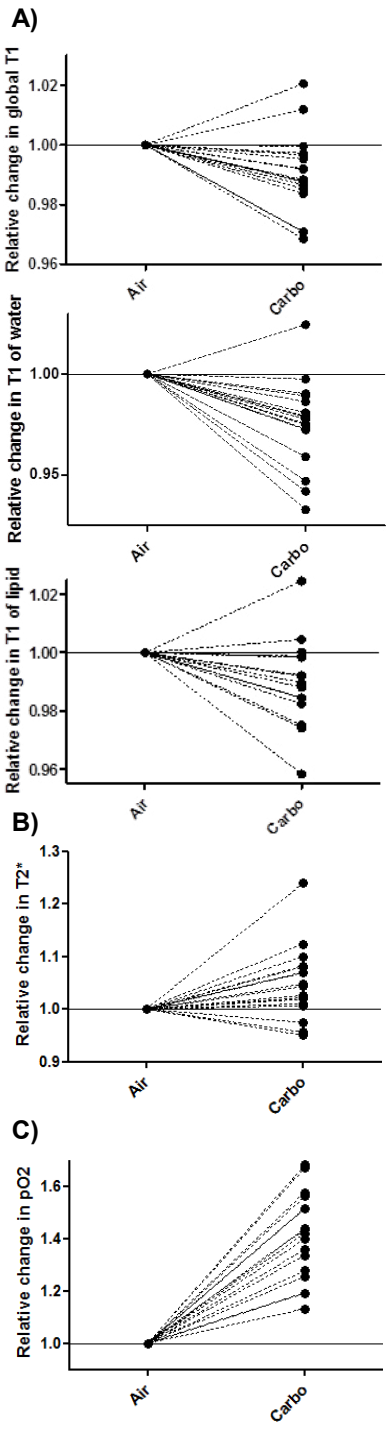

Fig. Relative changes in A) three parameters of T1-mapping, B) T2*, C) pO_2 by EPR oximetry before and after carbogen challenge

Discriminating low-grade from high-grade peripheral zone prostate cancer by multiparametric MRI: a multicenter study

Marnix Maas[1], Geert Litjens[2], Alan Wright[3], Masoom Haider[4], Katarzyna Macura[5], Kirsten Selnas[6], Daniel Margolis[7], Thomas Helbich[8], Berthold Kiefer[9], Jurgen Fütterer[1], Tom Scheenen[1]

[1]Department of Radiology and Nuclear Medicine, Radboud University Medical Center, Nijmegen, the Netherlands; [2]Department of Pathology, Radboud University Medical Center, Nijmegen, the Netherlands; [3]Cancer Research UK Cambridge Institute, University of Cambridge, Cambridge, United Kingdom; [4]Sunnybrook Health Sciences Center, University of Toronto, Toronto, ON, Canada; [5]Russell H. Morgan Department of Radiology and Radiological Science, Johns Hopkins University School of Medicine, Baltimore, United States; [6]Department of Circulation and Medical Imaging, Norwegian University of Science and Technology, Trondheim, Norway; [7]Department of Radiology, UCLA David Geffen School of Medicine, Los Angeles, United States; [8]Biomedical Imaging and Image-guided Therapy, Medical University Vienna - General Hospital Vienna, Vienna, Austria; [9]Siemens AG Healthcare, Erlangen, Germany

Introduction

Non-invasive assessment of prostate cancer grade is of great clinical importance for selecting and following-up patients for active surveillance with a minimum number of biopsies. All three imaging methods commonly employed in prostate multiparametric MRI (mpMRI), i.e. diffusion weighted imaging (DWI), ^{1}H MR spectroscopic imaging (^{1}H-MRSI) and dynamic contrast enhanced (DCE) imaging have been shown to correlate with Gleason scores. However, these correlations have to date not been explored in a multi-institutional setting, and no studies combining all three methods have been published. Here we present initial results for peripheral zone (PZ) prostate cancers in a multi-center study encompassing all 3 methods, using whole-mount section histopathology of resected prostates as the gold standard.

Methods

Fifty patients from 5 institutions (12, 10, 10, 10 and 8 patients) were included (mean±SD age 61±7y, PSA 7.4±3.5 ng/ml, Gleason score [GS] range 5-9). All centers used identical scanning protocols on 3T MRI systems (Siemens Healthcare, Erlangen) using external body and spine array coils. High-resolution T_2-weighted imaging was performed in three orthogonal directions, and DWI, 3D MRSI and DCE were acquired with identical protocols at all centers[1]. ADC maps were calculated from the DWI data using the scanner software (version VB17). MRSI data were quality checked and fitted accounting for contributions of choline (Cho), spermine (Spm), creatine (Cr) and citrate (Ci) using LCModel[2]. Ratios of (Choline+Spermine+Creatine)/Citrate (CSC/C) and Choline/(Spermine+Creatine) (C/SC) were calculated. DCE data were fitted with a semi-quantitative model yielding parameter maps of the initial area under the enhancement curve (iAUC), relative enhancement (RE), washin (WI), and washout (WO) using in-house developed software. Tumors were outlined and graded on histology slides according to a study-specific protocol[3]. Guided by histology and blinded to any functional imaging results, ROIs were drawn on T2w images in prostate cancer regions (volume >0.5 cc). Each ROI consisted of a central MRSI voxel and up to six directly neighboring MRSI voxels, provided they were located in the same tissue[1]. To correlate MRSI data with DWI and DCE, each MRSI voxel was represented by a sphere of its approximate true size (1.0 cc). Spheres were trimmed so as to contain only the tissue of interest. For each MRSI voxel/sphere the following quantities were calculated: 25th percentile (25p) for ADC, 75p for iAUC, RE and WI, and 25p for WO. The most deviating value of each parameter in each multi-MRSI-voxel ROI was used for further analysis. Tumors were stratified into low (L), intermediate (I) and high-grade (H) classes[4]. Spearman's correlation coefficients were calculated, and differences between low-grade and combined intermediate and high-grade tumors were assessed using mixed model analysis and ROC analysis with patient-level bootstrapping to account for within-patient correlations. The performance of combinations of parameters was analyzed using Logistic Regression modeling (LRM).

Results

A total of 45 PZ tumors from 39 patients with volume >0.5cc on histopathology and known GS were analyzed (L: 11, I: 16, H: 18), and 87 ROIs were annotated (average 5.2 MRSI voxels per ROI). Significant associations between tumor grade and parameter values were found for ADC, CSC/C and WI (Fig 1, Table 1). Significant differences between L and I+H cancers were found for ADC and CSC/C (Table 1). ROC analysis of these parameters resulted in areas under the curve (AUCs) of 0.80 ± 0.13 and 0.70 ± 0.19. A standardized threshold approach[5] (STA) with a C/SC cutoff of 0.4 yielded an AUC of 0.74. A Logistic Regression Model (LRM) including ADC and the MRSI-derived STA score yielded a slight improvement over using ADC alone (AUC 0.83 ± 0.15).

Discussion

Non-invasive assessment of prostate cancer aggressiveness is of high clinical importance, minimizing the number of biopsy needles to select and following up patients in active surveillance regimens. Multiparametric MRI has shown promising results for this purpose[6]. However, mpMRI methods need to be further validated in multi-center studies. These results show for the first time that good separation between L and I+H PZ tumors can be achieved in a multi-center setting, particularly with ADC maps. AUCs achieved with ADC and CSC/C were comparable to those reported in a recent single-center 3T study with similar design[4]. DCE-derived parameters were outperformed by DWI and MRSI-derived parameters, and performed slightly worse than in a recent single-center study[7]. Although this may be improved using patient-specific calibration methods and/or pharmacokinetic modeling, such methods may also introduce additional uncertainties. Combining CSC/C with C/SC with a standardized threshold approach lead to slightly improved MRSI performance, but LRM only lead to a small additional value of MRSI over ADC alone for separating L from I+H, in concordance with a previous report[4]. However, it has been suggested that MRSI-derived parameters may be more indicative of aggressiveness than ADC for TZ tumors[4]. Although TZ data are also available in this study, the low number of tumors available in this zone have thus far precluded drawing solid conclusions.

Conclusions

Using identical scanning protocols at 3T without an ERC in a multi-center setting yields good separation between low-grade and higher-grade tumor tissues with ADC maps.

References

[1]Maas, ISMRM 2014 (#4104); [2]Provencher, *Magn Reson Med* 30:672–79 (1993); [3]Epstein, *Am J Surg Pathol* 29:1228-42 (2005); [4]Kobus, *Radiol* 265:457–467 (2012); [5]Fütterer, *Invest Radiol* 42:116–112 (2007); [6]Pokorny, *Eur Urol* 66:22–29 (2014); [7]Vos, *Eur Urol* 64:448–455 (2013);

Acknowledgements: ERC Grant agreement n° [243115], Siemens Healthcare for research support, the PCaMAP consortium for collaborative support.

*Table 1: Statistical analysis. LMM: Linear mixed model. L: low-grade; I: intermediate grade; H: high-grade. *: p<0.05, **: p<0.01, ***: p<0.001, ns: not significant*

	Spearman's correlation		LMM L vs I+H	ROC analysis L vs I+H	
	r	p	p	AUC	p
ADC	-0.53	***	***	0.80 ± 0.13	***
CSC/C	0.42	***	*	0.70 ± 0.19	**
C/SC	0.10	ns	ns	0.58 ± 0.18	ns
iAUC	0.18	ns	ns	0.65 ± 0.24	ns
Rel.Enh.	0.10	ns	ns	0.61 ± 0.32	ns
WashIn	0.23	*	ns	0.63 ± 0.30	ns
WashOut	-0.09	ns	ns	0.58 ± 0.24	ns
LRM	--	--	***	0.83 ± 0.15	***

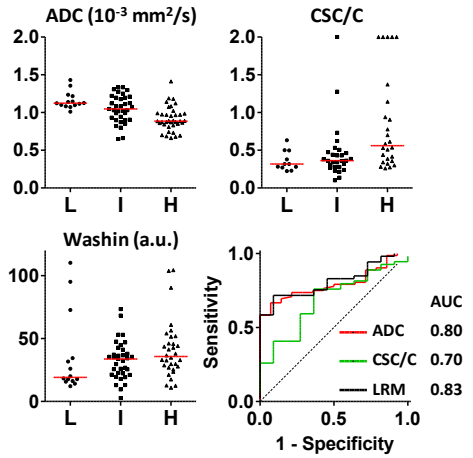

Fig. 1: Examples of separation between low (L), intermediate (I) and high (H) grade PZ tumors for ADC (a), CSC/C (b) and iAUC (c). d: ROC curves for L vs I+H for ADC (red), CSC/C (green) and a logistic regression model (LRM) including ADC and the MRSI-derived STA score (black).

Retrospective T^1 calculation based on DCE-MRI series with inhomogeneous B^1 at 7T in the breast

Erwin Krikken[1], Jaco J.M. Zwanenburg[1], Peter R. Luijten[1], Dennis W.J. Klomp[1], Jannie P. Wijnen[1]

[1]Department of Radiology, University Medical Center, Utrecht, the Netherlands

Introduction Kinetic modeling with dynamic contrast-enhanced MRI (DCE) for breast cancer patients allows estimation of quantitative parameters like the microvascular permeability (K^{trans}) and the extravascular extracellular space volume (v_e)[1]. This requires knowledge of the T_1. At high field MRI, the B_1+ field is inhomogeneous which influences the determination of T_1[2]. DESPOT1 is a method for T_1 mapping that allows correction for B_1+ field inhomogeneity using a B_1 map[3]. Optimal DCE protocols will combine high spatial resolution images and high temporal images to image the inflow of contrast agent. Due to gradient limitation, the high spatial resolution FFE images have different TR times and excitation flip angles from the images with high temporal resolution. The aim of this work is to investigate the feasibility of T_1 mapping (using the DESPOT1 method in a different way) based on existing DCE image series, and to quantify the influence of B1+ inhomogeneity on the determination of T_1.

Methods In a previous clinical study, patients have been scanned with a 7T MR system (Philips Healthcare) using a 4 channel breast coil (MR Coils, Utrecht, The Netherlands). Two FFE images with different flip angles (12^0 and 15^0) and different TR (4.0 and 4.3ms) and a B_1 map were acquired during that study. The signal of these images (S) is a function of the longitudinal relaxation time, T_1, repetition time, TR, flip angle, α, and a factor which is proportional to the equilibrium longitudinal magnetization, M_0:

$S = \frac{M_0(1-E_1)\sin(\alpha)}{1-E_1\cos(\alpha)}$ where $E_1 = e^{-TR/T1}$ [Eq. 1].

Signal from the two different FFE images (S1 and S2) with different flip angles are divided (S1/S2) and the T_1 are calculated[3].

Simulations: To quantify the influence of the B_1+ inhomogeneity, a simulation for a realistic T_1 range has been performed with different B_1. For each T_1, the S1 (for FA1 = 12°) and S2 (for FA2 = 15°) were calculated for a range of B_1 values (50-150%), using Eq 1. Next, the expected estimated T_1 was calculated assuming a perfect flip angle of 12 and 15 degrees, respectively. This results in a map that shows the influence of B_1+ inhomogeneity on calculating the T_1.

Phantom: Given the data from the clinical study, we acquired similar FFE images and a B_1 map of a phantom containing cylinders filled with gel with two different T_1's (Diagnostic Sonar). The T_1 was determined for 7T by look-locker inversion recovery T1 mapping where T_1 was calculated using Eq. 1 with and without correcting for the B_1.

Patient: A breast cancer patient was scanned as part of an ongoing study. The patient gave written informed consent. In vivo data has been corrected for B_1+ inhomogeneity's with the same method.

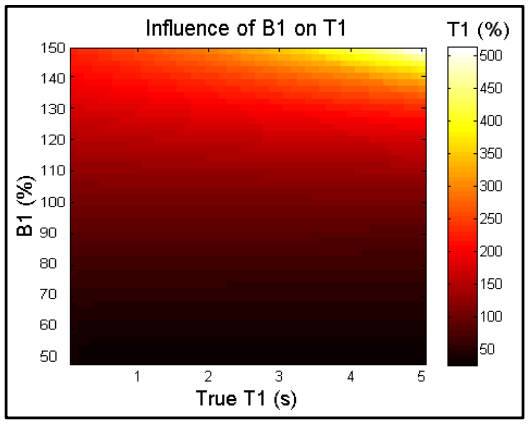

Figure 1 *Influence of B_1 on calculated T_1 values. For example, for a T_1 of 2.5s with a B_1 of 150% results in a calculated T_1 of 318% of the true value when not correcting for B_1+ inhomogeneity's*

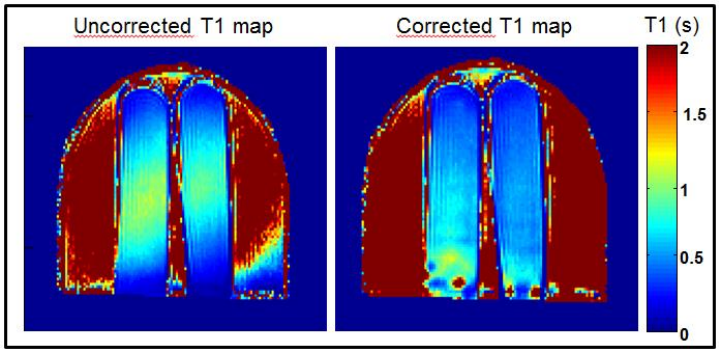

Figure 2 *Calculations of T_1 relaxation time in the two cylinders without (left) and with (right) correction of the B1 field using the B_1 map. Right cylinder is tube 1 and left cylinder tube 2*

Results For high T_1 relaxation times, the influence of B_1 on the calculated T_1 becomes larger (Figure 1). The calculated T_1 of the phantom without correction of B_1 shows more variation values of T_1 inside the cylinders (Figure 2). Table 1 shows the measured T_1 over the whole cylinders for the uncorrected and corrected T_1. In Figure 3, the corrected T_1 reductions of the contrast enhanced breast tumor are shown.

Table 1 Calculated T_1 in seconds

	True T1 times (S)	Uncorrected (s)	Corrected (s)
Tube 1	0.49	0.65 ± 0.20	0.47 ± 0.09
Tube 2	0.62	0.77 ± 0.23	0.58 ± 0.14

Discussion Simulations show that for physiological T_1 times found in the breast, variation in B_1 substantially influences the estimated T_1. Therefore it is important to correct for this by obtaining B_1 information. Figure 2 shows that correcting the T_1 map with the obtained B_1 map results in more reliable T_1 values. When applied in vivo data, B_1 insensitive values for contrast uptake can be assessed (Figure 3).

Conclusion We have shown that existing 7T DCE series with different flip angles and TR combinations in the high temporal and high spatial resolution images as acquired for breast cancer patients can be used to do quantitative T_1 mapping. We use an approach similar as presented by Deoni et al. Even though the acquisitions were not optimized for T_1 mapping, sufficiently reliable T_1 values can be obtained if B_1 correction is applied.

References [1]Tofts, P. S. et al. *Magn. Reson. Med.* 1991. [2]Kuhl, C. K. et al. *Radiology* 2007 [3]Deoni, S.C.L. et al. *Magn. Reson. Med.* 2003.

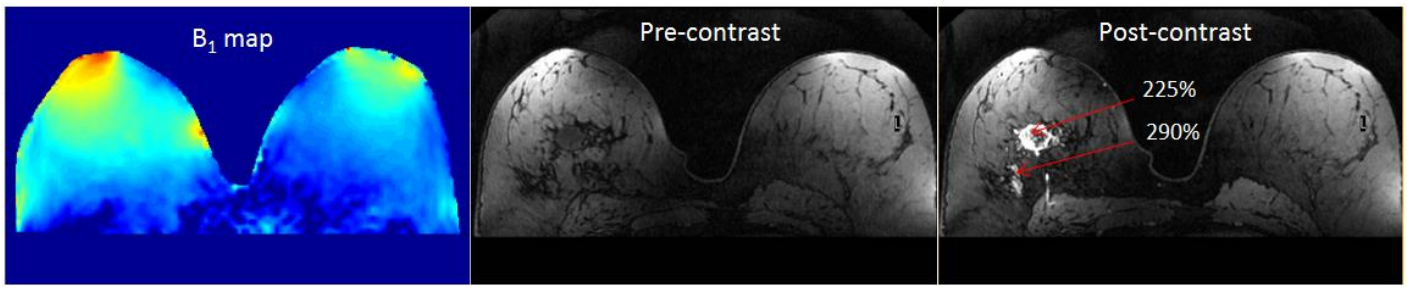

Figure 3 *7T DCE-MRI of breast cancer with B_1 corrected values for T_1 reduction caused by the contrast agent (left: B1map; middle: prior ; and right: 2min after contrast administration)*

Micro-vascular effects of photodynamic therapy in tumors evaluated with dynamic contrast-enhanced MRI

Tom Schreurs[1], Stefanie Hectors[1], Igor Jacobs[1], Holger Grüll[2], Klaas Nicolay[1], Gustav Strijkers[3]

[1]Department of Biomedical NMR, Eindhoven University of Technology, Eindhoven, the Netherlands
[2]Oncology Solutions, Philips Research Europe, Eindhoven, the Netherlands
[3]Department of Biomedical Engineering and Physics, Academic Medical Center, Amsterdam, the Netherlands

Target audience Researchers interested in dynamic contrast enhanced MRI for image guidance of cancer therapy

Purpose Photodynamic therapy (PDT) is an emerging cancer therapy. PDT is a local treatment which aims to induce tumor cell death by activation of a photosensitizer that produces reactive oxygen species under (laser) light irradiation. Apart from direct cell death, PDT treatment also induces vascular occlusion and immune response activation. Although successful results have been obtained with PDT[1,2], there is an unmet need to predict treatment outcome shortly after therapy. Therefore, the **aim** of this study was to use dynamic contrast-enhanced (DCE) MRI to study early vascular tumor effects of PDT. Besides, 4 types of endogenous MR contrast parameters were measured quantitatively, to detect structural tissue changes. We hypothesized that this information can be used to distinguish successfully treated (non-viable) tumor tissue from residual or recurrent (viable) tumor tissue.

Methods CT26 colon carcinoma cells were injected ~10 days before PDT subcutaneously into the hind limb of Balb/c mice. The PDT protocol consisted of an i.v. injection of 6.45 mL/kg body weight of the photosensitizer Bremachlorin (0.35% solution), activated 6 h later by 10 min illumination with 655 nm laser light, which was aimed onto the skin (120 J/cm^2) covering the tumor (n=5 animals). A control group (n=4) received no photosensitizer and no light treatment. Tumor size was monitored every 2-3 days until the animals were sacrificed 14 days after PDT. MRI was performed on a 7T Bruker BioSpec one day before, 3 h after, and 24 h after PDT. The protocol consisted of T2-weighted multi-slice spin echo scans, used as anatomical reference, followed by quantitative measurements of T1, T2, magnetization transfer ratio (MTR) and the apparent diffusion coefficient (ADC), all using 128^2 pixels multi-slice EPI readout acquisitions covering the whole tumor. Next, 3D FLASH scans were used for B1 mapping (FA = 145, 180, 215°), for quantitative measurements of pre-contrast T1 using a variable flip angle approach, and for the actual DCE scan. The latter had a scan time of 3.6 s, repeated for 15 min. After 2 min, an i.v. injection of contrast agent (4 mL/kg b.w. 75 mM Dotarem) was performed in 5 s using an infusion pump. From the DCE scans, contrast agent concentration curves were obtained for each pixel, which were used to calculate the transfer constant K_{trans} and fractional volume of the extravascular extracellular space v_e, using the standard Tofts-Kermode model.

Results Response to PDT was similar in all animals in the first 2-3 days after treatment: the whole or a large part of the tumor became necrotic. The necrotic mass subsequently shrunk and turned into a dry scab. In 2 mice, only a small scab was left 14 days after PDT. In the other mice, part of the tumor remained viable leading to recurrent tumor growth with a delay of approx 10 days as compared to controls. No significant treatment effects were observed in any of the endogenous parameter maps, except at the tumor surface (dry scab), and around the tumor (edema), see Fig 1. DCE-MRI analysis indicated that tumors were initially almost completely enhanced (Fig 1). In contrast, large tumor parts were non-enhanced right after treatment, which was even more pronounced after one day. The non-enhanced tumor fraction, averaged over all treated mice, increased from 1.9±1.5% before PDT, to 20.3±9.2 right after PDT, and 73.0±14.7 % after 1 day, whereas no significant increase was observed in controls. Parts of the tumor that still showed contrast agent uptake at 24h after PDT coincided with positions where tumor nodules regrew after some days (Fig 2), for the 3 mice with tumor recurrence. Pharmacokinetic modeling revealed that the average K_{trans} over all treated animals decreased from 0.25±0.07 before PDT, to 0.09±0.03 right after PDT. Non-decreased K_{trans} values at 1h after PDT spatially correlated with non-decreased K_{trans} at 24h after PDT.

Discussion The lack of enhancement in large tumor parts after PDT clearly indicates vascular occlusion. Remaining non-enhanced regions after 24h coincided with regions of tumor recurrence. The drop in K_{trans} right after PDT suggests that a decrease in perfusion can already be observed within 3h after PDT, which possibly enables monitoring of treatment efficacy at this very early time point. However, no treatment effects were found in endogenous parameter maps, suggesting that little or no structural tissue changes occur in the first 24 h. It is important to note that treatment also induced vascular occlusion in adjacent muscle tissue. However, these effects may be reversible, because slight limping was only observed in some mice for at most 2 days after PDT.

Conclusion DCE-MRI could be used to visualize the drastic microvascular effects of PDT in our tumor model. Therefore, the technique may be of clinical value for monitoring of treatment efficacy. In future experiments, the DCE-MRI data will be spatially compared to a histological viability essay (NADH-diaphorase staining), to assess if observed vascular changes are indicative of changes in tissue viability.

Acknowledgements This work is supported by NanoNextNL, a micro and nanotechnology consortium of the Government of the Netherlands and 130 partners

References 1) Dougherty *et al*., J. Natl. Cancer Inst. 55: 115-121, 1975; 2) Agostinis *et al*., CA Cancer J. Clin. 61: 250-281, 2011

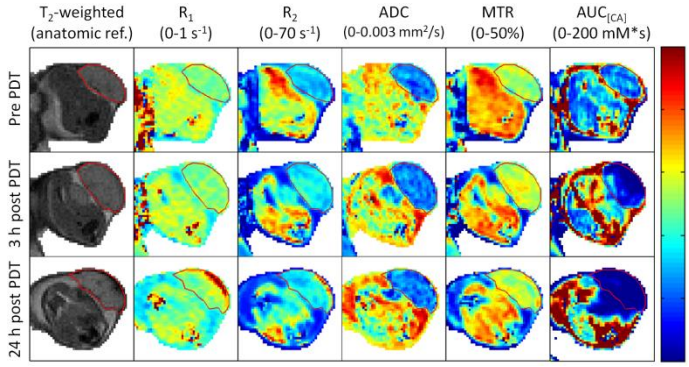

Figure 1: Parameter maps from a PDT-treated mouse in a cross-section of the hind limb. Column 1: T2-weighted anatomical reference images. The red outline indicates the tumor. Columns 2-5: endogenous parameter maps. Column 6: area under the time-curve (AUC) of contrast agent concentration, obtained by DCE-MRI. None of the endogenous parameters was strongly affected in the tumor core, but the tumor was surrounded by edema (high ADC, low R_2). According to the AUC maps, the tumor initially was completely perfused, whereas it was largely non-perfused 3h and 24h after PDT.

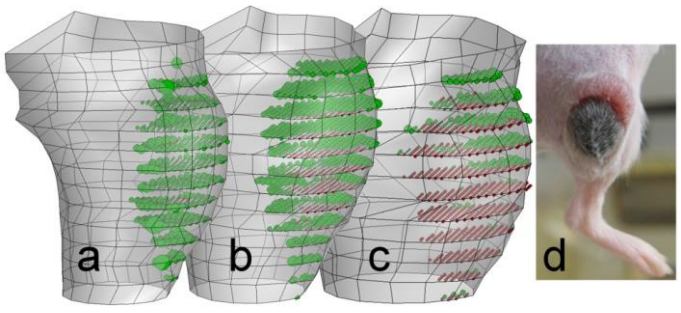

Figure 2: MRI-based 3D model of the hind limb before **(a)**, 3h post **(b)** and 24h post PDT **(c)**. Contrast-enhanced and non-enhanced tumor voxels are indicated in green and red, resp. After 3h, tumor perfusion was already shut down in the tissue close to the skin in the central slices. Only the upper part of the tumor was still enhanced after 24h, suggesting partially unsuccessful treatment. Indeed, tumor recurrence was seen in that part of the tumor after ~3 days. A photo of the tumor at day 7 is shown **(d)**, with a viable recurrence in the top.

Tumour relapse prediction using multi-parametric MR data recorded during follow-up of GBM patients

Adrian Ion-Margineanu[1], Sofie Van Cauter[2], Diana Sima[1], Frederik Maes[3], Stefaan Van Gool[4], Stefan Sunaert[2], Uwe Himmelreich[5], Sabine Van Huffel[1]

[1]STADIUS & ESAT, KU Leuven, Belgium; [2]Department of Radiology, University Hospitals Leuven, Leuven, Belgium; [3]PSI & ESAT, KU Leuven, Belgium; [4]Department Pediatric Neuro-Oncology, University Hospitals Leuven, Leuven, Belgium; [5]Department of Biomedical NMR (MOSAIC), Imaging & Pathology, KU Leuven, Belgium

Target audience: Researchers and doctors that use multi-parametric magnetic resonance imaging (MRI) data for brain tumor follow-up.
Purpose: The focus of our study is finding a relation between the multi-parametric MR data acquired during the follow-up of glioblastoma multiforme (GBM) patients and the relapse of the brain tumour after surgery, as described by the clinically accepted RANO criteria. Conventional MRI (cMRI) has a limited specificity in determining the underlying type of brain tumour and tumour grade. More advanced MR techniques like diffusion-kurtosis MRI (DKI), perfusion-weighted MRI (PWI), and MR spectroscopy are promising in the characterization of brain tumours as they give potentially more physiological information.
Methods: ***Acquisition:*** Twenty-nine GBM patients who underwent surgery were scanned using a 3 Tesla MRI unit (Philips Achieva, Best, The Netherlands). The protocol consisted of conventional imaging (T1-weighted MRI after contrast administration, T2-weighted MRI and FLAIR (fluid attenuated inversion recovery) MRI) and advanced imaging (DKI, dynamic-susceptibility weighted contrast (DSC) - MRI, and chemical shift imaging (CSI)). High resolution anatomical reference images were acquired with T1-weighted 3D spoiled gradient echo scan with fast field echo, TR/TE: 9.7/4.6 msec, flip angle: 8°, turbo field echo factor: 180, acquisition voxel size: 0.98x0.98x1 mm^3, 118 contiguous partitions, inversion time: 900 msec. Axial spin echo T2 images were acquired with TR/TE: 3000/80 msec, slice/gap: 4/1 mm, field of view (FOV): 230x184 mm^2, turbo factor: 10, acquisition matrix: 400x300. Axial FLAIR images were acquired with TR/TE/IR: 11000/120/2800 msec, slice/gap: 4/1 mm, FOV: 230x184 mm^2, acquisition matrix: 240x134. Regions of interest (ROI) were manually drawn around the solid contrast-enhancing (CE) region and the entire lesion (TO), while the ROI containing perilesional oedema (ED) was obtained by subtracting CE from TO. Another ROI was drawn around the contralateral normal appearing white matter (NAWM) to standardize the hemodynamic measurements of PWI. DKI data were acquired with a spin-echo echo-planar-imaging diffusion weighted imaging (SE-EPI-DWI) sequence with TR/TE: 3200/90 msec, δ/Δ: 20/48.3 msec, FOV: 240x240 mm^2, matrix: 96x96, 1 signal average acquired, section thickness/gap: 2.5/0, b-values: 700, 1000, and 2800 sec/mm^2 in 25, 40 and 75 uniformly distributed directions. Additionally, 10 images without diffusion sensitization (b=0) were obtained. The DKI data were processed as described in [1]. Fractional anisotropy (FA), mean diffusivity (MD) and mean kurtosis (MK) were derived from the tensors. After a nonlinear registration of the parameter maps to the anatomical MR images, average values of MK, MD and FA were determined in the CE and ED regions. PWI was obtained with a DSC-MRI protocol consisting of a gradient echo-EPI sequence, TR/TE: 1350/30 msec, section thickness/gap: 3/0 mm, dynamic scans: 60, FOV: 200x200 mm^2, matrix: 112x109. PWI data were analyzed using DPTools (www.fmritools.org), as described in [1]. The average values of the considered perfusion parameters were computed in the CE, ED, and NAWM regions. We compute relative regional Cerebral Blood Volume (rrCBV), relative regional Cerebral Blood Flow (rrCBF) and relative Decrease Ratio (rDR) by using the corresponding parameter value in the NAWM region as internal reference. A 2D-CSI short echo time protocol was used as validated in [2]. MR spectra were processed using the MATLAB 2010b environment (MathWorks, Massachusetts, U.S.A.) with SPID graphical user interface, as described in detail in [2]. Nine metabolites were quantified using AQSES-MRSI: N-acetyl aspartate (NAA), glutamine (Gln), glutamate (Glu), total creatine (Cre), phosphorylcholine (PCh), glycerophosphorylcholine (GPC), myo-inositol (Myo), and lipids (Lips) at 0.9 and 1.3ppm, referred to as Lip1 and Lip2 respectively. Glu+Gln and PCh+GPC were reported as Glx and tCho (total choline), respectively. Good quality voxels were selected in the CE region based on Cramer-Rao Lower Bounds and spectral quality. The following metabolite ratios are reported: NAA/tCho, NAA/sum, tCho/sum, NAA/Cre, Lips/tCho, tCho/Cre, Myo/sum, Cre/sum, Lips/Cre and Glx/sum.
Machine Learning: In total, from 29 patients, we have 178 data points and each of these has 27 features (3 volumes from cMRI, 6 from PWI, 6 from DKI, 10 from CSI and 2 parameters for indicating total resection of the tumor and another one for describing the treatment). After quality control for each advanced modality, we removed 30% of PWI data, 44% of DKI data and 66% of CSI data. This drop-out of data resulted in a subset of 18 patients with 45 measurements with complete features. We developed an imputation method to fill in the missing data. For each patient a label (i.e. responsive treatment or progressive disease) has been put by the doctors according to the RANO criteria. Each patient has been scanned at least twice, so we can divide every patient's time points into two classes: before the label was put (unlabeled data) and after the label was put (labeled data). We used several supervised classifiers (k-Nearest Neighbours (kNN), diagonal Linear Discriminant Analysis (dLDA), Support Vector Machine (SVM), Least Squares SVM (LSSVM), Random forests (RF), Classification Tree (CT), Boost ensembles, Neural networks (NN)) with the goal of testing whether the unlabeled data could have been reliably labeled before the actual labeling was performed in the clinic. We test these classifiers on all features, but also on subsets of features pertaining to a single advanced MR modality (PWI, DKI, CSI). We used a leave-one-patient-out testing method, where all time points that belong to the test patient are, in turn, excluded when training the classifier so that they can be used as test data. We compute the balanced error rate (BER) at each time point, using the assigned label as expected label for all time points of a patient. For each classifier we have a total of 17 time points, because there are patients with up to 6 time points after the labeling point and there are others with up to 11 time points before the labeling point. The overall performance of each classifier is reported as a weighted average of the BER values obtained at all time points, weighted BER (wBER).

Table 1. BER values before and after the labeling time point for the best six classifiers using complete features.

BER	RF	dLDA	SVM-lin	LogitBoost	RobustBoost	SVM-mlp
L+2	0	0	0	0	0	0
L+1	0	0	0	0	0	0
L	0	0.1	0.217	0	0	0.1
L-1	0	0.125	0	0	0	0.125
L-2	0.25	0.25	0.5	0.25	0.25	0.25

$$wBER = \frac{\sum W_i^p \cdot W_i^t \cdot BER_i}{\sum W_i^p \cdot W_i^t}$$

$$W_i^t = 1, i \geq \text{labeling time point}$$

$$W_i^t = 1 - \frac{0.5}{11} \cdot i, i < \text{labeling time point}$$

$$W_i^p = \frac{\text{Number of patients at time point } i}{\text{Total number of patients}}$$

Table 2. Overall performance (wBER) of the best six classifiers when using complete and imputed features.

wBER	RF	dLDA	SVM-lin	LogitBoost	RobustBoost	SVM-mlp
Complete features (PWI/DKI/CSI)	0.15 (0.15/0.36/0.57)	0.17 (0.26/0.26/56)	0.28 (0.22/0.26/0.6)	0.15 (0.15/0.37/0.61)	0.15 (0.15/0.37/0.62)	0.14 (0.19/0.35/0.63)
Imputed features (PWI/DKI/CSI)	0.29 (0.29/0.28/0.41)	0.22 (0.31/0.33/0.4)	0.24 (0.28/0.32/0.42)	0.34 (0.29/0.28/0.42)	0.33 (0.27/0.28/0.41)	0.35 (0.28/0.38/0.41)

Results: Table 1 shows the classifiers performance for several time points before and after the labeling time point. It contains the detailed BER performance of the best 6 classifiers, from a total of 23 different classifiers, when using complete features. Table 2 reports wBER of the best 6 classifiers when using complete and imputed features on the whole dataset, but also on the small subsets pertaining to a single advanced MR modality (PWI, DKI, CSI).
Discussion: By using either RF, LogitBoost or RobustBoost classifier on all complete features we can predict with 100% accuracy the outcome of clinical labeling with one time point (ca. 1 month) in advance. The same results are obtained when using only complete perfusion features. Classifiers trained only on complete diffusion or spectroscopy features yield worse results. If we use imputed data, linear classifiers (dLDA, SVM-lin) perform better than RF and Boost ensembles.
Conclusion: In this study we proved that it is possible to accurately predict at least one month earlier than doctors if a patient is responsive to the treatment or not, by using all complete features or just complete perfusion features. For future work we plan on integrating the temporal evolution of the features when classifying different MR sessions and also allow updating of the class labels in time.
Acknowledgements: FWO G.0869.12N; IUAP P7/19/ ; EU FP7/2007-2013, MC ITN TRANSACT 2012 n. 316679.
Refereces: [1] S. Van Cauter et al., *Neuro-Oncology*, 16(7), 1010-1021, 2014; [2] S. Van Cauter et al., *Journal of MRI*, vol. 37, no. 2, 445-456, 2013.

An MRI based mid-ventilation approach for radiotherapy of liver cancer on an MR-linac

Tessa van de Lindt[1], Gerald Schubert[2], Uulke van der Heide[1], Jan-Jakob Sonke[1]

[1]Department of Radiation Oncology, Academic Medical Center, Amsterdam, the Netherlands
[2]Philips Healthcare, Best, the Netherlands

Introduction: With an integrated MRI and linear accelerator (MR-linac) under development, it will become possible to visualize even low contrast tumors at the time of irradiation and new MRI-based strategies for motion management are required. In current practice, a 10 phase 4DCT is acquired and the phase which contains the time weighted average position of the tumor is extracted. This is called the mid-ventilation (midV) anatomy and is the preferred anatomy for treatment planning and delivery of free-breathing patients. Therefore, an efficient strategy to acquire a high quality MRI image in midV, for radiation therapy of the liver on an MR-linac, was developed and evaluated.

Concept: In midV, the velocity of the liver is high and images are thus susceptible to motion artifacts. Therefore, a fast, low resolution image is acquired in midV (LR midV) while a high resolution image is acquired in the more stable exhale phase (HR exhale). The HR image will then be deformably registered to the midV anatomy to obtain a high quality image in midV.

Methods: Diaphragmatic motion of a healthy volunteer was captured with a navigator beam on a 1.5T whole body MRI system (Philips Healthcare, Best). Two trigger levels were calculated: exhale and midV (fig1). The trigger levels were alternated so that in maximum exhale a multi-shot TSE (TE=100ms, TR=2180ms, shot length=234ms, res=1x1x4mm, NSA=3) was performed and in midV a T2-weighted single-shot TSE (TE=100ms, TR=222ms, shot length=166ms) was acquired. With deformable registration (B-splines, mutual information), the HR exhale scan was registered to the midV anatomy.

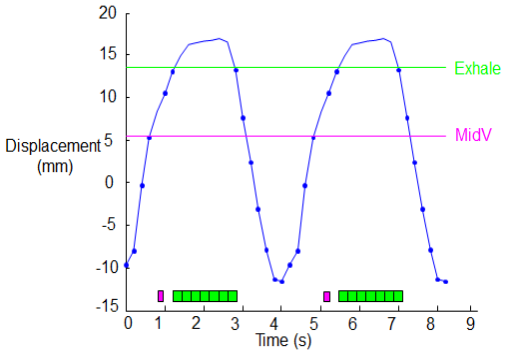

Fig1: Navigator signal (blue) of two respiratory cycles with, exhale (green) and midV (purple), rising edge trigger levels. The purple blocks represent the short acquisition of the scan in midV, while the green blocks represent the multi-shot HR acquisition in exhale.

Results: The high resolution anatomical image in maximum exhale shows minimal motion artifacts and the vascular structures of the liver are clearly visible. Because of the short shot-duration, the midV scan shows minimal motion artifacts as well, but has a lower resolution. After deformable registration of the exhale to the midV scan, a detailed, high quality image in midV anatomy (DR midV) was obtained (fig2). In a sagittal view it is visible that the deformable registered image fits the midV anatomy much better than the exhale image (fig3).

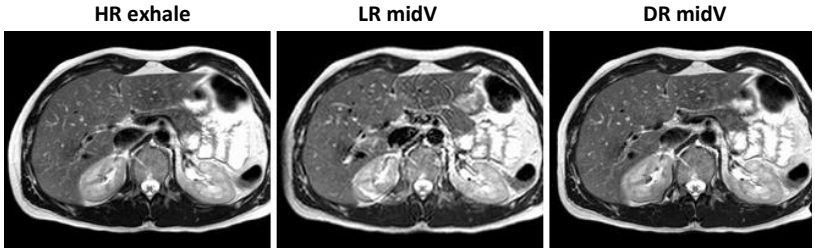

Fig2: Transverse T2-weighted images of the liver

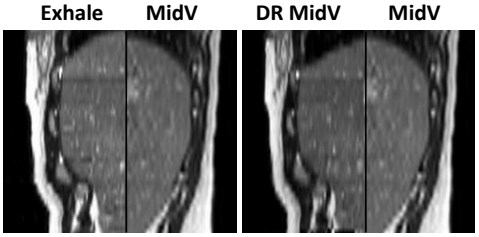

Fig3: In a sagittal view it is visible that the deformable registered image fits the midV anatomy better compared to the exhale image

Discussion & Conclusion: By using two alternating trigger levels, a fast T2-weighted image in midV and a high resolution image in the more stable exhale phase were acquired efficiently. By deformably registering the high resolution image to the midV anatomy, a high quality image in midV could be realized for treatment planning and guidance of liver cancer radiotherapy on an MR-linac.

Improved cortical bone segmentation using a spectral-spatial selective pulse to reduce water/fat in-phase echo time

Matteo Maspero[1], Peter R. Seevinck[2], Anna Andreych[1], Sjoerd Crijns[1], Alessandro Sbrizzi[3], Max Viergever[2], Jan J. Lagendijk[1], Cornelis A.T. van den Berg[1]

[1]Department of Radiotherapy, University Medical Center, Utrecht, the Netherlands
[2]Image Sciences Institute, University Medical Center Utrecht, Utrecht, the Netherlands
[3]Department of Radiology, University Medical Center, Utrecht, the Netherlands

TARGET AUDIENCE Researchers and medical physicist interested in segmenting bone structures from MRI data and/or in pseudo-CT generation for Radiation Therapy Planning (RTP) and/or MR-based attenuation correction for MR/PET.

PURPOSE MR-bone imaging is valuable for many applications, such as MR-based RTP. For this application a complete segmentation of bone is required together with a Digitally Reconstructed Radiography (DRR) to enable 2D position verification of the patient just prior to radiation delivery. Recently, promising results were obtained in the pelvic area with T_1-Dixon sequences [1,2]. Nevertheless, they suffer from false positive depictions due to misclassification of bone structures in areas characterized by short T_2(*) as occur e.g. in the bowel regions due to the presence of air gaps. Some methods have been proposed to solve the misclassification errors like, for example, the use of a probabilistic atlas [1] that requires prior knowledge of the anatomical area.

This work aims at reducing the in-phase time point for water and fat, by use of a spectral-spatial selective excitation pulse. In particular the use of a reduced echo time reduces signal voids due to T_2* dephasing. We demonstrate here that the shorter T_E in combination with a novel image processing approach leads to more specific black bone imaging by preventing misclassification of regions presenting with low T_2* at a conventional in-phase echo time.

METHODS *Subjects*: The data of two healthy volunteers were acquired on a Philips Achieva 1.5T using a 16-element Torso XL coil with SENSE factor 1.

Pulse: The scanner software was modified to allow the use of a spectral-spatial selective excitation pulse (the end of this pulse is the start of the T_E for the scanner). The RF pulse was designed using a binomial composition as introduced in [3]. The RF pulse length was 1.46 ms (*Fig. 1*) and has to be included when calculating the effective T_E. The first peak of the pulse corresponds to the magnetic moment. Whereas normal excitation pulses provide the same phase for both water and fat, the proposed pulse design enables excitation of water and fat with a relative phase difference. In the current study, the pulse was designed in such a way that at the effective T_E, water and fat was either in-phase, or out-of-phase.

Imaging parameters: Cartesian 3D spoiled GRE imaging parameters were as follow: T_E/T_R=0.86/3.82 ms, flip angle 7°, FOV 12.9x26.4x40 cm³, acquisition matrix 43x132x200, pixel bandwidth of 1.79 kHz and 21.3 s scan-time. The effective T_E corresponds to 2.3 ms.

In-Phase (IP) and Out-of-Phase (OP) images (*Fig. 2* left) were obtained with the aforementioned imaging scan parameter in two separated acquisitions by designing two RF pulses. The two pulses did not need to be designed repeatedly for different subjects.

Two cartesian 3D spoiled GRE images were also acquired as references (*Fig. 2* right). The imaging parameters were (if not specified they remained the same) T_E/T_R=2.3/3.6 ms, 19.7 s scan-time for the OP Ref image, and T_E/T_R=4.6/5.8 ms, 32.6 s acquisition time for the IP Ref image respectively. The pixel bandwidth was for both 1.67 kHz.

All the four sequences were acquired consecutively and the total acquisition time was within approximately 1.5 min (see in *Fig. 1* the exact acquisition timing) to minimize the probability of varying bowel filling between scans.

Imaging processing: Body masks of every transverse slice were obtained using an automatic 3 classes threshold Otsu algorithm [4] on the IP images and excluding the pixel below the first threshold. Two bone masks (*Fig. 3*) were generated applying a 3 classes k-mean clustering algorithm [5] based on Euclidean distance on the 2D topological space defined by all the correspondent pixels in every transverse slice of the IP and the OP images. Bone-only DRRs were reconstructed from the binary bone masks (*Fig. 4*).

RESULTS & DISCUSSION Even though the images are acquired with different sequences the total acquisition time is short enough not to expect considerable variation in the internal anatomy of the volunteers. The two OP images demonstrate very comparable contrast (*Fig. 2* bottom) as can be expected from similar effective echo times equal to 2.3 ms. Signal voids are present at water/fat interfaces and the bony structure results in black region (low magnitude) in the same anatomical area.

On the contrary, the two IP images (*Fig. 2* top) present differences localized in the central region that corresponds to the bowel: the Ref image depicts signal voids not visible in the image acquired with the proposed pulse. The bowel signal voids in the Ref image suggest that the bowel filling consists of a mixture of liquid and gas that causes intra-voxel dephasing for longer T_E. In this way the shortening of the T_E produces less signal voids by reducing the T_2* dephasing effects. This result is exploited in the image processing obtaining a reduction of false positive in the bone mask, as also visible in the bone-only DRRs in *Fig. 4*.

CONCLUSION Cartesian 3D spoiled GRE in-phase and out-phase images with reduced time point (2.3 ms) acquired with a spectral-spatial selective pulse resulted in good segmentation of cortical bones in the pelvis and in bone-only DRRs.

The main innovation is in the increased bone specificity related to improved discrimination between bone and short T_2* regions, such as air/fluid mixtures in the bowel region.

Furthermore the image processing proposed is fast and utilizes algorithms that are standard and easily implementable in a clinical department. Future work could focus on the development of a multi-echo acquisition in order to acquire in-phase and out-of-phase in a single sequence. The use of 2-point Dixon reconstruction based on the in-phase/out-phase could also allow a complete generation of Electron Density map valuable for RTP.

REFERENCES

[1] Schadewalt N et al. Int J Radiat Oncol 2014; 87(2): S474 [2] Helle M et al. ISMRM 2013 #0768 [3] Crijns S et al. ISMRM 2014 #1665 [4] Otsu N. Automatica 1975; 11(285-296): 23-7. [5] Lloyd S, Least squares quantization in PCM, 1982; IT IEEE (28.2): 129-37.

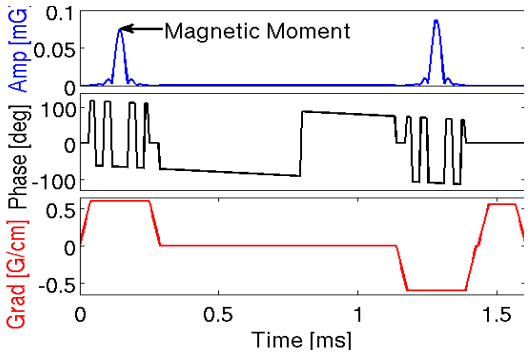

Fig. 1: RF amplitude, phase and gradient waveform for the IP spectral-spatial selective Pulse.

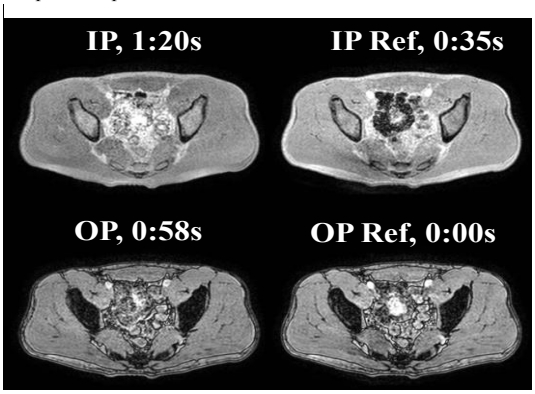

Fig. 2: In-Phase (IP) and Out-of-Phase (OP) images acquired with the custom pulse (left) and as reference (right). All the images have the same window level. The times are the relative start time from the beginning of the acquisition.

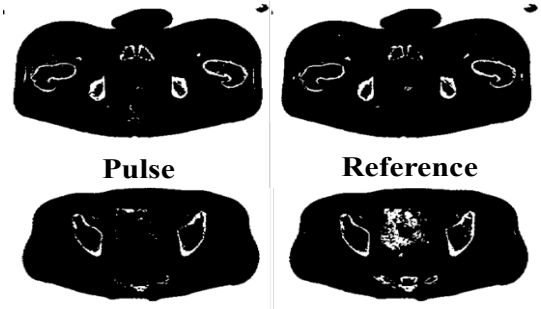

Fig. 3: Body and Bone masks of the Pulse images (left) and of the Reference ones (right) for two transverse slices: 17 (top) and 39 (bottom).

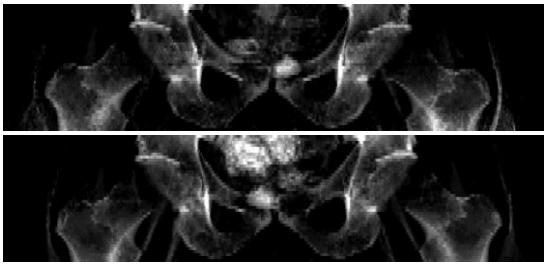

Fig. 4: Bone-only DRR from the Pulse images (top) and References ones (bottom).

Towards real-time monitoring of laser induced hyperthermia for photodynamic therapy with magnetic resonance thermometry at 7T

Robbert van Gorkum[1], Tom Schreurs[1], Larry de Greef[1], Gustav Strijkers[1], Klaas Nicolay[1]

[1] Department of Biomedical NMR, Eindhoven University of Technology, Eindhoven, the Netherlands

INTRODUCTION: Magnetic Resonance Thermometry (MRT) is a powerful modality to non-invasively measure the temperature inside tissue. Although extensively used at lower field strengths (≤3T), few studies exploit the possibilities of high field (≥7T) scanners for this purpose[1]. The most adopted MRT method uses phase mapping of the temperature-sensitive proton resonance frequency shift (PRFS), to determine temperature changes in tissue[2]. Localized cancer treatments, such as photodynamic therapy (PDT), could greatly benefit from real-time MRT by mapping the temperature change in tissue during laser induced hyperthermia to assess reported enhanced therapeutic effects[3-4]. However, applying this technique in a pre-clinical scanner poses unique setup problems due to coil size constraints and the requirement to correct for magnetic field inhomogeneities which, when left uncorrected, would strongly influence the MR-determined temperature. The aim of this study was to realize an MRT method to monitor the temperature in mice hind limb tumors during hyperthermia for PDT, accurately and in real-time.

METHODS: Experiments: All scans were performed with a BioSpec 70/30 USR system with a 72 mm volume coil (Bruker, Ettlingen, Germany). A Fast Low Angle Shot (FLASH) sequence was employed to obtain the phase images. Scan parameters were as follows: 256x256 matrix, 1 slice, coronal orientation, 1 mm thick, isodistance 0.1 mm, 8x8 cm² FOV, TE/TR 35ms/150ms, flip angle 11 degrees, scan time 38.4s per scan. The phantom setup consisted of a custom heating device, 2% agarose gel phantom, fiber optic temperature probe placed in the lower-center of the phantom (NIST traceable accuracy ≤0.05°C between 20 and 45°C, Opsens, Québec, Canada), a set of custom reference phantom holders, several reference phantoms containing mineral oil (IKEA, Leiden, The Netherlands) and a water bath to heat the phantom between 22 and 27°C (LAUDA-Brinkmann, Delran, NJ, USA). The phantom setup was acclimatized in the magnet bore for 1.5h to reach a thermal equilibrium prior to scanning. The following scan protocol was used:

1. A set of 10 baseline scans were acquired in rapid succession, total acquisition time circa 7.5 min. A global shim of the magnetic field was applied during the first baseline scan.
2. A total of 42 scans were acquired to monitor the temperature changes during heating and cooling at a scan rate of 1 scan per 5 min, total acquisition time approx. 3.5h.

Raw scan data was processed using custom-written MATLAB scripts (version 8.3, The MathWorks, Natick, MA, USA). Phase wraps in the images were unwrapped using the Goldstein, Zebken and Werner's algorithm[5]. The phase in the reference phantoms was linearly interpolated to create a phase correction map to correct for magnetic field inhomogeneities[6]. A 10x10 pixel ROI was used to determine the MR-derived temperature in the center of the image. MR-derived temperature data and fiber optic probe temperature data were statistically analyzed by means of goodness of fit (R^2) and mean square error (MSE).

RESULTS: Figure 1 shows a comparison of the PRFS phase mapping method with no correction map applied (A) and with a correction map applied (B). Note that the globally applied correction map was able to accurately correct for magnetic field inhomogeneities during the entire measurement period of 4h. The R^2 and MSE values given in table 1 indicate a good data correlation and six times decrease in the MSE when using a correction map. Figure 2 shows the correlation between the fiber optic probe measured temperature and the MR-derived temperature with no correction map applied (A) and with a correction map applied (B). Note that an arced symmetric pattern occurs during heating and cooling of the phantom. The arc in this pattern was most likely to be caused by the scan time of ~38s per point, which limits the capability of imaging phase differences during fast temperature changes.

Table 1	Pre-correction	Post-correction
R^2	0.94	0.99
MSE (°C²)	0.17	0.03

DISCUSSION: Phase mapping the PRFS has the ability to image temperature changes in tissue at high spatio-temporal resolution. The phantom data showed that the imaging method is capable of displaying the temperature real-time with great accuracy, even in the presence of magnetic field inhomogeneities. Future research will focus on using the PRFS phase mapping method in combination with a custom 72 mm coil laser setup in a therapy setting with mice.

REFERENCES: [1] Fite et al. PloS One, 2012, 7(4):e35509. [2] Hindman et al. JCP, 1966, 44:4582-4592. [3] Waldow et al. LSM, 1987, 7:12-22. [4] Mang et al. LSM, 1990, 10:173-178. [5] Goldstein et al. RS, 1988, 23 (4), 713-720. [6] Poorter et al. MRM, 1995, 33:74-81.

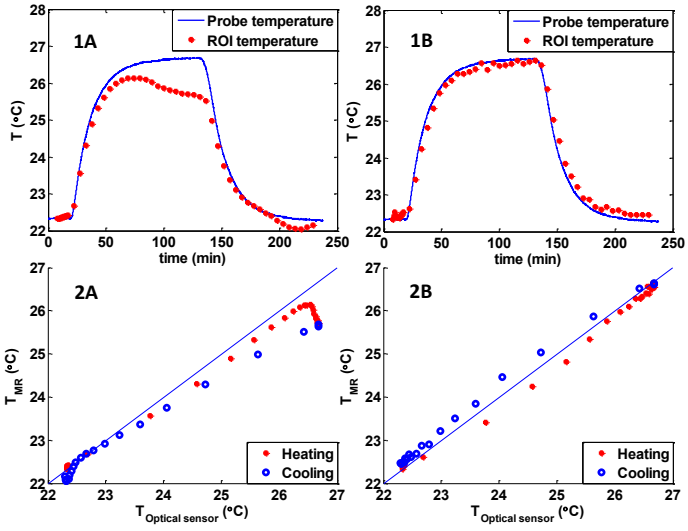

Figure 1: Comparison of the MR-derived temperature with the fiber optic probe temperature without (A) and with (B) a correction map applied. The blue lines and red dots indicate fiber optic probe measured temperature and MR-derived temperature, respectively. Note that the correction map was able to correct temporally separated magnetic field inhomogeneities over a total measurement period of 4h.

Figure 2: Correlation plots of MR-derived temperature (T_{MR}) versus fiber optic probe measured temperature ($T_{Optical\ sensor}$) without (A) and with (B) a correction map applied. Red dots and blue circles indicate the temperature changes during heating and cooling, respectively. The blue line represents the ideal theoretical relationship between the MR-derived temperature and the fiber optic probe measured temperature.

Revisiting the potential of alternating repetition time balanced steady state free precession imaging in the abdomen at 3T

Oliver J. Gurney-Champion[1], Remy Klaassen[2], Jaap Stoker[1], Arjan Bel[3], Hanneke W.M. van Laarhoven[2], Aart J. Nederveen[1], Sonia I. Goncalves[4]

[1]Department of Radiology, Academic Medical Center, Amsterdam, the Netherlands; [2]Department of Medical Oncology, Academic Medical Center, Amsterdam, the Netherlands; [3]Department of Radial Oncology, Academic Medical Center, Amsterdam, the Netherlands; [4]Institute for Biomedical Imaging and Life Sciences, University of Coimbra, Coimbra, Portugal

Targeted audience: Clinical scientists interested in 3D fat-saturation techniques, physicians interested in abdominal MRI

Purpose: Abdominal MR-imaging, for example in pancreatic cancer patients, is challenging as the pancreas is small, prone to respiratory motion and embedded in fat. Therefore, a fast and signal (contrast) to noise ratio (S(C)NR) effective sequence, preferably with fat saturation, is desired. A sequence that offers such properties is the alternating repetition time balanced steady state free precession (ATR-bSSFP). This 3D sequence can be obtained in a single breath hold at a high resolution and S(C)NR.[1] Furthermore, the alternation between different TRs (TR_1, TR_2), together with an adjusted RF phase cycling, modulates the frequency response function and creates broad stop-bands which can be used for inherent fat saturation.[2] Similar to bSSFP, image contrast depends on the ratio between tissue relaxation times, T_1/T_2. Despite the potential of ATR-bSSFP for clinical abdominal imaging, data acquisition strategies are still largely empirical and chosen heuristically. For example, the flip angle (FA) that yields the highest SNR, has been loosely determined for ATR-bSSFP only for $T_1/T_2<6$.[2] Furthermore, the FAs that yield the best fat saturation and contrast to noise ratio (CNR) are unknown. Therefore, the purpose of this research was to determine the optimal settings for $\tau=TR_1/TR_2$ and FA with respect to fat saturation effectiveness and CNR between abdominal tissues at 3T.

Methods: We ran Bloch simulations, using Spin-Bench,[3] to calculate ATR-bSSFP S(C)NR as function of FA (1–90°) and τ (1–3) for different T_1/T_2-ratios (3–50). We also calculated the S(C)NR of conventional bSSFP for comparison.[4] In addition, the CNR for T_1/T_2 from different abdominal organs (liver: T_1/T_2=23, pancreas: 17 and kidney cortex: 15) as function of FA and τ were calculated. We validated simulation results with phantom measurements on a 3T scanner. The phantom consisted of a rack with 14 tubes, one containing peanut oil and the remaining containing gels with different T_1/T_2 values (4–46).[5] The compromise between FA magnitude and SAR constraints limited the FAs to be ≤51° for τ=1, ≤35° for τ=2 and ≤21° for τ=3. We determined the effectiveness of fat saturation experimentally, by taking the ratio between the average signal from the tube containing peanut oil and the average signal of all other tubes, and compared to the fat saturation effectiveness of a Dixon sequence at FA=9°. Finally, in-vivo 3D ATR-bSSFP (1.7×1.7×2 mm^3 resolution, 400×350×95 mm^3 FOV, single breath hold of 19s) data was acquired in two healthy volunteers for different FA and τ values, and in one pancreatic cancer patient using the optimized parameters.

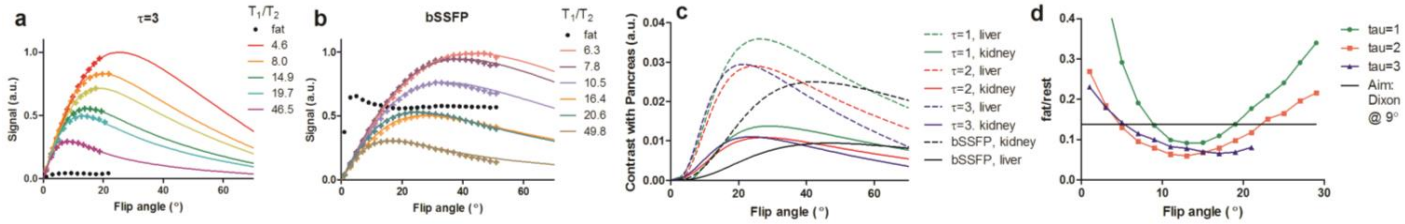

Fig 1: Measurements (crosses) and simulations (lines) of the signal as function of the FA for ATR-bSSFP τ=3 **(a)** as well as bSSFP **(b)** for different T_1/T_2. **c:** Simulated contrast between the pancreas and other organs as function of the FA for τ=1–3. **d:** Ratio of the signal from the tube containing fat, divided by the average signal from all other tubes. The black line indicates this value for Dixon with FA=9°.

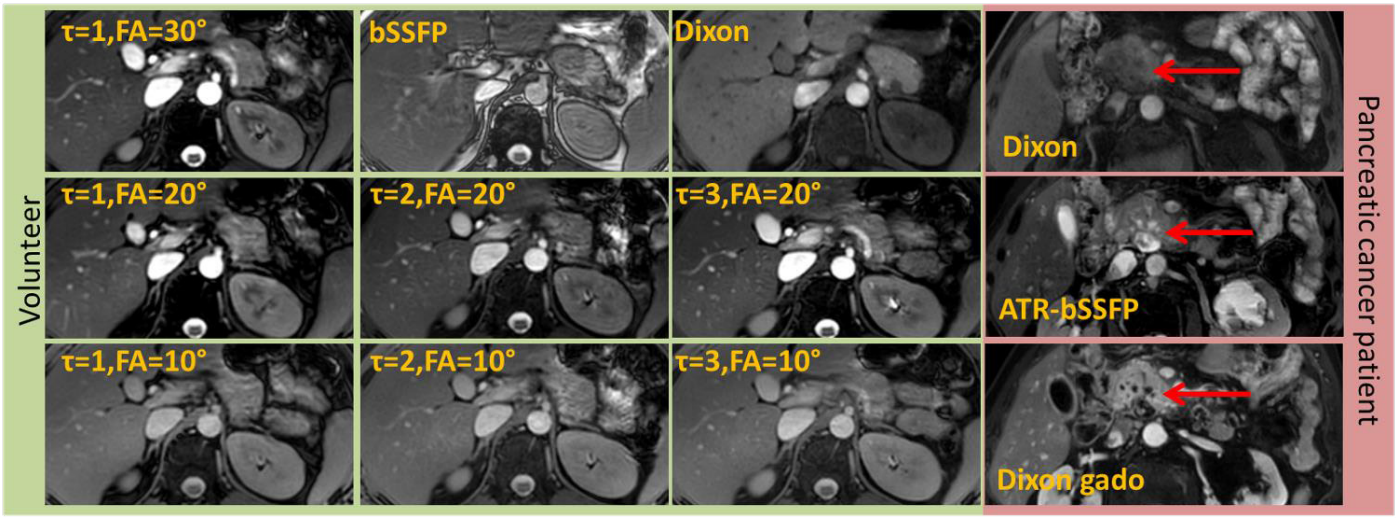

Fig 2: In-vivo ATR-bSSFP, Dixon and bSSFP images in a volunteer (green) and an ATR-bSSFP image without Gadovist compared to a Dixon image prior to and after injection of Gadovist in a pancreatic tumour patient (red). The arrow indicates the pancreas, where ATR-bSSFP had superior contrast over pre Gadovist Dixon.

Results: The simulations agreed with the measurements for all selected values of τ, FA and T_1/T_2 (Fig. 1 a, b). Simulations showed that for typical T_1/T_2 values in the abdomen, the signal as a function of FA is maximum for lower FAs for ATR-bSSFP (11.8°–18.2°) when compared to bSSFP (23.2°–29.0°). Furthermore, the FA value corresponding with maximum signal decreases with increasing τ. Simulations also showed that the FA that allows for the highest CNR varies per organ pair; for the organs investigated it was between 24–30° for τ=1, 22–28° for τ=2 and 20–24° for τ=3 for ATR bSSFP and 40–47° for bSSFP (Fig. 1c: example for pancreas). Experimentally, fat saturation effectiveness was best for τ=3 ATR-bSSFP (Fig. 1d), even outperforming fat saturation effectiveness in Dixon imaging. The in-vivo images showed the best contrast between pancreas, liver and kidneys for τ=3 and FA=20° (Fig. 2), in agreement with simulations. Due to the inherent T_2 contrast, fluid containing structures, like ductuli and cysts, were more pronounced on the ATR-bSSFP compared to the equivalent unenhanced Dixon images. In the pancreatic cancer patient, ATR-bSSFP showed structures in the pancreas as a positive contrast, which on the Dixon image only became visible as negative contrast after contrast injection (Gadovist).

Conclusion: In this study we showed that τ=3 and FA=20° yields the best compromise between contrast and f6at saturation in abdominal imaging. At these settings, the abdomen can be imaged within a breath hold at high resolution, with fat saturation and a T1/T2 contras that allows us to distinguish relevant pathological structures.

References: [1]: S.I. Gonçalves et al. Magn. Reson. Med. **67**(3), 595–600 (2012). [2]: J. Leupold et al. Magn. Reson. Med. **55**(3), 557–65 (2006). [3]: www.heartvista.com/SpinBench [4]: R.R. Ernst. Rev. Sci. Instrum. **37**(1), 93 (1966). [5]: C.M.J. de Bazelaire et al. Radiology **230**(3), 652–9 (2004).

Rapid online multiband RF peak power minimization for CAIPIRINHA and pTX-multi-slice shims by inter-slice phase relaxation

Alessandro Sbrizzi[1], Benedikt Poser[2], Desmond Tse[2], Hans Hoogduin[1], Peter R. Luijten[1], Cornelis A.T. van den Berg[1]

[1]Imaging Division, University Medical Center, Utrecht, the Netherlands
[2]Maastricht University

Target Audience MRI physicists and engineers.

Purpose Current multi-slice excitation schemes are based upon the superposition of single-band RF waveforms[1,2]. The different frequencies corresponding to different slice excitations, can constructively interfere, resulting in high peak powers. Through relaxation of the phase of the target magnetization profile, it is possible to minimize the constructive interference and thus to obtain lower peak amplitude[3]. A minimization problem has to be solved that considers the phase of each slice as part of the optimization. The algorithm from [3] requires a large amount of restarts (5000) and the minimization over a CAIPIRINHA phase cycling scheme and/or a pTx amplitude/phase shimming settings is not taken into account. In this work, we cast the problem as a linear objective function with quadratic equality and inequality constraints. This can be solved on the fly. Furthermore, the achieved peak power is lower than the existing phase relaxation method[3] and control of RF peak power over the whole CAIPIRINHA excitation scheme and/or a whole multi-channel transmit system with channel/slice dependent amplitude/phase shimming settings is obtained.

Theory Given a single band RF pulse waveform $b(t)$, the RF waveform that excites N slices at locations z_n (n indicates the slice) is given by Eq. (1). If a CAIPIRINHA phase cycling scheme, or a pTx channel system are employed, there are P pulses, each for a given phase cycling pattern or channel, respectively. The index p denotes the phase scheme or the channel for, respectively, the CAIPIRINHA and pTx case. Denoting by $\psi_{p,n}$ the desired phase (for each pulse p and each slice n), and by ϕ_n the interslice phase relaxation, the resulting p-th pulse is given by Eq. (2). Note that in Eq. (2), $\alpha_{p,n}$ denotes the amplitude shimming setting, thus for the CAIPIRINHA setup: $\alpha_{p,n}$=1. The minimum peak RF problem is then given by Eq. (3) and it returns a vector of optimal inter-slice phases ϕ=[ϕ_1 … ϕ_N]. This can be rewritten in matrix/vector form (Eq. 4) where **u** is the complex vector whose arguments are the inter-slice phases and **A** include all the given terms b, G, z_n, $\psi_{p,n}$ and $\alpha_{p,n}$. This particular problem can be rewritten as a linear program with quadratic inequality and equality constraints[4] given by Eq. (5). The vector **y** contains the real and imaginary part of **u** and thus the inter-slice phases. For lack of space, the details are omitted.

$$f(t) = \sum_{n=1}^{N} b(t) e^{i\gamma G t z_n} \tag{1}$$

$$f^p(t) = \sum_{n=1}^{N} \alpha_{p,n} b(t) e^{i\gamma G t z_n} e^{i(\psi_{p,n}+\phi_n)} \tag{2}$$

$$\arg\min_{\phi} \max |f^p(t)| \quad \text{for } t \in [0,T] \text{ and } p = 1,\ldots,P \tag{3}$$

$$\arg\min_{\mathbf{u}} \max |\mathbf{A}\mathbf{u}| \quad \text{with } |u_j| = 1 \tag{4}$$

$$\begin{aligned} &\text{minimize } \mathbf{c}^T\mathbf{y} \\ &\text{such that } \mathbf{y}^T\mathbf{Q}_i\mathbf{y} \le 0, \quad \forall i \\ &\qquad \mathbf{y}^T\mathbf{P}_n\mathbf{y} - 1 = 0, \quad n = 1,\ldots,N \end{aligned} \tag{5}$$

$$\Psi = \begin{pmatrix} 0 & 0 & 0 & 0 & 0 & 0 \\ 0 & \frac{\pi}{2} & \pi & \frac{3\pi}{2} & 0 & \frac{\pi}{2} \\ 0 & \pi & 0 & \pi & 0 & \pi \\ 0 & \frac{3\pi}{2} & \pi & \frac{\pi}{2} & 0 & \frac{3\pi}{2} \end{pmatrix} \tag{6}$$

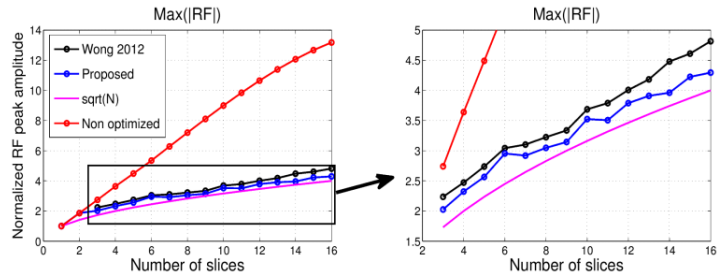

Fig 1 *Exp.1: peak amplitudes for multi-band configurations corresponding to N =2,… ,16. Values are normalized with respect to the peak amplitude of N = 1. For reference, also the theoretical minimum value √N is shown.*

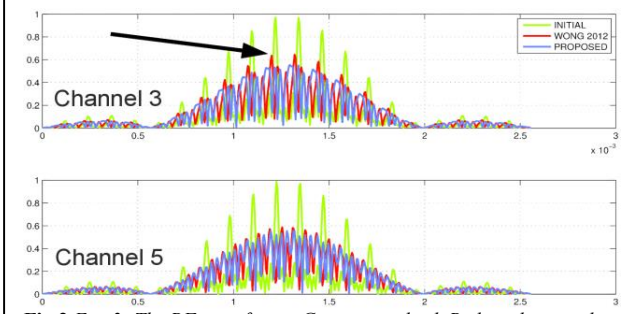

Fig 2 *Exp.3: The RF waveforms. Green: standard, Red: with inter-slice phase from [3], Blue: proposed.*

Methods We perform three inter-slice phase design experiments: *Exp.1:* multiband excitation for N = 2,3,…,16 (same as [3]), *Exp.2*: a CAIPIRINHA excitation scheme for phase cycling schemes given by the matrix $\Psi(p,n)= \psi_{p,n}$ given in Eq. (6); *Exp.3:* a Dynamic RF shimming problem for an 8 channel birdcage head-coil at 9.4T. The amplitude/phase shimming settings are optimized per channel p per slice n for a ROI covering the back of the brain (see Fig. 3). We consider a 6 slice excitation (SMS factor = 6), 3-lobes sinc pulse, 2mm slice thickness, slice distance: 16mm. Computations are carried out with Matlab on a desktop PC.

Results *Exp. 1:* Figure 1 shows the peak amplitudes for experiment 1. The computation time of each configuration is in the order of seconds and never longer that 10s. In the same figure, also the values obtained by Wong in [3] are reported. The proposed method achieves lower peak amplitude values for each multi-band excitation experiment and it approaches the √N curve. *Exp 2:* The peak amplitude corresponding to the CAIPIRINHA phase cycling scheme Ψ is 12.1μT. For comparison, the peak amplitudes obtained by the standard RF pulses for the same cycling scheme is 23.4μT. A reduction of approximately 50%. *Exp 3:* Finally, two of the eight RF waveforms for the pTx setup are shown in Fig. 2, normalized to the maximum peak of the standard (no phase relax) setup. Also the waveforms obtained by the phase relaxation from [3] are shown. The RF peak amplitude is reduced by 45% with respect to the standard setup. As indicated by the arrow, a 15% reduction is achieved with respect to the RF waveforms from [3]. To check the scanner implementation, the images obtained from the two phase relaxation methods are shown in Fig. 3. They look indeed the same, as they are supposed to be.

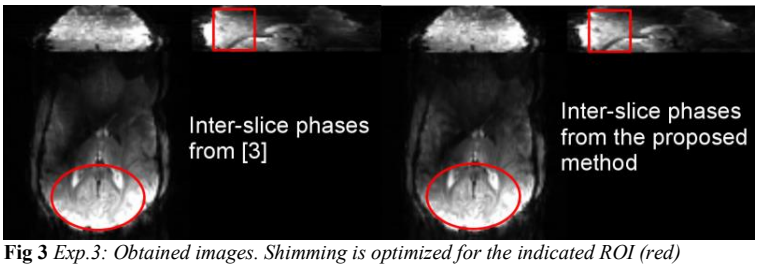

Fig 3 *Exp.3: Obtained images. Shimming is optimized for the indicated ROI (red)*

Discussion The minimum peak RF problem is generalized to the CAIPIRINHA and pTx setups. The reduction in peak RF is drastic with respect to standard design and larger than obtained in [3]. The compact formulation allows for quick computation and thus online implementation. This is essential for patient specific amplitude/phase shimming settings and CAIPIRINHA scans.

Conclusion Inter-slice phase relaxation is cast as a linear program with quadratic constraints and applied to more general setups as CAIPIRINHA and pTx shimming obtaining on-the-fly and patient-specific optimal inter-slice phase settings. **References** [1] Muller S. Magn Reson Med 1988. [2] Breuer FA et al. Magn Reson Med 2005, [3] Wong E. ISMRM 2012 p. 2209. [4] Boyd S and Vandenberghe L. Convex Optimization. 2004.

A fast method for T1 and T2 mapping of cerebrospinal fluid at 7T

Jolanda Spijkerman[1], Esben Petersen[1], Peter Luijten[1], Jeroen Hendriksen[1], Jaco Zwanenburg[1]

[1]Department of Radiology, University Medical Center, Utrecht, the Netherlands

Purpose: In previous studies it has been shown that brain perfusion decreases in Alzheimer's Disease (AD) patients [1], which could affect the oxygen content of cerebrospinal fluid (CSF) and perivascular fluids (PVF). Since both T_1 and T_2 of CSF (and PVF) depend on its oxygen level [2], T_1/T_2 mapping of CSF could potentially give important information on its oxygen content. However, at this point there is no fast, reliable method available to perform T_1/T_2 mapping in the brain specifically for CSF and PVF at higher field strengths. The purpose of this study was to develop a method for T_1/T_2 mapping of CSF and PVF for 7T MRI.

Methods: In Qin (2011) [3] the use of an MLEV pulse sequence for CSF imaging is described for mapping of the CSF volume fraction. We extended this method to perform T_1 and T_2 mapping, by varying the delay time (T_{delay}, for T_1) or the effective echo time (TE_{prep}, for T_2), which depends on the MLEV-spacing τ and the number of MLEV pulses. Table 1 summarizes the used variables. The readouts after the MLEV preparation consisted of a single shot 2D SE-EPI (4x4 mm^2, slice thickness 6 mm, SENSE 2.3). Both B_0 and B_1 dependency of the method were characterized by applying the method to a water phantom and using an extra linear shim gradient to induce +/- 250 Hz B_0 variation in the background. Reference T_1 and T_2 maps were made with a Look-Locker and a Spin Echo sequence, respectively (without the extra shim gradient). Four volunteers (1 male, aged 24-33) were scanned with the MLEV pulse sequence. All experiments were performed on a 7T MR scanner (Philips), using a volume transmit, and 32 channel receive coil (Nova Medical).

Results: For the water phantom the reference T_1 and T_2 were (mean±sd) 2510±15ms and 1581±11ms, respectively. The T_1 and T_2 resulting from the MLEV scans were 1972±186ms and 1382±197ms. The results of the B_0/B_1 characterization are shown in Figure 1. For the volunteers the mean T_1 and T_2 resulting from the MLEV scans were 4261±270ms and 918±34ms in the ventricles, and 3470±89ms and 754±32ms in the peripheral subarachnoid spaces. The T_1 and T_2 were homogeneous in both the ventricles and the subarachnoid spaces, for all volunteers. $\Delta B_0/B_1$ was approximately 0Hz/110% in the ventricles and 20Hz/70% in the subarachnoid spaces.

Discussion: The results show that the proposed method is relatively insensitive to B_1 variations, but T_2 scans in particular show sensitivity for B_0 variations; the method can be applied at 7T for B_0 +/-50%. Compared to the reference values, both T_1 and T_2 of the phantom were underestimated. The in vivo results were comparable to previous studies [3, 4]. A possible T_1/T_2 underestimation may not be a problem for comparison between groups of subjects or between regions within a subject. As B_0 and B_1 were within the range in which the method performs well, the results may suggest that the oxygen level in the peripheral CSF is different from that in the ventricles [2]. However, partial volume effects from the parenchyma in combination with the lower B_1 may play a role as well in the lower T_1 and T_2 in the peripheral CSF. Future work is needed to assess reproducibility and to gauge the effects of partial volume and oxygen dependence and/or protein content, and the effect of partial volume effects between tissue and CSF in the presence of reduced B_1 needs to be studied by simulations.

Conclusions: The MLEV method is suitable for T_1/T_2 mapping of CSF, also at high field strengths. This method is relatively insensitive to B_0 and B_1 variations.

Acknowledgment: This work was supported by the European Research Council, ERC grant agreement n°337333.

References: [1] Binnewijzend MA, et al., Eur Radiol, 2014; [2] Zaharchuk G, et al., Magn Reson Med, 2005; [3] Qin Q, Magnetic Resonance in Medicine, 2011; [4] Rooney WD, et al., Magn Reson Med, 2007

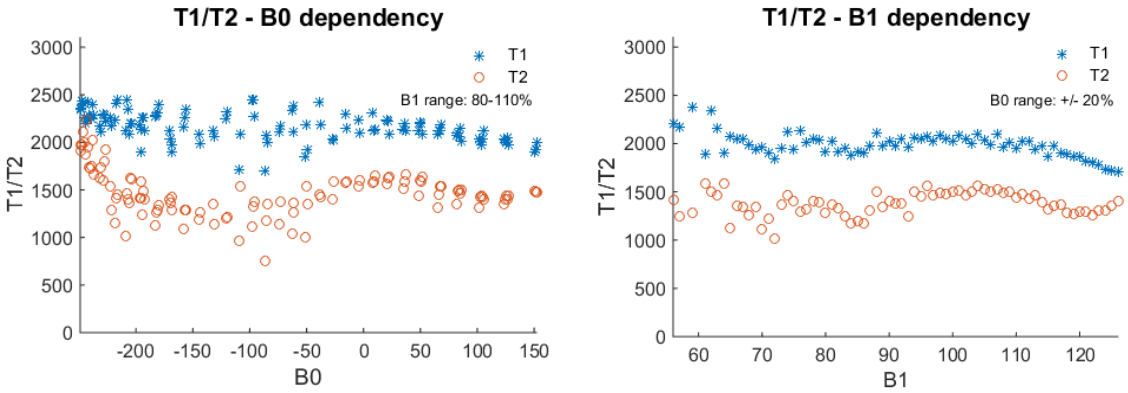

***Figure 1**: T_1/T_2 measurements in the water phantom showed that the method yielded consistent values for B_1 in the range of 80-110% of its nominal value, and for $B_0 \leq 20$ Hz off-resonance. Each point in the B_0-dependency graph represents the mean T_1 or T_2 over 1Hz bins for B_0, taking only pixels with 80-110% B_1. Each point in the B_1-dependency graph represents the mean T_1 or T_2 over 1% bins for B_1, taking only pixels with $B_0 \leq 20$ Hz off-resonance.*

***Table 1**: The parameters used to perform T_1/T_2 mapping with the MLEV method*

	T_{delay} [ms]	nr MLEV-pulses	τ [ms]	Scan time (single slice)
T_1 mapping	30000, 15000, 7500, 3750, 1875, 900, 450, 225, 100, 30	8	75	1:34 min
T_2 mapping	15000	0, 4, 8, 16, 32	75	1:45 min

Echo based correction of multiband multi-echo EPI improves task fMRI at 7T

Rasim Boyacioglu[1], Jenni Schulz[1], Markus Barth[2], David Norris[1]

[1]Donders Institute for Brain, Cognition and Behaviour, Radboud University Medical Center, Nijmegen, the Netherlands
[2]Centre for Advanced Imaging, The University of Queensland, Brisbane, Australia

Target audience: MR physicists, Neuroscientists, Data analyzers

Purpose: Recently we have implemented a multiband[1] (MB) multi-echo (ME) sequence and showed improvement in sensitivity at 7T for resting state (RS) fMRI with respect to standard ME[2] using combined echoes. The addition of FIX correction to the analysis framework also resulted in increased sensitivity and specificity leading to the discovery of additional networks that could not be observed with ME data and without FIX correction. In this study we explore the possibility of an automated echo based FIX correction scheme, i.e. using the uncombined echoes and compare its performance with the previously used FIX correction on MBME task fMRI data.

Methods: RS data (eyes open, 5 min. both acquisitions) and color-word Stroop task fMRI data (7 min.) were collected for 10 subjects (with informed consent) at a 7T Siemens scanner (Siemens Healthcare, Erlangen, Germany) with a 32 channel head coil. Acquisition parameters are summarized in Table 1. Reconstruction of MB data was performed offline in Matlab using a SENSE/GRAPPA reconstruction[3].

Table 1. Acquisition Parameters

	TR (s)	TEs (ms)	In plane GRAPPA	SMS factor	Excitation FA	BW (Hz/Px)	Slice gap	Res.(mm)
MBME task	0.74	11,23	3	3	40	2520	17%	3.5 isotropic
MBME RS	0.74	26,48		3				

Prior to each ICA the following preprocessing steps were applied: spatial smoothing (5 mm kernel), drift removal, MCFLIRT motion correction. All ICAs were carried out with Melodic (v3.14, http://www.fmrib.ox.ac.uk/fsl/) with automatic dimensionality estimation. Detection and removal of non-BOLD ICs was carried out with FSL_FIX[4] (http://fsl.fmrib.ox.ac.uk/fsl/fslwiki/FIX). Two different analysis pipelines are illustrated in Figure 1 and 2. In the standard case echoes were combined and then a standard FIX training dataset was used for the detection of noise ICs. In the second pipeline, for the echo based correction prior to echo combination of MBME task data, each echo time series was cleaned with FIX correction. The training datasets were obtained from the echoes of RS data. To ensure maximum specificity only the ICs with clear artifact characteristics were manually labeled as noise components for the creation of training datasets. The group level analysis of the two correction schemes were compared using a paired t-test.

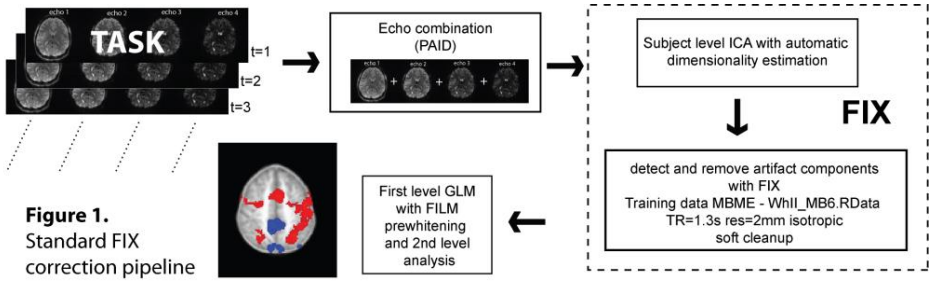

Figure 1. Standard FIX correction pipeline

Results & Discussion: Figure 3 shows the voxels which are **only** significantly activated for MBME with echo based FIX correction on a group level (N=10). The first row depicts the recovery of frontal clusters which are known to be involved for the Stroop task[5]. This improvement is most likely due to the better separation of noise sources that would be masked at later echoes and using a combined echo approach. As the earliest echo in the ME acquisition contributes most in regions with short T2* (e.g. inferior frontal), an improvement can be realized with an echo based correction scheme (yellow arrows). In addition, many other clusters (visual and parietal in row 2 and 3 respectively) start appearing with echo based correction. Using a commonly employed spatial resolution, MBME combined with echo based FIX correction offers improvements in the analysis of task fMRI data next to the commonly known advantages such as low distortion, the potential to acquire data over a broad range of T2* values and automatic elimination of non-BOLD ICs.

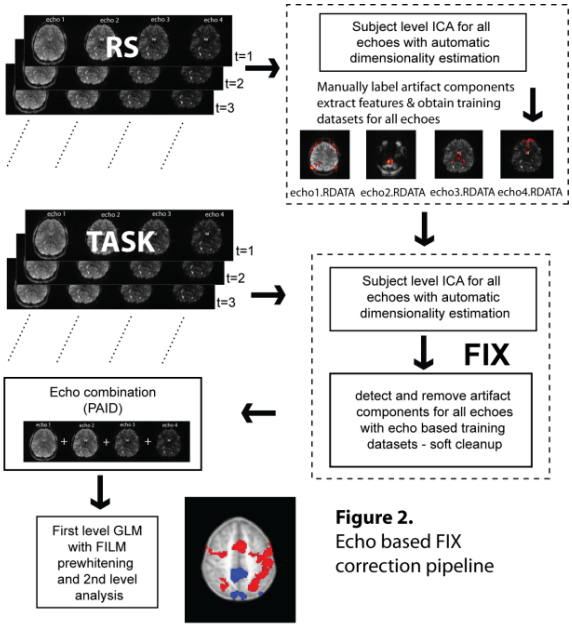

Figure 2. Echo based FIX correction pipeline

Conclusion: We have implemented a high temporal resolution (0.74s) MBME EPI sequence and showed that an echo based noise correction technique improves sensitivity particularly for activation in areas with susceptibility gradients.

References: 1) Larkman et al., JMR 2001. **2)** Boyacioglu et al., ISMRM 2014, p1502. **3)** Blaimer et al., JMRI 2006. **4)** Salimi-Khorshidi, Neuroimage 2014. **5)** Boyacioglu et al., Neuroimage 2014.

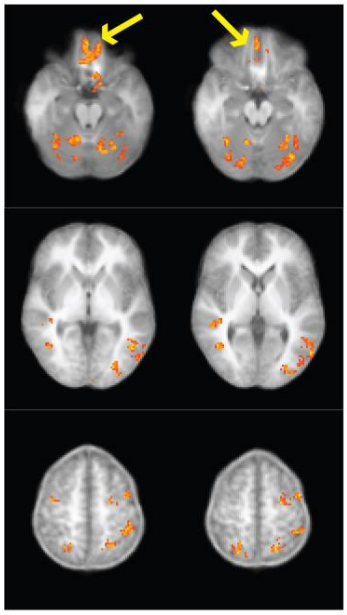

Figure 3. Examples of slices where echo based correction improves sensitivity with respect to standard correction

Characterization of respiratory induced B0 fluctuations in the breasts at 7 tesla

Tijl van der Velden[1], Vincent Boer[1], Peter Luijten[1], Dennis Klomp[1]

[1]Department of Radiology, University Medical Center, Utrecht, the Netherlands

Purpose: To spatially characterize B_0 fluctuations in the breast at 7 tesla.

Introduction: Breast MR examinations are likely to be influenced by B_0 and thereby f0 fluctuations caused by the respiratory cycle. Especially at higher field strengths, like 7 tesla, it is known that that the field or f0 fluctuations can be as much as 70 Hz[1]. These fluctuations can result in ghosting and blurring artefacts when long echo time imaging is performed and splitting of peaks in MR spectroscopy. However, until now these fluctuations were only assessed with B_0 maps with low resolution and limited field of view[1] or with field probes outside the tissue itself[2]. It is unknown what field fluctuations occur over both breasts and what the intra and inter subject variability is in the distortions. In this study we have acquired 3D B_0 maps which were, retrospectively, rearranged into different respiratory phases. Spatially varying B_0 fields were fitted to these data up to the 3rd order Laplace's spherical harmonics to investigate whether training sets may be an option to compensate for these dynamic field distortions.

Methods: Five healthy female volunteers were scanned at a Philips Achieve 7 tesla scanner (Philips Healthcare, Cleveland, OH, USA) equipped with a bilateral transmit/receive coil (MR Coils BV, Drunen, the Netherlands). From every volunteer, the raw data of two times 50 3D B_0 maps were acquired. Respiratory information was recorded simultaneously with a respiratory belt.
From the raw data, five k-spaces were constructed, each representing a different respiratory phase. The information of the respiration belt was pass-band filtered on 0.11 Hz to 0.49 Hz [3] and binned into five equal amplitude intervals per respiratory interval. Every acquired k-line was placed into one of the five k-spaces, based on the information from the respiration belt[4]. If multiple k-lines with the same phase encoding were binned into the same respiratory phase, complex averaging of these lines was performed. If any, k-lines from neighbouring respiratory phases were used to fill empty spaces in k-space. Reconstructions were performed in Matlab (Mathworks, Natick, MA) using the ReconFrame package (Gyrotools, Zurich, CH). From the reconstruction, relative B_0 fluctuations between the five different respiration phases was quantified by fitting up to the 3rd order spherical harmonic functions to the data using a least square error approach.

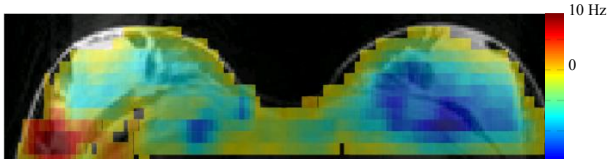

Figure 1: Example of a binned 3D B_0 map representing a field deviation caused by the respiratory cycle.

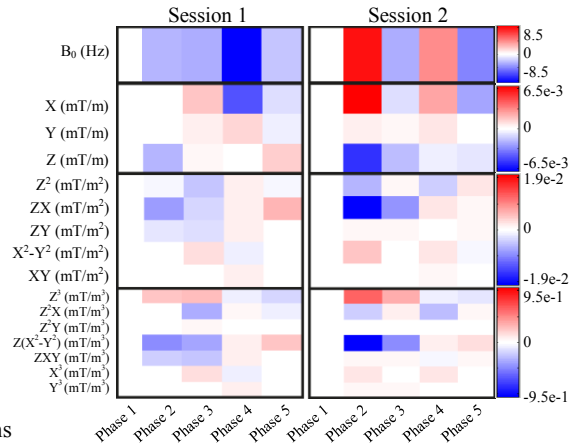

Figure 2: Shim variation in the breasts over the respiratory cycle for 1 volunteer for both sessions. Variations between the two sessions indicate that shimvariations are not reproducible over time within the same subject.

Results: An example of a binned B_0 map, representing a single respiratory phase, is displayed in figure 1. The changes over the respiratory phases for one subject is displayed in figure 2, showing intra subject variability. The maximum shim variations for each session is shown in figure 3, where it is seen that there is large variations between subjects, but in general there is a contribution of the ZX, Z^3, Z^2X and $Z(X^2-Y^2)$ terms.

Discussion and conclusion: As there is a large inter and intra subject variability in the field fluctuations, it is not expected that non-subject specific or subject specific training sets could account for these fluctuations. Therefore, a continuous monitoring system will be required when real time or retrospective correction are desired, such as field probes[5] or including navigator echoes with spatial encoding[6]. However, as some terms contribute much more to the distortions than others in all volunteers, a limited set of terms can be used when real time or retrospective correction is applied to reduce ghosting and blurring.

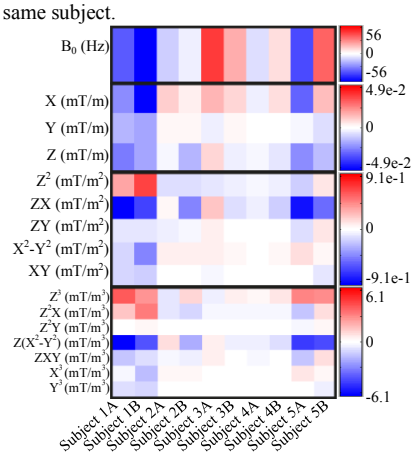

Figure 3: Maximum shim variation over the respiratory cycle for each session. The shim amplitude differs between subjects and sessions. Shims containing terms in the anterior-posterior direction (X) and feet-head direction (Z) are more profound than the left-right term (Y).

References:

[1] Boer et al. MRM 2012
[2] van der Velden et al. ESMRMB 2013, #85
[3] van Gelderen et al. MRM 2007
[4] Stemkens et al. Int. J. of Radiation Oncology, Biology, Physics, 2014
[5] De Zanche et al. MRM 2008
[6] Versluis et al. MRM 2012

Accelerating Bloch equation simulations by time-domain reduction of the RF pulse waveform

Willem van Valenberg[1], Gerard L.G. Sleijpen[2], Cornelis A.T. van den Berg[1], Peter R. Luijten[3], Alessandro Sbrizzi[1]

[1]Department of Radiotherapy, University Medical Center, Utrecht, the Netherlands
[2]Department of Mathematics, University Medical Center, Utrecht, the Netherlands
[3]Department of Radiology, University Medical Center, Utrecht, the Netherlands

Target Audience MRI physicists and engineers.

Purpose A large number of MR based research requires evaluating the response of a repeated radiofrequency (RF) pulse or pulse sequence through the Bloch equation. This is especially the case for MR fingerprinting[1] (MRF) which depends on many pseudorandom pulse sequence simulations to generate the lookup tables required for parameter estimation. Simulation time scales with the number of discretized time and spatial points, which means that the small time step on which RF pulses are generally defined, in combination with the demand for high resolution images, leads to heavy computational work. While the spatial dimension can be reduced by parallelizing calculations, the time domain requires a different approach. In this work, the responses of full RF pulses are accurately described using reduced pulses, defined on much fewer intervals, greatly reducing simulation time. Two reduced pulse types were designed and tested: the interpolated full pulse, which is expected to approximate smooth RF shapes well, and an optimized reduced pulse aimed at increasing accuracy.

Methods The reduced pulse has to approximate the response of the full pulse for a range of T_1, T_2, B_1^+ and ΔB_0 values. Therefore, we start by calculating the response of the full RF pulse with a slice-selecting gradient for 500 different test cases with parameters taken from uniform distributions with $|B_1^+| \leq 1$ and random phase, $\Delta B_0 \in [-500,500]$ Hz, $T_1 \in [0.4,1.4]$ s, and $T_2 \in [0.02,0.12]$ s. Per test case, the full pulse is simulated for 11 different frequencies, uniformly sampled in the excited slice, and the magnetization at the end of the pulse is marked as the target response. The accuracy of the response of a reduced pulse is quantified by the mean squared error (MSE) with the target response. The first reduced pulse is created by interpolating the full pulse on a coarse grid, reducing the number of time points from 2500 to 15. The second reduced pulse is calculated by using the built-in *fminunc* function of Matlab (Mathworks) to minimize the MSE over all reduced pulse shapes, taking the interpolated pulse as initial guess. This method was applied to RF pulse envelope shapes of different complexity: a Gaussian, and two sinc-shaped pulses with either two (*sinc*(2)) or eight (*sinc*(8)) side lobes. To validate the method, each pulse was tested with the simulation of two sequences: a balanced SE-EPI, and a pseudorandom sequence with randomly distributed repetition times and flip angles between respectively 10 and 15 ms, and 0 and 90 degrees. Both sequences have cartesian readout with 32 x 32 resolution and 8 acquisitions. These sequence simulations were done on a 4CPUs @3.30GHz PC, and the MSE of the response was calculated at the start of each readout.

Results Each optimized pulse was calculated between 60 and 100 seconds. Fig. 1 shows the waveforms of the full, interpolated and optimized *sinc*(2) pulse. For all pulse shapes the absolute difference between interpolated and optimized pulse was small. However Fig. 2 and 3 show that for most cases the optimized pulse has at least two orders of magnitude more accuracy. For the *sinc*(8) pulse, increasing the number of time points from 15 to 21 greatly improved results, especially for the optimized pulse. Simulating the SE-EPI sequences with a full pulse took at least 18 minutes while all 15 step pulses took only around 15 seconds, an acceleration factor of about 72. Taking 21 time points only led to a slight increase of simulation time to 17.6 seconds. For the pseudorandom sequence the speedup was 48 for 15 time points, and 41 for 21.

Discussion We have seen that the simulation time for MRI sequences can be drastically lowered by employing a reduced pulse. Small changes in reduced pulse shape led to large variation in the response approximation, indicating the need for optimized pulses for accurate sequence simulation. In order to describe the response of complex full pulse shapes with high precision, reduced pulses might need just a few more time points, keeping the acceleration factor for the simulation of the whole sequence nearly the same. The decrease in simulation time can have a positive impact in MRF research by reducing the computation time required for lookup table construction.

Conclusion The MRI sequence simulation time is drastically shortened by employing reduced pulses, whose responses accurately describe those of the full pulses.

References [1] Ma, Dan, et al. "Magnetic resonance fingerprinting." Nature 2013.

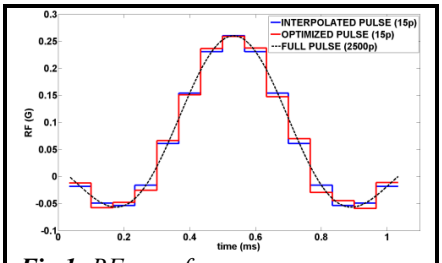

Fig 1: RF waveforms

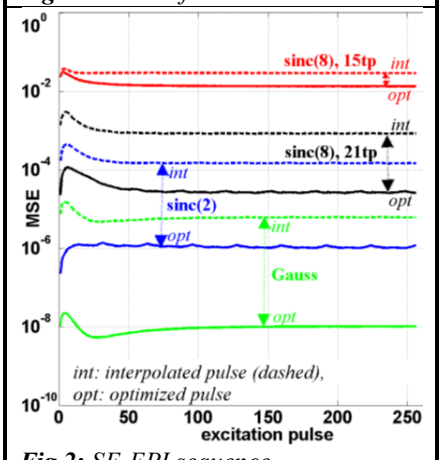

Fig 2: SE-EPI sequence

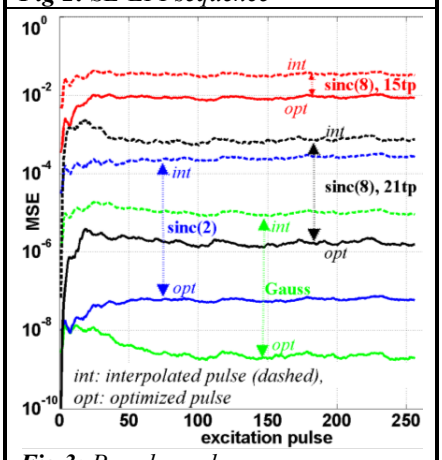

Fig 3: Pseudorandom sequence

Olefinic fat suppression in skeletal muscle DTI with combined 6- and 2-point dixon

Jedrzej Burakiewicz[1], Melissa T. Hooijman[1], Erik H. Niks[2], Jan J.G.M. Verschuuren[2], Andrew G. Webb[1], Hermien Kan[1]

[1]Department of Radiology, Leiden University Medical Centre, Leiden, the Netherlands
[2]Department of Neurology, Leiden University Medical Centre, Leiden, the Netherlands

Purpose: Quantitative MRI methods used in skeletal muscle such as Diffusion Tensor Imaging (DTI) require robust fat suppression [1]. This is particularly important in patients with muscular dystrophies, where significant fat infiltration of the muscle tissue is a common pathological feature. Presence of olefinic fat, often not suppressed by standard fat suppression methods, can have a large influence on quantitative DTI measurements [1]. Two methods were proposed to eliminate the olefinic fat signal in muscle tissue. Williams et al. [1] use spectral fat saturation. While usable in many applications, this technique reduces water signal by approximately 10% [1] and is susceptible to main magnetic field (B_0) inhomogeneities. Hernando et al. [2] use a chemical-shift encoded method. While more robust against B_0 inhomogeneities, it requires complex data acquisition, which enforces the use of longer echo times or causes loss of resolution in phase domain as a result of partial Fourier acquisition while using potentially unstable reconstruction with model fitting.In this study we propose an adapted method based on the latter approach which offers clinically acceptable resolution with shorter TE and significantly simplified reconstruction.

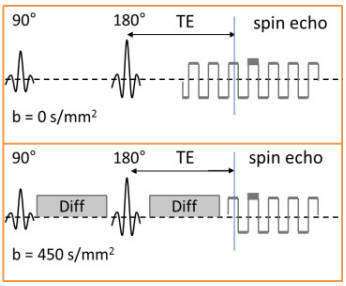

Fig. 1 Sequence diagram. Only magnitude data is needed from diffusion-weighted acquisition, allowing partial Fourier to compensate for the duration of diffusion gradients.

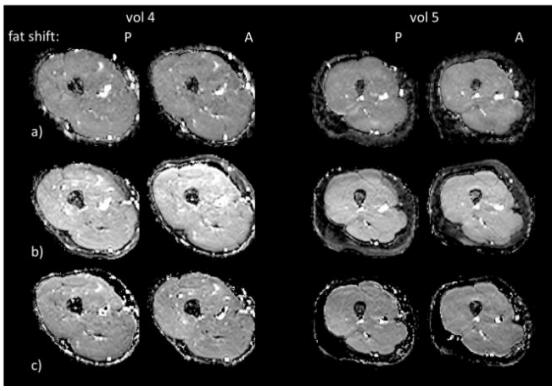

Fig. 2. Sample of DTI parameters (MD) calculated from images with olefinic fat suppression with a) fat saturation+SSGR, b) SSGR only, and c) Dixon + SSGR. Main fat is suppressed with SPAIR + SSGR in all acquisitions. To compare areas with and without presence of fat, fat shift direction is switched between A and P. Visual inspection shows good fat suppression.

Methods: Acquisitions were performed on a 3T Philips Ingenia system. 5 healthy volunteers were scanned (upper leg, unilateral), and informed consent was obtained from all participants. A standard spin-echo planar imaging DTI sequence with Spectrally Adiabatic Inversion Recovery (SPAIR) and Slice Selection Gradient Reversal (SSGR) fat suppression was modified to allow chemical-shift encoding. Diffusion-free (b=0) images were acquired with 6 shifted echoes (-1.05 ms to 9.38 with step of 2.08 ms). Diffusion-weighted images (b>0) were acquired with 2 shifted echoes (0 ms and 5.2 ms: in- and out-of-phase water-olefinic fat signal). b>0 acquisitions were repeated twice for purposes of signal averaging, and partial Fourier phase encoding was used (factor 0.69) to reduce TE. No partial Fourier was used in b=0 acquisition while keeping TE the same in both b=0 and b>0(Figure 1). Other typical acquisition parameters were: TE 50 ms, TR 3000 ms, 12 slices, voxel size 2 x 2 x 6 mm, b-value of 450 s/mm^2 , 6 diffusion directions. To further reduce TE, parallel imaging was used (SENSE, factor 1.7). For validation purposes, each acquisition was repeated with different fat shift directions, anterior (A) and posterior (P). Acquisition with similar parameters was performed in 2 volunteers using the triple fat suppression (triple fs) method proposed in [1].
In the reconstruction, initial olefinic fat separation was performed with 6-point IDEAL tuned to the resonant frequency of olefinic fat (90 Hz at 3 T) on b=0 images. b>0 magnitude images were reconstructed from in-phase and out-of-phase magnitude images. Ambiguity between water and fat [3] was resolved using a fat fraction map generated from reconstructed b=0 images and corrected to include diffusion weighting. Mean Diffusivity (MD) was calculated from reconstructed images and compared in a region of overlap in vastus lateralis.

Results: Sample images reconstructed with the proposed method are shown in Fig. 2, along with images using only SPAIR and SSGR, and triple fs. Visual inspection shows successful olefinic fat suppression, which is confirmed in quantitative measurements in water-fat overlap region (Table 1). Difference in MD calculated with and without overlapping fat in the Dixon-based method shows improvement compared to SPAIR+SSGR only, and comparable to triple fs in the 2 volunteers where this method was included. Dixon methods displays slightly higher standard deviation, possibly due to the method's susceptibility to motion, particularly close to the edge of the tissue: movement between Dixon acquisitions will prevent fat signal on the edge from cancelling out, resulting in large misestimation of MD.

Method/Dir	Vol 1	Vol 2	Vol 3	Vol 4	Vol 5
triple fs A	----------	----------	----------	1.74 ± 0.15	1.70 ± 0.13
triple fs P	----------	----------	----------	1.74 ± 0.14	1.75 ± 0.12
SPAIR SSGR A	2.27 ± 0.15	2.03 ± 0.19	1.98 ± 0.22	2.24 ± 0.24	2.04 ± 0.20
SPAIR SSGR P	2.23 ± 0.18	2.09 ± 0.17	2.07 ± 0.14	2.39 ± 0.19	2.14 ± 0.14
Dixon A	1.71 ± 0.19	1.53 ± 0.19	1.54 ± 0.15	1.88 ± 0.20	1.67 ± 0.18
Dixon P	1.68 ± 0.46	1.49 ± 0.37	1.49 ± 0.28	1.82 ± 0.32	1.61 ± 0.25

Table 1. Quantitative measurements (MD) in a small water-fat overlap region in the vastus lateralis, averaged over 12 slices for each volunteer and shown for both fat shift directions. Difference between A and P measurements in the proposed (Dixon) method is comparable to triple fat suppression and generally lower than SPAIR + SSGR only. In addition, SPAIR+SSGR appears to overestimate MD. Higher standard deviation in Dixon can be attributed to sensitivity of the method to motion near the edges.

Discussion: Use of Dixon for olefinic fat suppression results in greater robustness of the method against B_0 inhomogeneities and potentially allowing for acquisitions with larger field of view than the triple fs method. It also offers much better resolution compared to method proposed by Hernando et al. as well as simplified and more stable reconstruction, at the cost of being more susceptible to motion around the edges of the imaged area.

Conclusion: We demonstrated an improved approach to suppressing olefinic fat signal in muscle DTI which in comparison with previously described methods allows for shorter echo times and potential robustness to B_0 inhomogeneities typical of Dixon methods, while simplifying the reconstruction process and maintaining good standard of quantitative results.

Acknowledgments: This project has received funding from the European Union's Seventh Framework Programme for research, technological development and demonstration under grant agreement no. 602485.

References: [1] Williams et al. 2013, JMRI 38:1292-7; [2] Hernando et al. 2011, MRM 65:692-701; [3] Glover 1991, JMRI 1:521-530

Frequency offset method offers bias-field insensitive quantification of MPIO-labeled endogenous stem cell migration

Dimitri Roose[1], Maarten Naeyaert[1], Zhenhua Mai[1], Johan Van Audekerke[1], Marleen Verhoye[1]

[1]Bio-Imaging Lab, University of Antwerp, Antwerpen, Belgium

Target audience:

Purpose: Micron-sized paramagnetic iron oxide particles (MPIO) induce excellent negative contrast in T_2*-weighted MR images. However, the negative contrast does not exactly represent the size, shape and location of the superparamagnetic nanoparticles, due to the blooming artefact. Another issue is that negative contrast is less conspicuous than positive contrast. Especially for cell tracking experiments, these properties interfere with the visualization and quantification of cell migration. Positive contrast could be generated from T_2*-weighted images by applying frequency offsets during reconstruction[1]. In this work, the efficacy of frequency offset method was tested on *ex vivo* T_2*-weighted gradient echo images obtained in an animal model of iron oxide particle labeled endogenous stem cell migration. Positive contrast was therefore assessed after applying the frequency offset method. Moreover, a quantification method for migration on the positive contrast images was proposed.

Methods: MPIO-labeling was performed through a stereotactic injection in the mouse brain ventricles. At fifteen weeks after MPIO-labeling, a time at which many eNSC should have completed their migration to the olfactory bulb, mice were sacrificed for *ex vivo* MRI. Imaging was performed on a 7T Bruker Pharmascan system using a surface receiver coil. A high resolution 3D T_2*-weighted GE sequence was acquired.

The frequency offset method was studied by testing the two main parameters of the method, namely the number and size of the frequency steps, defining the frequency range of the offsets. The most optimal frequency range was then chosen empirically based on the quality of the images in the olfactory bulb region and used for the quantification of the MPIO-containing voxels.

For quantification of the migration towards a specific region, standard statistics are not appropriate since the intensity distribution of positive contrast images does not follow a normal distribution. Therefore, migration is quantified by combining intensity histogram analysis and kurtosis calculation.

Results: The frequency-offset method was implemented and optimized. The best results were obtained using fifty frequency offsets with a step size of 10 Hz resulting in a frequency range of 500 Hz. A comparison of debiased[2] positive and negative contrast images shows some voxels containing contrast are better visible on the positive contrast images (Figure 1).

For quantification purposes, the histograms were analyzed (Figure 2) and showed clearly higher intensities for the ipsilateral test region (with MPIO-labeled stem cell migration) versus the contralateral control region (no MPIO-labeled stem cell migration). When calculating the kurtosis values of the distributions, the test region's values are clearly higher than for the control region. Moreover, when comparing the quantification of the original images to images where the bias field of the surface coil was corrected for (debiased images), both for positive and negative contrast images, the difference between the kurtosis values of the biased versus debiased images are negligible in the positive contrast images, while significantly different in the negative contrast images (Figure 3).

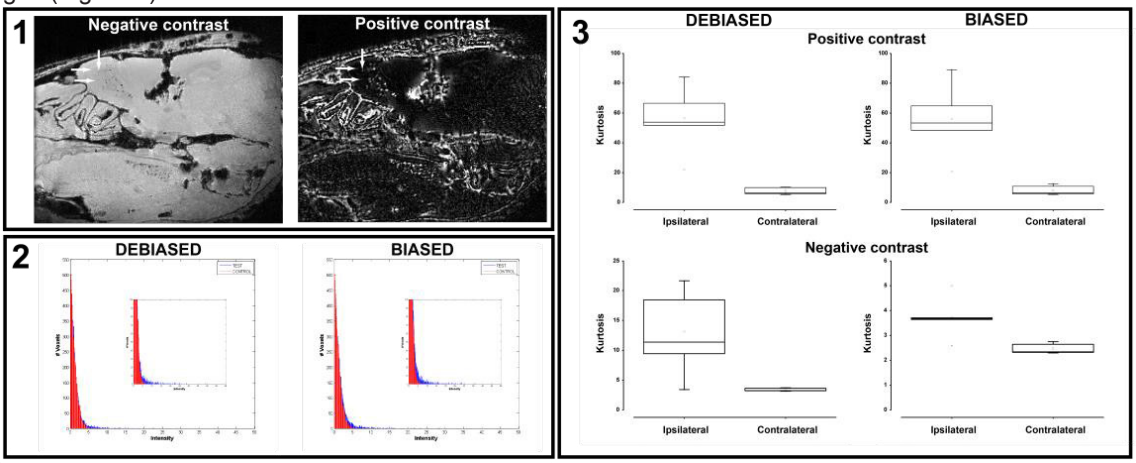

Discussion: Since it was proven that multiple MPIO are internalized in an eNSC and since multiple cells travel via the RMS, clusters of MPIO are formed with different sizes. These MPIO clusters could be considered as different field perturbing objects, which results in multiple optimal frequency offsets. Therefore, it was important to optimize the different parameters of the frequency-offset method. The positive contrast images provided a better visualization of voxels that contain a small amount of iron oxide particles.

More importantly, since the kurtosis values of biased and debiased datasets are alike in positive contrast images, the bias field does not seem to influence the quantification of positive contrast images. This is an important finding showing the advantage of the frequency-offset method combined with kurtosis to visualize and quantify migration.

Conclusion: The frequency offset method to generate positive contrast image datasets proved to be an excellent tool for the visualization of MPIO labeled cell migration in the mouse brain. Furthermore, migration could be quantified using the intensity histogram and kurtosis. More importantly, the quantification method proved not to suffer from the bias field present in the images.

References: 1. de Leeuw, H., Seevinck P.R., Bakker C.J., Center-out radial sampling with off-resonant reconstruction for efficient and accurate localization of punctate and elongated paramagnetic structures. Magn Reson Med, 2013. 69(6): 1611-22; 2. Mai Z., Hanel R., Batenburg J., Verhoye M., Scheunders P., Sijbers J. Bias field reduction by localized LloydMax quantization, Magnetic resonance imaging 2011. 29: 536-545.

Multiband multiecho 2D-EPI: maximizing BOLD CNR for fMRI at 3T

E. Daniel Gomez[1], Jenni Schulz[1], Rasim Boyacioglu[1], David Norris[1], Benedikt Poser[2]

[1]Donders Institute for Brain, Cognition and Behaviour, Radboud University Medical Center, Nijmegen, the Netherlands
[2]Faculty of Psychology and Neuroscience, Maastricht University, Maastricht, the Netherlands

TARGET AUDIENCE: Researchers interested in multiband (MB) and multiecho (ME) 2D-EPI sequences for fMRI studies.

INTRODUCTION: Multiband[1] Multiecho 2D-EPI with blipped-CAIPI[2] is an MR imaging sequence that allows the acquisition of multiple slices simultaneously – thus dramatically reducing acquisition time and repetition time (TR) – and of multiple echoes with different TEs after a single RF excitation, improving BOLD sensitivity in fMRI studies[3]. Nonetheless, crafting protocols which maximize the tSNR of MB accelerated experiments is not a straightforward task[4]. **In this contribution we compared the BOLD CNR of various MB-ME 2D-EPI protocols - different in their MB factors** (number of slices excited simultaneously), **in-plane acceleration factors** (referred to as GRAPPA[5] throughout this contribution) **and/or CAIPI factors** (2 for FOV/2, 3 for FOV/3, etc.) - under three constraints: 1. Equal number of volumes for all acquisitions, 2. As many echoes as possible using minimum TEs and TRs available, without violating the conditions TE_{max}=100ms and TR_{max}= 2000ms, and 3. Total acceleration = MB*GRAPPA < 10.

MATERIALS AND METHODS: MB-ME EPI data was acquired with a 32-channel head coil on a 3T Siemens Skyra MR scanner from N=3 subjects after written consent. For all acquisitions the following parameters were kept fixed: FA 65, BW 2030 Hz/px, voxel size 2.5mm^3, in-plane resolution 88 x 88, 36 slices, slice distance factor 0, and number of volumes =100. Acquisitions varied with respect to the multiband factor (MB), the GRAPPA factor, the CAIPI shift (CAIPI), measurement time (Time), TR, TE, echo spacing (ES) and number of echoes (Ec), as shown in table 1. Images were reconstructed online with the slice-GRAPPA[2] and GRAPPA algorithms. Echoes were combined offline by weighted summation, using as weighting factors the relative BOLD contrast[3] of each echo, resulting in a single time series. An effective tSNR map of each scheme was computed as the mean over the standard deviation of the weighted time series, divided by the square root of its respective TR. Finally, for each subject, the effective tSNR of voxels inside of a grey matter mask (extracted with FSL FAST, http://fsl.fmrib.ox.ac.uk/fsl/fslwiki/FAST) were averaged, yielding a relative BOLD (weighting) CNR value used as metric to compare different schemes. Masking is important for a fair comparison, to avoid influence from the difference in CSF/WM/GM contrast. This difference in contrast between acquisitions can be seen in Figure 1.

Table 1. Acquisition parameters for all tested MB-ME protocols.

	MB	GRAPPA	CAIPI	Time	TR	TE1	ES	Ec
1	2	2	1	3:33	1900	18	26	3
2	2	3	1	2:52	1460	15	19	3
3	2	3	2	2:52	1460	15	19	3
4	3	2	1	3:11	1630	19	26	4
5	3	2	3	3:11	1630	19	26	4
6	3	3	1	2:59	1440	15	19	5
7	3	3	2	2:59	1440	15	19	5
8	4	2	1	2:07	956	18	26	3
9	4	2	3	2:12	998	20	29	3

RESULTS: The relative BOLD CNR decreased with MB factor for all subjects, independent of the CAIPI and GRAPPA factors. For MB 2 and MB 3, higher relative BOLD CNR was obtained with GRAPPA 3, even though the total acceleration increased with respect to GRAPPA 2. For MB 4, results improved drastically by using the blipped-CAIPI technique. Figure 2 shows the relative BOLD CNR of all acceleration schemes tested.

DISCUSSION: The decrease in relative BOLD CNR for higher MB factors is partly attributable to the lower steady state signal intensity due to shorter TR, and the increase in the standard deviation of the time series arising as consequence of the reconstruction noise amplification (g-factor). Since the blipped-CAIPI technique reduces g-factor by reducing the degree to which the reconstruction relies on coil sensitivity encoding along the slice direction alone, it reduces artifactual variations in signal intensity thus improving the relative BOLD CNR. The better performance with GRAPPA factor 3 is likely to be caused by the shortening of the echo train length and the ES, reducing TEs and (for MB3) increasing the number of echoes acquired. These benefits seem to outweigh the reconstruction SNR g-factor penalty. The apparent outperformance of schemes 2 and 3 (MB2/PE3) will be further investigated, as it might be a consequence of the discrete character of the experiment.

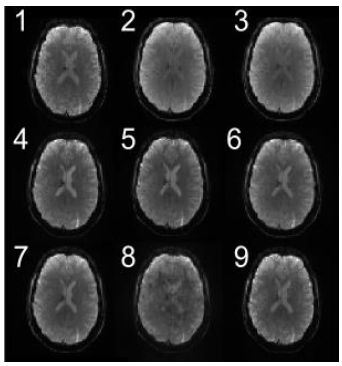

Figure 1. Central slice of the first volume of the weighted series.

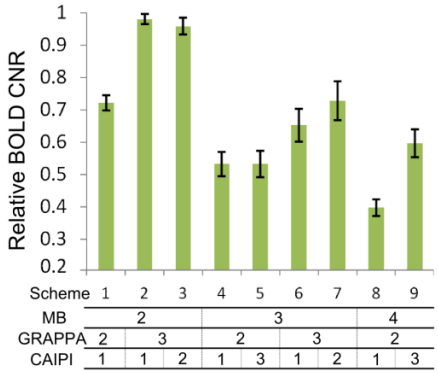

Figure 2. Relative BOLD CNR, averaged over all subjects. Error bars indicate standard deviation.

CONCLUSION: For a MB-ME 2D-EPI acquisition, with same amount of measurements, and within boundaries of achievable total acceleration factors for a given coil, **the relative BOLD CNR decreases with MB factor,** though blipped-CAIPI ameliorates this drawback substantially, **and the benefits of GRAPPA 3 outweigh g-factor losses when compared to GRAPPA 2.**

References: [1] Nunes et al., 2006. *Proc. Intl. Soc. Mag. Reson. 14.* p. 293 [2] Setsompop K. et al., 2012. *Magn. Reson. Med.* 67:1210-1224 [3] Poser B. et al., 2006. *Magn. Reson. Med.* 55:1227-1235 [4] Chen L. et al., 2014. *Neuroimage*. In Press. [5] Griswold M. et al., 2002. *Magn. Reson. Med.* 47:1202-1210

MR guidance of TMS for a patient specific treatment plan: MR based TMS field measurements and electromagnetic simulations

Stefano Mandija[1], P. Petrov, S.W.F. Neggers[2], A.D. de Weijer[3], P.R. Luijten[1], C.A.T. van den Berg[1]

[1]Imaging Division, University Medical Center Utrecht, Utrecht, the Netherlands
[2]Brain Center Rudolf Magnus, University Medical Center Utrecht, Utrecht, the Netherlands
[3]FMRIB Center, University of Oxford, Oxford, United Kingdom

Introduction: Transcranial magnetic stimulation (TMS) is a non-invasive neuro-stimulation method. For this purpose, a TMS coil applies a focal, time-varying incident magnetic field to a specific target region inducing an electric field and causing neuronal activation by locally exceeding the neuronal depolarization threshold[1]. The less painful inductive current generation makes this technique attractive to treat neurological disorders. Although a TMS-MRI setup already exists for fMRI studies, the positioning and power calibration of the TMS coil is still performed in a very simple way. The TMS power is increased until the thumb movement in response to a TMS pulse applied on the motor cortex is observed[2]. Here we demonstrate that MRI can provide guidance and dosimetry of the TMS treatment by mapping and quantifying the incident TMS magnetic field (B_{TMS}). For this purpose, we first describe a new combined TMS-MRI setup and MR sequence that allow us to map B_{TMS}. Then, starting from this map, we simulate the TMS induced electric field employing a patient specific brain model generated by automated segmentation of pre-treatment MR images. In this way, we can verify whether the TMS magnetic field focus overlays the target area. Subsequently, by means of the subject specific modelling we can quantify the electric field at the target area.

Materials and Methods: A TMS machine (Rapid, Magstim Company, Whitland, UK) is here integrated into a 3T MR scanner (Achieva, Philips, Best, The Netherlands) using different components to safely apply a TMS pulse.

Combined TMS-MRI setup: In fig.1, starting from the top left corner, for each 90° pulse of a Multi-SpinEcho sequence a TTL pulse is sent to a control box. This box synchronizes the TMS machine with the MR scanner triggering the TMS control signal. Every time a TMS pulse has to be delivered, the control box sends a pulse to a safety box that controls both the TMS machine and the relay box (Rapid, Magstim Company, Whitland, UK) enabling the closing of the relay that connects the TMS machine to the coil. Particular attention is paid to the time the relay takes:

- to close (15 ms), otherwise it will break due to the high level of current (15000 A) ;
- to open (2ms), to prevent image distortions by electrically disconnecting the TMS simulator from the coils.

All the signal time responses are verified using an oscilloscope (Fig. 2) to ensure the absence of delays in transmitting the signals between all the components shown in fig. 1. Finally, we use a dedicated TMS coil holder (Fig. 1.5) that enable placement of the TMS coil in different positions, paying attention not to exceed an angle of 30° between the coil plane and the B0 field to keep the Lorentz forces into mechanically tolerable limits[3].

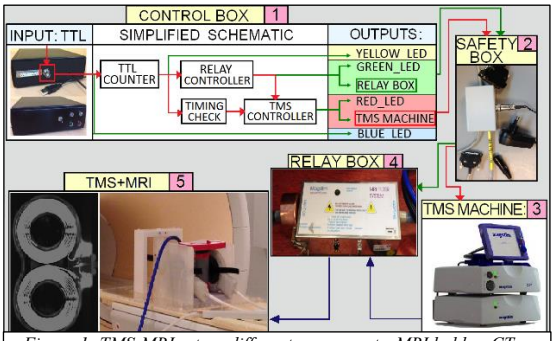

Figure 1: TMS-MRI setup: different components, MRI holder, CT scan of the TMS coil (resolution 1mm).

Measurements: We investigate the effect of a TMS pulse applied before the readout gradient in a conductive phantom (r = 12,5 cm, L = 20 cm, σ = 1.6 S/m: Agar 20 gr/L, NaCl 9.3 gr/L). In fig. 2, we show a Multi-SpinEcho sequence with the TMS integrated control signals: TR=1 sec, TE=50 ms, FOV= 160x160x88, RES=2.5x2.5x2.5 mm, G_x=29mT/m, slew rate=188 T/m/s. To safely apply a TMS pulse, a free gradient window is needed. Since we need 17 ms for the relay to open and close, this window is available only before the readout gradient. The measured accumulated phase at the spin echo is[4]:

$$\phi_{acc} = \phi_{RF} + \gamma \int_0^{TE} \Delta B_{0,eddy\_current}(\vec{r},t)dt + \gamma \int_0^{T_{TMS\_pulse}} \Delta B_{TMS,z}(\vec{r},t)dt\,.$$

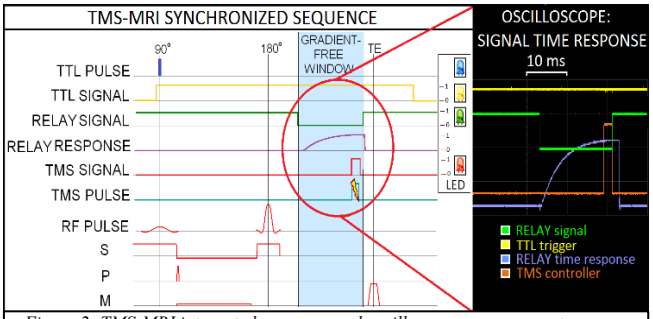

Figure 2: TMS-MRI integrated sequence and oscilloscope measurements.

After unwrapping the phase images (Fig. 3, c-d), it is possible to calculate the TMS incident magnetic field strength. To isolate the TMS phase contribution from other SE phase contributions such as the RF phase and the eddy current phase we subtract the phase image acquired with non-zero and zero power of the TMS pulse. Then we retrieve the z component of the incident TMS magnetic field: $\Delta B_{TMS,z}(\vec{r}) = \frac{\phi_{acc}^{TMS\neq 0} - \phi_{acc}^{TMS=0}}{\gamma \int_{t_{TMS\_pulse}} A(t)dt}$, where A(t) is the time integral over the TMS pulse waveform.

Simulations: Using SCIRun (SCI Institute's NIH/NIGMS CIBC Center, University of Utah, Utah), for the three different values of power we simulate $\Delta B_{TMS,z}$ to match the measured one. In this way, from these maps we can simulate the total electric field induced in the phantom (E_{ind}^{TMS}), assuming a quasi-static approximation (Fig. 3, m, n, o). By overlapping the electric field map on a pre-acquired anatomical image and on an anatomical image acquired during TMS session, we can precisely define the region that will be excited, since the electric field is very focal. Subtle changes in the position of the TMS coil allow us to target the focus of electric field to the region that has to be treated. Then, by changing the amount of current that runs into the TMS coil we can evaluate the minimum value needed to induce an E_{ind}^{TMS} capable to depolarize neuronal membranes inducing neuronal activation. In this way, we have created a very precise method to perform TMS magnetic field dosimetry.

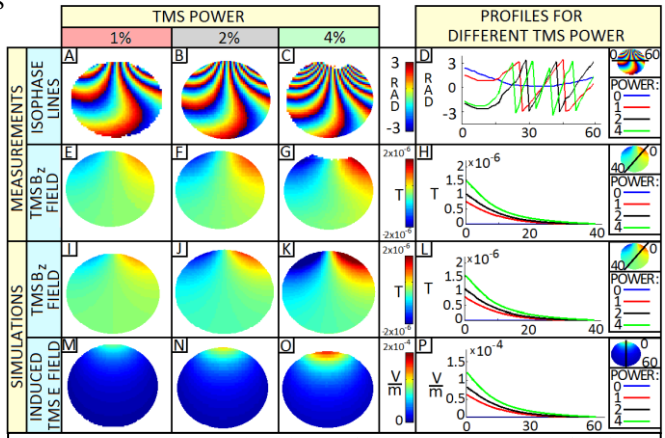

Figure 3: Measurements and simulations of the TMS incident magnetic field for three different intensities of the TMS pulse, and relative simulated induced electric fields.

Results: In fig. 3, a, b and c we clearly see both the increase of the phase wraps with higher TMS power values by a factor of $\sqrt{2}$ and a region closer to the TMS coil where intra-voxel dephasing occurs due to large intra-voxel ΔB_{TMS} field gradients. With the method described above, from measurements we retrieve the z component of the incident TMS magnetic field, the only measurable component (Fig. 3, e, f, and g). We can compare the measured magnetic fields maps with the simulated magnetic field maps (Fig. 3, i, j, k). As shown in fig. 3, the magnetic field drops approximately with $1/r^3$, where r is the distance from the coil, and it increases with the square root of the pulse power. As we can see, the region where E_{ind}^{TMS} is maximum is very constrained. Therefore guiding the positioning of the TMS coil with the MR scanner is crucial to precisely and correctly stimulate a predefined target brain area and subsequently quantify exactly the applied magnetic field at the focal region. An overlay of the measured magnetic field onto an anatomical scan acquired during TMS-MRI session records the applied treatment plan.

Conclusions: A precise MR based map of the TMS magnetic field, in combination with electromagnetic simulations and pre-acquired anatomical images, allows us to evaluate the behaviour of the induced TMS electric field and precisely target a certain functional area. In fact, with this new combined TMS-MRI setup we can now guide and provide dosimetry of TMS with the MR scanner for a patient specific treatment.

References: [1] D. E. Bohning et al, Neuroreport 1997, 8(11), 2535-2538. [2] M. Kobayashi, Lancet Neurology 2003, 2, 145-156. [3] A.D.de Weijer et al, Clin Neurophysiol 2014, 31(5), 474-487. [4] A. S. C. Peres et al, IFMBE Proceedings 2009, 25(7), 571-574.

Fat suppression for DW-FSE sequences using an integrated multi-acquisition Dixon method

Tim Schakel[1], Bjorn Stemkens[1], Hans Hoogduin[2], Marielle Philippens[1]

[1]Department of Radiotherapy, University Medical Center, Utrecht, the Netherlands
[2]Department of Radiology, University Medical Center, Utrecht, the Netherlands

Target audience: Researchers interested in diffusion weighted fast spin echo sequences.

Purpose: In oncology, diffusion weighted (DW) MRI can be used to detect and characterize lesions. In areas with large magnetic susceptibility variations, DW-MRI using the conventional single-shot-spin-echo-EPI can be very challenging and can lead to large image distortion artefacts. When geometric accuracy is vital, e.g. for radiotherapy applications, fast spin echo (FSE) based sequences can provide an alternative [1,2]. For these applications fat suppression is important, since fat can obscure lesions and make images harder to interpret. However, spectral based techniques also suffer from susceptibility variations which can result in incomplete fat suppression. In this work, we integrated a multi-acquisition Dixon method into a DW-SPLICE sequence (figure 1) to facilitate water-fat separation.

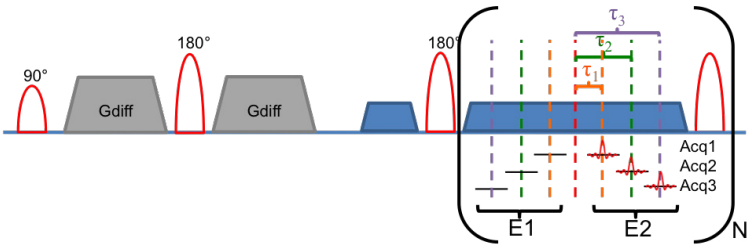

Figure 1: DW-SPLICE sequence diagram. Black bars: data acquisition windows. N = echo train length. For the b=0, the data acquisition windows are shifted by $\Delta\tau$ ($=\tau_2-\tau_1$) in subsequent measurements. The DW-SPLICE sequence utilizes a split-echo readout (E1 and E2) to mitigate phase errors due to motion during diffusion weighting [1].

Methods: The sequence was prototyped within the Philips Gyroscan software on a 3.0T Achieva system (Philips, Best, The Netherlands) (figure 1). The b0 (non diffusion weighted image) was acquired 3 times with the acquisition windows shifted by $\Delta\tau$ for each acquisition ($\tau_{1/2/3}$ = 1.12/1.70/2.28 ms). The b>0 measurements were acquired only for the middle acquisition (τ=1.70ms). The data from the different b0 acquisitions were suitable for water-fat separation, which was performed for the E1 and E2 SPLICE acquisitions separately and their results were combined afterwards. From these results water and fat fraction maps [3] were calculated. The b>0 measurements were reconstructed as usual and then multiplied by the water fraction map to suppress the fat and generate 'water weighted' images. ADC maps were generated using the non fat suppressed DW images. Data processing was performed offline in Matlab (The Mathworks, MA, USA) using ReconFrame (Gyrotools, LLC, Zurich, CH) and the hierarchical IDEAL algorithm [4] from the ISMRM fat-water toolbox.
Image acquisition parameters DW-SPLICE: echo spacing = 9.4 ms, echo train length = 49. TE/TR = 137/10598ms, refoc angle = 50°, halfscan=0.6, SENSE=1.5, FOV: 180x227x120 mm^3 (RLxAPxFH), voxelsize: 1.41x1.41x6 mm^3, b-values=0,300,800 s/mm^2 in 3 directions with a gradient overplus scheme. NSA=4. Total imaging time: 4m56s.

Results: Successful water-fat separation was achieved in the b0 images over the whole field of view; figure 2 shows 2 typical slices (a-e and f-j). By comparing 2c/h with d/i the effect of the fat suppression on the diffusion weighted b800 images can be observed.

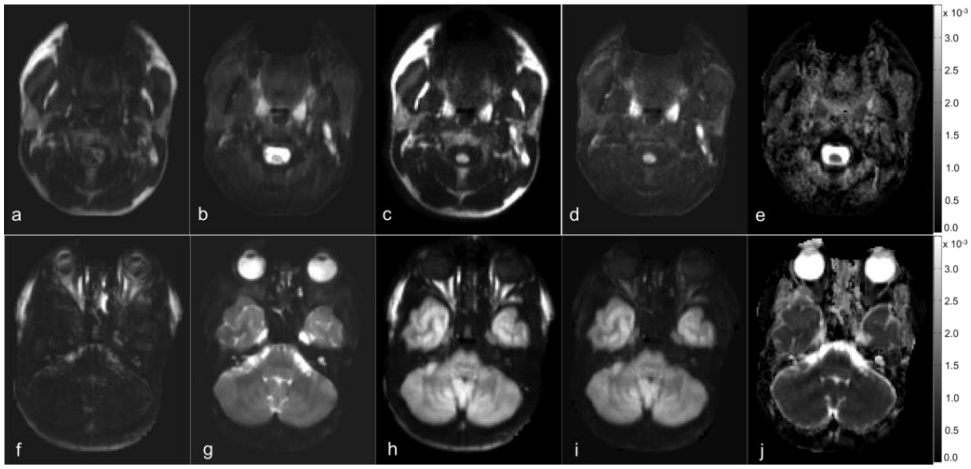

Figure 2: Two slices of DW-SPLICE sequence with integrated Dixon acquisition in the head-and-neck area of a healthy volunteer **(a,f)** b0-fat, **(b,g)** b0-water, **(c,h)** b800, **(d,i)** b800 water weighted, **(e,j)** ADCmap in mm^2/s.

Discussion: Water-fat separation could be performed using the hierarchical IDEAL algorithm. Even though the volunteer had a metal wire behind the teeth (signal void in figure 2 top row), water-fat separation was successful here. Only the b0 image needs to be acquired at different echo times. This could be included in the already present signal averages. In the presented results the echo spacing was increased by 2.4ms $(2(nAcq-1)\Delta\tau)$ compared to the normal DW-SPLICE sequence, lengthening the acquisition by 20%. Water-fat separation could not be performed in the b>0 measurements, due to the random phase offset introduced by bulk motion during the diffusion weighting gradients [1], which could not be accounted for in current water-fat separation algorithms. The ADC values in tissues containing a larger percentage of fat might be inaccurate due to the presence of signal from fat during acquisition. Since fat has a lower ADC value than water, this could lead to an underestimation of the ADC value. However, for lesion detection and delineation the undistorted, fat suppressed high b-value images are most important.

Conclusion: A multi-acquisition Dixon method has successfully been integrated in a DW-SPLICE sequence to achieve good fat suppression in an undistorted DW image in difficult areas, such as the head and neck region.

References: [1] Schick, Magn Reson Med 1997 Oct;38(4)638-44, [2] Schakel, In proc ISMRM 2013 #3443 [3] Liu, Magn Reson Med 2007 Aug:58(2):354-64, [4] Tsao & Jiang, Magn Reson Med 2013 Jul;70(1):155-9.

A comparison of 19F MRI recovery from compressed sensing

Sayuang Liang[1], Yipeng Liu[2], Tom Dresselaers[1], Sabine Van Huffel[2], Uwe Himmelreich[1]

[1]Department of Imaging & Pathology, KU Leuven, Leuven, Belgium
[2]ESAT, KU Leuven, Belgium

Introduction: Transplantation of pancreatic islets is a possible treatment option for patients suffering type I diabetic disease. However, the outcome of islet transplantation largely depends on the site of transplantation. Thus, monitoring the fate of transplanted islets using noninvasive imaging technique is necessary. Thanks to its high specificity without any background signal in biological tissue and potential for quantification of cell numbers, ^{19}F MRI is emerging as a useful tool for cell tracking[1]. Our previous study shows perfluorocarbon (PFCE) based particles have no significant effect on pancreatic islets' function and morphology. One major concern of ^{19}F MRI is the often essential long acquisition time due to the low concentration of the ^{19}F contrast agents and/or cell numbers. As the feasibility of using compressed sensing (CS) to accelerate ^{19}F MRI has been demonstrated by Zhong et al.[2], by applying different newly developed CS reconstruction algorithms, we want to validate the application of CS for imaging of perfluorocarbon (PFCE) labeled islets both in vitro and in vivo after subcutaneous transplantation.

Methods and Materials: The rodent pancreatic islets were obtained from Wistar rats (female, 8-10 weeks) using the collagenase digestion method[3]. Then the isolated islets were incubated overnight with cationic PFCE particles, which were prepared according to Dewitte et al.[4]. After washing with PBS three times, these pre-labeled islets were picked and separated equally for either making agar phantom or subcutaneous transplantation (each 200 islets). All MRI experiments were performed on a 9.4T Bruker Biospec small animal MR scanner (Bruker Biospin, Ettingen, Germany) equipped with a home built coil tuneable and matchable to both the ^{19}F and ^{1}H resonances. An 2D RARE sequence was used for both in vitro and in vivo ^{19}F acquisition with some parameters modification: TE/TR = 15.9 ms/1 s, FOV = 6.4 cm*6.4 cm/8 cm*4 cm, matrix size = 64*64/50*50, NA = 1000, slice thickness = 2.5 mm.
Different algorithms including SparseMRI[5]: a traditional convex based method for MRI application served as golden standard in this study; orthogonal multimatching pursuit[6] (OMMP): a recently proposed greedy algorithm; compressive sampling matching pursuit[7] (CoSaMP): a balanced algorithm between the faster greedy algorithm and more accurate convex algorithm; L1-reweighted minimization[8] : a slower non-convex algorithm with better accurate; two-level l1 minimization[9]: which approximates the reweighted L1 minimization method piecewise-linearly to generate similar results with faster speed are applied for CS reconstruction and comparison purpose. The sampling pattern was chosen by selecting lines in both readout and phase encoding direction with central k-space emphasized, points where the selected lines intersected are considered as sampled. By doing so, Cartesian k-space under-sample scheme normally done by the hardware for 3D imaging, where two phase encoding directions are under-sampled while readout direction is fully sampled, could be simulated. Under-sample factor (UF) from 2 to 8 was used.

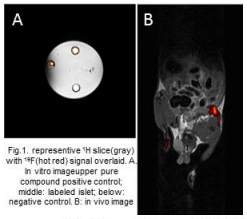

Fig.1. representive ^{1}H slice(gray) with ^{19}F(hot red) signal overlaid. A: In vitro imageupper pure compound positive control; middle: labeled islet; below: negative control. B: in vivo image

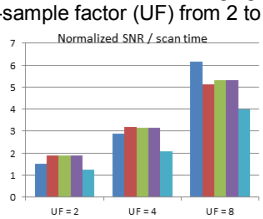

Fig.4. Normalized SNR/t value for in vivo reconstruction

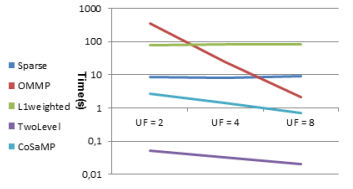

Fig.5. Computation time of diferent algorithms for in vivo image

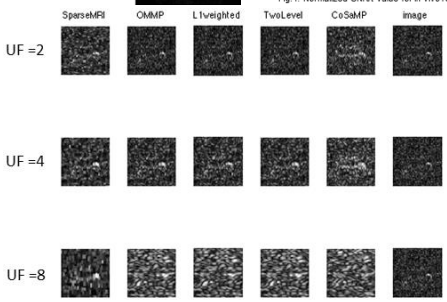

Fig.2. In vivo ^{19}F image reconstructed using different algorithm under different UFs

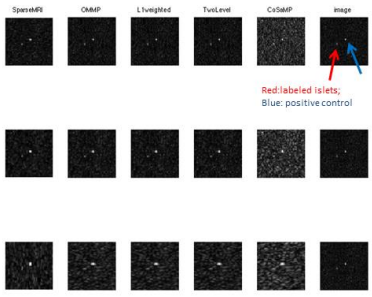

Fig.3. In vitro ^{19}F image reconstructed using different algorithm under different Ufs(left spot: labeled islets, middle spot: pure PFCE as positive control.

Results: The uptake of PFCE by islet cells was around 10^{15} ^{19}F spins/pancreatic islets according to in vitro NMR measurements. Thus, the total ^{19}F spins of 200 labeled islets is relative low considering the low sensitive of ^{19}F technique. In order to visualize the islets by ^{19}F MRI, a half hour scan time is necessary to get a 2D image with low resolution (1 mm x 1mm for in vitro & 1.6mm x 0.8mm for in vivo) resulting in SNRs of 9.86 for in vitro & 10.12 for in vivo (fig.1). Using different CS algorithms (fig.2 and 3), up to UF equals 4, for both in vitro and in vivo, signal from labeled islets could still be retrieved with a similar SNR as for the fully sampled image except for the CoSaMP method. This means that CS techniques effectively increase SNR/t (scan time) by a factor of around 3.2 (fig.4). If the detect limitation is set to SNR equals 5, for UF equals 8, there is still remaining detectable signal with some blurring noise around. Regarding the computational time of the different algorithms (fig.5), two-level methods gave the best performance, which is 10 times faster than SparseMRI.

Conclusion and Discussion: To the best of our knowledge, this study demonstrates and validates the application of CS for ^{19}F cell tracking using different CS algorithms for the first time. More importantly, in this study, we restrict the scope to the low SNR regime of ^{19}F images, which is the main concern of ^{19}F applications. Because of the low sensitivity, either huge amount of labeled cells or long scan times are needed. As for our application, increasing labeled islets requires sacrificing more animals for islets isolation and is as such not feasible; it is essential to improve the imaging approach. As we have demonstrated, several existing CS reconstruction algorithms could be applied to reduce the scan time by a factor of three or four with similar SNR and resolution. The experimentally determined acceleration rate we present here is lower than what was reported by Zhong et al.[2]. This may be partly explained by the much higher SNR level (44 vs. 10) for the fully sampled in vivo image in their study using a mouse model of localized inflammation. In addition, as the Cartesian k-space under-sample scheme was used in this study, it could affect the final reconstructed image quality. Especially for the UF = 8 reconstructed image, blurring effects happened for the signal of interested. This could be further improved by introducing non-Cartesian under-sample pattern in the future. As for both L1-reweighted and a two-level method, only L1 minimization was taken into account, the accuracy of the techniques could be further improved by importing other constrains, such as TV constrains used by SparseMRI[5]. We conclude that compressed sensing is a useful tool for accelerating ^{19}F MRI with low SNR. Among the different algorithms that we used in this study, the two-level method is preferable as it is considered the fastest method with relative good accuracy.

References: 1.Ahrens ET et al., Nature Biotechnology 2005; 23:983-987; 2.Zhong J et al., MRM 2013;69:1683-90; 3.Malaisse MWJ, Methods in Diabetes Research 1984;1:147-52; 4. Dewitte H et al.,Journal of Controlled Release 2013;169:141-149; 5.Lustig M, et al. MRM 2007;58:1182-95; 6. Liu E, et al. IEEE Trans 2012;58:2040-47; 7. Needell D, et al. Applied and Computational Harmonics Analysis 2009;26:301-21; 8. Candes EJ, et al. Journal of Fourier analysis and applications 2008;14:877-905; 9.Huang X, et al. accepted for publish in Signal Processing.

Improved line-shape estimation for in vivo MRS

Dirk van Ormondt[1], Ronald de Beer[1], Jan-Willem C. van der Veen[2], Diana M. Sima[3], Danielle Graveron-Demilly[4]

[1]ImPhys, Delft University of Technlogy, Delft, the Netherlands; [2]MRS Core Facility NIMH, NIH, Bethesda, USA; [3]Department of Electrical Engineering (ESAT), KULeuven, Leuven, Belgium; [4]Laboratoire CREATIS, Université Claude Bernard Lyon 1, Villeurbanne, France

Target audience – Users of metabolite-quantitation software.

Purpose – To devise a new, simple, fast method to improve estimation of the line-shape. At very high magnetic field, B_0 ≥11.7 T [1], micro-susceptibility in *human* tissue will have become the predominant contributor to the line-shape [2]. Under that condition, shimming, which alleviates macro-susceptibility effects only, is not sufficient. The line-shape resulting from micro-susceptibility in humans being unknown as yet, metabolite quantitation may become biased. Detection of bias can be difficult [3]. To avoid bias, one must estimate the line-shape from the metabolite data and use it in the quantitation. This work improves line-shape estimation through an alternative way of handling measurement noise.

Methods – First, recall that line-shape(v) = FFT [decay(t)], where v & t stand for frequency & time respectively. A well-known method to estimate the decay of the measured signal is from the division decay(t) = {|signal(t)+noise(t)| ÷ |simulated non-decaying signal(t)|} × exp(iϕ(t)), where |.| stands for absolute value, and ϕ(t) is the phase of the division [3]. In the present work, signal(t) and noise(t) are simulated, enabling one to judge the result. Intentionally, we made the line-shape non-Lorentzian [3]. The non-decaying denominator was simulated from a quantum-mechanically computed metabolite-signal database and from approximate metabolite concentrations obtained from quantitation with the familiar Lorentz line-shape (exponential decay). The division is highly perturbed at values of t where noise(t) ≥ signal(t), resulting in a 'spiky' form of decay(t). The spikes have an unknown, 'heavy-tailed' probability-distribution. Traditionally, this spiky result is smoothed with some filter, posterior to the division. Note that removal of spikes having a complicated probability distribution is no easy task, requiring expert setting of hyper parameters. Here, we smooth the numerator and the denominator separately, prior to the division, thus avoiding appearance of spikes altogether. Smoothing is done with a 3rd order Butterworth filter, needing one hyper-parameter. Filter end effects at t=0 are avoided by extending the numerator and denominator into echo's, thus maneuvering t=0 to the centre of the signal and filtering the entire echo rather than just the FID; see Figures below.

Results – **Fig.1** shows |signal(t) + noise(t)|, t= 0,…,1300 points. Values of t where noise(t) ≥ signal(t) are clearly visible. **Fig.2** shows the echo-version of Fig.1 (blue), for t= -2000,...,+2000 points; the yellow line is the smoothed version showing minimal filter-end effect in the centre, *i.e.*, at t=0. **Fig.3** is similar to Fig.2, but now for the denominator. Dividing the blue line of Fig.2 by the blue line of Fig.3 *produces spikes*. Dividing the yellow line of Fig.2 by the yellow line of Fig.3 *produces a smooth curve*. **Fig.4** summarises the smoothed parts of the division: blue = numerator, red = denominator, green = Re[phase factor], brown = Im[fase factor]. **Fig.5** shows the estimated decay, obtained from the four curves of Fig.4. Finally, **Fig.6** shows that the difference between the estimated decay(t) and the true decay(t) is small (see the vertical scale of the Figure).

Discussion – The goal of this work is to simplify estimation of the line-shape (decay) from the data, based on the formula in Section **Methods**. The aspect we wished to improve is the oversensitivity of the division to noise in the signal. We achieved this by smoothing the individual parts of the formula prior to carrying out the actual division. This not only removes noise but also the oscillating components. Note that these oscillating components have no relation to the decay and in fact contribute to the sensitivity to noise. By way of a Monte Carlo experiment with 1000 different noise-realisations, we verified that use of the estimated decay reduces the bias on metabolite quantitation to well below the standard deviation. This *warrants application of the Cramer-Rao Bounds*. All along, we assumed that the line-shape at B_0 ≥11.7 T is the same for each spectral component.

Conclusion – We devised a simple line-shape estimator, capable of reducing bias in metabolite quantation to well below the standard deviation.

References –

1. Kanithi H, Blasiak D, Vedrine P, *et al*. Production Results of 11.75 Tesla Iseult/INUMAC MRI Conductor at Luvat. IEEE Transactions on Applied Superconductivity, 2014; **24**(3):504.
2. Deelchand DK, Van de Moortele P-F, Adriany G, *et al*. In vivo ^{1}H NMR spectroscopy of the human brain at 9.4 T: Initial results. J Magn. Reson. 2010; **206**: 74-80.
3. Ormondt D van, Beer R de, Sima DM, *et al*. Biased metabolite-quantitation at 11.7 T. 2013; Proc. ISMRM-Benelux: PT4-09.

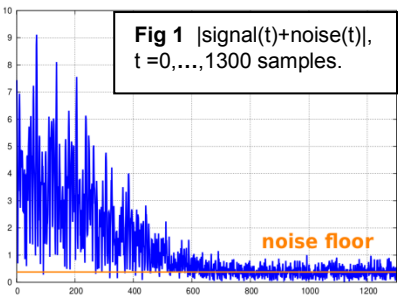

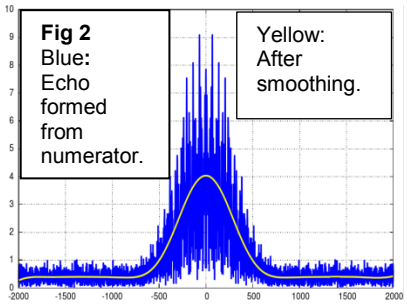

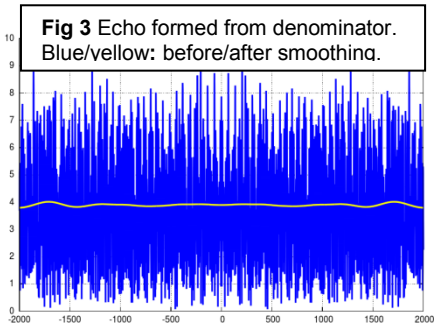

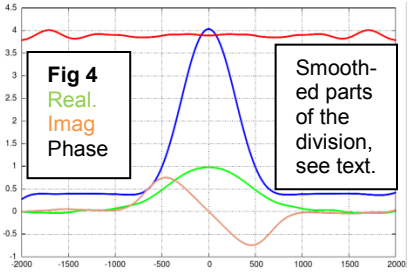

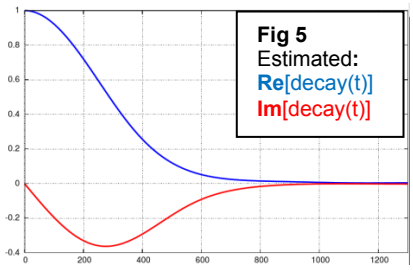

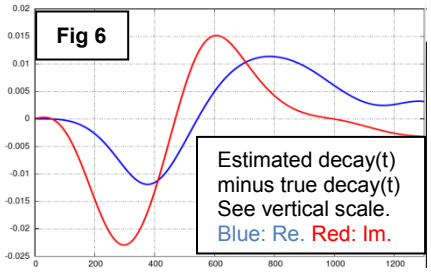

Bottom-up study of MRI positive contrast induced by superparamagnetic particles using the Off-Resonance Saturation sequence

Sebastien Delangre[1], Quoc Lam Vuong[1], Chrystelle Po[2], Bernard Gallez[2], Yves Gossuin[1]

[1]Biomedical Physics, UMONS, Mons, Belgium
[2]Biomedical Magnetic Resonance Unit, UCL, Louvain, Belgium

Magnetic Resonance Imaging (MRI) is a powerful non invasive medical imaging technique that provides images with excellent resolution and intrinsic contrast. However, MRI sometimes requires contrast agents to highlight regions of interest such as tumors. A kind of contrast agent are the Superparamagnetic Iron Oxide Nanoparticles (SPM particles)[1]. This biocompatible particles appear as hypointense spots in MRI images obtained with conventional imaging sequences due to their high r_2/r_1 ratio – and thus, belong to the negative contrast agent category.

Unfortunately, negative contrast can be difficult to interpret because it can also be produced by many sources independent of SPM nanoparticle such as air bubbles or tissue interfaces. To overcome this problem, new imaging sequences producing positive contrast with SPM nanoparticle were developed during the last few years. One of them is the Off-Resonance Saturation (ORS) technique[2]. The idea behind this sequence is to saturate the signal near the SPM particules and subtract the resulting image to an image obtained without saturation. The resulting image is an image with a positive contrast near the SPIO.

Different studies have shown that ORS is able to generate positive contrast experimentally both *in vitro* and *in vivo*[2,3]. However, a complete theoretical study of the ORS sequence is still lacking, which make impossible the optimization of the ORS sequence. For this reason, this work proposes a theoretical study of the ORS sequence, carried out with numerical simulations and experiments on agarose gel phantom on a 11.7T scanner system. A self-consistent analytical expression of the contrast dependence on the sequence parameters and the SPM particles properties was developed and compared with success to the experimental results. This expression provides a fundamental comprehension of the mechanisms leading to the ORS contrast, which allow an optimization of the ORS sequence. Therefore, the theoretical model can be useful for future in-vivo applications.

The influences on the contrast of the SPM particles relaxivities and concentration, the echo time and the saturation pulse parameters were investigated. The best contrast was achieved with SPM particles possessing the lower transverse relaxivity, an optimal particles concentration predicted by the theory and for the lower echo time.

1. Wang, Y. X., Hussain, S. M. & Krestin, G. P. Superparamagnetic iron oxide contrast agents: physicochemical characteristics and applications in MR imaging. *Eur. Radiol.* **11,** 2319–2331 (2001).
2. Zurkiya, O. & Hu, X. Off-resonance saturation as a means of generating contrast with superparamagnetic nanoparticles. *Magn. Reson. Med.* **56,** 726–732 (2006).
3. Khemtong, C. *et al.* In vivo Off-Resonance Saturation Magnetic Resonance Imaging of v 3-Targeted Superparamagnetic Nanoparticles. *Cancer Res.* **69,** 1651–1658 (2009).

Simultaneous group-wise rigid registration and T1 ML estimation for T1 mapping

Gabriel Ramos-Llordén[1], Arnold J. den Dekker[1], Gwendolyn van Steenkiste[1], Johan Van Audekerke[2], Marleen Verhoye[2], Jan Sijbers[1]

[1]iMinds-Vision Lab, University of Antwerp, Antwerp, Belgium
[2]Bio-Imaging Lab, University of Antwerp, Antwerp, Belgium

TARGET AUDIENCE: Scientists interested in quantitative relaxometry.

PURPOSE: T_1 mapping requires the acquisition of a series of T_1 weighted images prior to the estimation of the T_1 map[1]. Inter-frame subject motion and induced motion artifacts by MR scanner instabilities require alignment of the images. In T_1 mapping, the conventional approach involves registration prior to model fitting, i.e., a two-step approach[2]. This approach has serious drawbacks for accurate and precise T_1 map estimation. First, because the registration step is model-blind and does not account for inherent temporal intensity changes in the series of T_1 weighted images, motion may not be properly corrected. Secondly, the inherent image interpolation in the registration step will affect the statistical distribution of the images, and, if not correctly accounted for in the T_1 fitting, will introduce bias.

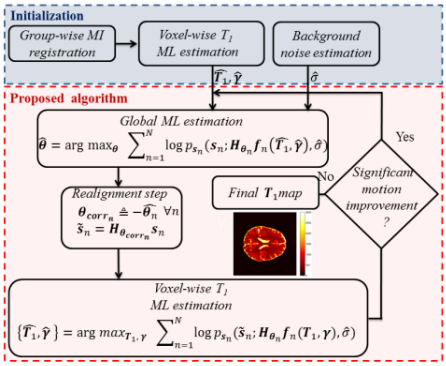

Fig.1

METHOD: We propose a simultaneous group-wise rigid registration and T_1 estimation method using a Maximum Likelihood (ML) approach[3] for brain T_1 mapping, thereby constructing a unified framework and circumventing the previously mentioned problems of the conventional two-step approach. Let N be the number of T_1 weighted images and $\boldsymbol{s}_n \in \mathbb{R}^M$ the vector which represents the n-th acquired T_1 weighted image, where M is the number of voxels. The noiseless and motion-free n-th T_1 weighted image is denoted as $\boldsymbol{f}_n \in \mathbb{R}^M$, being a function of the T_1 map, $\boldsymbol{T}_1 \in \mathbb{R}^M$, and other parameters $\boldsymbol{\gamma}$ (proton density, flip angle,...). The motion affected volume is modeled as $\tilde{\boldsymbol{f}}_n = \boldsymbol{H}_{\boldsymbol{\theta}_n}\boldsymbol{f}_n(\boldsymbol{T}_1, \boldsymbol{\gamma})$ where $\boldsymbol{H}_{\boldsymbol{\theta}_n} \in \mathbb{R}^{M \times M}$ is a linear operator defining rotation and translation[4] according to the n-th rigid transformation parameters $\boldsymbol{\theta}_n$. Assuming noise independence between acquisitions, the ML estimator of the $\boldsymbol{T}_1$ and $\boldsymbol{\gamma}$ maps and the motion parameters $\boldsymbol{\theta} = [\boldsymbol{\theta}_1^T, \boldsymbol{\theta}_2^T, \ldots, \boldsymbol{\theta}_N^T]^T$ is given by $\{\widehat{\boldsymbol{T}_1}, \widehat{\boldsymbol{\gamma}}, \widehat{\boldsymbol{\theta}}\} = \arg\max_{\boldsymbol{T}_1, \boldsymbol{\gamma}, \boldsymbol{\theta}} \sum_{n=1}^{N} \log p_{s_n}(\boldsymbol{s}_n; \tilde{\boldsymbol{f}}_n, \sigma)$ where $p_{s_n}(\boldsymbol{s}_n; \tilde{\boldsymbol{f}}_n, \sigma)$ is the joint-probability density function of the n-th acquired T_1 weighted image. The noise parameter σ is assumed to be known or can be estimated a priori. Because of the huge dimensionality of this maximization problem, we propose a splitting-type algorithm which combines a global motion ML estimation step for $\boldsymbol{\theta}$ (followed by an internal re-alignment step) with a voxel-wise ML estimation of $\boldsymbol{T}_1$ and $\boldsymbol{\gamma}$. The flowchart of the proposed algorithm is shown in Fig.1. A rough estimation of $\boldsymbol{T}_1$ and $\boldsymbol{\gamma}$ is provided by performing a prior group-wise registration with Mutual Information (MI) and subsequently a voxel-wise T_1 ML estimation. An initial motion estimate is obtained by substituting the initial estimates of the relaxation parameters in the global log-likelihood function and solving the maximization problem for $\boldsymbol{\theta}$. The re-alignment step produces a roughly corrected set of images by applying the inverse of the motion operator $\boldsymbol{H}_{\boldsymbol{\theta}_n}$. Voxel-wise ML estimation is then applied, providing more refined $\boldsymbol{T}_1$ and $\boldsymbol{\gamma}$ estimates. Both relaxation parameter maps serve again as input to the global motion ML estimation, yielding more precise motion estimation. The process is repeated until the difference between consecutive motion estimates iterations is smaller than a given tolerance level, providing a final motion corrected $\boldsymbol{T}_1$ map. The proposed method was evaluated both with synthetic and real experiments. The synthetic data were generated to mimic magnitude data, acquired with the Inversion Recovery (IR) spin echo sequence with a single coil. Therefore, $\boldsymbol{\gamma} = \{\boldsymbol{a}, \boldsymbol{b}\}$ and $\boldsymbol{f}_n(\boldsymbol{T}_1, \boldsymbol{\gamma}) = \boldsymbol{a} + \boldsymbol{b} \circ \boldsymbol{e}^{-\frac{TI_n}{T_1}}$, with TI_n being the n-th inversion time, $\circ$ the point-wise multiplication operator and $p_{s_n}(\boldsymbol{s}_n; \tilde{\boldsymbol{f}}_n, \sigma)$ a Rician probability density function[3] with envelope parameter $|\tilde{\boldsymbol{f}}_n|$ and noise standard deviation σ. We compared the performance of the proposed method with the conventional two-step approach used in our method's initialization. A 2D (M =128x128) proton density and T_1 map were created based on values provided in BrainWeb[5]. $\boldsymbol{f}_n(\boldsymbol{T}_1, \boldsymbol{\gamma})$ was created with $\boldsymbol{\gamma} = \{\boldsymbol{a}, \boldsymbol{b}\}$ defined as in *Barral et al.*[6] with TI_n, $n = 1, \ldots, N$ $(N = 18)$ equally spaced between 200 ms and 5000 ms. Motion parameters were created following a random walk model without drift, with the standard deviation of the x-shift, y-shift, and rotation angle, 0.1, 0.1 pixels and 0.8°, respectively. The signal-to-noise ratio (SNR) was defined as the spatial mean of the proton density map divided by σ. For each SNR between 10 and 90, 20 independent Rician realizations were created. Average absolute bias and root Mean Square Error (rMSE) between the estimated $\boldsymbol{T}_1$ map and the ground truth were calculated using a mask of the brain interior. Real data: One coronal slice of a single-coil acquisition with IR Echo Planar Imaging (TR=10s, 128x128 acquisition matrix, TI_n, $n = 1, \ldots, N$ $(N = 18)$ between 20 ms and 6000ms) of an *ex-vivo* rat brain was acquired. The T_1 weighted images suffered from motion artifacts due to scanner instabilities.

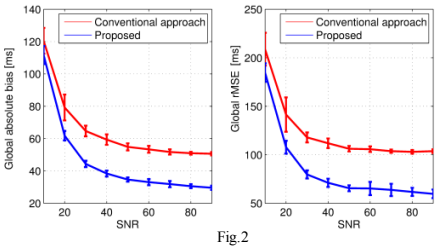

Fig.2

RESULTS: Fig.2 shows results from the synthetic experiments for the whole regime of SNR. The proposed method outperforms the conventional two-step approach in terms of bias and rMSE, which evidences the inadequacy of registration prior to T_1 estimation. In Fig.3, results with real data are presented. T_1 maps in the region denoted in Fig.3(a) with the proposed method and the conventional two-step approach are shown in Fig.3(b) and Fig.3(c), respectively. Visual results corroborate the effect of inaccurate motion estimation of the conventional approach in terms of removing important details (corpus callosum, see black arrow).

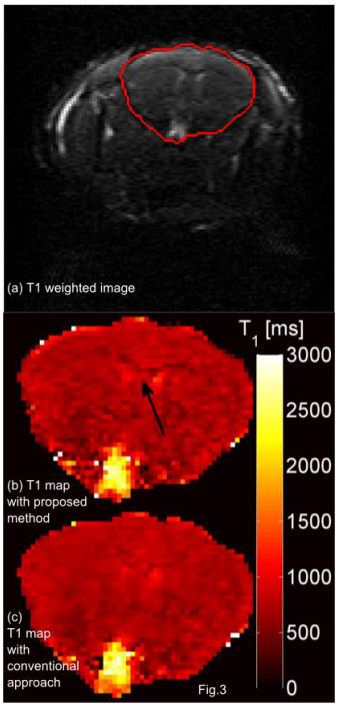

Fig.3

CONCLUSIONS: Registration prior to T_1 fitting introduces bias in the T_1 estimates due to motion estimation inaccuracy and interpolation effects. Our simultaneous group-wise registration and T_1 estimation method reduces this bias as well as the rMSE in the T_1 estimates for a wide range of SNR. Real data support the hypothesis that the inherent interpolation in prior registration has a negative effect on the final T_1 maps, producing blurring and thereby removing clinical important details, which are preserved by our proposed method.

REFERENCES: [1]Deoni S.C.L. et al., Top Magn Reson Imag 2010; 21(2);101-113, [2]Studler U. et al., Top Magn Reson Imag. 2010; 32(2): 394-398, [3]Sijbers J. et al., Int J Imag Syst Tech.1999; 10(2):109-114, [4]Cox R.W. et al., IEEE Trans Image Process. 1999; 8(9):1297-1299, [5]Cococo C.A. et al., Neuroimage.1997; 5(4), [6]Barral J.K. et al., Magn Reson Med. 2010 Oct; 64(4):1057-1067.

Comparison of multi-band multi-echo and multi-echo at 3T

Vincent Jansen[1], Rasim Boyacioglu[1], Jenni Schulz[1], David G. Norris[1]

[1]Donders Institute for Brain, Cognition and Behaviour, Radboud University Medical Center, Nijmegen, the Netherlands

Target Audience: MR physicists, Neuroscientists
Purpose: Following a recent implementation[1] of a Multi-Band[2] Multi-Echo[3] (MBME) sequence at 7T for resting state fMRI that showed improved sensitivity, the potential benefits of MBME with respect to a single band multi-echo (SBME) were investigated at 3T using an event related design.
Methods: Twelve subjects were scanned on a 3T Siemens Tim Trio system (Erlangen, Germany) while performing a cued Gabor grating task with visual feedback using a 32 channel head coil for signal reception. Responses were recorded via button boxes. In a single session, subjects performed the task twice, one with a MBME protocol and one with a SBME protocol, in pseudo-randomised order. Analysis of the reaction times and task performance showed no significant differences between the protocols ($p = 0.886$ and $p = 0.781$, respectively). Both of the protocols had an in-plane acceleration factor of 2 was and were reconstructed online with GRAPPA[4]. The multiband reconstruction was also carried out online with the slice GRAPPA algorithm[2]. The remaining protocol parameters are listed in Table 1.

Table 1. Acquisition parameters for SBME and MBME protocols.

Protocol	TR (s)	TEs (ms)	MB factor	Bandwidth (Hz/Px)	Resolution (mm^3)	Slice Gap	Flip Angle	No. of volumes
MBME	0.809	14,32,49	3	2368	3.5 x 3.5 x 3.0	17 %	56°	510
SBME	2.430	14,32,49	1	2368	3.5 x 3.5 x 3.0	17 %	80°	170

Echoes were combined using TE weighting[5] and concatenated in temporal direction to a 4D NIFTI file. All data were preprocessed with a 5 mm FWHM smoothing kernel, 100 s high pass filtering and exclusion of the first 6 volumes. The data were cleaned using FSL MELODIC (vs3.14, http://fsl.fmrib.ox.ac.uk/fsl/fslwiki/MELODIC) and FSL FIX[6,7] by removing non-BOLD related components. FIX was trained using the provided training sets with similar acquisition parameters: 'Standard' for SMBME and 'HCP_2000' for MBME. FSL FEAT (vs6.00, http://fsl.fmrib.ox.ac.uk/fsl/fslwiki/FEAT) was used for generalised linear modelling at the single subject level with the responses (left and right combined) as a single regressor and group level analysis using a two-sample paired T-test. Significance thresholds were calculated using mixture modeling (http://fsl.fmrib.ox.ac.uk/fsl/fslwiki/Mm)[8].

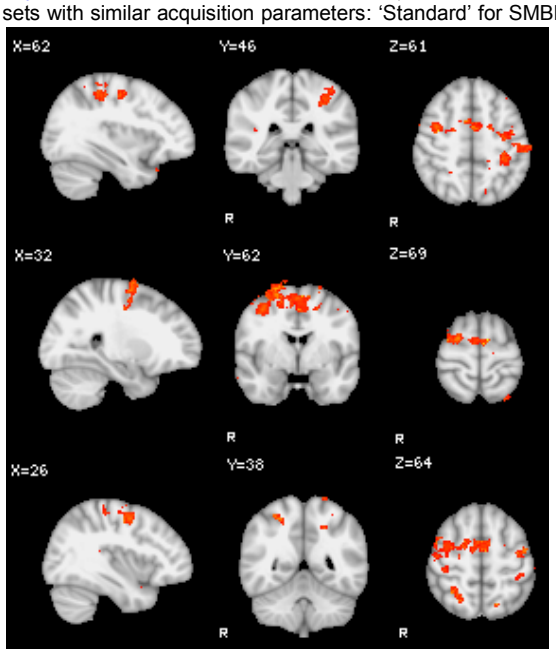

Figure 1. Saggital, coronal and axial slices (columns) showing significantly activated voxels only for MBME for several clusters (rows).

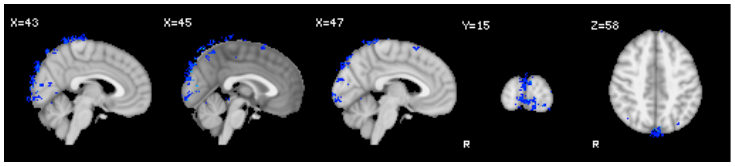

Figure 2. Three saggital, a coronal and an axial slice showing significantly activated voxels only for SBME.

Results: Figures 1 and 2 show significantly activated voxels, either **only** for MBME (red) or SBME (blue) group level analysis, respectively. Figure 1 shows that MBME performs significantly better than SBME in several parietal regions and the lateral frontal cortex, around areas which are generally activated during the Gabor task. Figure 2 shows that voxels activated **only** for SBME around cerebral spinal fluid (CSF), along the superior saggital sinus. The group difference image was masked with a binary non-brain, CSF, grey matter (GM) and white matter (WM) mask to calculate the number of significant voxels for both groups. Table 2 shows the number and percentage of significant voxels. SBME shows almost four times more significant voxels outside the brain than MBME, as is visualized in figure 2.
Discussion: These results show that the distribution of significant voxels between non-brain, CSF, GM and WM regions is different for MBME and SBME. MBME is significantly better than SBME in several GM areas. Most activation of CSF, WM and non-brain voxels is concentrated around GM voxels for MBME. This is probably due to the combination of relatively low resolution data and the 5 mm smoothing kernel. The results also show that for SBME, additional significant activation is concentrated in CSF, along the saggital sinus. This is probably artifactual signal which FIX was unable to remove. MBME has increased temporal resolution which allows for a more efficient removal of non-BOLD related components.
Conclusion: Implementation of Multi-Band in a Multi-Echo sequence shows improved sensitivity in several GM areas and benefits more from automatic non-BOLD related signal removal than a standard Multi-Echo sequence in a standard resolution, event related design at 3T.

Table 2. Table listing the number of significantly activated voxels and percentages in CSF, GM, WM and outside the brain.

Binary Mask	Voxel count	Percentage (%)
MBME group	2394	100.00
Non-brain	119	4.97
CSF	604	26.73
GM	849	35.46
WM	786	32.83
SBME group	2554	100.00
Non-brain	497	**19.46**
CSF	741	29.01
GM	929	36.37
WM	387	15.15

References: 1) Boyacıoğlu et al., ISMRM abstract 1502 2014. **2)** Blaimer et al., 2006 JMRI vol.24 p444-450. **3)** Poser et al., 2006 MRM vol.55 p1227-1235. **4)** Griswold et al., 2002 MRM vol.47 p1202-1210. **5)** Chiew and Graham, 2011 IEEE T-MI vol.30 p1691-1703. **6)** Salimi-Khorshidi et al.,2014 NeuroImage vol.90 p449-468. **7)** Griffanti et al., 2014 NeuroImage vol.95 p232-247. **8)** Woolrich et al., 2005 IEEE T-MI vol.24 p1-11.

Combined 8-channel transceiver fractionated dipole antenna array with a 16-channel loop coil receive array for body imaging

Ingmar Voogt[1], Dennis W.J. Klomp[1], Hans Hoogduin[1], Mariska P. Luttje[1], Peter R. Luijten[1], Cornelis A.T. van den Berg[1], Alexander J.E. Raaijmakers[1]

[1]Imaging Division, University Medical Center, Utrecht, the Netherlands

Target audience: RF coil engineers or MR scientists with an interest in body imaging at ultrahigh fields and/or dipole antennas as surface array elements.
Purpose: Body imaging at ultrahigh field strengths (UHF, 7 Tesla) is performed at various institutes with custom developed surface transmit/receive arrays. Recently, the fractionated dipole array has been presented where the antenna legs are segmented with inter-segment inductors to reduce SAR levels[1]. The 20 mm spacer towards the body leaves room for the placement of detunable loop coils, to realize a separate receive array. In this study, we developed an 8-element transceiver array consisting of fractionated dipole antennas, combined with a detunable 16-element receive-only loop coil array. Imaging performance is evaluated by coupling matrices, B_1^+ amplitude, SNR and T2w prostate images on 6 subjects with BMI ranging from 22.0 to 32.8.

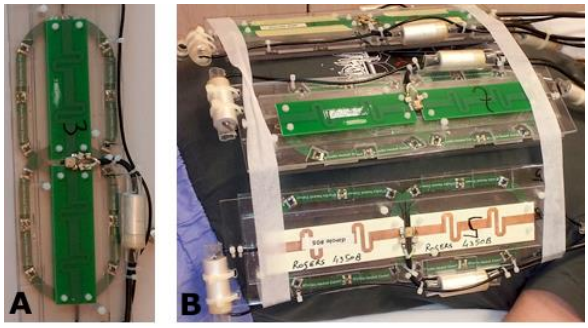

Figure 1: Fractionated dipole antenna with two loops (a) and array setup on a volunteer with removed covers (b)

Methods: Under each of the eight transceive antennas, two loops are positioned with mutual overlap (figure 1a). Spacing from the antenna towards the patient is assured by a 20 mm polycarbonate placeholder. Within this placeholder, receive loops are positioned at 8 mm distance from the patient. The antenna length is 28 cm with two meanders distributed evenly in each leg. The loops are oval shaped (10 cm short axis,16 cm long axis) with 8 capacitors (C_{total}=1pF) and preamp decoupling. Detuning networks block the current at two locations during transmit. Each antenna/two loop structure is one of eight separate elements that can be placed around the pelvis, abdomen or chest of the imaging subject. Volunteer images, with informed consent, were acquired on a Philips Achieve 7T platform with 8x2 kW multi-transmit system (maximum power at coil connector: 8x900W). Coupling matrices were acquired by directional couplers in the transmit line and a software based measurement procedure, carried out online in advance of each exam. After RF shimming, B_1^+ in the prostate was measured by the actual flip angle method[2]. SNR was measured by a dynamic noise scan with a low flip angle FFE measurement (2x2x2.5 mm^3, TE/TR=5/100ms, 124x214x10, FA=1°). Subject 6 was also scanned with an array of fractionated dipole antennas without Rx loops.

coupling antenna-adjacent loop (dB)				
	tuned		detuned	
ant.	loop1	loop2	loop1	loop2
1	-14.5	-20.9	-19.7	-21.7
2	-19.4	-18.4	-22.8	-23.4
3	-26.9	-29.6	-23.9	-25
4	-9.8	-18.1	-15.5	-29.9
5	-13.1	-29.6	-21.9	-41
6	-12.9	-17.6	-18.6	-30.7
7	-15.4	-24.9	-23.6	-28.5
8	-15.9	-18.8	-21.9	-32.8

coupling loop1-loop2 below corresponding antenna (dB)		
antenna	tuned	detuned
1	-16	-30.9
2	-17.5	-36
3	-13.7	-37.2
4	-16.6	-36
5	-16	-41
6	-16	-46
7	-15.9	-41.9
8	-13.5	-41.9

coupling antenna-neighbour loop (dB)			
tuned		detuned	
loop1	loop2	loop1	loop2
antenna 1-left neighbour			
-16.3	-22	-32.7	-44.6
antenna 1-right neighbour			
-23	-33	-43	-40.4
antenna 5-left neighbour			
-30.2	-26	-38.7	-38.2
antenna 5-right neighbour			
-24	-25.5	-42	-52.3

Table 1: Coupling levels between antenna and underlying loops, between two loops within one element and between antenna of one element and loops of the neighboring element.

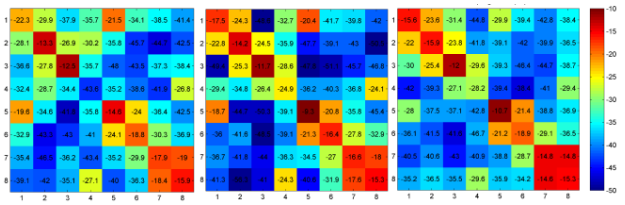

Figure 2: S-parameter matrices (in dB) of the antennas for three subjects with BMI of 22 (a) 26 (b) and 32.8 (c).

Results: By their symmetrical placement, the loop coils and the dipole antenna are remarkably well decoupled (< -9.8 dB without; < -15.5 dB with detuning, table 1). Matching of the antennas is acceptable (< 9 dB, most channels much better) and coupling is low (<-14 dB) for all investigated subjects, figure 2. B_1^+ amplitude ranges from 10 µT (BMI 32.8) to 15.4 µT (BMI 22). SNR values (SOS reconstruction) range from 21 to 27. The loop coils provide slightly higher SNR than the antennas alone (27 vs 22) but also reduced B_1^+ efficiency. Image quality of T2w prostate images is good for all subjects (figure 3).

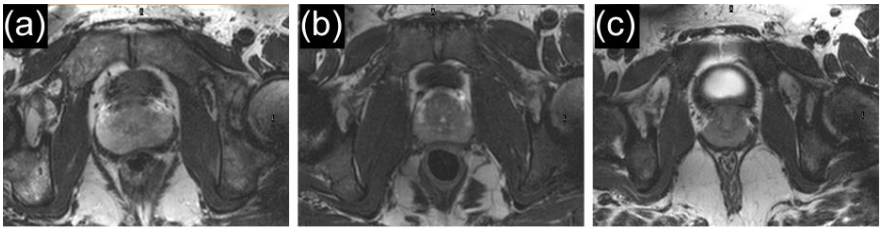

Figure 3: T2w TSE prostate images (TE/TR=130/2700 ms, 0.78x0.78x3 mm2, NSA=2) of volunteer subjects with BMI 22 (a) 26 (b) and 32.8 (c)

Conclusion: The combination of a 8-element fractionated dipole array with integrated 16-element loop coil receive array is a promising enhancement of the existing design. Its good imaging performance with extended acceleration potential (not evaluated yet) make it an attractive design for body imaging applications. Next step is to use the dipole antennas also for receive, resulting in a 24-element receive array with significantly higher SNR.

References: [1] Raaijmakers et al. ISMRM 21st Annual Meeting 2013
References: [2] Yarnykh (2007) MRM 57:192-200 (referentie over de B1+ mapping methode)

A phantom designed specifically for local SAR validation

Matthew Restivo[1], Ronald Mooiweer[1], Cornelis A.T. van den Berg[1], Alexander J.E. Raaijmaakers[1], Frank Simonis[1], Peter R. Luijten[1], Hans Hoogduin[1]

[1]Imaging Division, University Medical Center, Utrecht, the Netherlands

Introduction: SAR safety is an important issue for 7T MRI as localized SAR hot spots can potentially result in dangerous heating.[1] Safety decisions for peak local SAR must rely on numerical electromagnetic simulations of RF coil models loaded with human body models. However, prior to this SAR assessment it is important to obtain confidence in the coil models by validation using phantom experiments. Phantoms are typically dielectrically homogenous and therefore do not exhibit very localized heating. We built a phantom which exhibits significant localized heating and provides good conditions for measuring temperature rise with MR thermometry and/or using fiber optic temperature probes.

Methods: The phantom design consists of four 1 cm diameter tubes that run longitudinally through a 15 cm diameter cylinder, all made from PMMA (Fig. 1). The tubes are filled with a saline gel with a conductivity of 2.4 S/m at 298 MHz (measured using an Agilent 85070E dielectric probe). This is similar to the highest conductivity seen in a human head at 7T (CSF=2.2 S/m). Two of the tubes are narrowed to .5 cm diameter in the center so that current, and thus SAR, will be concentrated in that region (Fig.2). The larger cylinder is filled with oil. The oil is important in the phantom because it has near zero conductivity and will minimally heat with application of RF energy. Also, oil does not have a temperature dependent proton resonant frequency shift (PRFS), which allows us to use the phase change in the oil for field drift correction enabling more accurate PRFS thermometry.[2] Validation experiments were performed using a quadrature birdcage head coil. Proton Resonance Frequency Shift (PRFS) MR thermometry was performed using an FFE sequence with the addition of a high power pre-pulse every TR (455° flip angle at 10 kHz frequency offset to cause heating but not affect the MR image). The MR thermometry was performed using a 10° flip angle, TR=22ms, TE = 15ms, and minimal water-fat shift. The sequence was repeated consecutively 16 times for a total duration of 5 minutes.

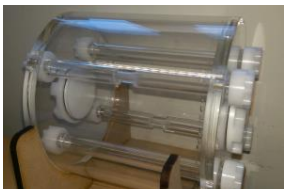

Figure 1: Photo showing the constructed phantom

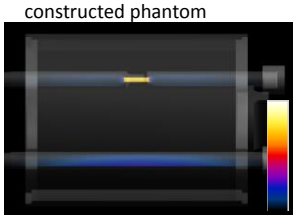

Figure 2: Sagittal view of simulated SAR distribution for the phantom in position 1. Very localized SAR is realized inside the narrowed tube compared to the straight tube

The SAR distribution was simulated using Semcad X (Speag AG, CH). Additionally, the Semcad thermo-solver, based on Pennes bioheat model, was used to simulate the temperature rise due to five minutes of heating. Temperature simulations were normalized to the same power used in MR experiments by comparing measured and simulated B1+.

Experiments were done with the phantom in two different positions. The first position was with the phantom centered in the longitudinal center of the coil, but 1.5 cm up from isocenter, so that the electric field would not be symmetric and un-even heating would occur. In the second position, the center of the phantom was moved to the longitudinal edge of the coil and rotated 90° with respect to position 1. This position was chosen because the birdcage produces higher electric fields near the edge of the coil compared to the center, and therefore should produce more heating. In previous experiments using this phantom, MR thermometry results have shown good agreement with fiber optic temperature probes inserted directly into the tubes. For this particular study, temperature probes were omitted because they are not included in simulations.

Results: The simulated peak 1g averaged SAR is 1.60 $W*kg^{-1}*\mu T^{-2}$ in position 1 when normalized to the average B1+ over the axial slice in the center of the coil. SAR1g increases to 2.80 $W*kg^{-1}*\mu T^{-2}$ when the phantom is moved to position 2. For comparison, the SAR1g in the head of a human model (Duke of the Virtual Family[3]) using the same coil is 2.61 $W*kg^{-1}*\mu T^{-2}$. Fig. 3 shows the maximum temperature rise observed using MR thermometry compared to the simulated SAR distribution for both positions. Fig. 4 shows the temperature rise measured by thermometry over time compared to the temperature rise expected from simulations at the center of each of the four tubes with the phantom at position 1. Maximum temp rise measured was ≈ 1.4°C vs. maximum temp rise simulated was ≈ 1.3° C. Much more heating was measured at position 2, where maximum temp rise measured was ≈ 5°C vs. maximum temp rise simulated was ≈ 3.4°C.

Discussion: Thermometry measurements for two different positions show reasonable agreement with temperature simulations. As expected, a larger temperature rise is observed in the narrowed tubes compared to the straight tubes. While the overall temperature difference is dependent on local SAR in the tubes as well as thermal effects (e.g. heat conductions), the initial slope of the temperature rise is directly indicative of the local SAR. The time course of heating in Fig. 3 shows that the initial slope of the temperature rise is predicted accurately by the simulation. Thus, there appears to be a match between actual and predicted local SAR levels. The most likely source of error in the simulations is positioning of the model with respect to the coil. The birdcage coil generates an electric field distribution that is strongly inhomogeneous. Small changes in position lead to large changes in electric field intensity within the conductive tubes. In the tube with the highest observed heating (Fig. 3, Tube A, Pos. 2), simulations underestimate heating by 1.6°C (5°C measured vs. 3.4°C simulated). More experiments must be done in similar high-heating situations to confirm whether this is an error related to model positioning, thermal properties, or a different cause.

Conclusion: A phantom has been constructed that exhibits high localized SAR, which is comparable to peak local SAR in the human head during 7T MRI. The local SAR in this phantom can be measured by means of temperature rise using PRFS thermometry or directly using fiber optic probes inserted into the tubes. Measurements with this phantom allow for local SAR validation for RF coil models, a necessary step prior to relying on SAR simulations for in-vivo safety decisions.

References: 1) Neufeld et al, PMB, 2011;56 (15):4649-59. 2) Salomir et al, IEEE, 2012;31(2):287-301. 3) Christ et al, PMB, 2010;55:N23. *This work was supported by the Initial Training Network, HiMR, funded by the FP7 Marie Curie Actions of the European Commission (FP7-PEOPLE-2012-ITN-316716)*

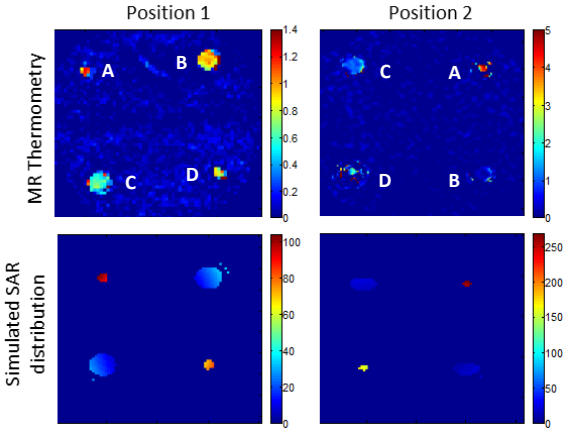

Figure 3: MR thermometry images show temperature rise in degrees Celsius over the center axial slice of the phantom after 5 min. Thermometry images show good agreement with simulated SAR distributions. SAR distributions are normalized to B1+ achieved in thermometry sequence. SAR has units of W/kg.

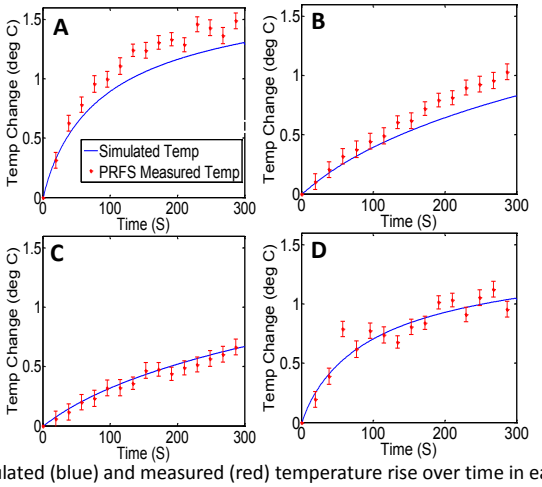

Figure 4: Simulated (blue) and measured (red) temperature rise over time in each of the four tubes (A-D) with the phantom placed in the center position (position 1). Error bars represent noise in the thermometry images computed from the standard deviation of temperature in an unheated region of the phantom.

RF safety validation of high permittivity pads at 7 tesla

Wyger Brink[1], Yassin Noureddine[2], Oliver Kraff[2], Andreas Bitz[3], Andrew Webb[1]

[1]C. J. Gorter Center for High Field MRI, Department of Radiology, Leiden University Medical Center, Leiden, the Netherlands
[2]Erwin L. Hahn Institute for Magnetic Resonance Imaging, University Duisburg-Essen, Essen, Germany
[3]Medical Physics in Radiology, German Cancer Research Center (DKFZ), Heidelberg, Germany

Target audience: Researchers with interest in RF shimming and RF safety at high fields

Purpose: RF shimming using dielectric pads has been shown to be useful by various authors, with an improved RF transmit field (B_1^+) fidelity [1,2]. Analyses of the specific absorption rate (SAR) in such configurations are typically based on electromagnetic (EM) simulations using approximate numerical methods and discretized body models [3]. The aim of this study is to further validate the accuracy of these methods inside a phantom configuration using RF near-field probes.

Methods: A homogeneous head and shoulders phantom was used to mimic the overall geometry of the human head and induce realistic coil loading. The phantom was filled with tissue simulating liquid which had a relative permittivity of ε_r = 50 and an electrical conductivity of σ = 0.603 S/m, as characterized using a dielectric probe kit (85070E, Agilent Technologies, Santa Clara, CA). Two sets of dielectric pads were constructed using aqueous suspensions of either $CaTiO_3$ (ε_r = 118, σ = 0.14 S/m) or $BaTiO_3$ (ε_r = 288, σ = 0.38 S/m), with dimensions of 18 × 18 × 1 cm^3 and lateral position as used in previous work [1,2]. A 16-rung high-pass birdcage resonator was built using a cylindrical former with an inner/outer diameter of 30/35 cm and rung length of 17 cm. The coil was tuned to 300 MHz and the reflection and coupling coefficients were below -15 dB for all experiments.

RF near-field measurements were performed within the phantom liquid using RF probes (EASY4, SPEAG, Zurich, Switzerland), with and without the dielectric pads present. The RF frequency was set to 300 MHz not to interfere with MR acquisitions at 297 MHz. The accepted power at the coil input was recorded using a directional coupler and power detector to correct for losses up to the coil port. The electric field magnitude was recorded along two lines, as indicated by the dashed lines in Figure 1.

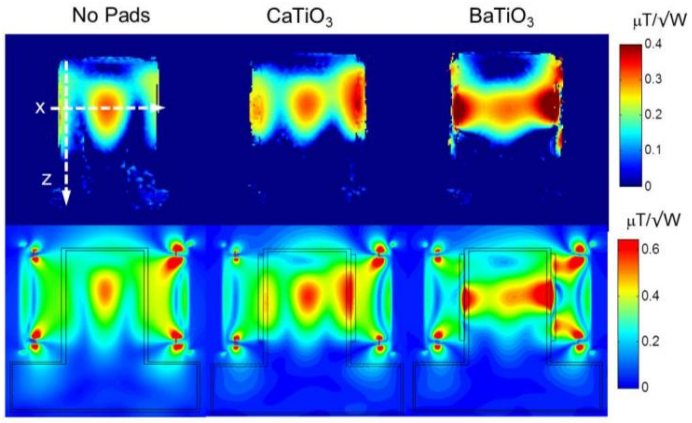

Fig. 1. Measured (top) and simulated (bottom) B_1^+ maps in the coronal view without and with pads. The dashed lines indicate the position of the line plots (cf. figure 2).

EM simulations were performed using the finite-integration time-domain method (CST Studio Suite, CST AG, Darmstadt, Germany) and circuit co-simulation to model the lumped elements. B_1^+ maps were acquired on a 7T system (Achieva, Philips Healthcare, Best, The Netherlands) using the double angle method [4], with nominal tip angles α_1/ α_2 = 60°/120°, TR/TE = 5000/4.0 ms and a 500 ms saturation delay. The transmit efficiency was determined by normalizing B_1^+ to accepted power, which included losses in the RF chain during MR experiments.

Results: Figure 1 shows simulated and measured B_1^+ maps in the coronal plane, without and with dielectric pads. The offset between measured and simulated data here, is due to losses in the RF chain during the MR experiments. Line plots of the E-field magnitude are shown in Figure 2. The relative changes in electric fields are within ~10% agreement with simulated data.

Discussion: Electric field measurements confirm that the electric fields within the phantom are affected by the dielectric pads. The largest E-field elevation is induced by the $BaTiO_3$ pads, which is in line with previous studies [2]. As can be appreciated from Figure 1, the B_1^+ 'focusing' induced by the $BaTiO_3$ pads leads to a local increase in transmit efficiency of up to ~300%. This can be of interest in localized applications such as MRS or high resolution imaging. The corresponding electric field data, which shows an increase in the order of 50-100%, indicates that the local SAR can be expected to remain in the same order of magnitude as when no pads are being used. The data presented here can only be indicative for the simulation error however; a realistic analysis of SAR requires the use of heterogeneous body models to relate these values to the in vivo case [3].

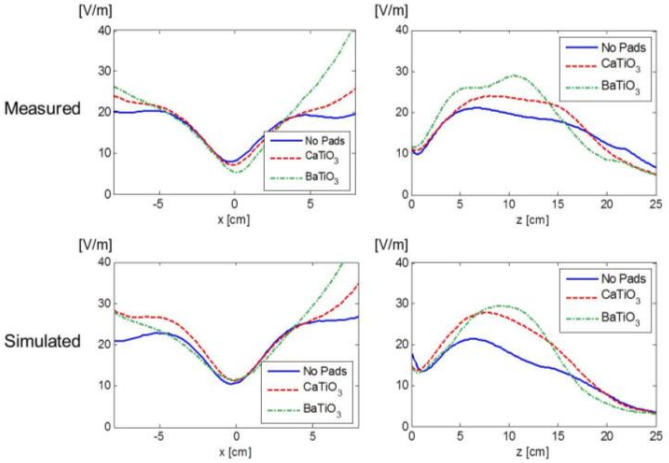

Fig. 2. Measured (top) and simulated (bottom) electric field magnitude without and with pads. The data were acquired along the dashed lines as shown in figure 1.

Conclusion: The data presented here indicate an agreement between simulations and measurements of electric and magnetic fields in the order of ~10%. This means that realistic scenarios can be evaluated with this error margin to provide SAR estimates for using pads in vivo.

References: [1] Teeuwisse et al., *MRM 2012*, 67:1285-93; [2] Brink et al., *Invest. Radiol. 2014*, 49:271-77; [3] Bitz et al., *Proc. ISMRM 2014*, 4892; [4] Cunningham et al., *MRM 2006*, 55:1326–33.

The three-dimensional shape of the myopic eye measured with MRI

Jan-Willem Beenakker[1,2], Denis Shaqmon[3], Andrew G. Webb[1], Gregorius Luyten[2], Berend Stoel[3]

[1]C. J. Gorter Center for High Field MRI, Department of Radiology, Leiden University Medical Center, Leiden, the Netherlands
[2]Department of Ophtalmology, Leiden University Medical Centre, Leiden, the Netherlands
[3]Division of Image Processing, Department of Radiology, Leiden University Medical Center, Leiden, the Netherlands

Target audience: MRI clinicians, researchers in ocular and vision science, ophthalmologists

Purpose: There is an increased interest in methods to measure and describe the three-dimensional shape of the retina, and its relation to myopia. For example, the refractive errors of the eye can partly be explained by the length of the eye along the optical axis, the axial length, which can be measured by optical techniques. Off-axis distances, however, cannot be measured by these techniques, because refraction induces potentially significant systematic errors.[1] Since it is not affected by refraction, in the recent years, MRI has become the main tool to measure the retinal shape.[2-4] One of the important findings is that the difference between the horizontal and vertical curvature of the retina leads to different refractive errors along the horizontal and vertical meridian.[2] However, the sensitivity of MRI to eye-motion has limited these evaluations to 2D or low-resolution 3D data of the eye. In this context, we describe a method that uses the advances in high field MRI to measure the full 3D ocular shape with high-resolution and we use this method to evaluate the relationship between 3D retinal shape and the refractive error.

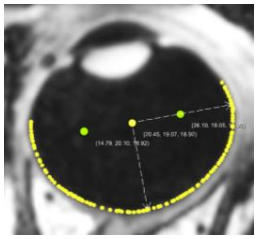

Fig. 1: Elliptic fit on high-resolution ocular MRI data

Methods: We examined 11 subjects with normal vision, |refractive error| < 0.5D, and 10 patients with mild to severe myopia (refractive error between -0.5D and -7D) with no further ocular pathologies. The examination consisted of an ocular MRI scan and auto-refraction measurement (Park 1, Oculus Inc., Arlington, WA). Four additional volunteers have been examined twice with MRI to assess the reproducibility of the method.

The ocular MRI was performed on a Philips Achieva 7 Tesla whole body magnet. The left eye was scanned with a custom-made dedicated 3-channel receive eye-coil, in combination with a volume transmit coil (Nova Medical Inc.,Wilmington, MA).[5] Eye-motion artefacts were minimized by the use of a cued-blinking protocol and the MR images were acquired using a 3D inversion recovery turbo gradient echo technique. The total MRI examination takes less than 15 minutes. The resulting MR-images were processed using an automatic segmentation algorithm, which detects the retinal contour with sub-pixel accuracy.[4]

The shape of the retina was quantified by fitting an ellipsoid to the detected contours and we used the obtained parameters as shape descriptors. In order to determine the number of contour points to be included in the ellipse fitting, a 2D fitting algorithm was applied and the accuracy and reproducibility of each fit was recorded for a range of percentages of included points. Subsequently, using this optimal percentage, 3D ellipsoid fitting was performed using the Sequential Least Squares Programming algorithm from the SciPy library. The fits were performed with the axes of the ellipsoid fixed to the optical axis, and the Left-Right and Feet-Head directions. An additional fitting procedure was programmed which allowed the ellipsoid to be rotated around the optical axis.

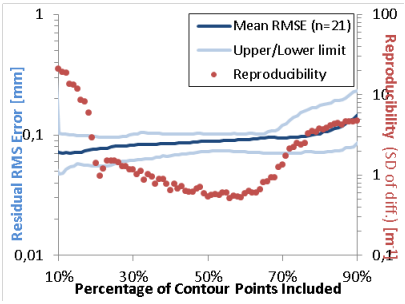

Fig 2. Goodness of fit and reproducibility as a function of amount of contour points included.

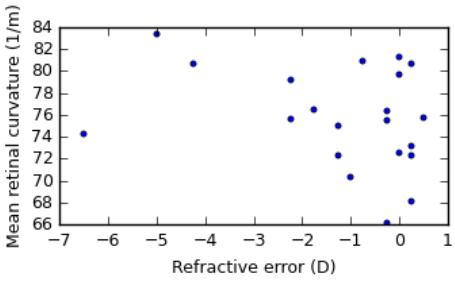

Fig 3. 3D fit results (A) The average retinal vertex curvature vs. myopia

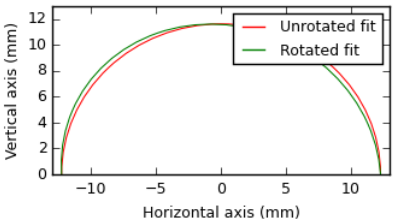

Fig. 4. 3D MRI data of eye allows for a better description of the retinal shape, since rotations around the optical axis can be taken into account. For this volunteer the maximal difference between an unrotated and rotated fit was 0.4mm.

Results: Fig. 1 gives an example of the 2D ellipse fit to the retina. The 2D fitting algorithms converged to ellipsoids with similar errors over a wide range of number of points used, fig 2, showing the retinal shape is well described by an ellipsoid. Only when more than 70% of the contour is used, the results start to deviate as the retinal shape starts to deviate from an ellipsoid near the crystalline lens and cilliary body. The reproducibility of the 2D ellipse fit was also stable for a wide range of number of included points (fig. 2). Therefore, for subsequent analysis 60% of the retinal contour was used as an input for the fit for subsequent analysis.

When the retinal shape is fitted in 3D with the axes of the ellipsoid fixed to the LR and FH directions, the previously described difference in horizontal and vertical vertex curvatures are reproduced ($73.8m^{-1}$ vs $77.5m^{-1}$ respectively).[2] When however the orientation of these two principle axes was left free as a fitting variable, for most (17/21) of the subjects a better fit is achieved by rotating the ellipsoid, fig 4 (mean maximal difference 0.2mm, range [0.0, 0.4]mm).

Discussion: The data supports the previously described increase of retinal curvature in emmetropia compared to myopia, fig. 3, ($74.8m^{-1}$ vs $77.0m^{-1}$).[2]

The main advantage of having full three-dimensional data is that it allows for a better description of the retinal shape that accounts for its potentially oblique orientation. Although this angle will average out over a large population, the improvements in descripting individual eyes are significant. This can be compared to astigmatism, the cylindrical component of spectacle glasses, whose angle also differs on the subject level. The 3D description of the retinal shape will be used in subject-specific ray-tracing eye models, enabling the evaluation of the refraction on the complete retina.

Conclusion: Ocular MRI is able to accurately measure and describe retinal shape. Our results extend the previous 2D measures of the ocular shape to 3D. Furthermore, the high reproducibility of the method makes it a powerful tool to study the hypothesized change of eye shape the development of myopia.[6,7]

References: 1. Atchison et al. Opt. Vis. Sci. 88: E601 (2011); 2. Atchison et al. IOVS 46: 2698 (2005); 3. Verkicharla et al. Ophth Phys Opt 32: 184 (2012)
4. Beenakker et al. IOVS (2014); 5. Beenakker et al. NMR Biomed 26: 1864 (2013); 6. Schmid, Opt Vis Sci 88: 674 (2011); 7. Smith et al, IOVS 46: 3965 (2005)

Correction of artifacts in ultrahigh Field T2* imaging using a training model for field probe based B0 measurements

Anders Garpebring[1], Joep Wezel[1], Vincent Boer[2], Tijl A. van der Velden[2], Andrew G. Webb[1], Dennis W. Klomp[2], Matthias J.P. van Osch[1]

[1]C. J. Gorter Center for High Field MRI, Department of Radiology, Leiden University Medical Center, Leiden, the Netherlands
[2]Department of Radiology, University Medical Center, Utrecht, the Netherlands

Targeted audience: Researchers interested in ultrahigh field MRI, field probes (FPs), and susceptibility induced MRI-artifacts

Purpose: Strongly T_2^*-weighted gradient echo (GE) imaging is frequently used at 7 T because of its superior quality, enabling detection of e.g. cortical layering and cerebral micro bleeds [1]. The improved contrast is partially due to the increased effects of magnetic susceptibility differences at higher field strengths. However, the increased sensitivity can at the same time lead to issues, i.e. breathing can cause phase-shifts during the collection of data resulting in artifacts. To make this type of imaging more robust B_0 maps obtained from navigators [2] or FPs [3] can be used for correction of the images. In the method based on FPs, a model is required for the extrapolation of the measured FP-values to a B_0-map. Usually this model is based on the assumption that there are no sources of the magnetic field in the imaged region, i.e., one can model the B_0-field using spherical harmonics (SH). This approach fails in case of sources within the imaged region, restricts the method to low order SH-models, and the extrapolation of FP-measurements to inside the head can be a potential source of error. The purpose of this work was to investigate if a model learned from simultaneous FP measurements and fast B_0-measurements could be used for FP-based correction of T_2^*-images, and whether this approach provides improvements over the conventional method.

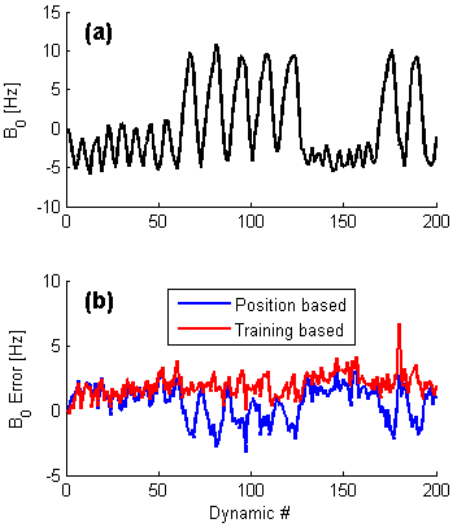

Fig 1. (a) Measured B_0 fluctuations. **(b)** Error in predicted B_0 fluctuations.

Methods: All imaging was performed on a 7 T Philips scanner using a 32-channel head coil and a FP system consisting of 15 ^{19}F transmit/receive probes (Skope Magnetic Resonance Technologies). A healthy volunteer was imaged and was instructed to do 30 s periods of normal and deep breathing during both fast EPI based B_0 imaging (the training data) and during the acquisition of the T_2^* weighted image. The EPI based B_0 imaging was repeated once to enable validation of predicted B_0. For the EPI sequence, transverse multi-slice single shot GE-EPI was used with a 64 × 64 × 10 matrix, 200 dynamics, a field of view (FOV) of 240 × 240 × 120 mm^3, TR/TE = 500/8.13 ms, flip angle (FA) = 20°, and a SENSE factor of 2.5. For the T_2^*-weighted imaging the acquisition matrix was 600 × 600 × 20, FOV 240 × 240 × 22 mm^3, TR/TE = 800/25.2 ms, FA = 35°, acquired without SENSE. FP-data were acquired during EPI and T_2^*-weighted scans with one measurement per slice and dynamic for the EPI sequence and one measurement per phase encoding line for the T_2^* sequence. A linear model was used to relate the FP values $\boldsymbol{\xi}(t)$ to $B_0(x,t)$:

$$B_0(x,t) = \mathbf{p}^T(x)\boldsymbol{\xi}(t) + \epsilon(x,t), \quad (1)$$

where $\mathbf{p}(x)$ are a set of coefficients for the pixel, found from least squares fitting to the training data, and $\epsilon(x,t)$ is noise. The resulting B_0 maps were fitted to a third order SH model to reduce noise and to extrapolate maps to regions with low SNR. The method developed by Wilm et al. [4] was used for reconstruction. For comparison, B_0 maps were also estimated using the positions of the probes and a second order SH model [3] (conventional method).

Results: Fig. 1a shows the variation in B_0 during the validation scan. In Fig. 1b the differences between the FP based predictions and the curve in Fig. 1a are shown for the proposed method and the conventional method. In Fig. 2 uncorrected and corrected T_2^*-images are shown.

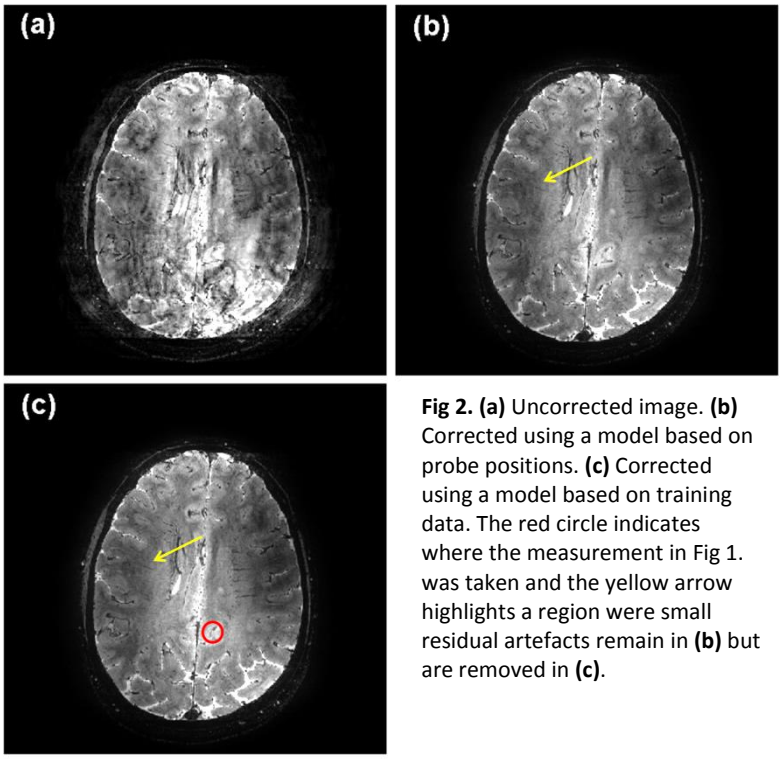

Fig 2. (a) Uncorrected image. **(b)** Corrected using a model based on probe positions. **(c)** Corrected using a model based on training data. The red circle indicates where the measurement in Fig 1. was taken and the yellow arrow highlights a region were small residual artefacts remain in **(b)** but are removed in **(c)**.

Conclusion: The proposed training based method was able to predict B_0 fluctuations in the validation dataset and correct for most artifacts in a T_2^*-image. The performance regarding the prediction of B_0 maps was better than for the conventional method, resulting in a small but detectable improvement in the corrected image. This study shows that B_0 maps based on training data and FPs could be a feasible approach for B_0 correction of T_2^* images and that it may provide some improvements over the conventional approach. Continued research will focus on evaluating the method in a larger group of subjects.

References: [1] Conijn M.M.A. et al. AJNR 2011 32(6):1043-9. [2] Versluis M.J. et al. MRM 2012 68(6):1836-45. [3] Vannesjo S.J. et al. MRM 2014 e-print (doi: 10.1002/mrm.25303). [4] Wilm B.J. et al. IEEE TMI 2012 31(6):1396-403.

Acknowledgements: This research is supported by the Dutch Technology Foundation STW, applied science division of NWO and the Technology Program of the Ministry of Economic Affairs.

Depth dependent safety analysis of peripheral arterial stents at 7 tesla

Janot Tokaya[1], Alexander Raaijmakers[1], Anja van der Kolk[1], Jurriaan Bakker[2], Peter Luijten[1], Dennis Klomp[3], Nico van den Berg[3]

[1]Department of Radiology, University Medical Center, Utrecht, the Netherlands
[2]Eindhoven Design Center, Medtronic, Eindhoven, the Netherlands
[3] Imaging Division, University Medical Center, Utrecht, the Netherlands

Introduction

At 7T the relatively short wave length of RF fields enhances energy deposition in tissue and allows resonance conditions to be met by relatively small structures. Therefore, excessive heating of arterial stents is anticipated and patients with stents are customarily excluded from 7T investigations. However, the enhanced electric fields induce currents and associated counteracting fields that cause the quality factors of the resonating stents to decrease, resulting in less pronounced heating. This has been confirmed recently for three stent lengths at 5 cm depth: local heating near the stent tips is inferior to direct heating ==at the surface by the local transmit antenna[1]. It is expected that for stents at shallower depths the enhancement of electric fields at the stent tips and its associated heating will exceed the heating of the surface layer nearest to the antenna, thus imposing additional restrictions on applied average transmit power. In this study the dependency of stent tip heating on stent depth is investigated in a phantom by proton resonance frequency shift (PRFS) thermometry validated with fiber optic probes (FOPs) and numeric electromagnetic simulations.

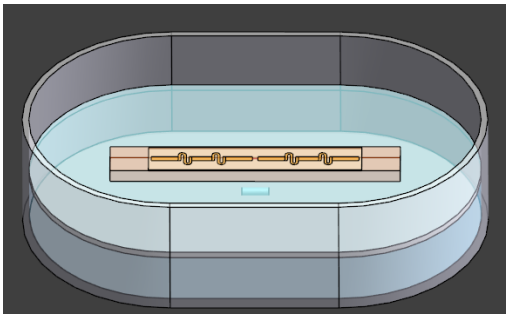

Fig. 1 ASTM phantom with stent and dipole antenna.

Methods

An elliptical ASTM phantom (fig.1) was filled with saline HEC gel (1.55g/L NaCl and 28g/L hydroxyethylcellulose, ε_r=76.5±0.6, σ=0.49±0.02 S/m, 9cm liquid height) closely resembling human tissue. An Xact 8X40mm arterial stent, which in previous studies proved to heat most prominently in a set of 20 arterial stents[2], was positioned at various depths under a fractioned dipole antenna[3]. PRFS MR thermometry was acquired in 5 coronal slices at 7 time intervals during an 11 min scan, with TE1/2/3 of 15/30/40ms and a TR of 150ms, with 4W average power. Potential field drift was corrected using near harmonic 2D reconstruction of the background phase utilizing a closed non-heating region around the implant[4]. A region of interest of 3x3 pixels around the FOPs (AccuSens; OpSens, Canada) was used to validate the PRFS temperatures against FOP measurements as presentenced in figure 2. Uncertainties in PRFS temperatures stem from local temperature gradients in the ROI and noise. Numerical simulations (Sim4Life, ZMT, Zurich) were used to acquire additional confidence in the measurements and investigate the variability of temperature increase with various tissue conductivities and the presence of an adipose layer between antenna and stent. The resulting SAR distribution were subsequently used as input for thermal simulations to determine the stent tip temperature. In simulations, the stents were represented as hollow cylindrical tubes, avoiding the computationally expensive mesh structure of the stent.

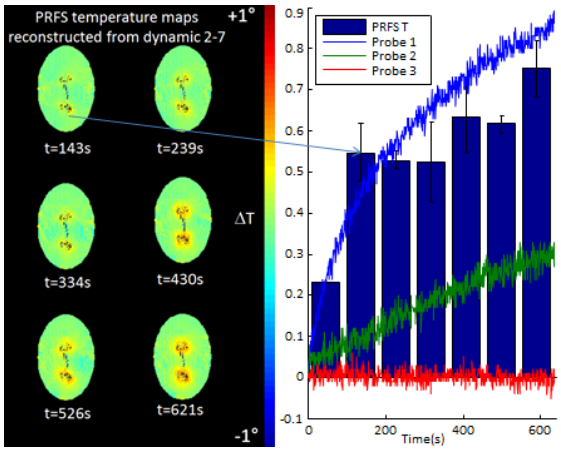

Fig. 2 PRFS temperature maps inside field drift masks. The error bars in PRFS T are the standard deviations in the ROI.

Results

A linear relation was found between stent tip heating and stent depth between 2-31mm as depicted by the gray line in fig.3, which is a fit to the black dashed line (probe and MR thermometry measurements). This result is expected since the penetration depth in our phantom exceeds the maximum stent depth that was investigated. The HEC layer directly under the dipole antenna was found to heat 0.12±0.02°C (uncertainty was determined from the standard deviation in non-heating regions) and shown as the red line in fig.3. A near linear relation was likewise found in the simulations with the phantom characteristics of the experiment. The dots in fig.3 represent the final stent tip heating found in a thermal simulation with 1.5W antenna output power. Increasing the conductivity of the phantom decreases heating and elucidates the exponential drop-off of the electric fields and its associated heating. Despite the apparent proportionality between SAR and conductivity the decay of the electric fields dominates the heating behavior of the stent in the investigated depth and conductivity domain. The presence of a 10mm adipose layer between the stent and the antenna increases heating with 13-41% and results in a shift towards the right (~7mm) of the exponential curve compared to the situation without an adipose layer, because electric field attenuation is relatively small in fatty tissue.

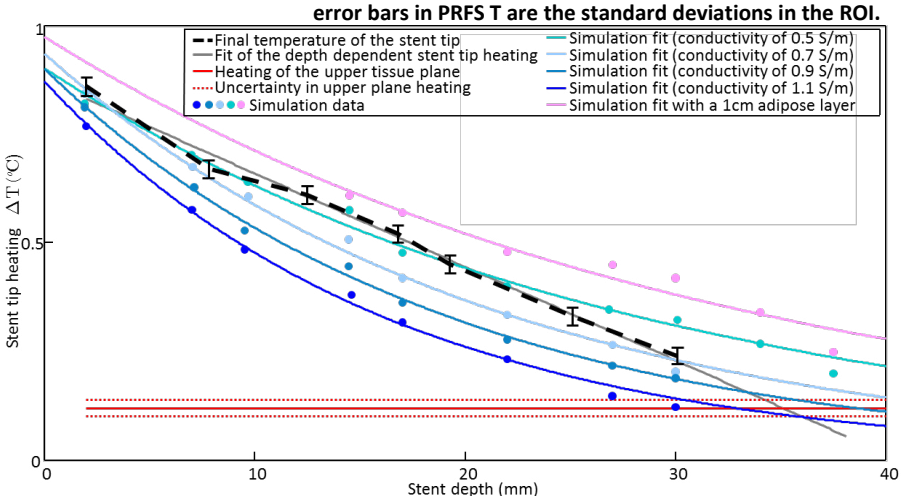

Fig. 3 Temperature increase of the stent tip at the end of the heating sequence as measured by the FOP and matched with thermometry and from numeric simulations.

Conclusion

For all investigated depths, stent tip heating exceeds heating at the upper tissue layer, resulting in a reduction of the safe average power level from 50% to 86% if the stent is not allowed to heat more than the upper skin layer. Extrapolation of the linear relation (grey line in fig. 3) between depth and heating suggests that stent heating remains below antenna heating if the stent is more than 35±1mm under the skin. It should however be noted that in more realistic models, including an adipose layer, more conservative estimates should be made and the depth for which stent tip heating drops below upper layer heating increases similar to adipose layer size. This also holds for less conducting tissue types since skin depth is inversely proportional with conductivity for a poor conductor. Still for all simulated situations similar relatively small temperature increases at the stent tips are found.

1.Winter, L. et al. Magn. Reson. Med. 2014.,2.Ansems, J. et al.ISMRM 2011.,3.Raaijmakers, A. et al. ISMRM 2013.,4.Salomir, R. et al. IEEE Trans. Med. Imaging, 2012.

New low-order pre-fractal geometries of high permittivity pads further increase sensitivity at high magnetic fields

Rita Schmidt[1], Andrew Webb[1]

[1]Department of Radiology, Leiden University Medical Centre, Leiden, the Netherlands

Target audience. Scientists working at 3T and 7T in applications with significant dielectric image artifacts.

Purpose. In previous work the concept of using high permittivity materials [1-4] to increase the strength and homogeneity of the B_1 field has been shown at 3T and 7T. However, it was also shown that at ultrahigh field (7 T and more) instead of a monotonic sensitivity improvement, high permittivity pads can also be a source of local signal decreases due to wavelength effects within the material, producing severe image artifacts. So far, all of the studies have used very simple rectangular geometries of homogeneous high permittivity material, without any exploration of different types of shape. In this study we investigate how the wavelength effects can be mitigated by using a low order prefractal geometry [5] for the dielectric pad, which maintains the overall coverage of the pad, but gives an increase in sensitivity and homogeneity in the relevant region of interest.

Methods. Electromagnetic simulations of B_1^+ field were performed using FDTD software (CST Microwave Studio). The setup included a birdcage coil that was loaded with the CST Bio model "Gustav": simulations were performed for both the head and leg regions. The geometry of the high dielectric pad with ε_r (relative permittivity) of 300 was designed in MATLAB and imported into CST Studio. The shaping of the prefactal pad was based on a cylindrical shell built from sub-sections of a "Sierpinski carpet" [5] up to a third order. The size of the central hole in the "Sierpinski carpet" base was 3.8x7 cm^2. As a comparison, fully filled pads of the same thickness (8 mm) with ε_r of 100 and 300 were designed. All B_1 maps were normalized to the accepted power of 1watt.

Figure 1: Simulations with different shaping of the pad in leg region

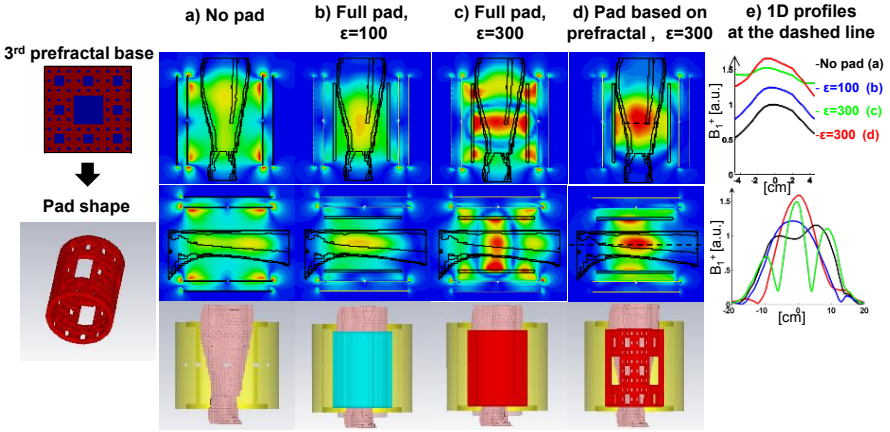

Results. Figure 1(b) shows that the ε_r =100 cylindrical pad increases the sensitivity by ~20%. Greater increases are shown in Figure 1(c) with a pad with ε_r =300, but there are significant inhomogeneities introduced by the higher dielectric. Using the prefractal geometry in Figure 1(d) maintains the high sensitivity but increases the longitudinal homogeneity significantly (the effect was improved from 1st – main holes only - to 3rd prefractal order). Figure 2 shows that results in the brain show similar behavior, but that the effects are even more pronounced in terms of the improved performance of the prefractal geometry. All maps are scaled to the same maximum value.

Figure 2: Simulations with different shaping of the pad in brain region

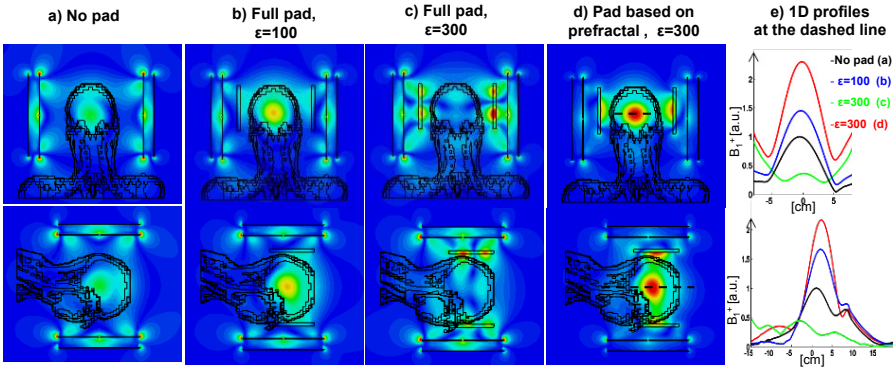

Conclusions. The results show that by using a prefractal geometry rather than a solid structure, as has been used in all previous studies, higher permittivity materials can be used to produce greater increases in sensitivity than currently possible, without introducing image artifacts associated with wavelength effects.

Acknowledgments. We are grateful to A. Seginer for discussions on prefractal geometries and to W. Brink for help with EM simulations.

References. [1] Haines K. et al. J.Magn.Reson. 2010; 203: 323-327. [2] Yang Q.X. et al., Magn Reson Med. 2011; 65:358–362. [3] Teeuwisse W.M. et al., Magn Reson Med. 2012; 67:912-918. [4] Brink W.M. et al. Magn.Reson.Med. 2014; 71: 1632-1640. [5] Allouche J-P. Cambridge University Press 2003.

Force compensated power supply cable for a local insert gradient in 7T MRI

Quincy van Houtum[1], Vincent Boer[1], Mark Gosselink[1], Dennis Klomp[1]

[1]Department of Radiology, University Medical Center, Utrecht, the Netherlands

Introduction. Local gradient inserts in MRI have the potential to increase the sensitivity in diagnostic imaging in for example DWI in breast cancer detection. Both the maximum strength and slew rate can be increased by a several-fold compared to the built-in whole body gradient system and consequently decrease voxel size thus allowing for higher spatial resolutions. While the design of insert gradients is a well-established field, the driving current still has to be supplied to the local insert gradient; preferably with a flexible cable. This is challenging as the strong magnetic field induces a substantial Lorentz force on the current-carrying wire. The resulting moving cable can hurt the patient or damage the system during scans as forces can become very large when using the full currents available in state of the art gradient amplifiers (Table 1). Though twisted-pairs reduce induced currents, the resulting net-force can still be significant as wire orientation can deviate from the alignment of the B0 field and particularly at the magnet ends, the B0 field is very inhomogeneous. In this study, a custom-designed multi-pole cable is built to cancel out forces and safely supply power to the local insert gradient.

Θ with B0 (rad) / Length (m)	0	π/4	π/2
	Lorentz force (N)		
1	0	3574	4200
0.05	0	179	210

Table 1. Forces on a wire inside the 7T magnetic field (B0) carrying a 600A current for different lengths and angles to B0. Lorentz force is calculated using F = B x I x L x Sin(Θ).

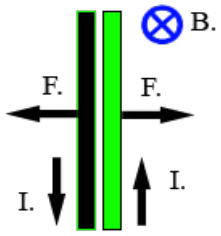

Figure 1. Schematic of Lorentz forces on two wires with alternate currents perpendicular to the magnetic field.

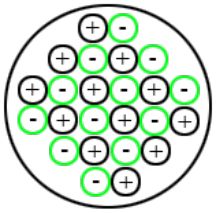

Figure 2. Schematic of designed cable. Thirteen twisted wire-pairs are bundled in one cable.

Method. To create a flexible cable and reduce forces at high currents in the 7T magnetic field, the current is split over multiple twisted-wire pairs and each pair will be used create a closed loop between amplifier and the insert gradient. Due to the parallel orientation, the opposite currents in each wire-pair and the reduced distance between pairs, the forces will be substantially reduced (Fig. 1). The first prototype was constructed using thirteen pairs of 4mm^2 stranded copper wires, insulated with an outer diameter of 4mm. All pairs of 13 meters in length were bundled for a total conductor surface of 52mm^2 per pole and insulated for safety using insulation tape (Fig. 2). For first experiments, the cable was connected to a custom-built dedicated breast insert. To assess worst case forces about 30cm of the cable was oriented perpendicular rather than aligned to the magnet while driving current through the cable. Forces were estimated by using a balance underneath the perpendicular part of the cable and weights on the other side. In addition, temperature was measured at the connection point.

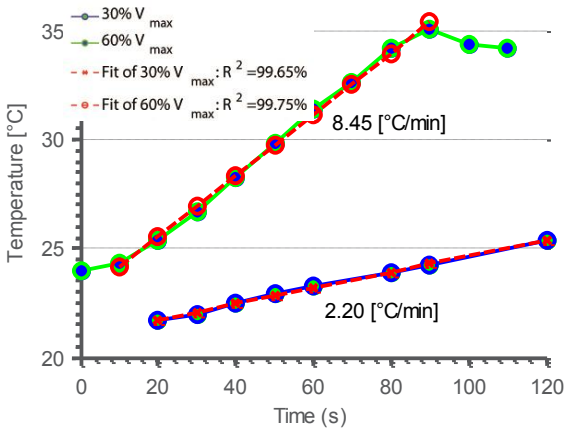

Figure 3. Measured temperature of cable-gradient coil connection at 18A and 36A versus the time in seconds. Fitting a linear equation in the data provided an estimate for the temperature increase rates per minute.

Results. First experiments at 125A showed no movement of the cable nor measurable forces (<1N) in a 7T field. The temperature at 18 and 36A increased at a rate of 2.20°C/min and 8.45°C/min (Fig. 3).

Discussion & Conclusion. The cable-design shows great potential for safe usage of high currents inside the 7T MRI system and implementing multiple pairs reduced forces significantly (7T x 125A x 0.3m > 262-fold). Future improvements will focus on a safe detachable connection between gradient and cable which allows for water input to cool down the gradient coil.

Assessment of hepatic glycogen turnover in mice by in vivo ^{13}C-MRS

Andreas Boss[1], Andor Veltien[1], Arend Heerschap[1]

[1]Department of Radiology and Nuclear Medicine, Radboud University Medical Center, Nijmegen, the Netherlands

Introduction and Aim: One of the important roles of the liver is the regulation of blood glucose levels. While in the postprandial state, excess carbohydrates are stored as glycogen, glucose is released from liver glycogen in the postabsorptive state. Studies using ^{13}C-MRS have, however, contributed to the notion that even during periods of net glycogen synthesis, a substantial amount of glycogen is degraded simultaneously[1,2]. This was concluded from pulse-chase experiments in which the ^{13}C-glycogen signal rose during the infusion of [1-^{13}C]-labeled glucose, and subsequently decreased upon switching to unlabeled glucose. These experiments were performed in both, humans[1] and rats[2], but to our knowledge glycogen turnover has not been assessed in mouse livers using *in vivo* ^{13}C-MRS. Next to glucose we evaluated galactose as tracer substance. This hexose is part of the dissacharide lactose found in milk, and is, in contrast to glucose, mainly metabolized in the liver. Furthermore, during the course of its hepatic metabolism UDP-glucose is produced, which is a direct precursor in the synthesis of glycogen. It can thus be speculated that turnover measurements can be achieved with lower amounts of tracer when galactose is used as a substrate. **Aim:** To test the feasibility of glycogen turnover assessment by *in vivo* ^{13}C-MRS in the liver of mice with glucose and galactose as tracer substrates.

Methods: Experiments were performed in 5 male, overnight-fasted **C57Bl6j mice** (weight: 22.6g ±2.0g [SD]). At 8 .a.m. mice were anesthetized using Isoflurane and subsequently a catheter was inserted in the jugular vein. **Infusion protocol:** [1-^{13}C]-labeled galactose or glucose was infused at a constant rate (1.2 and 2.4 µmol/min for galactose and glucose respectively) for a duration of 120min. Thereafter, the respective unlabeled substrate was infused for an additional 120 min. **MR acquisition:** The experiments were performed on a preclinical 11.7T MR scanner (Bruker BioSpin, Ettlingen). Mice were anesthetized with 1-2% Isoflurane in a gas mixture (O_2 to air ratio: 1 : 2) Respiration was monitored and kept constant at 60-100 breaths/min, temperature was maintained at 37°. A homebuilt ^{13}C surface coil (17x20 mm diameter) shaped and optimized for the liver was used for acquisition of ^{13}C-MR spectra, while an ^{1}H Alderman-Grant coil (43 mm diameter, 60 mm length) was used for imaging and ^{1}H-decoupling. First, the correct placement of the mouse liver on the ^{13}C surface coil was ensured (with help of a tube filled with a [1-^{13}C]-labeled acetate solution, surrounding the surface coil) and the mouse was repositioned if necessary. **^{13}C-MRS:** A simple pulse-acquire scheme was applied; pulse calibration was performed on the tube with [1-^{13}C]-labeled acetate surrounding the coil, using a block pulse. The pulse-chase experiments were then performed using a 180° pulse at the surface of the coil to minimize glycogen-signal contamination from the abdominal muscles close to the coil, while still reaching a ~90° pulse inside the liver. Further parameters were as follows: block pulse for excitation (duration: 43µs, center frequency on glycogen), ^{1}H-decoupling during acquisition (4k data points, spectral BW: 39000Hz), TR: 1260ms (3 times the estimated T1 of glycogen at 11.7T, extrapolated from[3]), 4 dummy scans, 471 averages, corresponding to a time resolution of 10 min per spectrum. **Post-processing:** MR spectra were post-processed using jMRUI. AMARES with prior knowledge was used for quantification. A two-step approach was used for fitting: For each experiment, line widths of the glycogen- and alpha-hexose peak were restricted to values found in spectra obtained at the end of the chase-period with high SNR. The decay of the alpha-hexose signals during ^{12}C-infusion was fitted with a monoexponential function: $A(t)=A_0*e^{-t/tau}+b$. **Estimation of turnover during galactose infusion:** Turnover was estimated for galactose based on differential equations, solved recursively with a finite time step using the solver function of Excel (c.f. **Fig.3A** for details).

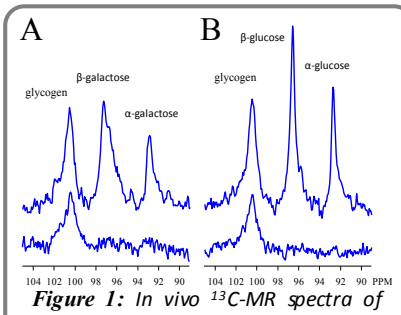

Figure 1: *In vivo ^{13}C-MR spectra of mice liver. **A:** Galactose-infusion; **B:** Glucose-infusion. The top spectra were obtained at the end of the 120min of ^{13}C-labeled substrate infusion. The bottom spectra were obtained at the end of the experiment.*

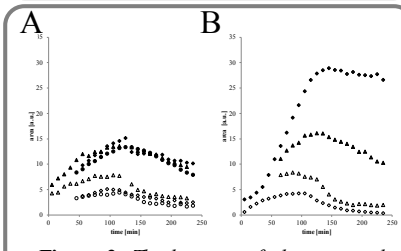

Figure 2: *The kinetics of glycogen and alpha-hexose signals .**A:**galactose-infusion (n=3), **B:**glucose-infusion (n=2). ^{13}C-labeled substrates were infused for 120min, followed by infusion of unlabeled substrates for the next 120min. Filled symbols: glycogen, corresponding open symbols: alpha-hexose.*

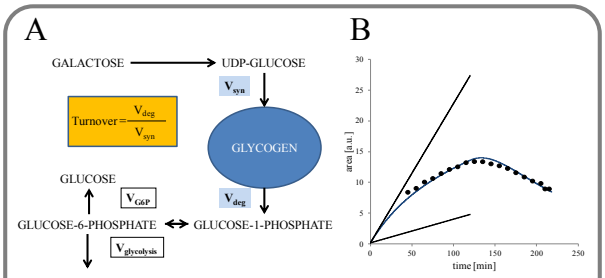

Figure 3A: *Metabolic model used to fit the time course of the glycogen curve during the galactose infusion. The rates of glycogen synthesis (V_{syn}) and degradation (V_{deg}) were assumed to be constant throughout the experiment. ^{13}C-enrichment of galactose as input-function for the model was assumed to be 100% during ^{13}C-infusion, and to be decreasing with the same time constant as the ^{13}C-galactose signals. Enrichment of UDP-glucose was estimated to be 30% lower than that of galactose, accounting for dilution by gluconeogenesis[2]. Fitted parameters include V_{syn}, V_{deg} and initial glycogen concentration. Turnover is the ratio of V_{deg} over V_{syn}. The model further assumes that true cycling (glycogen→ glucose-1-phosphate → UDP-glucose → glycogen) is negligible. i.e. most of the glucose-1-phosphate derived from glycogen is converted to glucose-6-phosphate and from there either released as glucose (V_{G6P}) or undergoing glycolysis ($V_{glycolysis}$). V_{deg} is therefore the sum of net V_{G6P} and $V_{glycolysis}$.*
***B**: Result of the fit (blue line) to the data points in one experiment with galactose infusion. The effect of initial glycogen levels is further illustrated: if they were very big, the signal would increase with V_{syn} (upper line), if initial glycogen was very low, the ^{13}C-glycogen signal is expected to increase with $V_{net}=V_{syn}-V_{deg}$ (lower line). Thus, in most cases, the apparent ^{13}C-signal increase will remain somewhere in between.*

Results/Discussion: ^{13}C-liver spectra obtained at the end of the 120 min infusion of ^{13}C-labeled substrates and corresponding spectra at the end of the experiment show signals reflecting the uptake and clearance of labeled galactose and glucose (**Fig.1**). The kinetics of glycogen and alpha-hexose ^{13}C labeling are shown in **Fig.2**. During the chase-period, the intensity of the alpha-hexose decays with a similar time constant for galactose (tau=28, 33, 88 min) and glucose (tau=22, 40 min), despite the fact that glucose was infused at double the concentration. Hepatic turnover was estimated to be 81, 83, and 87% for the galactose-infusion experiments (**Fig.3B**). A higher number of experiments is, however, needed to determine if the turnover of glycogen depends on the substrate infused. Furthermore, for a better kinetic modeling, blood enrichments of glucose and galactose need to be obtained.

Conclusion: We conclude that the assessment of glycogen turnover by ^{13}C-MRS is feasible in the livers of mice and can be used to study (transgenic) mouse models of diabetes or obesity.

References:

1. David, *The Journal of clinical investigation* 86, 612 (1990).
2. Magnusson, *The American journal of physiology* 266, E796 (1994)
3. Zang, *Biochemistry* 29, 6815 (1990)

Metabolic imaging of renal triglyceride content: validation by porcine kidney biopsies

Paul de Heer[1], Jacqueline Jonker[2], Evelien van Rossenberg[2], Marten Engelse[2], Trea Streefland[3], Ton Rabelink[1], Andrew Webb[1], Patrick Rensen[3,4], Hildo Lamb[5]

[1]C. J. Gorter Center for High Field MRI, Department of Radiology, Leiden University Medical Center, Leiden, the Netherlands; [2]Department of Nephrology, Leiden University Medical Centre, Leiden, the Netherlands; [3]Department of Endocrinology, Leiden University Medical Centre, Leiden, the Netherlands; [4]Einthoven Laboratory for Experimental Vascular Medicine, Leiden University Medical Centre, Leiden, the Netherlands; [5]Department of Radiology, Leiden University Medical Center, Leiden, the Netherlands

Target audience: nephrologists and radiologists interested in renal energy metabolism and MR spectroscopy

Purpose: The worldwide diabesity epidemic is a major public health problem. Obesity predisposes to the development of insulin resistance, type 2 diabetes and cardiovascular disease, which are associated with chronic kidney disease. However, obesity is also an independent risk factor for development of nephropathy. Evidence from animal (1-4) and limited human studies (5) suggest that obesity is associated with ectopic lipid accumulation, including renal lipid accumulation, which may lead to renal dysfunction, a process called lipotoxicity. However, human studies have been limited, because of the complication risk of repeated renal biopsies. Development of new noninvasive techniques to assess renal lipid content *in vivo* are crucial to gain more insight in the pathophysiology of obesity-related kidney disease. Therefore, we aimed to assess the reproducibility of renal triglyceride (TG) content measured by ^{1}H-MRS, compared to the gold standard, directly determining TG content by an enzymatic assay in kidney biopsies in an animal model.

Methods: In total fourteen left-sided porcine kidneys were obtained from two abattoirs. The kidneys were harvested within 30 min post-mortem to limit warm ischemia time. The kidneys were flushed with University of Wisconsin (UW) fluid and had a maximum cold ischemia time of 14 hours. Scans were performed on a 7Tesla Philips MRI scanner (Philips Healthcare, Best, Netherlands). The head coil was used for transmission and reception. A survey scan (Fig. 1a) was performed to position the MRS voxel (10x10x10 mm^3) within the cortex of the kidney. On a Dixon scan fat image (Fig. 1b) correct placement was confirmed, carefully avoiding extracellular (sinus or perirenal) lipids in the voxel. Measurements were performed in the upper and lower pole of each kidney, respectively. Two measurements had to be excluded from further analysis, due to a leak during the enzymatic assay and a corrupt MR data file, resulting in a total of twenty six measurements. Stimulated-echo acquisition mode (STEAM) spectra were acquired with an echo time of 8.2 ms without water suppression (repetition time (TR) 9 s, 3 averages) and with MOIST (1) water suppression (TR 9 s, 48 averages). TG were calculated as a percentage of the (unsuppressed) water peak. Directly after the scan protocol biopsies were taken at the same locations as the ^{1}H-MRS measurement. The renal tissue was snap frozen in liquid nitrogen, homogenized, and total lipids were extracted according to a modified protocol from Bligh and Dyer (6). TG was measured by an enzymatic kit (11488872, Roche Diagnostics). Numerical data are reported as mean values ± SD. A Pearson two-tailed correlation test was performed to compare the outcome of the MRS measurement and the biopsy result. Bland-Altman analysis was performed to evaluate the agreement between TG levels of the MRS measurement and the biopsies. For the Bland-Altman analysis the MRS and biopsy results were normalized.

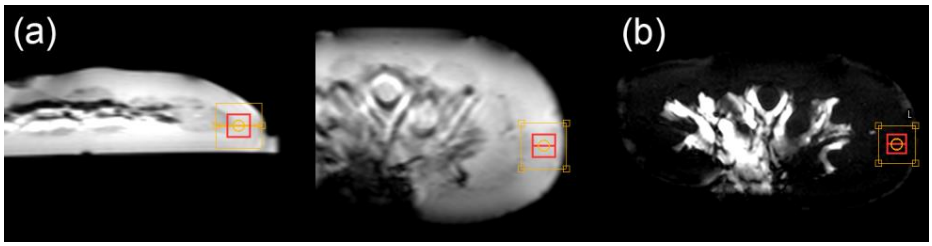

Figure 1. Placement of the VOI (red box) in one of the poles in the kidney cortex on a transverse and coronal survey (a) and Dixon fat image (b). The (outer) shim box is shown in orange.

Results: The average TG level in the renal cortex was 0.25±0.16% (range 0.068–0.768) measured by ^{1}H-MRS and 126±75 nmol/mg protein in the biopsy (range 36–331). Figure 2 shows two MR spectra with a large TG difference. The Pearson correlation (Fig. 3a) coefficient was 0.81 ($p < 0.0001$) showing good correlation. The Bland-Altman (Fig. 3b) has a bias of -0.07 and the limits of agreement were between 0.62 and -0.76.

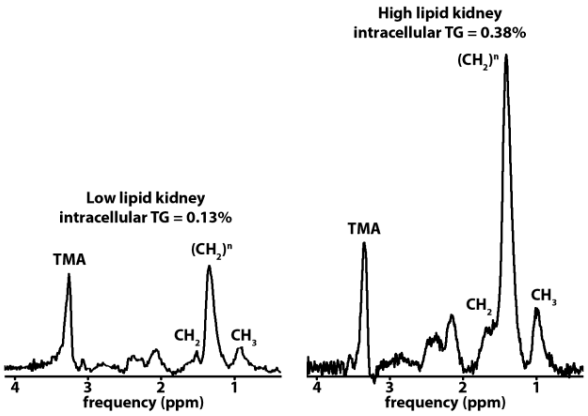

Figure 2. Two kidney MR spectra with a large difference in measured TG quantity. The increased chemical shift due to the high field strength allows to discriminate between various resonances that normally are not seen at lower field strengths. The spectra are scaled according to the water spectra to allow direct comparison.

Discussion and Conclusion: Our data show that porcine kidney TG levels measured by ^{1}H-MRS compared to a specific enzymatic assay are well correlated. The Bland-Altman analysis shows a bias close to zero and all but two measurements fall within the limits of agreement.

The non-invasive measurement of renal TG content is crucial in studying the relation between obesity and chronic kidney disease. ^{1}H-MRS opens a window for *in vivo* research into obesity-related lipotoxicity and nephropathy.

References [1] Wang Z et al, Diabetes 2005 Aug;54(8):2328-35. [2] Dominguez J et al, Am.J.Physiol Renal Physiol 2007 Sep;293(3):F670-F679. [3] Wu Y et al, Endocrinology 2006 Jan;147(1):44-50 [4]. Li Z et al, Am.J.Physiol Renal Physiol 2011 Nov;301(5):F1078-F1087. [5] Bobulescu IA, Magn Reson.Med. PLoS.One. 2014;9(8):e101285. [6] Bligh EG, Dyer WJ, Can.J.Biochem.Physiol 1959 Aug;37(8):911-7.

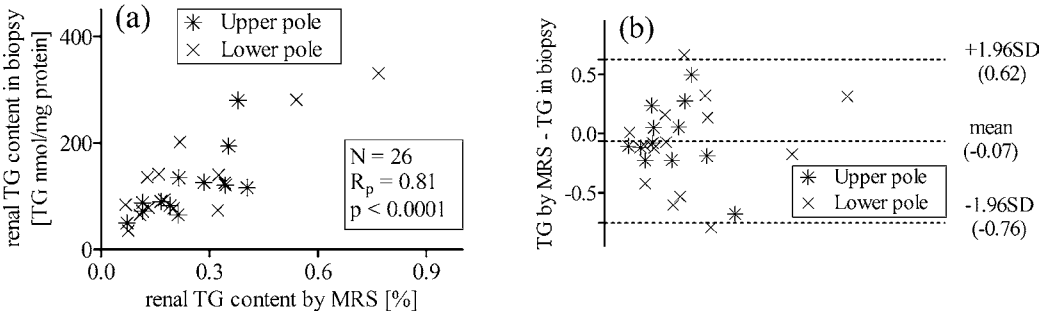

Figure 3. On the left a scatter plot is shown of all twenty six data points. The Pearson correlation coefficient was 0.81. On the right a Bland-Altman difference-average plot is shown of the TG ^{1}H-MRS determination vs the biopsy result. The upper and lower pole measurement have been grouped in this plot.

LC Model analysis of lactate edited MR single voxel spectroscopy of the hypoglycemic brain

Jack J.A. van Asten[1], Evita C. Wiegers[1], Arend Heerschap[1]

[1]Department of Radiology and Nuclear Medicine, Radboud University Medical Center, Nijmegen, the Netherlands

Target audience Scientists and researchers interested in spectral editing and data processing.

Purpose In the study of brain diseases by MR spectroscopy the signals of lactate are often used as relevant biomarkers. For instance in studies on hypoglycemia unawareness in diabetes, lactate metabolism in the brain may be very important [1]. As the lactate signals in MR spectra of the brain often overlap with those of lipids an editing technique is needed. With or without editing, the lactate signals are often small and detecting changes in these signals is challenging [2,3,4,5]. The aim of this work is to develop a robust and accurate analysis method dedicated to lactate detection, based on fitting a linear combination of metabolite signal models to the edited spectra.

Methods A semi-LASER pulse sequence [6] was adapted with small band refocusing MEGA pulses to perform lactate editing in voxels of ~32cc, located in the brain of two volunteers. Two times twelve MR spectra were collected during a stepped euglycemic-hypoglycemic clamp of approximately 1.5 hours. The editing MEGA pulse was applied at the CH group of lactate at 4.1 ppm at an alternating fashion. A long echo time (TE=144ms, TR=3s, NA=32) was used to get a positive and negative (or refocussed) lactate signal at 1.33 ppm. The spectra were phase corrected and frequency aligned and subsequently the edited and non-edited measurements were subtracted. These difference spectra were analyzed using LCModel [7] with a simulated basis set. It contained two metabolites, the only left-overs after subtracting the spectra produced by the editing sequence: lactate (CH_3) at 1.3 ppm and Cr (CH_2) at 3.9 ppm. Simulations were done with NMRSIM (Bruker Inc. Topspin 2.1) using the exact timing parameters and pulse shapes of the in vivo used sequence. The unsuppressed water measurement was used to estimate the absolute concentration of the metabolites, with lactate as the primary water scaling reference. Metabolite and water signals were corrected for T2 and T1 relaxation times (Lac: T2=240ms, T1=1250ms; water: T2=110ms, T1=832ms) [8,9]. The water concentration was assumed 38.888 M. The subtracted spectra were analyzed first one by one, and secondly after adding and filtering two measurements (n=6). A Student's ttest was used to assess the outcomes between the post and not processed difference spectra. The filter consisted of a 5 Hz apodization and zero filling by a factor of two. We also recorded a short echo time spectrum (TE=30ms, TR=3s, NA=32). And analyzed that with an appropriate basis set for these short echo time spectra.

Results Spectra of two volunteers were fitted and quantified. Numbers with standard deviations below 50% were considered qualitatively good enough for further evaluation. An example of a post processed and not processed fit result is depicted (Figure 1). The results are summarized in table 1.

The lactate and creatine concentrations are quantified equally good between the post processed and not processed spectra. The standard deviations, in LCModel based on CRLB's, were significantly better for the post processed values (P<0.01). The concentration of lactate and creatine of the short echo time spectra was slightly lower.

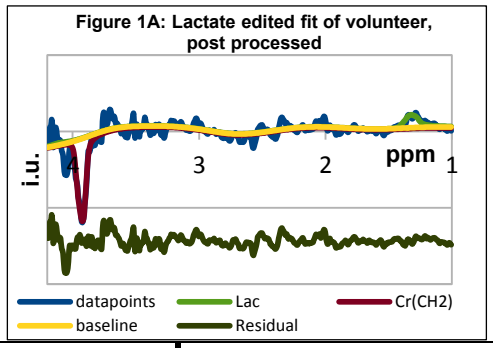

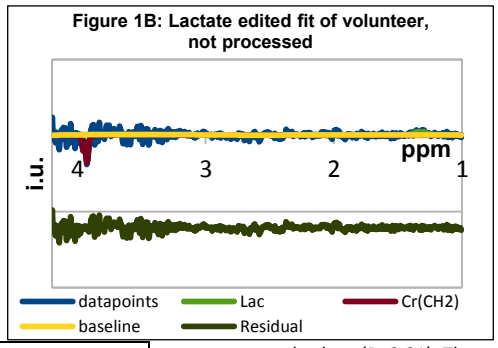

Table 1: [Lac]+[Cr] Std error of mean

	Volunteer 1						Volunteer 2					
	Long TE postproc		Long TE unproc		Short TE		Long TE postproc		Long TE unproc		Short TE	
	[mM]	Sem	[mM]	Sem	[mM]	Sem	[mM]	Sem	[mM]	Sem	[mM]	Sem
Lac	**0.71**	0.01	**0.72**	0.05	**0.56**	0.03	**0.80**	0.04	**0.76**	0.03	**0.68**	0.09
Cr (CH2)	**5.97**	0.29	**6.30**	0.46	**4.67**	0.27	**5.43**	0.51	**5.90**	0.64	**5.38**	0.16

Conclusion&Discussion Robust and accurate analysis of lactate edited MR spectra using LCModel with a simulated basis set with only two metabolites is very well possible. The collected spectra can be analyzed automatically without operator input and therefore less prone to errors. In absolute quantification the correction for T1 and T2 relaxation times needs special attention because relaxation times might differ regionally in the brain or between volunteers and patients. The assumed water content was an average between white and gray matter. The slightly lower lactate concentration in the short echo time spectra might be due to an overestimation of the lipid and macromolecular compounds in that area. Using the creatine signal as internal reference and the lactate signal from the edited spectra may improve the assessment of lactate at longer echo times.

References [1] De Feijter, H. DIABETES 2014:62. [2] Edden, R. JMRI 2010:32. [3] Artega de Castro, CS. NMR Biomed 2013 ;26. [4] Maddock R. NeuroImage 2011:57. [5] Smith, MA. JMRI 2008 :28. [6] Scheenen, TW. Magn Reson Med 2008:59. [7] Provencher Stephen W. NMR in BIOMEDICINE 2001:14. [8] Li, J Mol Imaging Dynam 2012:1. [9] Madan, A. MRM 2014.

Quantum coherence spectroscopy to measure 1D ^{1}H-[^{13}C]-lipid signals

Lucas Lindeboom[1,2], Robin de Graaf[3], Christine Nabuurs[2,4], Matthijs Hesselink[4], Joachim Wildberger[2], Patrick Schrauwen[1], Vera Schrauwen-Hinderling[1,2]

[1]Department of Human Biology, Maastricht University Medical Center, Maastricht, the Netherlands
[2]Department of Radiology, Maastricht University Medical Center, Maastricht, the Netherlands
[3]Department of Diagnostic Radiology, Magnetic Resonance Research Center, Yale University
[4]Department of Human Movement Sciences, Maastricht University Medical Center, Maastricht, the Netherlands

Target Audience
Researchers and clinicians interested in indirect ^{13}C spectroscopy (of lipids).

Purpose
Due to the low natural abundance of carbon-13 (^{13}C), and hence low incorporation in endogenous lipids, ^{13}C-enriched lipids are an excellent candidate to be used for *in vivo* tracer studies[1]. In order to enhance the detection sensitivity spectral editing techniques for the indirect detection of ^{13}C have been proposed. These techniques also offer the opportunity to use regular ^{1}H localization techniques. Gradient enhanced heteronuclear single and multiple quantum coherence spectroscopy (ge-HSQC or ge-HMQC respectively[2]) allows for acquisition of ^{1}H-[^{13}C] signals while simultaneously spoiling unwanted ^{1}H-[^{12}C] signals. Although intrinsically 50% of the ^{1}H-[^{13}C] signal is lost, this single shot acquisition technique may be preferable to subtraction-based editing methods (e.g. POCE[3]) for ^{13}C detection in tissues where movement artifacts and/or low ^{13}C fractional enrichments are expected. However, the large chemical shift of ^{13}C resonances of the lipid signal will lead to signal intensity loss and phase distortions when the conventional ge-HSQC and ge-HMQC sequences are applied as 1D editing technique. In this study we compared the use of modified ge-HSQC and ge-HMQC sequences, which were designed to refocus the chemical shift in the heteronuclear dimension to get 1D ^{1}H-[^{13}C]-lipid spectra.

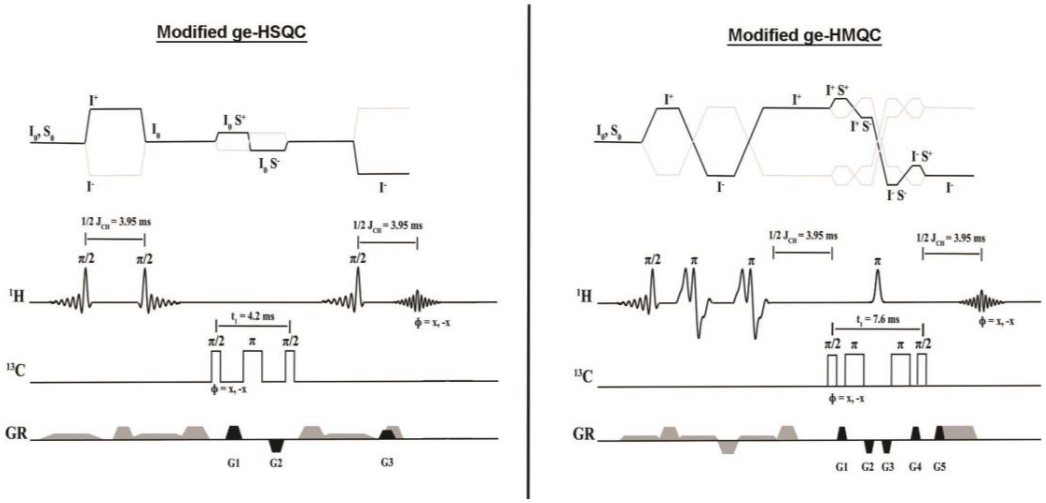

Figure 1. Modified ge-HSQC and ge-HMQC sequences as used in this study.

Methods
Experiments were performed on a 3T clinical MR system (Achieva 3T-X, Philips Healthcare, NL) using a butterfly-loop ^{1}H TX/TR quadrature coil combined with two 16cm ^{13}C TX/TR surface coils in quadrature-mode for optimal ^{1}H receiving sensitivity (RapidBiomed, GE). The two sequences used are depicted in figure 1. For ge-HSQC, the sequence represents a modification of a recently described method[4], where the coherences are formed during the TM mixing period of a STEAM localization sequence. A single ^{13}C inversion pulse was inserted during the evolution period. Coherence selection gradients (length 1 ms) were used in a ratio of 2:-2:1. The duration of the hard ^{13}C excitation pulse was 340 µs, leading to an evolution period of 4.2 ms. For the ge-HMQC, the quantum coherence module was placed after PRESS localization. In this case, two additional ^{13}C inversion pulses were inserted to refocus ^{13}C chemical shift. Selection gradients (length 0.5 ms) were used in a ratio of 1:-1:-1:1:1, leading to an evolution time of 7.6 ms. Total TE was 29 ms. In both sequences, the first ^{13}C pulse was phase cycled to improve spoiling of unwanted coherences. Offset of the ^{13}C pulses was set at the midchain ^{13}C-CH_2 resonance (~29 ppm). Four different spectra were acquired, to compare HSQC versus HMQC and to show the effect of the extra inversion pulse(s) in both sequences. All experiments were acquired from a 20 x 40 x 40 mm volume, placed in a phantom filled with Intralipid (a stable emulsion with of 20% soybean oil, 1.1 % ^{13}C) with TR = 2000 ms, 1/2J = 3.95 ms and NSA = 128. A lipid reference signal was obtained by turning off the dephasing gradients and by setting the frequency of the ^{13}C RF pulses far off resonance.

Results
The four different spectra acquired are depicted in figure 2. It is apparent that the insertion of the ^{13}C inversion pulses resulted in non phase distorted lipid signals with an increased signal intensity. The effective bandwidth of the ^{13}C refocusing pulse was sufficiently large for unambiguous detection of lipid methyl and methylene signals. The ^{1}H-[^{13}C]-CH_2 and –CH_3 signal is higher in the modified ge-HSQC sequence when compared to the modified ge-HMQC (calculated enrichment 0.9% vs. 0.6% respectively). The increased signal loss in ge-HMQC is likely due to the larger number of RF pulses as well as the non-refocused evolution of passive spin couplings in this sequence.

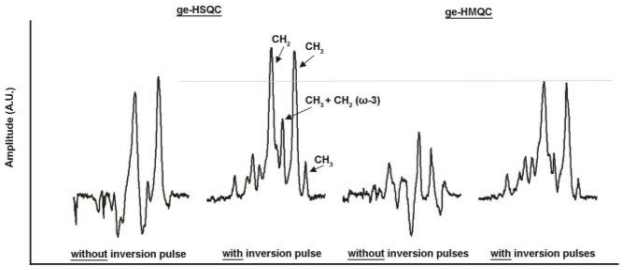

Figure 2. Comparison between the modified ge-HSQC and the modified ge-HMQC sequence, with and without additional ^{13}C inversion pulse(s).

Discussion and Conclusion
We have shown that the addition of ^{13}C inversion pulses to both the ge-HSQC and the ge-HMQC is essential to obtain ^{1}H-[^{13}C]-lipid signals without phase distortion. Due to the absence of ^{1}H-^{1}H couplings during the evolution time in the ge-HSQC, this sequence will yield higher signals than the ge-HMQC. The modified ge-HSQC sequence can be used in studies to follow the incorporation of ^{13}C lipid tracers.

References
1. Jonkers et al. MRM 2012. 2.Ruiz-Cabello et al. Journal of Magnetic Resonance, 1992. 3. Rothman et al., PNAS, 1985. 4. De Graaf et al. MRM (in press), 2014.

Acknowledgements
Funded by Top Institute Food and Nutrition (TIFN, WM003).

Measuring the metabolic effects of photodynamic therapy using ^{31}P MRSI

Sophie Peereboom[1], Tom Schreurs[1], Jeanine Prompers[1], Klaas Nicolay[1]

[1]Department of Biomedical NMR, Eindhoven University of Technology, Eindhoven, the Netherlands

Introduction

Photodynamic therapy (PDT) is a minimally invasive and specific cancer treatment method that is especially useful for superficial tumors. The procedure involves administration of a photosensitizing agent followed by irradiation at a wavelength corresponding to an absorbance band of the sensitizer[1]. When the excited photosensitizer falls back to its ground state, molecular oxygen is converted into highly reactive singlet oxygen. This singlet oxygen can destroy tumor tissue by means of both cellular and vascular effects. These effects are expected to show up within minutes after laser irradiation. Vascular effects can be measured using dynamic contrast enhanced (DCE) MRI, while ^{31}P spectroscopy can provide information about the energetic status of cells. Spectroscopic imaging is needed to assess the effects of treatment at different sites of the tumor. A good method for ^{31}P spectroscopic imaging is chemical shift imaging (CSI), but because of its phase encoding gradients in different directions, it is also a time consuming technique and is therefore not very suitable for measuring rapid dynamic changes.
The aim of this research was to design a fast 2D echo-planar ^{31}P spectroscopic imaging (EPSI) method to measure the metabolic effects of photodynamic therapy as a function of time, which will provide more insight in the mechanism of PDT and assist in assessing the efficacy of this treatment in an early stage.

Methods

To examine the time scale of the dynamic changes in the ^{31}P spectrum, localized ^{31}P spectra were measured in a CT26 tumor bearing BALB/c mouse up to 16 h post treatment. The spectra were measured with a 7T Bruker animal scanner, using an ISIS sequence for localized measurements in a single voxel (5×4×6 mm^3, TR=2000 ms), preceded by a localized shim. The baseline and 16 h post treatment scan were performed with 164 ISIS averages (acquisition time = 44.8 min), whereas the 40 min, 1 h and 1 h 20 min post treatment scans were performed with 64 ISIS averages (acquisition time =18.13 min).
For fast ^{31}P spectroscopic imaging, we designed a ^{31}P EPSI sequence which was based on a free induction decay CSI sequence that was adapted by replacing phase encoding in one direction by a so-called flyback gradient train[2], as is shown in Figure 1. The use of flyback gradient segments ensures that the phase of the spins always evolves in the same direction. This minimizes artifacts associated with the phase reversal in most echo planar spectroscopic and imaging techniques[3]. The gradients were designed in such a way that they respect both imaging parameters such as spatial resolution and number of spectral points, and scanner limitations concerning gradient rise time and acquisition. The pulse sequence was programmed in ParaVision v5.1. The acquired signal can be reconstructed by sinc interpolation in the time domain, followed by a 3D Fourier transform with zero-padding of the spectra.

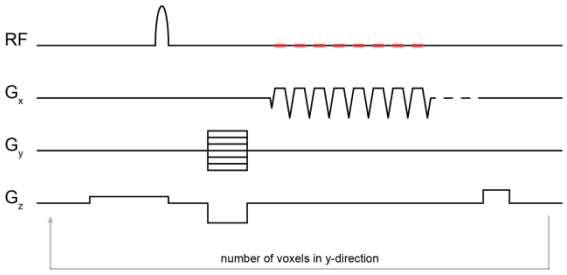

Figure 1: *Flyback echo-planar spectroscopic imaging sequence. A normal CSI sequence was modified in such a way that phase encoding in one direction is replaced by a flyback EPSI gradient train. Acquisition only takes place during the flat parts of the gradients.*

Results

The results of the in vivo scans are shown in Figure 2 and Figure 3. Figure 2 shows the spectra changing over time after treatment with PDT. From bottom to top the baseline scan, the 40 min post treatment, 1 h post treatment, 1 h 20 min post treatment and 16 h post treatment scans are shown, respectively. Changes in the inorganic phosphorus peak could already be observed 40 min post treatment, and after 16 h the three ATP peaks had disappeared.
The flyback EPSI sequence was successfully implemented. Typical imaging parameters are 6×6 voxels and a field of view of 2.413×2.413 cm^2, with a corresponding spectral bandwidth of 3874 Hz (23.9 ppm). Thus far, we did not measure ^{31}P spectroscopic images using this sequence in vivo.

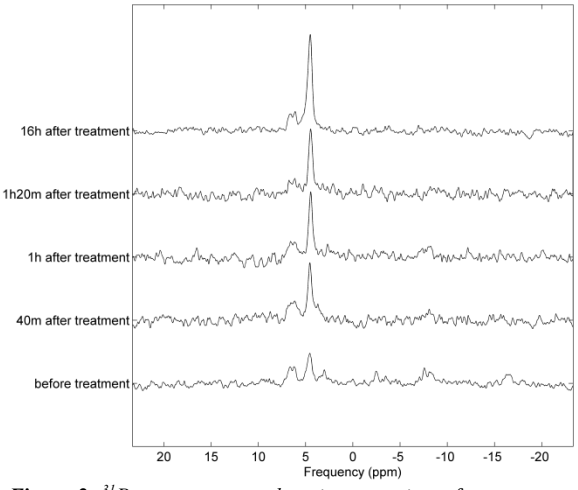

Figure 2: *^{31}P tumor spectra changing over time after treatment with PDT. All spectra are scaled according to their number of averages.*

Discussion

The advantages of the flyback EPSI sequence are that it is faster than CSI, it has an easy reconstruction and it is less sensitive to pulse sequence timing errors, eddy currents and B_0 inhomogeneity than normal EPSI[3]. A disadvantage is that this sequence requires fast gradient switching and is therefore highly dependent on a good gradient system. This limitation causes the fact that at this moment the sequence cannot be used with its theoretical minimal TR; a larger repetition time must be used and this slows the sequence down.
Future work includes the design of an experimental setup in order to make murine PDT treatment inside the scanner possible. This enables to measure spectra during and directly after treatment, and makes it possible to compare spectra before and after PDT treatment in a fair way. Despite the acceleration already achieved, still a lot of averages will be necessary to measure a reasonable ^{31}P signal. To make this sequence even faster, it will be combined with compressed sensing by adding gradient blips in y-direction[4].

Conclusion

PDT treatment causes rapid changes in energy metabolism, therefore fast measurements are necessary. ^{31}P flyback EPSI is a promising technique to provide more information about the metabolic effects of PDT treatment.

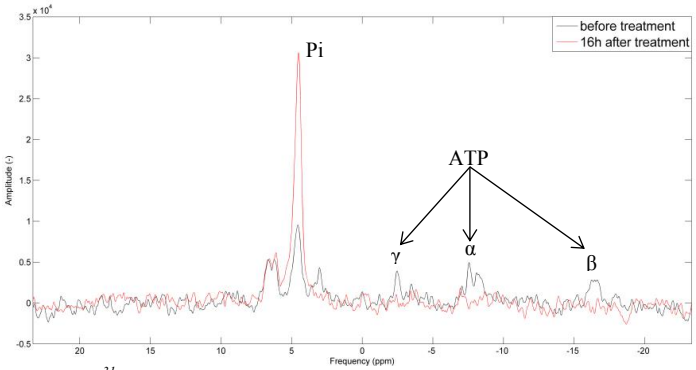

Figure 3: *^{31}P tumor spectra; in red the baseline scan, in black the 16 h post treatment scan. ATP disappears after treatment, while the amount of inorganic phosphate increases.*

References

1. Agostinis et al. CA Cancer J Clin 2011; 61:250-281
2. Feinberg et al. Magn Reson Med 1990; 33:461-466
3. Cunningham et al. Magn Reson Med 2005; 54:1286-1289
4. Hu et al. J Magn Reson 2008; 192(2):258-264

2D-^{1}H Localized PRESS-COSY and 2D-^{31}P EXSY spectra of the mouse hindleg at 11.7T

Devashish Das[1], Andor Veltien[1], Arend Heerschap[1]

[1]Department of Radiology and Nuclear Medicine, Radboud University Medical Center, Nijmegen, the Netherlands

Purpose

2D NMR enables the characterization of a wide variety of chemical and biochemical systems *in vitro* and *in vivo*; in the later case usually in combination with different localization schemes like L-COSY [1], SLO-COSY [3] and/or PRESS localized COSY reported in literature [3]. At ultrahigh field (11.7Tesla), there is an advantage to detect metabolites by exploiting increased chemical shift separation as well as high SNR. The aim of this project was to develop and validate 2D-^{1}H (PRESS)-COSY and 2D-^{31}P EXSY MR sequences for improved detection of ^{1}H and ^{31}P metabolites in the mouse hindleg at 11.7Telsa Bruker horizontal bore (9cm) Biospec MR system.

Methods

First 2D-Proton PRESS COSY sequence was implemented using the following radio frequency (slice selective soft) pulses and delays. (A) 90ss-TE/6-180ss-TE/3-t1-Δ-90ss-TE/6-acquire, where delay TE is the sum of (2*TE/6+TE/3+t1+Δ) compensation delays, and t1+Δ = (TE/2-TE/6), where delay t1 incremented for each F1 time domain experiment. Incrementing delay in such a manner is also reported for semi-constant time experiments (4). That is for a given t1 increment, delay Δ is compensated, such that both chemical shift and J-coupling Hamiltonian (Hcs and Hj) remain active in the period (t1+Δ), which result in the build of diagonal and cross peaks in the F1 and F2 dimensions. Second sequence 2D-^{31}P-EXSY (Exchange spectroscopy) was implemented using a series of hard pulses and delays represented as (B) 90-t1-90-tm-90-acquire, where t1 is the increment delay and tm is the mixing time (delay). At first we validated both sequences on a phantom, and then we acquired mouse hindleg ^{1}H and ^{3}1P spectra. Acquired data were processed using Bruker Topspin 2.1 software, and reconstructed in magnitude mode.

Results

Figure 1 is a series of 2D-proton PRESS-COSY spectra acquired using sequence (a) described in the method section. Excellent water suppression was achieved in all proton spectra. Figure 1a was recorded in the 2ml tube containing 40mM fructose dissolved in water. In this figure clear cross peaks between J-coupled protons of fructose molecule can be seen, each proton has a separate chemical shift that has component in F1 and F2 dimensions. This 2D spectrum of fructose demonstrates superior resolving power of 2D-Proton PRESS-COSY, because one cannot discriminate such complex spin network in a 1D-spectrum. In Figure 1b, recorded in the hindleg of mouse with TE=24ms, show distinct cross peak for CH2 group of lipid. Figure 1c, also recorded in the hindleg show clear cross peaks for two protons of Taurine. In this experiment we used TE=134ms, which eliminated lipid resonances overlapping with taurine peaks at 3.1-3.5ppm. In figure 2 we show ^{31}P-EXSY spectra of the mouse hindleg. In both case CK enzyme mediated exchange cross peaks between PCr and γATP can be seen. Figure 2a intensity of PCr→ γATP, γATP→ PCr cross peaks remain constant, before ischemia. However, during ischemia cross peak intensity is decreased due to rapid Pi levels as shown in figure 2b.

Conclusion

We independently developed ^{1}H and ^{31}P 2D-spectroscopy at 11.7Telsa Bruker, horizontal small bore (9cm) Biospec MR system. Both sequences were implemented to obtain hindleg spectra at high temporal and spatial resolution.

References

[1]Thomas et,al MRM, 26:58 (2001) [2] Blackband et.al JMR 79:184-189 (1988)
[3] Braakman et.al ,MRM, 60:449-456(2008) [4] Aitio et.al, JMR, 143,391-396 (2000)

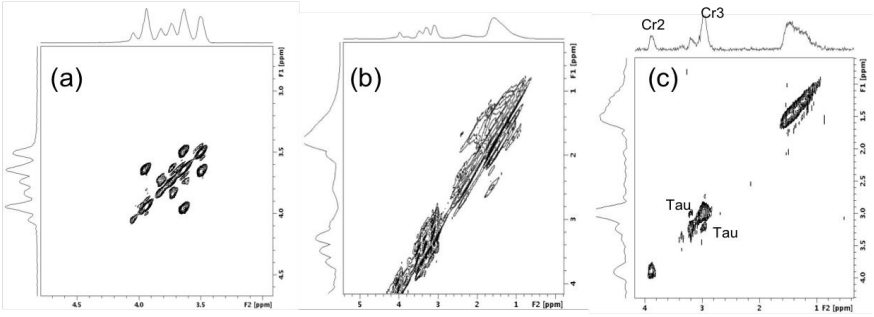

Figure 1: Localized 1H-PRESS-COSY Spectra (a) Fructose phantom, NS=2, 8ul voxel, TE=11.4ms, TR=1.5s, F2=2500Hz, F1=2500Hz,TD2=4096, TD1=128. (b) Mouse hindleg, NS=8, TR=2s, 64ul, TE=24ms, F2=5000Hz, F1=5000Hz, TD2=4096, TD1=128. (c) Mouse hindleg, NS=8, TR=2s, voxel 64ul, TE=134ms, F2=5000Hz, F1=5000Hz, TD2=4096, TD1=128.

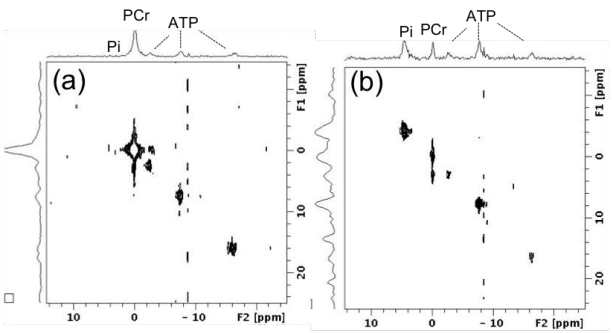

Figure 2: 2D-^{31}P-EXSY hindleg mouse spectra (a) Pre-Ischemia hindleg spectra, exchange cross peaks between PCr and γATP can be seen. (b) Ischemic hindleg spectra, exchange cross peaks intensity between PCr and γATP is reduced. Spectra parameters, NS=48, TR=1s, mix (tm)=400ms, F2=8012Hz, F1=8012Hz, TD2=4096, TD1=48.

Measuring brain lactate with ^{1}H-MRS during hypoglycemia in humans; preliminary results

Evita Wiegers[1], Hanne M.M. Rooijacker[2], Cees J. Tack[2], Arend Heerschap[1], Bastiaan E. de Galan[2], Marinette van der Graaf[1]

[1]Department of Radiology and Nuclear Medicine, Radboud University Medical Center, Nijmegen, the Netherlands
[2]Department of Internal Medicine, Radboud University Medical Center, Nijmegen, the Netherlands

Target audience: (Clinical) researchers interested in diabetes, hypoglycemia or brain metabolism in general.
Purpose: Iatrogenic hypoglycemia is the most frequent acute complication of insulin therapy in people with type 1 diabetes (T1DM). Recurrent hypoglycemia initiates a process of habituation, characterized by suppression of hypoglycemic symptoms and compromised hypoglycemic awareness, resulting in a high risk of severe hypoglycemia. Recent evidence suggests a pivotal role for increased brain lactate transport capacity as underlying mechanism.[1,2,3] The primary objective of this study is to investigate the effect of hypoglycemia on brain lactate content.
Methods: *Subjects and procedure:* After an overnight fast, 3 healthy volunteers (2 males, mean age: 23.6 ± 1.5 yrs, mean BMI: 22.8 ± 1.85 kg/m^2) underwent a stepped hyperinsulinemic (60 mU·m^2·m^{-1}) euglycemic-hypoglycemic glucose clamp, during which arterial plasma glucose levels were kept at 5.0 mmol/l for the euglycemic phase (30 min) and at 2.8 mmol/l for the hypoglycemic phase (45 min). Arterial plasma glucose levels and plasma lactate levels were determined every 5 minutes.

Brain lactate detection with ^{1}H-MRS: MR data were acquired at 3.0 T (Siemens, Trio) from a 31.25 cm^3 MRS voxel (2.5 x 5 x 2.5 cm), placed in the supraventricular cortex. ^{1}H-MR spectra were acquired with an interleaved J-editing semi-LASER sequence with TE 144 ms and TR 3000 ms and 32 averages. J-editing was performed with MEGA-pulses with a bandwidth of 7 Hz centered on the lactate quartet at 4.11 ppm. The power of the MEGA-pulse was switched on and off in an interleaved fashion, resulting in spectra where the lactate doublet at 1.33 ppm is negative (MEGA power off) or positive (MEGA power on). As a consequence, difference spectra contained only the (positive) lactate doublet, removing all other signals from the spectra.

Post-processing and quantification All spectra were zero-filled (from 1024 to 2048 points) and phase and frequency aligned with respect to the first recorded 'reference' spectrum. Alignment was done by maximizing the normalized scalar product between this reference spectrum and the other spectrum in Matlab (R2014a, the MathWorks). Apodized (5 Hz Lorentzian) difference spectra were created from every couple of spectra with the MEGA-pulse on and off, and subsequently two consecutive difference spectra were averaged to enable accurate measurement of the lactate doublet. The lactate signal was quantified using the AMARES algorithm in jMRUI[4] and the unsuppressed water signal, recorded with a shorter TE (30 ms), from the same voxel (sLASER, TR 5000 ms, 8 averages). The following assumptions were made for quantification of brain lactate levels: a T2-value of 240 ms for lactate[5] and 110 ms for water, 70% water content in the brain[6] and, regarding the used TRs, neglectable T1-effects. The amount of brain lactate measured during stable euglycemia and hypoglycemia was averaged. Data are presented as mean ± standard error of the mean. A paired sample t-test was performed to determine significant differences (p<0.05) between both glycemic conditions.
Results Plasma glucose levels stabilized at 4.68 ± 0.21 mmol/l and 2.90 ± 0.02 mmol/l during euglycemia and hypoglycemia, respectively. Plasma lactate levels increased significantly from 1.27 ± 0.23 mmol/l during euglycemia to 1.67 ± 0.17 mmol/l during hypoglycemia (mean change: 0.40±0.07 mmol/L, p=0.03).^{1}H-MRS was successful in detecting brain lactate as the lactate doublet was visible in all difference spectra. An example of a representative edited spectrum is shown in Fig. 1. We did not find changes in brain lactate levels between both glycemic conditions (euglycemia 0.39 ± 0.05 µmol/g, hypoglycemia 0.30 ± 0.02 µmol/g; mean change -0.09±0.03 µmol/g, p=0.12), as shown in Fig. 2.
Discussion and conclusion These preliminary data, obtained in healthy volunteers, suggest that increased plasma lactate levels during hypoglycemia are not accompanied by an increase in lactate content in the brain. Our data, which appear in line with those of Terpstra et al. 2014,[7] indicates either that excess lactate is not taken up by the brain, due to a relatively low amount of monocarboxyl-transporters (MCT),[8] or that lactate does not accumulate in the brain because it is immediately utilized. Further research, in both healthy subjects and (hypoglycemia unaware) T1DM patients, will determine the effect of hypoglycemia on brain lactate in these groups in more detail.

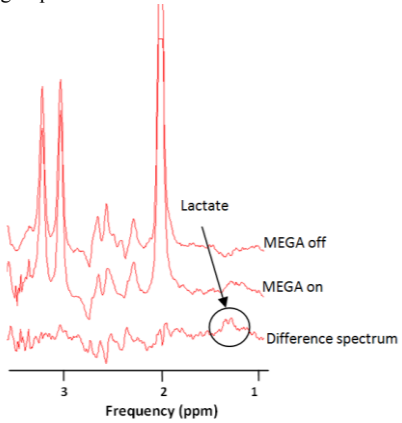

Fig. 1 MEGA off, MEGA on and difference spectrum. The lactate doublet is clearly visible at 1.33 ppm in the difference spectrum.

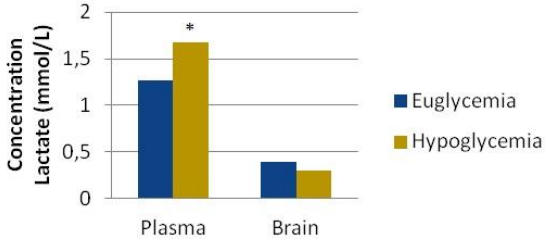

Fig. 2 Mean concentrations of lactate in the plasma and in the brain during euglycemia and hypoglycemia. The * determines a significant change in lactate concentration compared to euglycemia (p < 0.05).

References
1. De Feyter, H.M., et al., Increased brain lactate concentrations without increased lactate oxidation during hypoglycemia in type 1 diabetic individuals. Diabetes, 2013. 62(9): p. 3075-80. **2**. Wyss, M.T., et al., In vivo evidence for lactate as a neuronal energy source. J Neurosci, 2011. 31(20): p. 7477-85 **3.** van Hall, G., et al., Blood lactate is an important energy source for the human brain. J Cereb Blood Flow Metab, 2009. 29(6): p. 1121-9. **4**. Vanhamme, L., et al., Improved method for accurate and efficient quantification of MRS data with use of prior knowledge. J Magn Reson, 1997. 129(1): p. 35-43. **5.** Madan, A., et al., Proton T2 measurement and quantification of lactate in brain tumors by MRS at 3 Tesla in vivo. Magn Reson Med, 2014. **6.** Mandal, P.K., et al. In vivo proton magnetic resonance spectroscopic signal processing for the absolute quantitation of brain metabolites. Eur J Radiol, 2012. 81(4): p. e653-64**. 7.** Terpstra, M., et al., Changes in human brain glutamate concentration during hypoglycemia: insights into cerebral adaptations in hypoglycemia-associated autonomic failure in type 1 diabetes. J Cereb Blood Flow Metab, 2014. 34(5): p. 876-82. **8**. Aveseh, M., et al., Endurance training increases brain lactate uptake during hypoglycemia by up regulation of brain lactate transporters. Mol Cell Endocrinol, 2014. 394(1-2): p. 29-36.

Robust 3D ^{1}H MRSI of the prostate without endorectal coil at 3T

Nassim Tayari[1], Isabell K. Steinseifer[1], Caixia Fu[2], Elisabeth Weiland[3], Jack J.A. van Asten[1], Tom W.J. Scheenen[1], Marnix C. Maas[1], Arend Heerschap[1]

[1]Department of Radiology and Nuclear Medicine, Radboud University Medical Center, Nijmegen, the Netherlands
[2]MR Application Development, Siemens Shenzhen Magnetic Resonance Ltd., Chi
[3]MR Applications Development, Siemens Healthcare, Erlangen, Germany

Target Audience: Clinicians and researchers interested in MRSI of the prostate

Introduction: Proton MR Spectroscopic Imaging (MRSI) can improve detection, localization and the determination of aggressiveness of prostate cancer [1,2]. ^{1}H MRSI of the prostate is mostly performed with PRESS volume selection [3]. Recently, it was shown that a semi-LASER sequence adapted with low power, high bandwith GOIA-WURST refocusing pulses, in combination with an endorectal coil (ERC) and shortened echo times provides well-resolved spectra with high SNR and little lipid contamination [4]. Since the positioning of an ERC is time consuming and uncomfortable for patients, hospitals increasingly prefer to perform prostate MR without an ERC. Therefore it becomes very relevant that good MRSI data of the prostate can be obtained without this coil. The purpose of this study is to test if high quality ^{1}H MRSI data of the prostate can be acquired with the GOIA-sLASER pulse sequence in patient examinations without an ERC.

Methods: MR was performed on a 3T MR system (MAGNETOM Skyra Siemens Healthcare, Erlangen, Germany) with a 32 channel body coil for signal reception. Seven patients, suspicious of prostate cancer (PCa), received Buscopan to reduce peristalsis and underwent a multi-parametric MRI exam. As these measurements involved a cancer detection protocol, whole mount validation of PCa presence was not routinely performed in these patients. For MRSI a non-product sLASER sequence with GOIA-Wurst (16,4) refocusing pulses was used [4]. All measurements were performed with TE=88ms, variable TR (SAR limited) and matrix size (see table), 3 averages and weighted phase encoding, resulting in measurement times between 4:50 and 8:44 min. Nominal voxel size was 6x6x6 mm^3 for one patient, and 7x7x7 mm^3 for the others (after apodization corresponding to spherical voxels of 0.64 and 1.01 cc, respectively). MR spectra were fitted with LCModel using a basisset of simulated metabolite signal shapes of citrate (Cit), creatine (Cr), spermine (Spm), choline (Cho) and myo-inositol (mI) [5].

Results: Magnitude shim values for the selected volumes around the prostate were 21-33 Hz. Without ERC the GOIA-sLASER sequence produced MR spectra with little lipid contamination and resonances for Cit, Cr, Spm, Cho and mI, as shown in the Fig.(a) for 2 MRSI voxels with the LCModel fit in Fig (b). From the Cit signal a metabolic map was reconstructed showing a variable distribution of this compound over the prostate (Fig. (c))
To quantify the performance of the sequence we determined the voxel fraction of high quality signals (CRLB <30%) in 6x6 voxels in 3 transversal slices through the prostate (108 voxels/patient). For Cit, this fraction was >90% in all patient measurements (Table). For the other metabolites the fraction of reliably quantifiable voxels was more variable. e.g. for Cho, the most important other metabolite in PCa detection, it was between 38 and 77% (Table). The best overall results were obtained in the patient measured with longest TA (8:44 min, see Table). In the exam with nominal voxels of 6x6x6 mm^3 the fraction of good Cho signals was least (Table).

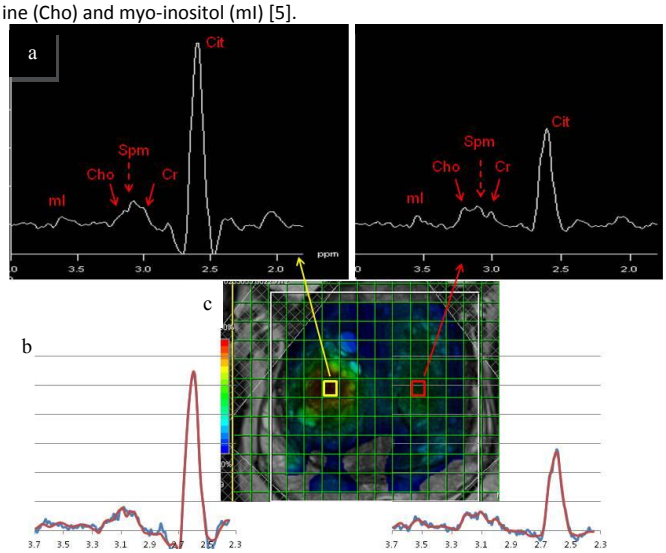

Figure. a) 3D MRSI spectra, acquired with the sLASER sequence with GOIA pulses, of a detection patient examination with body array coil only. The measurement time was 8:44. b) LCModel fitting for the two spectra . Fit is shown in red. c) Citrate map

	TR	Shim	Matrix Size	TA	Cho	Cit	Cre	Spm
1	740	21	14x10x12	8:11	15%	100%	87%	47%
2	630	22	12x14x11	8:44	69%	100%	92%	72%
3	630	21	12x10x10	4:50	59%	92%	50%	23%
4	630	25	12x10x10	4:50	38%	100%	67%	67%
5	820	22	12x10x10	6:45	77%	100%	80%	83%
6	900	28	12x10x10	6:55	76%	100%	73%	28%
7	900	33	12x10x10	6:55	48%	100%	68%	43%

Table. Percentages of voxels in which the fit of the metabolite signals of Cit, Cho, Cr, Spm reached a CRLB <30 %. The central 6x6 voxels of three slices within the prostate of the patients were taken for this analysis (voxel size for patient one is 6x6x6 mm^3 and7x7x7 mm^3 for the others)

Discussion: The GOIA-sLASER sequence without an ERC shows excellent performance as reflected by small lipid contamination, almost 100% voxel detection of Cit, which is due to its high SNR (favorable modulation of citrate spins with this sequence and TE [4]), and distinguishable signals for Cho, Spm, Cr and mI.
To detect PCa at least also the Cho signal is needed to calculate a relevant metabolite ratio. The current measurements indicate that voxels of 1.01 cm^3 with a TR of at least 900ms or an acquisition time of about 9 min are required for proper detection of Cho in the majority of voxels (at shorter TR there is more saturation of the Cho signal). This is comparable to GOIA-sLASER measurements with ERC, but with voxels of 0.64cm^3 (4). Shorter examination times down to about 5 min still may be of value in tumor detection, as the Cho signal is expected to increase. Compared to an endorectal coil, the phased array has the advantage of a more homogenous reception profile, enabling the reconstruction of single metabolite maps.
In conclusion, the GOIA-sLASER sequence allows robust ^{1}H MRSI examinations of the prostate in patients *without* an endorectal coil in a time acceptable for widespread clinical implementation.

References: [1] T.Scheenen et al., Invest. Radiol 2011;46(1):25-33; [2] Kobus et al. NMR Biomed 2104;27:39–52 [3] T.Scheenen et al., MRM 2005;53:1268–1274; [4] Steinseifer et al., Magn Reson Med 2014; [Epub ahead of print] [5] Provencher et al., Magn Reson Med 1993;30

Acknowledgments: This project received funding from the European Union's Seventh Program for research, Technological Development and Demonstration under Grant Agreement No ITN-GA-2013-316679 and ERC Grant agreement n° [243115].